Geochemistry of Phanerozoic carbonaceous black shales, sandstones and cherts in Malaysia: insights into gold source rock potential

By

Charles Makoundi
B.Sc. M.Sc. (UMNG), M.Sc. (UM), M.Sc. (UTAS)
GradCertRes (UTAS)

UNIVERSITY OF TASMANIA

A research thesis submitted in fulfillment of the requirements for the degree of Doctor of Philosophy

CODES

ARC Centre of Excellence in Ore Deposits
University of Tasmania

June 2016

ABSTRACT

The trace element geochemistry of marine black shales has been successfully used to interpret sediment provenance and deep ocean conditions during sedimentation. More recently, it has been proposed that certain pyritic black shales may act as sources of gold and arsenic for orogenic gold deposits. Four aspects of the geochemistry of the Phanerozoic black shales from the central gold belt/East Malaya terrane and the Sibumasu terrane in Malaysia are investigated in this thesis: 1) the whole rock major and trace element geochemistry of shales has been used to determine provenance and redox depositional conditions; 2) relationships of whole rock gold concentration to other elements in the shales has been used to assess the mechanism of gold transport and concentration; 3) textures and Laser Inductively Coupled Plasma Mass Spectrometry (LA ICP-MS) geochemistry of pyrite in the shales is employed to determine origin of the pyrite; sedimentary, metamorphic or hydrothermal; and 4) LA-ICP-MS gold content of the sedimentary pyrite is determined to assess the source rock potential of the shales to form orogenic deposits.

The oldest, organic-poor, grey shales of the Late Cambrian-Early Ordovician Machinchang Formation have a felsic provenance (Th/Sc>1; La/Th>2.8) and were deposited under oxic conditions as determined by the absence of framboidal pyrites. The Machinchang Formation shales display a good relationship among alumina (Al_2O_3) and Au, V, Cr, Ni, Co, Sn, and Sb implying that these trace elements were deposited attached to clay particles into the sedimentary basin.The shales have Au contents that range from 43 to 49 ppb (mean 46 ppb). LA ICP-MS gold content is present from 0.05 to 3.6 ppm

(0.6 ppm) within euhedral pyrite. The texture and composition (Ag/Au<1; As/Ni>10) suggests a hydrothermal origin for pyrite in Malaysia. A lack of visible sedimentary pyrite in the Machinchang Formation grey shales in Malaysia leaves a gap in the understanding of the Late Cambrian-Early Ordovician ocean chemistry in Malaysia. Consequently, trace metals in existing euhedral pyrites may have an epigenetic origin related to circulation of hydrothermal fluids and deposition of trace elements into pyrite after sedimentation. The hydrothermal activity is also evidenced by the occurrence of quartz veins containing euhedral pyrite grains.

The Early Ordovician-Silurian Setul Formation sandstones are very siliceous, alumina poor but organic carbon-rich. The negative europium anomaly and the ratio Th/Sc>1 suggest a felsic provenance. The sandstone gold content varies from 5 to 75 ppb (mean 26 ppb) and shows a strong positive relationship with alumina indicating gold content is clay-related. The geochemistry indicates a strong control of organic processes during deposition of trace metals due to a positive correlation between total organic carbon and V, U, Cr, Se, As, Zn and Ni.

The Pennsylvanian-Early Permian Singa Formation black shales from the Sibumasu terrane show a ratio of Th/Sc>1 indicative of felsic-intermediate provenance. Framboidal pyrites are bigger than 10 μm across with a consistent ratio of V/Cr<2 suggesting that they were deposited in an oxic marine environment. The black shales display a positive relationship between Al_2O_3 and the trace elements Ni, Cu, Zn, As, Sb and the organic carbon content is low (<0.5 wt %). The gold content in the shales ranges from 40 to 62 ppb (51 ppb) and correlates weakly with V supporting a possible control of organic processes during deposition of gold in the sediments. Gold content in sedimentary pyrite

ranges from 0.05 to 1.6 ppm (mean 0.3 ppm) and varies positively with As, Co, Ag, Sb, Te and Bi. The pyrites are enriched in Mn, Co, Ni, Cu, Zn, As, Cd, Sb, Te, Au, Pb, and Bi but depleted in Ag, Mo, and strongly depleted in Tl compared to Worldwide Diagenetic Pyrite (WDP, Gregory et al., 2015).

The Late Devonian BRSZ Unit 1 black shales have a Th/Sc ratio that ranges from 0.6 to 1, suggesting an intermediate provenance likely related to the East Malaya terrane granitoids as parent rocks. The shales contain framboidal pyrite commonly less than 10 µm implying deposition under anoxic to euxinic conditions. The gold concentrations in shale ranges from 4 to 39 ppb (mean 23 ppb). Whole rock trace elements such as V, Cr, Zn, As, Se, Mo, Sn, Sb, and U show a positive correlation with both alumina and organic carbon implying a sedimentary (clay) and organic matter control for these trace elements during their deposition into basin. Sedimentary pyrites of the BRSZ Unit 1 are enriched in Mn, Zn, Te, Au, and Pb and depleted in Co, As, Mo, Cd, Sb, Tl, and Bi relative to WDP. Gold content in sedimentary pyrite varies from 0.06 to 5 ppm (mean 1 ppm).

The Selinsing gold deposit is hosted by the Carboniferous-Permian Raub Group. Framboidal pyrites, proximal to the orebody, are enriched in Mn, Zn, and Au depleted in Ni, Cu, As, Se, Mo, Ag, Cd, Sb, Te, Bi and strongly depleted in Tl compared to WDP. The gold content in diagenetic pyrite varies from 0.03 to 0.84 ppm (mean 0.3 ppm). In the Middle Triassic Karak Formation, gold content ranges from 0.4 to 0.6 ppm (mean 0.5 ppm) in diagenetic pyrite whereas it ranges between 0.06 and 0.8 ppm (mean 0.2 ppm) in metamorphic pyrite. The good correlation of V with Au, Zn, Cd, and Sb in diagenetic pyrite suggests that these trace elements were all concentrated by organic processes.

The Middle Triassic Semantan Formation black shales have ratios of Th/Sc<1 indicating a mafic provenance. Framboidal pyrites are mostly less than 10 µm indicating deposition under anoxic to euxinic conditions. Both alumina and organic carbon contents vary positively with V, Cr, Mo, Sb, and U indicating these trace elements were introduced adsorbed onto clays or alumino-silicates and organic matter into the Semantan basin. Gold content in sedimentary pyrite varies between 0 and 4.6 ppm (mean 0.8 ppm) and changes positively with Se, Zn, and Cd. Compared to WDP, the Semantan pyrites are strongly enriched in Zn, moderately enriched in Cu, As, Se, Ag, Cd, Te, Au, and Bi but depleted in Mo, Sb, and Tl.

The Middle Triassic Gua Musang Formation black shales have a ratio of Th/Sc<1 implying an intermediate-mafic provenance. The shales contain framboidal pyrites which diameter is higher than 20 µm indicative of oxic-dysoxic conditions. Gold content in black shales varies from 3 to 51 ppb (mean 28 ppb). Al_2O_3 content shows a weak positive correlation with Au, Ni, Cr, and Sn suggesting that Au, Ni, Cr and Sn may have been introduced into sediments attached to clay minerals or contained in the aluminosilicate mineral structure. The gold content of framboidal pyrite varies from 0.2 to 1.8 ppm (mean 0.8 ppm) whereas in metamorphic pyrite, it is between 0 to 0.1 ppm (mean 0.02 ppm). Compared to WDP, the Gua Musang framboidal pyrites are enriched in Au, Te, and midly in Ag, and depleted in Co, As, Mo, Sb, Tl, Pb, and Bi. The Late Triassic BRSZ Unit 2 cherts that crop out in the vicinity of the BRSZ have elevated contents of SiO_2, S, Cu, Mo, and U and depleted in other major elements including Cr, Zn, Ga, and Th compared to PAAS. Framboidal pyrites are enriched in Au, Zn, Cd, Sb and depleted in Ni, Cu, Te and strongly depleted in Bi, Tl, Pb, Mo, Co relative to WDP.

Through time, there are two peaks of Au, Se, Cd, Tl contents in sedimentary pyrite that have been revealed by the study in black shales from Malaysia. A peak in the period from 207 to 237 Ma in sediments of East Malaya terrane (e.g. Gua Musang and Semantan formations) when the seawater conditions were dysoxic to euxinic across the Central Gold Belt. Additionally, a peak of Au, Se, Cd, Tl concentrations at 368 Ma has been found in sedimentary rocks of intermediate provenance (e.g. the BRSZ Unit 1) when the redox depositional conditions were dominantly anoxic to euxinic. The highest gold contents which vary from 0.01 to 5 ppm were measured from sediments that deposited under anoxic-euxinic depositional conditions. Overall, both in the Central Gold Belt and the Northwest Domain in Langkawi Islands, gold content in sedimentary pyrite correlates strongly with V, U, and Se suggesting a strong control of organic processes on Au introduction into sedimentary pyrite.

There is considerable variation in the Pb isotopic composition of the sedimentary pyrite across the region. Machinchang and Semantan formation pyrites tend to be less radiogenic than the BRSZ Unit 1 pyrite. Partial variation in each sample is related to the in situ decay of U and Th but the remainder relates to initial isotopic differences during crystallization of pyrite. The Singa Formation contains pyrites with two different compositions: one is similar to the pyrite found in the Machinchang and Semantan formations but slightly lower in $^{207}Pb/^{204}Pb$, and the other is much more radiogenic than the BRSZ Unit 1 pyrite. The Pb isotope model age of sedimentary rock-hosted gold-bearing pyrite do not coincide with the age of tuffs which is 233 Ma in the southern part of the Central Gold Belt indicating no link between gold mineralisation in the Semantan Formation and volcanism. Gold-bearing ore pyrites from the Selinsing and Tersang gold

deposits have isotopic composition indicating Pb model age around 250 ± 50 Ma. This age may be interpreted as the age of gold mineralisation in the district. The S isotope data from sedimentary pyrites ranges from -32.1 ‰ to 6.2 ‰ (mean -12.4 ‰) and show a broadly parallel trend to the seawater sulphate curve suggesting that sulphur originated from reduction of seawater sulphate.

This study has clearly demonstrated that diagenetic pyrites from black shales located far from gold deposits are enriched in gold. The gold content of all sedimentary pyrites ranges from 0.01 to 5 ppm (mean 1 ppm). The mean value of 1 ppm (1000 ppb) is far above the value of 250 ppb documented by Large et al. (2011) in diagenetic pyrite indicative of carbonaceous shale source rocks with the potential to produce economic gold deposits. Sedimentary pyrites are enriched in both Au and As, whereas igneous rock-hosted pyrites sampled in this study are commonly depleted in Au and As. Geochemically, Au and As are the two key elements in the local gold deposits thus the sedimentary pyrites hosted in black shales are the likely gold and As sources in the district. Commonly, gold and other trace elements are remobilised from sedimentary pyrites during recrystallization by metamorphic-hydrothermal fluids (Large et al., 2009). The trace metals are dissolved in the fluids and precipitate elsewhere.

Statistically, the Middle Triassic Gua Musang has gold contents greater than 250 ppb. The Laser mass spectrometry analyses suggest that this gold is dissolved in the pyrite lattice and not in the form of gold inclusions. Similarly, the Late Devonian BRSZ Unit 1 and the Middle Triassic Karak formations also have 100 % of invisible content in pyrite above 250 ppb.

These three formations are thus concluded to be the best gold source rocks in the province. Additionally, the Singa Formation has 59 % of invisible gold in pyrite over 250 ppb. In contrast, the igneous rock-hosted pyrite has 11 % of invisible gold above 250 ppb, making them unlikely gold source rocks in the district. Currently, exploration activities are focused on the Carboniferous (319-337 Ma) and Permian (259-264 Ma) host rocks as documented in Makoundi (2012). To maximize the possibility of further discovery, gold exploration should be extended to new stratigraphic horizons of Pennsylvanian-Early Permian, Late Devonian and Middle Triassic ages which contain elevated Se and Au contents in sedimentary pyrite.

Declaration of Originality

"This thesis contains no material which has been accepted for a degree or diploma by the University or any other institution, except by way of background information and duly acknowledged in the thesis, and to the best of my knowledge and belief no material previously published or written by another person except where due acknowledgement is made in the text of the thesis, nor does the thesis contain any material that infringes copyright."

Signed

Charles Makoundi
B.Sc. M.Sc. (UMNG), M.Sc. (UM), M.Sc. (UTAS)
GradCertRes (UTAS)
(June, 2016)

Authority of access

This thesis may be made available for loan and limited copying and communication in accordance with the Copyright Act 1968.

Signed

Charles Makoundi
B.Sc. M.Sc. (UMNG), M.Sc. (UM), M.Sc. (UTAS)
GradCertRes (UTAS)
(June, 2016)

TABLE OF CONTENTS

CHAPTER 1: INTRODUCTION

CHAPTER 2: REGIONAL GEOLOGICAL SETTING, GEOLOGY OF THE FORMATION SAMPLES AND U-Pb ZIRCON DATING

CHAPTER 3: PALAEOZOIC FORMATIONS

CHAPTER 4: MESOZOIC FORMATIONS

CHAPTER 5: RARE EARH ELEMENT (REE), PROVENANCE, TECTONIC SETTING AND PALEOREDOX CONDITIONS

CHAPTER 6: RADIOGENIC AND STABLE ISOTOPES OF LEAD, SULPHUR AND ORGANIC CARBON

CHAPTER 7: DISCUSSION AND CONCLUSIONS

LIST OF FIGURES

Chapter I

Chapter II

Chapter III

Chapter IV

Chapter V

Chapter VI

Chapter VII

LIST OF TABLES

Chapter I

Chapter II

Chapter III

Chapter IV

Chapter V

Chapter VI

Chapter VII

ACKNOWLEDGMENTS

Many thanks go to my supervisor Prof. R.R. Large who for his constructive criticism contributed enormously to the writing and completion of this thesis. Countless thanks also go to my co-supervisor Prof. Khin Zaw, who initiated and motivated me to start this PhD research project and has also been instrumental in the completion of this thesis. I also strongly thank him for his advice and in-depth comments related to this study. I am indebted to Dr. Sebastien Meffre who provided assistance in Pb isotope analysis on pyrite and K-feldspar and his review of the sulphur, lead and carbon isotope chapter. Mrs. Christine Cook at the Central Science Laboratory is thanked for the sulphur isotope conventional analysis and organic carbon isotope determination.

I also thank Peter and Katie McGoldrick for their help on XRF analysis and total organic carbon determination. This study received financial and logistic support from the Langkawi Environmental Institute (LESTARI) and Universiti Kebangsaan Malaysia, (UKM), CODES Scholarships and Ore Deposits of SE Asia" Project as well as the Trace Element in the Ocean (TEO) project. Many thanks go to Prof. Shafeea Leman and Associate Prof. Kamal Roslan from Universiti Kebangsaan Malaysia (UKM) for their assistance during field work in Malaysia. Over my PhD candidature at CODES, some colleagues have been a source of psychological support and inspiration such as Jeff Steadman, Dan Gregory, Jing cheng, and Indrani Mukerje, Sean Johnson, Nathan Steeves to name a few. Many thanks also go to the administrative and technical staff of CODES, University of Tasmania such as Ian Little, Sarah Gilbert, Isabella von Lichtan (Izzy), June Pongratz, Jane Higgins, Steve Calladine, Debora Macklin, and Elena Lounejeva for

their multiform help. A tribute goes to my late father and mother who left me too early. May their souls rest in peace!

Above all, this thesis is dedicated to the glory of God as it is known that the steps of a good man are ordered by the Lord (Psalm 37:23). This thesis is a jewel to my lovely wife who endlessly goes along with me through the odds and happiness sustained by a joyful love.

CHAPTER 1
INTRODUCTION

1.1. Foreword

Clastic sedimentary rocks such as black shales are important hosts for a range of trace elements, including Zn, Pb, Cu, Mo, Se, V, U, Ni, As, Ag, Cr, and Au (Pašava et al., 1993; Rimmer, 2004; Tribovillard et al., 2006; Pi et al., 2013). The trace element (TE) enrichment in shales has significance for two reasons: 1) economic significance when the concentrations of particular elements are abnormally high; and 2) they can be used to interpret seafloor redox conditions and trace element concentration in the palaeo-ocean (Hatch and Leventhal, 1992; Riquier et al., 2005; Large et al., 2014). Recent research has emphasized the source rock potential of particular black shales for gold ore deposits (Pitcairn et al., 2006; Large et al., 2009, 2011; Tomkins, 2013). This study is focussed on black shale sequences that occur in Phanerozoic continental margin basins throughout the Sibumasu and East Malaya Terranes of Malaysia. These terranes were selected because of (1) the presence of a large number of black shale-bearing formations; (2) the occurrence of gold deposits associated with some black shale; and (3) the presence of granites which may be an alternative source rock for the gold deposits.

1.2. Research aims

The major objective of this PhD research is to establish the lithological and geochemical characteristics of Phanerozoic black shales and associated sandstones and cherts in Malaysia and determine if there exists a relationship to gold mineralisation in the district. The main objective can be divided into six aims as follows:

1) To document lithostratigraphy of the selected Phanerozoic black shale-bearing sedimentary sequences.

2) To determine the maximum depositional age of the selected sedimentary units and the crystallisation age of S-type granites intruded into the sedimentary units.

3) To measure and interpret the major and trace element compositions, including rare earth elements, of the selected Phanerozoic sedimentary sequences.

4) To determine the composition of sedimentary pyrite contained in black shales and volcaniclastic rocks in order to evaluate the contemporaneous ocean chemistry and gold source rock potential of the shales.

5) To investigate timing relationships of gold mineralisation using the lead isotope composition of ore related pyrites.

6) To suggest the likely sources of gold, major controls on gold deposition, and implications on gold exploration in the district.

In order to achieve these aims, 129 sedimentary rock samples were collected in the field of which 88 fresh or unweathered rock samples were analysed for major and trace element analyses including total organic carbon and rare earth elements (REE). In addition, 477 spot analyses were undertaken for sedimentary pyrite trace element chemistry. Moreover, for age determination, 381 zircon grains were analysed across all the formations. Additionally, 60 analyses were conducted on carbon and sulphur isotope compositions plus 178 spot analyses were undertaken on pyrite and K-feldspar to determine their lead isotope composition.

1.3. Previous work and research significance

This section summarizes the research questions and identifies knowledge gaps in relation to the research work. This study attempts to resolve a long-standing debate as to whether the sedimentary rocks or the granitoids in the Sibumasu and East Malaya Terranes are the likely source of gold for sediment-hosted orogenic gold deposits such as the Selinsing gold deposit, the Penjom gold deposit, the Tersang gold deposit, and the Bukit-Koman gold deposit in Central Malaysia. A sedimentary source of gold relates to Au enrichment in diagenetic pyrites coupled with sedimentary sulphur signature from stable isotope determination. Gold content in diagenetic pyrites should vary positively with Mn, Ag, V, Mo, and Ni contents. By contrast, a granite source commonly shows a magmatic sulphur isotope composition. And the Pb isotopic age of K-feldspar in granite should approximate the age of gold mineralisation at a given gold deposit in the district. Previous research works completed at the Selinsing, Tersang, Bukit-Koman and Penjom gold deposits concentrated on U-Pb zircon dating, mineral paragenesis, and fluid inclusion studies (Ng, 1986; Yeap, 1993; Kamar et al., 1994; Wan Fuad and Purwanto, 2002; Makoundi, 2012). However, there is little published research on the sedimentary host rocks, in particular their lithogeochemistry, chemical environment of deposition and potential to be the source of gold in the ore deposits.

Previous researchers had considered that gold mineralisation in the Central Belt is related to a granitic source (Scrivenor, 1928; Willbourn and Ingham, 1933; Richardson, 1939). Unfortunately, there is little evidence in relation to the timing, and geochemical fingerprinting of gold mineralisation in Central Malaysia. In addition, Yeap (1993, p.343) asserted that gold was probably sourced from the lower crust or mantle, based on the Pb isotope character of the Maran ore in Central Malaysia. Nevertheless, there is a lack of convincing arguments to support the type of granitoid (magnetite or ilmenite-series), which relates to the source of gold in the district.

Goh et al. (2005) claimed that the main factors that controlled the input of gold were sedimentary and metasedimentary rocks, heating and depositional structures; however, little evidence was given on the source rock characteristics that controlled the emplacement and formation of gold mineralisation in the district. Again, Goh et al. (2005) reported that the granitoids generated heat that induced hydrothermal fluids to circulate through the volcanic-sedimentary rocks. Generally, recent geochemical studies have shown that some black shales contain anomalous levels of gold and arsenic (Pitcairn et al., 2006; Large et al., 2010). It has been suggested that syngenetic gold in black shales within sedimentary basins is sourced by erosion of the hinterland, attached to detrital clay particles and transported as colloidal gold by high-volume river systems (Thomas et al., 2011; Bull and Large, 2014). These authors strongly argue that carbonaceous rocks are good gold source rocks in sedimentary sequences (Pitcairn et al., 2006; Tomkins, 2010; Large et al., 2011).

The majority of gold in the shales occurs in sedimentary pyrite (Pitcairn et al., 2006; Large et al. 2009) and is regarded as an early sedimentary stage of the pre-concentrated gold to form source rocks favourable for later orogenic gold formation (Large et al., 2010). A related question that is being addressed in this study is "did detrital clays and/or organic matter play a role as a metal carrier to sedimentary basins in Malaysia? If that is so, then it provides a link between the shales and ore deposits and has huge implications for the genesis of gold in the sediment-hosted, orogenic gold deposits which are found in the Central Gold Belt of Peninsular Malaysia. In previous research work, organic carbon concentrated gold into sediments. For instance, good correlation was found between total organic carbon and gold content from three carbonaceous gold-bearing formations of South China implying the role of organic carbon in concentrating gold into sediment (Hu Kai, 2000). Clay minerals are produced from the breakdown of pre-existing rocks and are transported together with trace metals and deposited in black shales. Trace elements (Zn, Pb, Cu, Mo, Se, V, U, Ni, As, Ag, Cr, and Au) are adsorbed

onto clays and deposited into basin during formation of black shales. In this thesis, the roles of clays and organic matter in transporting gold into sedimentary basins and deposition in black shales are investigated. Ore genesis studies at the Selinsing gold deposit in Malaysia (Makoundi, 2012; Makoundi et al., 2014) have yielded little data on whether granite-related fluids or sedimentary fluids contributed to the deposition of gold in the area.

Recent investigations at Selinsing concentrated on sulphur and lead isotopes attempting to resolve the source of metals, including gold. In this regard, the data suggest that sulphur was derived from a sedimentary local source and lead was sourced from the upper crust (Makoundi, 2012; Makoundi et al., 2014). These authors suggested a two-stage model of gold mineralisation at the Selinsing gold deposit in the Central Gold Belt. The early stage characterised by initial Au enrichment in organic-rich sediments and a late stage marked by remobilisation of Au and deposition in structural traps (Makoundi et al., 2014). At a larger scale, there was no evidence to indicate which types of sedimentary rocks are potential gold source rocks for the Malaysian mineral deposits. Answering this question is the ultimate aim of the current study.

1.4. Texture and chemistry of sedimentary and metamorphic-hydrothermal pyrites

Pyrite is the most abundant and ubiquitous sulphide mineral in the earth's crust, occurring in diverse geological settings as well as modern sedimentary basins (Mann et al., 1990; Berner et al., 2013). It is also a common sulphide mineral in numerous ore deposits and may host a great number of trace elements (Huston et al., 1995; Large et al., 2009). Pyrite is also present in many Phanerozoic marine sedimentary rocks, especially those formed in anoxic or euxinic basin settings (Milner, 1962; Vallentyne, 1963; Love and Amstutz, 1966, Greensmith et al., 1971). In previous metallogenetic studies, trace elements in pyrite were used as a genetic fingerprint (Loftus-Hills and Solomon, 1967; Bralia et al., 1979; Roberts, 1982; Huston et al.,

1995; Barton and Hallbauer, 1996; Raymond, 1996; Clark et al., 2004; Barker et al., 2009; Large et al., 2009; Ulrich et al., 2011). Recently, texture and chemistry of sedimentary pyrites have been studied in detail for a) determining the gold source-rock potential of black shales (Pitcairn et al., 2006; Large et al., 2009; Sack et al., 2014; Gregory et al., 2015) and b) tracking trace element variations in the ocean through time (Berner et al., 2013; Large et al., 2014).

Because of the emphasis on pyrite chemistry in this thesis, I will summarise previous research on the textures and chemistry of sedimentary pyrites (diagenetic or syngenetic) and how it may be used to solve particular geological issues relevant to this thesis study. Iron sulphides are ubiquitous throughout the geological record. Pyrite is the most commonly found sulphide mineral in a wide variety of rock types from deep sea to continental environments (e.g. Schieber, 2011; Agangi et al., 2013). Pyrite textures and chemical characteristics discussed in this Chapter serve as criteria for discriminating diagenetic/syngenetic pyrite from metamorphic-hydrothermal pyrite. Given the fact that pyrite texture and chemistry go hand in hand, several trace element ratios are also used to infer the origin of pyrite. Recent research has given insights on Co/Ni, Ag/Au ratios to discuss the origin of pyrite (Large et al., 2009; Large et al., 2011; Gregory et al., 2015). The terms diagenetic pyrite means pyrites formed in the mud during sedimentation whereas syngenetic pyrites are those formed in the water column. In contrary, epigenetic pyrites are those formed later during circulation of hydrothermal fluids either infilling fractures (e.g. vein pyrite) or overgrown on previous pyrites. Authigenic pyrites form in a sediment during or after deposition.

1.4.1. Pyrite texture and formation

Authigenic pyrite forms following the reaction between Fe and H_2S, which are produced by the reduction of dissolved sulphate (SO_4^{2-}) by bacteria that use organic matter as a reducing

agent and an energy supply (Berner, 1970, 1984). The amount of pyrite formed initially relies on the availability of these parameters in the sediment or sea water controlled by the seafloor redox conditions. Authigenic pyrites are found in marine sediments and they often have a framboidal textures (Fig. 1.1). The term framboid is derived from "framboise" the French for raspberry. The framboidal pyrites commonly settle from the water column and grow within the sediments after deposition, reflecting pore water composition, which in turn depends primarily on the sea water composition and contained organic component. Diagenetic pyrites extract heavy metals from the pore waters during growth (Huerta-Diaz and Morse, 1990). However, syngenetic pyrites are smaller (i.e. a few microns) generally enriched in As, Mo, and Sb and under euxinic conditions precipitates above the sediment seawater boundary directly from the seawater, thus reflecting a direct seawater composition (Large et al., 2014).

The geochemical variation in these sedimentary pyrites thus reflects changes in sea water composition. Previous research has also documented that sedimentary pyrite can form syngenetically if the chemocline lies above the sediment-water interface, or diagenetically if the chemocline lies at or below the sediment–water interface (Tribovillar, 2006). A chemocline is a cline caused by a strong, vertical chemistry gradient within a body of water. Syngenetic pyrite consists of fine-grained, euhedral crystals (<5 μm in diameter), whereas diagenetic pyrite is made up of larger (>10 μm in diameter), spherical framboids (Wilkin et al., 1996; Tribovillar, 2006). Raiswell (1982); and Coleman and Raiswell (1995) have argued that framboidal pyrite forms during the early stage of diagenesis, with euhedral pyrite forming later in burial as dissolved sulphide concentrations decreased. Iron-sulphide commonly precipitates from solutions oversaturated in its components (Morse et al., 1987; Schoonen and Barnes, 1991), but may also form by in-situ replacement of solid Fe-bearing mineral phases in contact with aqueous sulphur species (Canfield and Raiswell, 1991; Raiswell and Canfield, 2012). Laboratory observations indicate that framboidal pyrite does not form directly, but via a metastable

precursor Fe-sulphide phase (‘amorphous’ FeS, mackinawite and greigite) from iron-rich waters where, locally, sulphide production rates were high enough to reach supersaturation as for FeS (Morse et al., 1987; Schoonen and Barnes, 1991; Wilkin et al., 1996; Benning et al., 2000; Rickard and Luther, 2007; Taylor and Macquaker, 2011).

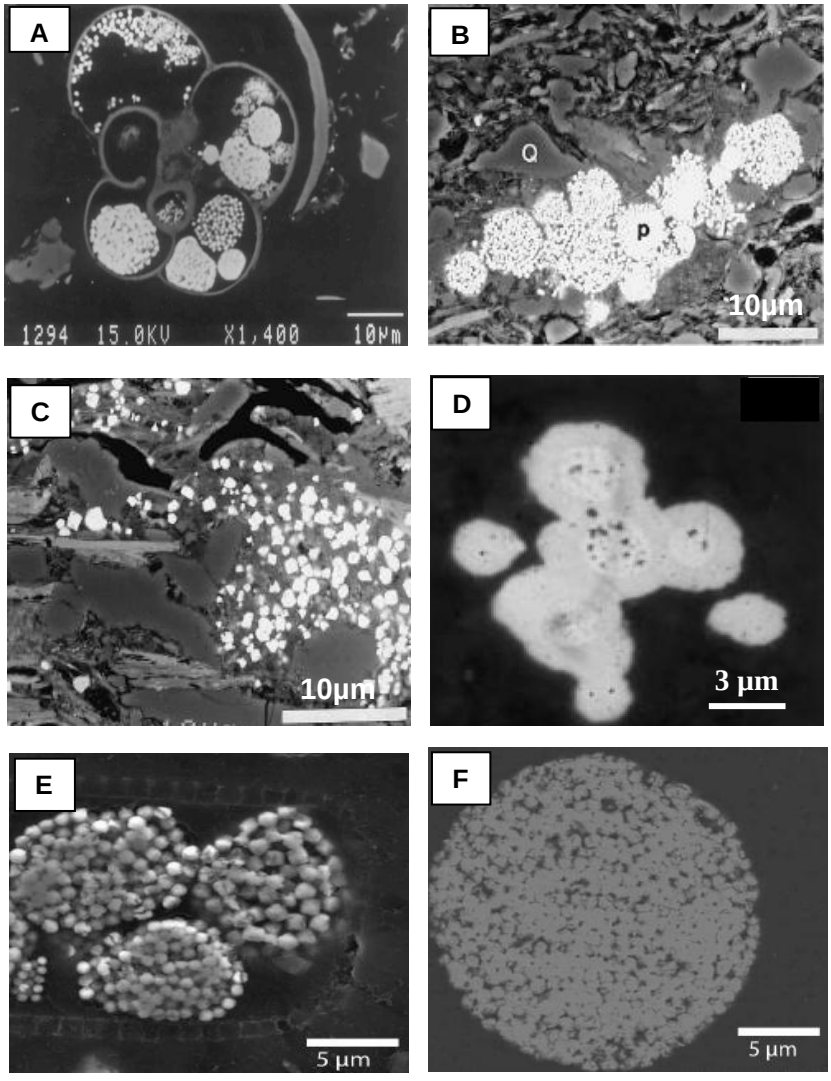

Fig. 1.1. Pyrite microtextures. **A**) Diagenetic framboidal pyrite with microcrystals <1µm surrounded by shells within sapropel (Passier et al., 1997). **B**) Cluster of framboidal pyrite in clay-rich mudstone in the sediments of Cleverland Ironstone Formation (Taylor and Macquaker, 2000). **C**) Syngenetic euhedral pyrite cluster in clay within mudstone in the sediments of Cleverland Ironstone Formation (Taylor and Macquaker, 2000). **D**) Pyrite framboids with overgrowths from the euxinic sediments of Green Lake (Suits and Wilkin, 1998). **E**) Cluster of diagenetic framboidal pyrite discovered from the Derwent Estuary sediments, Tasmania (Gregory et al., 2014). **F**) Aggregate of pyrite framboid from the Huon Estuary, Tasmania (Gregory et al., 2014).

The transformation of mackinawite to greigite was proposed experimentally as follows by Lennie et al., 1995: $12FeS + 2O_2 \longrightarrow 3Fe_3S_4$ (greigite) + Fe_3O_4 and $12FeS + 4H_2O \longrightarrow 3Fe_3S_4 + Fe_3O_4 + 4H_2$. The transformation of FeS to pyrite is controlled by the availability of an oxidant to produce sulphur species with intermediate oxidation states (Schoonen and Barnes, 1991; Neumann et al., 2005). Lennie et al. (1997) argued that the transition from greigite to pyrite (FeS_2) requires addition of S to greigite and reduction of Fe^{3+} to Fe^{2+} to form pyrite or marcasite. Raiswell and Canfield (2012) argued that available reactive iron minerals and reactive organic matter are essential during pyrite formation within the sediments. These two factors control the rate at which sulphide is produced by sulphate-reducing bacteria (Berner, 1970). Other experiments (Huerta-Diaz and Morse, 1992; Morse and Arakaki, 1993) have shown that a wide range of trace elements are incorporated into the precursor iron monosulphide (mackinawite or greigite) at an early stage, including As, Hg, Mo, Co, Cu, Mn, Ni, Cr, Pb, Zn and Cd, which are absorbed from seawater and local pore waters in seafloor muds (Large et al., 2007, 2009; Gregory et al., 2014). Work by Taylor and Macquaker (2000) shows that euhedral pyrite precipitates directly from pore waters oversaturated with respect to pyrite, but not Fe-monosulphides.

Recent research work has shown a wide range of pyrite textures, which have been discussed in terms of their origins and chemical characteristics (Guy et al., 2010; Thomas et al., 2011, Large et al., 2011; Pisarzowska et al., 2014). Guy et al. (2010) have documented three main types of pyrites including detrital, diagenetic, and epigenetic pyrites (Fig. 1.2). All captions in this Figure come from the work of Guy et al. (2010). Detrital pyrites (Fig. 1.2A) were found in conglomerate, sandstone, siltstone, wackestone and diamictite. They are inclusion free, compact non-porous and often show rounded cubes to well-rounded grains. The irregular microcrystal pyrite aggregates (Fig. 1.2B) are framboid-like and irregular. The framboid-like patches are 15 µm in diameter and contain cemented 0.5µm sized microcrystals.

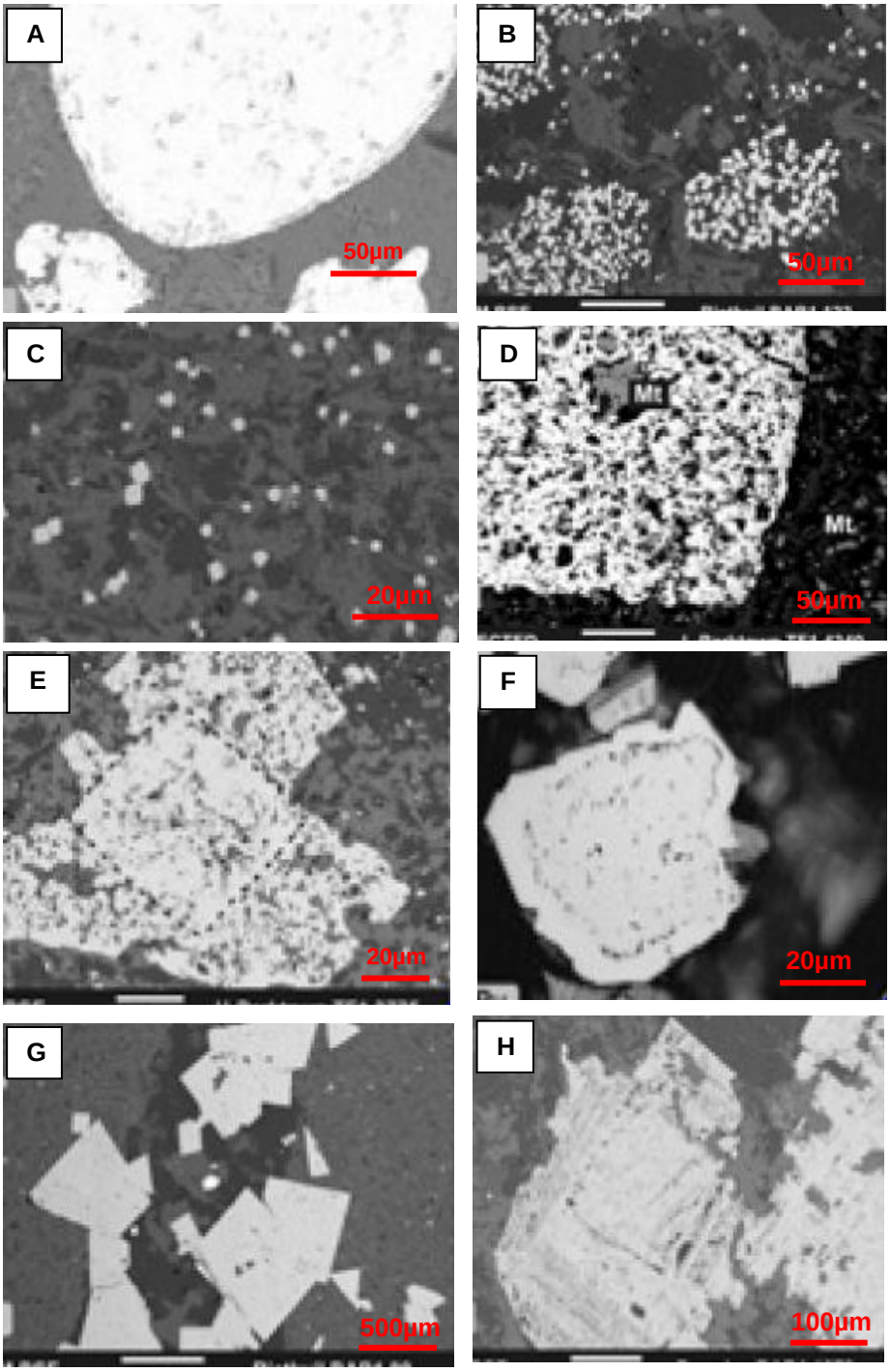

Fig. 1.2. Pyrite textures from the MESOARCHEAN Witwatersrand Supergroup, South Africa (Data and descriptions from Guy et al., 2010). **A**) Detrital pyrite. **B**) Diagenetic, microcrystal aggregates of pyrite. **C**) Diagenetic, small euhedral crystals in mudstone. **D**) Diagenetic, inclusion-rich euhedral pyrite. **E**) Inclusion-rich overgrowth in carbonate-oxide BIF. **F**) Inclusion-free overgrowth around a tiny pyrite nodule. **G**) Epigenetic, pyrite formed by biogenic replacement of quartz. **H**) Epigenetic pyrite consists of crystallographically aligned porous overgrowths.

These pyrite grains were found in carbonaceous shales. They are interpreted to be of diagenetic origin. The small euhedral crystals are of syngenetic origin (Fig. 1.2C). The euhedral to subhedral pyrite crystals (Fig. 1.2D) which are inclusion-rich were found in sandstone, siltstone, diamictite, and carbonaceous mudstone. They are interpreted to have formed at a later stage of diagenesis marked by migrating pore waters within permeable siltstone beds or laminae (Alonso-Azcarate et al., 1999). Pyrite overgrowths, inclusion-rich and inclusion-free (Figs. 1.2E-F) often form at a later stage of metamorphism and/or hydrothermal activity (Wagner and Boyce, 2006); however, these pyrite overgrowths were interpreted to have formed during diagenesis as they have been found in impermeable beds (e.g., mudstones). Epigenetic pyrite types which are documented herein are non-porous (or inclusion-free) and porous (Figs. 1.2G-H). These pyrite types are commonly found in sandstone and siltstone and they are larger than diagenetic pyrite with size ranging up to 500 μm or more in diameter. They contain crystallographically aligned pores indicative of fast growth and metamorphism (Ramdohr, 1958; Craig et al., 1998). Additionally, non-porous pyrite may reach similar sizes especially when they are in the form of veinlets, individual crystals or aggregates.

Some of the epigenetic pyrite crystals may occur near early diagenetic pyrite. These crystals were interpreted to represent remobilized/recrystallized early diagenetic pyrite (Wagner and Boyce, 2006). Pyrite overgrowths (Fig. 1.2H) were observed close to diagenetic pyrite. They were interpreted to be of epigenetic origin. Other pyrite types such as pyrite veinlets or replacive pyrite were all interpreted to be of epigenetic origin (Guy et al., 2010). Work by Thomas et al. (2011) adds to that of Guy et al. (2010) and presents textural characteristics of pyrite at Bendigo Gold Mine, Australia. Some key textures of diagenetic pyrites are fine acicular diagenetic pyrite hosted in black shales (Fig. 1.3A), and fine-grained pyrite nodules (Fig. 1.3B). Diagenetic pyrite cores (py1) followed by later diagenetic overgrowths (py2) which in turn is overgrown by euhedral metamorphic-hydrothermal pyrite (py3) (Fig. 1.3C). Metamorphic-hydrothermal

pyrites are often coarse grained euhedral with an outermost rim (Figs. 1.3D-E) and euhedral zoned in the overgrowth pyrite (Fig. 1.3F).

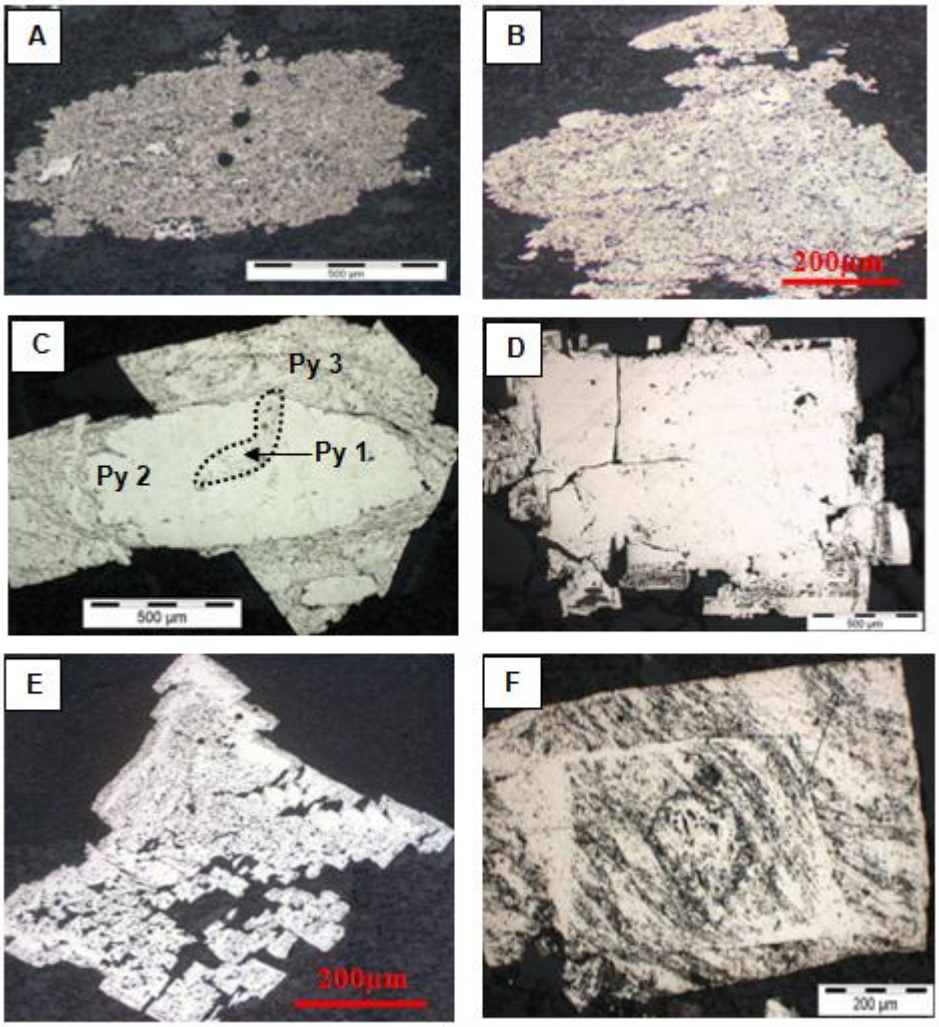

Fig. 1.3. Pyrite textures in sediments from the Bendigo Gold Mine, Australia (Data from Thomas et al., 2011). **A**) Fine acicular grained pyrite, diagenetic py1 after marcasite. **B**) Fine-grained diagenetic pyrite in shale. **C**) Early diagenetic core of py1, followed by a later diagenetic overgrowth nodule (py2), overgrown by euhedral metamorphic-hydrothermal py3. **D**) Coarse-grained euhedral metamorphic-hydrothermal py3, with an outermost rim. **E**) Coarse-grained euhedral metamorphic-hydrothermal pyrite aggregate overgrowing a silt-shale boundary. **F**) Zoned euhedral metamorphic-hydrothermal pyrite showing the metamorphic fabric of the shale preserved in the overgrowth pyrite; revealed by acid etch (Data and descriptions from Thomas et al., 2011).

1.4.2. Chemical characteristics of pyrite

Thomas et al. (2011) have shown that early diagenetic pyrites are characterized by a high Ag/Au ratio with elevated contents of Bi, Ni, Cu, Mo, Ag, Zn, Mn, V and Pb; however, late metamorphic-hydrothermal pyrites are usually zoned (Fig. 1.4) and having a lower Ag/Au ratio. Some images of sedimentary pyrites (Figs. 1.4 A-D) as they appear on a LA ICP-MS pyrite maps (Large et al., 2009). Large et al. (2009) have provided some textural and chemical criteria to distinguish diagenetic and metamorphic-hydrothermal pyrites based on their work on the sediment-hosted gold deposits including Bendigo in Victoria, Spanish Mountain in British Columbia, Sukhoi Log in Siberia, and northern Carlin Trend in Nevada (Tables 1.1 and 1.2).

Table 1.1. Textural and Chemical Criteria to help in the distinction between diagenetic and metamorphic-hydrothermal pyrites in Sediment-Hosted Gold Deposits (Data and descriptions from Large et al., 2009)

Criteria	Early diagenetic pyrite (Bendigo, Spanish Mountain, Sukhoi Log, and Carlin Trend0	Hydrothermal pyrite (Bendigo, Spanish Mountain, and Sukhoi Log)	Hydrothermal pyrite (Carlin Trend main stage)
Texture: Size and shape	Fine-grained (<5 μm), stratiform, clusters of microeuhedral crystals (50–150 μm), framboidal, sooty or microneedles (after marcasite); rounded shapes are common	Coarse-grained (0.5–50 mm), strata bound or crosscutting, euhedral with cubic shape, may be zoned	Fine-grained; rims (2–20 μm) on preexisting pyrite, cubic, or needle shapes, porous spongy aggregates
Texture: Internal	Abundant inclusions of sediment matrix material randomly oriented	Commonly clear, inclusion-free; etching with HNO_3 may reveal deformation fabric of sedimentary host rock replaced by pyrite	Abundant inclusions; etching with HNO_3 gives brownish coloration due to high As content
Composition of pyrite: General	Abundant trace elements; commonly, but not always, As, Ag, Ni, V, Pb, Mn, Zn, Cu, Mo, Se, Te	Low levels of most trace elements, except As, Co, Ni, Se	Enriched in As, Sb, Tl, Cu, Hg, Ag, Pb
Outermost pyrite rims	Rarely present	Two types of rims: Au-As–rich in high-grade ores; Co-Ni–rich in low-grade ores	High enrichment in Au and As
Silver	1 < Ag < 400 ppm	0.01 < Ag < 10 ppm	50 < Ag < 1,000 ppm
Vanadium	3 < V < 10,000 ppm	0.01 < V < 60 ppm	0.1 < V < 60 ppm
Nickel	100 ppm < Ni < 2 wt %	5 < Ni < 1,000 ppm	5 < Ni < 100 ppm
Zinc	2 < Zn < 5,000 ppm	0.1 < Zn < 20 ppm	0.1 < Zn < 30 ppm
Molybdenum	0.4 < Mo < 3,000 ppm	0.01 < Mo < 4 ppm	4 < Mo < 150 ppm
Selenium	2 < Se < 5,000 ppm	2 < Se < 140 ppm	4 < Se < 220 ppm
Manganese	1 < Mn < 3,000 ppm	0.1 < Mn < 50 ppm	0.5 < Mn < 60 ppm
Arsenic	400 < As < 7,000 ppm	60 ppm < As < 1.6 wt %	1 wt % < As < 10 wt %
Gold	0.01 < Au < 200 ppm	0.01 < Au < 30 ppm	50 < Au < 2,000 ppm

Table 1.2. Summary of Enriched Trace Elements (>100 ppm) in Major Pyrite Types at Sukhoi Log, Spanish Mountain, Bendigo, and Northern Carlin Trend (elements in order from maximum to minimum) (Data from Large et al., 2009)

Deposits	Trace elements enriched in diagenetic pyrite (>100 ppm)	Trace elements enriched in metamorphic and /or hydrothermal pyrite (>100 ppm)	Trace elements enriched in outermost pyrite rim (>100 ppm)
Sukhoi Log	As, Ni, Mn, Pb, Co, Ti, Cu, Zn	As, Ni, ±Co	Ni, ±Co
Spanish Mountain	As, Ni, Cu, Pb, Se, Ti	As, Ni, Se, ±Co	Ni, Co
Northern Carlin Trend	Cu, As, Ni, Se, V, Mo, Sb, Mn, Pb, Tl, Ag, Ti	As, Sb, Tl, Cu, ±Ag, Pb	As, Au, Cu, Sb, Tl, ±Pb, Ag
Bendigo	As, Ni, Pb, Co, Ti, Cu, Sb, Bi	As, Ni, ±Co, Pb, Sb	As, Pb, minor Au

A composite pyrite grain which contains a sedimentary core overgrown by later metamorphic-hydrothermal pyrite is shown in Figs. 1.4E-F.

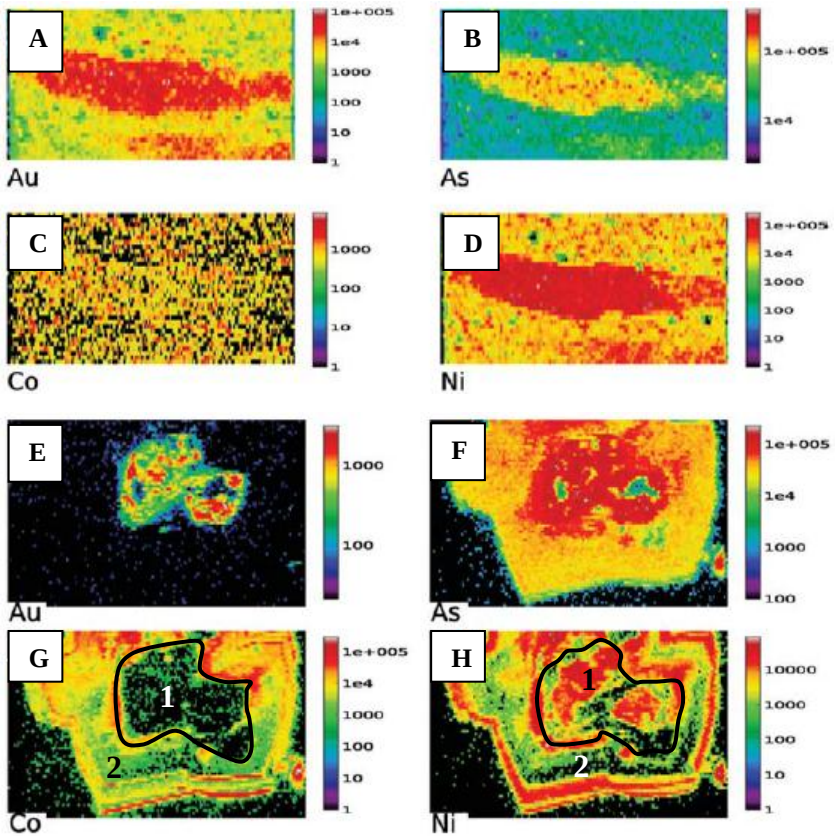

Fig. 1.4. LA ICP-MS images of sedimentary pyrite and metamorphic-hydrothermal pyrites (data from Large et al., 2009). Note zone 1 in Fig. 1.4G is for sedimentary pyrite whereas zone 2 is for metamorphic-hydrothermal pyrite in Fig. 1.4.H.

Some trace elements are preferentially enriched in either sedimentary or metamorphic-hydrothermal pyrite. The difference in chemistry also helps discriminate both pyrite types (Table

1.2). Makoundi (2012) has documented that coarse grained pyrite crystals that are zoned with low Ag/Au, and high Co/Ni ratios may likely be of metamorphic-hydrothermal origin. Additionally, Guy et al. (2012) have shown that early diagenetic pyrites display Co/Ni ratios ranging from 0.1 to 1.0 in carbonaceous mudstones and between 1.0 and 2.0 in diamictite and sandstone. However, other researchers found that early diagenetic pyrites are characterised by Co/Ni ratios around unity (Clark et al., 2004). In early diagenetic pyrite, there is covariance amongst Co, Ni, and As (Guy et al., 2010). These authors also argue that epigenetic pyrite is characterized by low trace element concentrations and steep positive correlation between Co and Ni. Volkov and Fomina (1974) reported that pyrite formed in silty clays (in the Black Sea) had greater Co/Ni ratios compared to that which formed in carbonaceous muds. These authors interpreted this as due to the mobility of cobalt and the likelihood of Ni to incorporate into authigenic silicates. Another possibility is that such variations may be due to the oxidation state of the diagenetic pore waters in the environment of pyrite formation (Scott et al., 2009). A particular example of Co-Ni and Ag-Au plots for sedimentary pyrite is shown below (Fig. 1.5). Recent research by Gregory et al. (2015) has developed new criteria adding to previous data. Overall, sedimentary pyrite is enriched in a suite of trace elements in the following order of abundance: As ≥ Ni > Pb ≥ Cu ≥ Co ≥ Mn > Sb ≥ Zn ≥ Se ≥ Mo > Ag ≥ Bi > Te ≥ Cd > Au. These authors defined the specific values and composition limits of sedimentary pyrite as follows: 0.01 < Co/Ni < 2, 0.01 < Cu/Ni < 10, 0.01 < Zn/Ni < 10, 0.1 < As/Ni< 10, Ag/Au > 2, 1 < Te/Au < 1000, Bi/Au > 1, Sb/Au > 100 and As/Au > 200.

The Au content of sedimentary pyrite (far from gold productive basins) has a mean of 160 ppb, with more than 67% of the data ranging from 10 ppb to 5000 ppb (Gregory et al., 2015). Elements such as Se, Ag, Sb, Mo and to a lesser extent As contribute to the sedimentary pyrite composition due to their higher proportions in the ocean at times of elevated global oxygenation. Other elements such as Mn and Cu in pyrite may have been transferred from the water column to

the sediment interface via the Mn (hydr)oxide complex. In this study, ratios such as Ag/Au, As/Au, and Te/Au combined with pyrite texture are used to determine the origin of pyrite.

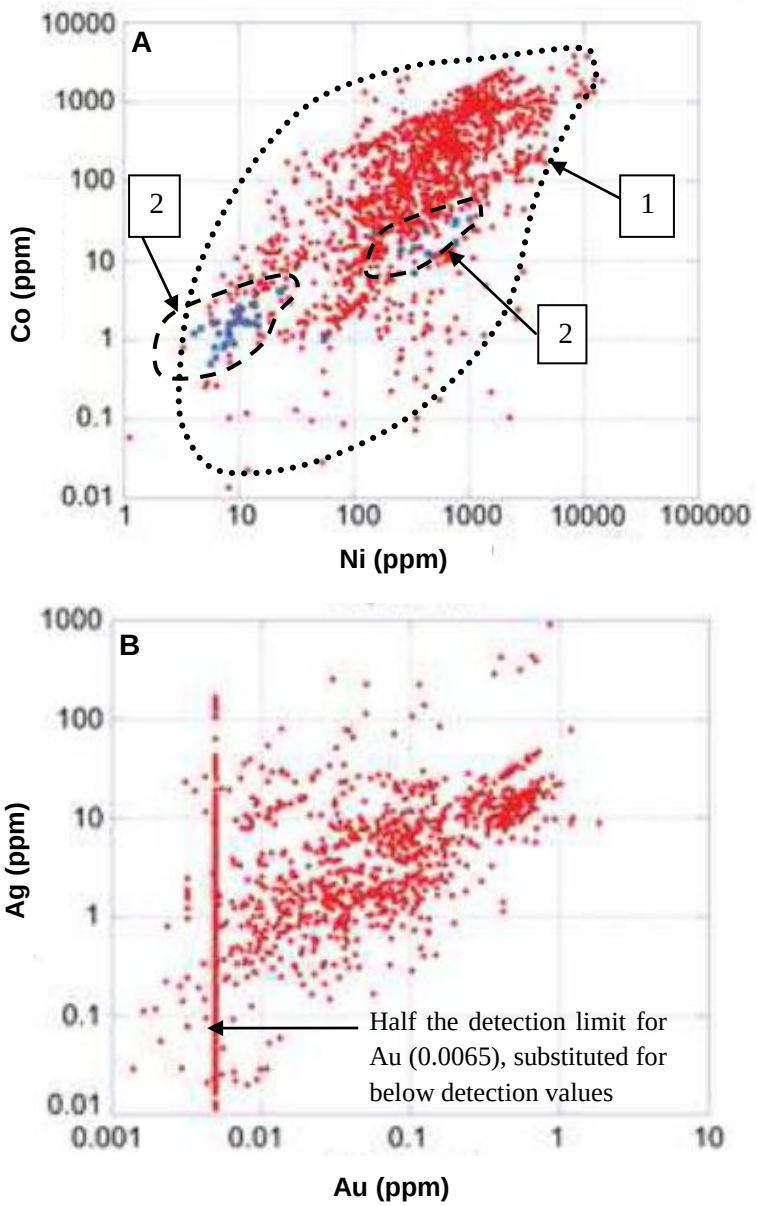

Fig. 1.5. Binary log-log plots showing relationships between **A**) Co and Ni; and **B**) Ag and Au for the sedimentary pyrites. Note: polygon 1 represents the sedimentary pyrites studied by Gregory et al. (2015). In addition, polygon 2 corresponds to the sedimentary pyrite field of Berner et al. (2013).

1.5. Methods of study

The methods of study include field work and sampling in Malaysia and laboratory work at Centre of Excellence in Ore Deposits (CODES), University of Tasmania. Field work includes describing and sampling the sedimentary rocks and granites, as well as drawing lithologic logs consistent with sample stratigraphic positions. The laboratory work includes the following analyses: (1) Whole rock geochemistry of sedimentary rocks to determine variation in trace elements; (2) Petrographic and textural studies to define different types of pyrites; (3) Laser Ablation Inductively Coupled Plasma Mass Spectrometer (LA ICP-MS) analysis of pyrite found in sedimentary rocks and granites to determine trace element distribution and zonation; (4) Laser stable isotope analysis of sulphur in pyrite and radiogenic isotope study of lead in pyrite, as well as isotopic carbon composition to discuss sources of organic matter, approximate age of formation, metal source, comparisons between formations; and (5) Total sulphur and total carbon determination to determine relationships between organic matter and gold concentration and accompanied metals in the Phanerozoic basins in Malaysia. Details of these methods are given in appendix A at the back of the thesis.

1.6. Thesis structure

This PhD thesis comprises seven chapters. Chapter 1 introduces the aims of the thesis, highlights the methods used, updates previous work and research significance, summarises common textures and chemistry of pyrite and presents the thesis organisation. Chapter 2 presents the regional geological setting, geology of the formations including description of outcrops, lithological and textural features of samples, and sedimentary logs. It also documents newly constrained U-Pb zircon ages. Chapter 3 documents the major and trace element compositions including total organic carbon and total sulphur for the Palaeozoic formations. It also presents

comparison with PAAS (Post-Archean Australian Shales; Taylor and McLennan, 1985). Chemical differences among the Palaeozoic formations are also investigated. Chapter 4 covers the major and trace element compositions including total organic carbon and total sulphur for the Mesozoic formations. It also includes comparison of formation sample compositions with PAAS (Post-Archean Australian Shales). Chapter 5 documents the Rare Earth Element (REE) composition of the studied formations. It also covers provenance and tectonic studies of selected formations including an interpretation of paleoredox conditions on the seafloor during the Phanerozoic in Malaysia. This Chapter combines results of lithogeochemical analyses of shales with redox conditions to discuss whether changes from oxic to anoxic/euxinic conditions in sea water affected the trace element compositions both in whole rocks and sedimentary pyrites. Relationships between provenance of sedimentary rocks and sedimentary pyrite trace element compositions are discussed. Chapter 6 presents the lead radiogenic isotope composition of pyrite, sulphur and carbon isotope compositions from selected Phanerozoic formations. The Pb isotope composition for the Selinsing and Tersang gold deposits are compared in detail with those from the sedimentary units. The age of mineralisation is also inferred from this study. Chapter 7 combines all lithogeochemical, zircon ages, pyrite trace element chemistry, and Pb isotope composition of the studied formations to characterise gold source rocks and discuss exploration implications. A new detailed chemostratigraphy of some sedimentary units is also documented. Chemical criteria for sedimentary pyrite of selected Phanerozoic formations (this study) combined with those from worldwide diagenetic pyrites are also presented in this Chapter. This chapter also proposes prospective stratigraphic horizons for gold exploration.

CHAPTER 2
REGIONAL GEOLOGICAL SETTING, GEOLOGY OF THE FORMATION SAMPLES AND U-Pb ZIRCON DATING

2.1. Introduction

This chapter covers regional geological setting and documents the lithological and textural features of selected formation samples including newly constrained U-Pb zircon ages. Southeast Asia has a wealth of mineral resources and comprises a number of terranes associated with accreted volcanic arc or back-arc basins (Khin Zaw et al., 2014). The boundaries, nature and shapes of the terranes have been a subject of hot scientific debates (Hutchison, 1977; Şengör, 1986; Metcalfe, 2011, 2013; Khin Zaw et al., 2014). The major terranes in Southeast Asia are South China, Indochina, Sibumasu, West Myanmar-Sumatra and Southwest (SW) Borneo Terranes (Fig. 2.1). The study areas include the Central Gold Belt in Malaysia and the Langkawi Islands as shown in Fig. 2.1.

2.2. Tectonic terranes in Southeast Asia

The Sibumasu (Siam, Burma, Malaysia, and Sumatra) and Indochina Terranes, in the north, are separated by the Inthanon Suture Zone and the Sukhothai Terrane, which are known to be an accretionary complex and a volcanic arc before the closure of the extinction of the Palaeo-Tethys Ocean and a volcanic arc respectively (Sone et al., 2008). The Changning-Menglian Suture Zone (CMSZ) divides the Sibumasu and the Sukhothai Terranes (Fig. 2.1). The Nan-Uttaradit-Sra Kaeo Suture zone separates the Sukhothai Fold Belt from Indochina. In Malaysia, the Sibumasu Terrane is separated from the Indochina/ East Malaya Terranes by the Bentong-Raub Suture Zone (BRSZ) (Barber and Crow, 2009; Metcalfe, 2013). The terranes moved away from the northwest Gondwana margin during the

Phanerozoic and resulted in the opening and closure of the Palaeo-, Meso- and Neotethyan (or Cenotethys) Oceans (Metcalfe, 2011).

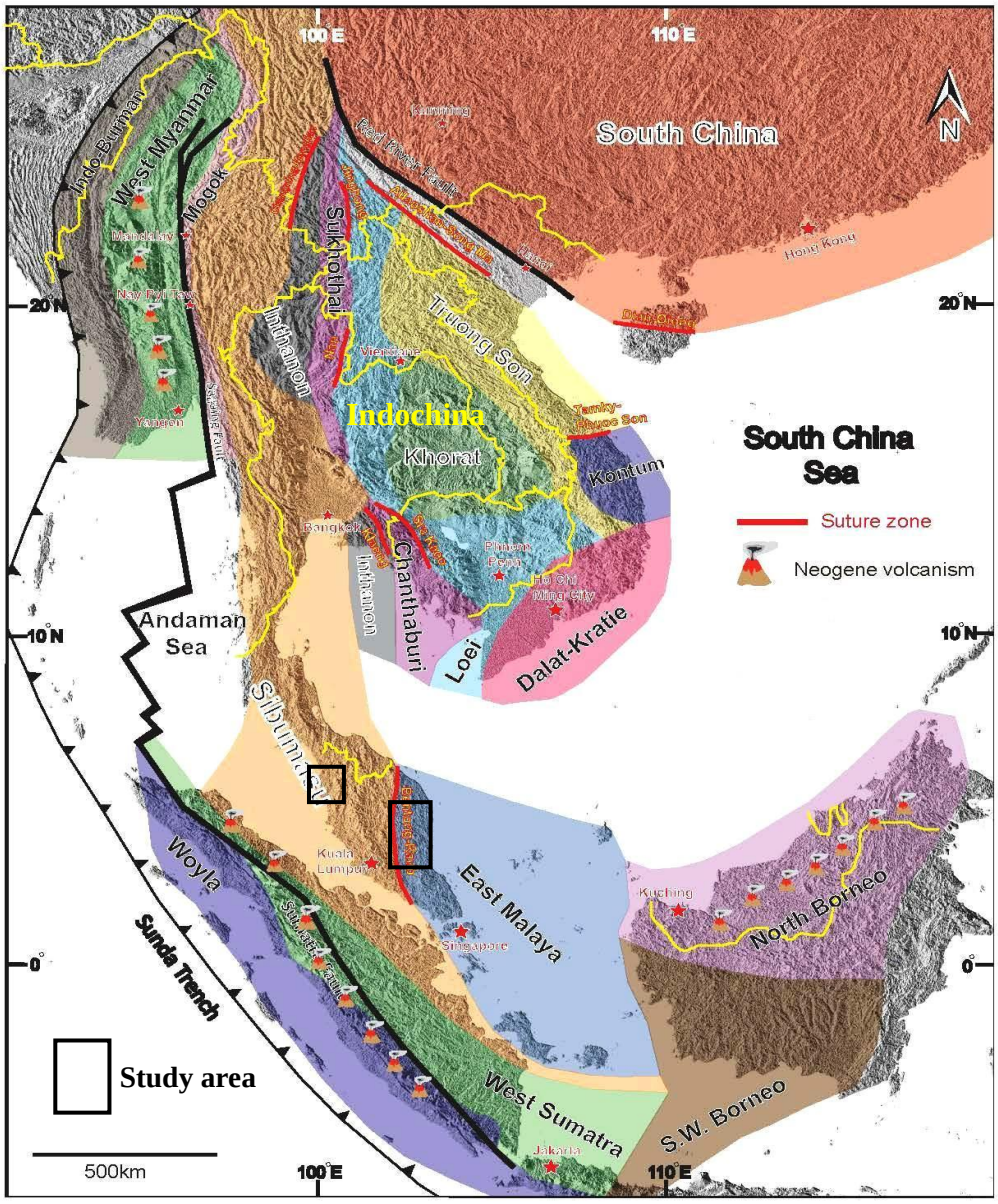

Fig. 2.1. Sketch map showing the main terranes in Southeast Asia (Khin Zaw et al., 2014) and the study area for this research. Terranes on this map include Indochina Terrane, Truong Son Fold Belt, Loei Fold Belt, Dalat-Kratie, Fold Belt, East Malaya Fold Belt, Sukhothai, Inthanon, Sibumasu, West Myanmar, and Sumatra.

2.2.1. Tectonic belts in Malaysia

In Malaysia, there are three NS trending tectonic belts (Fig. 2.2). Yeap (1993) characterized these terranes as the Western Belt, Central Gold Belt and Eastern Belt after Scrivenor (1928). The distribution of the selected study areas are delineated by the Semantan Formation, Karak Formation, Bentong-Raub Suture rocks (BRSZ Units 1 and 2), Gua Musang Formation, plus the ilmenite-series and magnetite-series granitoids (Fig. 2.2). Recently, the partition of Malaysia into three terranes was also invoked with the Sibumasu Terrane lying in the west and the Sukhothai Arc (East Malaya Fold Belt) in the east (Metcalfe, 2013). The NW domain which is part of the Sibumasu Terrane comprises the Langkawi Islands and other units such as the Kubang Pasu Formation (Figs. 2.1 and 2.2).

2.2.1.1. The Western Belt of Malaysia

This belt lies within the Sibumasu Terrane and contains Early Palaeozoic continental margin sequences, Late Palaeozoic platform carbonates, Triassic carbonates, deep water clastic sequences and Jurassic-Cretaceous continental deposits (Harbury et al., 1990; Uyop et al., 2007). This belt was derived from the NW Australian Gondwana margin in the Late Early Permian (Metcalfe, 2013). Quaternary sediments are present in coastline areas. The Western Belt is also associated with the tin-bearing Main Range Granitoid Province, a large plutonic belt that extends from Malaysia to the southern Peninsular Thailand and western Thailand. The other belts are the Central and Eastern Belts. The Eastern Belt is equivalent to the Sukhothai Arc, which was formed in the Late Carboniferous-Early Permian. This Arc was then separated from Indochina by back-arc spreading in the Permian (Metcalfe, 2013). This belt contains tin-bearing S-type granites of Triassic age.

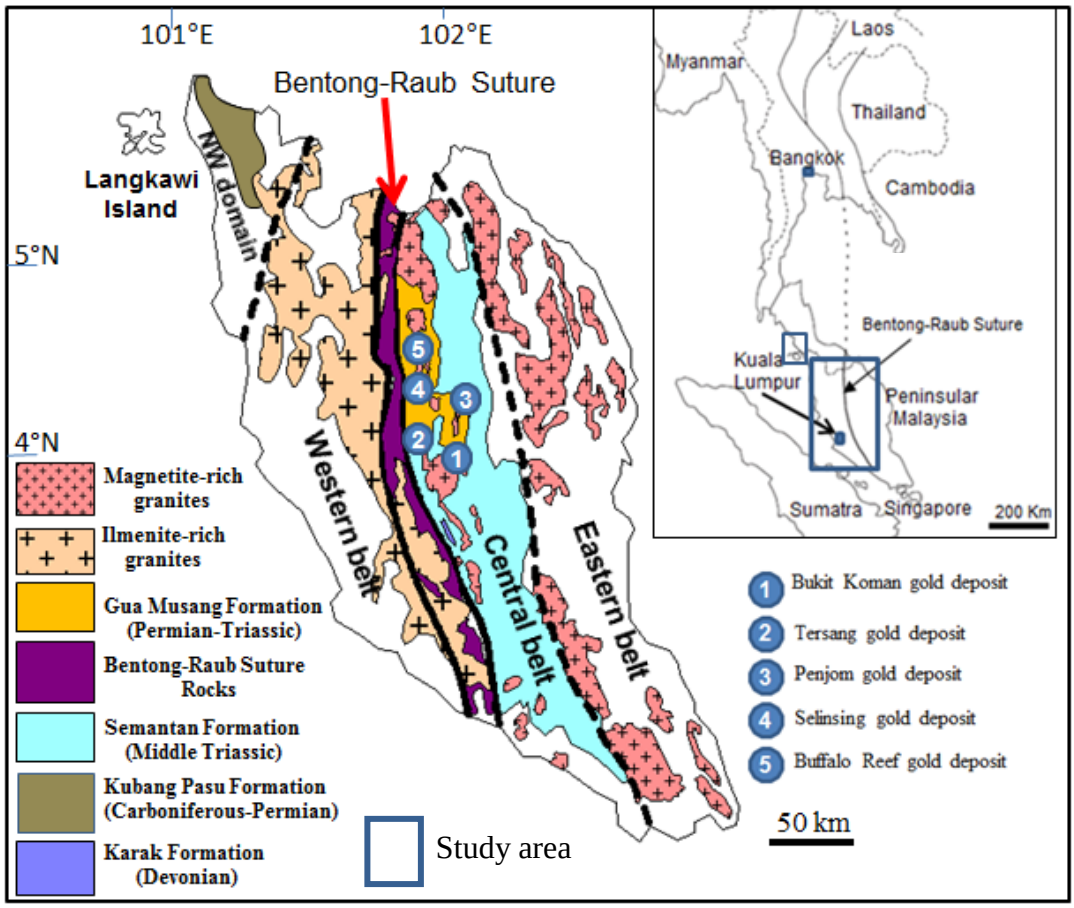

Fig. 2.2. Map of Malaysia showing distribution of Phanerozoic formations, magnetite and ilmenite-rich granites, the Bentong-Raub Suture Zone and the selected sediment-hosted gold deposits (modified after Cobbing et al., 1986).

The granites are also enriched in uranium and thorium. U-Pb zircon dating for the granites ranges from Late Triassic (230-9 Ma) to early Jurassic (207-14 Ma) with a peak around 210 Ma (Hutchison, 1989; Cobbing et al., 1992). In northwest, close to the boundary with Thailand, there is the Carboniferous-Permian Kubang Pasu Formation (Fig. 2.2), which contains black shale-bearing sequences. The Bentong-Raub Suture Zone that is shown in Fig. 2.2 resulted in the closure of the Palaeo-Tethys Ocean in Late Triassic (Oliver et al., 2014).

2.2.1.2. The Central Gold Belt of Malaysia

The Central Gold Belt is located to the east of the Bentong-Raub Suture Zone. It comprises Permo-Triassic metamorphic rocks, and deep to shallow marine sedimentary rocks (Kobayashi and Tamura, 1968; Makoundi, 2004). This belt also contains limestone with intermediate to felsic volcanic and volcaniclastic rocks, deposited in a fore-arc portion of the Palaeo-arc basin (Richardson, 1939; Gobbett and Hutchison, 1973; Leman, 1994; Metcalfe, 2002). The plutonic rocks in the Central Gold Belt have many similarities with those from the Eastern Belt (Cobbing et al., 1992). In the Central Gold Belt, particularly, the mapped zone in this study comprises plutonic units known as the Benom or the Benta alkali series. This series is composed of the Gunung Benom granite of calc-alkali affinities and the Benta intermediate to mafic rocks of alkalic type (Jaafar Ahmad, 1979). In this belt, granites yield Middle Triassic ages (Liew, 1983 and Darbyshire, 1988). The granites are mainly ilmenite series (S-type) with few exceptions of magnetite (I-type) series occurrences. Most magnetic susceptibility measurements (n= 100) which were determined during field work (this study) range from 0.01 to 44.4 x 10^{-3}SI. Only three measurements have values above 3.10^{-3}SI indicating an I-type series. The evidence strongly suggests predominance of S-type granites in the sampled areas. The Central Gold Belt is characterised by numerous occurrences of sediment-hosted gold deposits.

2.2.1.3. The Eastern Belt of Malaysia

This belt is part of the East Malaya Fold Belt made up of poly-deformed Late Palaeozoic sequences which are unconformably overlain by Late Permian continental conglomerate and Jurassic-Cretaceous continental deposits. In this belt, granitoids yield a compositional range from biotite granite to hornblende-biotite granite/granodiorite and diorite-gabbro (Schwartz et al., 1995). This belt also includes a suite of shoshonitic trachyte

in the Segamat area (Johor), dated by the K/Ar method to 62 Ma (Bignell and Snelling, 1977). Oliver et al. (2014) documented U-Pb ages for the granite and gabbro ranging from 238 to 285 Ma. In addition, the Eastern Belt plutons consist of biotite or hornblende-biotite-bearing I-type granitoids with Triassic Rb-Sr ages. The magnetite-rich granitoids are typical of modern-day Andean-type active margins where oceanic plates are subducted under continental margins or island arcs producing andesite volcanoes (Yeap, 1993).

2.2.1.4. Bentong-Raub Suture Zone (BRSZ)

The Bentong-Raub Suture Zone is a significant structure in Southeast Asia (Fig. 2.2). The suture is also suggested to be genetically related to the gold mineralisation in the central gold belt (Wan Fuad and Purwanto, 2002). According to Hutchison (1989), the Malay Peninsula underwent orogenic compression during the Triassic. The separation of East Malaya and Indochina from Gondwanaland gave rise to the Palaeo-Tethys Ocean that was closed in the Late Triassic (Oliver et al., 2014) producing the BRSZ. Some authors propose that this Triassic collision triggered the deformation of the Pre-Mesozoic strata and the intrusion of the Mesozoic S-type granitic plutons (Mitchell, 1981; Sengör, 1984; Hutchison, 1989). Other authors reported that the BRSZ of the Malay Peninsula represents the site of closure for the Palaeo-Tethys ocean basin forming the boundary between the Sibumasu Terrane in the west and the Sukhothai Arc in the east (Metcalfe, 2013; Khin Zaw et al., 2014). The suture extends up to 20 km in width and contains oceanic radiolarian cherts ranging in age from Devonian to Late Permian (Metcalfe, 2011). Within this suture, there are mélanges composed of clasts of ribbon-bedded chert, limestone, sandstone, conglomerate, blocks of turbidites, volcanic and volcaniclastic rocks. Additionally, it also contains bodies of serpentinite interpreted to be originally oceanic peridotites (Metcalfe, 2000). Chert and

limestone clasts in the mélange were dated by radiolarians, conodonts and foraminifera, and yielded Carboniferous and Permian ages (Metcalfe, 2000). The orogenic compression during the Triassic is called the Indosinian Orogeny. This orogeny occurred when the stitching of the Sibumasu Terrane with the East Malaya Fold Belt commenced in the Late Permian, evolved in the Early to Middle Triassic and ended in the Late Triassic (Metcalfe, 2011). Oliver et al. (2014) reported that the closure of the Palaeo-Tethys resulted in the formation of the Bentong-Raub Suture Zone in the Late Triassic (230-200 Ma).

2.3. Geology and stratigraphic framework of Langkawi Islands

Langkawi Islands are located in the NW domain (Fig. 2.3) and its geological setting is presented in Figure. 2.3. In this study, the Sibumasu and East Malaya Terranes (Fig. 2.1) are of interest as they contain black shale-bearing sequences. The formations selected in the Sibumasu Terrane on the Langkawi Islands are: (1) the Late Cambrian-Early Ordovician Machinchang Formation; (2) the Early Ordovician-Silurian Setul Formation; and (3) the Pennsylvanian-Early Permian Singa Formation. The geology of the island shows the main lithological units which comprise the Machinchang Formation, the Setul Formation, the Singa Formation, the Chuping Formation, and the intruding Triassic granites (Fig. 2.3). The oldest Palaeozoic sequence is the Machinchang Formation, which is located in the NW Domain in Langkawi Islands. The Machinchang Formation consists mainly of three Members. The oldest Hulur Member, which is a coarsening upward sequence that contains interbedded graded siltstone, grey shale, and clayey sandstone, is interpreted as having been deposited in a prodelta environment (Lee, 2006). The Chinchin Member (F5 sequence), which consists of a fining upward sequence of quartzose conglomerate and sandstone, was

deposited in upper shoreface to beach environment (Lee, 2006). Stratigraphy of the Phanerozoic formations in the Sibumasu Terrane in Langkawi is presented in Fig. 2.4.

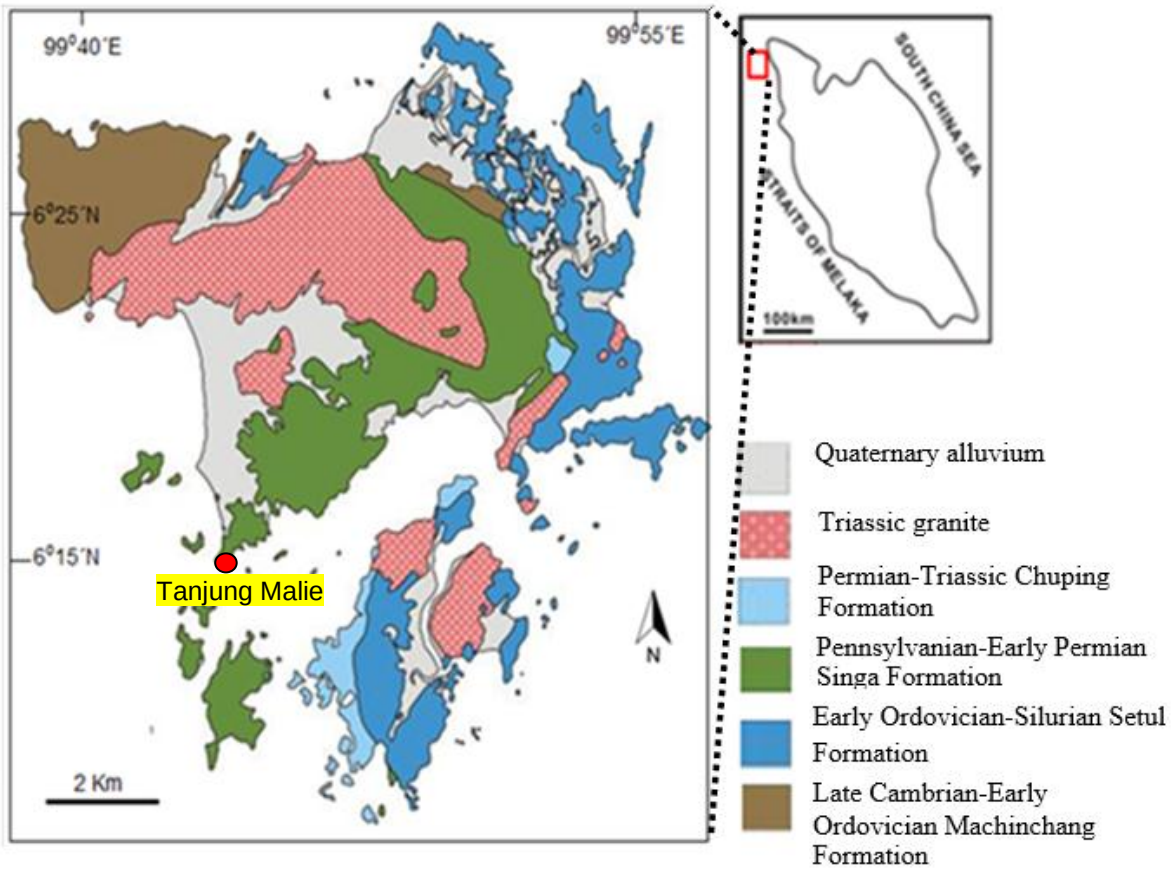

Fig. 2.3. Sketch map of the geological map of the Langkawi Islands, Malaysia (modified after Che et al., 2008).

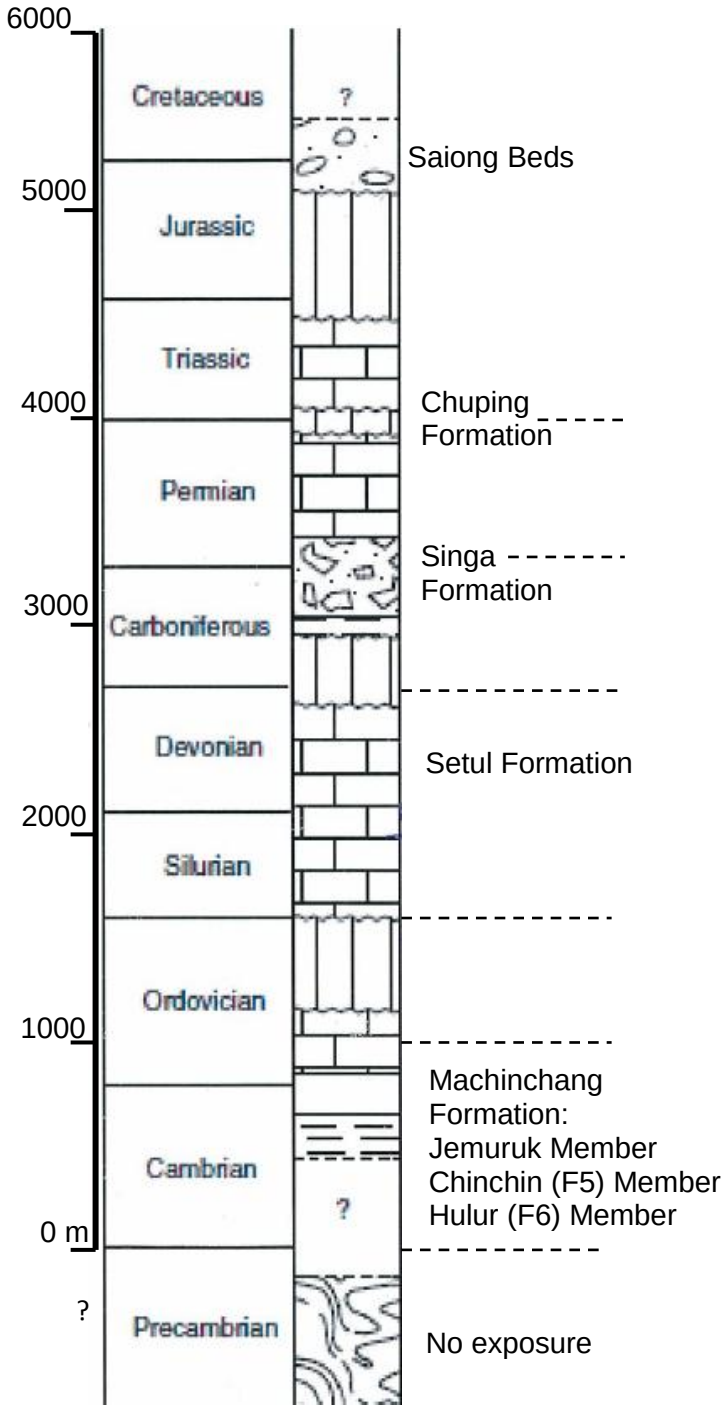

Fig. 2.4. Simplified chronostratigraphy of the Phanerozoic sedimentary sequences of Langkawi Islandss and the Northwest Domain (NWD), part of the Sibumasu Terrane (modified from Metcalfe, 2013). Note: Palaeozoic formation names in red colour are those selected in this study. Sketch not to stratigraphic scale. Note: Fm= Formation.

The youngest Jemuruk Member made up of fining upward succession of siltstone, shale, hummocky cross-bedded sandstone, and thin beds of limestone, accumulated in storm-derived shoreface to back barrier lagoon with tidal channel environment. In this thesis, the lowest Hulur Member sequence and Jemuruk Member were not sampled as a result of restriction to outcrops due to government regulations in private lands. Jones (1961) reported that the Early Ordovician-Silurian Setul Formation conformably overlies the Late Cambrian-Early Ordovician Machinchang Formation. The Setul Formation comprises two Members including the Lower Detrital Band (LDB) and the Upper Limestone Member that represent transgressive sediment input onto the shelf limestone (Lower Ordovician) during sedimentation (Jones, 1968; Cocks et al., 2005). Some researchers identified Lower Devonian graptolites and tentaculites in this formation (Cocks et al., 2005). Che et al. (2008) reported that the Setul Formation was deposited during Ordovician to Early Ordovician-Silurian time.

The Pennsylvanian-Early Permian Singa Formation comprises thin to poorly bedded alternating pebbly black mudstone, silty shale and lithic to quartz arenite. In Langkawi, Stauffer and Lee (1986) recognised six lithofacies as follows: (1) Laminated 0.5 to 2 m thick, well sorted, medium-grained clean sandstone facies with hummocky cross-bedding structures; (2) Interbedded sandstone and dark sandy mudstone showing flaser bedding and containing burrows; (3) Metric scale interbedded sand-mud facies displaying gentle deformation with scattered megaclasts of boulder size, which are found above the interbedded sandstone and dark sandy mudstone; (4) Sandy mudstone with graded sandstone facies and rare megaclasts; (5) Diamictite facies composed of clay and silt to big boulders with punctual burrows; and (6) Laminated sandstone-siltstone facies gently deformed with channel-like truncations with variety of megaclasts.

Previous work reported that the Singa Formation has been metamorphosed to hornfels due to its close proximity to the Raya granite of Langkawi (Foo, 1964). The megaclasts found in the Singa Formation have been interpreted to be of glacial origin (Stauffer and Lee, 1986). The Singa Formation is interpreted as having been deposited in glacial marine environment evidenced by the presence of matrix-located fresh feldspars, granitic clasts, angular limestone clasts, and brachiopods (Mohd Shafeea and Asmaniza, 2002). Che et al. (2008) reported that this formation may have been deposited in a shallow marine environment under the influence of polar glaciation and glacial melting. According to Che et al. (2008), the Singa Formation can be correlated to the Kubang Pasu Formation, which crops out in the northwestern domain of Malaysia.

The Permo-Triassic Chuping Formation crops out in the northwest of Malaysia. It contains fossils such as foraminifera, algae and conodonts. The limestone is "massive, light to dark grey in colour, fine-grained and poorly fossiliferous" (Fontaine et al., 1988). The fossils indicate an age between Ladinian and Carnian. Floral and foraminifera assemblages show strong similarity to the Alpine and European ones indicating a warm and shallow sea environment. The Jurassic-Cretaceous Saoing beds are continental sediments. The work of Khoo (1977) and Harbury et al (1990) documented the Jurassic-Cretaceous continental deposits in Peninsular Malaysia. The beds are conglomerate associated with sandstone, mudstone and shale (Ong, 1969). The conglomerate is polymictic and composed of quartz clasts, chert, sandstone, shale, quartzite and volcanic rocks in a sandy clay matrix. Clasts are aligned implying paleocurrent directions towards the east. Mudstone and shale contain plant fragments. Ong (1969) interpreted the Saiong beds as being a molasse facies deposited in a fluvial environment and correlated this unit with the Tembelling Group (Fig. 2.5).

2.4. Stratigraphy of the Central Gold Belt in Malaysia

The formations that were selected (Fig. 2.5) in the Central Gold Belt are: the Late Devonian BRSZ Unit 1; the Middle-Triassic Karak Formation; the Middle-Triassic Semantan Formation; the Middle-Triassic Gua Musang Formation, the Late Triassic BRSZ Unit 2, the Carnian-Norian Kerum Formation and the Cretaceous Tembelling Group. The Late Devonian BRSZ Unit 1 consists of interbedded carbonaceous black shale, sandstone and phyllite to the north underlain by layers of carbonaceous shales to the south along the Bentong-Raub road in the state of Pahang, Malaysia.

The Middle-Triassic Karak Formation (Fig. 2.5) was first described by Jaafar (1976) who reported occurrences of metamorphosed argillaceous sediments, which he attributed to the Bentong Group. Previous studies described this formation as 4800m of schists but this study shows that the schists and hornfels are interbedded with chert, quartzite, shale, phyllite, conglomerate, breccia and rhyolitic tuff. This formation was deposited in an open marine basin between the Sibumasu and Indochina terranes (Metcalfe, 2000). Current field observation shows that the Karak Formation is mostly made up of repetitive layers of siltstone and black shales. The black shales (up to 4 cm thick layers) contain wavy and flaser laminations. The siltstones show parallel laminations. The Middle Triassic Semantan Formation (Fig. 2.5) is part of the most extensive outcrop in the Central Gold Belt sedimentary basin that was named by Jaafar (1976). It is composed of carbonaceous shales interbedded with rhyolitic tuff of Triassic age. This formation was intruded by felsic and intermediate igneous rocks (Jaafar, 1980). Sedimentary rocks in close proximity to the igneous rocks are metamorphosed to hornfels.

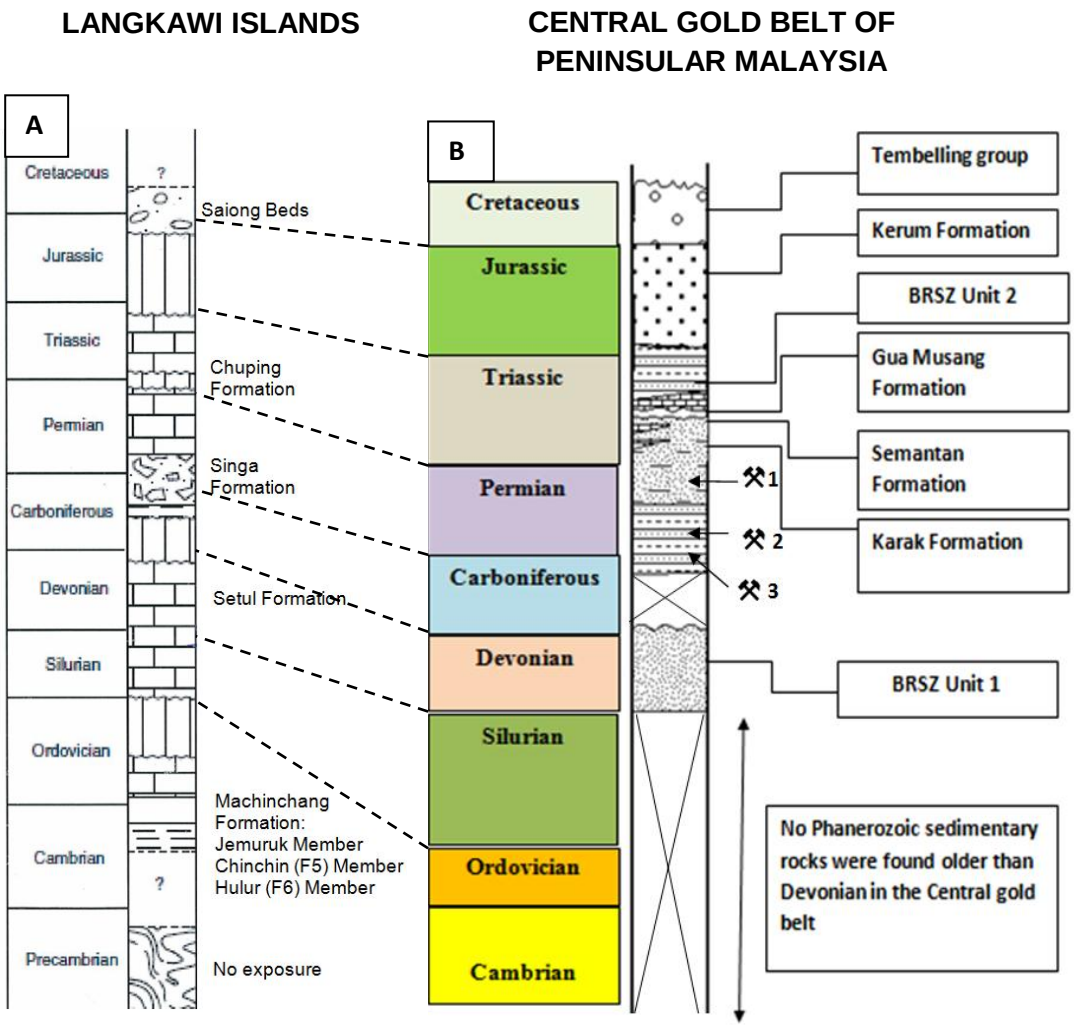

Fig. 2.5. Simplified chronostratigraphy of the Phanerozoic Formations in Malaysia. **A**) Chronostratigraphy of the Langkawi Islands as shown in Fig. 2.4. **B**) Chronostratigraphy of the Central Gold Belt, part of the East Malaya block, Malaysia (modified from Metcalfe, 2013). Note: the BRSZ Unit 1, Unit 2, Semantan, Karak, and Gua Musang are the selected formations in this study. Stratigraphic positions of the gold deposits are indicated by the mining logos (crossed hammers): 1) Penjom gold deposit (259-264 Ma); 2) Tersang gold deposit (261-333 Ma); 3) Selinsing gold deposit (324-246 Ma) (U-Pb zircon data from Makoundi, 2012). This sketch is drawn on a geological time scale.

The presence of shallow water bivalves indicates a neritic environment (Metcalfe, 1985). In the Semantan Formation, tuff beds contain cross or parallel laminations. Laminated mudstone beds are associated with fine tuffs and layers of mud pellets. Beds of pebbly mudstone were also documented by Mohd Shafeea and Sone (2001). A few species of bivalves were found by Jaafar (1976). Two fossil assemblages were found including Myophoria or shallow-water fauna, and the pelagic fauna characterised by the occurrence of Daonela, Halobia and Posidonia. The presence of *Daonela indica and Daonela Pahangensis* indicates a Ladinian age for the pelagic sediments (Khoo, 1988). Myphoria fauna is characterised by the occurrence of *Costatoria malayensis, Costatoria chegarperahensis and Neoschizodus ovutus* implying an Anisian to Early Ladinian age.

The Middle Triassic Gua Musang Formation (Fig. 2.5) crops out in the Central Gold Belt and belongs to the Raub Group. Most sediment-hosted orogenic gold deposits such as Selinsing, Buffalo Reef, Tersang and Penjom gold deposits are hosted within this formation. The Gua Musang Formation comprises two facies: Middle Permian to Triassic carbonate facies and Triassic argillaceous facies. Black shale units of Triassic age belonging to the Gua Musang Formation were reported in and around the town of Kuala Lipis in the Central Gold Belt (Makoundi, 2004). These black shales are also present within the host stratigraphy of a number of sediment-hosted gold deposits located in the eastern part of the Bentong-Raub Suture Zone (Makoundi, 2012; Makoundi et al., 2014). In addition, some bivalves such as *Costatoria sp.* and plant fragments were reported in shale sequences belonging to the Gua Musang Formation (Makoundi, 2004). In the work of Makoundi (2004), this formation was interpreted to have been deposited in deep-water marine environment. The Late Triassic BRSZ Unit 2 is made up of carbonaceous shale with interbedded chert. Small-scale folds

occur in this unit together with multiple quartz and pyrite veins. Some pyrite veins ranging from 2 to 3 mm thick cut across bedding.

Other thicker pyrite veins, with thickness between 1 and 1.5 cm, are concordant to bedding and rarely cutting the bedding. Underlying the Tembelling Group is the Jurassic to Cretaceous Kerum Formation (Fig. 2.5) composed of volcanic rocks, shale, siltstone, sandstone, and conglomeratic sandstone. The lower part of Kerum Formation is made up of a tuffaceous unit that resembles the Semantan Formation (Fig. 2.5).

The Cretaceous Tembelling Group (Fig. 2.5) comprises the Lower Cretaceous Termus shale, which is composed of mudstone, siltstone, shale, sandstone and breccia (Khoo, 1977). The sediments of the Tembelling Group are interpreted to be continental because of the presence of plant fossils, palynomorphs and fresh water bivalves. The presence of cross-bedding, cross-lamination and pebble imbrication indicates a subaqueous environment. Tectonically, a wider part of the eastern margin of the Tembeling basin is controlled by the NNW-SSE Lebir and the NW-SE Lepar fault zones suggesting local uplift that supplied sediments into the basin. Similarly, Mustaffa (2000a) suggested that dextral strike-slip faults may have led to the inversion of the Semantan Formation causing uplift and emplacement of intrusions such as the Upper Triassic granites, which were probably the source of the sediments.

2.5. Description of formation samples, logging, and newly constrained ages

2.5.1. Machinchang Formation (Late Cambrian-Early Ordovician)

The Late Cambrian-Early Ordovician shales crop out in the Machinchang Formation on the Island of Langkawi. In this thesis, the Machinchang Formation was selected. From

field observation, the sedimentary sequences are mapped as lower and upper sequences. The outcrop photographs of these sequences are shown below (Fig. 2.6).

The Cambrian lower F5 sequence is characterised by rhythmically interbedded grey shales (5-60 cm thick) and grey to brown fine-grained sandstones (3-120 cm thick) (Fig. 2.6A). The sandstones contain high-angle cross-bedding. The Ordovician upper F6 sequence also consists of sandstone beds which are interbedded with grey shales (Fig. 2.6B). The outcrops are exposed along the beach in Langkawi and their sedimentary log is displayed in Fig. 2.7 together with each rock sample in stratigraphic position.

Fig. 2.6. Outcrop photographs of the Machinchang Formation, Langkawi Islands, Malaysia. **A**) The F5 clastic sequence (as noted in Fig. 2.5A) which shows sandstone with cross-bedding facies and shale. **B**) The F6 clastic sequence that contains thick sandstone with low angle, cross-bedding structures interbedded with grey shales.

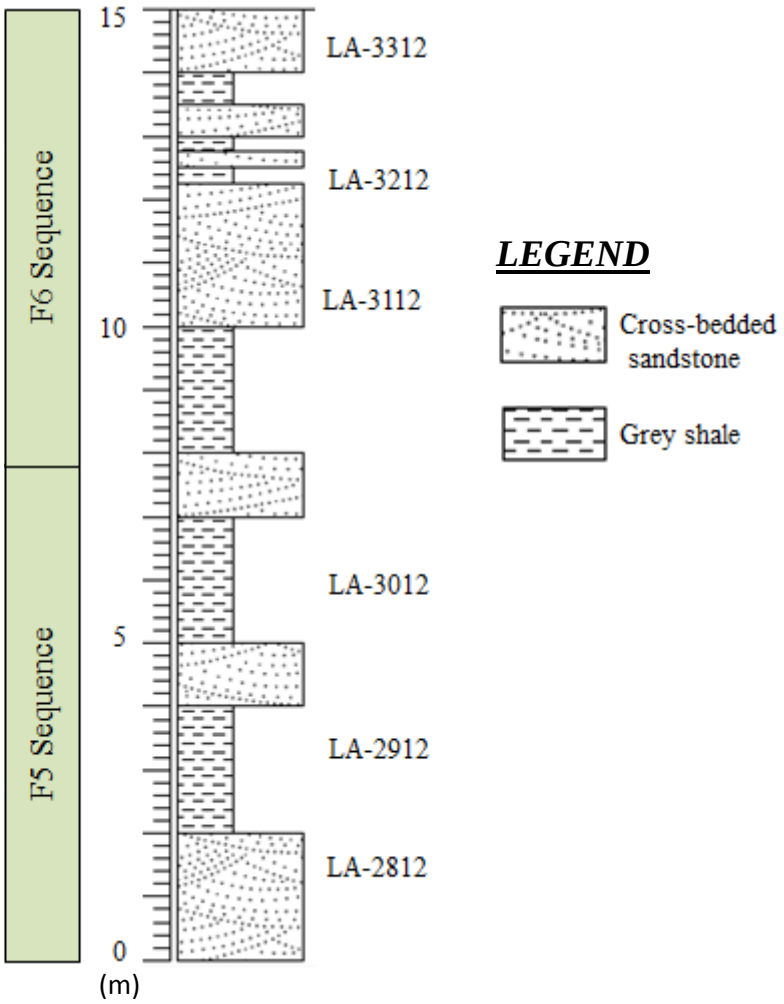

Fig. 2.7. Sedimentary log of the Machinchang Formation showing the stratigraphic position of the collected samples. Location: Langkawi Islands, Malaysia. Stratigraphic thickness is in meter. The transition from F5 to F6 sequence is not sharp; however, the F5 sequence shows low angle cross-bedding whereas the F6 sequence is characterised by high angle cross-bedding.

From the sedimentological evidence, the Machinchang Formation is interpreted as "the deposits of a highly destructive, wave-influenced delta and associated estuary and beach-ridge complex" (Lee, 1983; 2009). A number of collected samples were examined under the microscope. The textural and lithological characteristics of selected grey shale and sandstone samples are shown in Fig. 2.8.

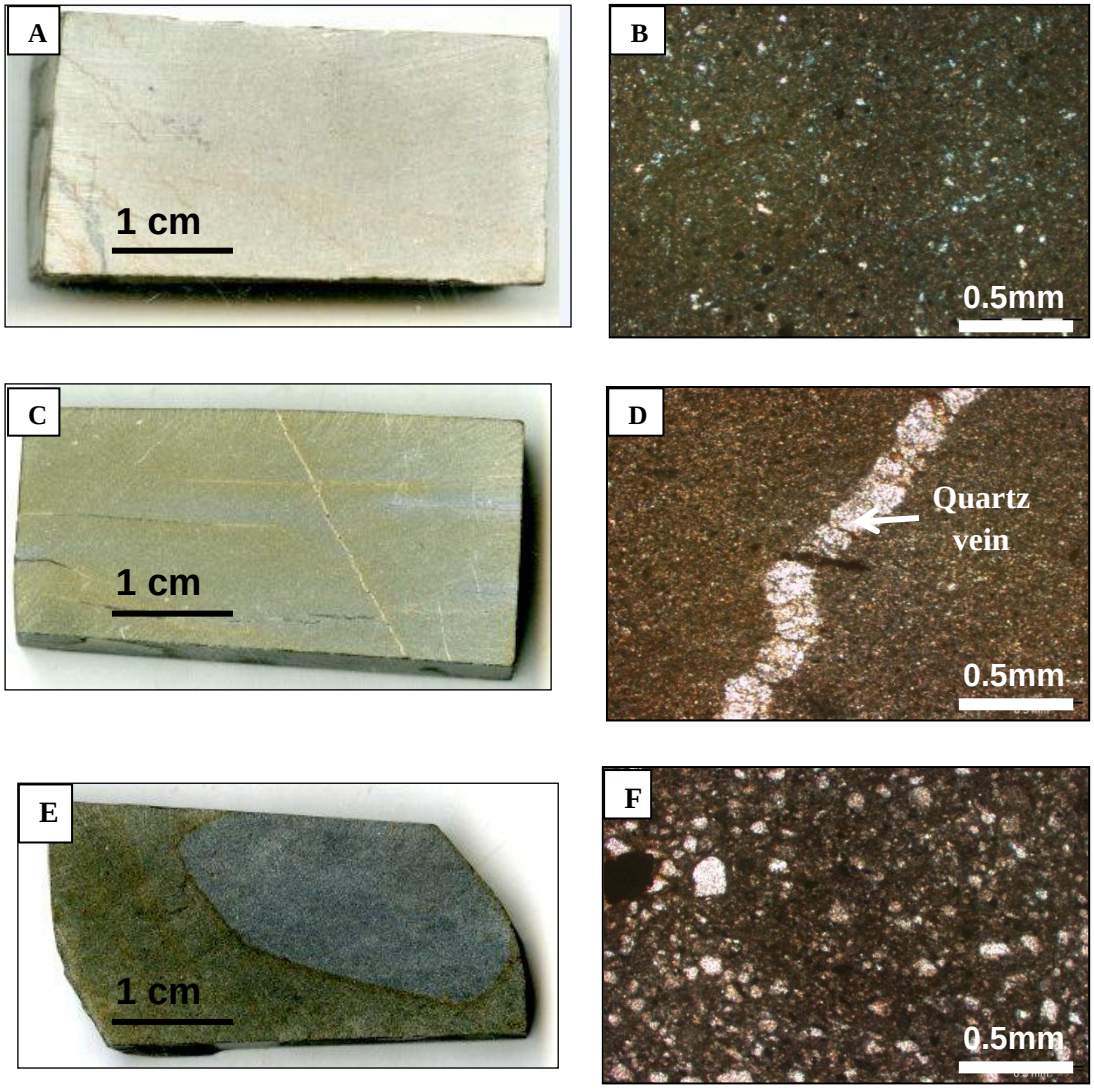

Fig. 2.8. Lithologic and textural characteristics of the F5 and F6 detrital sequences of the Machinchang Formation in Langkawi, Malaysia. **A**) Hand specimen of the grey shale of the Lower F5 sequence (sample LA-2812). The grey shales contain sub-rounded and sub-angular monocrystalline quartz grains (65 vol. %), sericite (20 vol. %), muscovite (5 vol. %), few pyrite grains and rock fragments including iron oxides (5 vol.5 %). **B**) Photomicrograph of the grey shale in cross polarised light (sample LA-2812). **C**) Hand specimen of the grey shale of the upper F6 sequence (LA-3112). **D**) Photomicrograph of the grey shale in cross polarised light. Under the microscope, it is made of monocrystalline quartz (60 vol. %), feldspar (30 vol. %), iron oxides and organic matter (10 vol. %). Some tiny quartz veinlets (up to 0.25 mm thick) also cut the bedding. **E**) Hand specimen of the sandstone of the F6 sequence (sample LA-3312). **F**) Photomicrograph of the sandstone in cross polarised light. The sandstone is poorly sorted, contains sub-angular quartz grains (65 vol. %), potassic feldspar altered to sericite (20 vol. %), muscovite (5 vol. %), some fragment of quartzite (15 vol. 15%), euhedral pyrite grains are common (up to 400µm across).

Paleontological evidence has shown the presence of *trilobite* and *brachiopods* attributing a Late Cambrian age (Hutchison and Tan, 2009). The age of 449 Ma (Fig. 2.9) is much

younger and appears unreliable probably due to laboratory contamination, sampling of the wrong unit or sample confusion.

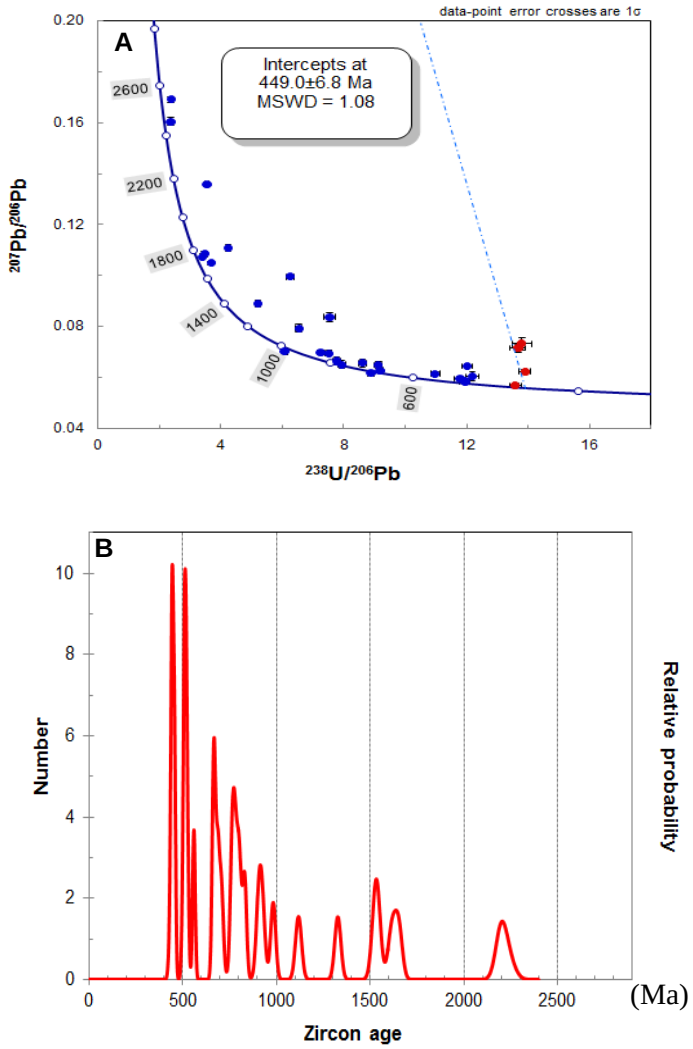

Fig. 2.9. Geochronology of the Machinchang Formation. **A**) U–Pb inverse concordia diagram of zircon (Sample No. LA-3312). **B**) Probability plot of the zircon age showing highest peak at 449 Ma. The accuracy between different labs is between 1 to 3% (Klötzli et al., 2009). In this study, a 1% error when the error from the weighted average of a sample is less than 1% is recommended in the subsequent Chapters.

2.5.2. Setul Formation (Early Ordovician-Silurian)

Outcrops of the LDB for the Setul Formation were found in northeast of the Langkawi Islands at approximately 10 km from the coastline. The exposures are made up of black, fine-grained, bedded sandstone (Fig. 2.10A). A typical section of the Setul Formation consists of

up to 50 m thick laminated dark, fine-grained sandstones (Fig. 2.10B). The Setul Formation sandstone sequence below that was sampled for this study is known as the Lower Detrital Band (LDB) belonging to the "Tanjong Dendang rocks (Fig. 2.10B).

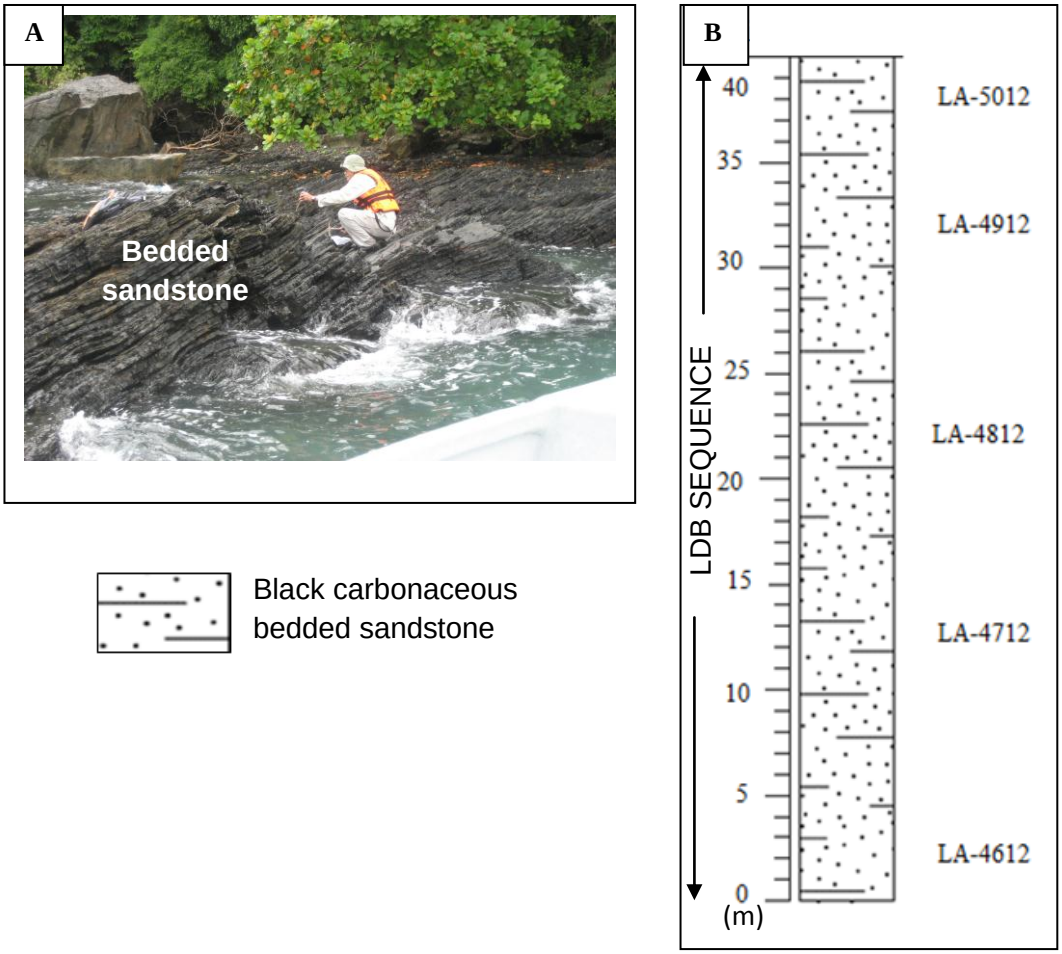

Fig. 2.10. Field observation of the Early Ordovician-Silurian Setul Formation in Langkawi Islands, south of Teluk Mempelam, northwest Pulau Langgun, Langkawi, Malaysia. **A**) Outcrop of bedded organic-rich sandstone. **B**) Sedimentary log of a type section of the Tanjong Dendang rocks known as the Lower Detrital Band or LDB. Note: stratigraphic positions of samples (LA-4612 to LA-5012) collected in the field.

Fossil age of the Setul Formation ranges from Early Ordovician (Tremadoc) to Silurian (Jones, 1961; Jones 1968; Cocks et al, 2005). LA ICP-MS, U-Pb dating carried out at the University of Tasmania as part of this study returned a maximum age of Early Silurian (427 Ma; MSWD= 0.32) calculated from six youngest detrital zircons out of 30 age measurements

(Fig. 2.11). The uncertainty on ages is recorded at 1σ values. Results of zircon dating are presented in Appendix B.

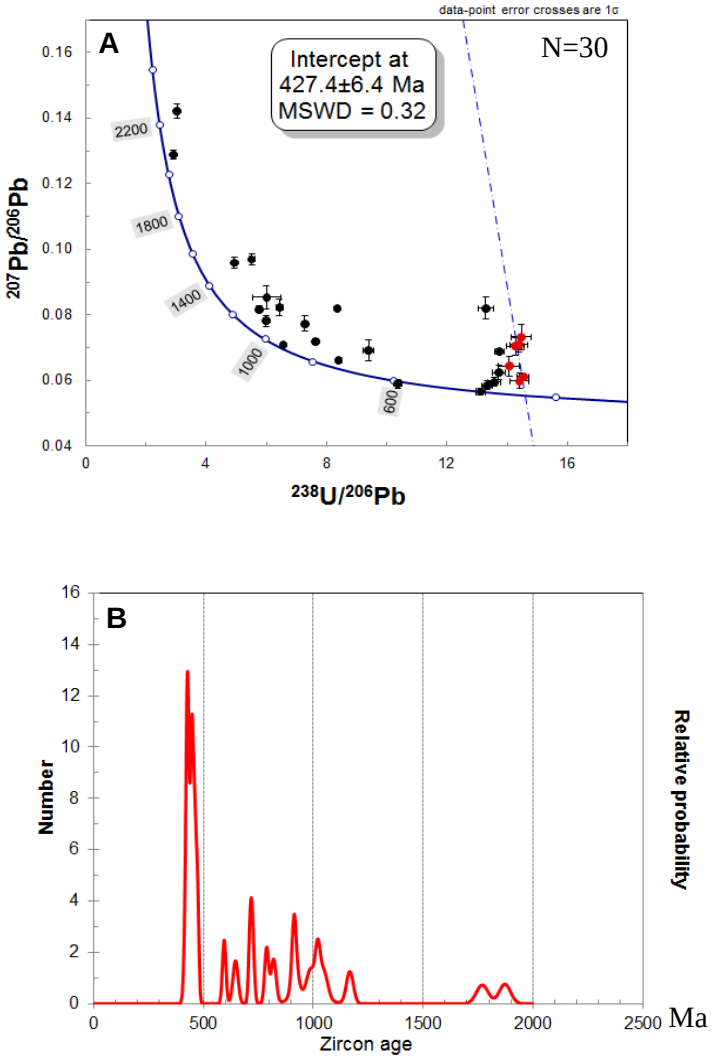

Fig. 2.11. Geochronology of the Setul Formation (Sample No. LA-4912). **A**) U–Pb inverse concordia diagram. **B**) U-Pb age Probability Density Plot.

The Setul sequence is chiefly composed of bedded, poorly to moderately sorted sandstone. Under the microscope, the sandstone (Sample No. LA-5012) is composed of sub-rounded to sub-angular monocrystalline and polycrystalline quartz (vol. 60 %), feldspar crystals (vol. 20 %) and rock fragments (vol. 5 %), and about vol. 15 % of clay minerals. In addition, the

sandstone is cross-cut with tiny quartz carbonate veinlets (1 mm). Lithological and textural features of the Setul Formation are shown in Fig. 2.12.

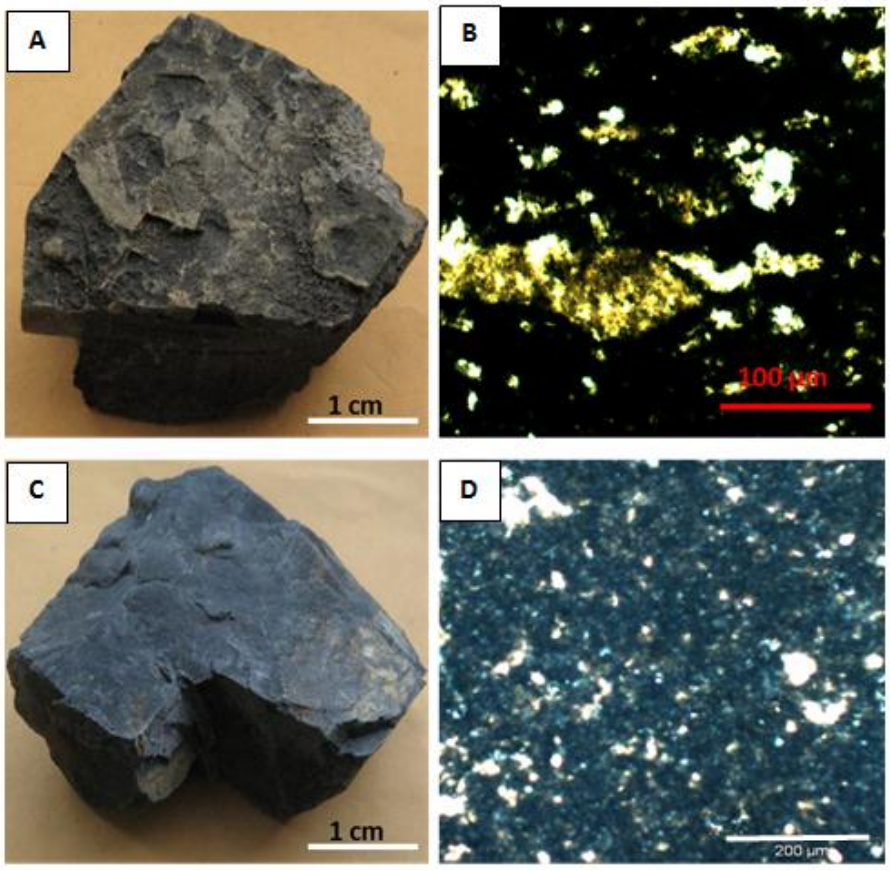

Fig. 2.12. Lithologic and textural characteristics of the Setul Formation in Langkawi, Malaysia. **A**) Hand specimen of sandstone (Sample No. LA-4912). **B**) Photomicrograph of sandstone in cross polarised light (Sample No. LA-4912. **C**) Hand specimen of the poorly sorted sandstone (Sample No. LA-5012). **D**) Photomicrograph of the sandstone in cross polarised light (Sample No. LA-5012).

Sample No. LA-4912 is a moderately sorted sandstone which contains organic matter in the form of parallel bands, muscovite (vol. 5%), quartz (vol. 60%), sericitised feldspar (vol. 30%), and some rock fragments (vol. 5%). Few framboidal pyrites (5 µm across) are present but not analysed due to their smaller diameter.

2.5.3. Singa Formation (Pennsylvanian-Early Permian)

The Singa Formation crops out on the Island of Langkawi in Malaysia. It has an outcrop area of about 178 sq. km and shares a boundary with the Triassic granite and Quaternary alluvium. Previous geological mapping has shown that this formation comprises thinly interbedded pebbly black mudstones, silty shales and lithic sandstones to quartz arenites. In Langkawi, six lithofacies were recognized by Stauffer and Lee (1986) as follows: (1) Laminated 0.5 to 2 m thick, well sorted, medium-grained clean sandstone facies with hummocky cross-bedding structures, (2) Interbedded sandstone and dark sandy mudstone with flaser bedding containing burrows, (3) Meter scale interbedded sand-mud facies with disseminated megaclasts of boulder size, (4) Sandy mudstone with graded sandstone facies and rare megaclasts, (5) Diamictite facies composed of clays and silts with minute burrows, and (6) Laminated sandstone-siltstone facies gently deformed with channel-like truncations and megaclasts. The presence of unsorted pebbles in this formation is indicative of glacial origin (Stauffer and Lee, 1986).

The Singa Formation is interpreted as having been deposited in a glacial-marine environment evidenced by the presence of matrix-hosted fresh feldspars, granitic clasts, angular limestone clasts, and brachiopods (Mohd Shafeea and Asmaniza, 2002; Basir et al., 2003). Selected field photographs of the Singa Formation are shown in Fig. 2.13. All samples collected in the field were placed on the sedimentary log according to their key lithologies and stratigraphic positions as shown in Fig. 2.14. In this study, the diamictite facies was recognized at the Tanjung Malie beach (Fig. 2.3) where most exposures are made up of massive sandstones associated with pebbly mudstones. Pebbly mudstones (Fig. 2.13C) contain clasts (also called lonestone) of up to 10 cm in diameter implying a glacial environment for the Singa Formation.

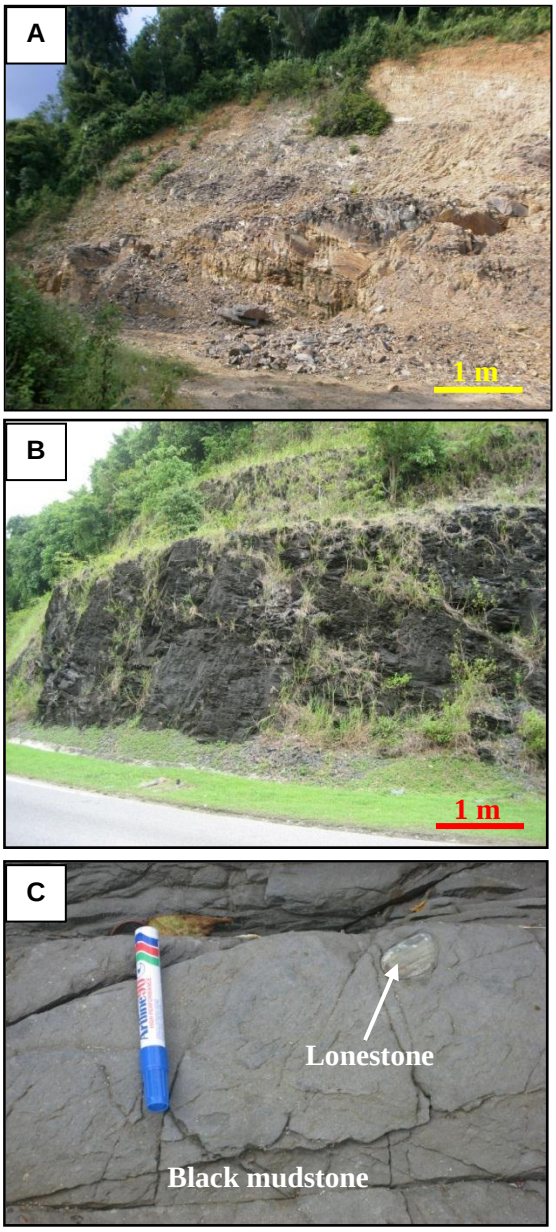

Fig. 2.13. Field photographs of the Singa Formation in Malaysia. **A**) Outcrop of dark-brown to grey bedded sandstone. **B**) Exposure of black shale. **C**) Lonestone in black mudstone.

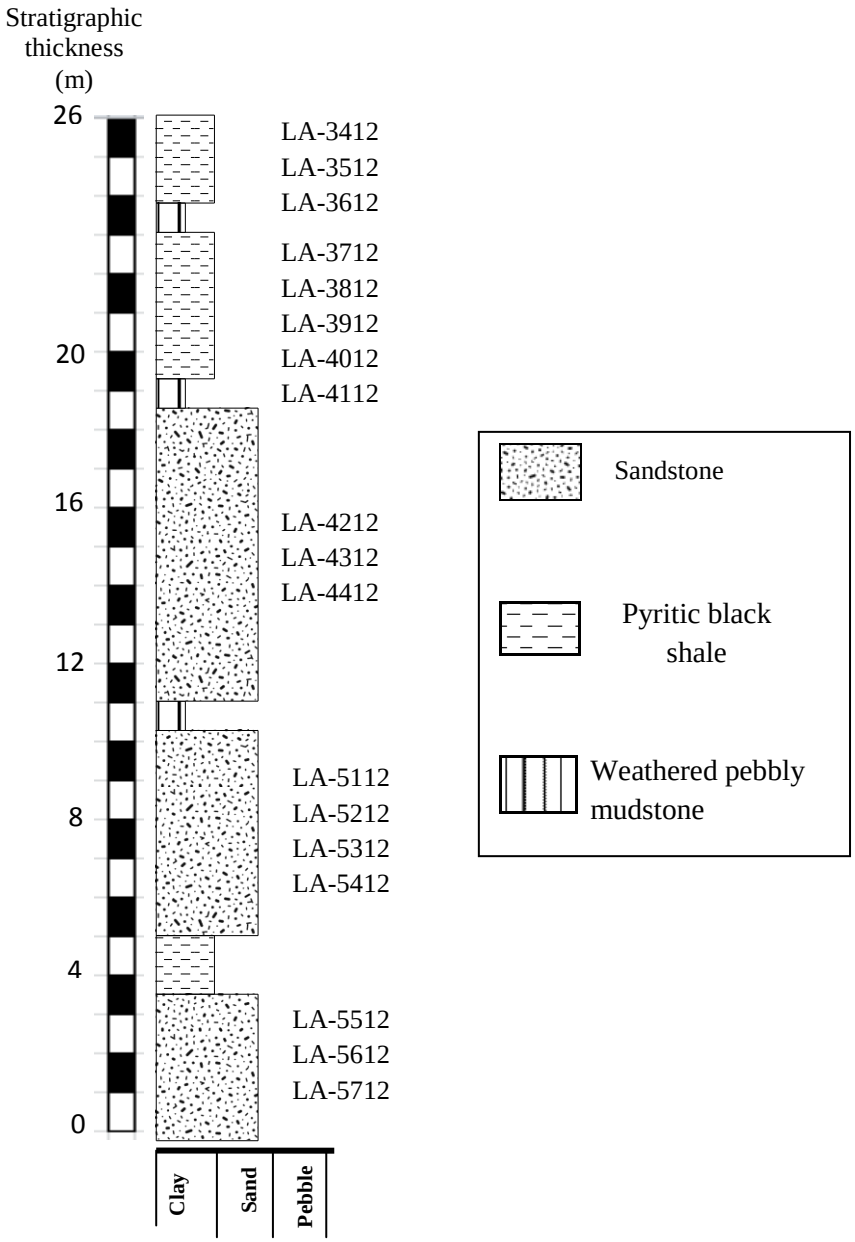

Fig. 2.14. Sedimentary log showing a Singa Formation sequence at Langkawi Islands, Malaysia. The fining upward sedimentary sequence is dominated by sandstone interbedded with black shale. The log shows gaps representing absence of exposure or highly weathered rocks.

The sedimentary log depicts a record of lower and higher energy environments. The black shales were probably deposited during relatively low energy conditions as they contain more aluminosilicate minerals such as clays whereas the sandstones were accumulated over higher energy conditions in the depositional environment. Basir et al. (2003) reported the presence of radiolarian in black siliceous mudstone and cherts which ages are Ordovician-Silurian,

Upper Devonian-Lower Carboniferous, and Middle Permian. U-Pb zircon dating has returned a maximum depositional age of 418.6 Ma (Fig. 2.15). The Late Silurian age maximum deposition age is much older than the Pennsylvanian-Early Permian stratigraphic age provided by the fossils (Waterhouse, 1982). The lack of young zircon in this formation is supported by a previous study which has shown that detrital zircons between 320-360 Ma are rare throughout south east Asia (Burrett et al., 2014).

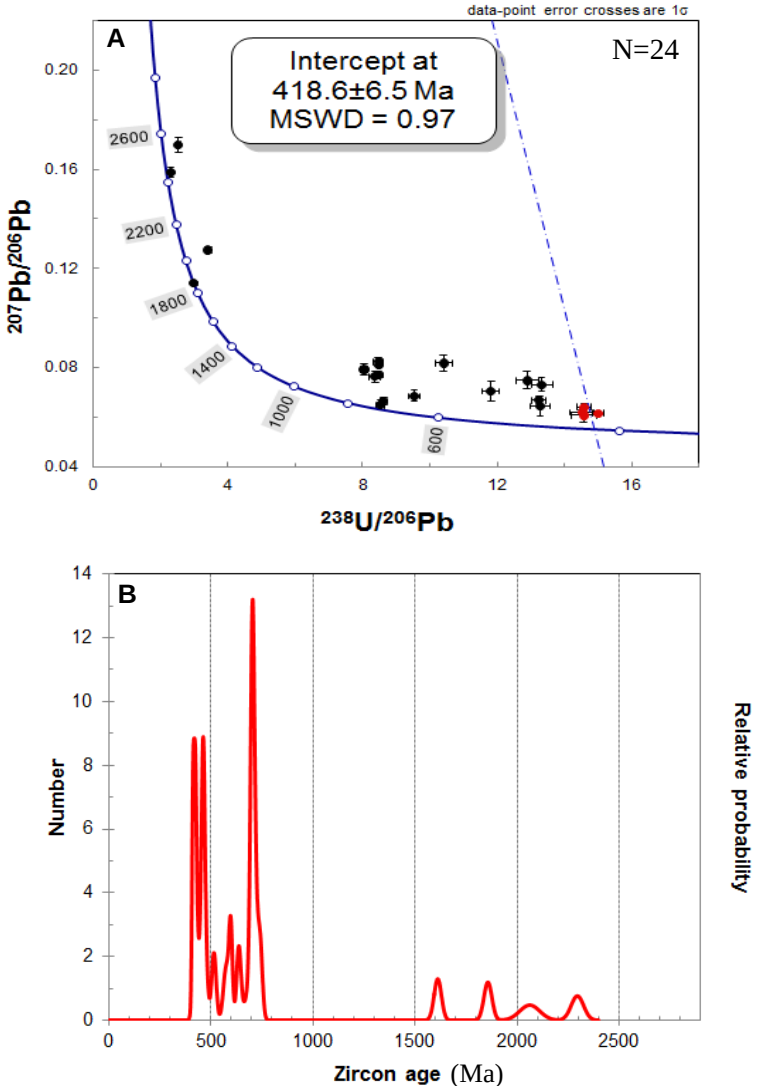

Fig. 2.15. Geochronology of the Singa Formation (Sample No. LA-3412). **A**) U–Pb inverse concordia diagram. **B**) U-Pb Probability density plot. The youngest peak is at 417.6 Ma. The age value of 418.6 Ma is the mean value of calculated age. Results of zircon dating are presented in Appendix B.

Lithologic and textural characteristics of the Singa Formation are given in Fig. 2.16.

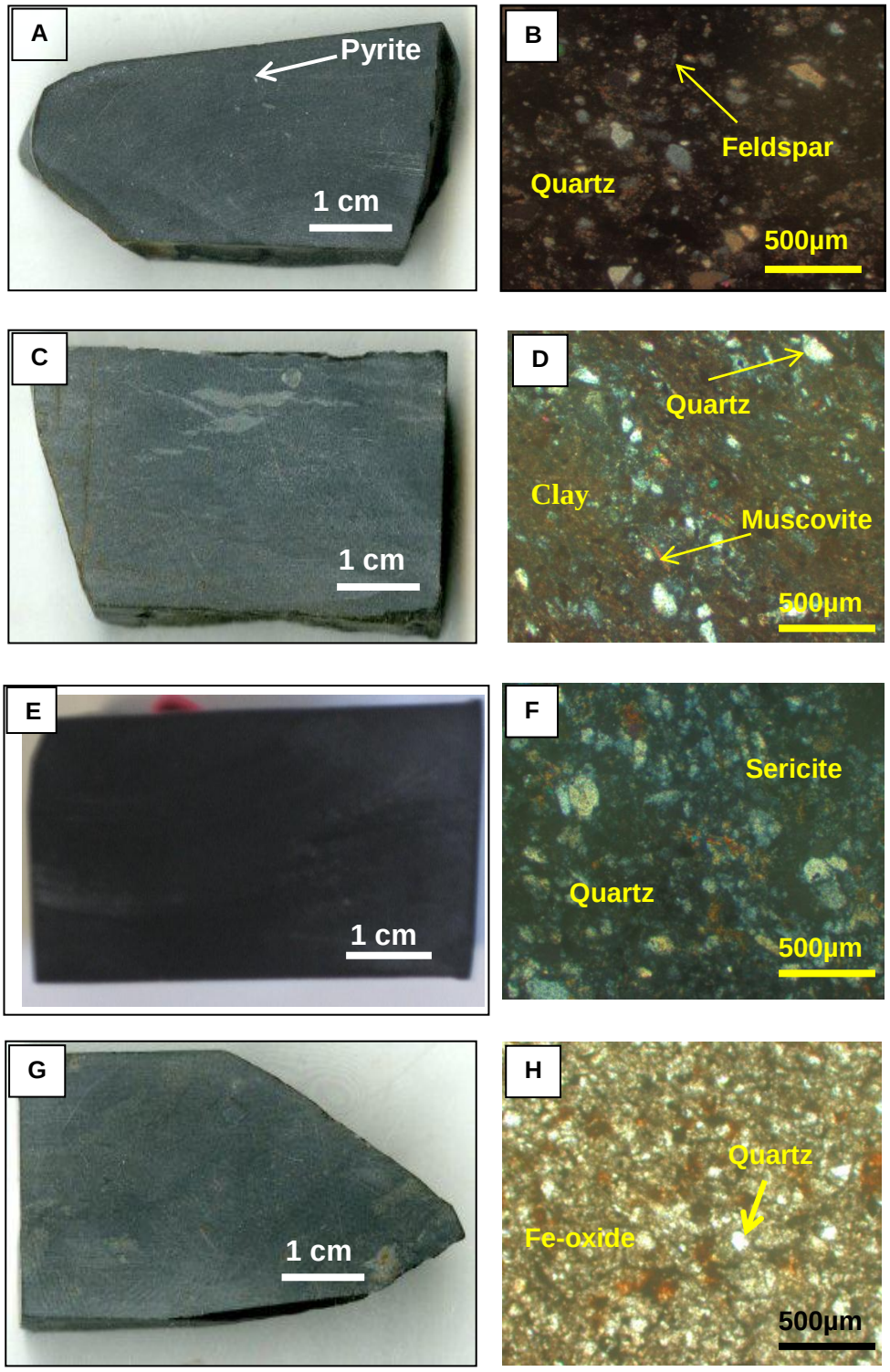

Fig. 2.16. Lithologic and textural characteristics of the Singa Formation. **A**) Hand specimen sample of feldspathic black shale (sample LA-4112). **B**) Photomicrograph of the black shale in cross polarized light. **C**) Hand specimen sample of black shale (sample LA-3512). **D**) Photomicrograph of the black shale in cross polarized light. **E**) Black shale (sample LA-4212). **F**) Photomicrograph of the black shale in cross polarized light. **G**) Hand specimen of black shale (sample LA-3412). **H**) Photomicrograph of black shale in plane polarised light. Annotation: Fel=Feldspar; Qtz= Quartz.

Petrographic analysis of the shales and sandstones is summarised in Table 2.4 below.

Table 2.1. Mineral composition of shale and sandstone from the Pennsylvanian-Early Permian Singa Formation.

	Lithology	Sorting	Qtz	Feldspar	Mica	Lithic fragments	Other	Comments
LA-3412	Shale	-	60	10	25	5	clay	-
LA-3512	Shale	-	65	10	25	-	clay	Sericite alteration
LA-3712	Shale	-	65	5	30	-	Some qtz veinlets	-
LA-3812	Shale	-	50	10	40	-	pyrite	-
LA-4012	Shale	-	60	10	25	5	clay	Mono and polycrystal line qtz
LA-4112	Shale	-	60	5	30	5	clay	-
LA-4212	Shale	-	60	5	20	10	clay	-
LA-4312	Sandstone	poor	65	25	5	5	Zircon and clay	-
LA-5312	Sandstone	good	85	5	10	-	clay	-
LA-5612	Sandstone	poor	70	10	20	5	5% iron oxides and clay	-
LA-5712	Shale	-	60	5	20	-	5% iron oxides and clay	-

2.5.4. BRSZ Unit 1 (Late Devonian)

The BRSZ Unit 1 rocks are part of the Bentong Group (Jaafar, 1976) and were deposited in an open deep-water basin between the Sibumasu and Indochina Terranes (Metcalfe, 2000). The BRSZ Unit 1 black shales are similar to those that crop out at the Selinsing gold deposit. Outcrop images of the BRSZ Unit 1 are shown in Fig. 2.17 and the

sedimentary log is shown in Fig. 2.18. The sedimentary rocks composed of black shales are similar to those that crop out at the Bukit-Koman gold deposit, which is located about 15 km north of the mapped BRSZ Unit 1 sequence.

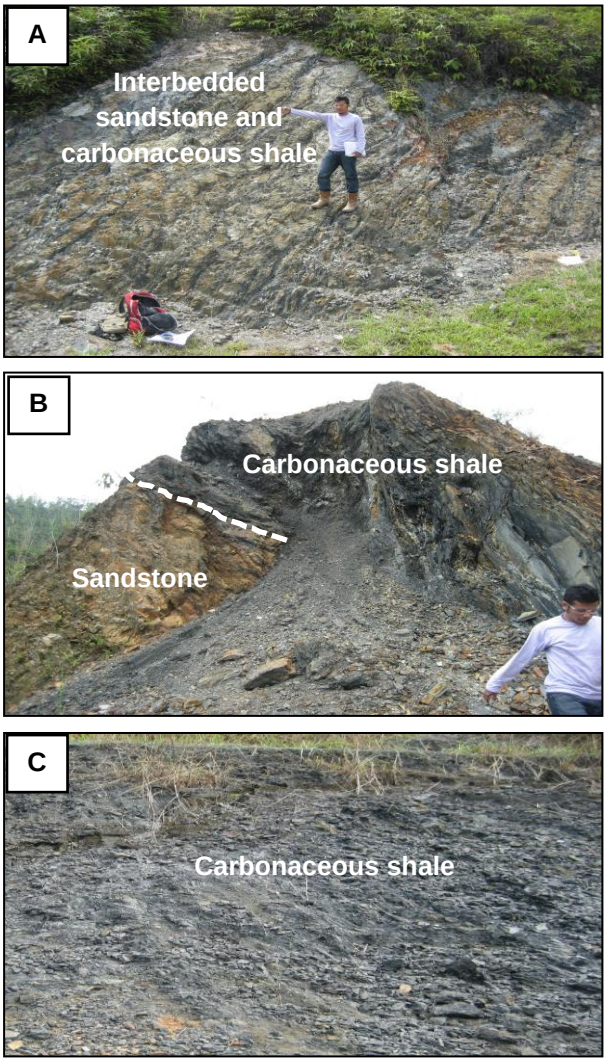

Fig. 2.17. Outcrop photographs of the BRSZ Unit 1 at Lurah Bilut, Central Basin of Peninsular Malaysia. **A**) The sedimentary sequence is made up of interbedded sandstone and black shale. **B**) Geologic contact between the sandstone and carbonaceous shale within the lower sequence. **C**) Road cut showing the carbonaceous shale in the lower turbiditic sequence.

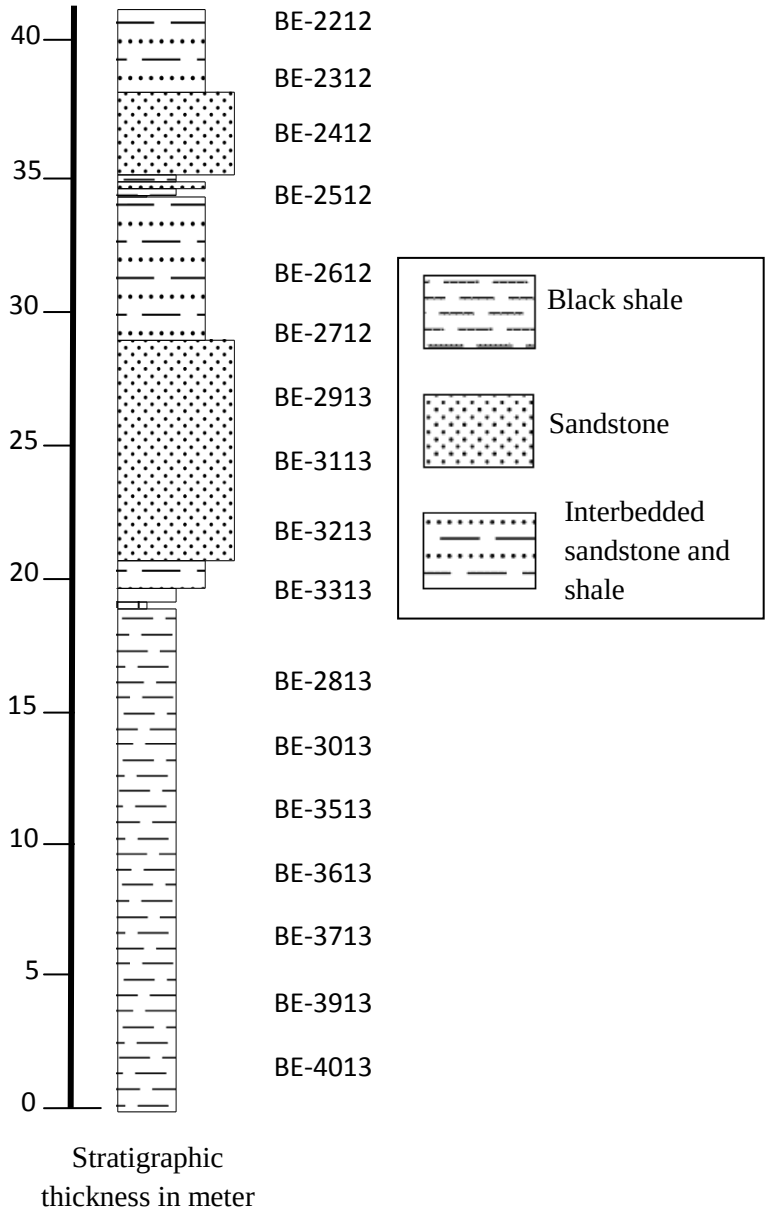

Fig. 2.18. Sedimentary log of the BRSZ Unit 1 (Late Devonian) that shows stratigraphic position of collected samples. Location: Lurah Bilut, Malaysia. This clastic turbiditic sequence is made up of sandstone interbedded with black shales. The sandstone is grey to brown/pink in colour and the beds are 2 to 10 cm thick. The black shale bed laminations are 1 to 8 mm thick. The Black shales show parallel laminations (up to 1cm thick), convolute laminations and contain tiny quartz lenses (1-2 cm long).

Previous studies report the occurrence of Late Devonian *radiolarians* and Early Devonian *graptolites* such as *Monograptus cf. Praehercynians Jaeger* (Metcalfe, 2000). Currently, the maximum depositional age of the BRSZ Unit 1 determined using LA-ICP-MS, U-Pb zircon dating indicates a Late Devonian age (367±5.8 Ma; MSWD= 0.52) similar to the previous stratigraphic age from the radiolarian (Fig. 2.19). Results of zircon dating are presented in Appendix B.

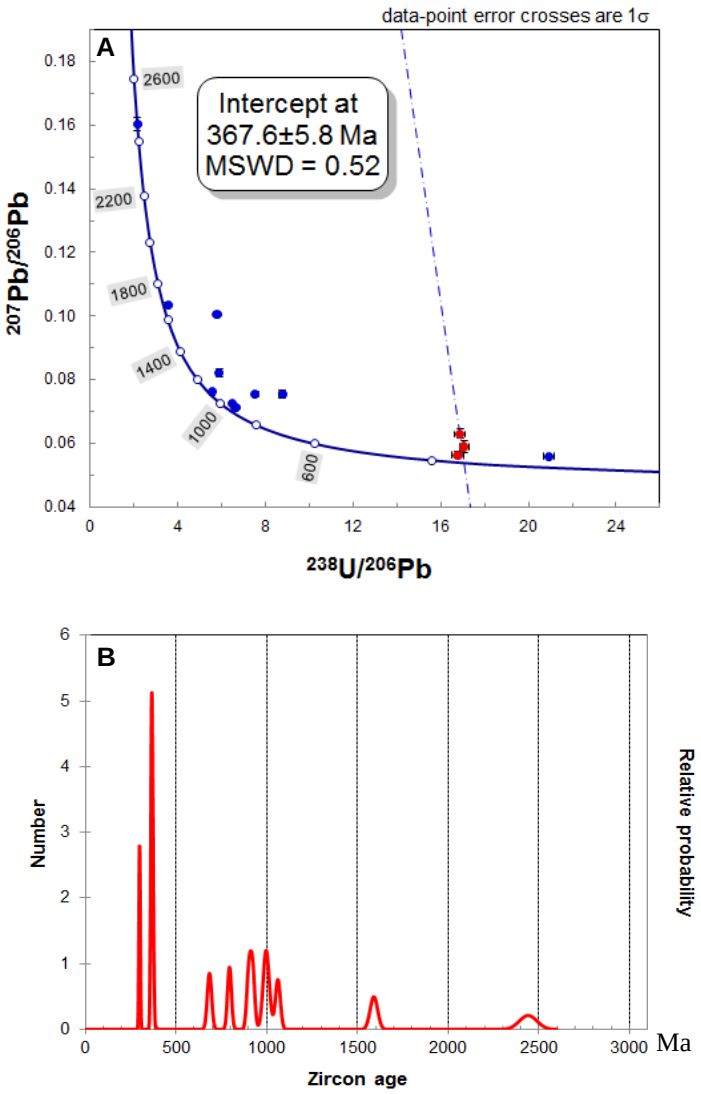

Fig. 2.19. Geochronology of the BRSZ Unit 1 (Late Devonian) in the Bentong-Raub Suture Zone (Sample No. BE-3213). **A**) Inverse concordia plot of U-Pb zircon dating. **B**) U-Pb Probability density plot.

Lithological and textural characteristics of the BRSZ Unit 1 are shown in Figs. 2.20 and 2.21.

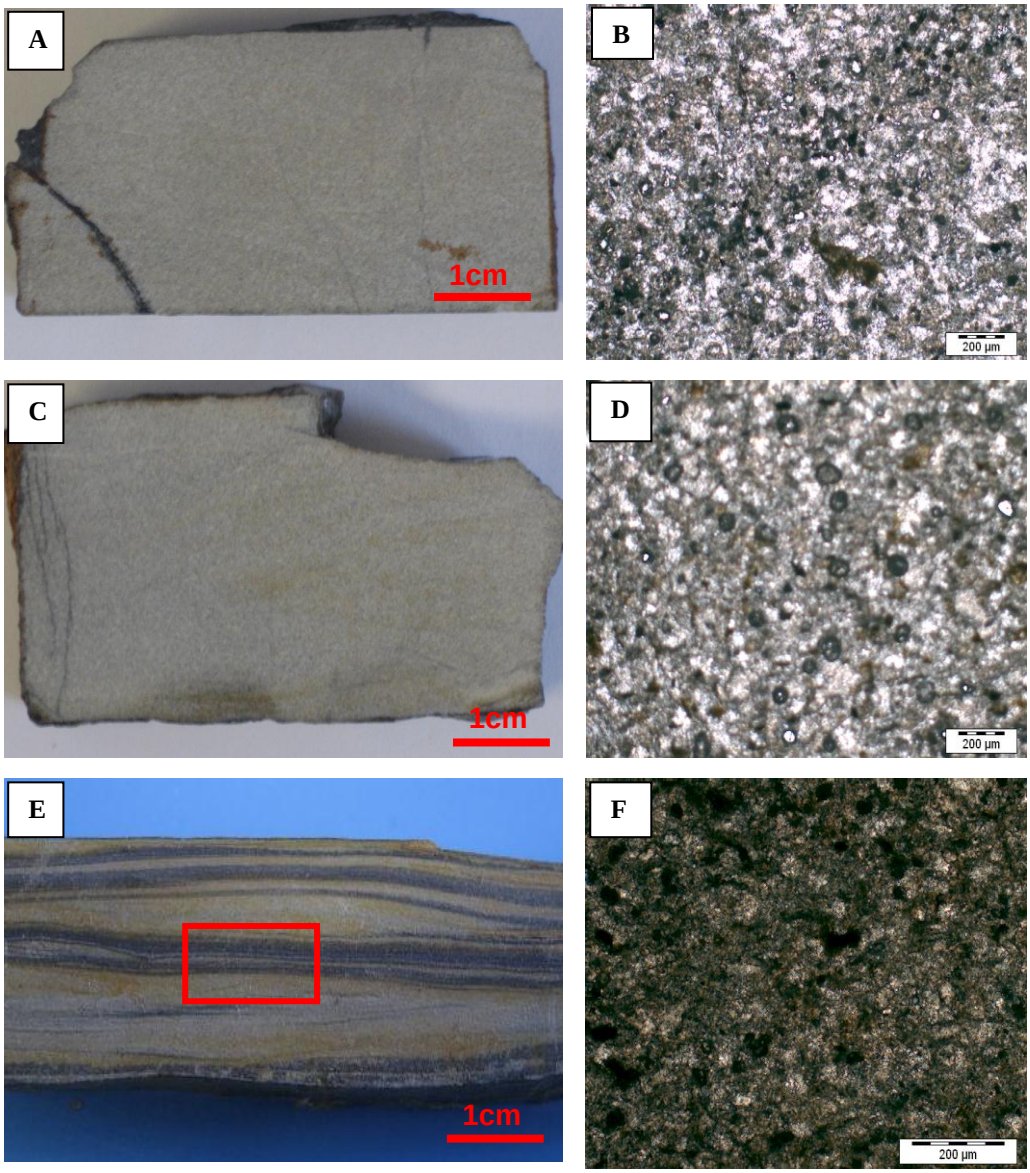

Fig. 2.20. Lithological and textural characteristics of the BRSZ Unit 1 sandstones and black shales, Malaysia. **A**) Hand specimen of sandstone (Sample No. BE-3213). **B**) Microphotograph of the sandstone (Sample No. BE-3213). The sample is composed of mono and polycrystalline quartz (vol. 65%), altered feldspar (vol. 20%), rock fragments (vol. 5 %), and iron oxide and pyrite crystals (vol. 10 %). **C**) Hand specimen of sandstone (Sample No. BE-3313). **D**) Microphotograph of the sandstone (Sample No. BE-3313). It comprises monocrystalline and polycrystalline quartz grains (vol. 70%), altered feldspar (vol. 20%), disseminated pyrite (vol. 5%), lithics (vol. 5%). **E**) Black shale interbedded with sandstone (Sample No. BE-2312). **F**) Microphotograph of the black shale lamination (red rectangle). Under the microscope, the shale comprises sub-rounded quartz grains (vol. 60%), potassic feldspar (vol. 30%), and rock fragments (vol. 10%).

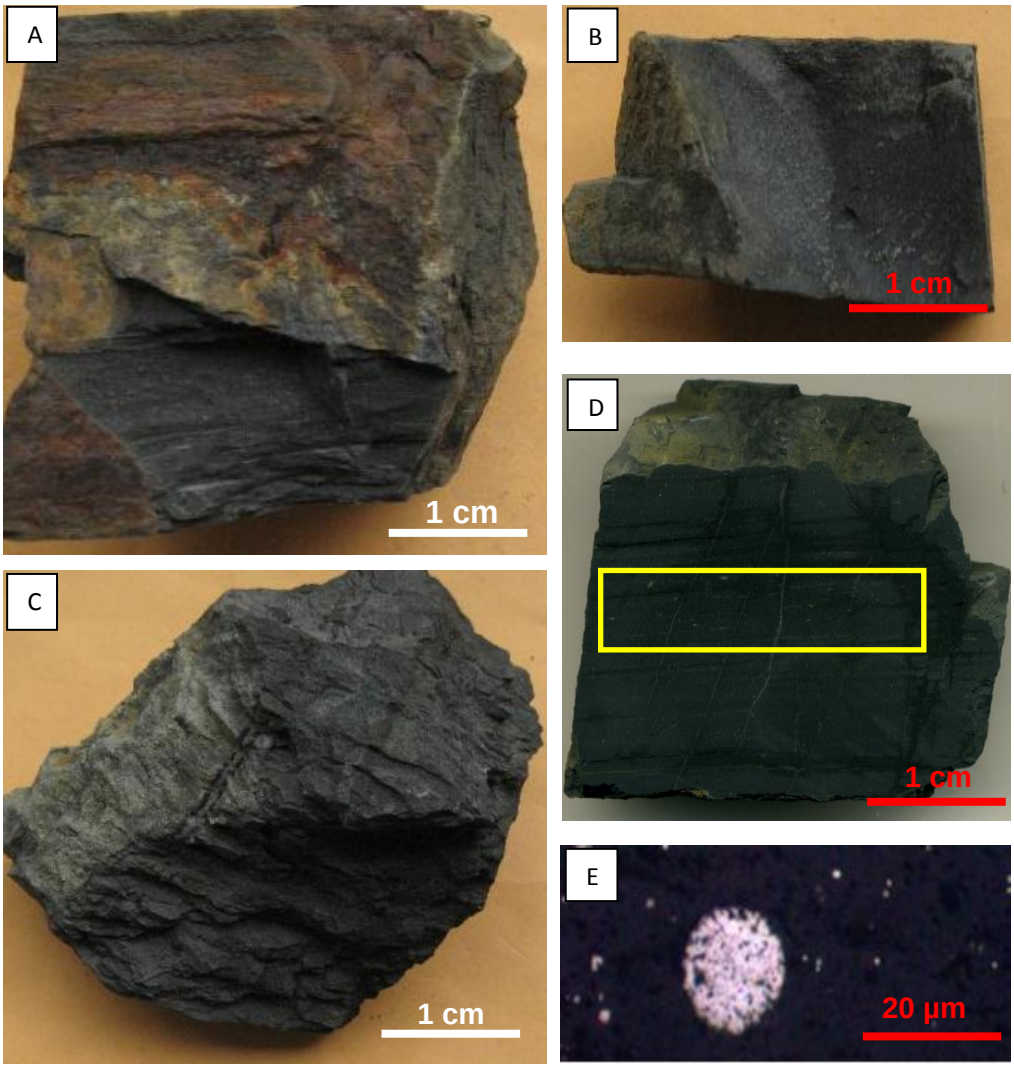

Fig. 2.21. Some hand samples of carbonaceous pyritic black shales enriched in gold from the BRSZ Unit 1, Malaysia. **A**) Black shale (Sample No. BE-2412). **B**) Black shale (Sample No. BE-2512). **C**) Carbonaceous black shale (Sample No. BE-2612). **D**) Pyritic carbonaceous black shales with tiny quartz veinlets (Sample No. BE-2712). The yellow rectangle represents an area rich in framboidal pyrites. **E**) Microphotograph of pyrite framboids from the yellow area (Sample No. BE-2712).

2.5.5. Carboniferous black shale at the Selinsing gold deposit

Selinsing gold deposit is located in the northwest of Pahang and approximately 50 km north of Raub Town in Malaysia (Fig. 2.22). The Selinsing gold deposit and its extension

northward known as the Buffalo Reef prospect have an approximate area of 20 sq. km. In the Selinsing area, mining started prior to 1888 and has operated over many years. The Selinsing property was acquired in 2007 for the purpose of exploration with plans to build a gold treatment plant under a new name "Monument Mining Company".

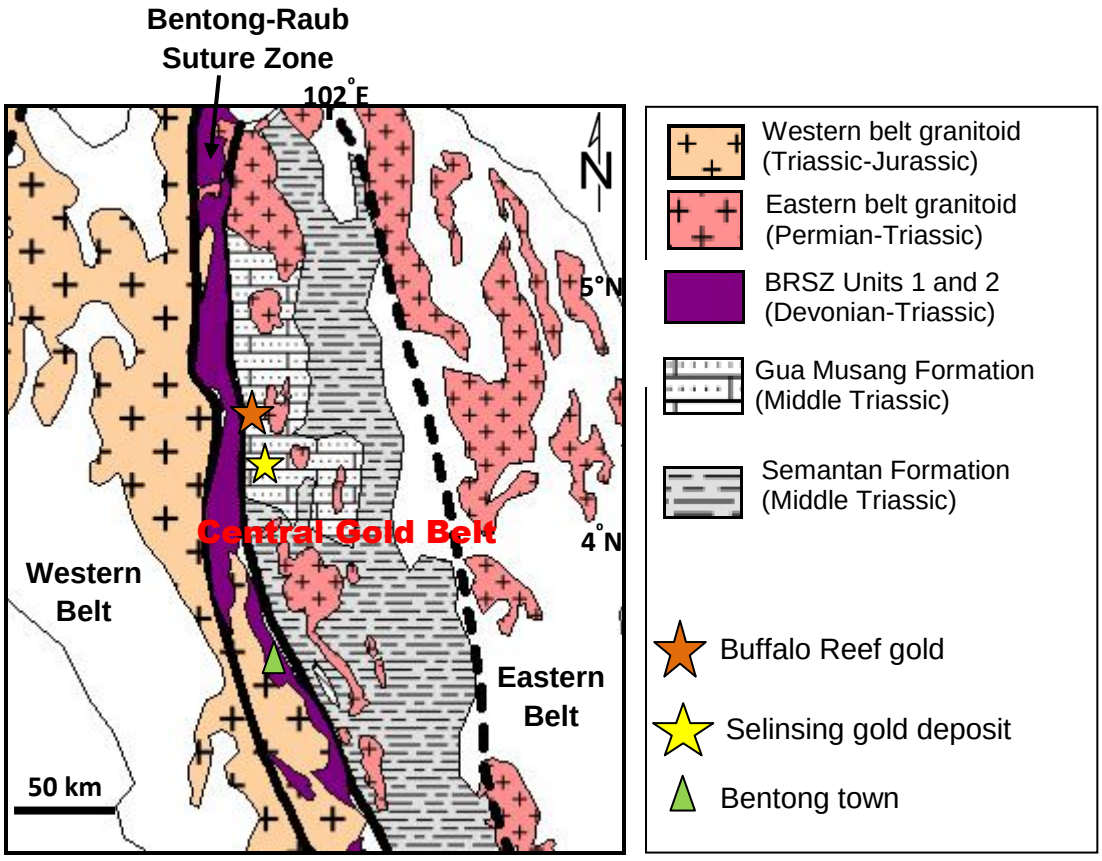

Fig. 2.22. Local geological map showing the Selinsing and Buffalo Reef and the extent of the BRSZ Unit 1 and BRSZ Unit 2 in Malaysia.

In 2013, the company Snowden estimated the resources for both the Selinsing and Buffalo Reef as follows: (1) Proven resources were estimated at 2,626,000 tonnes for oxides and sulphide at an average grade of 0.3 and 0.62 g/t respectively; (2) Measured resources were calculated at 2,682,000 tonnes at an average grade of 0.27 and 0.56 for oxides and sulphide

respectively; and (3) Indicated resources were fixed at 3,624,000 tonnes for the above cut-off grades. The Selinsing gold deposit is located east of the Bentong-Raub Suture Zone where the BRSZ Units 1, and 2 (Fig. 2.22).The host rocks consist of phyllite, black shales, tuffaceous siltstone and sandstone which belong to the Carboniferous-Permian Raub Group (Foo, 1983). The sedimentary host sequence has undergone low grade regional metamorphism. The maximum depositional age of the black shales has been constrained using U-Pb analyses of zircons and returned an age ranging from 300 Ma (Pennsylvanian) to 331 Ma (Mississippian) (Makoundi et al., 2014). The black shales contain framboidal pyrites with size ranging from 5 to 30 µm (Fig. 2.23).

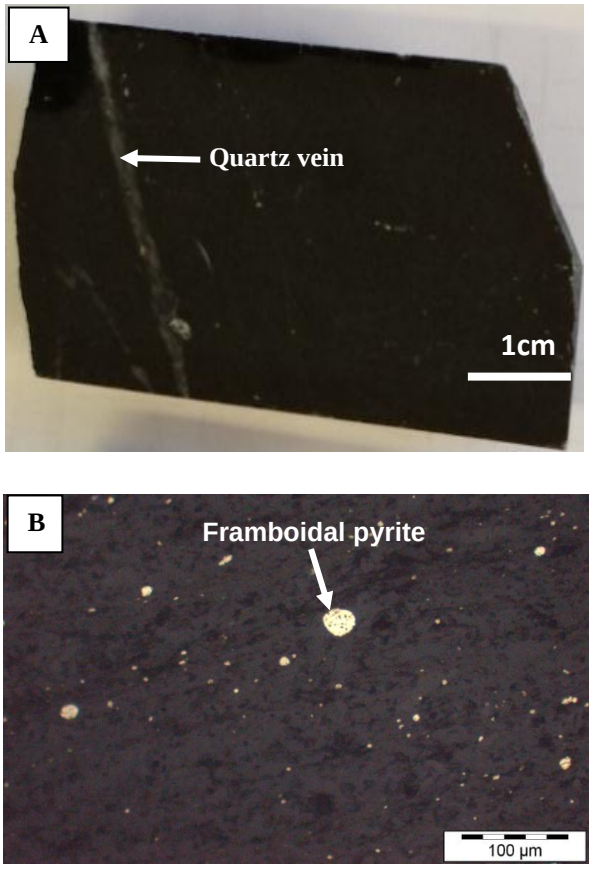

Fig. 2.23. Hand specimen and photomicrograph of pyrite in black shales away from the orebody at the Selinsing gold mine. Sample No. SEL-103B, depth: 68.5 m and Sample No. SEL-R076, depth: 41.9 m. **A**) Black shale specimen containing quartz veins. **B**) Photomicrograph under the microscope showing pyrite framboids in black shale.

2.5.6. Karak Formation (Middle Triassic)

Current field observation shows that the Karak Formation is made up of repetitive thin layers of sandstone, siltstone and black shales (Fig. 2.24). The black shales (up to 7 cm) contain wavy and flaser laminations. The siltstones have a variable thickness ranging from 2 to 8 cm and show parallel laminations. Few microfaults are found in some horizons of the formation. The Karak Formation is composed of interbedded sandstone, siltstone and black shales. This formation is interpreted to have been deposited in a marine deep-water environment (Abdul Hadi and Mustaffa Kamal, 2000).

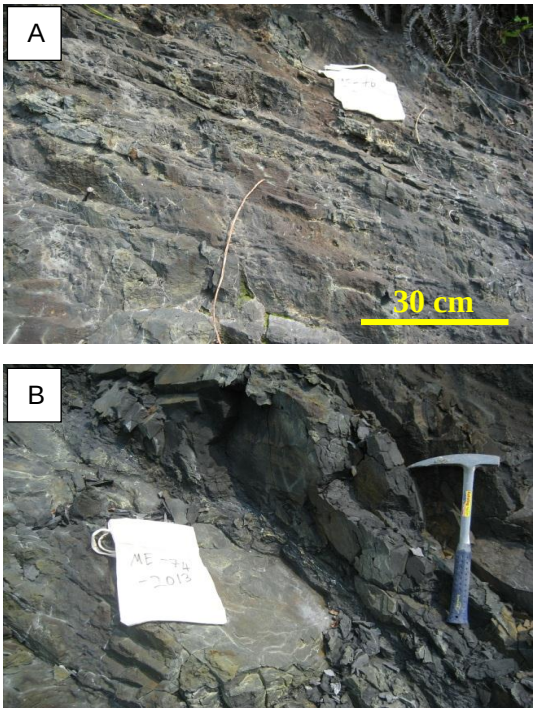

Fig. 2.24. Outcrop photograph of the Karak Formation in Central Malaysia. **A**) Bedded sandstone. **B**) Close-up view of black shale.

Lithologic and textural characteristics are presented below (Fig. 2.25). Hand specimens are dark in colour for the shales and some organic matter laminations.a

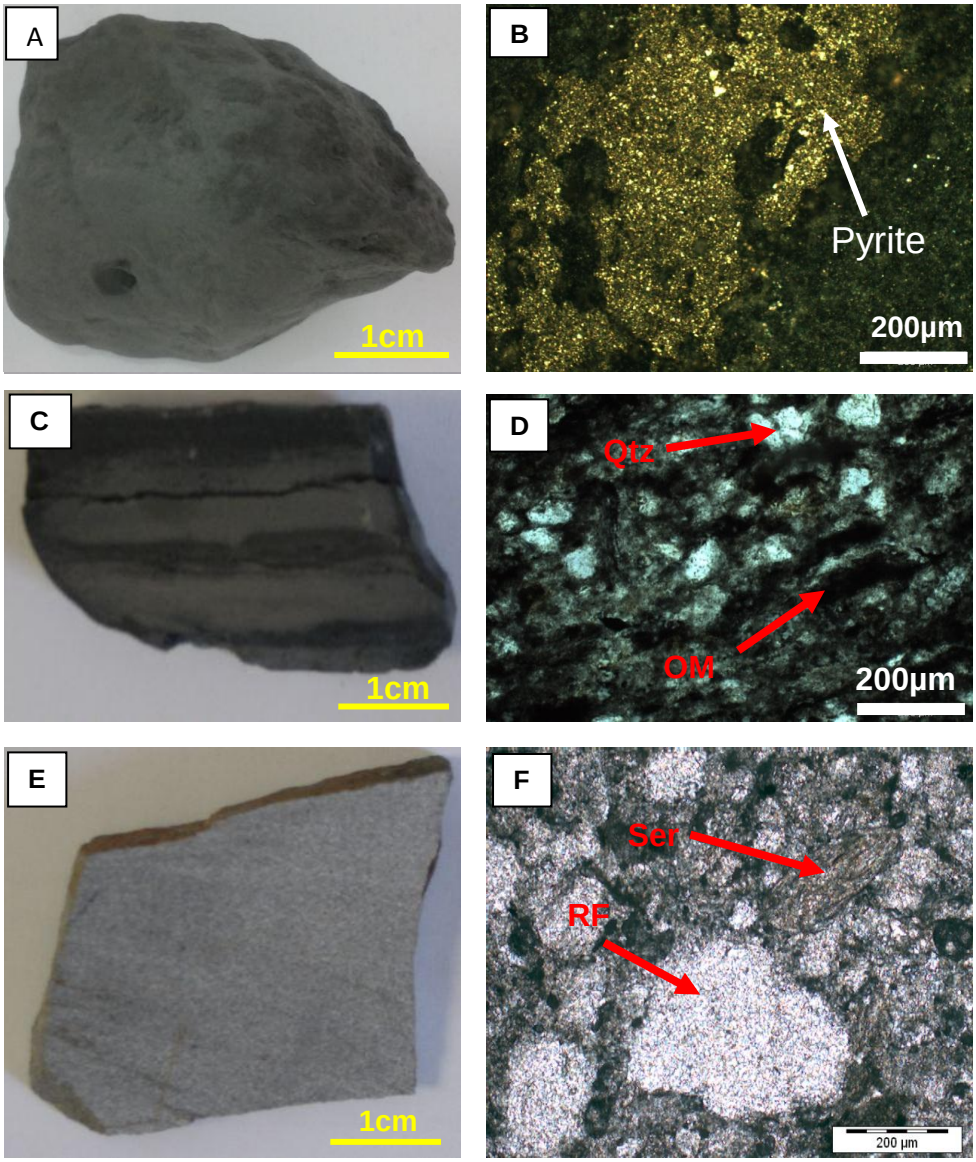

Fig. 2.25. Lithologic and textural characteristics of the volcaniclastic Karak Formation. **A**) Black shale hand specimen. **B**) Pyrite in black shale. **C**) Black shale. **D**) Bands of organic matter (OM) in black shale. Thin section shows poorly sorted, angular quartz grains (vol. 55%), altered feldspar (vol. 40%), and rock fragments (vol. 5%). **E**) Tuffaceous siltstone hand specimen. **F**) Microphotograph of the tuffaceous siltstone showing quartz grains, altered mica and a cement made of clay surrounding quartz grains. Note: RF= rock fragment; Ser= sericite; OM= organic matter; Qtz= quartz.

Previously, fossils were found in shale including *Paraceratites sp. and Costatoria chegarpahangensis* of Late Middle Triassic age (Hasnol et al., 2007). U-Pb zircon dating returned a maximum depositional age of Middle Triassic (Anisian) (236.7±3.9 Ma, MSWD= 1.8) as indicated on the concordia plot below (Fig. 2.26). Results of zircon dating are presented in Appendix B.

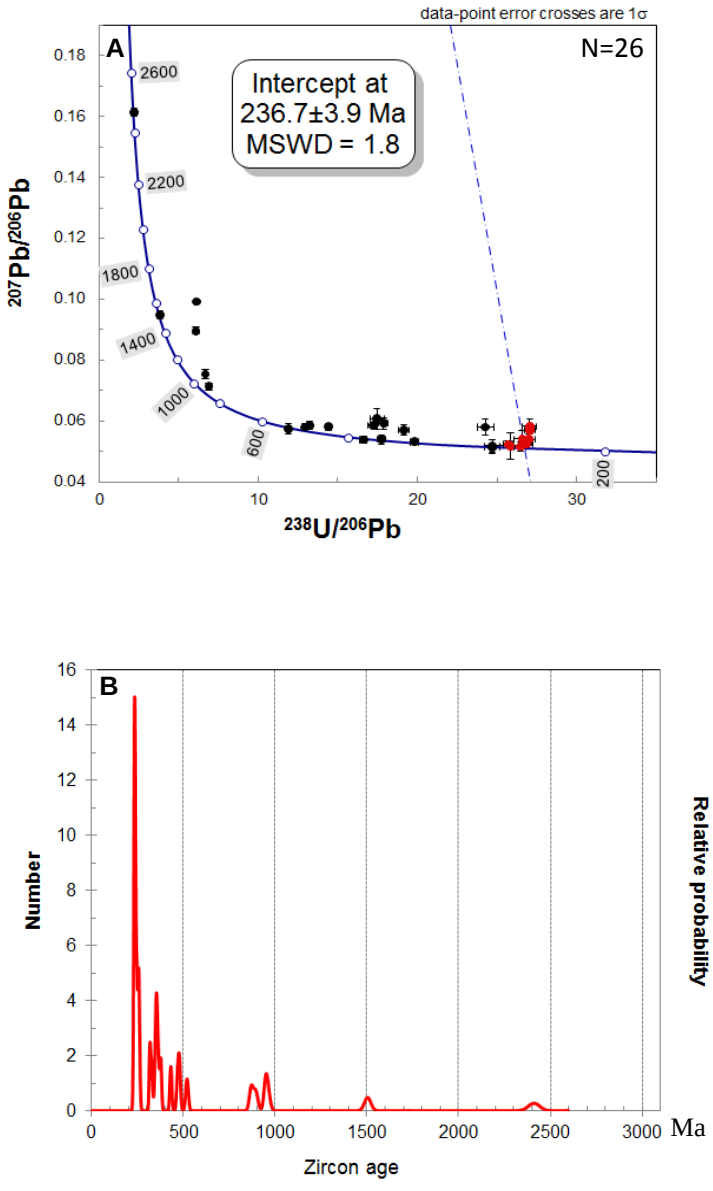

Fig. 2.26. Geochronology of the Karak Formation in Malaysia (Sample No. ME-7213). **A**) U–Pb inverse concordia plot of zircon. **B**) Probability plot of zircon age.

2.5.7. Semantan Formation (Middle Triassic)

Field mapping has shown that the Semantan Formation is made up of interbedded tuffaceous siltstone (1-3 cm thick layers) and tuffaceous black shales (up to 2 cm thick layers) (Fig. 2.27). The shales contain organic matter laminations (2-3 mm). Clusters of microcrystals of pyrite are present in organic-rich shale layers within the upper part of the sedimentary sequence. The geologic contact between the tuffs and black shales is not visible in the field. Sedimentary structures in the Semantan Formation (Fig. 2.28).

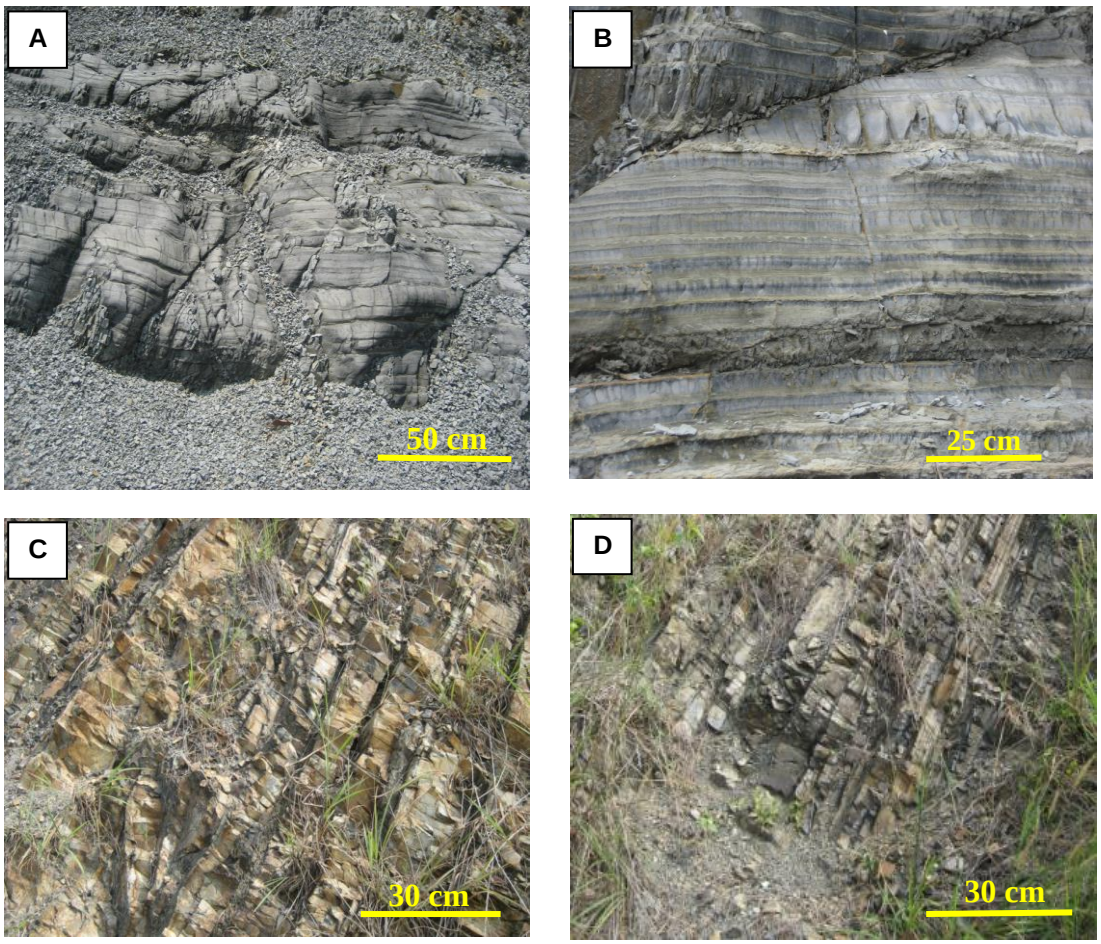

Fig. 2.27. Outcrop photographs of turbidite-volcaniclastic rocks of the Semantan Formation. **A**) Interbedded black tuffaceous siltstone and black shales. **B**) Close-up view of the turbidite sequence. **C**) Coarse grained bedded tuff. **D**) Fine-grained bedded tuff.

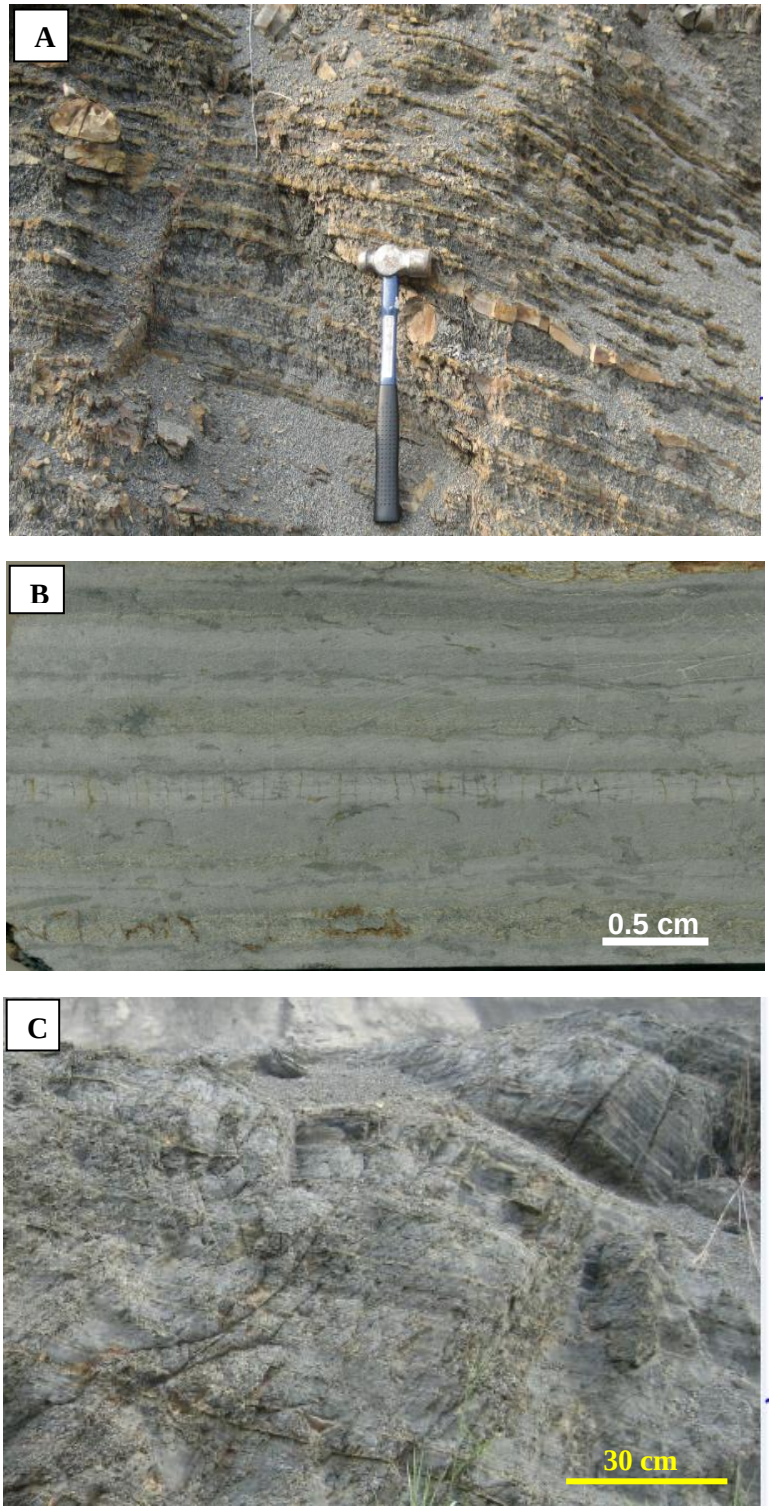

Fig. 2.28. Outcrop photographs of turbidite-volcaniclastic rocks of the Semantan Formation **B**) Polished slab showing planar bedding in interbedded tuffaceous black shale and grey siltstone. **C**) Parallel bedding sedimentary structure.

Previous work reports that the Semantan Formation is characterized by an assemblage of slumping, turbidity current and debris flow deposits interpreted to have been deposited in

deep marine environment (Hasnol et al., 2007). Occurrences of *Halobia* and *Posidonia* indicate a deep marine environment (Mustaffa Kamal and Abdul Hadi, 2000).

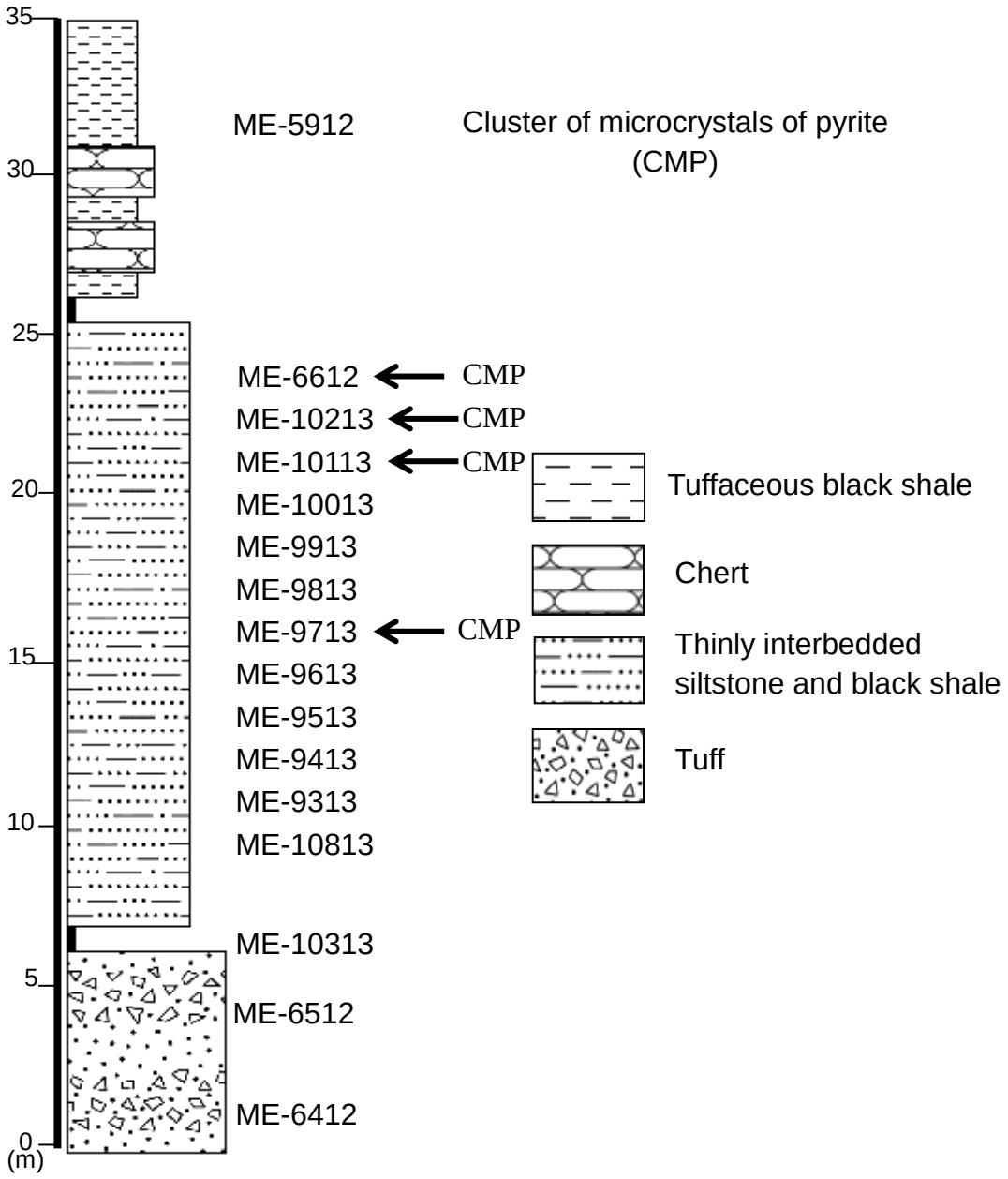

Fig. 2.29. Lithostratigraphy of the Semantan Formation showing the stratigraphic position of samples collected in Malaysia. Note: the stratigraphic thickness is in meter.

Paleontological evidence has shown the presence of *Entolium subdemisum Muenster* and *Costatoria Pahangensis* of Middle-Upper Triassic age (Hasnol et al., 2007) for the Semantan Formation. In this study, the tuffaceous sandstone returned a Middle Triassic (Ladinian) maximum depositional age (231.6±3.6 Ma; MSWD= 1.3) using U-Pb zircon dating. Likewise, the tuffs have a Ladinian age (233.1± 1.6 Ma; MSWD= 0.97) (Figs. 2.30 and 2.31). Results of zircon dating are presented in Appendix B.

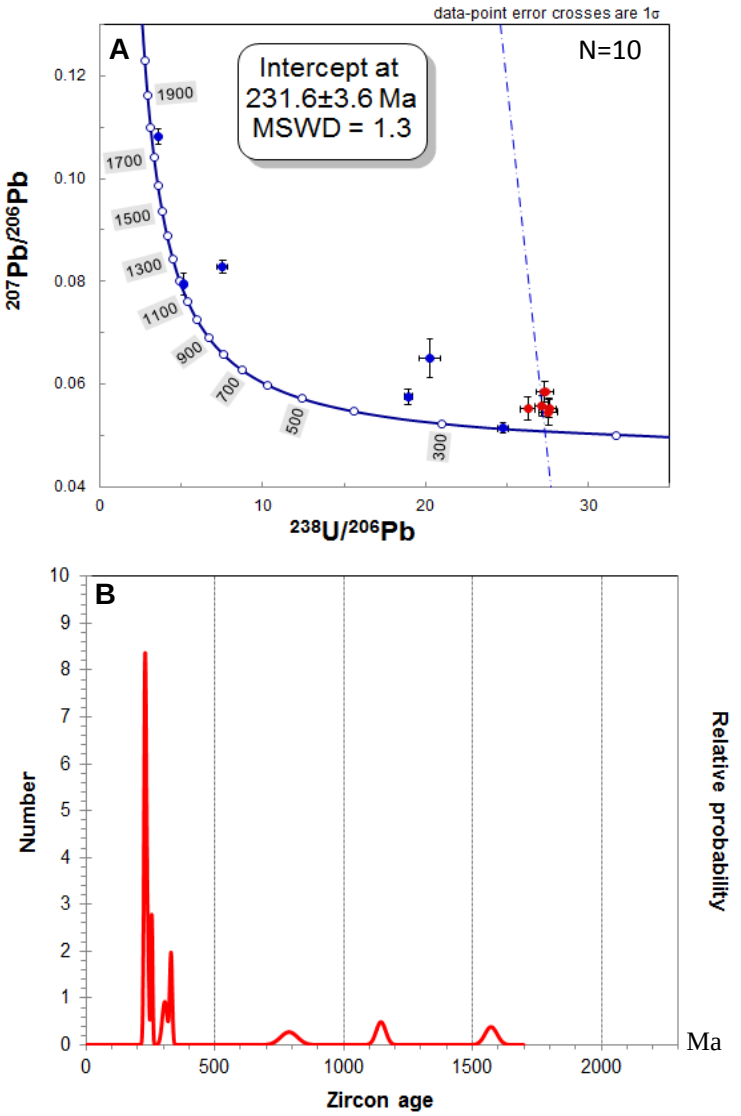

Fig. 2.30. Maximum depositional age of the Semantan tuffaceous sandstone (Sample No. ME-10813). **A**) U-Pb inverse concordia plot indicating a Ladinian age. **B**) Probability plot of the zircon age. The age of the youngest is at

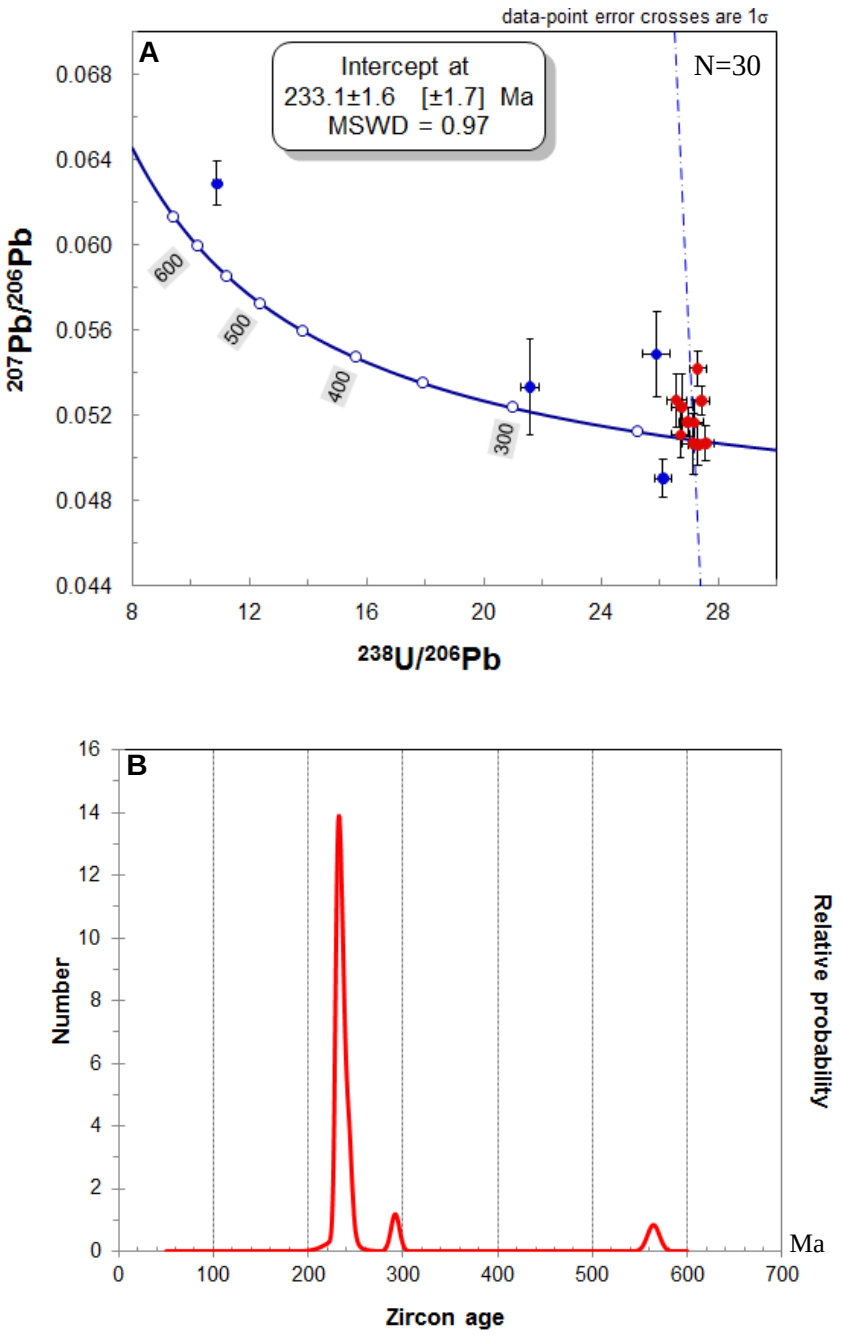

Fig. 2.31. Maximum depositional age of the Semantan tuff (Sample No. ME-6512). **A**) U-Pb inverse concordia plot indicating a Ladinian age. **B**) Probability plot of the zircon age. The age of the youngest zircon is 230 Ma and the calculated mean age of eleven zircon grains is 233 Ma.

Lithologic and textural characteristics of the Semantan Formation are shown in Fig. 2.32 and a summary of mineral composition is presented in Table 2.2.

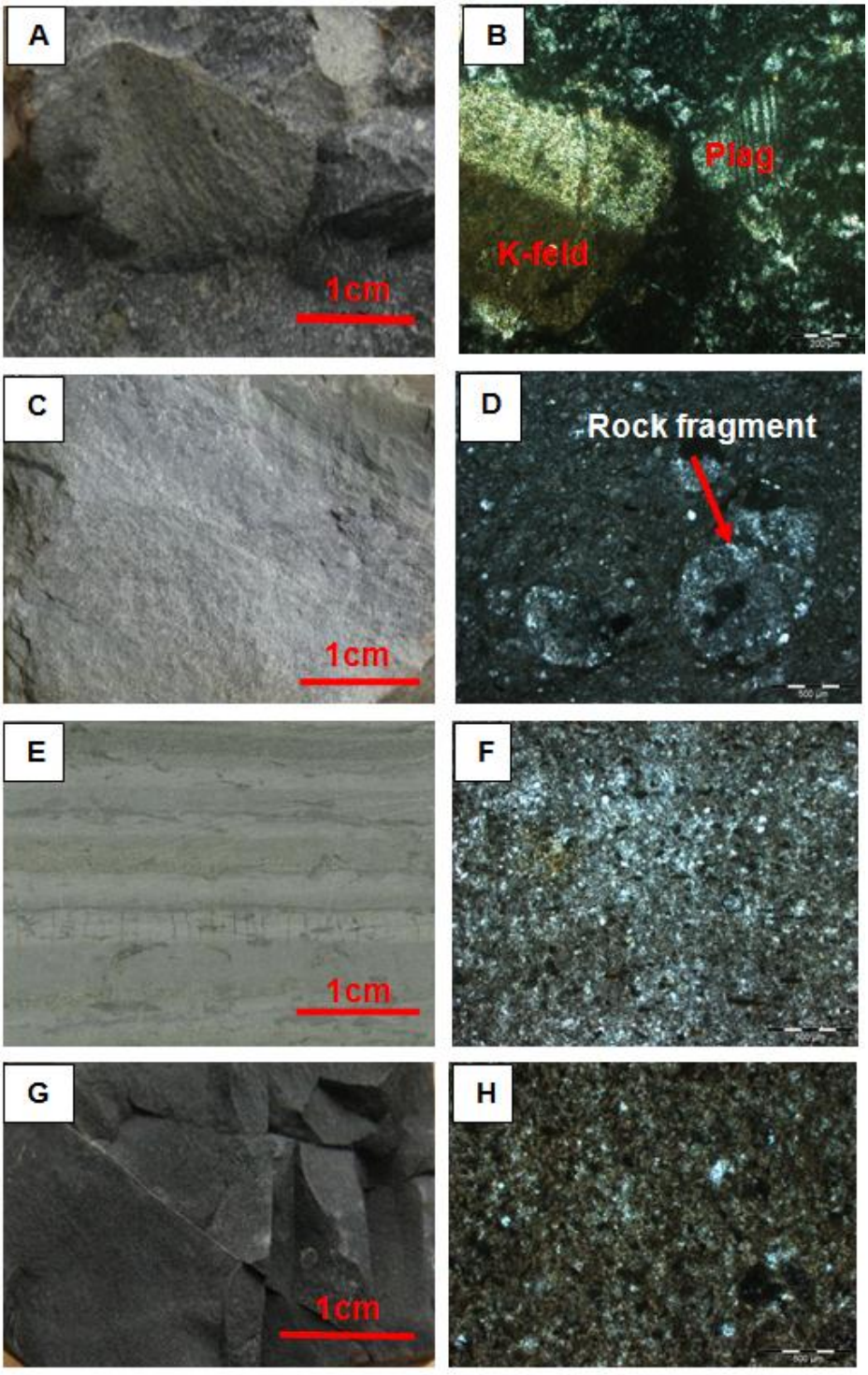

Fig. 2.32. Lithologic and textural characteristics of the Semantan Formation (Middle Triassic). **A**) Hand specimen of crystal-rich tuff (Sample No. ME-6512). **B**) Photomicrograph of tuff in cross polarised light. **C**) Hand specimen of pale grey fine-grained tuff (Sample No. CH-0812). **D**) Photomicrograph of tuff in cross polarised light. **E**) Hand specimen of shale layers with organic matter laminations (Sample No. ME-6612). **F**) Photomicrograph of tuffaceous sandstone in cross polarised light. **G**) Hand specimen of black fine-grained tuff (Sample No. ME-6412). **H**) Photomicrograph of tuff in cross polarised light. Red scale bar is 1 cm long.

Table 2.2. Summary of mineral composition of some tuff and black shale samples for the Semantan Formation, Malaysia.

	Lithology	Quartz	Feldspar	Mica	Lithics	Other
CH-0812	Tuff	Monocrystalline quartz (20%)	Plagioclase (20%);	Muscovite (10%)	Schist fragments (40%); quartzite (10%)	-
ME-6412	Tuff	Monocrystalline quartz (45%)	Orthoclase (25%)	-	Rock fragments (30%)	-
ME-6512	Tuff	Polycrystalline, xenomorphic quartz grains – 30%; straight extinction	Microcline with cross-hatched twinning texture, altered (20%) plagioclase (20 %); sanidine? (10%)	-	20% of rhyolite? Fragments;	-
ME-6612	Black shale	Xenomorphic quartz (60%)	Altered feldspar (20%)	Muscovite (10%)	Rock fragments (10%)	-

2.5.8. Gua Musang Formation (Middle Triassic)

Outcrop images of the Gua Musang Formation and a sedimentary log with stratigraphic positions of collected samples are presented in Figs. 2.33 and 2.34 below.

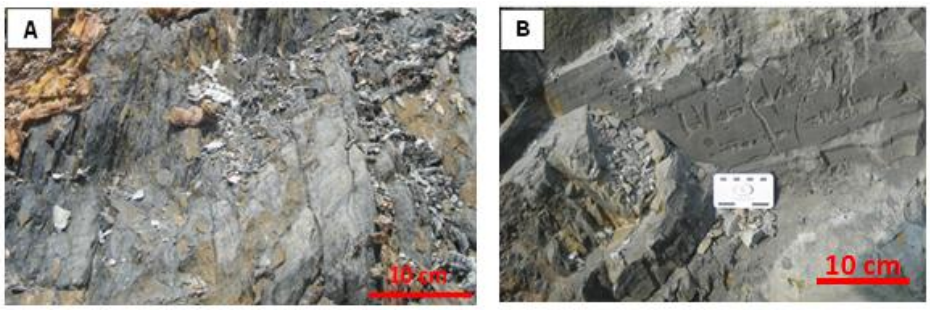

Fig. 2.33. Outcrop photographs of the black shales and greywacke in the Gua Musang Formation. **A**) Black shale exposure. **B**) Close view of the black shale showing the pyrite staining in the red rectangle. 1. The Gua Musang Formation is comprised of interbedded black shales and sandstones. The presence of convolute and parallel laminations in the argillaceous facies and cherts concretions is indicative of deep water, slope basin environment (Makoundi, 2004).

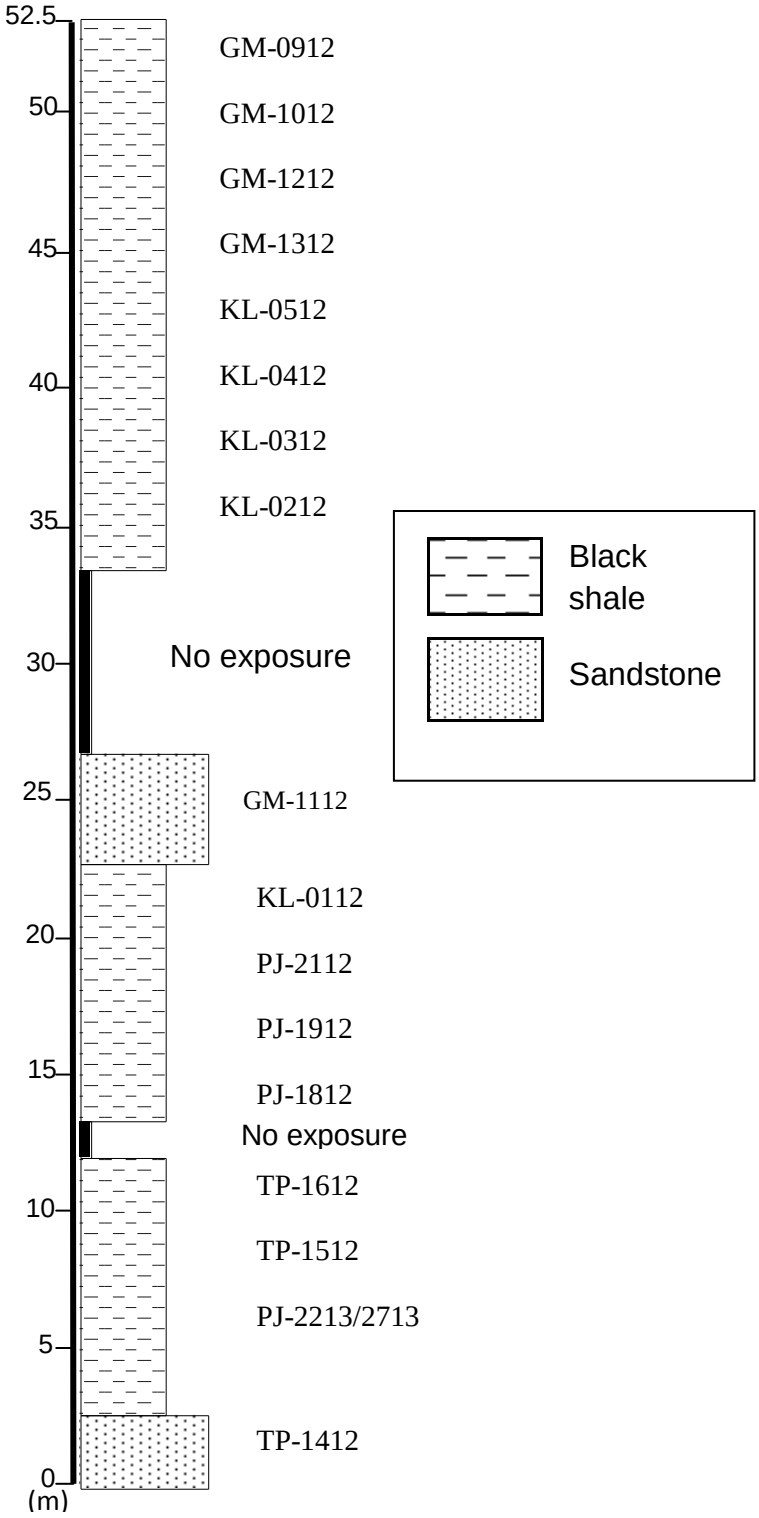

Fig. 2.34. Sedimentary log of a Gua Musang Formation section at Kuala Lipis in Malaysia. The log shows interbedded black shale and sandstone layers. Gaps represent absence of exposures.

Previous work reports the presence of Middle-Upper Anisian *foraminifers* such as *Meandrospira dinarica and Pilamminella grandis* and Middle to Upper Triassic bivalves in shales (Fontaine et al., 1994). The presence of convolute and parallel laminations in the argillaceous facies and cherts concretions is indicative of deep water, slope basin environment (Makoundi, 2004). LA-ICP-MS U-Pb zircon dating (Fig. 2.35) indicates a Middle Triassic age (231 ± 2.9 Ma). Results of zircon dating are presented in Appendix B.

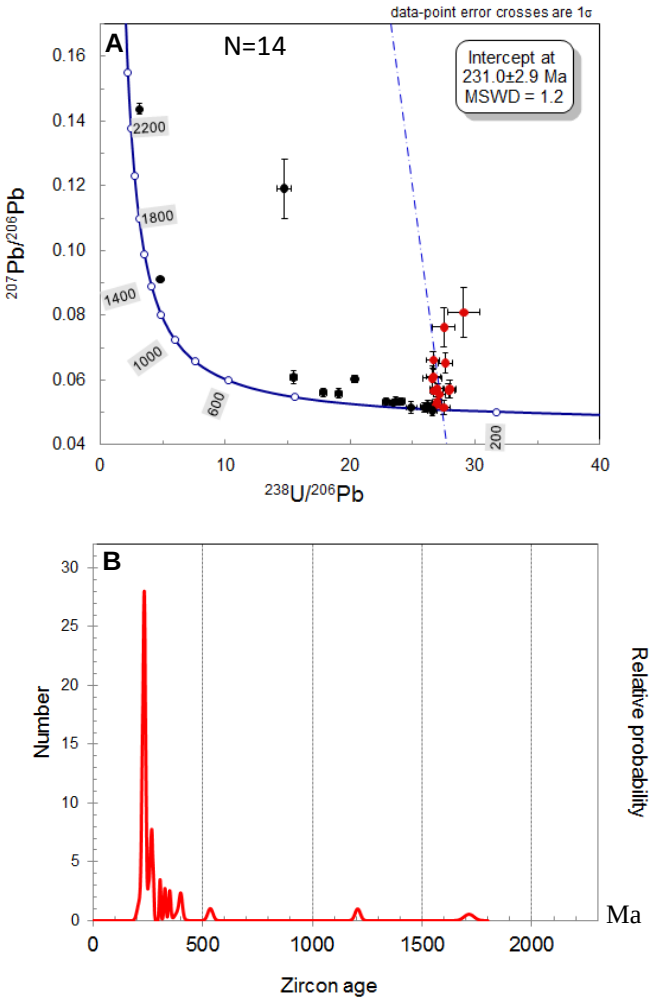

Fig. 2.35. Maximum depositional age of the Gua Musang Formation. **A**) Inverse concordia plot of zircon (Sample No. GM-1112). **B**) Probability plot of the zircon samples.

Lithology and textures of the Gua Musang Formation are shown in Fig. 2.36 below.

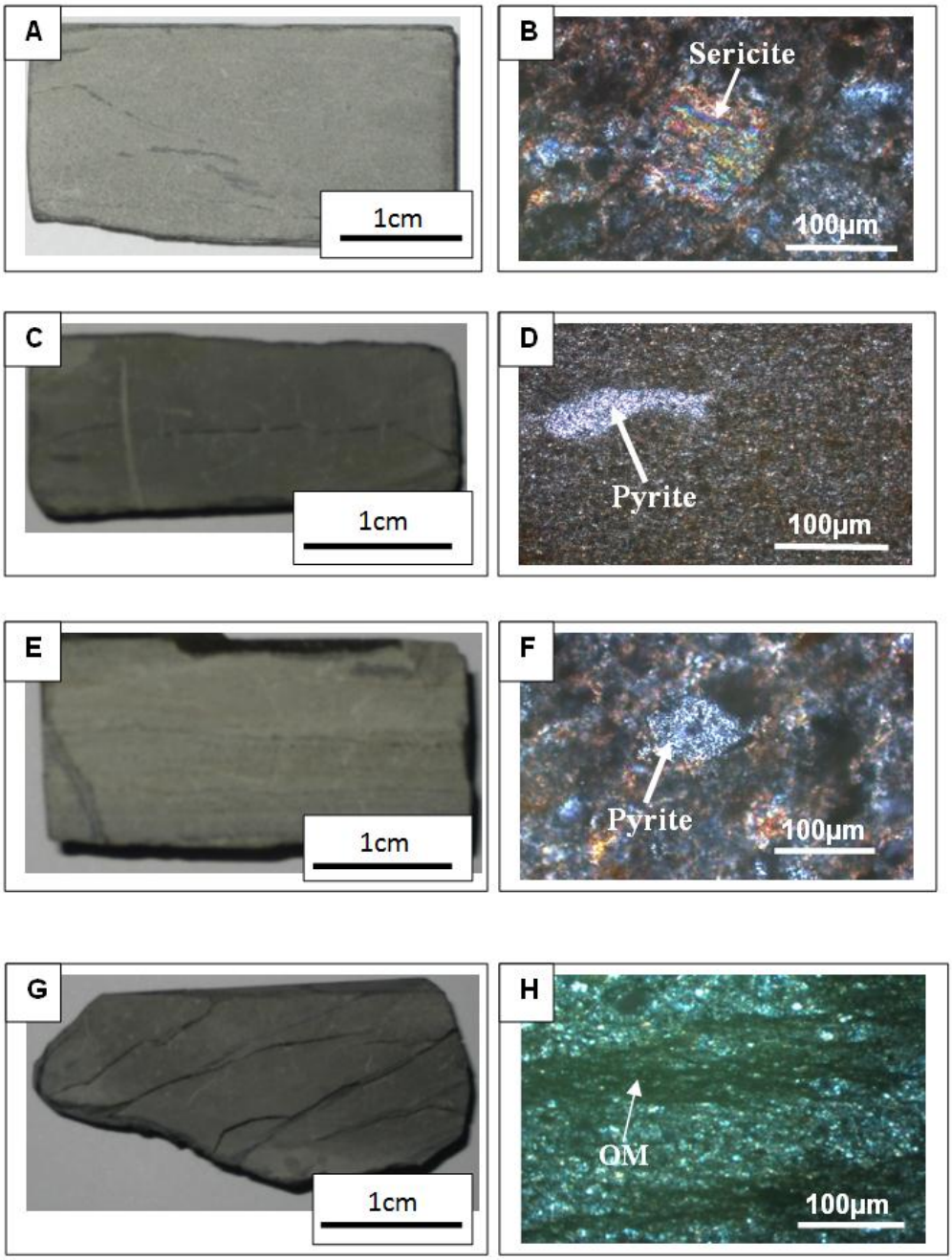

Fig. 2.36. Lithological and textural characteristics of the Black shale in the Gua Musang Formation, Malaysia. **A**) Hand specimen of black shale contains laminations of organic matter (sample KL-0112). **B**) Microscopic picture showing quartz grains (vol. 55%), numerous altered feldspars (40%), and few rock fragments (vol. 5%). Picture taken under crossed polarized light. **C**) Hand specimen of black shale (sample PJ-1812). **D**) Photomicrograph of the black shale showing angular quartz grains (vol. 60%), few rock fragments (vol. 5%), and altered feldspars to sericite (vol. 35%). **E**) Hand specimen of the grey shale (sample KL-0512) showing thin organic matter laminations. **F**) Photomicrograph showing monocrystalline quartz (vol. 45%), clays (vol. 50%) and some altered feldspar (vol. 5%). **G**) Hand specimen of the black shale (sample KL-0312). **H**) Photomicrograph showing quartz grains (vol. 65%), altered K-feldspar (vol. 25%), plagioclase (vol. 5%), and rock fragments (up to vol. 5%). Note: bands of organic matter (OM).

2.5.9. BRSZ Unit 2 (Late Triassic)

The Late Triassic BRSZ Unit 2 is a chert exposure (Fig. 2.37) which extends up to 100 m wide and crops out in the Bentong-Raub Suture Zone (BRSZ). The suture is thought to be genetically related to the gold mineralization in the Central Gold Belt of Malaysia (Wan Fuad and Purwanto, 2002). The exposure is comprised of bedded cherts interbedded with few sandstone layers and cross-cut by quartz veins (Fig. 2.37).

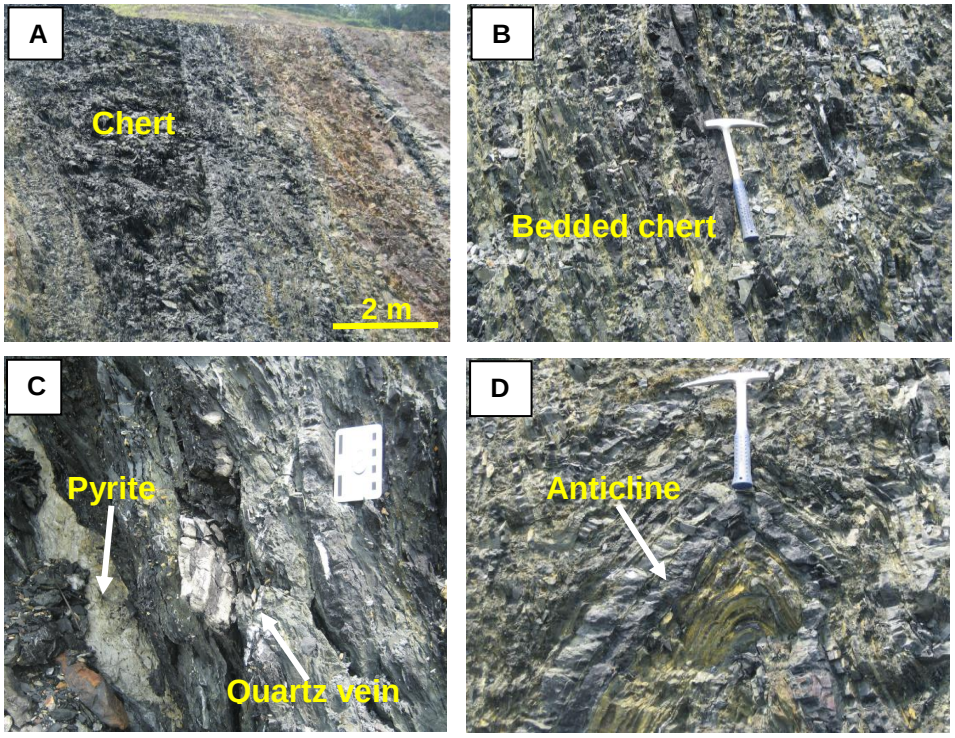

Fig. 2.37. Outcrop photographs of cherts in the BRSZ Unit 2 in Malaysia. **A**) Main chert outcrop. **B**) Bedded chert. **C**) Massive pyrite boudinaged band in chert. **D**) Folded cherts.

Mustaffa Kamal (2000) reported that these bedded cherts were found intercalated with sandstone and shales layers. The cherts contain radiolarian and associated with olistostromes (chaotic sedimentary deposits) which were interpreted to have deposited in a deep marine

environment. Dextral transcurrent movements resulted in the uplift and inversion of the chert-argillite units. As a consequence, by Late Triassic these deposits would have been further tectonized in a dextral transpressive regime. Sedimentary log of this unit is shown in Fig. 2.38.

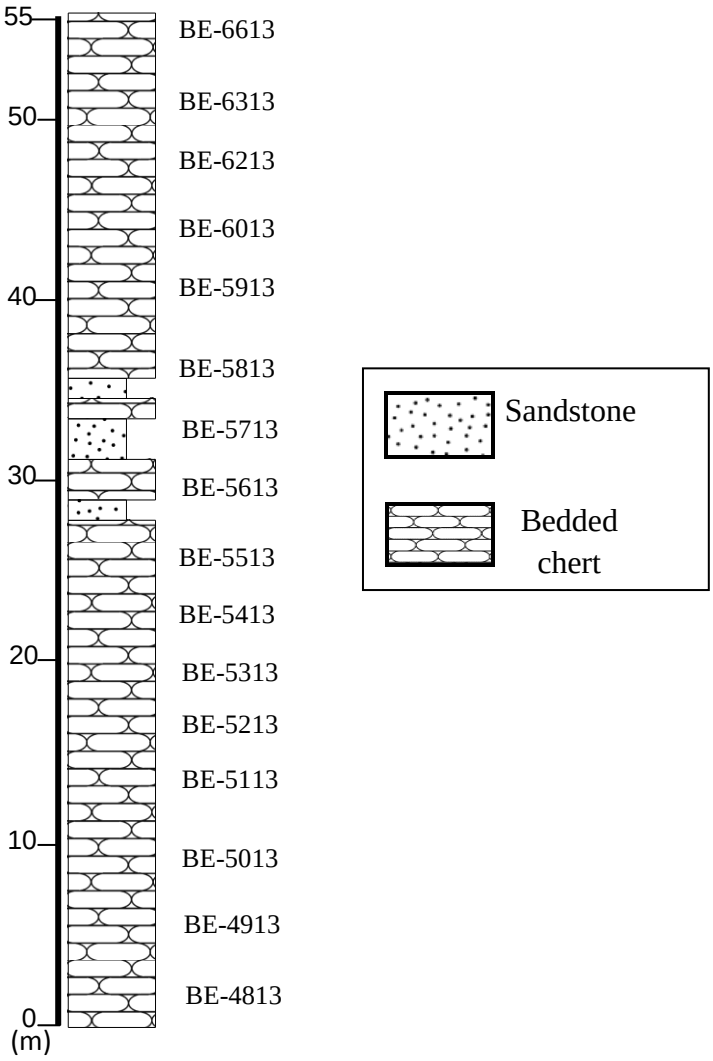

Fig. 2.38. Sedimentary log of the Late Triassic BRSZ Unit 2 (Fig. 2.37) showing stratigraphic position of collected samples. Location: West of Bentong town (see location in Fig. 2.22), Malaysia. The sequence is made of bedded black cherts interbedded with massive sandstone.

Occurrences of radiolarian were reported from the black bedded cherts as having Late Devonian age (Basir, 2013). Those cherts were not mapped at the same location with the

samples collected in this study. LA-ICP-MS U-Pb zircon dating result indicates a Late Triassic (Norian) age (207.1±3.2 Ma) (Fig. 2.39) for the sandstones. Results of zircon dating are presented in Appendix B.

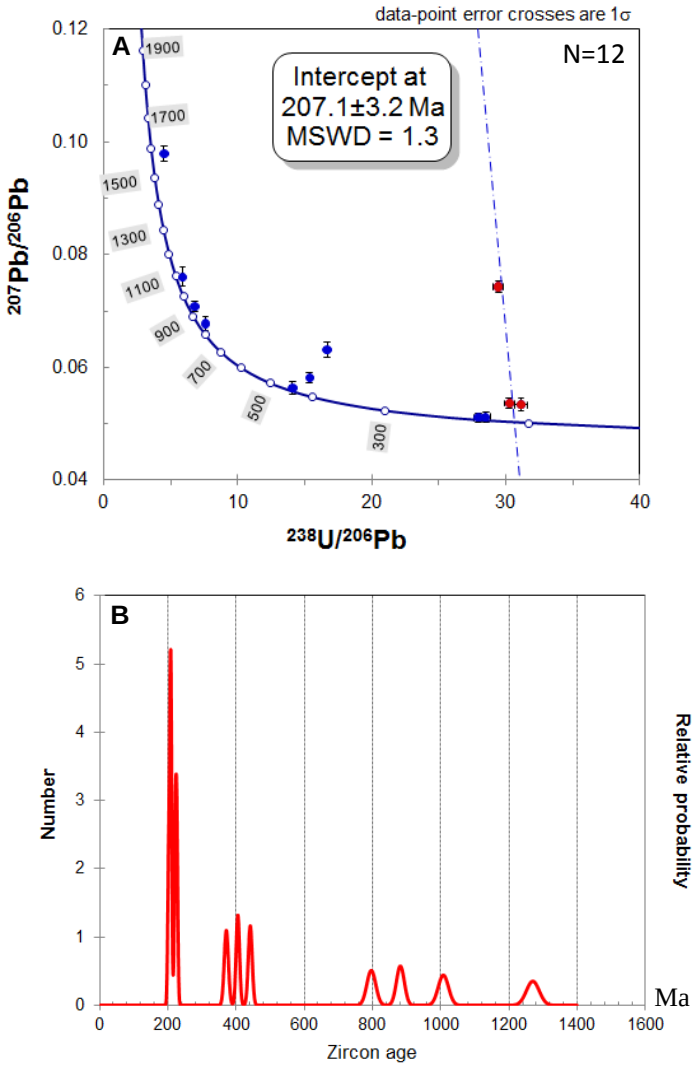

Fig. 2.39. Geochronology of the BRSZ Unit 2 sandstones which are interbedded with cherts. **A**) U–Pb inverse concordia plot of zircons (Sample BE-5913). **B**) Probability plot. In this thesis, the Semantan and Karak volcaniclastic sequences zircon ages are taken as accurate ages excluding other formations (i.e. non volcaniclastic sequences). Similar volcaniclastic sequences ages were determined in past research (Amato and Pavlis, 2010).

2.6. Discussion of U-Pb zircon dating (this study) and fossil data (previous work)

The age determination from zircon grains and paleontological data show some inconsistencies. In the Palaeozoic, the Machinchang Formation should have an age ranging from Late Cambrian to Early Ordovician; however, the maximum depositional age from the detrital zircon dating returned an age of Late Ordovician. This age is much younger and unreliable due to perhaps sample contamination or the bed of sampled Machinchang Formation may have been wrongly attributed to the F6 sequence. The sampled horizon may be the lower part of the Setul Formation. Therefore, in the following chapters, for the Machinchang Formation, the fossil age will be taken into account for age accuracy and trace element variation plots through time. *Trilobite* faunas found within the Machinchang Formation plus lithostratigraphic correlation with the Tarutao Formation 10km away in Thailand give consistent age which ranges from Late Cambrian to Early Ordovician (Stait et al., 1984 and 1987; Shergold et al., 1988; Wongwanich et al., 2001; Burrett et al., 2014).

The Setul Formation fossil age ranges from Early Ordovician (Tremadoc) to Silurian. The detrital zircon age is 427 Ma which matches with the fossil age. As mentioned previously (section 2.3), the Setul Formation is subdivided into the lower Setul (Tremadoc to Hirnantian) and the upper Setul Limestone (Silurian). The sampled section in this thesis is the detrital band that separates the lower and upper Setul Formation. The Singa Formation detrital zircon age is 418 Ma. Nevertheless, this age does not preclude a younger age. All other evidences (fossils and glacial deposits) point to a Pennsylvanian to early Permian age. This fossil age is also supported by data from the Kaeng Krachan Group (formely Phuket Group) just across the border in Thailand (Mitchell, 1970; Waterhouse, 1982). Detrital zircon ages for other formations such as BRSZ Unit 1, Semantan, Karak, Gua Musang, and BRSZ Unit 2 are consistent with the fossil ages and have been considered in this thesis.

CHAPTER 3
PALAEOZOIC FORMATIONS

3.1. Introduction

This chapter covers the lithostratigraphy and geochemistry of the Palaeozoic formations. The formations that have been studied are the Late Cambrian-Early Ordovician Machinchang, Early Ordovician-Silurian Setul, Pennsylvanian-Early Permian Singa, Carboniferous black shales at the Selinsing gold deposit, and the Late Devonian BRSZ Unit 1. It summarizes the petrographic features of the sedimentary rocks and extends into the lithogeochemistry and pyrite chemistry. Chemical comparison is discussed among the Palaeozoic formations throughout the chapter. A discussion of controls on gold deposition and relationship among gold and some trace elements are explored. This Chapter also presents the results of pyrite chemistry to evaluate whether sedimentary or magmatic-hydrothermal processes prevailed during pyrite formation. A sketch map that shows the distribution of the Palaeozoic formations is shown in Figure 3.1.

3.2. Machinchang Formation (Late Cambrian-Early Ordovician)

3.2.1. Major element compositions

The aims of major and trace element analysis in this chapter are: 1) To determine the composition of major, and trace elements in whole rocks, and 2) To compare whole rock compositions with standard shales (e.g. PAAS) and upper continental crust sediments (UCC). Mean of major and trace element compositions of each Palaeozoic formation are compared to the average composition of Post-Archean Australian Shale (PAAS) from Taylor and McLennan (1985).

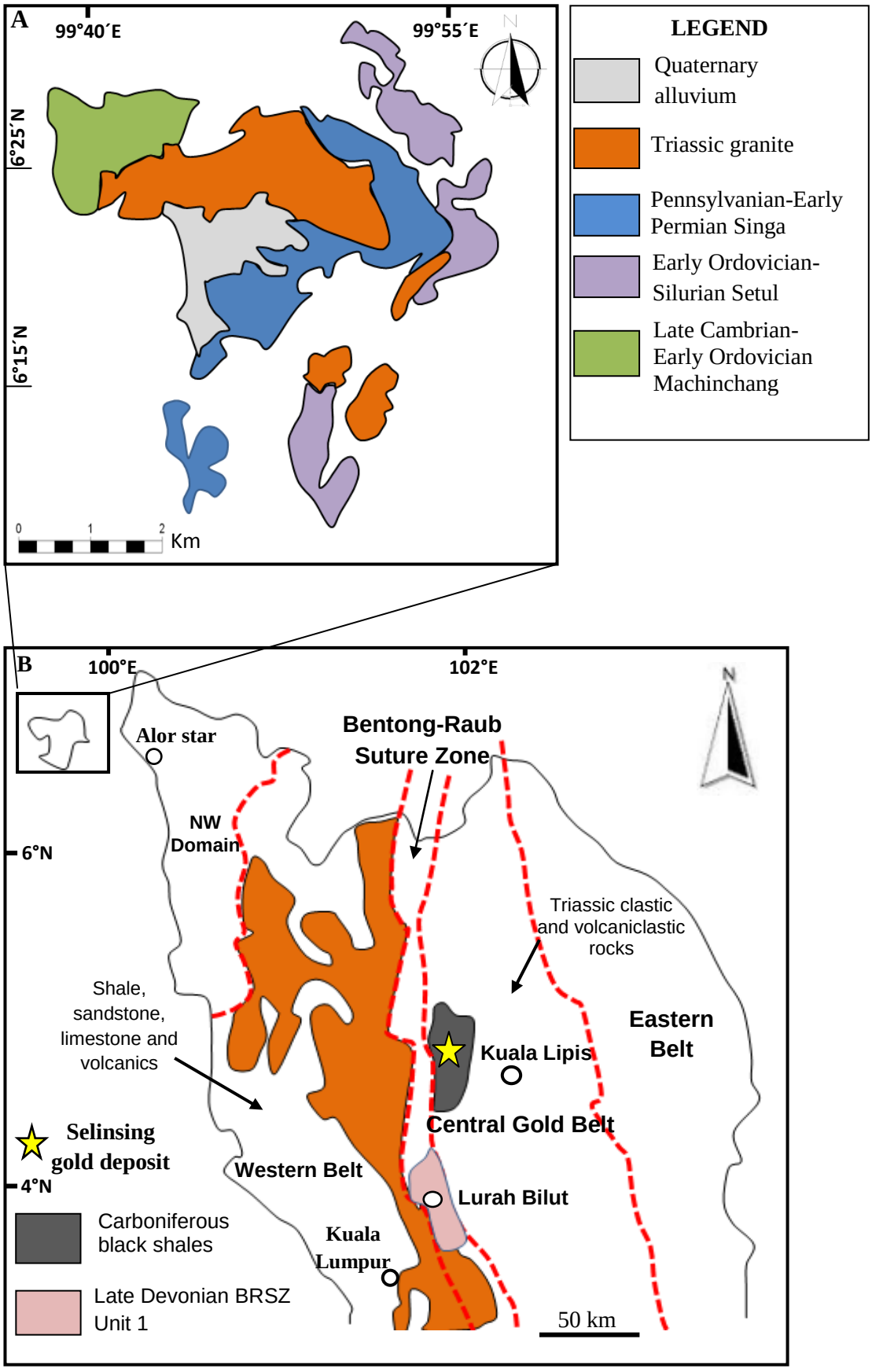

Fig. 3.1. Geological map of selected Palaeozoic formations in this study. **A**) Geological map of the Langkawi Island showing the three Palaeozoic formations Machinchang, Setul and Singa. **B**) Mainland Peninsular Malaysia map displaying the two Palaeozoic formations which include the Selinsing black shales and the BRSZ Unit 1.

The Wedephol's Average Shale (WAS) from Wedephol (1985), the North American Shale Composite (NASC) from Gromet et al. (1984), and the Upper Continental Crust (UCC) from Taylor and McLennan (1985) are also shown in Table 3.1. Fresh and less weathered sandstone and shale samples were collected from both the F5 and F6 sequences of the Late Cambrian-Early Ordovician Machinchang Formation. These samples were analysed for their major, and trace elements using LA ICP-MS (Laser Ablation Inductively Coupled Plasma Mass Spectrometry) and XRF (X-ray fluorescence analysis) techniques at University of Tasmania. In the dataset, detection limit for all the major element including total sulphur content is 0.01 wt %. In addition, the detection limits of analysed trace elements are: Sc (1.5 ppm), Ba (4 ppm), V (3 ppm), Cr (1 ppm), Ni (1 ppm), Cu (1 ppm), Zn (1 ppm), Ga (2 ppm), As (3 ppm), Se (1 ppm), Rb (0.5 ppm), Sr (1ppm), Y (1 ppm), Zr (1 ppm), Nb (0.5 ppm), Mo (0.5 ppm), Ag (2 ppm), Sn (1 ppm), Sb (2 ppm), Te (2 ppm), Tl (2 ppm), Pb (1 ppm), Bi (2 ppm), U (2 ppm), Th (2 ppm), La (4 ppm), Ce (6 ppm), and Nd (4 ppm).

The grey shales are enriched in K_2O and depleted in Fe_2O_3, MgO, Na_2O, and P_2O_5 compared with PAAS, WAS, NASC and UCC. Mean contents of major elements in the grey shales are SiO_2 (57.05 wt %), Al_2O_3 (23.4 wt %), MgO (1.4 wt %), Na_2O (0.07 wt %), K_2O (8.5 wt %), Fe_2O_3 (4.7 wt %), MnO (<0.01 wt %), CaO (<0.01 wt%), TiO_2 (0.9 wt %), and P_2O_5 (0.07 wt %). A spider plot of major elements in grey shales compared with PAAS is shown in Fig. 3.2 and emphasises the enrichment in K_2O and depletion in Na_2O. The Al_2O_3 versus K_2O plot (Fig. 3.3) further indicates that the composition of these major elements may have been significantly controlled by microcline perthite from the source rocks coupled with a weak clay control (illite presence) as shown on Fig. 3.3. The mean compositions of the sandstone and shale samples for the Machinchang Formation are shown in Table 3.1. LA ICP-MS solution gold data is given in Appendix B.

Table 3.1. The mean composition of the major and trace elements in sandstones and shales for the Machinchang Formation in comparison with the average of well-known standards.

	Sandstone (n=3)	Grey shale (n=3)	PAAS	WAS	NASC	UCC
SiO_2 (wt %)	67.88	57.05	62.8	58.9	64.8	61.6
TiO_2	0.76	0.90	1	0.8	0.78	0.67
Al_2O_3	16.55	23.44	18.9	16.7	16.9	15.2
Fe_2O_3	4.48	4.67	7.22	6.9	5.7	6.2
MnO	<0.01	<0.01	0.11	-	0.06	0.09
MgO	1.28	1.38	2.2	2.6	2.9	3.7
CaO	0.20	<0.01	1.3	2.2	3.4	5.5
Na_2O	0.61	0.07	1.2	1.6	1	3.2
K_2O	5.35	8.53	3.7	3.6	3.8	3.4
P_2O_5	0.11	0.07	0.16	-	0.13	0.17
Loss	2.92	3.74	-	-	-	-
Total	100.02	99.87	-	-	-	-
TOC (wt %)	0.03	0.12	-	-	-	-
S (wt %)	0.01	0.01	-	-	-	697
Sc	15.76	22.76	16	-	14.9	16
Ba	752.00	1003.67	650	580	636	584
V	124.67	171.33	150	130	-	98
Ni	16.27	25.08	55	68	58	56
Cu	9.46	4.17	50	45	-	25
Zn	67.94	30.30	85	95	-	65
Cr	82.90	118.77	110	90	125	126
Ga	21.46	30.76	20	-	-	15
As	13.87	5.03	-	10	28.4	1.7
Co	11.03	4.37	23	19	-	10
Au (ppb)	42.67	49.33	-	2.3	-	-
Se	0.50	0.50	-	0.5	-	0.12
Rb	213.13	319.36	160	140	125	78
Sr	51.50	32.73	200	300	142	333
Y	32.73	50.23	27	-	-	24
Zr	246.07	202.43	210	160	200	203
Nb	17.37	19.63	19	-	-	19
Mo	0.63	0.97	1	1	-	1.1
Ag	-	0.30	-	0.07	-	0.07
Cd	-	-	-	-	-	-
Sn	4.73	6.17	4	6	-	2.3
Sb	3.83	5.10	-	1.5	2.09	0.3
Te	-	0.10	-	-	-	0.005
Tl	0.84	1.31	-	0.68	-	0.52
Pb	86.01	38.77	20	22	-	0.0004
Bi	0.13	0.35	-	0.1	-	0.085
Th	19.70	25.08	14.6	-	12.3	8.5
U	3.31	5.33	3.1	3.7	2.66	1.7

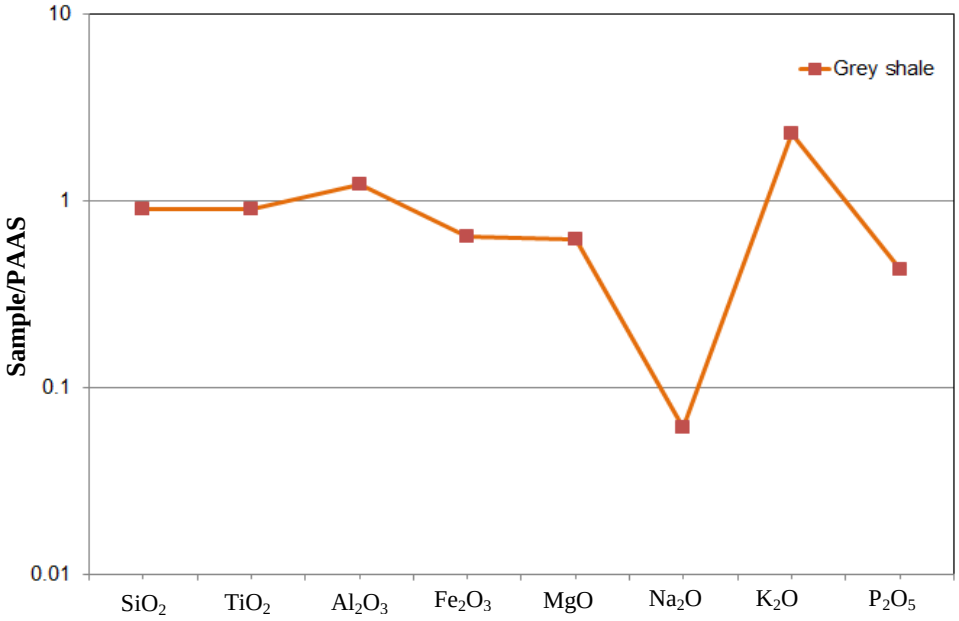

Fig. 3.2. Spider plot of major element composition (mean values) of the Machinchang grey shales normalized to PAAS. The CaO and MnO contents are not shown as they are below detection limit (less than 0.01).

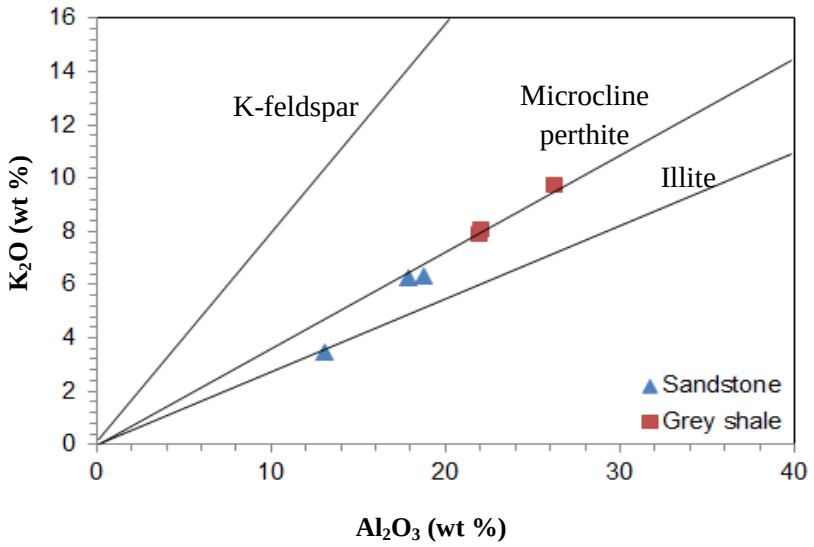

Fig. 3.3. Relationship between alumina and K_2O in sandstone and grey shales for the Late Cambrian-Early Ordovician Machinchang Formation. The plot also displays the K-feldspar, microcline perthite and illite lines. Noticeably, the contents of K_2O and Al_2O_3 are plotted along the microcline perthite and illite lines. The microcline perthite and illite compositional lines are drawn based on data from Deer et al. (1966).

3.2.2. Trace element compositions

In this section, the mean compositions of selected trace elements are normalised to PAAS in order to discuss the relative enrichment and depletion of trace elements. The trace elements are arranged in order of increasing atomic number. The grey shales are enriched in Sn, Th, and U and depleted in Co, Ni, Cu, and Zn compared to PAAS (Fig. 3.4). Previous researchers have used Al_2O_3 content as a proxy for detrital control (aluminosilicate fraction in the sediments) to suggest detrital origin of trace elements absorbed onto clay particles or enclosed in the structure of aluminosilicate minerals (Calvert and Pedersen, 1993; Tribovillard et al., 1994; Hild and Brumsack, 1998; Böning et al., 2004; Tribovillard et al., 2006). In the grey shales, elements that show a positive correlation with Al_2O_3 are Au, Sn, Ni, Cr, V, and organic carbon but those that display a negative correlation include As, and Mo. In the sandstones, positive correlation is shown by Au, Sn, Cr, V, Mo; however, the elements such as Ni, As, and organic carbon display a negative correlation with Al_2O_3 (Figs. 3.5-3.7).

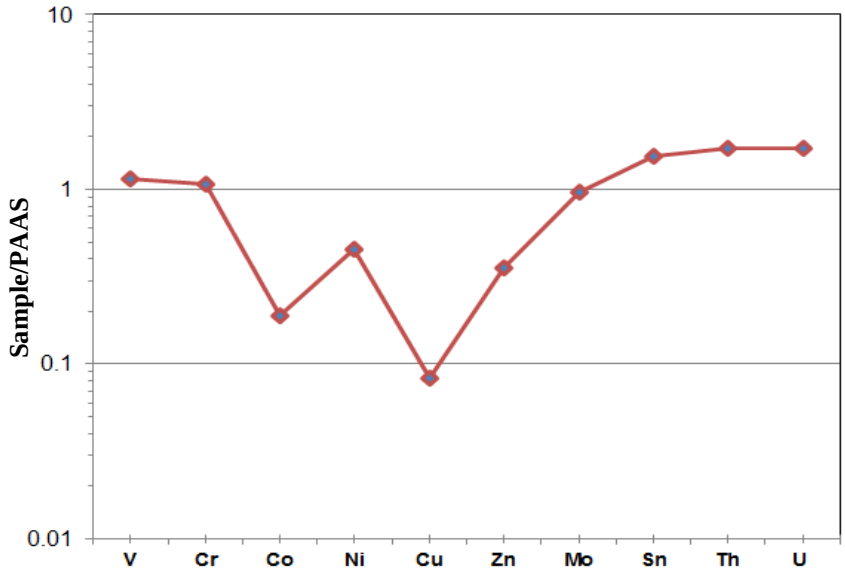

Fig. 3.4. Average composition of selected trace elements in grey shales normalised to PAAS for the Machinchang Formation.

Correlation coefficients for the sandstones and shales are shown in Table 3.2 below.

Table 3.2. Values of Pearson's coefficient of correlation of Al_2O_3, organic carbon and selected trace elements in grey shales of the Late Cambrian-Early Ordovician Machinchang Formation. Because of the low numbers of samples these correlation coefficients are a first order approximation. Highlighted numbers represent values equal to or greater than 0.5.

Correlation	Al_2O_3_wt %	Org.C_wt %	S_wt %	V_ppm	Cr_ppm	Ni_ppm	Cu_ppm	Zn_ppm	As_ppm	Mo_ppm	Co_ppm	Sn_ppm	Sb_ppm	Au_ppb
Al_2O_3_wt %	1													
Org.C_wt %	-0.15	1												
S_wt %	6.00E-16	9.70E-17	1											
V_ppm	1	-0.17	1.20E-15	1										
Cr_ppm	0.92	-0.51	1.20E-15	0.93	1									
Ni_ppm	0.99	-0.25	4.30E-16	1	0.96	1								
Cu_ppm	-0.6	0.88	0	-0.62	-0.86	-0.68	1							
Zn_ppm	-0.47	-0.8	-1.40E-16	-0.45	-0.098	-0.38	-0.42	1						
As_ppm	-0.97	-0.086	0	-0.97	-0.81	-0.94	0.4	0.66	1					
Mo_ppm	-0.47	-0.8	-3.10E-16	-0.46	-0.1	-0.38	-0.42	1	0.67	1				
Co_ppm	0.79	0.49	1.80E-16	0.78	0.5	0.72	0.016	-0.91	-0.91	-0.91	1			
Sn_ppm	0.84	0.41	8.70E-16	0.83	0.57	0.78	-0.068	-0.87	-0.94	-0.88	1	1		
Sb_ppm	0.88	-0.6	2.00E-16	0.89	0.99	0.92	-0.91	0.0056	-0.75	-1.60E-16	0.4	0.48	1	
Au_ppb	0.95	-0.44	9.50E-16	0.96	1	0.98	-0.81	-0.18	-0.86	-0.19	0.57	0.64	0.98	1

Table 3.2 (continued) Values of Pearson's coefficient of correlation of Al_2O_3, organic carbon and selected trace elements in sandstones of the Late Cambrian-Early Ordovician Machinchang Formation. Highlighted numbers represent values equal to or greater than 0.5.

Correlation	Al_2O_3_wt %	Org.C_wt %	S_wt %	V_ppm	Cr_ppm	Ni_ppm	Cu_ppm	Zn_ppm	As_ppm	Mo_ppm	Co_ppm	Sn_ppm	Sb_ppm	Au_ppb
Al_2O_3_wt %	1													
Org.C_wt %	-0.93	1												
S_wt %	-0.99	0.97	1											
V_ppm	1	-0.93	-0.99	1										
Cr_ppm	1	-0.93	-0.99	1	1									
Ni_ppm	-0.99	0.86	0.95	-0.99	-0.99	1								
Cu_ppm	-0.92	1	0.97	-0.92	-0.92	0.84	1							
Zn_ppm	-0.087	0.45	0.24	-0.084	-0.097	-0.071	0.48	1						
As_ppm	-0.84	0.98	0.91	-0.84	-0.84	0.74	0.99	0.61	1					
Mo_ppm	0.63	-0.29	-0.5	0.63	0.62	-0.74	-0.26	0.72	-0.1	1				
Co_ppm	-1	0.93	0.99	-1	-1	0.99	0.92	0.1	0.85	-0.62	1			
Sn_ppm	1	-0.95	-1	1	1	-0.97	-0.94	-0.15	-0.87	0.57	-1	1		
Sb_ppm	0.71	-0.39	-0.59	0.71	0.7	-0.81	-0.37	0.64	-0.21	0.99	-0.7	0.66	1	
Au_ppb	0.93	-0.73	-0.87	0.93	0.93	-0.98	-0.71	0.28	-0.59	0.87	-0.93	0.91	0.92	1

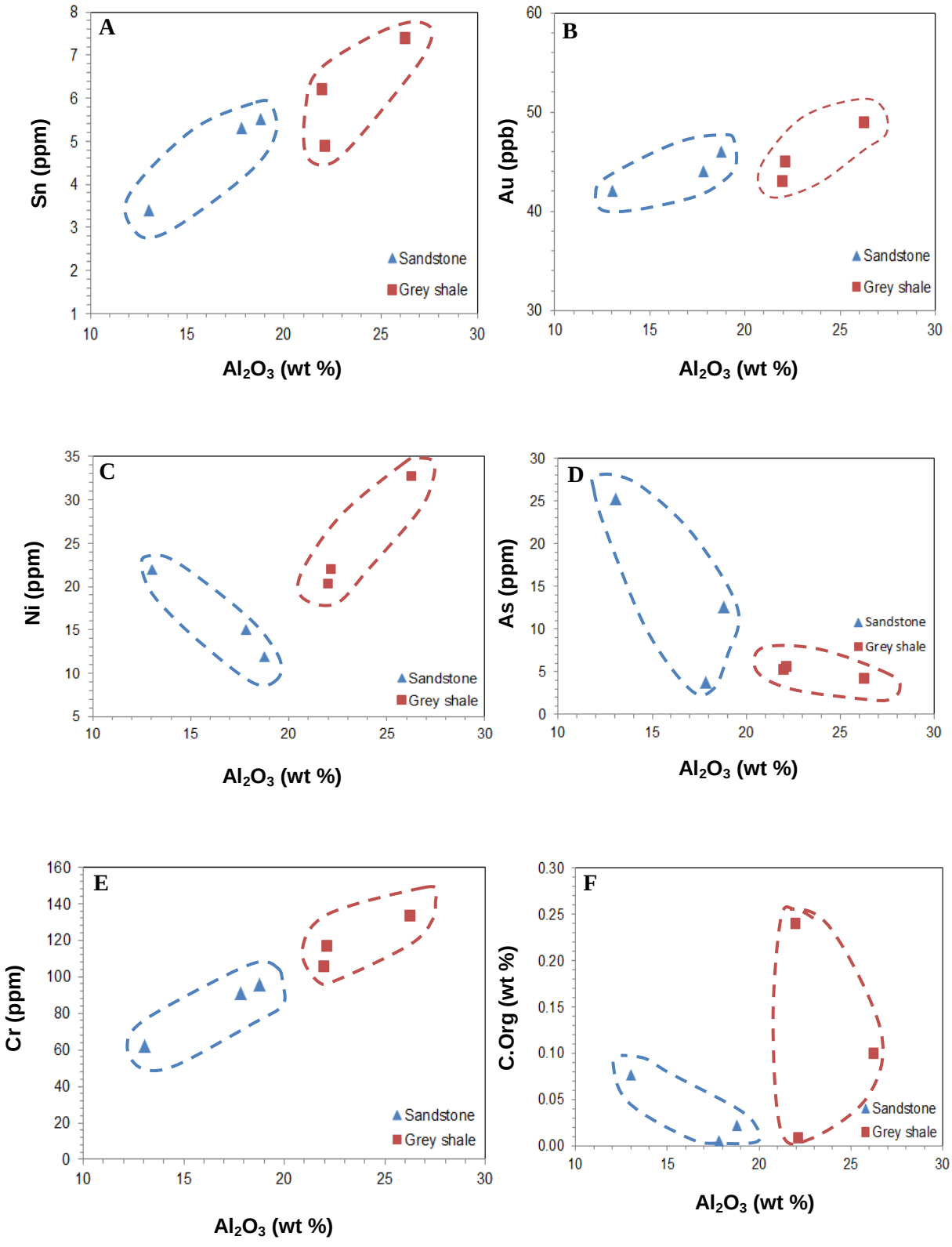

Fig. 3.5. Binary plots showing relationships of alumina to Sn, Au, Ni, As, Cr, and organic carbon in the Late Cambrian-Early Ordovician Machinchang Formation. **A**) Al_2O_3 vs Sn. **B**) Al_2O_3 vs Au. **C**) Al_2O_3 vs Ni. **D**) Al_2O_3 vs As. **E**) Al_2O_3 vs Cr. **F**) Al_2O_3 vs Organic carbon (C. Org).

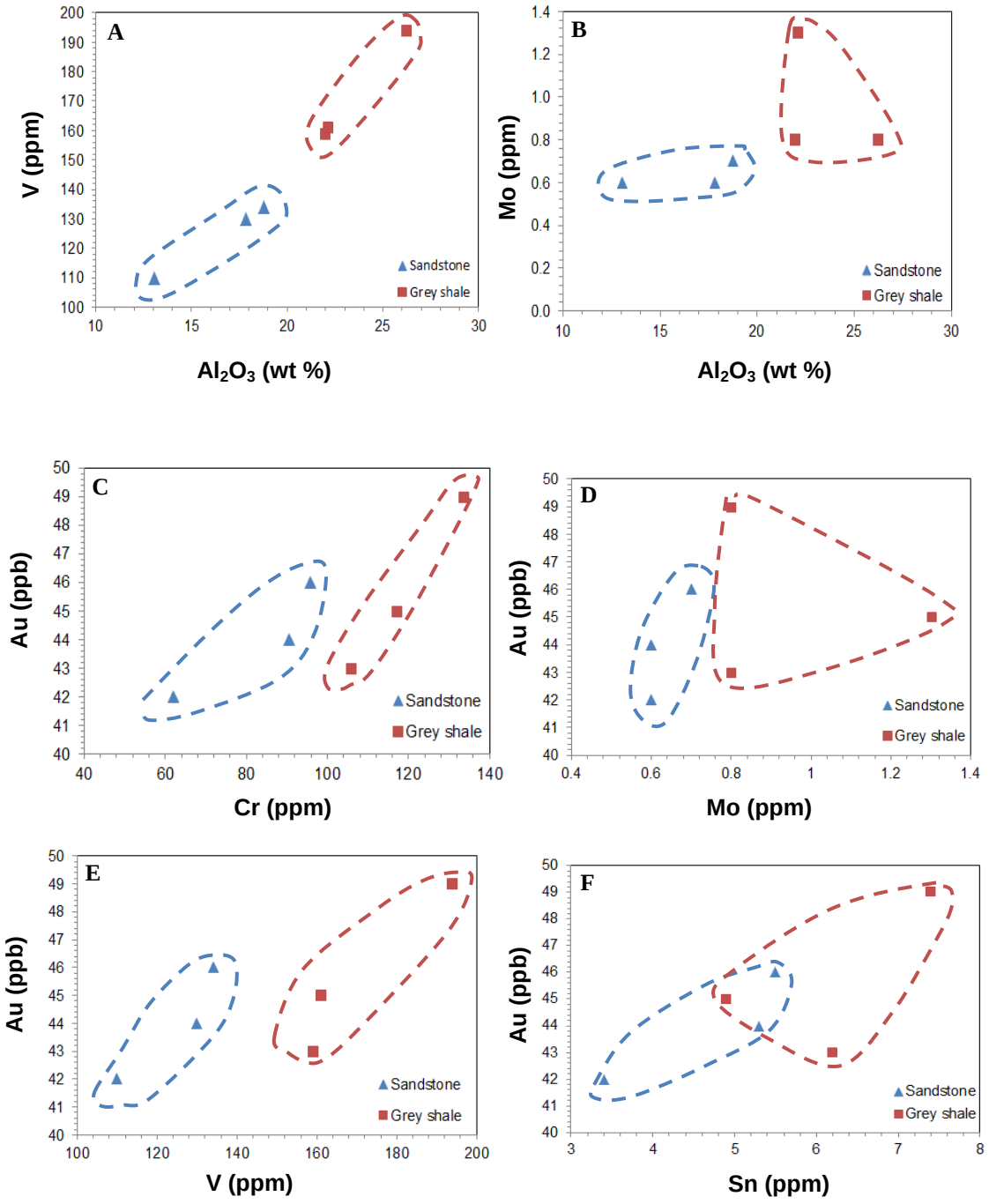

Fig. 3.6. Geochemical binary plots of the sandstones and grey shales for the Late Cambrian-Early Ordovician Machinchang Formation. **A**) Al_2O_3 vs V. **B**) Al_2O_3 vs Mo. **C**) Au vs Cr. **D**) Au vs Mo. **E**) Au vs V. **F**) Au vs Sn.

In the shales, gold shows a positive correlation with Al_2O_3, V, Cr, Ni, Co, Sn and Sb. Organic carbon relations to some trace elements are shown in Fig. 3.6. There is no clearly consistent pattern of trace element variation with organic carbon in the shales (Fig. 3.7).

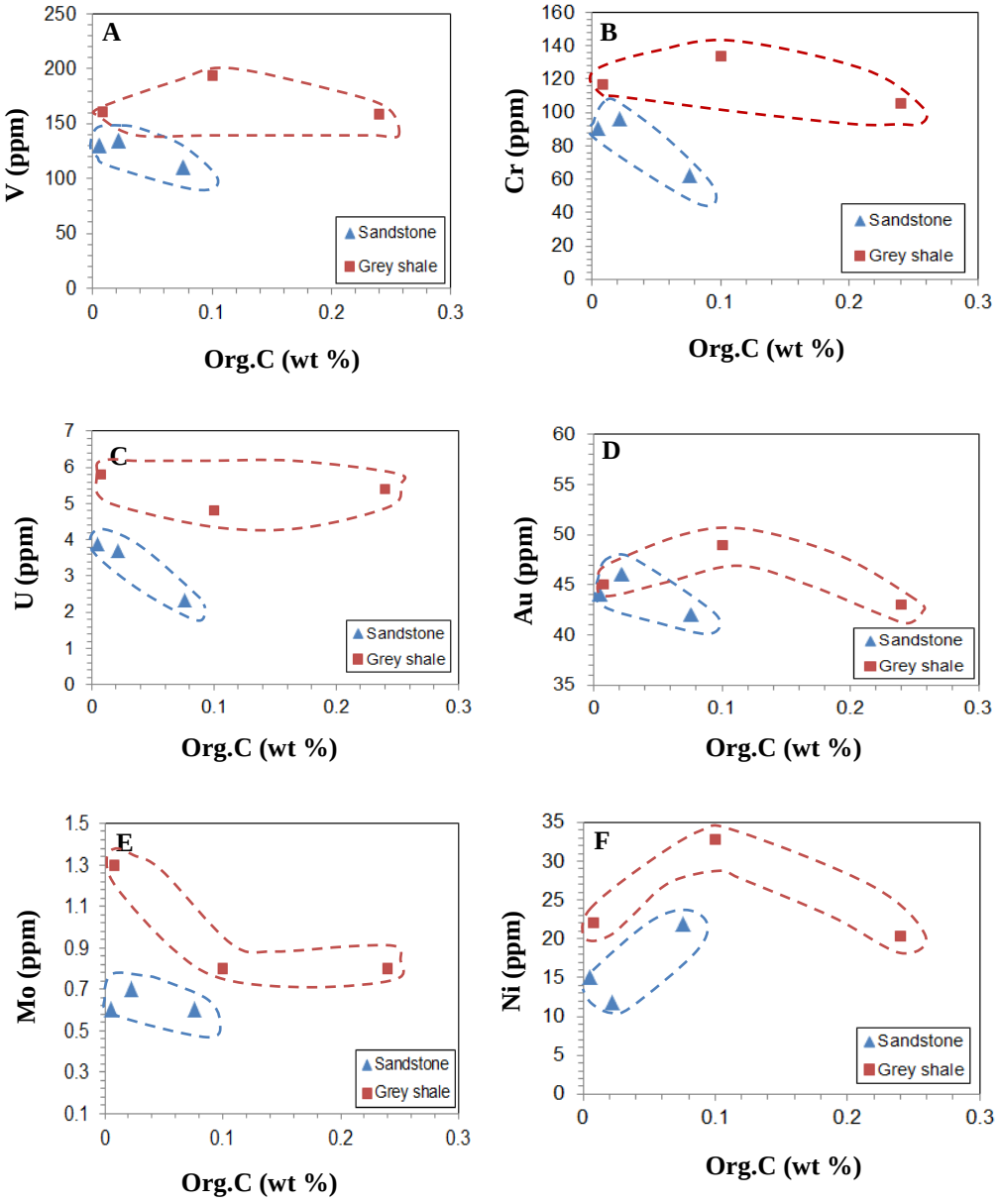

Fig. 3.7. Binary plots of relationships between organic carbon and selected trace elements for the Late Cambrian-Early Ordovician Machinchang Formation. **A**) Organic Carbon versus V. **B**) Organic carbon versus Cr. **C**) Organic carbon versus U. **D**) Organic carbon versus Au. **E**) Organic carbon versus Mo. **F**) Organic matter versus Ni.

The positive correlation among Al_2O_3 and V, Cr, Ni, Co, Sn, Sb, and Au as shown in the correlation Table 3.2 suggests that these trace elements are being introduced to the sedimentary environment attached to aluminous clay minerals. However, the negative or flat correlation of Al_2O_3 with As, Mo and organic carbon suggests these trace elements are unrelated to clay sedimentation. The low levels of organic carbon in the shales (< 0.3 wt %) and lack of consistent correlation indicates that organic carbon has little control on trace element concentration in the sedimentary rocks. Gold shows a weak positive correlation with Al_2O_3 in both the sandstones and shales suggesting that it has also been introduced to the basin attached to clay particles. This is supported by the positive correlation of gold with Cr, V, and Sn.

3.2.3. Pyrite texture and composition

The aims of pyrite analysis in this chapter are: 1) determine trace element concentration in different pyrite generations; 2) investigate relationships between gold and other trace elements in pyrite; and 3) compare trace element content in sedimentary pyrite from recent research with the current dataset. Pyrite is mostly found in the lithic sandstone of the F6 sequence (sample LA-3312); however, the underlying F5 sequence grey shales have not shown any visible ore minerals. The lithic sandstone in F6 clastic sequence contains euhedral, moderately oxidized pyrite grains, which are disseminated in the matrix (Fig. 3.8). The pyrite grains are 100-200 µm across. Rutile is in the form of inclusions with size ranging from 50 to 100 µm in the pyrite and disseminated in the matrix. Goethite grains are common with a size between 100 and 150 µm across and randomly distributed in the sandstone matrix. The euhedral pyrite texture is not common for syngenetic or diagenetic pyrite and suggests either a metamorphic or hydrothermal origin (Large et al., 2009; Guy et al., 2010).

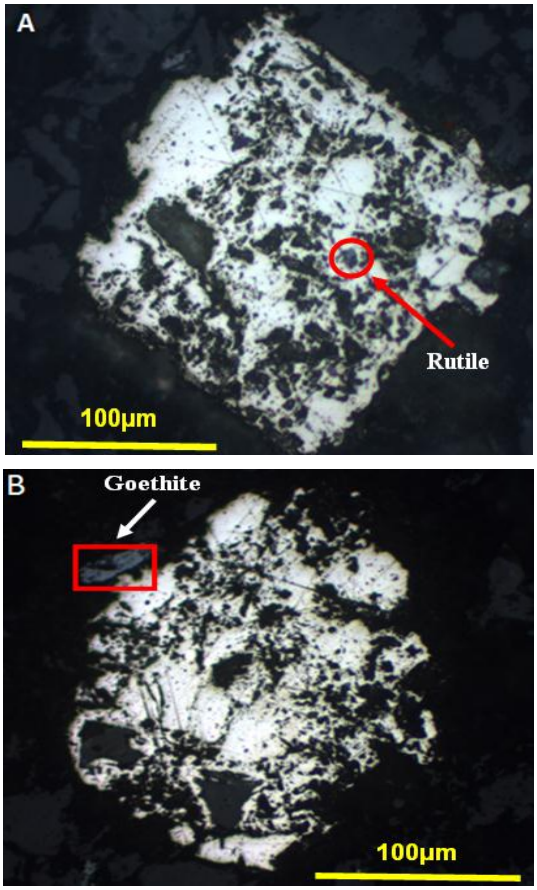

Fig. 3.8. Pyrite textures in reflected light from the Machinchang Formation (Late Cambrian-Early Ordovician). **A**) Euhedral pyrite with inclusions of rutile. **B**) Subhedral pyrite with goethite in the matrix.

Results of the spot analyses are given in Table 3.3. Laser Ablation Inductively Coupled Plasma Mass Spectrometry (LA-ICP-MS) was undertaken on pyrite. The Machinchang pyrite spot analyses do not plot consistently within the field of sedimentary pyrites as shown in Fig. 3.9. The discriminatory plots Co-Ni, Cu-Ni, Mo-Se, and As-Ni confirm that the Machinchang pyrites are not of sedimentary origin. The ratio Ag/Au which varies from 0.05 to 2.4 (mean 0.6) is typical of a hydrothermal-metamorphic origin of pyrite (Gregory et al., 2015).

Table 3.3. LA ICP-MS analyses of pyrite from the Machinchang Formation, Malaysia

Analysis no.	V	Cr	Mn	Co	Ni	Cu	Zn	As	Se	Mo	Ag
LA-3312A-1	3.23	8.91	11.21	1.81	7.27	15.88	7.73	6788.30	35.04	0.31	0.14
LA-3312A-2	0.00	0.00	0.83	0.10	1.81	3.49	0.00	6731.30	42.83	0.01	0.05
LA-3312A-3	0.58	0.08	0.00	1.89	4.01	18.25	0.78	4659.40	18.70	0.03	0.46
LA-3312A-4	0.00	0.29	0.00	0.11	0.97	2.26	0.65	5263.80	42.54	0.01	0.05
LA-3312A-5	22.02	34.99	53.16	136.23	121.12	299.44	168.08	6966.20	30.07	18.58	0.43
LA-3312A-6	32.40	42.57	40.22	140.08	152.88	449.21	175.64	6979.20	28.12	26.14	0.59
LA-3312A-7	6.73	7.71	8.10	33.70	39.57	195.41	67.84	4420.90	51.41	10.87	0.16
LA-3312A-8	295.26	105.99	2233.63	16.91	18.29	48.54	847.02	70.62	2.47	1.50	0.02
LA-3312A-9	42.43	43.09	104.52	79.96	110.05	743.18	304.75	9271.30	23.29	44.34	0.43
LA-3312A-10	53.06	53.22	58.24	66.98	121.51	1063.50	460.45	9321.60	27.30	73.41	0.49
LA-3312A-11	69.49	62.61	132.31	114.23	168.19	1122.40	702.62	5160.60	11.07	88.40	0.20
LA-3312A-12	28.55	33.83	24.38	40.23	57.11	537.11	205.62	8164.90	41.31	31.10	0.47
LA-3312B1A	8.77	12.81	5.03	26.36	34.44	15.87	2.93	5128.40	33.18	0.53	0.14
LA-3312B1B	17.48	28.47	8.98	41.69	57.68	28.62	7.76	6497.90	29.09	0.59	0.13
LA-3312B1C	0.06	0.00	0.29	0.07	0.56	1.50	0.00	2894.60	39.15	0.00	0.01
LA-3312B1D	0.00	0.00	0.71	3.57	13.68	1.47	0.02	9860.30	24.98	0.00	0.03
LA-3312B-1E	0.00	0.00	0.42	0.42	1.48	1.35	1.40	5307.80	25.80	0.01	0.02
LA-3312B-1F	24.24	27.35	44.26	197.61	543.18	60.16	17.18	8383.60	69.00	1.12	0.49
LA-3312B1G	25.61	34.15	23.02	144.61	235.10	78.42	24.49	5932.80	33.23	1.84	0.27
LA-3312B1H	0.08	0.00	0.48	2.80	5.91	5.34	2.57	6082.50	37.71	0.02	0.08
LA-3312B-1I	561.09	173.32	719.73	23.78	40.76	26.52	812.61	51.15	4.15	12.97	0.07
LA-3312B 10A	0.00	1.08	0.36	1.76	8.45	4.48	0.23	7787.90	42.30	0.02	0.16
LA-3312B-10B	29.89	59.52	25.86	130.71	176.15	64.78	37.90	9088.40	54.60	3.79	0.90
LA-3312B-10C	0.12	0.00	0.04	0.62	2.05	2.35	0.00	2418.00	21.84	0.01	0.13
LA-3312B-10D	0.06	0.37	0.29	18.37	50.97	4.09	0.44	5362.20	35.95	0.13	0.03
LA-3312B-10E	0.29	2.95	0.75	7.52	21.90	4.12	0.38	2621.50	31.34	0.00	0.10
LA-3312B-10F	5.02	6.57	4.00	61.81	148.83	28.06	12.79	4438.80	31.89	1.24	0.25
LA-3312B-10G	0.32	0.95	0.00	1.80	11.67	3.66	0.00	6075.80	33.49	0.01	0.07
LA-3312B-10H	10.72	20.10	11.71	124.16	176.37	19.26	4.67	6168.30	30.09	0.04	0.25
LA-3312B-10I	6.14	7.03	6.26	36.01	109.67	22.20	18.75	8548.90	44.36	1.34	0.20
Mean	41.45	25.60	117.29	48.53	81.39	162.36	129.51	5881.57	32.54	10.61	0.23

Table 3.3 (continued) LA ICP-MS analyses of pyrite from the Machinchang Formation, Malaysia

Analysis no.	Cd	Sn	Sb	Te	Au	Tl	Pb	Bi
LA-3312A-1	0.05	0.17	20.86	4.22	0.39	0.03	46.66	5.31
LA-3312A-2	0.06	0.06	9.76	6.29	0.46	0.02	19.35	2.89
LA-3312A-3	0.17	0.00	13.98	2.73	0.19	0.01	250.65	11.87
LA-3312A-4	0.08	0.01	0.45	5.20	0.26	0.01	1.68	0.20
LA-3312A-5	0.15	0.51	47.03	8.67	0.25	0.21	424.63	31.80
LA-3312A-6	0.09	0.98	72.42	10.92	0.34	0.24	532.22	51.77
LA-3312A-7	0.01	0.26	29.14	12.85	0.23	0.04	224.50	14.54
LA-3312A-8	0.03	13.98	65.02	0.15	0.05	0.41	96.82	0.84
LA-3312A-9	0.64	1.63	131.74	8.00	0.43	0.23	922.29	69.28
LA-3312A-10	0.39	1.22	151.41	16.12	1.63	0.32	1305.80	92.88
LA-3312A-11	0.70	1.83	167.79	12.23	0.18	0.41	1618.70	144.12
LA-3312A-12	0.09	1.13	78.72	16.88	0.60	0.24	668.81	48.50
LA-3312B-1A	0.01	0.34	35.00	5.64	0.24	0.07	64.88	19.36
LA-3312B-1B	0.08	0.50	36.47	4.59	0.39	0.14	64.14	16.22
LA-3312B-1C	0.02	0.00	3.11	3.37	0.15	0.00	8.77	0.55
LA-3312B-1D	0.02	0.00	2.84	2.90	0.42	0.00	10.55	1.21
LA-3312B-1E	0.03	0.00	1.11	1.51	0.18	0.00	4.42	0.38
LA-3312B-1F	0.14	0.61	151.45	10.91	2.36	0.31	254.68	82.54
LA-3312B-1G	0.07	0.73	141.15	11.70	0.54	0.24	205.21	75.05
LA-3312B-1H	0.03	0.15	5.69	5.27	0.55	0.01	12.40	2.00
LA-3312B-1I	0.24	19.17	35.52	0.00	0.09	0.75	42.86	8.82
LA-3312B-10A	0.02	0.04	1.22	7.10	1.85	0.01	4.82	0.77
LA-3312B-10B	0.17	0.89	111.71	16.47	3.53	0.30	171.78	63.58
LA-3312B-10C	0.01	0.00	3.58	0.91	0.21	0.00	9.89	0.54
LA-3312B-10D	0.03	0.00	10.78	4.12	0.24	0.02	15.26	1.30
LA-3312B-10E	0.03	0.07	8.56	2.88	0.09	0.00	26.93	1.24
LA-3312B-10F	0.06	0.24	34.52	3.71	0.17	0.10	65.17	17.85
LA-3312B-10G	0.02	0.00	8.01	5.11	0.35	0.01	25.50	2.02
LA-3312B-10H	0.01	0.38	55.72	3.73	0.31	0.19	91.46	15.41
LA-3312B-10I	0.05	0.57	53.53	8.59	2.06	0.09	75.97	19.72
Mean	0.12	1.52	49.61	6.76	0.62	0.15	242.23	26.75

The high As/Ni ratio (As/Ni> 10) (Fig. 3.9D) of the pyrites is clearly outside the sedimentary pyrite field, and supports a hydrothermal source for As. Pyrite composition indicates that gold correlates well with Ag, Te, As, Ni and Se (Table 3.4; Fig. 3.10). In contrast, there is a weak correlation among Au, Co and Sb. V correlates with Zn, Cr, Sn, and Tl. Using V in

pyrite as a proxy for organic matter suggests that Cr, Zn, Sn and Tl concentration is organic-related. Otherwise, the other metals (Au, Ag, Te, As, and Se) likely have a hydrothermal source. The plots Co-Ni, Cu-Ni, Se-Mo and As-Ni are used in this thesis to help discriminate sedimentary pyrite from metamorphic-hydrothermal pyrite (Figs. 3.9A-D).

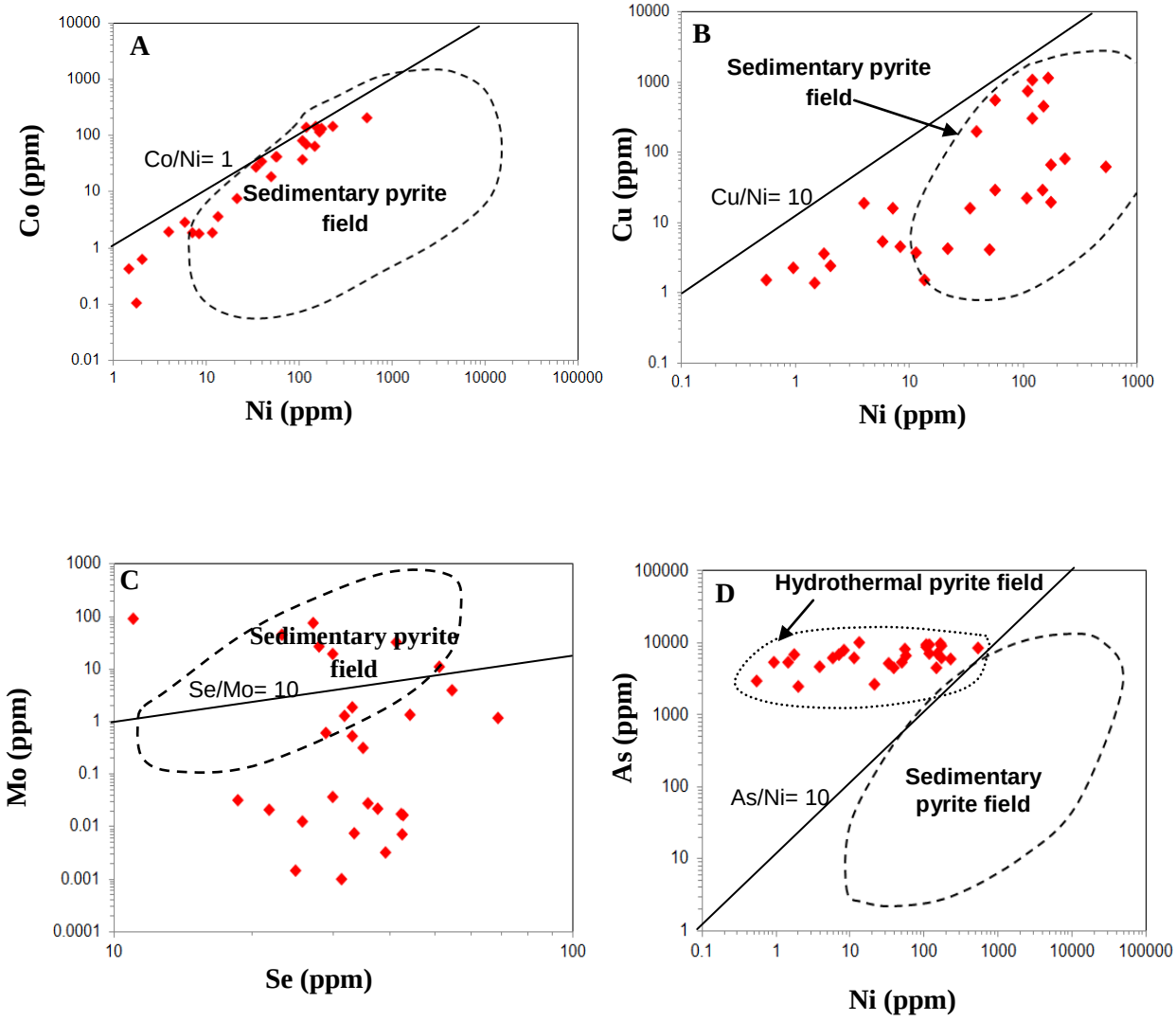

Fig. 3.9. Geochemical binary plots of pyrite in the Machinchang Formation. **A**) Co versus Ni. **B**) Cu versus Ni. **C**) Mo versus Se. **D**) As versus Ni. Dashed polygon represents the field of sedimentary pyrite (Gregory et al. (2015). The pyrite composition is not contained in the sedimentary pyrite field (plots A-D).

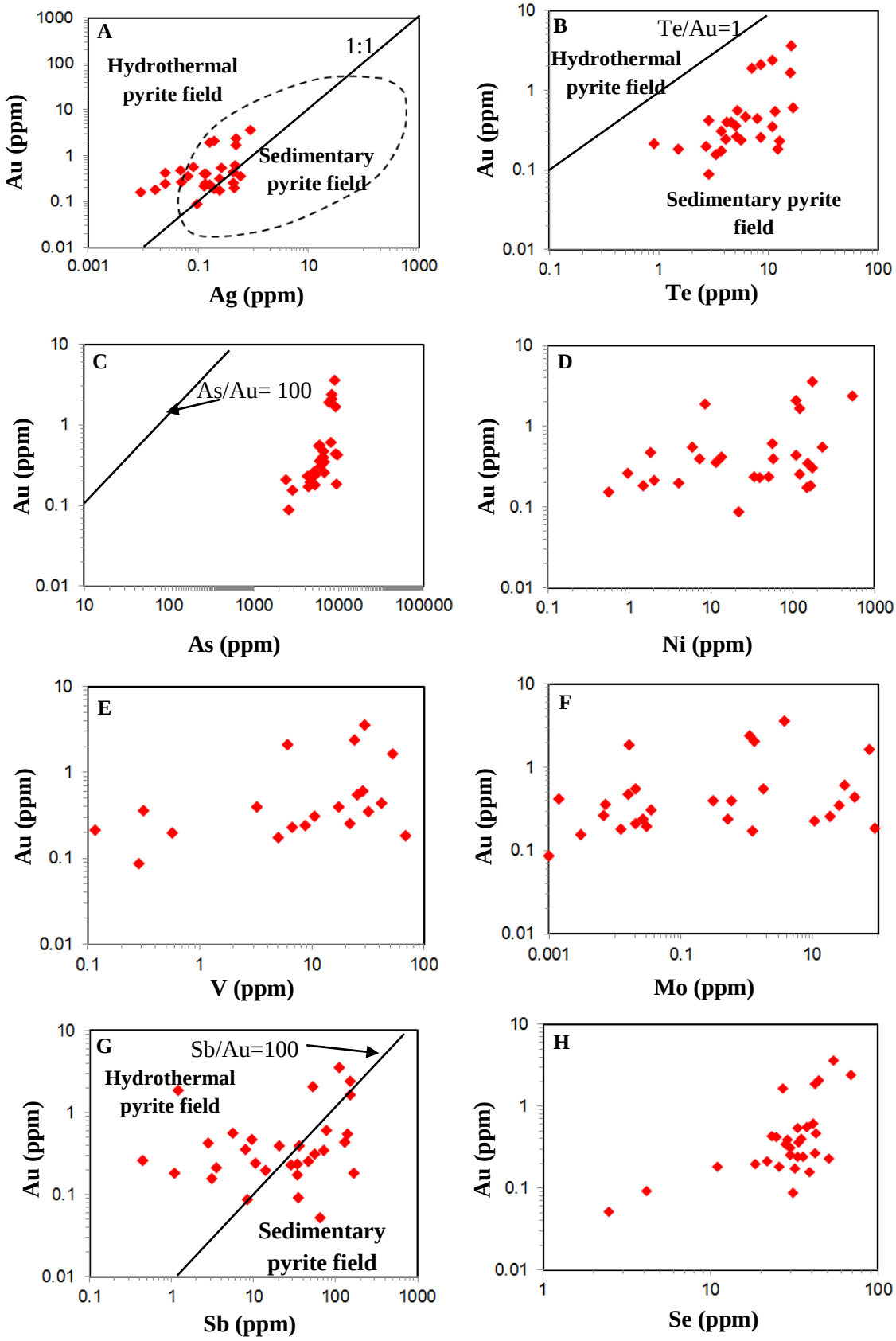

Fig. 3.10. Gold relations to other trace elements in pyrite for the Machinchang Formation. **A**) Au versus Ag. **B**) Au versus Te . **C**). Au versus As. **D**) Au versus Ni. **E**) Au versus V. **F**) Au versus Mo. **G**) Au versus Sb. **H**) Au versus Se. The dashed polygone in Fig 3.18A represents the sedimentary pyrite field (Gregory et al., 2015).

Coefficients of correlation among trace elements in pyrite are summarized in Table 3.4.

Table 3.4. Correlation coefficients of analysed trace elements in pyrite from the Late Cambrian-Early Ordovician Machinchang Formation. Highlighted numbers are equal to or greater than 0.5 pointing to positive correlation between two variables.

Correlation	V_ppm	Cr_ppm	Co_ppm	Ni_ppm	Cu_ppm	Zn_ppm	As_ppm	Se_ppm	Mo_ppm	Ag_ppm	Cd_ppm	Sn_ppm	Sb_ppm	Te_ppm	Au_ppm	Tl_ppm	Pb_ppm	Bi_ppm
V_ppm	1																	
Cr_ppm	0.92	1																
Co_ppm	-0.016	0.29	1															
Ni_ppm	-0.032	0.18	0.89	1														
Cu_ppm	0.037	0.3	0.38	0.22	1													
Zn_ppm	0.81	0.87	0.13	0.036	0.54	1												
As_ppm	-0.54	-0.33	0.35	0.34	0.31	-0.37	1											
Se_ppm	-0.56	-0.51	0.24	0.4	-0.24	-0.66	0.51	1										
Mo_ppm	0.12	0.37	0.34	0.2	0.99	0.6	0.23	-0.3	1									
Ag_ppm	-0.12	0.19	0.69	0.55	0.41	0.021	0.51	0.29	0.34	1								
Cd_ppm	0.2	0.42	0.36	0.27	0.83	0.57	0.21	-0.32	0.86	0.35	1							
Sn_ppm	0.99	0.9	-0.054	-0.065	-0.0051	0.81	-0.57	-0.58	0.071	-0.15	0.15	1						
Sb_ppm	0.12	0.45	0.79	0.74	0.71	0.45	0.35	0.032	0.68	0.62	0.69	0.097	1					
Te_ppm	-0.25	0.063	0.57	0.47	0.61	0.042	0.62	0.48	0.55	0.71	0.37	-0.29	0.69	1				
Au_ppm	-0.13	0.043	0.39	0.49	0.045	-0.14	0.58	0.6	0.025	0.61	0.079	-0.15	0.41	0.57	1			
Tl_ppm	0.81	0.96	0.5	0.42	0.43	0.83	-0.17	-0.38	0.48	0.34	0.52	0.77	0.64	0.24	0.15	1		
Pb_ppm	0.031	0.31	0.44	0.3	0.99	0.53	0.3	-0.23	0.98	0.44	0.86	-0.013	0.76	0.61	0.075	0.45	1	
Bi_ppm	0.003	0.33	0.74	0.66	0.81	0.39	0.39	0.027	0.8	0.6	0.77	-0.051	0.94	0.73	0.35	0.54	0.86	1

3.2.4. Discussion for the Machinchang Formation

In most sedimentary rocks, aluminium is seen as an indicator of the aluminosilicate component of the sediments with low mobility during diagenesis (Brumsack, 1989; Calvert and Pedersen, 1993; Piper and Perkins, 2004). In this study, whole-rock chemistry of the Machinchang grey shales shows that there is a good relationship between gold and alumina suggesting that gold along with Sn, Cr, Ni, Co, and V may have been deposited attached to clay particles into the Machinchang basin. Likewise, previous studies have also reported gold associated with clay minerals in the form of nanoparticles at the clay mineral grain rims (Hanlie et al., 1999). Thomas et al. (2011) also argued that gold may be deposited in the Bendigo sedimentary basin as a result of large-scale erosion and deposition of gold together with clays. This view consolidates the understanding of a sedimentary control on gold deposition into sedimentary basins. However, on the micro-scale, Au measured by LA ICP-MS is associated with euhedral pyrite, suggesting hydrothermal remobilisation, also supported by the ratios Ag/Au< 1, As/Ni> 10 and correlation of Au with Te, Se, As and Ag. Alumina has a good correlation with Sn that implies adsorption of Sn to clay particles which

is a common feature in sedimentary rocks (Slingerland and Smith, 1986). Recent research on the Sn-W and U deposits in the Central European Variscan Belt (Bohemian Massif) has shown that Sn mineralisation is commonly associated with the clay mineral assemblage (Rene, 2012). Whole rock data indicates a good control of organic matter during incorporation of S, Ni, Cu, Zn, As, and Co into pyrite in sandstone. The significantly low amount of organic matter (mean 0.06 wt %) coupled with low contents in Mo suggests that conditions were not favorable enough for sulfate-reducing bacteria to govern the oxidation of organic matter hence producing sedimentary pyrite. These organic-poor sedimentary rocks of the Machinchang Formation contain Au content that ranges from 40 to 57 ppb (mean 46 ppb). Extremely low organic carbon and Mo, Ni, V contents suggests suboxic to oxic seawater conditions as higher organic carbon contents with elevated redox sensitive trace elements generally accumulate in anoxic seawater conditions (Tribovillard et al., 2006).

The absence of sedimentary pyrite in the collected shale samples from the Machinchang Formation leaves a knowledge gap in the understanding of the Late Cambrian-Early Ordovician ocean chemistry in the Sibumasu Terrane in Malaysia. Therefore, the gold source rock potential of these grey shales on the basis of sedimentary pyrite composition cannot be assessed in this study. Consequently, trace metals in existing euhedral pyrites may have an epigenetic origin as they were probably transported by hydrothermal fluids and deposited into pyrite long after sedimentation. This hypothesis is consistent with the occurrence of quartz veins which cross-cut bedding in sandstones and grey shales as noticed in thin sections.

3.3. Setul Formation (Early Ordovician-Silurian)

3.3.1. Major and trace element compositions

As expected for sandstones, the Early Ordovician-Silurian Setul Formation sandstones are enriched in Si_2O and depleted in TiO_2, Al_2O_3, Fe_2O_3, MgO, CaO, Na_2O, K_2O, and P_2O_5 relative to UCC (Fig. 3.11, Table 3.5).

Table 3.5. The average chemical composition of sandstones from the Setul Formation (Early Ordovician-Silurian) with mean compositions of PAAS, WAS, NASC, and UCC.

	Sandstone (n=5)	**PAAS**	**WAS**	**NASC**	**UCC**
Wt %					
SiO_2	90.83	62.80	58.90	64.80	61.60
TiO_2	0.17	1.00	0.80	0.78	0.67
Al_2O_3	3.19	18.90	16.70	16.90	15.20
Fe_2O_3	0.56	7.22	6.90	5.70	6.20
MnO	<0.01	0.11	-	0.06	0.09
MgO	0.29	2.20	2.60	2.90	3.70
CaO	0.03	1.30	2.20	3.40	5.50
Na_2O	0.10	1.20	1.60	1.00	3.20
K_2O	1.29	3.70	3.60	3.80	3.40
P_2O_5	0.01	0.16	-	0.13	0.17
Loss	3.46	-	-	-	-
Total	99.94	-	-	-	-
TOC	1.56	-	-	-	-
ppm					
S	0.16	-	-	-	697.00
Sc	2.12	16.00	-	14.90	16.00
Ba	199.51	650.00	580.00	636.00	584.00
V	128.38	150.00	130.00	-	98.00
Ni	11.59	55.00	68.00	58.00	56.00
Cu	12.12	50.00	45.00	-	25.00
Zn	4.75	85.00	95.00	-	65.00
Cr	17.46	110.00	90.00	125.00	126.00
Ga	4.70	20.00	-	-	15.00
As	6.22	-	10.00	28.40	1.70
Co	34.71	23.00	19.00	-	10.00
Au (ppb)	26.51	-	2.30	-	-
Se	1.30	-	0.50	-	0.12
Rb	45.51	160.00	140.00	125.00	78.00
Sr	25.88	200.00	300.00	142.00	333.00
Y	8.67	27.00	-	-	24.00
Zr	42.44	210.00	160.00	200.00	203.00
Nb	2.76	19.00	-	-	19.00
Mo	9.78	1.00	1.00	-	1.10
Ag	0.70	-	0.07	-	0.07
Cd	-	-	-	-	-
Sn	0.90	4.00	6.00	-	2.30
Sb	3.26	-	1.50	2.09	0.30
Te	0.10	-	-	-	0.01
Tl	0.33	-	0.68	-	0.52
Pb	11.37	20.00	22.00	-	0.00
Bi	0.10	-	0.10	-	0.09
Th	4.87	14.60	-	12.30	8.50
U	5.13	3.10	3.70	2.66	1.70

Note: dash means no available data or not analysed.

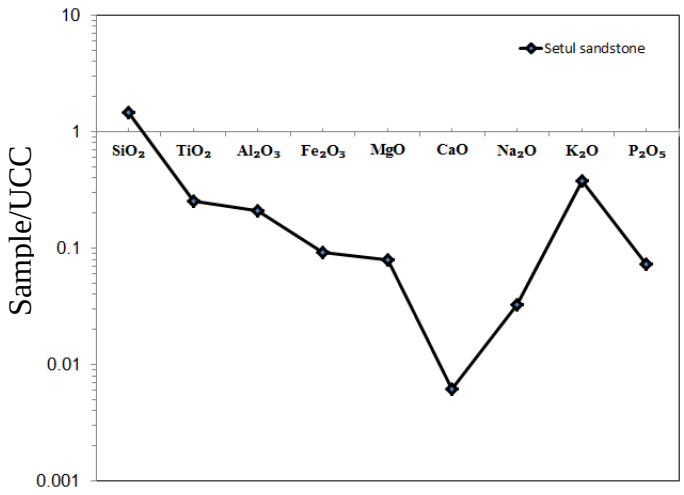

Fig. 3.11. Spider plot of major element chemical composition (mean values) of the Setul sandstones normalised to UCC.

The comparative plot of selected trace elements shows that the Setul Formation sandstones are enriched in V, As, Co, Se, Mo, Sb, and U and depleted in Ni, Cu, Zn, Cr, Sn, Tl, and Th relative to UCC (Fig. 3.12). By comparison, relationships between alumina and selected trace elements are shown below in binary plots (Fig. 3.13).

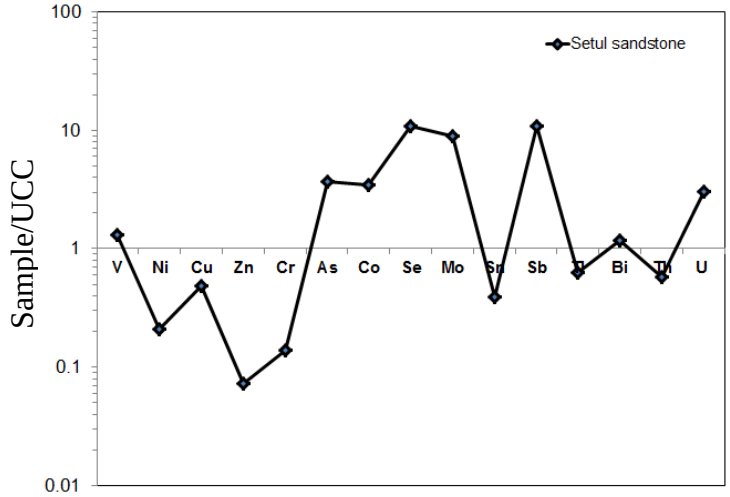

Fig. 3.12. Spider plot of selected trace element composition (mean values) of the Setul sandstones normalised to UCC.

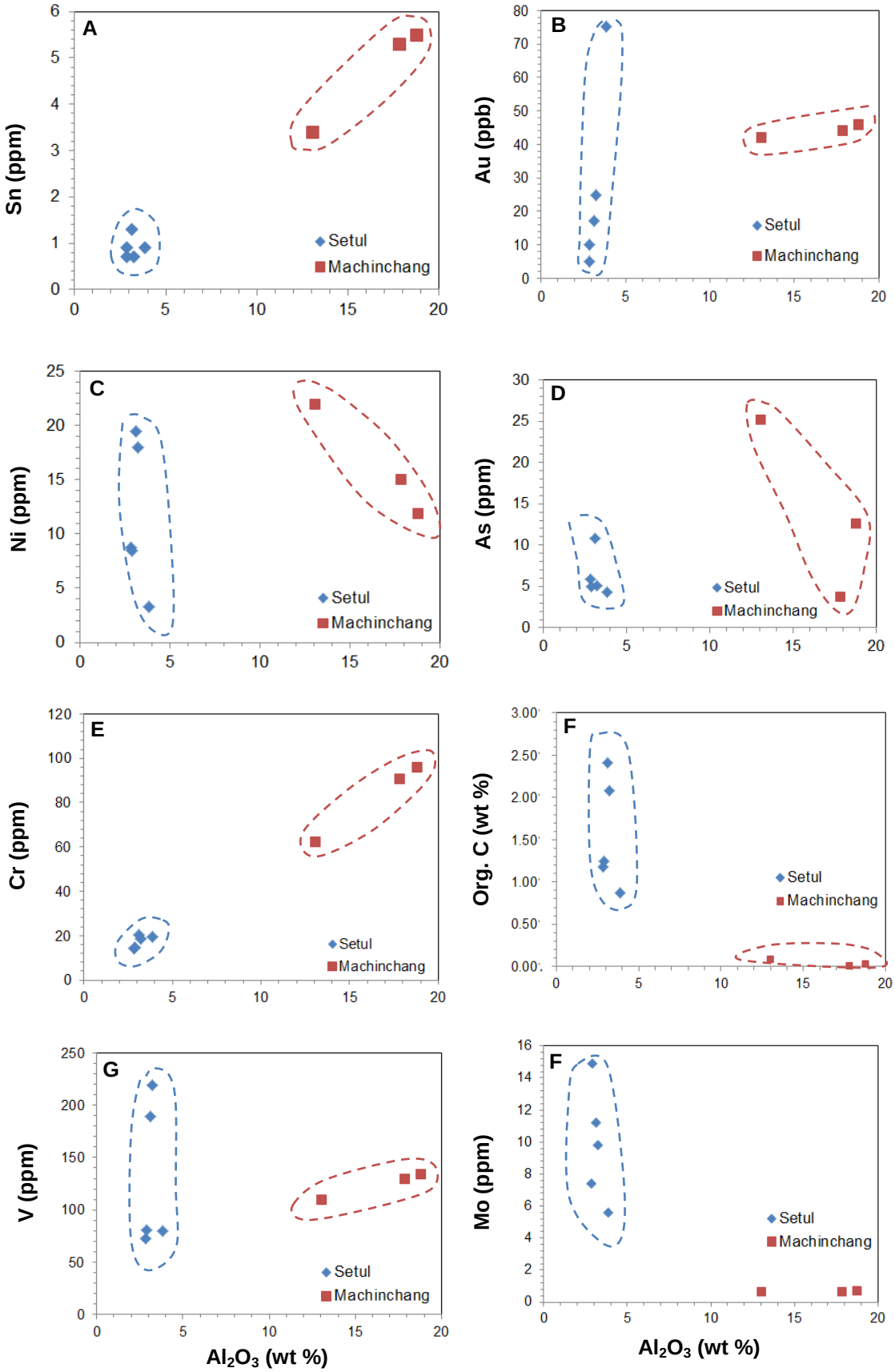

Fig. 3.13. Alumina relationships with selected trace elements and organic carbon in the Setul and Machinchang Formation sandstones. **A**) Alumina versus Sn. **B**) Alumina versus Au. **C**) Alumina versus Ni. **D**) Alumina versus As. **E**) Alumina versus Cr. **F**) Alumina versus organic carbon. **G**) Alumina versus V. **H**) Alumina versus Mo.

Comparatively, the Late Cambrian-Early Ordovician Machinchang sandstones are enriched in more trace elements than the Setul sandstones (Fig. 3.12). Moreover, the highest trace element contents are those of Se, Mo, and Sb in the Setul sandstones. In the Setul Formation, alumina content varies positively with Au and Cr and negatively with Ni, and As (Fig. 3.13). Relationships between gold and other trace elements plus organic carbon are shown in Figs. 3.14-3.15 and Table 3.6.

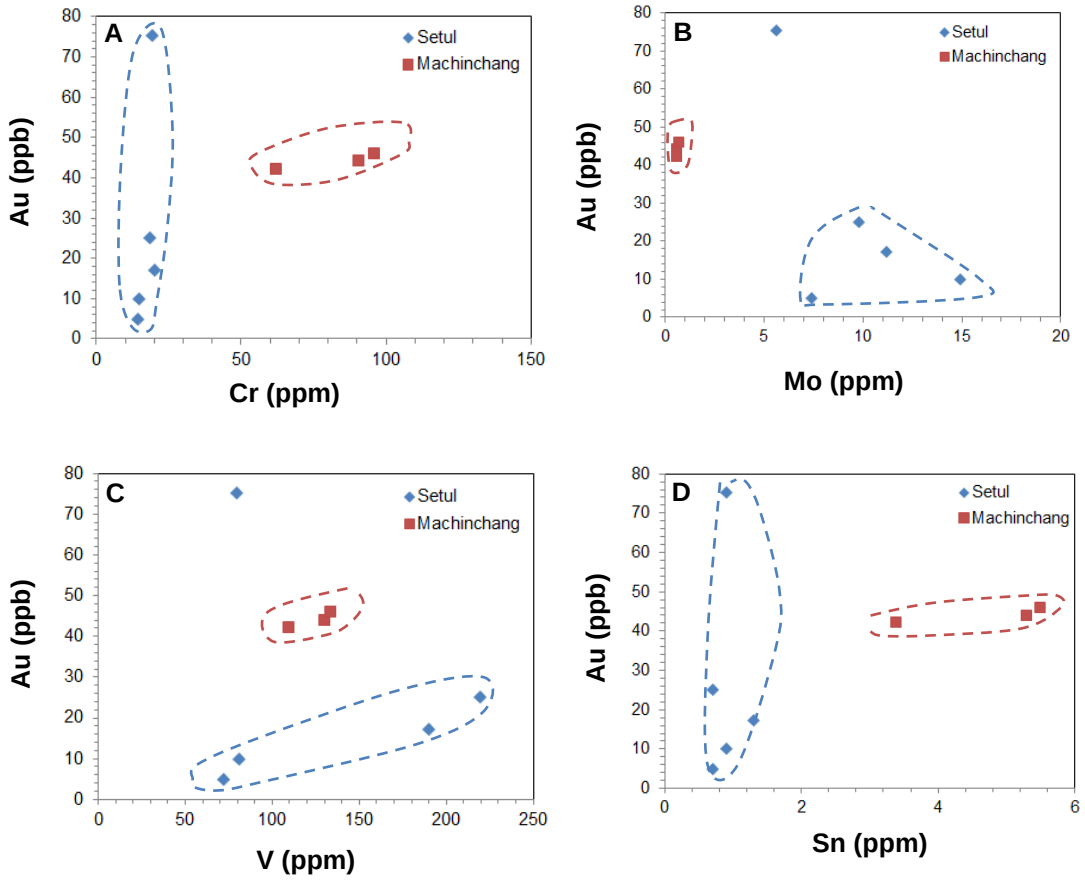

Fig. 3.14. Relationships of Au to Cr, Mo, V, and Sn in the Setul and Machinchang sandstones. **A**) Au versus Cr. **B**) Au versus Mo. **C**) Au versus V. **D**) Au versus Sn.

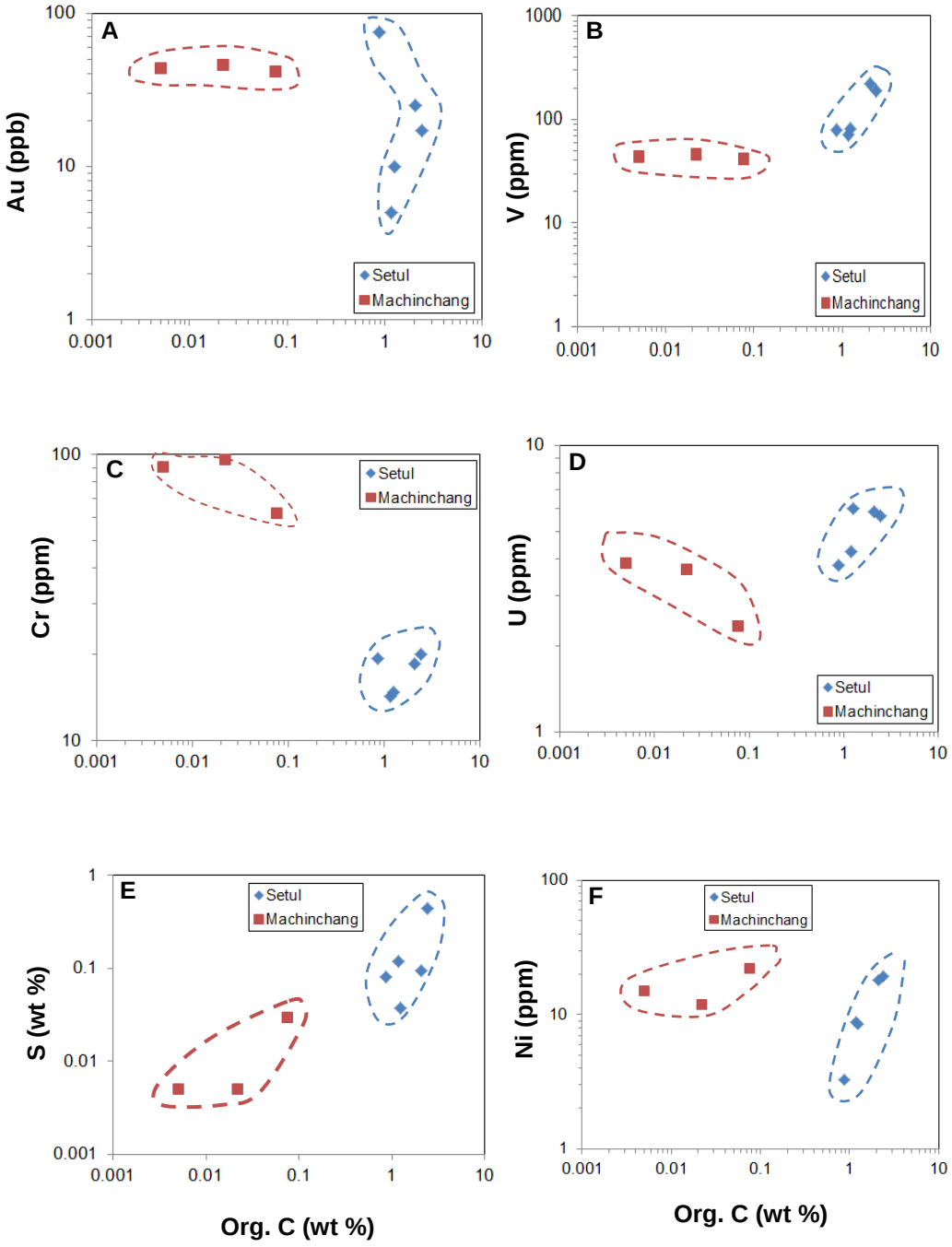

Fig. 3.15. Log-log binary plots showing relationships of organic carbon (Org. C wt %) to selected trace elements in the Early Ordovician-Silurian Setul Formation and the displayed Late Cambrian-Early Ordovician Machinchang sandstone field for comparison. **A**) Organic carbon versus Au. **B**) Organic carbon versus V). **C**) Organic carbon Cr. **D**) Organic carbon versus U. **E**) Organic carbon versus sulphur. **F**) Organic carbon versus Ni.

Table 3.6. Correlation coefficients for the Early Ordovician-Silurian Setul Formation sandstones. Highlighted numbers are equal to or greater than 0.5.

Correlation	Al_2O_3_wt %	Org.C_wt%	S_wt %	Au_ppb	V_ppm	Cr_ppm	Co_ppm	Ni_ppm	Cu_ppm	Zn_ppm	As_ppm	Se_ppm	Mo_ppm	Sn_ppm	Sb_ppm	Tl_ppm	Pb_ppm	U_ppm
Al_2O_3_wt %	1																	
Org.C_wt %	-0.25	1																
S_wt %	-0.087	0.74	1															
Au_ppb	0.99	-0.39	-0.19	1														
V_ppm	0.02	0.92	0.51	-0.14	1													
Cr_ppm	0.7	0.5	0.56	0.59	0.63	1												
Co_ppm	-0.48	-0.69	-0.76	-0.34	-0.73	-0.96	1											
Ni_ppm	-0.34	0.99	0.66	-0.48	0.92	0.4	-0.6	1										
Cu_ppm	0.021	-0.27	-0.84	0.045	0.024	-0.33	0.48	-0.17	1									
Zn_ppm	0.11	0.57	-0.052	-0.009	0.83	0.38	-0.36	0.63	0.57	1								
As_ppm	-0.27	0.75	0.98	-0.36	0.47	0.41	-0.64	0.69	-0.83	-0.093	1							
Se_ppm	-0.087	0.73	0.98	-0.18	0.49	0.56	-0.75	0.64	-0.85	-0.085	0.98	1						
Mo_ppm	-0.62	0.36	0.088	-0.62	0.18	-0.27	0.17	0.37	-0.015	0.051	0.24	0.22	1					
Sn_ppm	0.086	0.49	0.84	0.032	0.26	0.56	-0.66	0.36	-0.87	-0.29	0.83	0.91	0.3	1				
Sb_ppm	-0.12	0.69	0.91	-0.2	0.43	0.5	-0.67	0.59	-0.83	-0.13	0.93	0.97	0.41	0.96	1			
Tl_ppm	0.67	0.54	0.57	0.54	0.67	0.99	-0.96	0.45	-0.3	0.44	0.42	0.55	-0.34	0.49	0.46	1		
Pb_ppm	-0.73	0.08	-0.39	-0.69	0.015	-0.65	0.59	0.17	0.49	0.2	-0.22	-0.31	0.81	-0.32	-0.17	-0.67	1	
U_ppm	-0.51	0.68	0.21	-0.58	0.59	0.0067	-0.12	0.7	0.1	0.47	0.33	0.31	0.89	0.25	0.43	-0.026	0.72	1

3.3.2. Discussion for the Setul Formation

Chemically the Setul sandstones are very siliceous, alumina (Al_2O_3) poor but organic carbon-rich compared to the Machinchang sandstones and shales (Figs. 3.13-3.15). Consequently, rather than Al_2O_3 variation controlling trace element concentration, the organic carbon content of the sandstones appears to be the major control. In Table 3.6, it is clear that V, U, Cr, Se, As, Zn and Ni all have a positive relationship with organic carbon in the Setul sandstones. Gold shows a negative relationship to organic carbon (correlation coefficient of -0.39 in Table 3.6) but a strong positive relationship with Al_2O_3 (correlation coefficient of 0.99 in Table 3.6). Gold content is clay-related in the sandstones. Additionally, alumina content varies positively with Au and Cr; however, gold content varies positively with Tl (correlation coefficient is 0.54). The evidence indicates a strong control of organic processes during deposition of the trace metals V, U, Cr, Se, As, Zn, and Ni because of good correlation among V and other trace elements.

3.4. Singa Formation (Pennsylvanian-Early Permian)

Black shales and sandstones were analysed for their major and trace element composition (Table 3.7).

Table 3.7. The average chemical composition of black shales and sandstones for the Singa Formation in comparison with the average chemical composition of well-known standards

	Black shale (n= 10)	Sandstone (n= 8)	PAAS	WAS	NASC	UCC
(wt %)						
SiO_2	65.02	80.02	62.8	58.9	64.8	61.6
TiO_2	0.77	0.44	1	0.8	0.78	0.67
Al_2O_3	14.48	8.18	18.9	16.7	16.9	15.2
Fe_2O_3	5.75	2.80	7.22	6.9	5.7	6.2
MnO	0.08	0.10	0.11	-	0.06	0.09
MgO	2.62	1.35	2.2	2.6	2.9	3.7
CaO	2.02	1.39	1.3	2.2	3.4	5.5
Na_2O	1.91	1.20	1.2	1.6	1	3.2
K_2O	3.56	2.17	3.7	3.6	3.8	3.4
P_2O_5	0.16	0.09	0.16	-	0.13	0.17
Loss	3.43	2.11	-	-	-	-
Total	99.80	99.80	-	-	-	-
TOC	0.21	0.33	-	-	-	-
S	0.18	0.23	-	-	-	697
(ppm)						
Sc	13.33	7.18	16	-	14.9	16
Ba	553.20	396.25	650	580	636	584
V	129.82	115.74	150	130	-	98
Ni	28.98	15.69	55	68	58	56
Cu	23.57	19.15	50	45	-	25
Zn	91.11	44.46	85	95	-	65
Cr	79.91	43.40	110	90	125	126
Ga	19.07	9.76	20	-	-	15
As	17.01	15.96	-	10	28.4	1.7
Co	20.21	-	23	19	-	10
Au (ppb)	58.28	20.59	-	2.3	-	-
Se	0.50	0.50	-	0.5	-	0.12
Rb	143.02	76.79	160	140	125	78
Sr	131.70	95.44	200	300	142	333
Y	33.08	20.71	27	-	-	24
Zr	275.16	161.29	210	160	200	203
Nb	24.95	13.16	19	-	-	19
Mo	0.99	6.30	1	1	-	1.1
Ag	0.58	1.00	-	0.07	-	0.07
Cd	0.15	-	-	-	-	-
Sn	3.22	5.40	4	6	-	2.3
Sb	1.80	2.59	-	1.5	2.09	0.3
Te	0.54	1.00	-	-	-	0.005
Tl	0.77	1.00	-	0.68	-	0.52
Pb	25.54	12.68	20	22	-	0.0004
Bi	0.69	1.00	-	0.1	-	0.085
Th	18.21	9.21	14.6	-	12.3	8.5
U	2.91	3.51	3.1	3.7	2.66	1.7

Standards: Post-Archean Australian Shale (PAAS) from Taylor and McLennan (1985), the Wedephol's Average Shale (WAS) from Wedephol (1985), the North American Shale Composite (NASC) from Gromet et al. (1984), and the Upper Continental Crust (UCC) from Taylor and McLennan (1985). –: Not analysed or no data available.

3.4.1. Major element compositions

The Pennsylvanian-Early Permian Singa Formation black shales are similar to PAAS but show minor enrichment in Na_2O (Fig. 3.16). The plot K_2O-Al_2O_3 shows that most analysed samples scatter along the anorthoclase and illite lines indicating that these major oxide contents in the Singa sediments may have been controlled by feldspar (e.g. anorthoclase) and illite from the source rocks (Fig. 3.17).

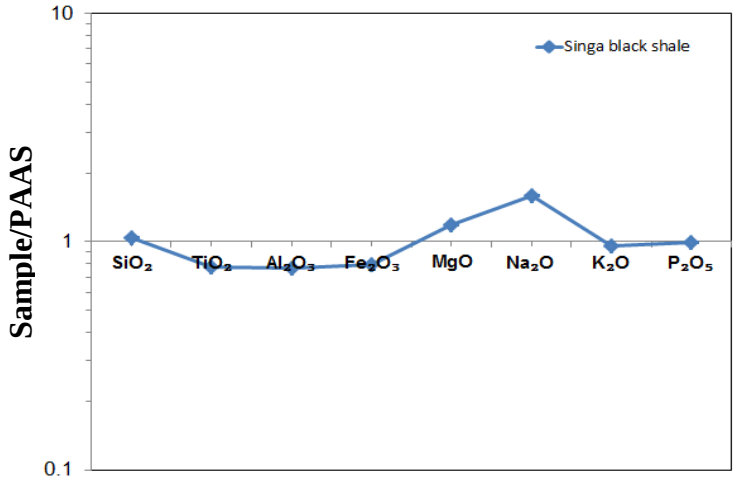

Fig. 3.16. Spider plot of major element composition (mean values in wt %) of the Singa Formation black shales normalised to PAAS.

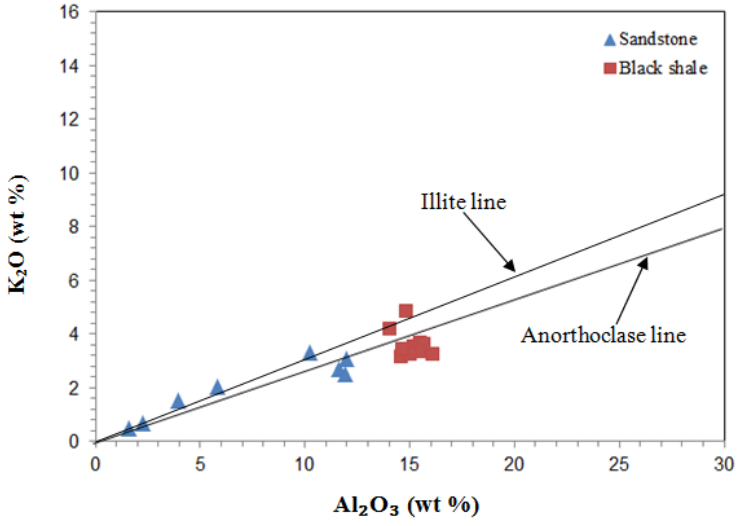

Fig. 3.17. Binary plot of Al_2O_3 against K_2O in the Singa Formation. Anorthoclase line drawn with data from Deer et al. (1966). Anorthoclase composition at Grand Caldeira, Azores. Illite analysed from Fithian, Illinois, USA.

3.4.2. Trace element compositions

A number of trace elements in the Singa Formation black shales are compared to PAAS (Post-Archean Australian Shale, data from Taylor and McLennan, 1985) in order to discuss enrichment and depletion. The trace elements are presented in order of elevated atomic number. The Singa Formation black shales have a trace element pattern very similar to PAAS (Fig. 3.18).

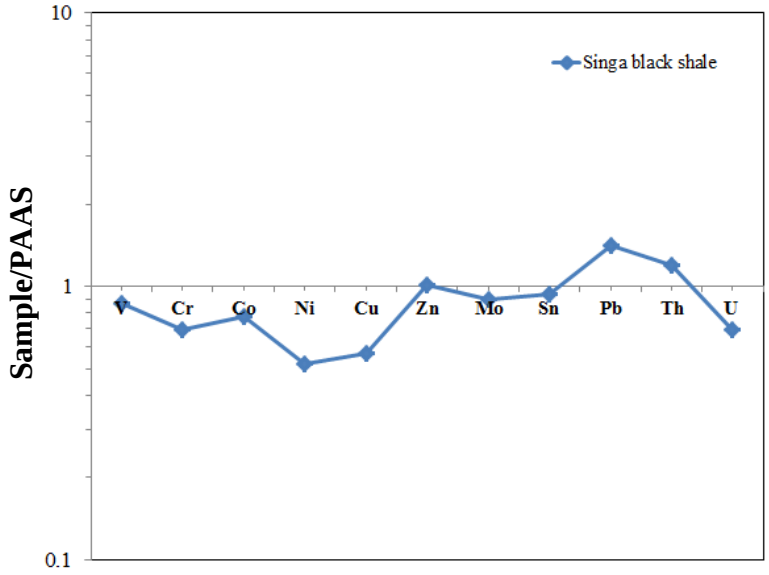

Fig. 3.18. Mean composition of selected trace elements in black shales for the Singa Formation normalised to PAAS.

As discussed previously, alumina (Al_2O_3) content is used as a proxy to imply detrital origin of trace elements absorbed onto clay particles or enclosed in the structure of aluminosilicate minerals (Calvert and Pedersen, 1993; Tribovillar et al., 1994; Hild and Brumsack, 1998; Böning et al., 2004; Tribovillar et al., 2006). The following plots (Figs. 3.19-3.20) show the patterns of alumina contents against some trace elements.

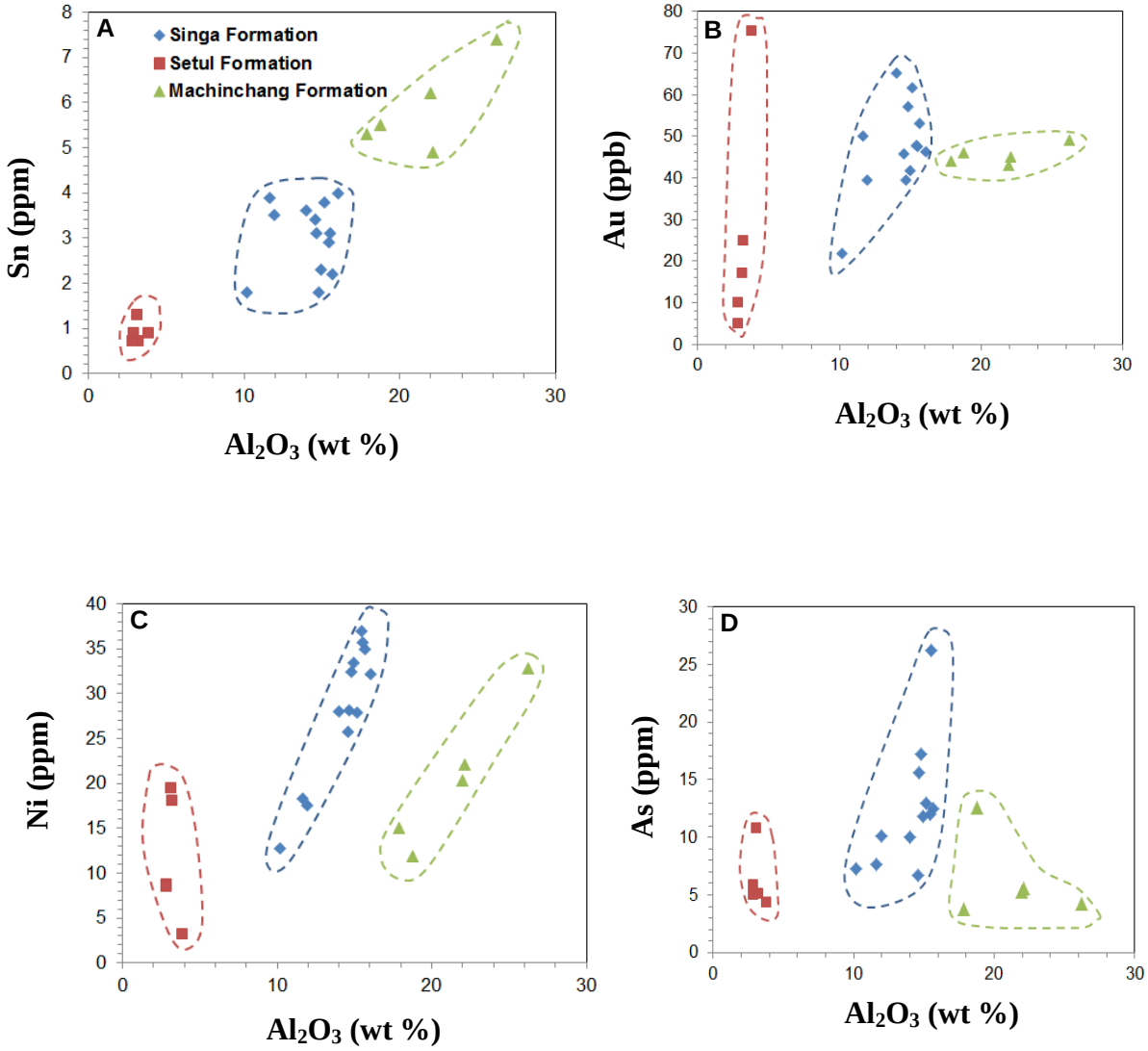

Fig. 3.19. Comparative plots showing alumina relationships with Sn, Au, Ni and As in the Palaeozoic formations including the Late Cambrian-Early Ordovician Machinchang, Early Ordovician-Silurian Setul and Pennsylvanian-Early Permian Singa formations. **A**) Alumina versus Sn. **B**) Alumina versus Au. **C**) Alumina versus Ni. **D**) Alumina versus As.

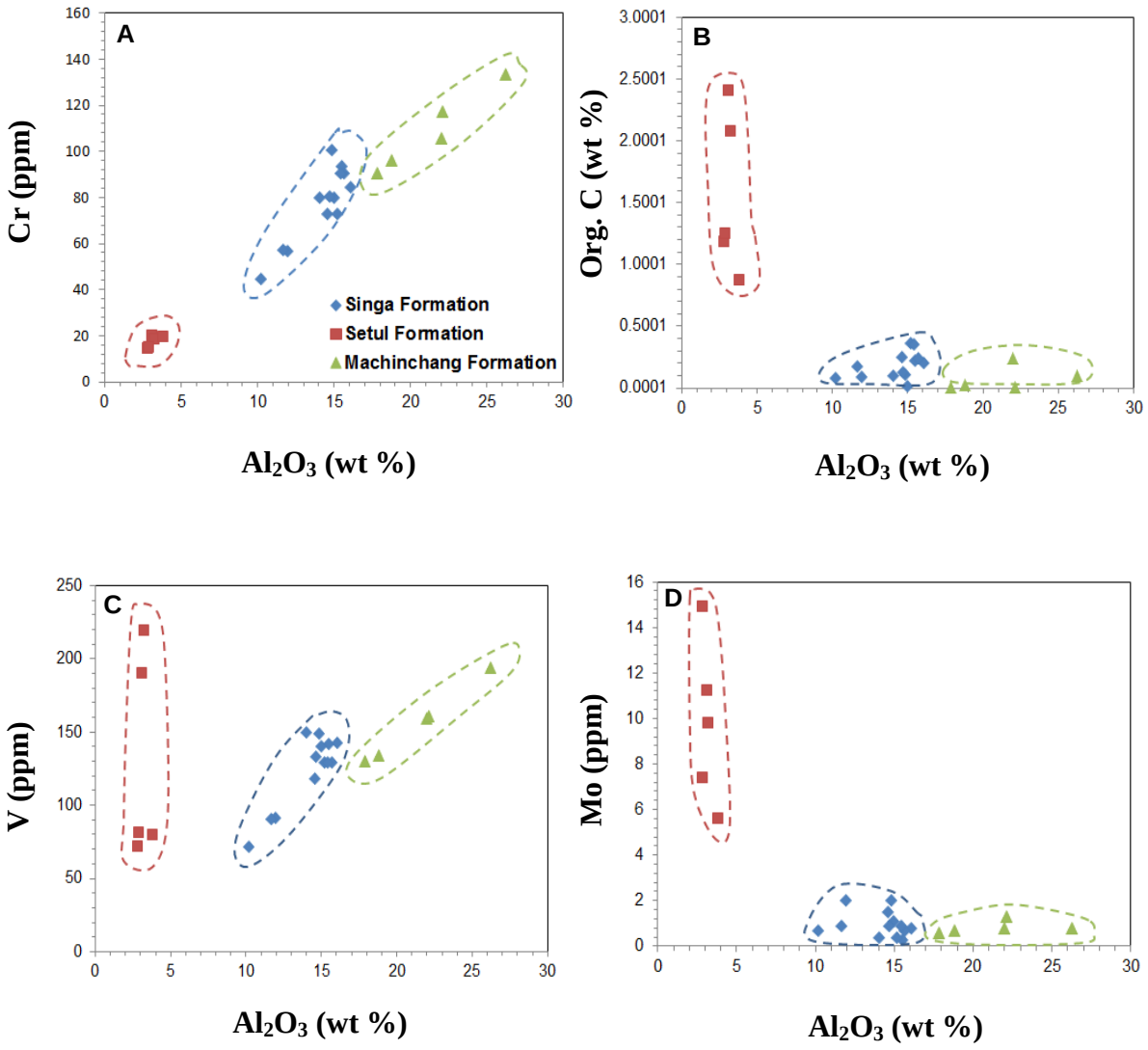

Fig. 3.20. Comparative plots showing alumina relationships with Cr, organic carbon, V and Mo in the Palaeozoic formations including the Late Cambrian-Early Ordovician Machinchang, Early Ordovician-Silurian Setul and Pennsylvanian-Early Permian Singa Formations. **A**) Alumina versus Cr. **B**) Alumina versus organic carbon. **C**) Alumina versus V. **D**) Alumina versus Mo.

In the Singa Formation, the alumina content varies positively with As, Ni, Cr, and weakly with organic carbon. Remarkably, alumina and gold contents vary positively in all three formations but with different slopes (Fig. 3.19B). In the Singa Formation, gold content varies positivily with V content. In contrast, Au has no correlation with Sn and Mo (Fig. 3.21). Relationships of organic carbon content to some trace elements are shown in Fig. 3.22, and indicates no strong correlation in the Singa Formation (Table 3.8).

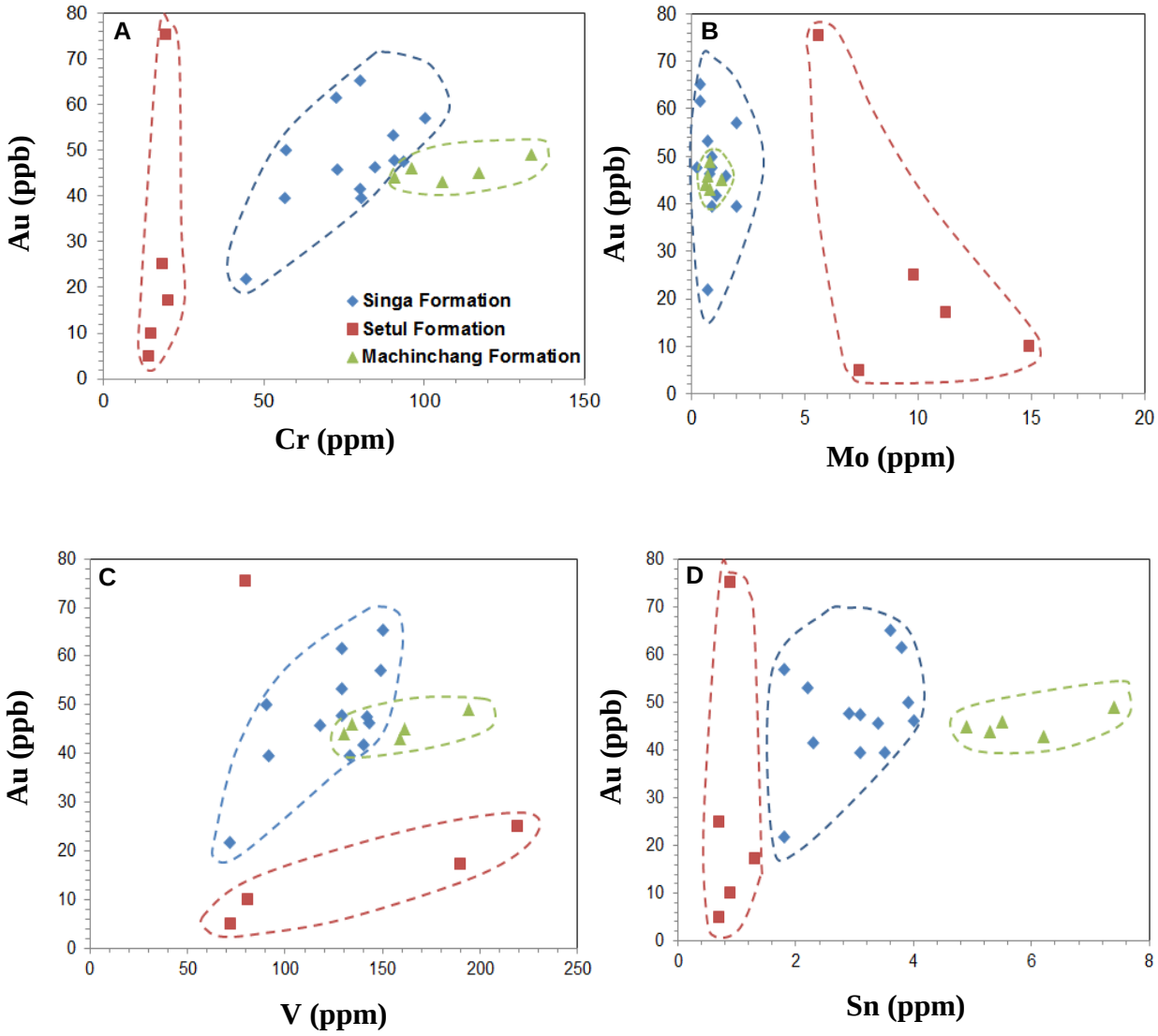

Fig. 3.21. Comparative plots showing relationships of Au to Cr, Mo, V, and Sn in the Singa Formation with the Setul, and Machinchang formation fields are shown for comparison. **A**) Au versus Cr. **B**) Au versus Mo. **C**) Au versus V. **D**) Au versus Sn.

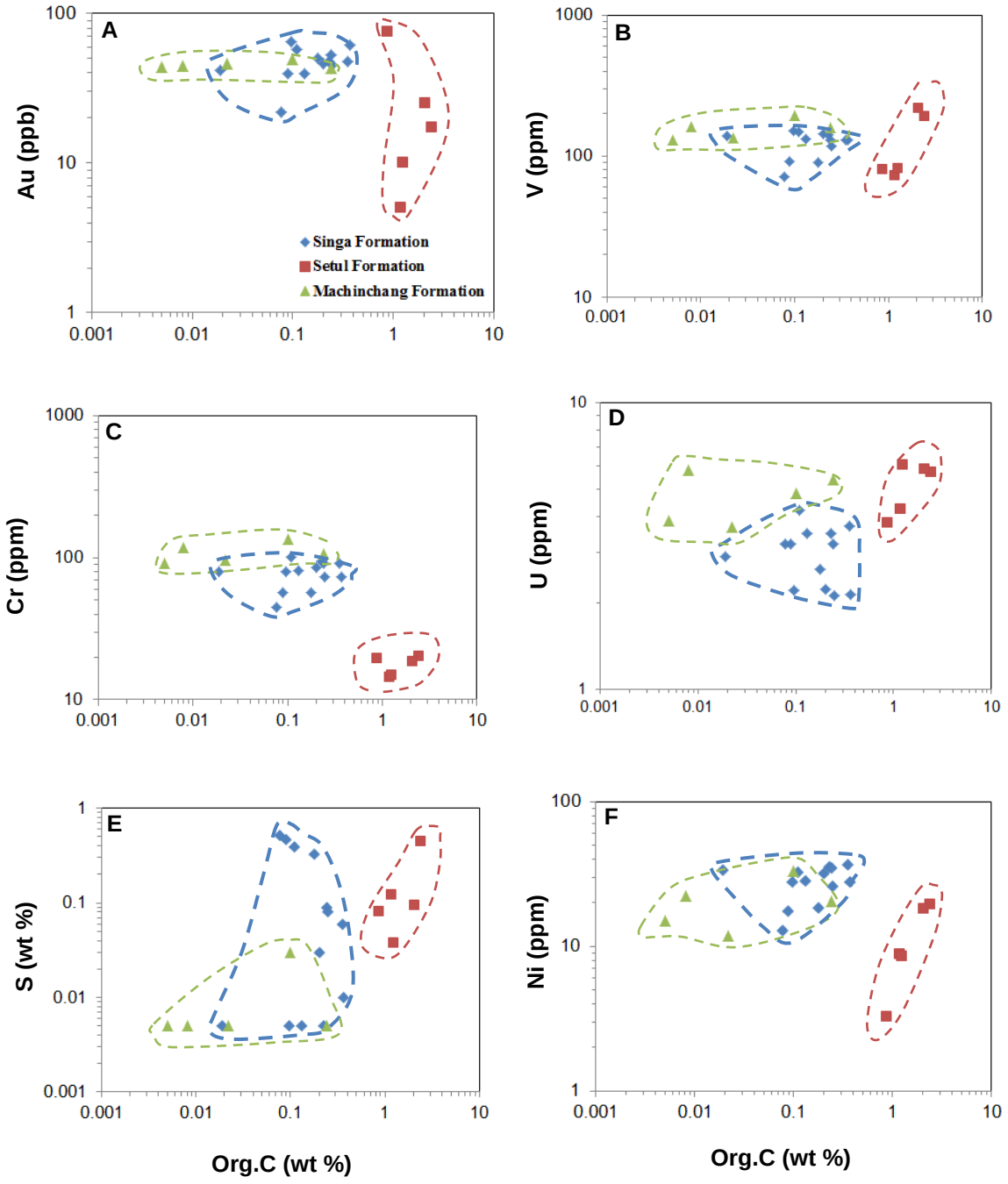

Fig. 3.22. Log-log comparative binary plots showing relationships of organic carbon (Org. C wt %) to selected trace elements in the Pennsylvanian-Early Permian Singa Formation and the displayed fields of the Late Cambrian-Early Ordovician Machinchang and the Early Ordovician-Silurian Setul formations for comparison. **A**) Organic carbon versus Au. **B**) Organic carbon versus V. **C**) Organic carbon versus Cr. **D**) Organic carbon versus U. **E**) Organic carbon versus sulphur. **F**) Organic carbon versus Ni.

Table 3.8. Correlation coefficients of selected trace elements with alumina and organic carbon from the Singa black shales. Highlighted numbers are equal to or greater than 0.5 between two variables.

Correlation	Al_2O_3_wt %	Org.C_wt %	S_wt %	Au_ppb	V_ppm	Cr_ppm	Ni_ppm	Cu_ppm	Zn_ppm	As_ppm	Mo_ppm	Sn_ppm	Sb_ppm	U_ppm
Al_2O_3_wt %	1													
Org.C_wt %	0.44	1												
S_wt %	-0.074	-0.15	1											
Au_ppb	-0.29	0.17	0.24	1										
V_ppm	-0.11	-0.62	0.25	0.32	1									
Cr_ppm	0.35	-0.1	0.62	0.026	0.48	1								
Ni_ppm	0.65	0.1	0.12	-0.2	0.22	0.75	1							
Cu_ppm	0.62	0.28	0.4	0.15	0.18	0.29	0.24	1						
Zn_ppm	0.89	0.34	0.11	-0.46	-0.17	0.49	0.75	0.45	1					
As_ppm	0.66	-0.0082	-0.071	-0.21	0.38	0.23	0.24	0.69	0.42	1				
Mo_ppm	-0.21	-0.31	0.79	-0.21	-0.048	0.24	-0.11	0.24	0.044	-0.15	1			
Sn_ppm	0.025	0.37	-0.63	0.12	-0.14	-0.63	-0.48	0.15	-0.31	0.38	-0.55	1		
Sb_ppm	0.69	0.032	-0.17	-0.29	0.31	0.25	0.32	0.6	0.44	0.96	-0.24	0.38	1	
U_ppm	0.12	-0.13	0.55	-0.23	0.23	0.83	0.61	-0.076	0.48	-0.11	0.36	-0.76	-0.1	1

3.4.3. Discussion for the Singa Formation

The Singa Formation shales have an intermediate Al_2O_3 content (10-16 wt %) between the Setul Formation sandstones and Machinchang Formation shales (Fig. 3.22). Similar to the Machinchang Formation, the Singa Formation shales show a positive relationship (Table 3.8) between Al_2O_3 and the trace elements Ni, Cu, Zn, As, Sb. The organic carbon content of the Singa Formation is low (<0.5 wt %) similar again to the Machinchang Formation. Gold shows no strong correlation with other elements (Table 3.8). Other elements Ni, Cu, Zn, As, Sb were deposited into the basin attached to clay particles based on correlation among Al_2O_3 and these trace elements.

3.4.4. Pyrite trace element composition

Six pyrite types were identified in the Singa Formation which include disseminated framboidal pyrites (pyrite 1) (<20 µm), up to 30 µm wide and 50 µm long diagenetic aggregates of pyrite nodules (pyrite 2), clusters of euhedral clean pyrite (pyrite 3), coarse

grains of subhedral pyrite (pyrite 4), inclusion-rich pyrite (pyrite 5), coarse euhedral clean pyrite (pyrite 6)(Fig. 3.23). Results of the LA-ICPMS spot analyses are given in Table 3.9.

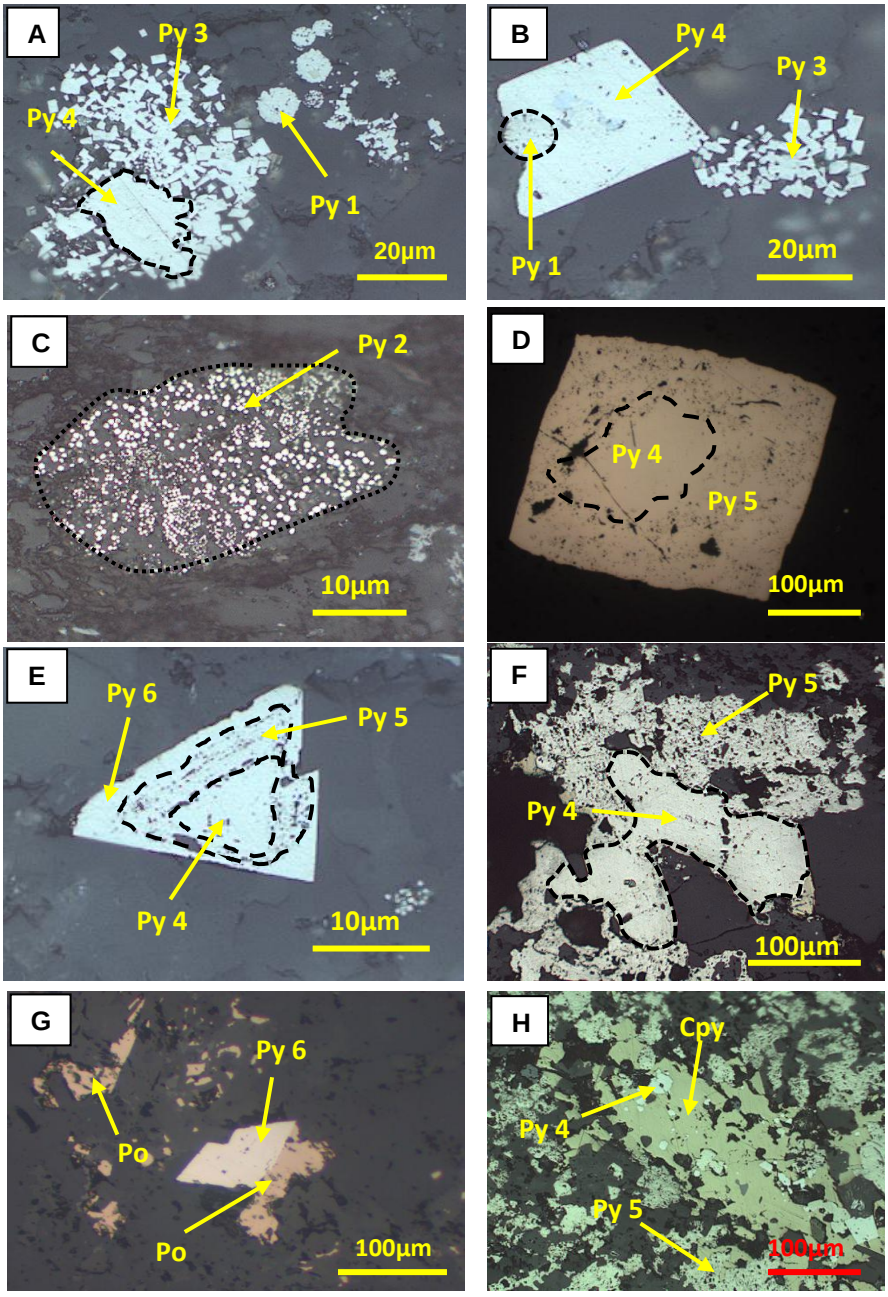

Fig. 3.23. Textural characteristics of pyrite with other sulphide minerals in the Singa Formation, Langkawi. **A**) Diagenetic pyrites (py 1), microcrystals of euhedral pyrite 3, and clean subhedral pyrite 4 (sample LA-3812A). **B**) Diagenetic pyrite 1 overgrown by euhedral pyrite 4 and associated with pyrite 3 (sample LA-3812B). **C**) Aggregate of micro-nodules of pyrite (py 2) (sample LA-3812C). **D**) Subhedral pyrite 4 overgrown by pyrite 5 (sample LA-5312). **E**) Zoned pyrite grain showing pyrite 4 (core) overgrown by pyrite 5, which in turn, rimmed by pyrite 6 (sample LA-3812A). **F**) Pyrite 4 associated with pyrite 5 (sample LA 4112). **G**) Pyrite 6 and pyrrhotite (Po) in the form of patches which size ranges from 5 to 200 µm across (sample LA-4112). **H**) Chalcopyrite (Cpy) formed around microcrystals of pyrite 4 associated with pyrite 5 (sample LA-4112). Sample identification: LA-3812 and LA-4112 represent black shales; LA-5312 is a sandstone sample.

Table 3.9. LA ICP-MS analyses of pyrite from the Pennsylvanian-Early Permian Singa Formation, Malaysia.

Analysis No.	Pyrite type	Mn	V	Co	Ni	Cu	Zn	As	Se
MA05A012	Py 1	1256	4.11	3767	956	775	107	3643	67
MA05A013	Py 1	1610	3.88	2714	903	293	146	3552	-
MA05A014	Py 1	11474	1.96	2296	1720	8325	1331	2330	-
MA05A015	Py 1	7334	21.43	4193	765	315	125	3516	-
MA05A031	Py 1	54	1.61	1095	663	145	182	1063	68
MA05A034	Py 1	4989	13.59	5344	720	4341	687	5033	-
MA05A035	Py 1	4889	3.51	2116	17721	311	1432	1461	99
MA05A036	Py 1	5995	1.61	1788	13812	244	1461	2138	72
MA05A037	Py 1	8639	1.09	650	13551	334	538	993	60
MA05A038	Py 1	3543	3.31	2860	413	428	2282	3351	-
MA05A039	Py 1	7268	0	787	7046	280	460	1747	50
MA05A061	Py 1	-	2.35	1121	323	206	475	4226	-
MA05A062	Py 1	283	1.86	4764	910	691	1990	2605	-
MA05A064	Py 1	9543	1.23	413	115	90	329	4790	-
MA05A053	Py 1	642	0.74	3182	1022	371	342	3427	-
MA05A069	Py 1	-	0	296	97	85	198	454	66
MA05A070	Py 1	-	0	380	150	68	79	413	42
MA05A071	Py 1	335	1.21	885	480	150	343	800	72
MA05A072	Py 1	3435	3.39	137	148	46	167	470	-
MA05A074	Py 1	5331	0.1	128	46	66	461	298	-
MA05A075	Py 1	1139	0.86	791	234	218	1049	832	-
MA05A076	Py 1	614	0.01	232	116	110	474	435	-
MA05A093	Py 1	673	4.18	269	371	130	784	682	65
MA05A098	Py 1	-	1.1	3654	939	307	114	3716	14
MA05A099	Py 1	1235	5.75	2875	664	12574	1592	2800	42
MA05A113	Py 1	3630	10.38	3572	898	299	352	3834	-
MA05A115	Py 1	12465	6.74	2483	695	223	76	2655	-
MA05A118	Py 1	-	0.53	5162	1557	973	1165	4555	-
MA05A120	Py 1	4777	2.81	1975	742	409	747	1992	-
MA05A122	Py 1	-	1.73	3859	994	6317	30925	3538	545
MA05A123	Py 1	-	32.5	6558	2182	480	141	6485	-
MA05A126	Py 1	2984	3.17	3495	899	363	3725	3674	-
MA05A017	Py2	-	19.95	1887	389	217	149	6111	-
MA05A018	Py2	-	13.09	971	233	178	158	8819	-
MA05A019	Py2	-	7.12	1452	265	380	85	5979	-
MA05A020	Py2	-	7.52	1971	335	181	559	6189	-
MA05A021	Py2	-	12.8	1510	258	174	100	5703	-
MA05A044	Py3	2171	2.61	1838	402	415	457	10671	-
MA05A058	Py3	-	1.39	333	234	121	540	562	51
MA05A059	Py3	529	0.2	266	199	139	779	549	61
MA05A060	Py3	988	0	271	193	132	752	520	80
MA05A067	Py3	5280	15.27	270	102	87	704	434	73
MA05A068	Py3	1172	10.45	259	137	40	394	700	53
MA05A088	Py3	813	13.05	366	314	145	634	650	49
MA05A089	Py3	-	0.5	1465	674	508	1301	1514	68
MA05A090	Py3	169	1.33	345	347	141	400	746	77
MA05A116	Py3	-	0.82	617	397	116	290	767	77
MA05A117	Py3	-	0	687	301	143	198	687	72
MA05A097	Py3	1235	0	625	801	275	1210	1029	66

Note: - = not detected

Table 3.9 (continued)

Analysis No.	Pyrite type	Mn	V	Co	Ni	Cu	Zn	As	Se
MA05A101	Py3	-	0	811	472	148	1146	914	56
MA05A086	Py3	-	0.09	642	384	135	782	853	62
MA05A092	Py3	1	2.93	239	349	115	535	493	57
MA05A065	Py4	1361	0	467	138	145	1117	1166	48
MA05A066	Py4	564	0.1	357	105	99	903	1146	53
MA05A073	Py4	-	0.38	366	129	69	220	423	55
MA05A094	Py4	-	9.38	135	888	60	368	565	51
MA05A087	Py4	281	0.11	341	166	140	645	587	53
MA05A091	Py4	1360	0.98	408	580	90	436	646	80
MA05A100	Py4	22	0.16	515	686	93	406	774	72
MA05A121	Py4	692	20.15	1127	974	319	58	1970	-
MA05A040	Py5	-	5.59	125	20	9	0.715	102	-
MA05A041	Py5	-	11.48	68	25	20	-	74	-
MA05A102	Py5	-	0.42	26	51	12	-	100	19
MA05A103	Py5	-	1.24	26	257	24	3	97	20
Ap09A007	Py5	53.97	2.32	665.82	2214.2	27.44	15.38	0.88	44.86
Ap09A008	Py5	62.27	17.77	565.56	1081.5	115.99	18.57	1.98	33.46
Ap09A010	Py5	47.64	26.66	499.3	1394.2	12.37	7.81	1.03	37.99
Ap09A012	Py5	15.19	5.07	585.75	2504.9	253.38	3.59	1.65	42.16
Ap09A013	Py5	3.26	1.02	607.52	1450	65.84	2	0.95	38.15
Ap09A043	Py5	1.47	14.54	2.7	65.37	12.79	0.69	28.86	12.23
Ap09A044	Py5	1.01	14.79	1.96	65.05	25.48	1.28	50.43	13.67
Ap09A045	Py5	0.27	4.97	2.42	199.46	16.33	1.17	60.08	11.74
Ap09A046	Py5	1.06	0.65	2.25	28.98	55.21	0.84	115.04	27.5
Ap09A054	Py5	0.64	23.52	1.78	24.38	34.28	2.34	57.32	13.21
Ap09A055	Py5	0.72	19.5	2.04	19.43	20.34	0.89	22.61	10.89
Ap09A056	Py5	0.4	9.34	2.73	36.91	25.38	1.15	31.81	9.26
MA05A008	Py5	-	6.99	143	73	78	-	353	-
MA05A009	Py5	119	0.54	124	95	93	1.925	539	-
MA05A007	Py6	-	4.2	48	24	25	0.705	68	-
MA05A010	Py6	26	0.25	39	22	45	2.545	208	-
MA05A011	Py6	265	4.75	62	92	73	1.875	143	-
MA05A042	Py6	-	1.93	100	46	9	1.685	93	-
MA05A043	Py6	-	0.86	49	50	22	-	117	-
MA05A055	Py6	-	0.01	112	19	4.655	1.895	140	-
MA05A056	Py6	-	2.34	12	42	24	2.1665	74	-
MA05A095	Py6	-	0.35	26	764	47	-	729	107
MA05A096	Py6	-	2.13	61	57	117	11	1115	65
MA05A106	Py6	-	1.67	64	49	8	2	354	33
Ap09A009	Py6	9.98	5.6	507.92	991	106.81	2.57	1.1	32.27
Ap09A011	Py6	11.21	6.96	500.42	1187.9	120.09	2.51	2.34	25.43
Ap09A014	Py6	0.04	0.08	384.9	743.18	5.55	0.78	0	25.8
Ap09A015	Py6	38.69	8.2	498.47	1151.4	12.91	10.85	3.9	36.93
Ap09A016	Py6	5.28	1.75	591.4	1363.3	4.71	1.65	1.04	45.16
Mean		2023.97	5.21	1084.84	1059.26	497.82	792.14	1584.54	58.58
Mean (WDP)		545	-	303	829	436	131	1360	71

Note: - = not detected or data not available; WDP= worldwide diagenetic pyrite (Gregory et al., 2015)

Table 3.9 (continued)

Analysis No.	Pyrite type	Mo	Ag	Cd	Sb	Te	Au	Tl	Pb	Bi
MA05A012	Py 1	76.38	12	1.71	221	38	0.9	2.8	977	234
MA05A013	Py 1	66.52	11	1.65	184	30	0.72	1.9	664	178
MA05A014	Py 1	48.07	11	2.75	131	25	0.17	2.15	1635	119
MA05A015	Py 1	105.01	20	0.47	214	36	1.61	0.52	992	237
MA05A031	Py 1	43.56	3	2	53	15	0.07	0.34	604	57
MA05A034	Py 1	41.69	14	4	215	37	0.59	2.24	1738	211
MA05A035	Py 1	34.4	10	4	218	23	0.24	1.62	8903	100
MA05A036	Py 1	26.8	4	22	197	15	0.10	1.15	6309	91
MA05A037	Py 1	40.95	5	1.68	266	8	0.24	1.28	2269	46
MA05A038	Py 1	78.01	8	19	247	43	0.33	1.94	908	226
MA05A039	Py 1	23.1	3	2.00	295	22	0.26	1.44	2166	104
MA05A061	Py 1	28.66	5	1.84	89	7	0.31	0.57	600	58
MA05A062	Py 1	40.23	4	7	146	17	0.34	0.62	1149	108
MA05A064	Py 1	28.69	4	2.17	51	3.85	0.14	0.21	242	35
MA05A053	Py 1	95.05	6	1.84	245	26	0.58	1.29	784	84
MA05A069	Py 1	216.78	3	1.91	46	3.38	0.13	0.19	1515	33
MA05A070	Py 1	33.98	1	0.77	42	7	0.06	0.17	937	28
MA05A071	Py 1	12.22	3	1.88	63	9	0.13	0.18	748	50
MA05A072	Py 1	5.53	0.48	1.98	34	3.52	0.13	0.19	722	12
MA05A074	Py 1	9.78	0.50	2.04	32	3.61	0.14	0.20	785	7
MA05A075	Py 1	41.47	4	1.82	86	3.23	0.12	0.18	795	31
MA05A076	Py 1	19.75	2	1.89	65	3.35	0.13	0.18	591	19
MA05A093	Py 1	27.05	1	1	42	6	0.05	0.07	779	35
MA05A098	Py 1	113.19	13	0	237	44	0.69	2.79	0.40	213
MA05A099	Py 1	56.56	12	3	216	38	0.65	1.8	3.29	166
MA05A113	Py 1	126.63	12	3.33	240	41	0.83	1.62	<6.66	185
MA05A115	Py 1	61.23	8	7.57	164	35	0.43	1.72	<7.57	153
MA05A118	Py 1	80.24	13	10	227	60	0.28	0.85	9.70	198
MA05A120	Py 1	54.4	8	3.60	21	24	0.41	0.78	<7.19	215
MA05A122	Py 1	60.59	15	72	140	34	0.38	1.07	71.78	180
MA05A123	Py 1	82.49	16	4.07	209	43	1.29	0.97	<8.14	234
MA05A126	Py 1	58.25	11	10	38	44	0.41	1.07	9.51	200
MA05A017	Py2	12.86	4	2.02	349	63	0.29	2.85	620	295
MA05A018	Py2	6.38	2	1.83	154	30	0.11	1.24	413	160
MA05A019	Py2	10.2	4	1.80	225	31	0.11	1.19	463	201
MA05A020	Py2	5.61	4	1.80	303	55	0.11	1.53	682	312
MA05A021	Py2	6.83	3	1.92	239	37	0.24	1.77	660	231
MA05A044	Py3	29.83	7	1.57	233	58	0.32	1.94	901	288
MA05A058	Py3	35.19	2	1.83	49	10	0.12	0.18	341	32
MA05A059	Py3	36.62	1	1.92	54	8	0.13	0.19	483	32
MA05A060	Py3	40.1	1	0.74	39	6	0.06	0.07	382	27
MA05A067	Py3	29.37	0.49	2.00	36	3.54	0.13	0.19	476	11
MA05A068	Py3	19.35	0.48	1.97	28	3.50	0.13	0.19	232	6
MA05A088	Py3	17.38	2	3	45	7	0.11	0.12	730	36
MA05A089	Py3	31.25	5	1	117	14	0.33	0.19	1245	95
MA05A090	Py3	154.53	3	1	59	11	0.18	0.11	2812	64
MA05A116	Py3	23.25	3	1.62	54	13	0.23	0.13	<3.24	51
MA05A117	Py3	11.92	3	1.56	42	13	0.25	0.121	<3.12	42
MA05A097	Py3	33.31	3	8	65	11	0.18	0.18	913	54

Note: - = not detected or data not available.

Table 3.9 (continued)

Analysis No.	Pyrite type	Mo	Ag	Cd	Sb	Te	Au	Tl	Pb	Bi
MA05A101	Py3	64.53	5	1	66	13	0.17	0.19	1.01	63
MA05A086	Py3	24.66	2	1	47	8	0.12	0.09	416	44
MA05A092	Py3	15.85	2	1	44	7	0.11	0.15	505	35
MA05A065	Py4	54.89	1	1.82	60	3.22	0.121	0.18	688	19
MA05A066	Py4	65.3	0.45	1.83	56	3.24	0.121	0.18	580	17
MA05A073	Py4	6.71	1	1.95	32	3.46	0.13	0.19	203	22
MA05A094	Py4	8	2	0	53	4	0	0.02	563	26
MA05A087	Py4	26.25	2	1	59	10	0.19	0.12	649	49
MA05A091	Py4	21.62	2	2	46	9	0.11	0.1	756	33
MA05A100	Py4	62.21	3	1	62	14	0.12	0.16	0.55	50
MA05A121	Py4	23.08	4	1.84	139	25	0.53	1.02	1.84	122
MA05A040	Py5	1.1	0.33	1.47	25	2.28	0.094	0.39	66	1
MA05A041	Py5	3.26	0.36	1.57	46	2.44	0.101	0.87	79	2
MA05A102	Py5	0.05	0	0.29	58	0.18	0.07	0.16	<0.58	3
MA05A103	Py5	0	0	0	23	1	0.01	0.11	0.31	3
Ap09A007	Py5	630.06	6.69	0.1	103.78	11.65	0.11	1.5	1004	83.98
Ap09A008	Py5	0.52	2.95	0.05	70.96	3.64	0.04	1.59	511.62	9.76
Ap09A010	Py5	5.73	5.82	0.03	56.63	9.02	0.08	1.69	679.87	75.45
Ap09A012	Py5	346.54	13.4	0.06	114.71	11.56	0.09	2.36	1125.4	104.48
Ap09A013	Py5	0.52	2.04	0	68.65	1.6	0.02	1.49	319.98	11.03
Ap09A043	Py5	2.52	0.02	0.16	1.46	0.14	0.01	0.98	11.18	0.01
Ap09A044	Py5	2.04	0.07	0.15	1.86	0.1	0.01	1.65	17.89	0.02
Ap09A045	Py5	2.42	0.02	0.16	1.51	0.09	0.02	0.85	11.53	0.03
Ap09A046	Py5	45.34	0.01	0.03	0.58	0.19	0.01	0.07	2.79	0
Ap09A054	Py5	3.27	0.11	0.24	2	0.51	0.02	1.15	20.5	0.03
Ap09A055	Py5	5.75	0.12	0.07	0.39	0.09	0	1.28	16.82	0.02
Ap09A056	Py5	3.36	0.07	0.1	0.75	0.09	0.01	1.14	13.73	0.03
MA05A008	Py5	2.86	1	1.65	174	2.43	0.10	0.84	699	31
MA05A009	Py5	0.50	1	1.54	184	2.28	0.09	0.94	784	24
MA05A007	Py6	0.51	0.45	1.59	64	2.35	0.10	0.87	221	9
MA05A010	Py6	0.49	2	1.54	136	2.24	0.09	1.07	545	8
MA05A011	Py6	0.50	2	1.54	151	2.28	0.09	1.84	506	15
MA05A042	Py6	0.43	0.33	1.43	25	2.22	0.09	0.126	105	2
MA05A043	Py6	1.69	0.35	1.52	77	2.36	0.10	2.44	174	1
MA05A055	Py6	0.71	0.44	1.8	25	3.20	0.12	0.84	29	0
MA05A056	Py6	0.71	0.44	1.79	72	3.17	0.12	1.67	90	<0.21
MA05A095	Py6	0.09	0	0	59	8	0	0.04	273	12
MA05A096	Py6	2.16	1	0	167	7	0.08	0.23	1423	34
MA05A106	Py6	0.15	0	1	9	1	0	0.25	0.71	6
Ap09A009	Py6	0.17	2.25	0.06	27.36	1.44	0.01	1.84	172.07	7.36
Ap09A011	Py6	0.09	3.26	0.04	211.02	1.72	0.02	7.95	324.36	5.03
Ap09A014	Py6	0.03	0.07	0	72.66	0.29	0	1.64	42.74	0.45
Ap09A015	Py6	0.35	3.08	0.05	78.45	2.14	0.01	1.71	282.4	8.07
Ap09A016	Py6	0.04	0.47	0	24.95	0.28	0	0.82	80.71	1.03
Mean		40.63	3.93	2.91	102.81	14.09	0.21	0.98	723.90	73.06
Mean (WDP)		88	9.2	3	90	4.9	0.1	36	387	13

Note: WDP= worldwide diagenetic pyrite in Gregory et al. (2015)

The textures of pyrite 1, 2, and 3 are similar to those of diagenetic-syngenetic pyrites as documented in Chapter 2. Additionally, these pyrites have the following ratio ranges: Co/Ni (0.05-7); Zn/Ni (0.04-39), Cu/Ni (0.02-6), As/Ni (0.07-42), Te/Au (22-500), As/Au (>2184), Ag/Au (4-65), Sb/Au (51-2755), and Bi/Au (46-2836). The textures and geochemical ratio values of pyrites 1, 2, and 3 are indicative of a diagenetic origin. Plots of Co-Ni, Cu-Ni, Mo-Se, and As-Ni are shown below (Fig. 3.24). Relationships of Au to some trace elements are also shown in Fig. 3.25 and their correlation coefficients are summarised in Table 3.10.

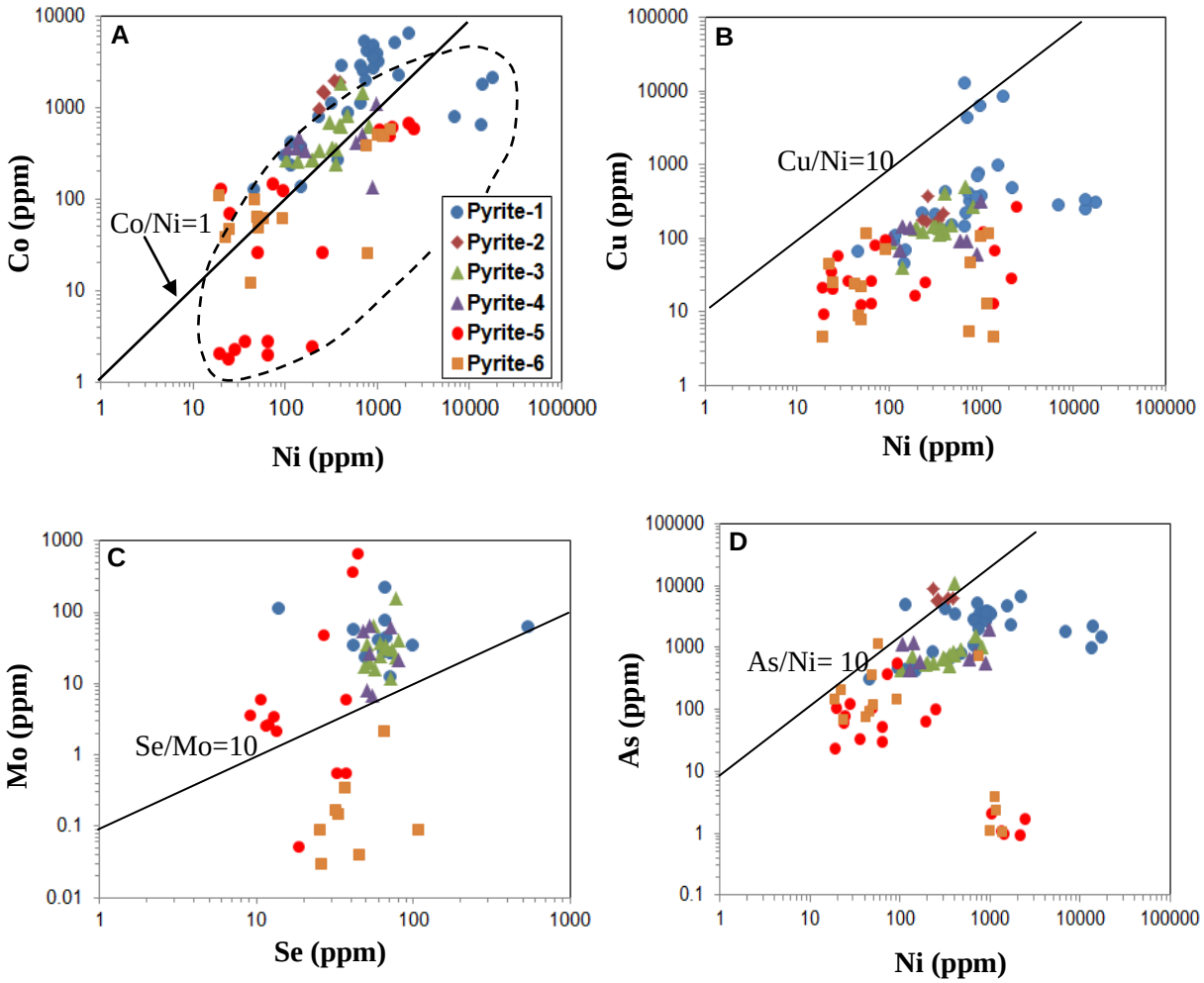

Fig. 3.24. Geochemical binary plots of pyrite in the Pennsylvanian-Early Permian Singa Formation. A) Co versus Ni. B) Cu versus Ni. C) Mo versus Se. D) As versus Ni. Dashed polygon (Fig. 4.30A) represents the field of sedimentary pyrite (Gregory et al., 2015).

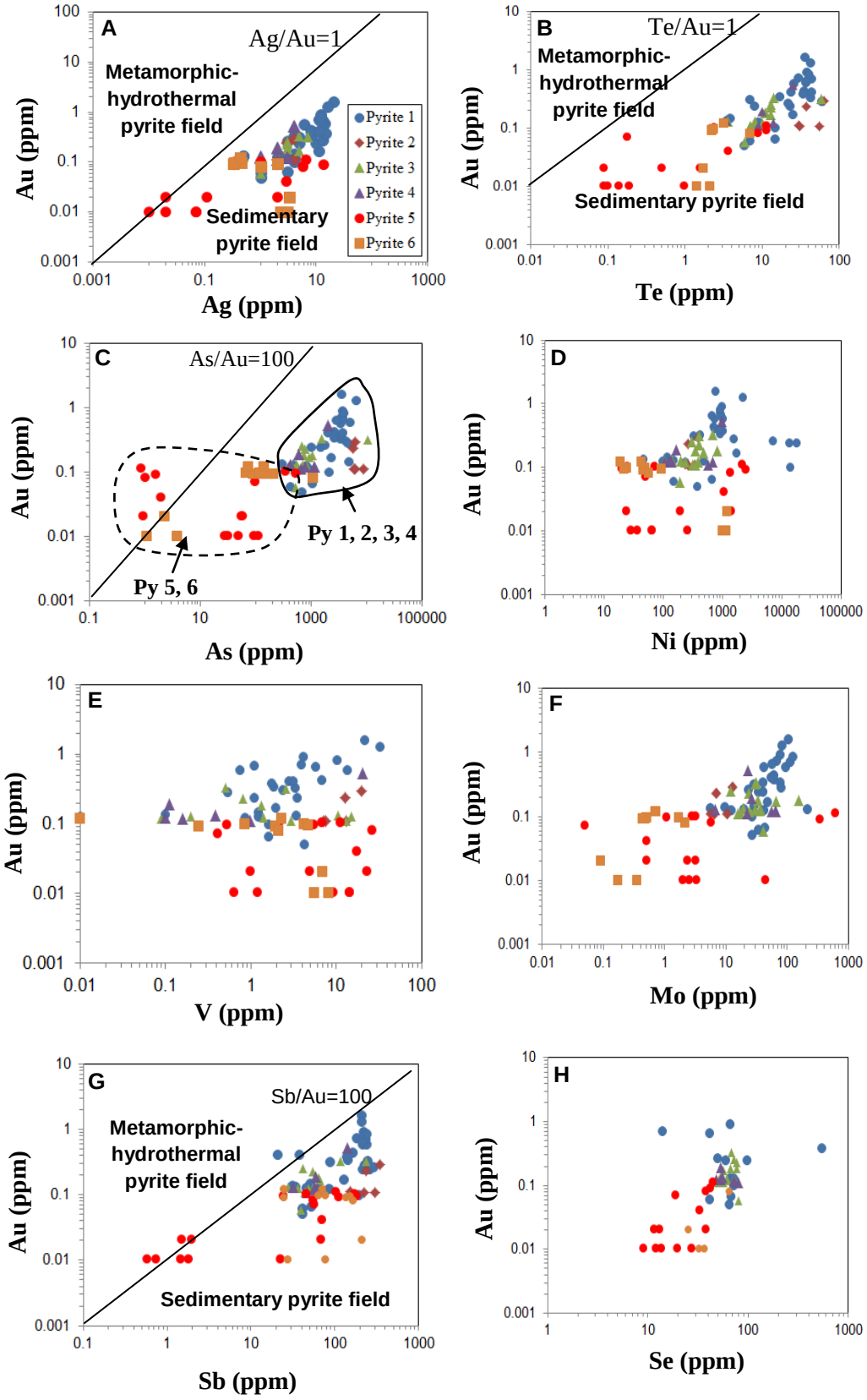

Fig. 3.25. Gold relationships to other trace elements in pyrite for the Pennsylvanian-Early Permian Singa Formation. **A**) Au versus Ag. **B**) Au versus Te. **C**) Au versus As. **D**) Au versus Ni. **E**) Au versus V. **F**) Au versus Mo. **G**) Au versus Sb. **H**) Au versus Se.

Table 3.10. Correlation of coefficient of trace elements from framboidal pyrites (pyrite 1). Highlighted numbers are equal to or greater than 0.5 between two variables.

Correlation	Au_ppm	Mo_ppm	Se_ppm	As_ppm	Mn_ppm	Co_ppm	Ni_ppm	Cu_ppm	Zn_ppm	Ag_ppm	Cd_ppm	Sb_ppm	Te_ppm	Tl_ppm	Pb_ppm	Bi_ppm
Au_ppm	1															
Mo_ppm	0.43	1														
Se_ppm	0.027	-0.022	1													
As_ppm	0.65	0.27	0.36	1												
Mn_ppm	0.036	-1.30E-05	-0.0026	0.19	1											
Co_ppm	0.71	0.34	0.42	0.8	-0.053	1										
Ni_ppm	-0.14	-0.19	-0.086	-0.15	0.28	-0.084	1									
Cu_ppm	0.086	-0.02	0.34	0.16	0.092	0.24	-0.094	1								
Zn_ppm	-0.038	-0.0046	0.99	0.12	-0.11	0.19	-0.027	0.36	1							
Ag_ppm	0.81	0.42	0.47	0.74	0.21	0.83	-0.022	0.37	0.27	1						
Cd_ppm	-0.062	3.70E-05	0.96	0.17	0.11	0.24	0.062	0.29	0.95	0.26	1					
Sb_ppm	0.51	0.26	-0.077	0.47	0.19	0.55	0.42	0.17	-0.013	0.54	0.071	1				
Te_ppm	0.62	0.39	0.23	0.72	0.086	0.85	-0.069	0.27	0.16	0.84	0.23	0.61	1			
Tl_ppm	0.41	0.24	-0.07	0.47	0.24	0.52	0.19	0.35	0.017	0.59	0.063	0.71	0.67	1		
Pb_ppm	-0.16	-0.14	-0.11	-0.2	0.27	-0.082	0.88	-0.13	-0.11	-0.043	0.0044	0.28	-0.12	0.15	1	
Bi_ppm	0.74	0.39	0.27	0.73	0.092	0.84	-0.093	0.23	0.17	0.88	0.23	0.54	0.92	0.67	-0.1	1

Framboidal pyrites (pyrite 1) show gold concentration that varies positively with Ag, Te, As, Co, Sb, and Bi as shown in Table 3.10 and Fig. 3.25. Compared to early pyrites (pyrite 1, 2, and 3), the later pyrites (py 4, 5, and 6) have the following ratio limits: Co/Ni (0.01-6), Zn/Ni (0.001-9), Cu/Ni (0.003-2), As/Ni (0.0008-20), Te/Au (3-214), As/Au (>8), Sb/Au (>58), and Bi/Au (>1). These geochemical values are much lower relative to those of diagenetic pyrites (Gregory et al., 2015). Therefore, the textures of pyrite 4, 5, and 6 combined with their geochemical ratio values suggest a metamorphic or hydrothermal origin for pyrite.

The fact that all the pyrites plot on or below the line Ag/Au = 1 (Fig. 3.25A) strongly suggest that pyrites 4, 5, and 6 are metamorphic rather than hydrothermal (Thomas et al., 2011; Gregory et al., 2015) and formed by the recrystallization of pyrites 1, 2, and 3. The evidence of metamorphism is supported by the occurrence of hornfels in this formation (Foo, 1964). Additionally, the sedimentary pyrites (pyrites 1, 2, and 3) are enriched in most trace elements except Tl compared to metamorphic pyrites (pyrites 4, 5, and 6) (Fig. 3.26). This feature is commonly observed in metamorphic pyrites formed by the recrystallization of sedimentary pyrites (Large et al., 2007; Thomas et al., 2011).

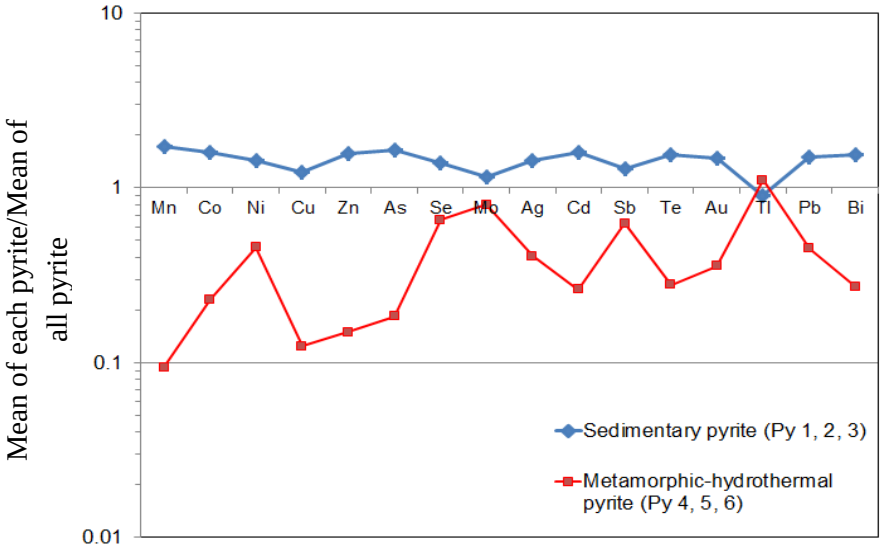

Fig. 3.26. Spider plot showing normalised mean values of selected trace element contents in pyrite for the Pennsylvanian-Early Permian Singa Formation. The trace elements are arranged in order of increasing atomic weight.

Compared with WDP (worldwide diagenetic pyrite, Gregory et al., 2015), the Singa sedimentary pyrites (pyrites 1, 2, and 3) are enriched in Mn, Co, Ni, Cu, Zn, As, Cd, Sb, Te, Au, Pb, and Bi and depleted in Ag, Mo, and strongly depleted in Tl (Fig. 3.27).

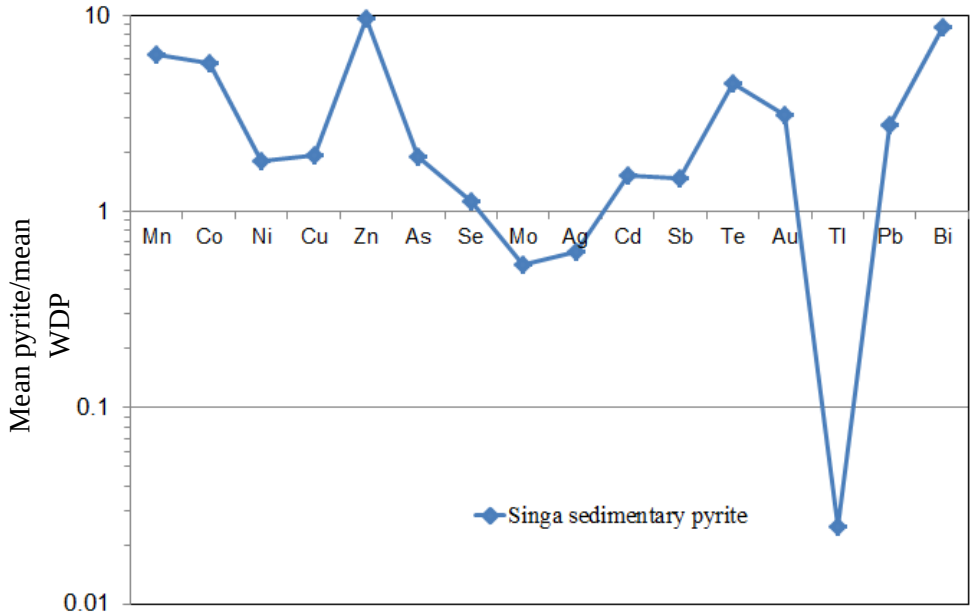

Fig. 3.27. Spider plot showing mean values of selected trace elements in pyrite normalised to WDP (worldwide diagenetic pyrite, Gregory et al., 2015) in the Pennsylvanian-Early Permian Singa Formation. The trace elements are arranged in order of increasing atomic weight.

3.5. BRSZ Unit 1 (Late Devonian)

A total of fifteen samples of sandstone and black shale were analysed for major and trace elements. The samples were collected from a sedimentary section belonging to a BRSZ Unit 1 sequence, which crop out along the Bentong-Raub road in the Central Gold Belt of Peninsular Malaysia. Total organic carbon content and quantification of gold content in sandstones were not determined for the BRSZ Unit 1 due to limited research budget. Results are shown in Table 3.11 for the major and trace element analyses of the BRSZ Unit 1 compared to the average composition of Post-Archean Australian Shale (PAAS) from Taylor and McLennan (1985), the Wedephol's Average Shale (WAS) from Wedephol (1985), the Global Subducting Sediment (GLOSS) from Plank and Langmuir (1998), the North American Shale Composite (NASC) from Gromet et al. (1984), and the Continental Upper Crust (UCC) from Taylor and McLennan (1985).

3.5.1. Major element compositions

On the basis of SiO_2 and Al_2O_3 contents in the sedimentary rocks, the BRSZ Unit1 turbidites display increased silica content in the sandstone (consistent with high SiO_2/Al_2O_3 ratios, 5.1-21.2) whereas the black shales have elevated alumina content (consistent with low SiO_2/ Al_2O_3 ratios, 2.5-3.9). The elevated Al_2O_3 content in the black shales varies from 17.8 to 22.3 wt % relative to sandstones, which have values ranging from 4 to 14 wt %. This chemical difference in Al_2O_3 content is due to higher content of clays in the black shales relative to the sandstones.

Table 3.11. Major (wt %) and trace element (ppm) mean values for the BRSZ Unit 1 compared to PAAS, WAS, GLOSS, NASC and UCC

	Shale	Sandstone	PAAS	WAS	GLOSS	NASC	UCC
SiO2	63.00	78.85	62.80	58.90	58.57	64.8	61.6
TiO2	0.92	0.53	1.00	0.80	0.62	0.78	0.67
Al2O3	19.70	9.03	18.90	16.70	11.91	16.9	15.2
Fe2O3	2.79	2.77	7.20	6.90	-	5.7	6.2
MnO	0.01	0.01	0.11	-	0.32	0.06	0.09
MgO	1.35	0.78	2.20	2.60	2.48	2.9	3.7
CaO	0.01	0.01	1.30	2.20	5.95	3.4	5.5
Na2O	0.10	0.06	1.20	1.60	2.43	1	3.2
K2O	4.62	2.06	3.70	3.60	2.04	3.8	3.4
P2O5	0.03	0.03	0.16	-	0.19	0.13	0.17
Loss	7.19	6.06	-	-	-	-	-
Total	99.70	100.18	-	-	-	-	-
S	0.34	0.87	-	0.20	-	-	697
ppm		-					
Sc	20.54	10.50	16.00	-	13.10	14.9	16
Ba	689.55	353.45	650.00	580.00	776.00	636	584
V	294.25	215.68	150.00	130.00	110.00	nd	98
Cr	122.64	78.32	110.00	90.00	78.90	125	126
Ni	37.17	30.21	55.00	68.00	70.50	58	56
Cu	72.90	25.71	50.00	45.00	75.00	-	25
Zn	29.52	30.62	85.00	95.00	86.40	-	65
Ga	27.27	11.79	20.00	-	-	-	15
As	15.64	14.71	-	10.00	-	28.4	1.7
Se	1.85	27.67	-	0.50	-	-	0.12
Rb	229.90	100.56	160.00	140.00	57.20	125	78
Sr	34.25	32.53	200.00	300.00	327.00	142	333
Y	36.00	22.61	27.00	-	29.80	-	24
Zr	213.07	163.56	210.00	160.00	130.00	200	203
Nb	22.58	13.92	19.00	-	8.94	-	19
Mo	7.07	3.66	1.00	1.00	-	-	1.1
Ag	-	2.72	-	0.07	-	-	0.07
Au (ppb)	23.00	-	-	2.30	-	-	-
Sn	5.66	2.48	4.00	6.00	-	-	2.3
Sb	2.96	3.89	-	1.50	-	2.09	0.3
Te	2.35	2.60	-	-	-	-	0.005
Tl	2.33	-	-	0.68	-	-	0.52
Pb	50.98	24.93	20.00	22.00	19.90	-	0.0004
Bi	-	-	-	0.10	-	-	0.085
U	7.31	4.22	3.10	3.70	1.68	2.66	1.7
Th	17.81	10.48	14.60	-	6.91	12.3	8.5

- = data not available; Detection limit for the major element is 0.01 wt %. TE: trace element

The K_2O/Al_2O_3 ratio for the BRSZ-U1 black shales ranges from 0.21 to 0.15 (mean 0.23) and that of sandstones is between 0.18 and 0.33 (mean 0.25) compared to 0.24 for North American Shale Composite (NASC; Gromet et al., 1984), 0.22 for Wedephol's Average Shale (WAS; Wedephol, 1995), 0.19 for Post Archean Average Shale (PAAS; Taylor and McLennan, 1985), 0.17 for Global Subducting Sediment (GLOSS; Plank and Langmuir, 1998), 0.17 for Upper Continental Crust (UCC; Taylor and McLennan, 1985). Compared to PAAS, the black shales have slightly higher K_2O contents and lower Fe_2O_3, MgO, Na_2O, and P_2O_5 contents (Fig. 3.28).

The values of K_2O/Al_2O_3 ratio that range from 0.18 to 0.33 (mean 0.24) for the BRSZ Unit 1 correspond to the presence of hydromuscovite as the principal K-Al-bearing mineral (Fig. 3.29). In addition, the data indicates that the proportion of Zr (mean 213 ppm) is much higher in the shales than in the sandstones (mean 164 ppm) indicative of heavy minerals existence in the shales of the BRSZ Unit 1 turbidites. There is little variation in Fe_2O_3 content in the turbidite section of the BRSZ Unit 1 both in the black shales and sandstones. However, elevated iron is observable in individual pyrite-rich samples, which under the microscope showed the presence of disseminated pyrite framboids and coarse euhedral to subhedral pyrites.

The MgO content is low in both sandstones and black shales, which is indicative of a reduced phase of Mg-rich minerals such as garnet or magnesite commonly found in sediments. Compared to sandstones, the higher proportion of TiO_2 in the shales may be related to the existence of heavy minerals such as rutile and zircon.

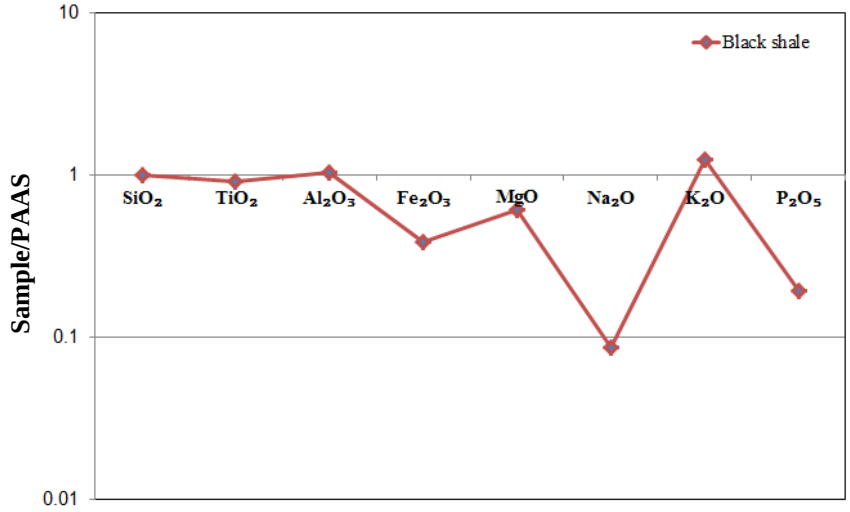

Fig. 3.28. Spider plot of major elements (mean values in wt%) in black shale for the BRSZ Unit 1 normalised to PAAS.

The low content of Na_2O in the sedimentary rocks suggests that they are mature, which is related to the removal of alkali elements. The P_2O_5 content of the sedimentary rocks is low (0.008-0.078 wt %) suggesting that the amount of detrital apatite is negligible in the sedimentary matrix. It is noticeable that most Fe-rich samples have higher amounts of sulphur, which is likely present as sedimentary pyrite in the Late Devonian BRSZ Unit 1 turbidites (Fig. 3.30). Petrographic observation shows that the highest peak in the organic-rich sandstone actually indicates a stratigraphic position (e.g. Sample no. BE-2712) bearing greater amounts of framboidal and euhedral pyrites across the whole formation.

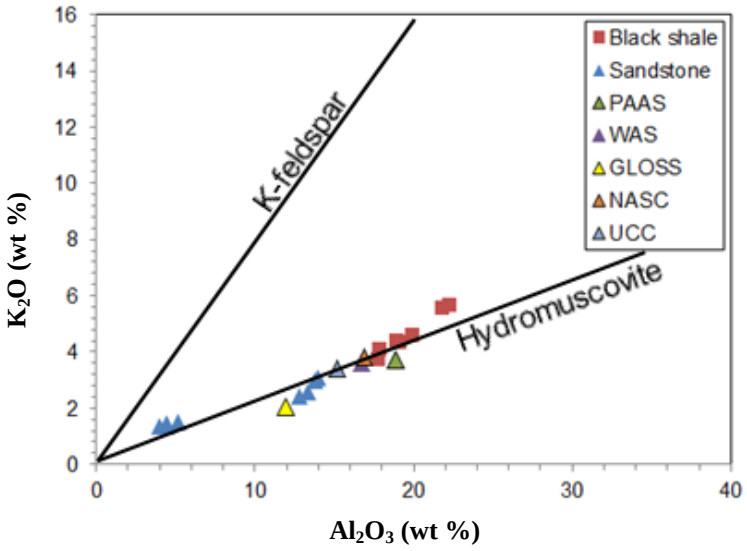

Fig. 3.29. Lithogeochemical plots for the BRSZ Unit 1. **A**) Al_2O_3-K_2O for the BRSZ Unit 1 showing a linear trend for the black shale facies passing through NASC, WAS, and UCC and close to PAAS. There is a curvilinear trend that passes near GLOSS for the sandstone facies. The K-feldspar and hydromuscovite lines are drawn based on data from Deer et al. (1966).

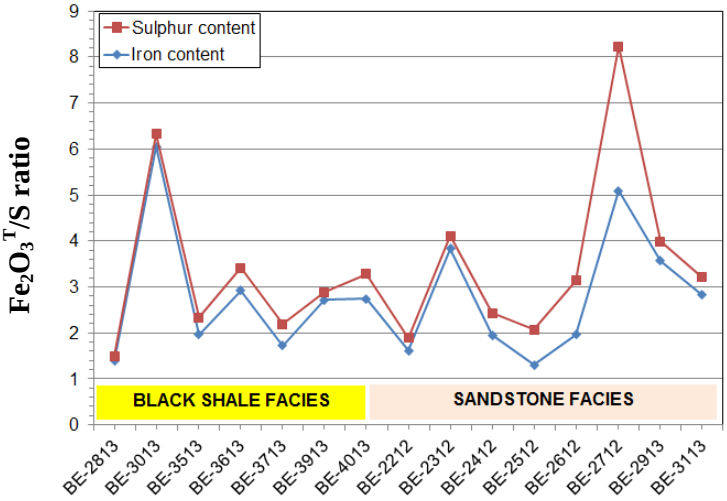

Fig. 3.30. Line plot showing variation in sulphur and iron contents from the BRSZ Unit 1 black shales and sandstones.

3.5.2. Trace element compositions

As documented in Table 3.11, a number of trace elements were analysed from whole rock samples of the BRSZ Unit 1. However, some trace elements such as Te, Tl, Bi, and Ag were not plotted against Al_2O_3 because their results were mostly close to the detection limit. The trace element content in the BRSZ Unit 1 show significant variations in the sandstones

and black shales. As expected, the black shales have elevated levels of trace elements compared to sandstones. The black shales have elevated contents of V, Cr, Ba, Zr, Mo, Sn, Pb, U, Cu, Ni, and Zn. However, the sandstones have higher contents in Se, Te, and As and lower contents in other trace elements (Table 3.11). In order to investigate the controls on trace element deposition, binary plots of alumina against trace elements are shown in Figs. 3.31-3.32. Previous researchers have used Al_2O_3 content as a proxy for detrital fluxes (aluminosilicate fraction in the sediments) to infer detrital origin of metals adsorbed onto clay particles or within the structure of aluminosilicate minerals (Calvert and Pedersen, 1993; Tribovillar et al., 1994; Hild and Brumsack, 1998; Böning et al., 2004; Tribovillar et al., 2006).

In view of the trace element patterns in black shales, three groups have been identified based on the correlation coefficients for each trace element. The first group has trace elements that show strong positive correlation with Al_2O_3 (Table 3.12) including Cr, V, Sn, Mo and As. The second group, which contains trace elements that exhibit weak correlation with Al_2O_3, include Sb, Se, and Zn. The third group comprises trace elements that show no or negative correlation with Al_2O_3 are Ni, Cu, and Au. Trace elements that exhibit a good correlation with Al_2O_3 may have been introduced with detrital aluminosilicates into the basin. Many of the trace elements in the shales that correlate positively with Al_2O_3 also correlate with organic carbon; particurlay V, U, Cr, Se, Mo, Sb, and Sn suggesting that both clays and organic matter have acted to concentrate the elements. Trace elements that have weak and negative correlation with Al_2O_3 may have been adsorbed onto organic matter or syngenetic pyrite with partial input from detritus. Remarkably, Al_2O_3 content varies positively with Cr, Ni, Zn, Sn and U in the sandstones (Table 3.13).

Table 3.12. Correlation coefficients for the BRSZ Unit 1 black shales. Highlighted numbers are equal to or greater than 0.5 for positive correlation between two variables.

Correlation	Al_2O_3_wt %	Org.C_wt %	S_wt %	Au_ppb	V_ppm	Cr_ppm	Ni_ppm	Cu_ppm	Zn_ppm	As_ppm	Se_ppm	Mo_ppm	Sn_ppm	Sb_ppm	U_ppm
Al_2O_3_wt %	1														
Org.C_wt %	0.76	1													
S_wt %	0.31	0.42	1												
Au_ppb	-0.34	-0.54	-0.39	1											
V_ppm	0.83	0.99	0.35	-0.47	1										
Cr_ppm	0.99	0.81	0.39	-0.41	0.87	1									
Ni_ppm	0.21	0.52	0.89	-0.42	0.41	0.33	1								
Cu_ppm	0.15	0.29	0.42	-0.94	0.22	0.22	0.37	1							
Zn_ppm	0.54	0.058	0.18	0.31	0.14	0.53	0.091	-0.32	1						
As_ppm	0.71	0.6	0.18	-0.23	0.67	0.75	0.056	0.18	0.43	1					
Se_ppm	0.64	0.85	0.045	-0.53	0.87	0.64	0.072	0.29	-0.25	0.52	1				
Mo_ppm	0.75	0.91	0.083	-0.3	0.94	0.79	0.2	0.04	0.18	0.74	0.84	1			
Sn_ppm	0.79	0.61	0.35	-0.29	0.68	0.82	0.16	0.26	0.49	0.97	0.51	0.67	1		
Sb_ppm	0.58	0.91	0.11	-0.44	0.91	0.61	0.25	0.16	-0.22	0.46	0.95	0.9	0.41	1	
U_ppm	0.76	0.79	-0.17	-0.25	0.85	0.75	-0.065	-0.029	0.17	0.65	0.85	0.94	0.57	0.85	1

Table 3.13. Correlation coefficients for the BRSZ Unit 1 sandstones. Highlighted numbers are equal to or greater than 0.5 for positive correlation between two variables.

Correlation	Al_2O_3_wt %	Org.C_wt %	S_wt %	V_ppm	Cr_ppm	Ni_ppm	Cu_ppm	Zn_ppm	As_ppm	Mo_ppm	Sn_ppm	Sb_ppm	U_ppm
Al_2O_3_wt %	1												
Org.C_wt %	-0.82	1											
S_wt %	-0.77	0.89	1										
V_ppm	-0.39	0.84	0.76	1									
Cr_ppm	0.91	-0.8	-0.59	-0.42	1								
Ni_ppm	0.97	-0.84	-0.79	-0.44	0.86	1							
Cu_ppm	-0.26	-0.0054	-0.2	-0.41	-0.29	-0.24	1						
Zn_ppm	0.85	-0.9	-0.7	-0.61	0.88	0.92	-0.16	1					
As_ppm	0.24	0.17	0.25	0.61	0.16	0.28	-0.86	0.14	1				
Mo_ppm	0.47	-0.014	-0.13	0.46	0.22	0.49	-0.66	0.2	0.87	1			
Sn_ppm	0.89	-0.7	-0.62	-0.23	0.77	0.94	-0.54	0.82	0.57	0.7	1		
Sb_ppm	0.054	0.39	0.049	0.61	-0.21	-0.071	-0.17	-0.46	0.3	0.59	0.018	1	
U_ppm	0.83	-0.43	-0.57	0.058	0.59	0.81	-0.37	0.52	0.53	0.83	0.84	0.51	1

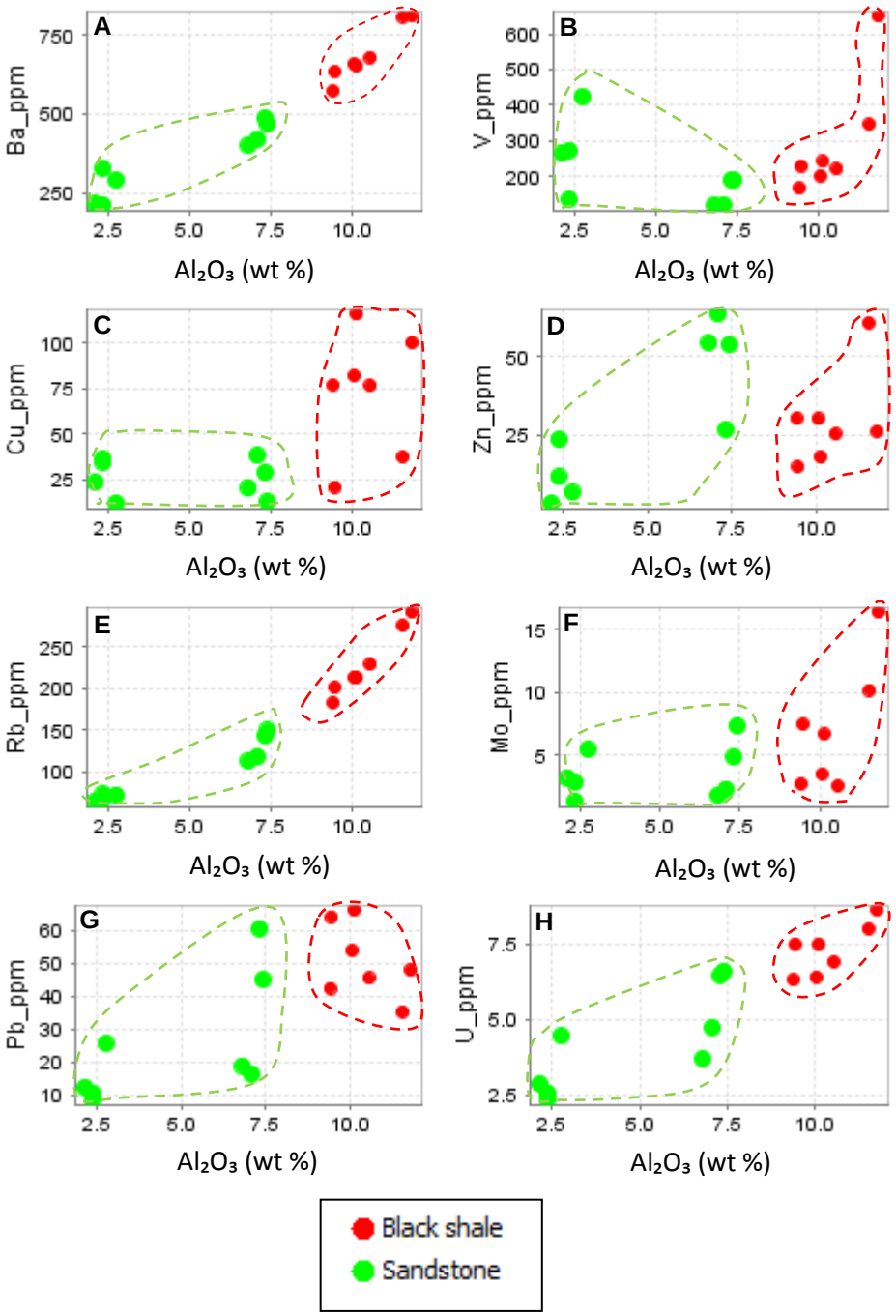

Fig. 3.31. Trace element relationships with Al_2O_3 in black shales and sandstones of the BRSZ Unit 1, Malaysia.

The positive relationship of Al_2O_3 to Sn, Ba and Rb is consistent with these elements being locked in alumina-silicate clays probably linked to a prolonged transport history of detrital

clays from their source rocks in the region (Reid and Frostick, 1985; Slingerland and Smith, 1986).

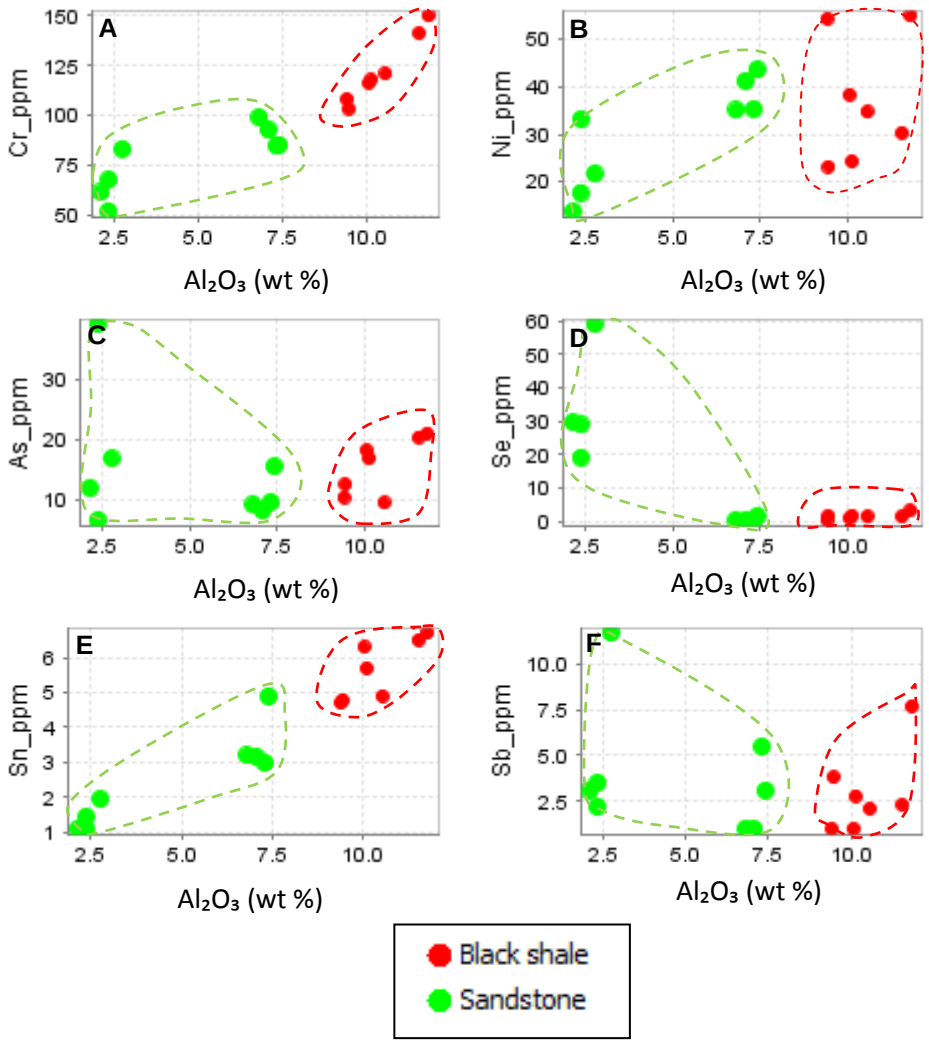

Fig. 3.32. Relationships of trace elements with Al_2O_3 in black shales and sandstones of the BRSZ Unit 1.

Comparing with Wedephol's Average Shale (WAS, Wedephol, 1995), the enrichment factors of trace elements in the BRSZ Unit 1 black shales indicate that the elements such as As, S, Ba, V, Cr, Cu, Se, Zr, Sb, Tl, Pb and U are enriched 1-3 times over the average shale. But Mo is enriched 7 times over the average shale. In the black shales, organic carbon content varies

positively with V, U, Cr, and alumina (Fig. 3.33, Table 3.12). In the sandstones, organic carbon content varies positively with V and S but it shows a negative correlation with Cr, Ni, Zn, and alumina (Fig. 3.33, Table 3.13).

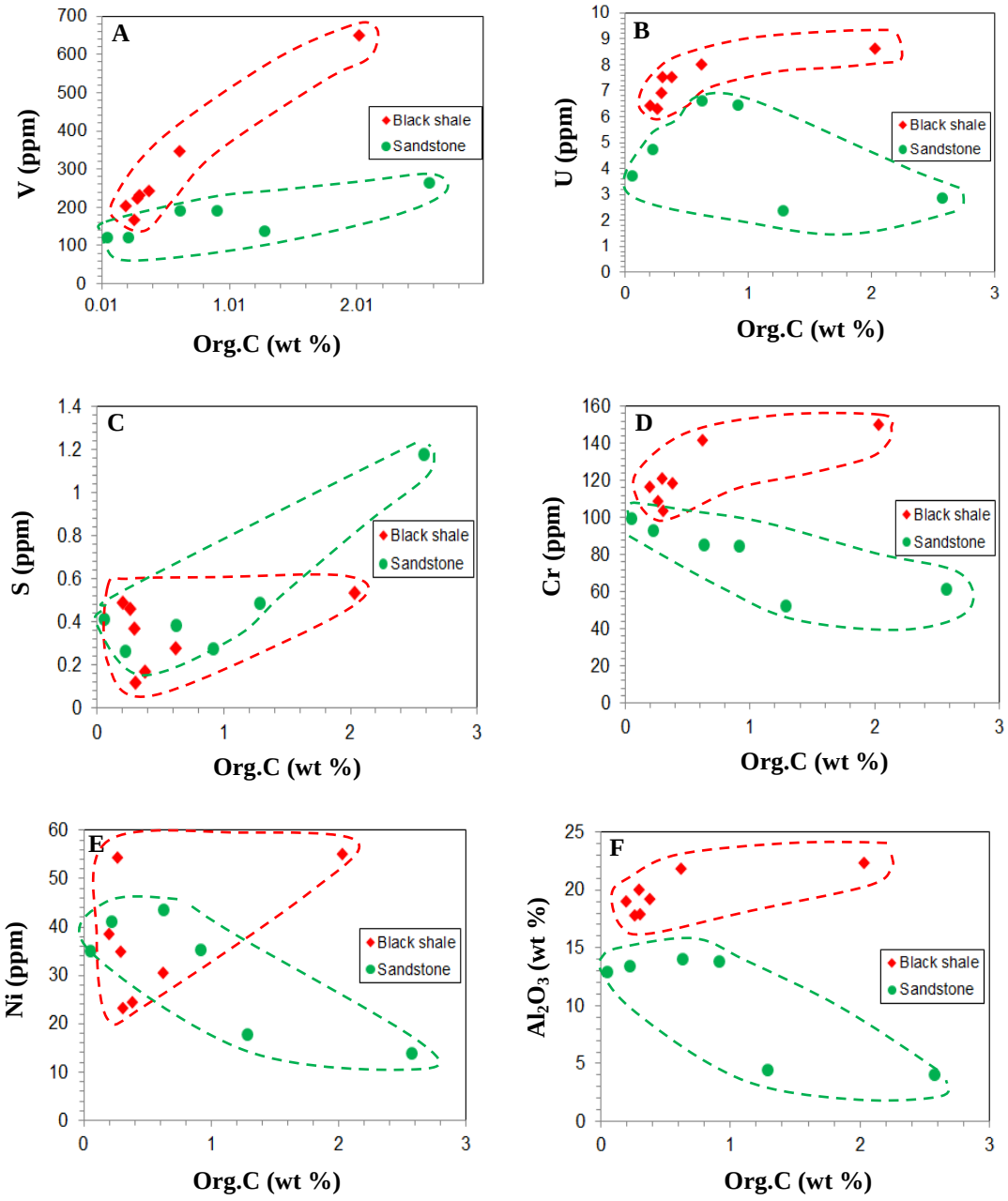

Fig. 3.33. Relationships of organic carbon to trace elements in the BRSZ Unit 1. **A**) Organic carbon versus V. **B**) Organic carbon versus U. **C**) Organic carbon versus sulphur. **D**) Organic carbon versus Cr. **E**) Organic carbon versus Ni. **F**) Organic carbon versus alumina.

3.5.3. Comparative lithogeochemistry of Palaeozoic shales from the Late Cambrian-Early Ordovician Machinchang (MCF), Pennsylvanian-Early Permian Singa (SGF), and Late Devonian BRSZ Unit 1 (BU1)

In an attempt to compare the major element composition in shales, mean values for the Late Cambrian-Early Ordovician MCF shales, the Pennsylvanian-Early Permian SGF shales, and the Late Devonian BU1 shales are plotted in Fig. 3.34. The Silurian shales are elevated in SiO_2, Fe_2O_3, MgO, MnO, Na_2O, CaO, and P_2O_5 compared to the Late Cambrian-Early Ordovician and Devonian shales; but depleted in Al_2O_3, TiO_2, and K_2O. The MCF grey shales and the BU1 black shales obviously contain no Ca-bearing phases which is indicated by values below detection limit (0.01 wt %). The only recorded elevated CaO content is in the Pennsylvanian-Early Permian SGF black shales. This is due to some amount of CaO in the Singa Formation black shales related to the presence of calcite veinlets in few hand specimens. The relatively elevated contents in Fe_2O_3 in the Pennsylvanian-Early Permian SGF black shales may be explained by the abundance of disseminated diagenetic and hydrothermal pyrites as well as goethite in some samples evidenced by petrographic observation.

In view of the existing trends, it is concluded that the MCF grey shales are relatively enriched in Al_2O_3, and K_2O compared to the other formations. The SGF black shales contain elevated Fe_2O_3, MgO, MnO, Na_2O, CaO, and P_2O_5 relative to other shales. However, the BU1 black shales have highest contents of TiO_2 and lower values in other major elements compared to other shales. It is important to notice that although the MnO content is higher in the SGF black shales, it is still low and only slightly above the detection limit (0.01 ppm).

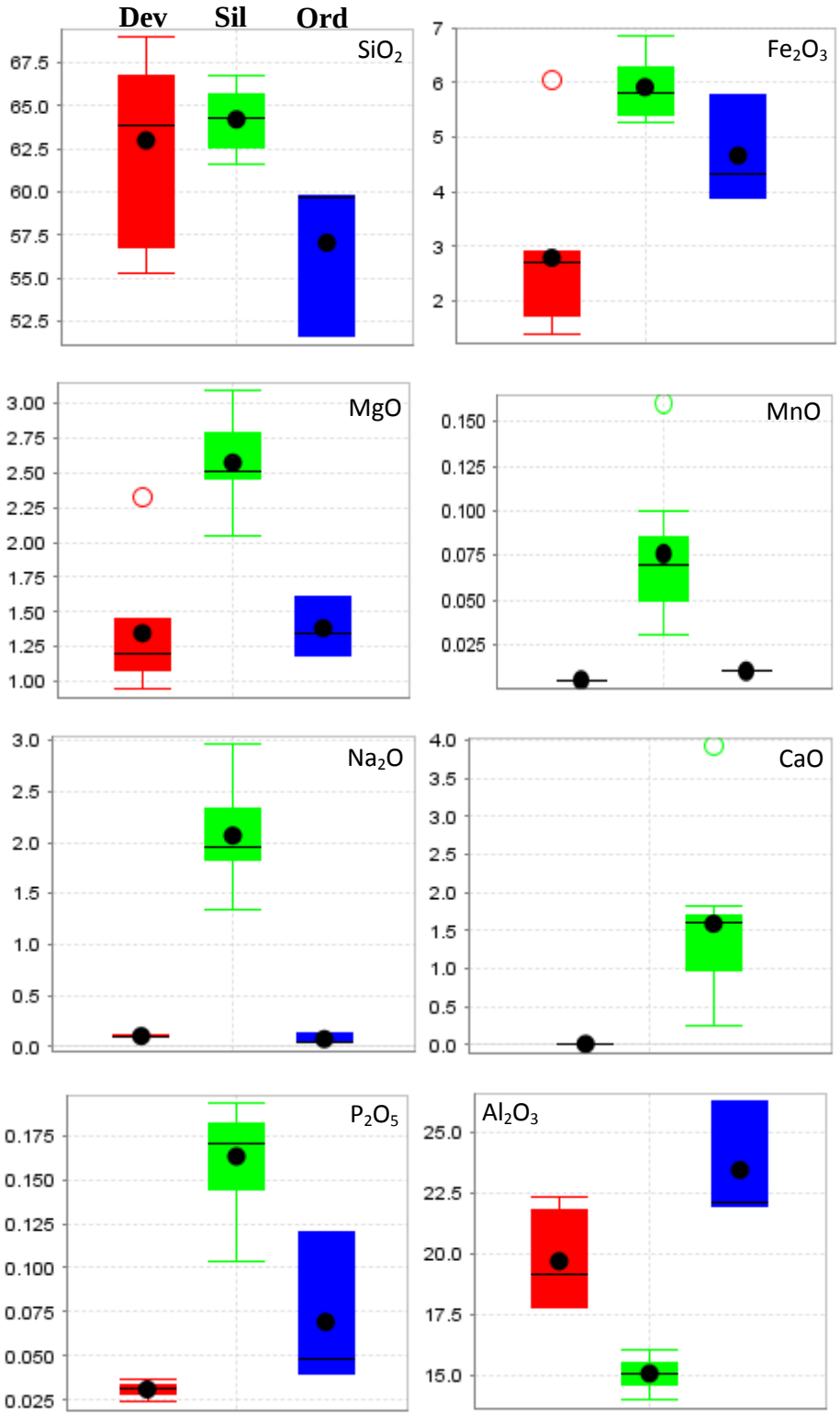

Fig. 3.34. Turkey box plot of mean major element contents (wt %) of grey and black shales from the Late Cambrian-Early Ordovician Machinchang (blue), the Pennsylvanian-Early Permian Singa (green) and the Late Devonian BRSZ Unit 1 (red). Note: Age abbreviations are **Dev** for Devonian, **Sil** for Silurian, and **Ord** for Ordovician.

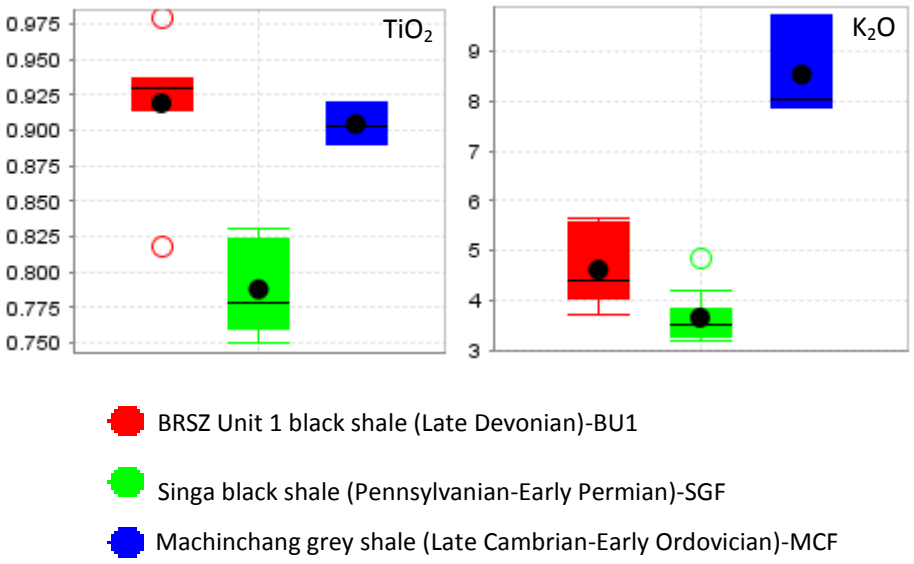

Fig. 3.34 (continued) Turkey box plot of mean major element contents of grey and black shales from the Late Cambrian-Early Ordovician Machinchang, the Pennsylvanian-Early Permian Singa and the Late Devonian BRSZ Unit 1. The black circle represents the mean value. The open circle represents an outlier, which is the top and bottom 5% of the data.

An approach on evaluating the original detrital mineralogy in Palaeozoic shales is to use the Index of Compositional Variability (ICV) and ratio of K_2O/Al_2O_3 (Cox et al., 1995). ICV is defined as: ICV = $(Fe_2O_3+K_2O+Na_2O+CaO+MgO+MnO)/ Al_2O_3$. According to Cox et al. (1995), more mature mudstones or shales with mostly clay minerals should display lower ICV values that are <1.0. The ICV discrimination plot is shown in Fig. 3.35A. The ICV values for the MCF grey shales vary from 0.6 to 6.20 (average 3.51), those of the SGF black shales range from 0.97 to 1.12 (average 1.04) and those of the BU1 black shales are between 0.36 and 0.64 (average 0.45). The evidence indicates that the MCF grey shales major element composition may have been controlled by feldspars with lesser amount of clays. The SGF black shale major element composition implies a mixed control of clays and non-clay silicates particularly K-feldspar. This observation is consistent with the presence of altered feldspar and plagioclase crystals in thin sections.

The major element contents in the Late Devonian BU1 black shales were controlled by the input of clay minerals as these major elements plot below the K_2O/Al_2O_3= 0.3 line (Fig. 3.35B).

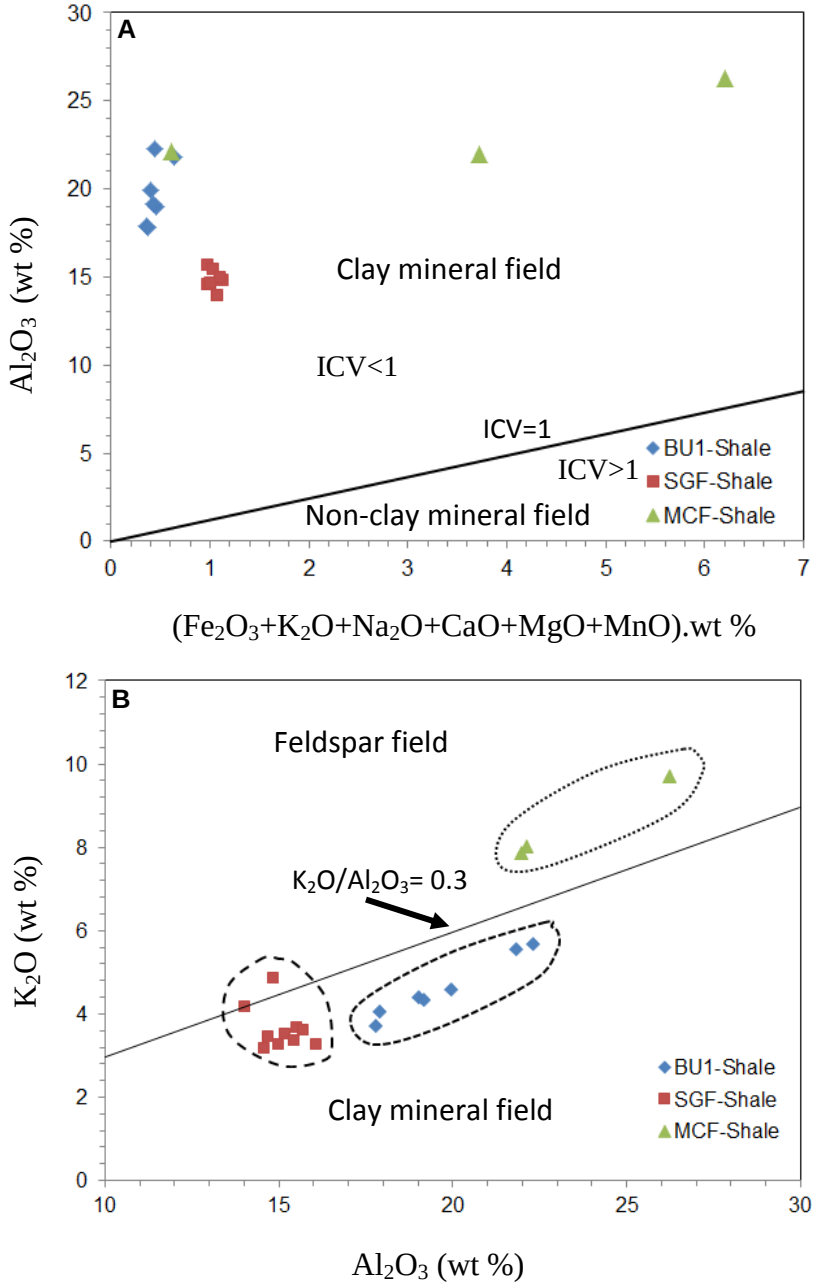

Fig. 3.35. Major element composition plots of shales. **A**) Index of compositional variation of oxides. **B**) Binary discrimination diagram of K_2O versus Al_2O_3 for shales from the Late Cambrian-Early Ordovician Machinchang Formation (MCF), the Pennsylvanian-Early Permian Singa Formation (SGF), and the Late Devonian BRSZ Unit 1 (BU1) (after Cox et al., 1995).

Comparison of trace element concentrations in Fig. 3.36 indicates that BRSZ Unit 1 is the most enriched in V, Cr, Mo, Pb, and U. Singa Formation is comparatively enriched in Zn and the Machinchang Formation is comparatively enriched in Ba and Th.

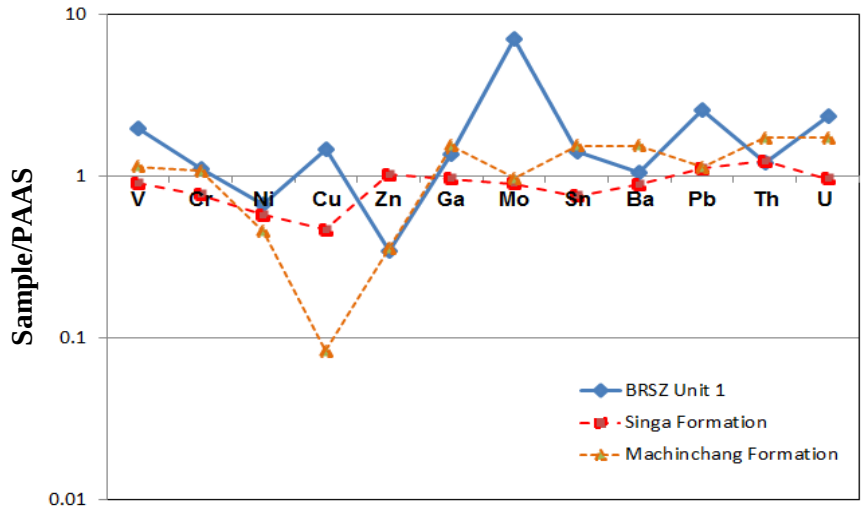

Fig. 3.36. Comparative spider plot of selected trace elements in whole rocks (mean values) from the Late Devonian BRSZ Unit 1 normalised to PAAS (Post-Archean Australian Shale, Taylor and McLennan, 1985) with the Late Cambrian-Early Ordovician Machinchang and Pennsylvanian-Early Permian Singa Formations as background for chemical comparison.

3.5.4. Pyrite texture and composition

The BRSZ Unit 1 black shales contain framboidal and euhedral pyrites that can be grouped into two types as follows: (1) Type 1 comprises cluster of pyrite framboids (up to 100 µm across) and disseminated coarse grained framboids (up to 30 µm across); and (2) Type 2 has micro sized euhedral to subhedral clean pyrite (up to 60 µm wide) (Fig. 3.37).

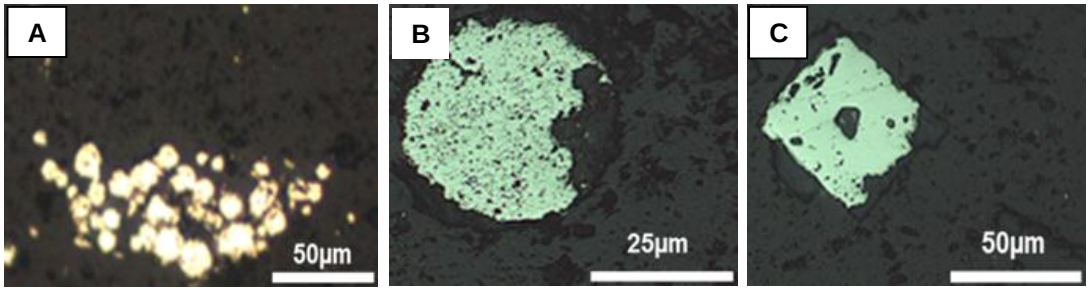

Fig. 3.37. Pyrite textures in the BRSZ Unit 1 black shales. **A**) Cluster of microcrystals of pyrite (Type 1). **B**) Framboidal pyrites (Type 1). **C**) Euhedral pyrite (Type 2).

Composition of trace elements in pyrite from the BRSZ Unit 1 is documented in Table. 3.16. Relationships of Ni to Co and Cu as well as Se to Mo are shown in Fig. 3.38. The Co content in pyrite 1 varies from 1 to 71 (mean 15 ppm) and that of Ni ranges from 97 to 7712 (mean 1047 ppm). In addition, the Cu content is between 68 and 1653 (mean 586 ppm). The Co and Ni values plot within the field of sedimentary pyrite of Gregory et al. (2015). Likewise, for the Cu-Ni, Mo-Se, and As-Ni plots, all pyrite data are confined to the field of sedimentary pyrite (Fig. 3.38). In framboidal pyrite 1, the trace element content varies significantly. In pyrite 1, the mean concentration of trace elements in decreasing order is as follows: Pb>Ni>Cu>Zn>As>Se>Sb>Ag>Te>Co>Mo>V>Tl>Cd>Au=Bi. However, in the euhedral pyrite 2, the mean concentration of trace elements in decreasing order is as follows: Pb>Ni>Cu>Zn>Se>As>Co>Sb>Ag>Te>V>Tl>Mo>Au>Cd>Bi. There is a negligible variation in trace element content between both pyrite types.

The gold content in pyrite 1 varies from 0.07 to 5 ppm (mean 0.9 ppm). In comparison, the gold content in pyrite 2 ranges up to 4 ppm (mean 1.2 ppm). Relationships between Au and other trace elements are shown in Fig. 3.39. There is a positive correlation between Au, Ag and As and a weak correlation with Te. In contrast, V, Mo, and Ni have no correlation with Au (Fig. 3.39). The texture and composition of both pyrite 1 and pyrite 2 strongly suggest a sedimentary origin as all data plot within the sedimentary pyrite field and

have Ag/Au>1 and As/Ni<10. Correlation coefficients for pyrite 1 and pyrite 2 are presented in Tables 3.14 and 3.15. Results of pyrite spot analyses are shown in Table 3.16.

Table 3.14. Correlation coefficient in framboidal pyrite (pyrite 1) in the BRSZ Unit 1. Highlighted numbers are equal to or greater than 0.5 indicate positive correlation between two variables.

Correlation	Mn_ppm	V_ppm	Co_ppm	Ni_ppm	Cu_ppm	Zn_ppm	As_ppm	Se_ppm	Mo_ppm	Ag_ppm	Cd_ppm	Sb_ppm	Te_ppm	Au_ppm	Tl_ppm	Pb_ppm	Bi_ppm
Mn_ppm	1																
V_ppm	0.21	1															
Co_ppm	0.2	-0.12	1														
Ni_ppm	-0.23	0.24	-0.4	1													
Cu_ppm	0.34	0.15	0.67	0.39	1												
Zn_ppm	-0.27	0.15	0.35	0.96	0.53	1											
As_ppm	0.16	-0.13	0.46	-0.1	0.28	-0.047	1										
Se_ppm	0.5	0.45	0.37	0.68	0.49	0.19	-0.2	1									
Mo_ppm	0.14	-0.027	-0.38	-0.52	-0.31	-0.54	-0.2	0.052	1								
Ag_ppm	0.044	0.046	0.71	0.77	0.7	0.89	0.3	0.53	-0.51	1							
Cd_ppm	0.33	-0.11	-0.11	-0.11	0.18	0.0095	-0.13	0.095	0.23	-0.2	1						
Sb_ppm	0.12	-0.11	0.61	0.053	0.45	0.36	0.13	0.47	0.08	0.64	-0.078	1					
Te_ppm	0.84	0.053	0.15	-0.25	0.26	-0.16	0.05	0.39	0.042	-0.011	0.39	0.054	1				
Au_ppm	-0.12	0.0023	0.61	0.37	0.36	0.58	0.019	0.76	-0.37	0.65	-0.11	0.63	-0.12	1			
Tl_ppm	-0.14	0.18	-0.041	0.6	0.27	0.58	2.30E-04	0.3	0.061	0.51	0.0087	0.49	-0.25	0.29	1		
Pb_ppm	0.08	-0.057	0.86	1	0.67	0.87	0.42	0.35	-0.59	0.89	-0.24	0.58	-4.90E-04	0.55	0.19	1	
Bi_ppm	0.54	-0.047	0.18	-0.63	0.065	-0.43	-0.057	0.56	0.35	-0.18	0.24	0.13	0.62	0.026	-0.36	-0.15	1

Table 3.15. Correlation coefficients in euhedral fine-grained pyrite (pyrite 2) in the BRSZ Unit 1. Highlighted numbers are equal to or greater than 0.5 indicate positive correlation between two variables.

Correlation	Mn_ppm	V_ppm	Co_ppm	Ni_ppm	Cu_ppm	Zn_ppm	As_ppm	Se_ppm	Mo_ppm	Ag_ppm	Cd_ppm	Sb_ppm	Te_ppm	Au_ppm	Tl_ppm	Pb_ppm	Bi_ppm
Mn_ppm	1																
V_ppm	-0.15	1															
Co_ppm	0.15	0.32	1														
Ni_ppm	0.16	0.19	-0.13	1													
Cu_ppm	0.39	0.22	0.29	0.54	1												
Zn_ppm	0.0079	0.24	-0.027	0.89	0.09	1											
As_ppm	0.67	-0.16	0.065	0.71	0.43	0.26	1										
Se_ppm	0.41	0.077	0.41	0.48	0.098	0.11	0.67	1									
Mo_ppm	0.24	-0.098	0.26	-0.33	-0.026	-0.32	0.12	0.7	1								
Ag_ppm	0.6	-0.097	0.0099	0.94	0.46	0.85	0.91	0.48	-0.062	1							
Cd_ppm	0.41	0.3	0.64	2.30E-04	0.6	0.071	0.32	0.4	0.51	0.23	1						
Sb_ppm	0.46	-0.24	-0.099	0.64	0.38	0.17	0.83	0.29	0.039	0.83	0.2	1					
Te_ppm	0.84	-0.19	0.013	0.41	0.42	-0.022	0.87	-0.074	0.055	0.83	0.22	0.67	1				
Au_ppm	0.49	-0.094	-0.12	0.91	0.52	0.69	0.76	-0.24	-0.12	0.8	0.19	0.88	0.67	1			
Tl_ppm	0.63	-0.097	-0.06	0.5	0.42	0.55	0.68	0.68	0.066	0.73	0.32	0.73	0.6	0.83	1		
Pb_ppm	0.36	-0.011	-0.011	0.92	0.61	0.72	0.79	-0.47	-0.21	0.86	0.19	0.81	0.62	0.78	0.57	1	
Bi_ppm	0.37	-0.087	0.28	-0.4	0.22	-0.17	0.16	0.12	0.22	0.2	0.26	0.12	0.29	-0.045	0.13	0.098	1

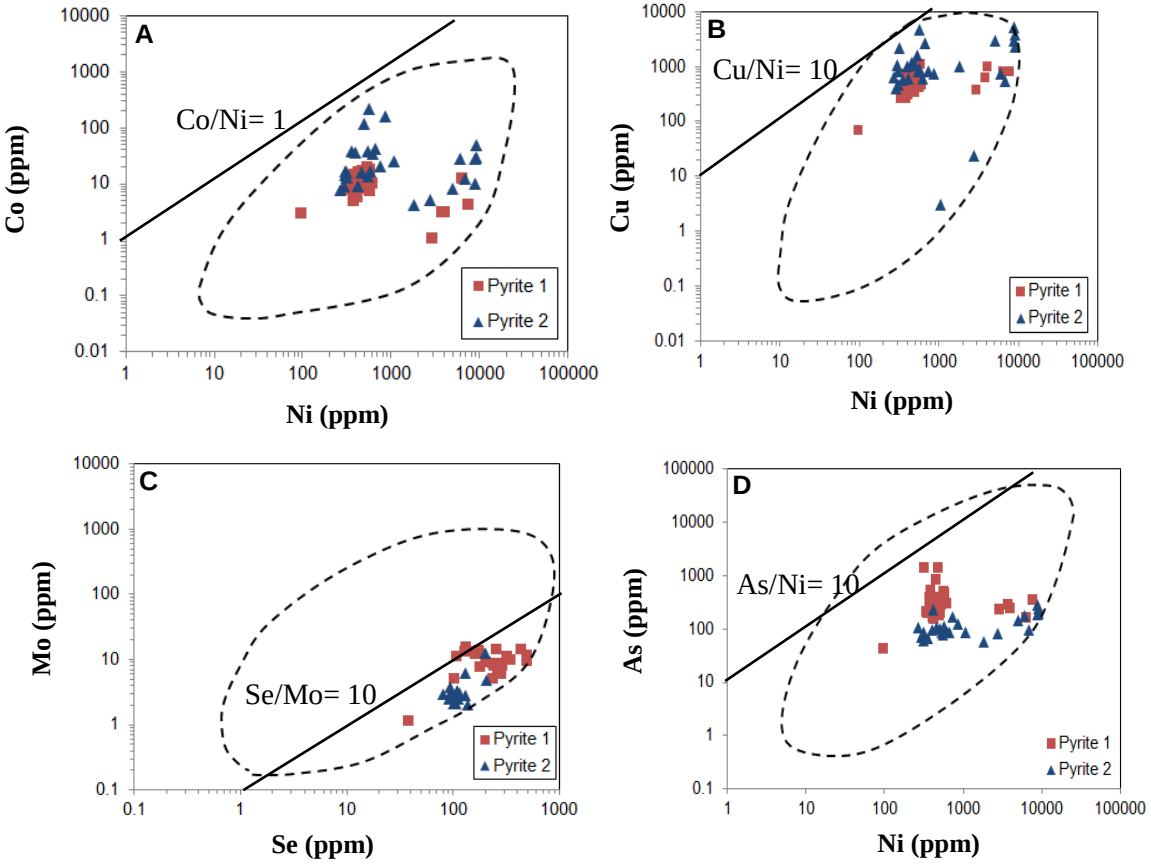

Fig. 3.38. Binary plots of framboidal and euhedral pyrites from the BRSZ Unit 1, Malaysia. **A**) Co-Ni plot. **B**) Cu-Ni plot. **C**). Se-Mo plot. **D**) As-Ni plot. Dashed polygon represents the outline for sedimentary pyrite (Gregory et al., 2015).

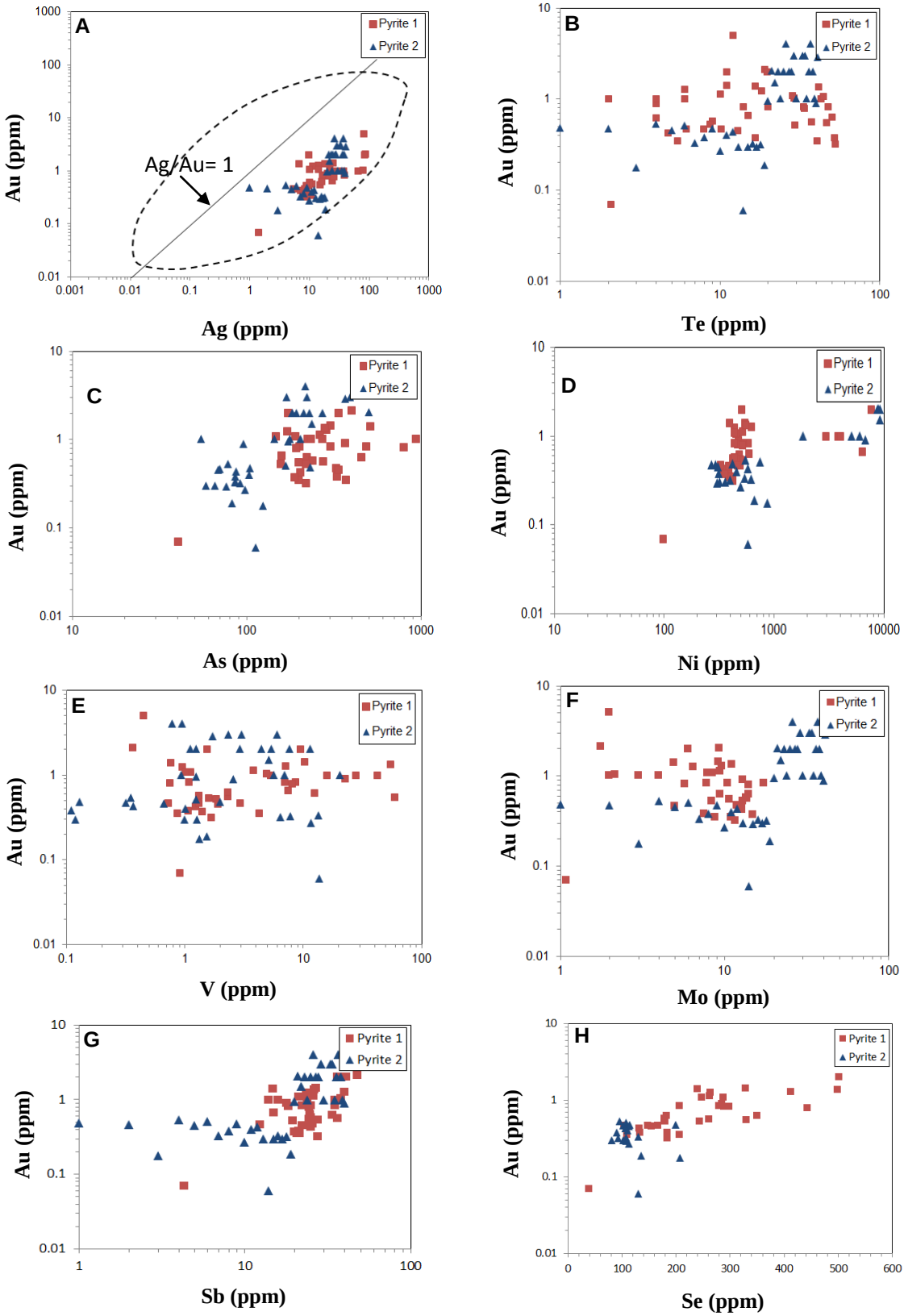

Fig. 3.39. Binary plots of framboidal and euhedral pyrites from the BRSZ Unit 1, Malaysia. **A**) Ag-Au plot. **B**) Te-Au plot. **C**) As-Au plot. **D**) Ni-Au plot. **E**) V-Au plot. **F**) Mo-Au plot. **G**) Sb-Au plot. **H**) Se-Au plot. Dashed polygon in Fig. 3.39A represents the field of sedimentary pyrite (Gregory et al., 2015). All data plots in the field Ag>Au (plot A) and confirms the sedimentary origin of the pyrite and associated gold.

Table 3.16. LA ICP-MS Analyses of pyrite from the BRSZ Unit 1 turbidites, Malaysia.

Analysis no.	Pyrite type	Mn	V	Co	Ni	Cu	Zn	As
Ap16A007	Pyrite 1	2571.00	6.97	7.00	578.00	404.00	24.00	488.00
Ap16A008	Pyrite 1	427.00	7.06	10.00	621.00	459.00	21.00	286.00
Ap16A009	Pyrite 1	1032.00	3.77	8.00	518.00	426.00	17.00	262.00
Ap16A010	Pyrite 1	2343.00	8.60	9.00	521.00	524.00	20.00	303.00
Ap16A011	Pyrite 1	733.00	10.27	15.00	539.00	628.00	14.00	304.00
Ap16A012	Pyrite 1	253.00	22.41	12.00	476.00	480.00	9.00	369.00
Ap16A013	Pyrite 1	343.00	12.36	12.00	481.00	743.00	27.00	222.00
Ap16A024	Pyrite 1	1847.00	7.41	12.00	6378.00	783.00	-	158.00
Ap16A026	Pyrite 1	144.00	0.36	55.00	-	1045.00	5640.00	399.00
Ap16A050	Pyrite 1	5695.00	5.29	53.00	-	1653.00	-	938.00
Ap16A046	Pyrite 1	1318.00	0.45	71.00	-	1069.00	-	451.00
Ap16A035	Pyrite 1	6951.00	4.92	60.00	-	1166.00	-	1580.00
Ap16A072	Pyrite 1	859.00	15.82	1.00	2946.00	361.00	1987.00	224.00
Ap16A078	Pyrite 1	144.00	42.51	3.00	3851.00	633.00	1954.00	273.00
Ap16A077	Pyrite 1	529.00	27.86	3.00	4051.00	971.00	3657.00	233.00
Ap16A074	Pyrite 1	1653.00	9.54	4.00	7712.00	782.00	5050.00	337.00
My01a007	Pyrite 1	3393.43	0.75	12.78	467.06	477.33	36.42	800.67
My01a008	Pyrite 1	2901.69	1.06	10.04	386.72	288.30	24.27	329.23
My01a010	Pyrite 1	5236.63	4.23	10.85	385.35	717.27	324.57	372.60
My01a011	Pyrite 1	6615.96	59.53	12.93	485.57	658.04	77.24	198.51
My01a013	Pyrite 1	17.89	0.91	2.80	96.96	67.76	4.81	40.41
My01a014	Pyrite 1	3866.96	1.84	10.28	419.43	379.26	98.71	156.83
My01a015	Pyrite 1	2308.50	0.95	11.29	432.84	360.35	35.12	170.83
My01a016	Pyrite 1	4192.52	1.09	8.76	437.01	376.55	85.12	201.40
My01a017	Pyrite 1	2822.56	1.53	11.10	503.09	335.12	30.25	173.64
My01a018	Pyrite 1	3942.88	1.11	15.47	453.10	887.49	1169.87	190.74
My01a027	Pyrite 1	5192.19	8.02	12.18	515.06	1039.81	149.02	192.11
My01a028	Pyrite 1	3338.89	1.01	10.00	434.46	368.79	261.58	146.95
My01a029	Pyrite 1	5445.79	2.31	5.54	421.05	417.71	70.71	275.54
My01a030	Pyrite 1	4597.74	1.68	8.98	419.67	304.98	33.34	218.39
My01a031	Pyrite 1	5154.23	2.32	16.75	588.41	1079.01	184.04	454.38
My01a032	Pyrite 1	1907.71	0.76	12.34	390.92	251.47	37.82	510.93
My01a033	Pyrite 1	638.10	1.23	12.00	347.40	374.34	26.06	204.15
My01a034	Pyrite 1	1456.27	1.32	15.12	434.09	488.51	20.25	238.18
My01a035	Pyrite 1	7063.65	54.59	18.73	546.94	670.95	238.55	279.74
My01a043	Pyrite 1	581.17	0.72	11.57	328.37	258.88	17.85	1356.21
My01a044	Pyrite 1	1156.45	2.92	16.02	489.98	464.00	17.76	1384.13
My01a045	Pyrite 1	692.69	0.86	13.75	400.68	393.25	11.48	199.32
My01a046	Pyrite 1	2558.59	1.39	7.66	354.29	366.01	72.77	188.24

Table 3.16 (continued)

Analysis no.	Pyrite type	Se	Mo	Ag	Cd	Sb	Te	Au	Tl	Pb	Bi
Ap16A007	Pyrite 1	207.00	17.33	21.00	2.00	35.00	14.00	0.83	6.08	79.00	1.00
Ap16A008	Pyrite 1	412.00	9.71	14.00	1.00	40.00	6.00	1.27	5.24	74.00	1.00
Ap16A009	Pyrite 1	262.00	9.47	22.00	1.00	26.00	10.00	1.13	4.13	68.00	1.00
Ap16A010	Pyrite 1	280.00	10.50	39.00	1.00	25.00	20.00	0.83	4.24	69.00	1.00
Ap16A011	Pyrite 1	329.00	9.23	25.00	1.00	27.00	11.00	1.42	4.28	64.00	1.00
Ap16A012	Pyrite 1	285.00	12.91	20.00	1.00	18.00	4.00	0.90	3.05	54.00	1.00
Ap16A013	Pyrite 1	183.00	14.02	10.00	2.00	34.00	4.00	0.62	4.24	70.00	1.00
Ap16A024	Pyrite 1	-	0.87	24.00	1.00	15.00	15.00	0.66	1.53	3173.00	0.00
Ap16A026	Pyrite 1	-	1.78	87.00	1.00	48.00	19.00	2.12	3.54	11399.00	1.00
Ap16A050	Pyrite 1	-	3.00	66.00	-	35.00	43.00	1.00	5.00	7351.00	1.00
Ap16A046	Pyrite 1	-	2.00	81.00	1.00	51.00	12.00	5.00	4.00	9082.00	1.00
Ap16A035	Pyrite 1	-	2.15	78.00	1.00	38.00	29.00	1.03	3.53	12450.00	1.00
Ap16A072	Pyrite 1	-	4.00	32.00	1.00	24.00	6.00	1.00	5.00	1743.00	0.00
Ap16A078	Pyrite 1	-	2.00	26.00	1.00	14.00	2.00	1.00	5.00	1920.00	0.00
Ap16A077	Pyrite 1	-	2.00	37.00	2.00	16.00	4.00	1.00	6.00	1965.00	0.00
Ap16A074	Pyrite 1	-	6.00	85.00	3.00	41.00	11.00	2.00	13.00	4020.00	0.00
My01a007	Pyrite 1	288.94	5.78	20.00	1.96	18.31	47.50	0.81	2.54	56.34	1.69
My01a008	Pyrite 1	184.46	7.57	9.03	1.96	21.24	51.91	0.38	2.54	41.80	1.10
My01a010	Pyrite 1	206.20	8.76	10.74	3.99	20.76	40.41	0.35	2.72	49.60	1.85
My01a011	Pyrite 1	329.50	10.73	14.97	2.19	24.63	46.63	0.55	3.70	53.36	1.63
My01a013	Pyrite 1	38.96	1.10	1.39	0.43	4.31	2.08	0.07	0.62	5.82	0.31
My01a014	Pyrite 1	243.06	8.39	9.86	2.86	19.52	29.52	0.52	2.63	44.22	1.01
My01a015	Pyrite 1	263.83	6.43	11.42	1.97	23.62	18.11	1.24	3.34	50.09	1.19
My01a016	Pyrite 1	297.68	7.83	16.37	2.75	22.27	33.34	0.83	2.97	47.07	0.94
My01a017	Pyrite 1	501.92	9.35	9.64	2.26	36.53	19.65	2.00	4.03	44.86	1.40
My01a018	Pyrite 1	287.67	8.52	14.21	10.70	21.13	44.48	1.08	2.89	53.44	1.25
My01a027	Pyrite 1	443.03	14.11	25.70	2.97	24.56	33.70	0.79	3.59	57.94	1.77
My01a028	Pyrite 1	248.13	7.92	10.14	3.46	21.91	28.41	1.09	2.29	40.04	1.25
My01a029	Pyrite 1	261.01	13.82	10.89	2.07	36.57	37.12	0.56	3.94	37.81	0.71
My01a030	Pyrite 1	184.47	11.65	8.25	1.75	27.50	52.52	0.32	2.23	36.59	1.36
My01a031	Pyrite 1	350.29	9.40	15.81	3.01	24.81	50.44	0.63	3.07	69.29	1.47
My01a032	Pyrite 1	239.89	4.92	6.69	1.59	14.74	16.59	1.39	1.78	31.95	1.59
My01a033	Pyrite 1	132.56	12.85	7.01	2.31	24.96	4.71	0.43	3.84	51.56	1.06
My01a034	Pyrite 1	178.42	13.62	10.03	3.24	24.98	9.00	0.58	4.58	73.19	0.65
My01a035	Pyrite 1	498.76	11.17	18.40	2.68	26.45	41.34	1.35	3.38	66.76	1.44
My01a043	Pyrite 1	103.50	4.98	5.44	1.55	12.37	6.17	0.46	1.90	38.58	0.37
My01a044	Pyrite 1	148.22	12.77	8.83	2.58	24.65	7.89	0.47	4.13	66.65	0.43
My01a045	Pyrite 1	110.08	10.96	7.70	2.31	21.42	5.40	0.35	3.12	53.45	1.04
My01a046	Pyrite 1	133.14	14.90	9.12	1.95	20.03	16.60	0.37	3.01	45.15	1.28

Table 3.16 (continued)

Analysis no.	Pyrite type	Mn	V	Co	Ni	Cu	Zn	As
My01a047	Pyrite 1	1634.08	1.60	14.19	527.89	484.34	20.14	218.30
My01a049	Pyrite 1	2192.48	1.32	9.87	462.62	472.49	26.32	326.26
My01a050	Pyrite 1	2466.21	1.89	4.69	389.00	485.42	30.32	335.77
My01a048	Pyrite 2	4381.57	1.99	8.99	422.47	578.31	42.64	230.28
My01a051	Pyrite 2	1918.49	0.32	8.86	293.15	398.12	32.97	70.40
My01a052	Pyrite 2	4492.89	1.34	154.72	869.51	733.39	130.28	123.47
My01a053	Pyrite 2	4186.18	0.35	13.47	549.17	783.49	42.04	78.31
My01a054	Pyrite 2	1445.85	0.67	16.69	307.55	791.00	26.06	68.82
My01a055	Pyrite 2	5559.71	1.26	20.09	749.76	799.88	52.98	166.83
My01a056	Pyrite 2	1466.89	13.44	37.15	541.25	1537.56	53.54	85.81
My01a057	Pyrite 2	2001.66	0.11	12.89	313.38	464.07	32.29	86.12
My01a066	Pyrite 2	3616.26	0.13	7.74	270.84	617.80	41.12	104.20
My01a067	Pyrite 2	4256.38	11.66	111.71	501.87	1023.51	111.61	97.83
My01a068	Pyrite 2	4625.77	1.02	15.58	460.96	1115.45	47.97	103.11
My01a069	Pyrite 2	2578.30	0.37	16.11	581.54	867.87	31.31	87.30
My01a070	Pyrite 2	532.92	1.00	15.50	318.95	2120.59	29.97	58.13
My01a071	Pyrite 2	4089.45	13.79	208.89	575.38	4489.90	2898.64	111.90
My01a072	Pyrite 2	189.90	0.12	14.06	306.32	1035.41	16.25	76.39
My01a073	Pyrite 2	369.01	7.79	32.67	625.81	591.42	29.66	85.73
My01a074	Pyrite 2	1185.43	1.28	37.03	357.82	548.73	111.44	65.68
My01a075	Pyrite 2	937.65	6.43	35.34	402.38	997.22	47.07	91.57
My01a076	Pyrite 2	1463.85	1.55	40.39	664.31	2596.48	157.96	82.59
Ap16A027	Pyrite 2	3658.00	1.26	13.00	-	1384.00	7819.00	173.00
Ap16A028	Pyrite 2	7841.00	1.25	56.00	-	3052.00	-	502.00
Ap16A036	Pyrite 2	3070.00	5.16	28.00	9291.00	2203.00	-	236.00
Ap16A037	Pyrite 2	3654.00	5.42	27.00	8988.00	5207.00	-	183.00
Ap16A038	Pyrite 2	1007.00	0.93	8.00	5060.00	2845.00	-	144.00
Ap16A039	Pyrite 2	7952.00	4.44	10.00	8810.00	2897.00	-	273.00
Ap16A047	Pyrite 2	7440.00	0.95	22.00	-	2400.00	-	507.00
Ap16A049	Pyrite 2	9294.00	7.68	12.00	-	3077.00	-	228.00
Ap16A051	Pyrite 2	6692.00	1.12	26.00	-	2276.00	-	213.00
Ap16A052	Pyrite 2	3358.00	6.05	34.00	-	3171.00	-	170.00
Ap16A053	Pyrite 2	1315.00	20.52	4.00	1842.00	966.00	4102.00	55.00
Ap16A054	Pyrite 2	-	0.16	24.00	1072.00	3.00	-	83.00
Ap16A055	Pyrite 2	422.00	7.06	5.00	2759.00	23.00	1658.00	81.00
Ap16A062	Pyrite 2	7282.00	2.35	77.00	-	2926.00	-	390.00
Ap16A063	Pyrite 2	4607.00	3.03	34.00	-	3321.00	-	222.00
Ap16A064	Pyrite 2	2775.00	5.65	84.00	-	2487.00	-	203.00
Ap16A065	Pyrite 2	1439.00	11.52	48.00	9257.00	3734.00	-	193.00
Ap16A066	Pyrite 2	2627.00	0.78	18.00	-	1798.00	-	217.00
Ap16A067	Pyrite 2	4184.00	2.91	12.00	-	3528.00	-	183.00
Ap16A068	Pyrite 2	395.00	6.95	27.00	6041.00	735.00	4325.00	176.00
Ap16A022	Pyrite 2	2691.00	2.58	12.00	6856.00	517.00	7729.00	96.00
Ap16A025	Pyrite 2	2663.00	1.73	40.00	-	1234.00	-	369.00
Mean (this study)		2949.77	6.10	24.81	1625.05	1162.27	824.08	274.24
Mean (WDP)		545.00	-	303.00	829.00	436.00	131.00	1368.00

Table 3.16 (continued)

Analysis no.	Pyrite type	Se	Mo	Ag	Cd	Sb	Te	Au	Tl	Pb	Bi
My01a047	Pyrite 1	179.77	12.92	8.97	2.61	27.63	8.69	0.53	4.03	58.42	0.96
My01a049	Pyrite 1	166.37	11.95	8.50	2.73	25.76	10.19	0.47	3.65	57.28	0.53
My01a050	Pyrite 1	154.45	12.59	8.44	2.66	22.23	12.97	0.45	3.57	52.08	0.39
My01a048	Pyrite 2	200.11	12.49	10.04	2.43	27.49	13.08	0.48	4.99	58.80	0.67
My01a051	Pyrite 2	102.28	2.45	3.46	0.09	13.34	12.24	0.47	0.53	41.50	0.37
My01a052	Pyrite 2	208.43	4.70	3.81	0.70	12.58	8.55	0.18	1.23	25.29	0.49
My01a053	Pyrite 2	96.53	3.07	5.65	0.22	17.01	16.27	0.53	1.19	70.79	0.96
My01a054	Pyrite 2	112.81	2.40	3.81	0.13	17.40	5.89	0.45	0.62	79.46	0.23
My01a055	Pyrite 2	108.52	3.15	6.30	0.21	19.15	26.66	0.51	1.70	56.36	0.78
My01a056	Pyrite 2	130.32	2.81	4.14	0.53	16.74	8.79	0.33	0.57	59.86	0.50
My01a057	Pyrite 2	91.00	2.46	2.49	-	12.14	11.33	0.38	0.33	37.83	0.36
My01a066	Pyrite 2	114.41	3.06	3.79	0.24	15.89	22.48	0.47	0.49	49.83	0.12
My01a067	Pyrite 2	113.71	2.76	4.47	0.26	14.21	16.47	0.27	0.81	49.79	0.88
My01a068	Pyrite 2	110.89	3.28	5.84	0.15	17.55	26.07	0.40	0.92	87.82	1.29
My01a069	Pyrite 2	106.98	2.88	5.66	0.20	19.35	13.07	0.43	0.76	92.42	0.71
My01a070	Pyrite 2	102.37	2.09	3.04	-	14.25	4.45	0.30	0.23	83.73	0.21
My01a071	Pyrite 2	131.24	5.98	3.32	5.70	9.50	9.86	0.06	0.86	24.29	0.83
My01a072	Pyrite 2	107.93	2.08	2.70	0.00	17.55	1.75	0.29	0.23	77.01	0.12
My01a073	Pyrite 2	107.75	2.47	4.59	0.07	19.38	5.90	0.32	0.38	72.30	0.40
My01a074	Pyrite 2	81.58	2.85	3.06	0.23	11.17	10.82	0.30	0.26	84.86	0.33
My01a075	Pyrite 2	93.68	3.66	3.64	0.11	14.15	8.80	0.32	0.30	123.85	0.51
My01a076	Pyrite 2	136.44	2.00	4.25	0.34	11.15	8.69	0.19	0.70	47.50	0.72
Ap16A027	Pyrite 2	-	1.26	32.00	0.00	25.00	18.00	0.95	5.63	5060.00	1.00
Ap16A028	Pyrite 2	-	3.40	100.00	1.00	50.00	59.00	2.04	5.80	14432.00	1.00
Ap16A036	Pyrite 2	-	1.88	26.00		33.00	19.00	1.50	2.45	7153.00	0.00
Ap16A037	Pyrite 2	-	2.00	24.00	1.00	26.00	21.00	2.00	2.00	8851.00	1.00
Ap16A038	Pyrite 2	-	2.00	13.00	-	24.00	9.00	1.00	1.00	5461.00	0.00
Ap16A039	Pyrite 2	-	2.00	28.00	-	28.00	46.00	2.00	2.00	4940.00	0.00
Ap16A047	Pyrite 2	-	3.00	62.00	1.00	48.00	52.00	4.00	12.00	7194.00	0.00
Ap16A049	Pyrite 2	-	2.00	43.00	2.00	33.00	32.00	2.00	14.00	3464.00	1.00
Ap16A051	Pyrite 2	-	3.00	37.00	1.00	26.00	27.00	2.00	8.00	4643.00	0.00
Ap16A052	Pyrite 2	-	3.00	41.00	1.00	28.00	18.00	3.00	11.00	5290.00	0.00
Ap16A053	Pyrite 2	-	1.00	16.00	0.00	8.00	9.00	1.00	1.00	1807.00	0.00
Ap16A054	Pyrite 2	-	-	-	-	-	-	-	-	44.00	-
Ap16A055	Pyrite 2	-	0.00	1.00	-	1.00	1.00	0.00	0.00	361.00	0.00
Ap16A062	Pyrite 2	-	3.00	69.00	2.00	41.00	54.00	3.00	7.00	8158.00	1.00
Ap16A063	Pyrite 2	-	3.00	43.00	1.00	41.00	27.00	3.00	9.00	8405.00	1.00
Ap16A064	Pyrite 2	-	1.00	22.00	1.00	21.00	17.00	1.00	5.00	6599.00	1.00
Ap16A065	Pyrite 2	-	2.00	30.00	-	28.00	20.00	2.00	3.00	8802.00	0.00
Ap16A066	Pyrite 2	-	2.00	32.00	1.00	60.00	17.00	4.00	9.00	7413.00	0.00
Ap16A067	Pyrite 2	-	2.00	29.00	-	32.00	22.00	2.00	5.00	7778.00	1.00
Ap16A068	Pyrite 2	-	1.00	22.00	-	32.00	4.00	1.00	1.00	8091.00	0.00
Ap16A022	Pyrite 2	-	0.87	16.00	0.00	15.00	12.00	0.89	2.53	2167.00	0.00
Ap16A025	Pyrite 2	-	2.37	70.00	1.00	54.00	32.00	2.84	6.37	9709.00	1.00
Mean (this study)		125.34	3.39	20.14	0.96	23.94	18.12	1.15	3.28	1957.36	4.22
Mean (WDP)		71.00	88.00	9.20	3.00	90.00	4.90	0.10	36.00	387.00	13.00

WDP= Worldwide Diagenetic Pyrite (Gregory et al., 2015); - = no data available.

By comparing the sedimentary pyrites (pyrite 1 and 2) of the BRSZ Unit 1 with the global diagenetic pyrite (WDP) (Gregory et al., 2015), the BRSZ Unit 1 pyrites are strongly enriched in Mn, Zn, Te, Au, and Pb, moderately enriched in Ni, Cu, Se, Ag and depleted in Co, As, Mo, Cd, Sb, Tl, and Bi relative to the global diagenetic pyrites (Fig. 3.40). Given the Au mean content of WDP (mean 0.104 ppm), the BRSZ Unit 1 are richer in gold by one order of magnitude.

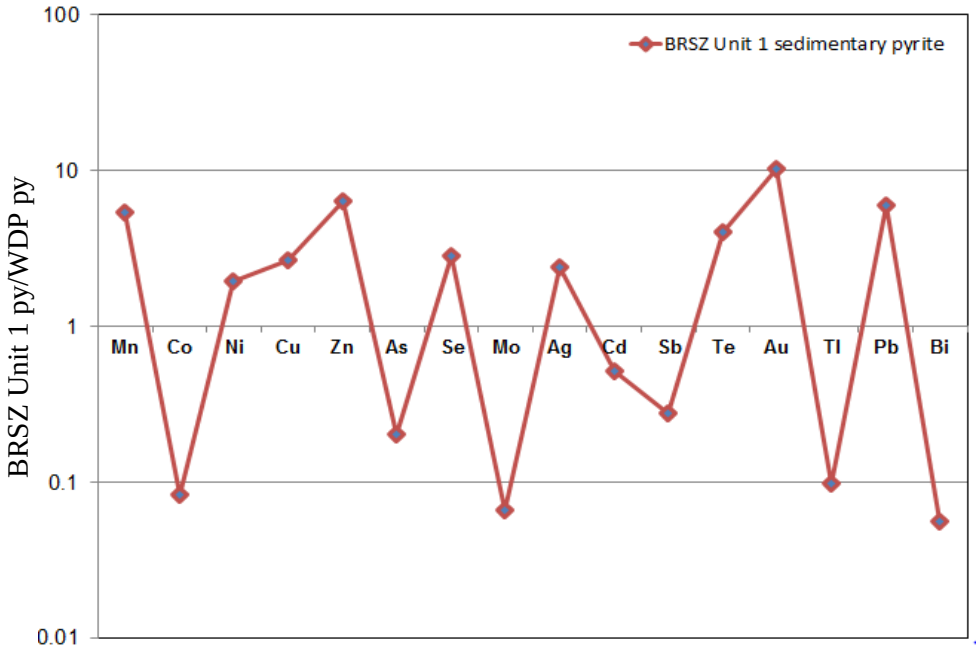

Fig. 3.40. Spider plot comparing the mean TE values of sedimentary pyrites (pyrite 1 and 2) of the BRSZ Unit 1 with the overall mean for worldwide diagenetic pyrite (WDP). Pyrite data from the BRSZ Unit 1 are normalised to WDP. Note: py= pyrite in the figure caption.

3.5.5. Discussion for the BRSZ Unit 1

Comparatively, the Late Devonian BRSZ Unit 1 black shales are characterised by elevated concentrations of Al_2O_3, TiO_2, MgO, Na_2O, and K_2O compared with the Late

Cambrian-Early Ordovician Machinchang grey shales and the Pennsylvanian-Early Permian Singa Formation black shales. The evidence suggests that the major element composition is related to the amount of clays in the studied samples. This interpretation is consistent with the index of compositional variability (ICV) which is less than 1 and the K_2O/Al_2O_3 ratio being less than 0.3. In the BRSZ Unit 1, whole rock trace elements such as V, U, Ni, Cr, Se, and Mo have positive correlation with both Al_2O_3 and organic carbon implying a sedimentary (clay) and organic carbon control for these trace elements during their transport into basin. The small euhedral pyrite crystals (pyrite 2) in the BRSZ Unit 1 (BU1) are interpreted to be of early to late diagenetic origin. Taylor and Macquaker (2000) researched that these small euhedral crystals precipitate from solution in the early to late stages of early diagenesis. In addition, in the Late Devonian BU1, there is no relationship among Au, V, Mo, and Ni which implies no involvement of organic processes during metal uptake into diagenetic pyrites.

3.6. Pyrite trace element composition from the Selinsing gold deposit

Plots of selected trace elements in framboidal pyrites are presented in Figs. 3.41-3.42. Apart from Na, Mg, Al, Si, K, and Ca contents which are usually elevated in framboidal pyrite due to matrix inclusions, the framboidal pyrites are enriched in As (mean 233 ppm), Co (mean 327 ppm), Cu (mean 277 ppm), Ni (mean 364 ppm), Zn (mean 203 ppm) and Sb (mean 37 ppm). The Selinsing framboidal pyrite gold content ranges from 0.03 to 0.84 (mean 0.29 ppm). Results of LA-ICP-MS spot analyses are presented in Table 3.17. There is a strong correlation between Co and Ni and the ratio Co/Ni is less than 1, which indicates enrichment of Ni over Co in the framboidal pyrites (Fig. 3.41A). The Cu-Ni and Se-Mo plots show a positive correlation (Figs. 3.41B and 3.41C).

Table 3.17. LA ICP-MS analyses of framboidal pyrite in the Selinsing gold deposit, Malaysia.

Analysis No.	Mn	V	Cr	Co	Ni	Cu	Zn	As	Se	Mo	Ag	Cd
A070	6341.89	17.00	12.64	185.07	271.11	213.97	483.90	209.01	2.22	3.07	5.27	0.00
A071	4355.27	9.39	4.61	255.17	334.32	313.03	381.17	183.18	6.89	2.81	4.33	2.11
A072	2493.81	23.68	22.63	1322.19	693.49	740.36	400.22	388.94	18.84	9.14	2.54	2.12
A073	616.52	3.81	2.30	200.21	312.91	155.64	102.21	197.63	4.74	1.13	4.94	0.21
A074	1449.82	11.39	0.71	248.43	280.91	265.61	100.97	142.41	0.81	1.12	3.32	0.79
A075	4528.97	0.23	1.39	137.63	221.87	80.60	350.57	138.47	5.33	3.76	3.70	0.29
A076	1626.84	0.53	2.19	297.74	568.23	232.30	266.59	315.85	5.30	2.56	10.70	0.60
A077	1409.42	1.08	0.61	151.33	267.96	117.07	183.66	154.22	11.99	7.10	8.47	0.39
A078	4925.77	3.42	0.92	332.12	625.65	315.33	196.62	333.90	5.38	4.96	13.24	0.26
A079	1588.72	5.43	11.41	452.94	459.21	427.09	130.86	185.65	2.55	4.56	5.13	0.03
A080	2888.30	1.75	11.75	243.64	328.18	222.41	150.53	157.17	5.65	2.84	5.82	0.04
A081	3005.59	0.05	7.01	204.70	404.28	262.79	132.98	168.21	5.84	2.20	4.02	1.82
A082	4325.07	1.73	0.52	898.06	602.41	1051.97	203.66	411.72	4.15	20.08	9.68	0.82
A083	667.60	0.13	1.10	162.86	196.37	95.81	180.30	115.51	0.63	0.22	4.57	0.05
A084	20.68	0.30	12.99	153.99	122.28	54.85	28.23	310.48	1.73	6.68	2.61	0.32
A091	797.53	0.30	0.69	57.87	122.59	171.82	151.93	170.90	2.97	4.59	9.55	0.02
A092	15.87	0.04	1.10	134.56	73.36	44.00	18.43	208.94	1.35	1.37	5.76	0.02
A093	1119.66	1.07	14.55	137.13	236.69	118.44	196.50	124.52	2.82	4.10	3.66	0.30
A094	970.41	2.21	10.62	327.51	483.69	277.02	159.62	294.04	5.54	2.25	5.27	0.21
A095	3071.16	37.53	30.74	628.19	682.13	389.09	245.56	452.77	11.69	6.12	11.30	1.89
Mean	2310.95	6.05	7.52	326.57	364.38	277.46	203.23	233.18	5.32	4.53	6.19	0.61
Mean (WDP)	545.00	-	-	303.00	829.00	436.00	131.00	1368.00	71.00	88.00	9.20	3.00

Analysis No.	Sn	Sb	Te	W	Pt	Au	Tl	Pb	Bi	Th	U
A070	0.83	34.43	4.15	0.22	0.07	0.62	0.35	312.63	11.88	0.88	1.57
A071	0.52	30.95	0.03	1.54	0.18	0.31	0.23	395.09	9.91	1.34	2.24
A072	0.46	51.94	2.39	0.28	0.23	0.08	1.71	756.13	11.56	0.02	0.63
A073	0.17	35.84	3.64	0.10	0.00	0.19	0.14	306.99	10.12	0.01	0.03
A074	1.30	22.45	2.70	0.08	0.01	0.08	0.41	246.70	6.81	0.10	0.02
A075	0.04	26.24	1.32	0.05	0.03	0.39	0.33	194.54	4.80	0.03	0.01
A076	0.33	65.35	4.34	0.22	0.03	0.45	0.54	598.12	17.66	0.01	0.02
A077	0.01	25.55	1.69	0.22	0.03	0.56	0.40	256.24	6.54	0.02	0.01
A078	0.52	64.63	3.57	0.18	0.03	0.58	0.32	549.85	14.28	0.01	0.01
A079	0.42	30.19	0.78	0.57	0.06	0.03	0.63	375.25	9.51	0.17	0.05
A080	0.38	31.94	2.58	0.13	0.05	0.09	0.70	323.67	8.10	0.11	0.02
A081	0.12	23.42	1.83	0.30	0.06	0.15	0.23	293.53	7.15	0.02	0.03
A082	0.39	51.33	4.67	0.07	0.20	0.36	0.15	598.49	11.99	0.00	0.08
A083	0.08	26.63	3.77	0.11	0.01	0.22	0.03	213.09	8.34	0.04	0.00
A084	0.34	13.05	1.77	1.99	0.01	0.10	0.14	114.44	4.40	0.02	0.06
A091	0.13	23.31	1.66	0.05	0.01	0.14	0.88	254.09	5.25	0.01	0.01
A092	0.11	21.38	1.22	0.10	0.02	0.11	0.60	144.21	6.10	0.00	0.00
A093	0.08	24.09	0.17	0.06	0.02	0.38	0.04	244.20	6.06	0.01	0.03
A094	0.10	45.02	1.17	0.72	0.03	0.18	0.37	355.36	10.53	0.00	0.01
A095	0.47	90.88	4.20	0.09	0.00	0.84	0.53	737.05	18.81	0.25	0.46
Mean	0.34	36.93	2.38	0.35	0.05	0.29	0.44	363.48	9.49	0.15	0.26
Mean (WDP)	-	90.00	4.90	-	-	0.10	36.00	387.00	13.00	-	-

Note: WDP= Worldwide Diagenetic pyrite (Gregory et al., 2015); dashes indicate no data.

The As and Ni plot indicates that the framboidal pyrites show a As/Ni ratio less than 10 indicative of their sedimentary origin (Fig. 3.41D) (Gregory et al., 2015). Correlation coefficients are shown in Table 3.18. Au shows positive correlation (Fig. 3.42) with Ag (cc= 0.61), V (cc= 0.43), Sb (cc=0.42), Te (cc= 0.42), As (cc= 0.35), and Ni (cc= 0.34). The elements such as V, As, Ag, Ni and Se are commonly contributed to marine sediments by organic matter and introduced into pyrite during its formation in sediments (Large et al., 2011; Makoundi et al., 2014). Gold content in framboidal pyrite varies positively with Mn, Ag, and Sb.

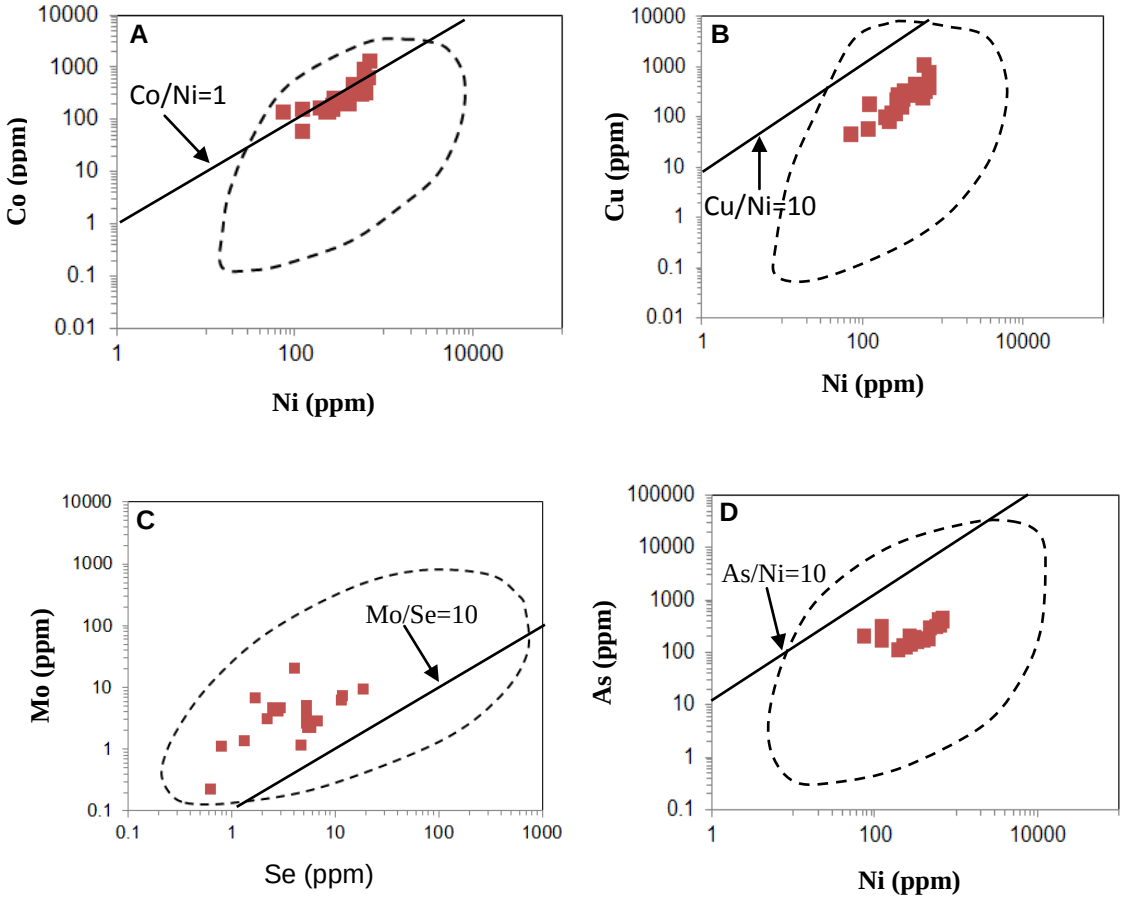

Fig. 3.41. Binary log-log plots of pyrite geochemistry in framboidal pyrites from Selinsing gold deposit black shales, Malaysia. **A**) Scatter plot of Co-Ni. **B**) Scatter plot of Cu-Ni. **C**). Scatter plot of Se-Mo. **D**) Plot displaying As and Ni values. Dashed polygon represents the field of sedimentary pyrite (Gregory et al., 2015) in this figure and also in Fig. 3.42 (next page).

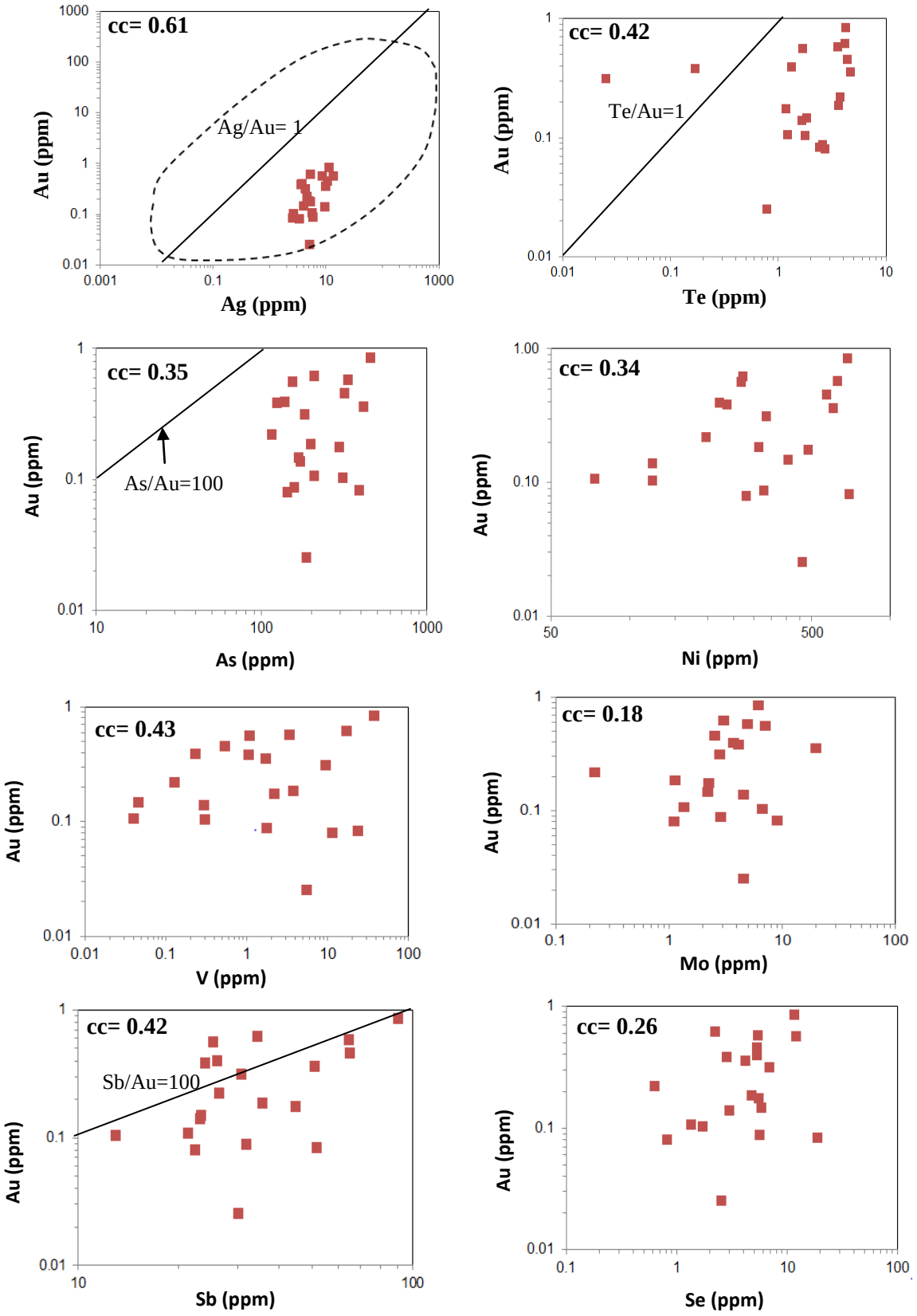

Fig. 3.42. Log-log plots showing relationships between Au-Ag, Au-Te, Au-As, Au-Ni, Au-V, Au-Mo, Au-Sb, and Au-Se in pyrite for the Selinsing gold deposit black shales, Malaysia. The Ag>Au content of all pyrite analyses, confirms a sedimentary origin (Thomas et al., 2011). Note: cc is coefficient of correlation.

Table 3.18. Coefficients of correlation for the Selinsing framboidal pyrites. Highlighted numbers equal to or greater than 0.5 indicate positive correlation between two variables.

Correlation	Mn_ppm	V_ppm	Co_ppm	Ni_ppm	Cu_ppm	Zn_ppm	As_ppm	Se_ppm	Mo_ppm	Ag_ppm	Cd_ppm	Sb_ppm	Te_ppm	Au_ppm	Tl_ppm	Pb_ppm	Bi_ppm
Mn_ppm	1																
V_ppm	0.32	1															
Co_ppm	0.23	0.56	1														
Ni_ppm	0.4	0.52	0.77	1													
Cu_ppm	0.38	0.34	0.87	0.73	1												
Zn_ppm	0.74	0.47	0.34	0.35	0.28	1											
As_ppm	0.2	0.53	0.72	0.75	0.64	0.15	1										
Se_ppm	0.19	0.55	0.67	0.6	0.4	0.44	0.47	1									
Mo_ppm	0.28	0.12	0.65	0.43	0.8	0.13	0.6	0.32	1								
Ag_ppm	0.23	0.098	0.068	0.45	0.21	0.0047	0.47	0.11	0.3	1							
Cd_ppm	0.28	0.58	0.56	0.53	0.46	0.37	0.41	0.65	0.22	-0.072	1						
Sb_ppm	0.35	0.61	0.55	0.86	0.47	0.33	0.79	0.49	0.29	0.68	0.38	1					
Te_ppm	0.28	0.3	0.29	0.43	0.34	0.15	0.49	0.037	0.27	0.51	-0.018	0.59	1				
Au_ppm	0.53	0.43	0.011	0.34	0.025	0.48	0.35	0.26	0.18	0.61	0.14	0.62	0.42	1			
Tl_ppm	-0.027	0.42	0.6	0.33	0.33	0.25	0.3	0.63	0.13	-0.0037	0.29	0.23	-0.038	-0.24	1		
Pb_ppm	0.39	0.63	0.81	0.94	0.74	0.45	0.79	0.66	0.47	0.5	0.58	0.89	0.48	0.4	0.46	1	
Bi_ppm	0.37	0.57	0.48	0.82	0.44	0.39	0.71	0.37	0.18	0.62	0.34	0.94	0.64	0.59	0.15	0.85	1

The gold content in framboidal pyrite varies from 0.03 to 0.84 (mean 0.3 ppm). The arsenic content ranges from 116 to 453 (mean 233 ppm). The Ag/Au ratio varies from 8.5 to 202.5 (mean 37 ppm) indicating enrichment in Ag content relative to Au in the diagenetic pyrite. The textural features of pyrite grains combined with the Co/Ni and Ag/Au ratios strongly suggest a diagenetic origin. The Selinsing framboidal pyrite are enriched in Mn, Zn, and Au depleted in Ni, Cu, As, Se, Mo, Ag, Cd, Sb, Te, Bi and strongly depleted in Tl compared to worldwide sedimentary pyrite (Gregory et al., 2015) (Fig. 3.43).

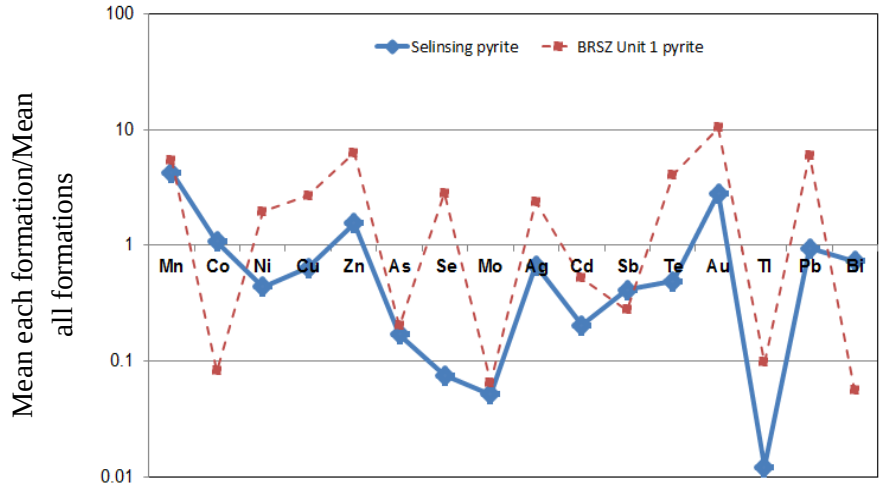

Fig. 3.43. Comparative spider plot of the mean trace element composition in framboidal pyrites contained in black shales of the Selinsing gold deposit normalised against the overall means for worldwide diagenetic pyrite (WDP; Gregory et al., 2015). Note: the BRSZ Unit 1 pyrite in dashed line as background for comparison.

3.6.1. Discussion for the Selinsing gold deposit

The disseminated small framboidal pyrites which size ranges from 20 to 40 µm from the Selinsing gold deposit are interpreted to have formed during diagenesis due to the Ag/Au ratio> 1 and all data plot within the sedimentary pyrite field. Most pyrite framboids that were laser-ablated have a size greater than 20 µm. It is suggested that pyrite framboids larger than 10 µm form diagenetically (Wilkin et al., 1996). There is a weak to strong correlation between Au and redox sensitive trace elements such as V, Ag, Ni, Sb, and As. These trace elements can form organometallic complexes with humic substances and get reduced and incorporated into sedimented organic matter (Calvert and Pedersen, 1993; Wood, 1996; Tribovillar et al., 2006).

CHAPTER 4
MESOZOIC FORMATIONS

4.1. Introduction

This chapter covers the lithostratigraphy, whole-rock geochemistry, U-Pb zircon dating, and pyrite trace element chemistry of the Mesozoic formations which include the Middle Triassic Karak Formation, the Middle Triassic Semantan Formation, the Middle Triassic Gua Musang Formation, and the Late Triassic BRSZ Unit 2. In this Chapter, major and trace elements compositions of whole rocks are compared to PAAS (Post-Archean Australian Shale, Taylor and McLennan, 1985) to discuss enrichment and depletion. Relationships among alumina, organic carbon and some trace elements are also explored to verify whether clays or organic matter played a significant role in metal concentration in sedimentary basin. Pyrite trace element compositions are documented. The pyrite composition helps evaluate the origin of each pyrite generation and discuss the gold potential in these formations. Major and trace element analyses in whole rocks for the Karak Formation are not included in this thesis due to budgetary restriction. A sketch map of the selected Mesozoic formations is presented in Fig. 4.1.

4.2. Karak Formation (Middle Triassic)

4.2.1. Pyrite texture and trace element composition

The aims of pyrite chemistry in this chapter are the following: 1) to determine trace element concentration in pyrite; 2) to investigate relationships among gold and some trace elements in pyrite; and 3) to compare trace element composition in sedimentary pyrite to the worldwide diagenetic pyrite (Gregory et al., 2015).

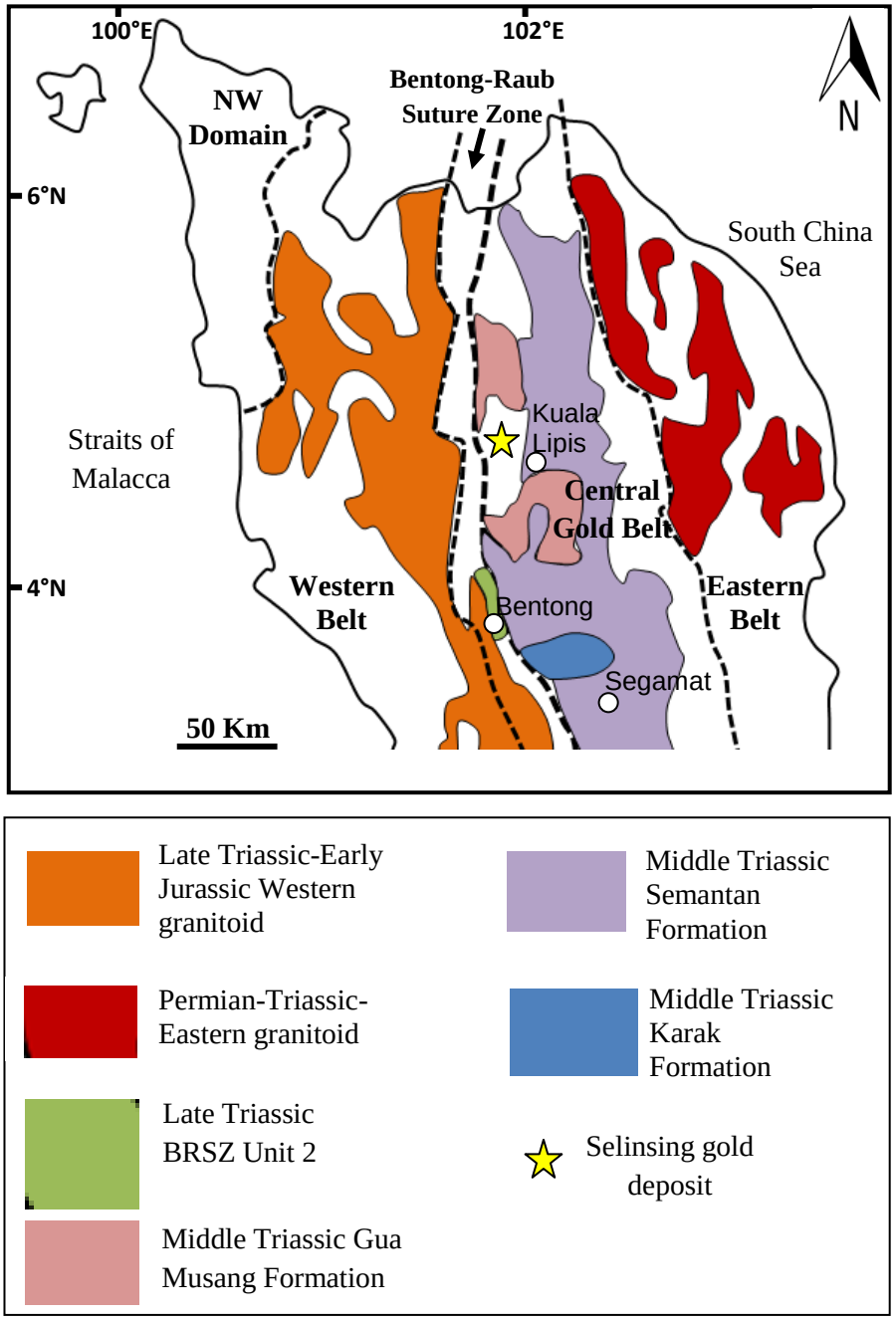

Fig. 4.1. Geological map of the selected Mesozoic formations in this study.

In the Karak Formation, two types of pyrite were found in tuffaceous black mudstones and siltstones. The fine grained pyrites (type 1) are mostly framboids with size from 30 to 400 µm across. The coarse-grained pyrite (pyrite 2) that also contain inclusions of pyrrhotite, are in places elongated and disseminated patches having size between 400 and 600 µm (Fig. 4.2). Results of spot LA-ICPMS analyses are presented in Table 4.1.

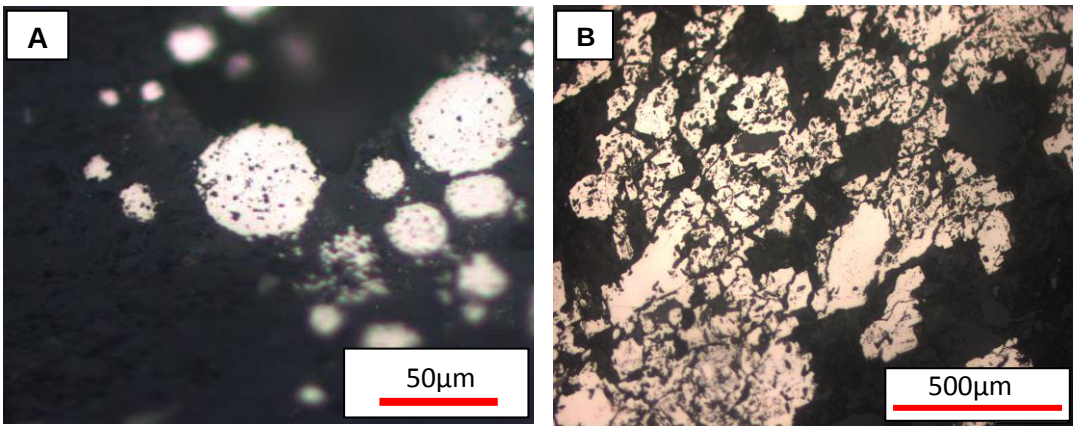

Fig. 4.2. Pyrite textures in volcaniclastic rocks of the Karak Formation, Malaysia. **A**) Framboidal pyrite (pyrite 1). **B**) Coarse, patchy and disseminated pyrite (pyrite 2).

Framboidal pyrites (pyrite 1) are characterised by the following ratios: Co/Ni>1, Cu/Ni<1, Se/Mo>10, and an increasing Ni content with decreasing As content (Fig. 4.3). The ratio Se/Mo = 10 appears to discriminate fairly well the two types of pyrite; however, in other binary plots coarse pyrite (pyrite 2) data are largely scattered. Pyrite 2 grains show large crystals and partial dissolution comparable to the metamorphic pyrite found in the sediment-hosted Pb-Zn deposits in the Canadian Cordillera (McClay and Ellis, 1983).

Table 4.1. LA ICP-MS analyses of pyrite (in ppm) from the Anisian Karak Formation, Malaysia.

Analysis No	Pyrite type	V	Mn	Co	Ni	Cu	Zn	As	Se	Mo
JA28A072	Py 1	18.5	4.6	1423.4	270.0	608.0	55.3	5536.9	56.6	99.5
JA28A073	Py 1	26.3	15.2	893.8	342.2	149.3	272.0	3301.1	43.0	48.0
JA28A074	Py 1	41.2	4.0	1153.1	303.6	858.7	484.1	3573.2	59.5	73.5
JA28A075	Py 1	6.9	8.0	880.9	186.5	266.0	166.1	8091.7	89.1	82.8
JA28A078	Py 1	10.7	15.8	2579.8	656.3	597.6	103.7	1059.6	55.9	10.1
JA28A082	Py 1	22.5	3.2	1190.8	286.1	283.0	38.5	4962.6	99.4	87.6
JA28A084	Py 1	42.3	23.3	2135.8	517.1	553.0	207.3	832.9	56.0	13.4
JA28A085	Py 1	1.0	14.1	1483.5	557.2	327.7	139.3	779.1	47.5	7.7
JA28A049	Py 2	15.9	6.2	176.0	24.9	28.3	171.3	434.5	59.5	1.5
JA28A050	Py 2	14.7	2.3	16.6	20.8	33.9	29.4	550.7	59.7	1.2
JA28A051	Py 2	8.6	0.6	27.7	41.0	21.3	4.6	414.8	76.4	0.8
JA28A052	Py 2	8.2	1.0	27.4	35.1	25.3	32.7	728.1	67.5	1.3
JA28A054	Py 2	13.5	0.7	287.3	3241.1	13.6	3.0	140.2	42.7	1.3
JA28A055	Py 2	6.4	4.7	19.6	76.1	17.0	15.8	387.0	65.8	0.8
JA28A056	Py 2	18.8	5.5	80.4	112.0	30.0	5.2	247.3	45.4	1.5
JA28A057	Py 2	8.1	3.3	202.8	3735.7	69.8	7.7	79.5	30.3	4.8
JA28A058	Py 2	6.1	4.0	477.6	1370.0	162.5	1871.7	132.0	61.8	1.6
JA28A059	Py 2	8.5	2.6	375.1	1293.7	21.7	5.0	14.3	32.3	0.6
JA28A080	Py 2	25.1	2.8	1389.9	2141.3	65.3	30.0	2108.8	56.3	2.0
Mean (this study)		16.0	6.4	780.1	800.6	217.5	191.7	1756.5	58.1	23.2
Mean (WDP)		-	545.0	303.0	829.0	436.0	131.0	1360.0	71.0	88.0

Analysis No	Pyrite type	Ag	Cd	Sn	Sb	Te	Au	Tl	Pb	Bi
JA28A072	Py 1	20.6	0.8	1.4	75.7	11.5	0.5	3.5	940.3	41.9
JA28A073	Py 1	20.4	3.5	10.6	83.0	10.0	0.5	8.1	455.8	38.3
JA28A074	Py 1	20.9	4.3	1.7	80.3	11.6	0.6	8.9	742.6	36.7
JA28A075	Py 1	13.3	1.3	5.0	64.0	8.1	0.4	7.9	1495.6	39.8
JA28A078	Py 1	26.7	0.6	6.8	78.4	11.7	0.6	0.7	447.3	35.9
JA28A082	Py 1	22.4	0.6	1.0	75.7	9.1	0.6	3.7	2908.3	47.8
JA28A084	Py 1	20.6	2.0	5.9	76.3	9.0	0.6	1.3	301.3	29.4
JA28A085	Py 1	10.8	1.2	0.4	50.2	5.3	0.4	0.3	378.1	19.9
JA28A049	Py 2	0.7	0.3	0.5	12.1	2.0	0.3	0.1	59.6	7.6
JA28A050	Py 2	1.3	0.2	1.0	14.6	10.1	0.2	0.1	71.2	15.2
JA28A051	Py 2	0.9	0.0	0.6	9.6	19.6	0.2	0.1	49.3	10.2
JA28A052	Py 2	1.5	0.1	0.5	14.0	12.2	0.1	0.0	55.2	12.8
JA28A054	Py 2	0.3	0.1	1.2	13.7	1.9	0.1	0.1	19.6	4.8
JA28A055	Py 2	0.7	0.1	0.5	12.9	16.0	0.1	0.0	58.4	13.9
JA28A056	Py 2	0.8	0.2	0.9	11.0	5.7	0.1	0.1	37.1	8.5
JA28A057	Py 2	1.0	0.1	0.9	16.1	1.8	0.1	0.0	64.6	8.5
JA28A058	Py 2	3.1	3.2	0.8	101.1	4.0	0.9	0.1	440.4	36.1
JA28A059	Py 2	0.7	0.2	0.7	15.1	0.7	0.1	0.1	19.6	3.9
JA28A080	Py 2	5.3	0.2	3.7	17.2	5.6	0.2	0.1	65.6	12.5
Mean (this study)		9.1	1.0	2.3	43.2	8.2	0.3	1.9	453.2	22.3
Mean (WDP)		9.2	3.0	-	90.0	4.9	0.1	36.0	387.0	13.0

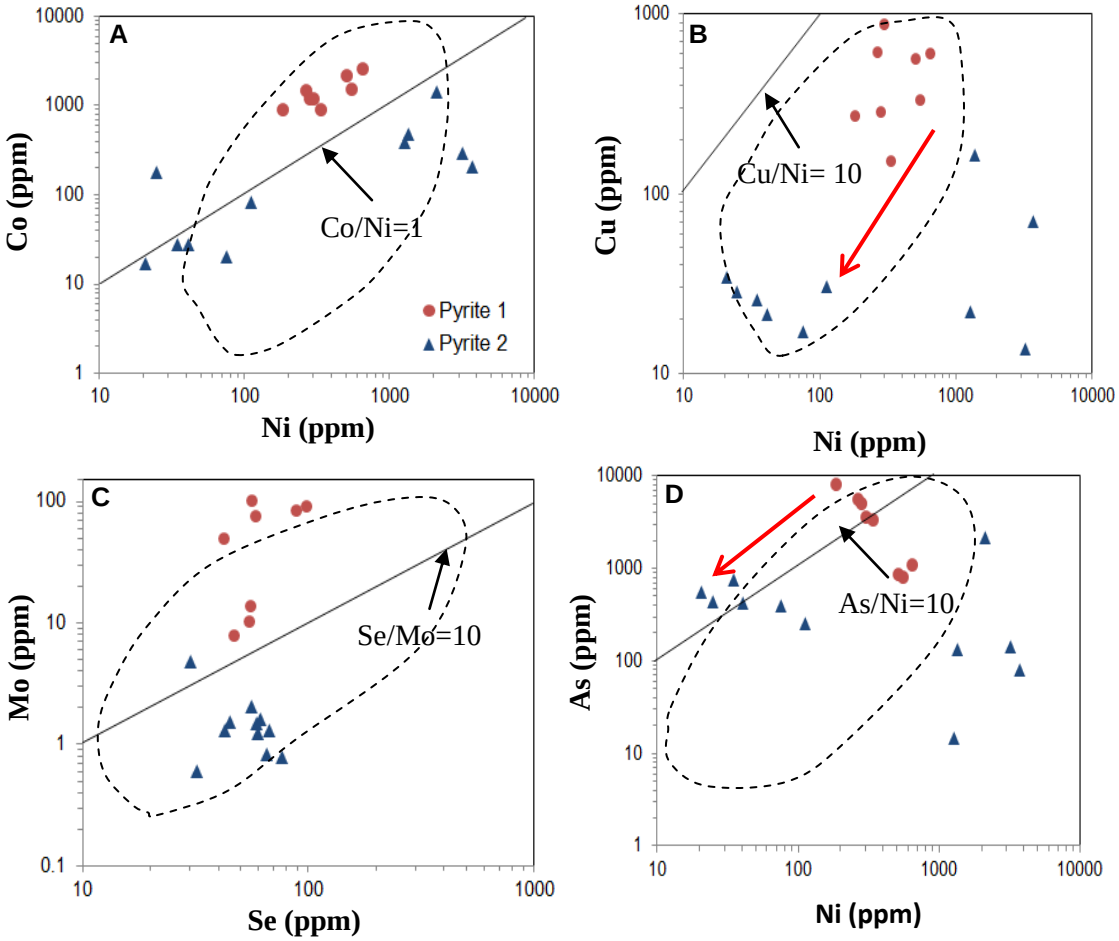

Fig. 4.3. Log-log plots of trace elements in pyrite from the Anisian Karak Formation, Malaysia. A) Co-Ni plot. **B**) Cu-Ni plot. There is loss of Cu and Ni from pyrite 1 to pyrite 2. **C**). Se-Mo plot. **D**) As-Ni plot. Dashed polygon represents the outline for sedimentary pyrite (Gregory et al., 2015). The red arrow indicates loss of As and Ni from pyrite 1 to pyrite 2. Red arrow showing loss in As, Cu and Ni from pyrite 1 to pyrite 2.

Additionally, the framboidal pyrites spots are clustered subparallel to the line Co/Ni= 1. Moreover, pyrite framboid data plot perpendicular to the line As/Ni= 10. However, the trend is not shown by coarse pyrite (pyrite 2). The texture and chemical ratios indicate that pyrite 1 has a diagenetic origin whereas pyrite 2 has a metamorphic origin. Pyrite 2 mostly likely formed by metamorphic crystallisation of pyrite 1 and loss of most trace elements. This is a common process of pyrite cleaning due to recrystallisation (Large et al., 2007). The relationships among gold and other trace elements are shown in Fig. 4.4.

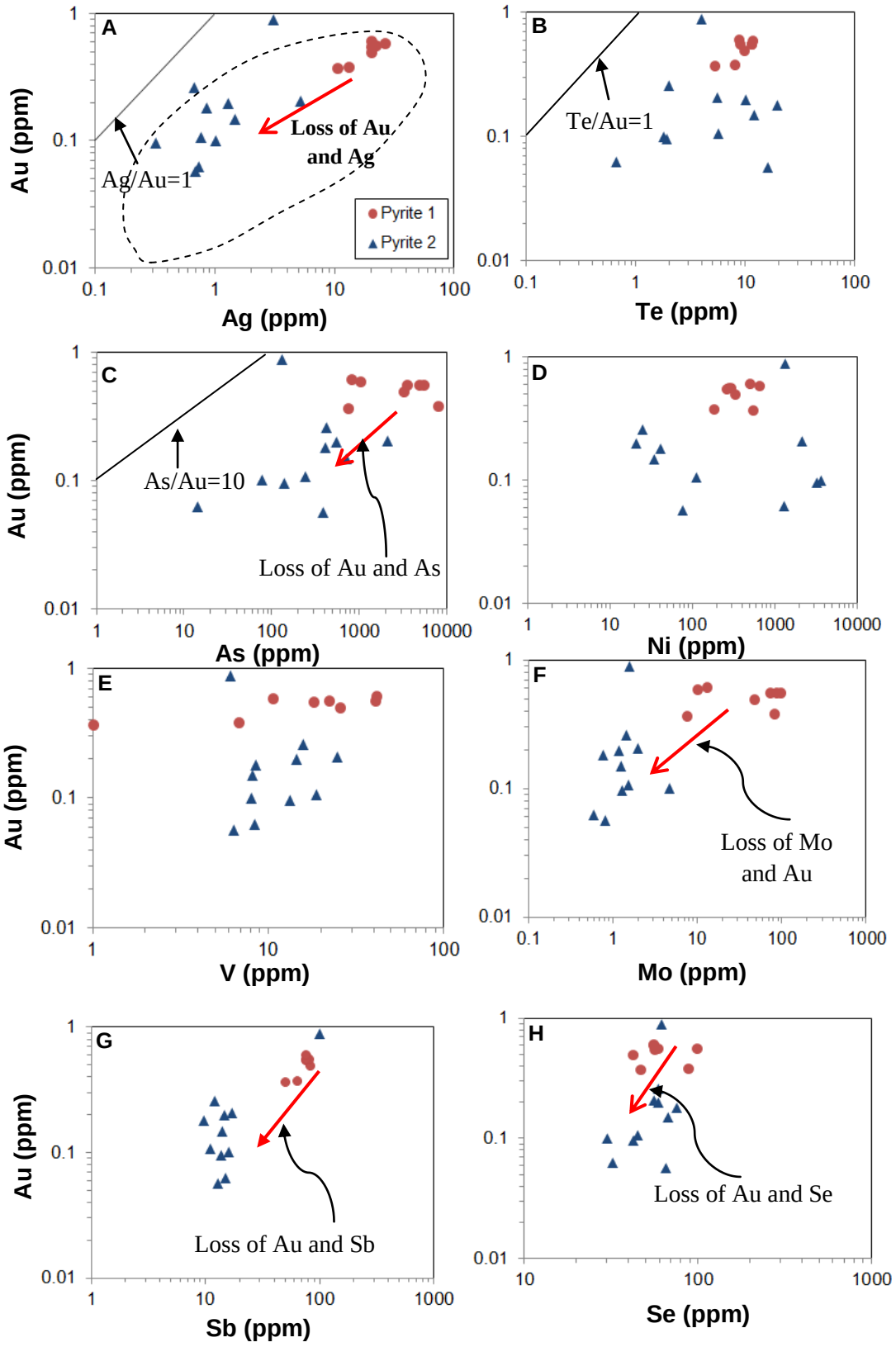

Fig. 4.4. Bivariate log-log plots showing trace element relationships. **A**) Au-Ag. **B**) Au-Te. **C**) Au-As. **D**) Au-Ni. **E**) Au-V. **F**) Au-Mo. **G**) Au-Sb. **H**) Au-Se in pyrite for the Karak Formation, Malaysia.

Relationships amongst trace elements in pyrite 1 and pyrite 2 are illustrated by the coefficients of correlation (Tables 4.2 and 4.3). It is clear from Fig. 4.4 that Au and most other trace elements are depleted in pyrite 2 compared to pyrite 1; the Au-Ag, Au-As, Au-Mo, Au-Sb and Au-Se plots all show this feature.

Table. 4.2. Coefficients of correlation of selected trace elements in framboidal pyrite (pyrite 1) from the Middle Triassic Karak Formation. In this Table, correlation coefficients range from 0.5 to 0.9 implying good correlation between two variables.

Correlation	Ag_ppm	Cd_ppm	Sn_ppm	Sb_ppm	Te_ppm	Au_ppm	Tl_ppm	Pb_ppm	Bi_ppm
Mo_ppm	0.024	0.025	-0.32	0.25	0.34	3.00E-04	0.62	0.66	0.8
Se_ppm	-0.018	-0.39	-0.34	-0.058	-0.095	-0.061	0.2	0.92	0.63
V_ppm	0.46	0.65	0.16	0.7	0.47	0.7	0.3	-0.094	0.18
Mn_ppm	0.015	0.025	0.59	-0.047	-0.25	0.1	-0.47	-0.67	-0.63
Co_ppm	0.49	-0.39	0.11	0.092	0.21	0.53	-0.78	-0.41	-0.34
Ni_ppm	0.22	-0.21	0.17	-0.15	-0.12	0.21	-0.78	-0.57	-0.66
Cu_ppm	0.4	0.25	-0.33	0.31	0.59	0.56	-0.059	-0.3	-0.065
Zn_ppm	-0.021	0.95	0.17	0.29	0.23	0.064	0.63	-0.39	-0.18
As_ppm	-0.2	-0.094	-0.13	0.035	0.11	-0.3	0.64	0.62	0.7
Ag_ppm	1	0.0057	0.31	0.86	0.84	0.9	-0.082	0.067	0.51
Cd_ppm	0.0057	1	0.28	0.39	0.23	0.085	0.68	-0.37	-0.1
Sn_ppm	0.31	0.28	1	0.48	0.24	0.13	0.23	-0.39	0.059
Sb_ppm	0.86	0.39	0.48	1	0.87	0.81	0.36	0.032	0.61
Te_ppm	0.84	0.23	0.24	0.87	1	0.74	0.28	-0.046	0.58
Au_ppm	0.9	0.085	0.13	0.81	0.74	1	-0.17	8.50E-04	0.35
Tl_ppm	-0.082	0.68	0.23	0.36	0.28	-0.17	1	0.19	0.47
Pb_ppm	0.067	-0.37	-0.39	0.032	-0.046	8.50E-04	0.19	1	0.72
Bi_ppm	0.51	-0.1	0.059	0.61	0.58	0.35	0.47	0.72	1

Correlation	Mo_ppm	Se_ppm	V_ppm	Mn_ppm	Co_ppm	Ni_ppm	Cu_ppm	Zn_ppm	As_ppm
Mo_ppm	1	0.57	0.1	-0.86	-0.67	-0.93	0.018	-0.034	0.89
Se_ppm	0.57	1	-0.11	-0.55	-0.3	-0.54	-0.22	-0.33	0.66
V_ppm	0.1	-0.11	1	0.1	0.018	-0.13	0.47	0.6	-0.16
Mn_ppm	-0.86	-0.55	0.1	1	0.58	0.72	-0.14	0.0062	-0.7
Co_ppm	-0.67	-0.3	0.018	0.58	1	0.85	0.42	-0.27	-0.69
Ni_ppm	-0.93	-0.54	-0.13	0.72	0.85	1	0.17	-0.13	-0.92
Cu_ppm	0.018	-0.22	0.47	-0.14	0.42	0.17	1	0.42	-0.23
Zn_ppm	-0.034	-0.33	0.6	0.0062	-0.27	-0.13	0.42	1	-0.11
As_ppm	0.89	0.66	-0.16	-0.7	-0.69	-0.92	-0.23	-0.11	1
Ag_ppm	0.024	-0.018	0.46	0.015	0.49	0.22	0.4	-0.021	-0.2
Cd_ppm	0.025	-0.39	0.65	0.025	-0.39	-0.21	0.25	0.95	-0.094
Sn_ppm	-0.32	-0.34	0.16	0.59	0.11	0.17	-0.33	0.17	-0.13
Sb_ppm	0.25	-0.058	0.7	-0.047	0.092	-0.15	0.31	0.29	0.035
Te_ppm	0.34	-0.095	0.47	-0.25	0.21	-0.12	0.59	0.23	0.11
Au_ppm	3.00E-04	-0.061	0.7	0.1	0.53	0.21	0.56	0.064	-0.3
Tl_ppm	0.62	0.2	0.3	-0.47	-0.78	-0.78	-0.059	0.63	0.64
Pb_ppm	0.66	0.92	-0.094	-0.67	-0.41	-0.57	-0.3	-0.39	0.62
Bi_ppm	0.8	0.63	0.18	-0.63	-0.34	-0.66	-0.065	-0.18	0.7

Table 4.3. Coefficients of correlation of selected trace elements in coarse-grained pyrite (pyrite 2) from the Middle Triassic Karak Formation. In this Table, correlation coefficients (numbers in pink colour) range from 0.5 to 0.9 implying good correlation between two variables.

Correlation	Ag_ppm	Cd_ppm	Sn_ppm	Sb_ppm	Te_ppm	Au_ppm	Tl_ppm	Pb_ppm	Bi_ppm
Mo_ppm	0.16	-2.40E-04	0.2	0.044	-0.4	2.40E-04	-0.093	0.062	-0.014
Se_ppm	0.18	0.15	-0.11	0.13	0.8	0.29	0.069	0.23	0.43
V_ppm	0.46	-0.28	0.75	-0.32	-0.26	-0.18	0.75	-0.31	-0.27
Mn_ppm	-0.0068	0.23	-0.11	0.15	-0.31	0.18	0.16	0.2	0.14
Co_ppm	0.88	0.18	0.92	0.21	-0.36	0.22	0.68	0.17	0.14
Ni_ppm	0.19	0.034	0.41	0.11	-0.6	-0.022	-0.016	0.034	-0.13
Cu_ppm	0.59	0.91	0.2	0.92	-0.28	0.9	0.36	0.93	0.86
Zn_ppm	0.37	1	-0.079	0.99	-0.19	0.97	0.24	0.99	0.91
As_ppm	0.8	-0.18	0.85	-0.16	0.16	-0.05	0.6	-0.12	0.03
Ag_ppm	1	0.38	0.83	0.42	-0.087	0.46	0.72	0.43	0.49
Cd_ppm	0.38	1	-0.06	0.99	-0.21	0.97	0.27	0.99	0.9
Sn_ppm	0.83	-0.06	1	-0.018	-0.21	0.0034	0.73	-0.039	0.004
Sb_ppm	0.42	0.99	-0.018	1	-0.21	0.96	0.25	0.99	0.91
Te_ppm	-0.087	-0.21	-0.21	-0.21	1	-0.14	-0.2	-0.12	0.12
Au_ppm	0.46	0.97	0.0034	0.96	-0.14	1	0.35	0.97	0.91
Tl_ppm	0.72	0.27	0.73	0.25	-0.2	0.35	1	0.26	0.3
Pb_ppm	0.43	0.99	-0.039	0.99	-0.12	0.97	0.26	1	0.95
Bi_ppm	0.49	0.9	0.004	0.91	0.12	0.91	0.3	0.95	1

Correlation	Mo_ppm	Se_ppm	V_ppm	Mn_ppm	Co_ppm	Ni_ppm	Cu_ppm	Zn_ppm	As_ppm
Mo_ppm	1	-0.5	0.036	0.14	0.16	0.67	0.36	0.0024	0.0041
Se_ppm	-0.5	1	-0.089	-0.13	-0.15	-0.68	0.013	0.19	0.32
V_ppm	0.036	-0.089	1	0.2	0.59	0.044	-0.14	-0.31	0.69
Mn_ppm	0.14	-0.13	0.2	1	-0.0036	-0.24	0.21	0.21	-0.096
Co_ppm	0.16	-0.15	0.59	-0.0036	1	0.44	0.39	0.16	0.74
Ni_ppm	0.67	-0.68	0.044	-0.24	0.44	1	0.28	0.037	-0.021
Cu_ppm	0.36	0.013	-0.14	0.21	0.39	0.28	1	0.9	0.025
Zn_ppm	0.0024	0.19	-0.31	0.21	0.16	0.037	0.9	1	-0.18
As_ppm	0.0041	0.32	0.69	-0.096	0.74	-0.021	0.025	-0.18	1
Ag_ppm	0.16	0.18	0.46	-0.0068	0.88	0.19	0.59	0.37	0.8
Cd_ppm	-2.40E-04	0.15	-0.28	0.23	0.18	0.034	0.91	1	-0.18
Sn_ppm	0.2	-0.11	0.75	-0.11	0.92	0.41	0.2	-0.079	0.85
Sb_ppm	0.044	0.13	-0.32	0.15	0.21	0.11	0.92	0.99	-0.16
Te_ppm	-0.4	0.8	-0.26	-0.31	-0.36	-0.6	-0.28	-0.19	0.16
Au_ppm	2.40E-04	0.29	-0.18	0.18	0.22	-0.022	0.9	0.97	-0.05
Tl_ppm	-0.093	0.069	0.75	0.16	0.68	-0.016	0.36	0.24	0.6
Pb_ppm	0.062	0.23	-0.31	0.2	0.17	0.034	0.93	0.99	-0.12
Bi_ppm	-0.014	0.43	-0.27	0.14	0.14	-0.13	0.86	0.91	0.03

In framboidal pyrite (pyrite 1), there is a good correlation amongst Au and V, Co, Cu, Ag, Sb, Te, Bi as indicated by the coefficients of correlation (Table 4.2). Elements such as Ag, V, and Te are typically adsorbed onto organic matter and concentrated into framboidal pyrite during diagenesis (Large et al., 2009). Pyrite 1 has a Au content that varies from 0.36 to 0.60 ppm Au (mean 0.5 ppm) whereas pyrite 2 has Au content ranging from 0.05 to 0.87 ppm Au (mean 0.2 ppm). The pyrite framboids (pyrite 1) have more Co than Ni, whereas the

crystalline pyrite 2 has more Ni than Co (Table 4.1,). Elements that correlate well with Au in pyrite 2 are Cu, Zn, Cd, Sb, Pb, and Bi (Table 4.3). The correlation of coefficients of Au relative to Cu, Zn, Cd, Sb, Pb, and Bi vary from 0.90 to 0.97 (Table 4.3).Compared to the worldwide diagenetic pyrite average (Gregory et al., 2015), the Karak pyrites are enriched in Co, As, Ag, Te, Au, Pb, Bi and depleted in Ni and strongly depleted in Mn, and Tl (Fig. 4.7). It is uncommon for framboidal pyrites to have Co>Ni and Mo>Se as shown by the worldwide database (Gregory et al., 2015) and therefore suggest that the Karak pyrite may have been affected by low grade metamorphic processes. This interpretation has previously been invoked to explain the trace element patterns in Triassic marine pyrite from the Otago black shales in New Zealand with the same feature (Large et al., 2009). The Otago black shales underwent low grade metamophism (greenschist facies) that have affected the chemistry of the diagenetic pyrites.

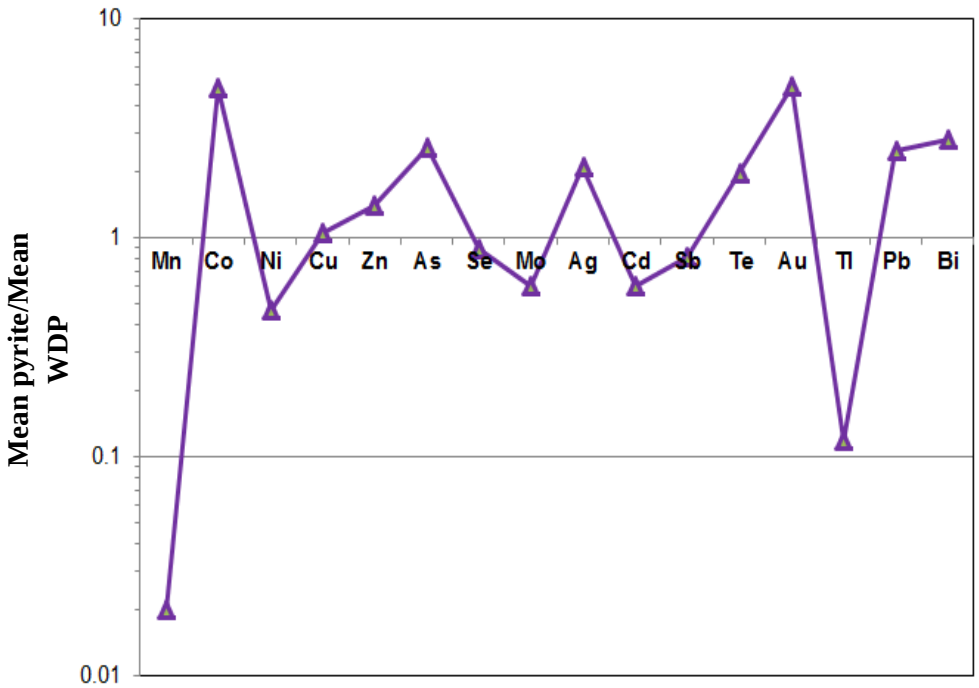

Fig. 4.5. Spider plot of mean values of selected trace elements in sedimentary pyrites normalised to WDP (worldwide diagenetic pyrite, Gregory et al., 2015) from the Karak Formation, Malaysia. Mean values are for the Karak Formation sedimentary pyrite dataset.

Comparing both pyrite types, framboidal pyrite (pyrite 1) is moderately enriched in V, Mn, Co, Cu, As, Mo, Ag, Cd, Sn, Sb, Au, Tl, Pb, Bi and depleted in Ni whereas metamorphic pyrite (pyrite 2) is moderately enriched in Ni and depleted in V, Mn, Co, Cu, As, Ag, Cd, Sn, Sb, Au, Pb, Bi (Fig. 4.6 Additionally, Mo and Tl are strongly depleted in pyrite 2 (Fig. 4.6).

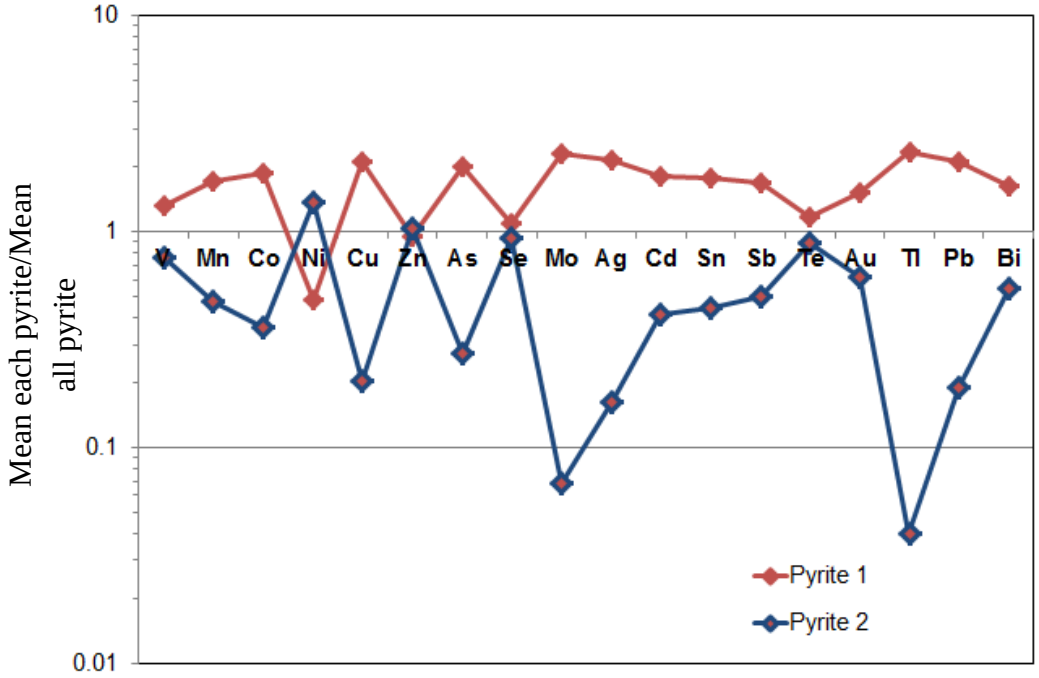

Fig. 4.6. Normalised spider plot showing chemical composition of selected trace elements in framboidal pyrite (pyrite 1) and metamorphic pyrite (pyrite 2) in the Karak Formation, Malaysia. The average of the whole dataset is presented in this plot.

4.2.2. Discussion for the Karak Formation

Gold content in diagenetic pyrite ranges from 364 to 602 ppb (mean 508 ppb) whereas gold concentration in metamorphic pyrite is between 62 and 876 ppb (mean 207 ppb). The result indicates that gold was liberated from framboidal pyrite during crystallisation and conversion to metamorphic pyrite. This implies that the tuffaceous black shales in the Karak Formation containing higher amounts of gold in sedimentary

pyrites may be considered to be good Au source rocks. Diagenetic pyrite shows an unusual geochemical signature of higher Co content relative to Ni which suggests a volcanic contribution of cobalt into the structure of framboidal pyrites during diagenesis. In contrast, framboidal pyrites are known to commonly have higher Ni content relative to Co content (Large et al., 2011; Makoundi et al., 2014). Interestingly, Au and Ag have a strong correlation in the framboidal pyrites (pyrite 1) and in metamorphic pyrites (pyrite 2). Moreover, Au has no correlation with Mo in both pyrite types. The good correlation of V with Au, Zn, Cd, and Sb in diagenetic pyrite 1 suggests they were all concentrated by organic processes (Rimmer, 2004; Large et al., 2009). Vanadium is commonly introduced to the sediments by organometallic ligands in the organic matter (Athur and Sagenan, 1994; Morford and Emerson, 1999).

4.3. Semantan Formation (Middle Triassic)

4.3.1. Major element composition

The Semantan Formation black shales have the following compositional limits, SiO_2 (54.5-65.8 wt %), TiO_2 (0.52-0.78 wt %), Al_2O_3 (15-21 wt %), Fe_2O_3 (0.8-16 wt %), MnO (0.01-0.90 wt %), MgO (0.3-2.5 wt %), CaO (0.01-0.20 wt %), Na_2O (0.03-1.5 wt %), K_2O (0.9-3.7 wt %), P_2O_5 (0.02-0.20 wt %). The total organic carbon (TOC) varies from 0.3 to 0.7 wt % (mean 0.4 wt %); however, the total sulphur ranges from 0.03 to 1.5 wt % (mean 0.2 wt %). Result of major and trace elements are presented in Table 4.4. Note the MnO and CaO contents are low and mostly close to the detection limit (0.01 wt %). The Semantan black shales have a similar major element composition compared to PAAS (Fig. 4.7) except for significant depletion in K_2O and P_2O_5.

Table 4.4. The mean composition (major element in wt %; trace element in ppm) of black shales from the Semantan Formation (Middle Triassic) with average compositions of PAAS, WAS, NASC, and UCC.

	Black shale (n= 15)	PAAS	WAS	NASC	UCC
(wt %)					
SiO_2	62.81	62.8	58.9	64.8	61.6
TiO_2	0.66	1	0.8	0.78	0.67
Al_2O_3	18.33	18.9	16.7	16.9	15.2
Fe_2O_3	6.52	7.22	6.9	5.7	6.2
MnO	0.12	0.11	-	0.06	0.09
MgO	1.67	2.2	2.6	2.9	3.7
CaO	0.07	1.3	2.2	3.4	5.5
Na_2O	0.88	1.2	1.6	1	3.2
K_2O	2.22	3.7	3.6	3.8	3.4
P_2O_5	0.06	0.16	-	0.13	0.17
Loss	6.70	-	-	-	-
Total	100.00	-	-	-	-
TOC	0.38	-	-	-	-
S	0.23	-	-	-	697
(ppm)					
Sc	21.68	16	-	14.9	16
Ba	305.59	650	580	636	584
V	160.08	150	130	-	98
Ni	46.31	55	68	58	56
Cu	40.24	50	45	-	25
Zn	65.94	85	95	-	65
Cr	57.84	110	90	125	126
Ga	20.60	20	-	-	15
As	12.32	-	10	28.4	1.7
Se	1.15	-	0.5	-	0.12
Rb	97.58	160	140	125	78
Sr	70.29	200	300	142	333
Y	29.26	27	-	-	24
Zr	159.64	210	160	200	203
Nb	9.47	19	-	-	19
Mo	1.35	1	1	-	1.1
Ag	-	-	0.07	-	0.07
Sn	3.07	4	6	-	2.3
Sb	1.76	-	1.5	2.09	0.3
Te	0.85	-	-	-	0.005
Tl	0.62	-	0.68	-	0.52
Pb	22.32	20	22	-	0.0004
Bi	0.38	-	0.1	-	0.085
Th	10.47	14.6	-	12.3	8.5
U	3.18	3.1	3.7	2.66	1.7

Note: - = not analysed

They are consistently enriched in Al_2O_3 and K_2O contents and depleted in Na_2O relative to PAAS. The Al_2O_3-K_2O plot shows that the two major elements may have been partially controlled by Na-rich orthoclase cryptoperthite, alkali feldspar (Fig. 4.8).

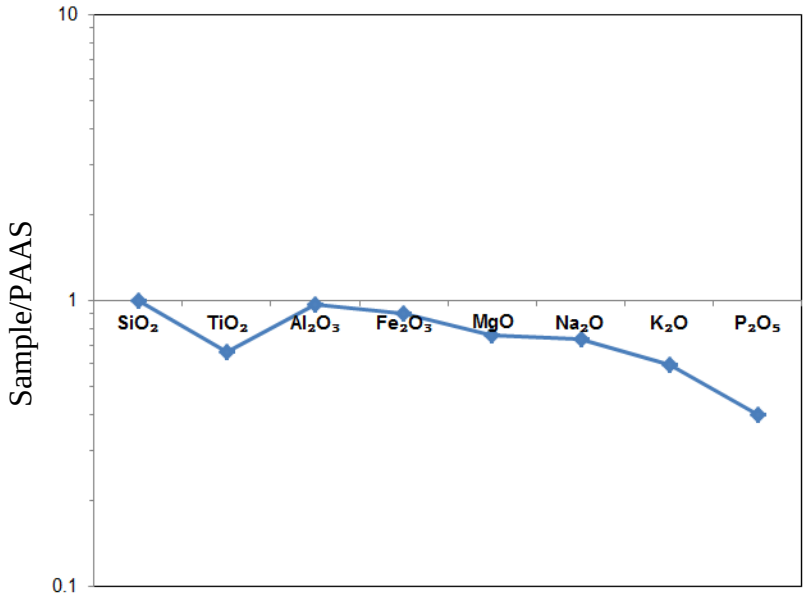

Fig. 4.7. Spider plot of major element composition normalised to PAAS for the Semantan black shales featuring patterns of the Machinchang, Singa, and BRSZ Unit 1 shales as background for comparison.

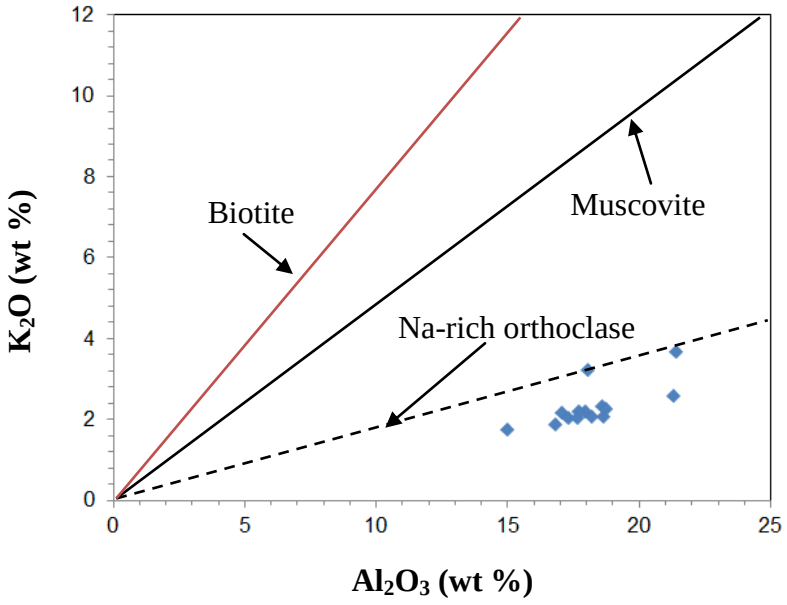

Fig. 4.8. Binary plot of Al_2O_3 against K_2O in the Semantan black shale. The dashed line represents the Na-rich orthoclase cryptoperthite (data from Deer et al., 1966).

4.3.2. Trace element composition

The Semantan black shales were analysed for Ni, Cu, Zn, Cr, As, Sn, Sb, Te, Tl, Pb, Bi, Th and U (Table 4.4). Concentrations of these elements are similar to PAAS as they are close to 1 on the normalisation plot (Fig. 4.9).The mean compositions of these trace elements which are presented in Table 4.4 are normalised to PAAS (Post-Archean Australian Shales, Taylor and McLennan, 1985) and discussed for their enrichment and depletion (Fig. 4.9).

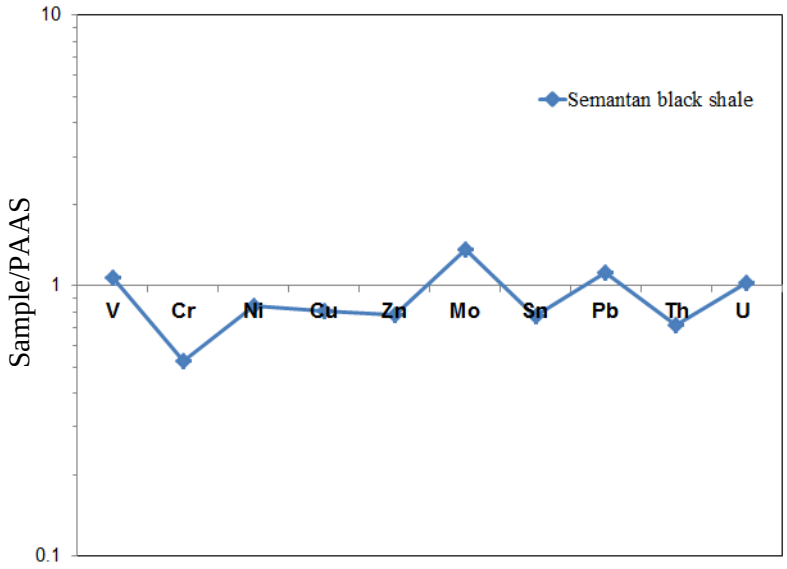

Fig. 4.9. Spider plot of trace element compositions normalised to PAAS for the Semantan black shales.

The Semantan black shales are similar to PAAS in trace element composition. Relations of Al_2O_3 to some trace elements are shown in Fig. 4.10 in order to verify whether clay or aluminosilicate minerals controlled the accumulation of such elements into the basin.

Previous researchers used alumina content as a proxy for detrital control to imply detrital origin of trace elements adsorbed onto clay particles or enclosed in the structure of aluminosilicate minerals (Calvert and Pedersen, 1993; Tribovillar et al., 1994; Hild and Brumsack, 1998; Böning et al., 2004; Tribovillar et al., 2006).

Minerals such as amphibole, biotite, and garnet have been found hosting significant amounts of V, Cr, and Zn in their structure (Canet et al., 2003; Donohue and Essene, 2005). Alumina relationships with certain trace elements have shown that in the Semantan Formation black shales, Al_2O_3 content varies positively with V, Cr, Mo, Sb, U and organic carbon whereas it correlates negatively with As and Zn (Fig. 4.10, Table 4.5). Comparatively, there is no correlation between Cr and organic carbon in the Singa black shales.

In contrast, there is a positive correlation between alumina and both vanadium and Nickel in the shales. Relationships of organic carbon to selected trace elements including sulphur content are shown in Fig. 4.11. In this figure, the logarithmic scale is used to depict correlation trends and fit the organic carbon contents as they range between 0 and 2.5 wt %. The relations of organic carbon to some trace elements are used to imply control of organic matter (via organometallic complexes) on certain trace elements during their introduction into organic-bearing sediments (Tribovillard et al., 2006).

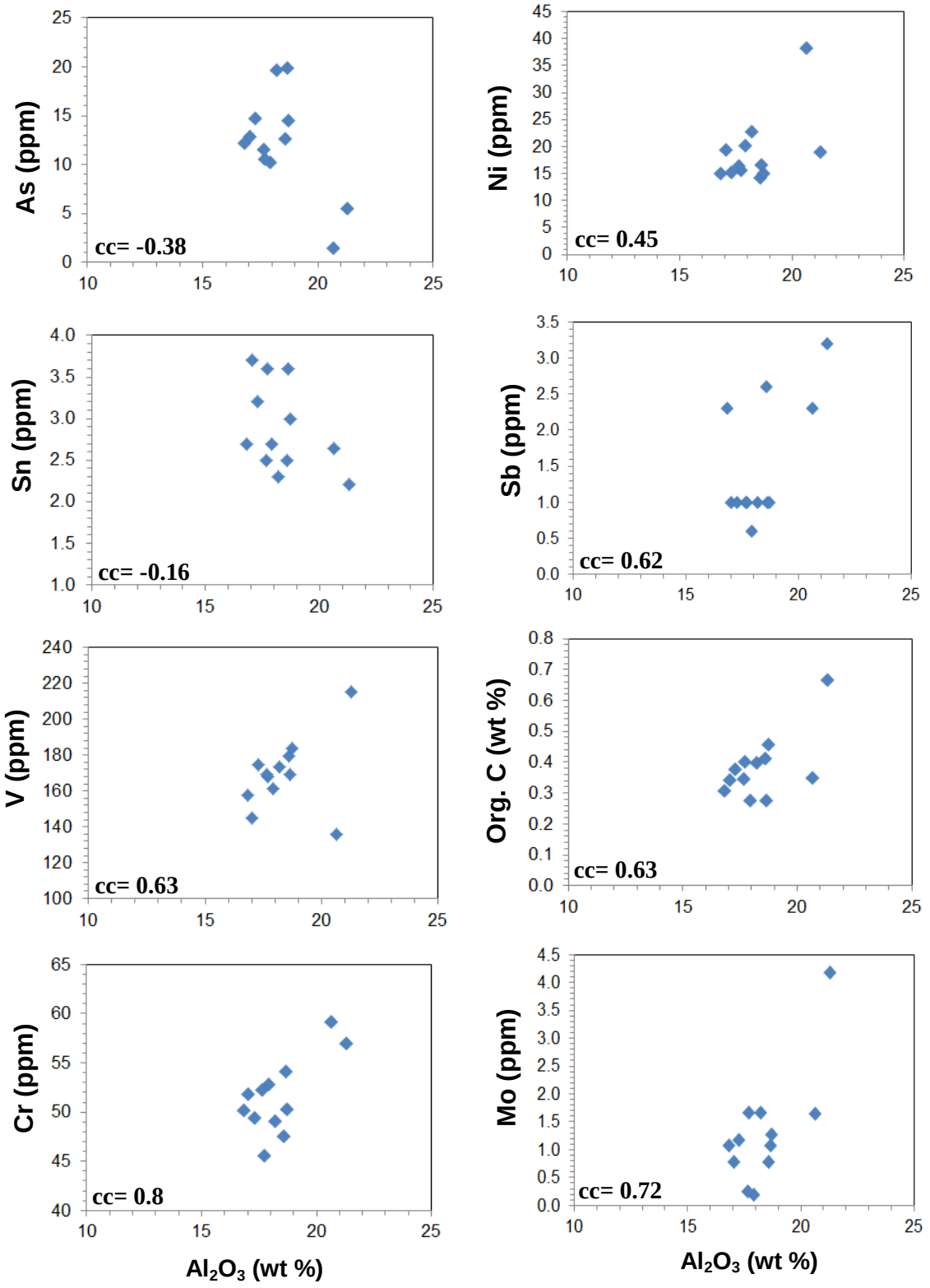

Fig. 4.10. Alumina relationships with selected trace elements including organic carbon content in the Semantan Formation. Note: cc is the coefficients of correlation as shown in Table 4.5. Alumina correlates well with organic carbon, Sb, V, Cr and Mo.

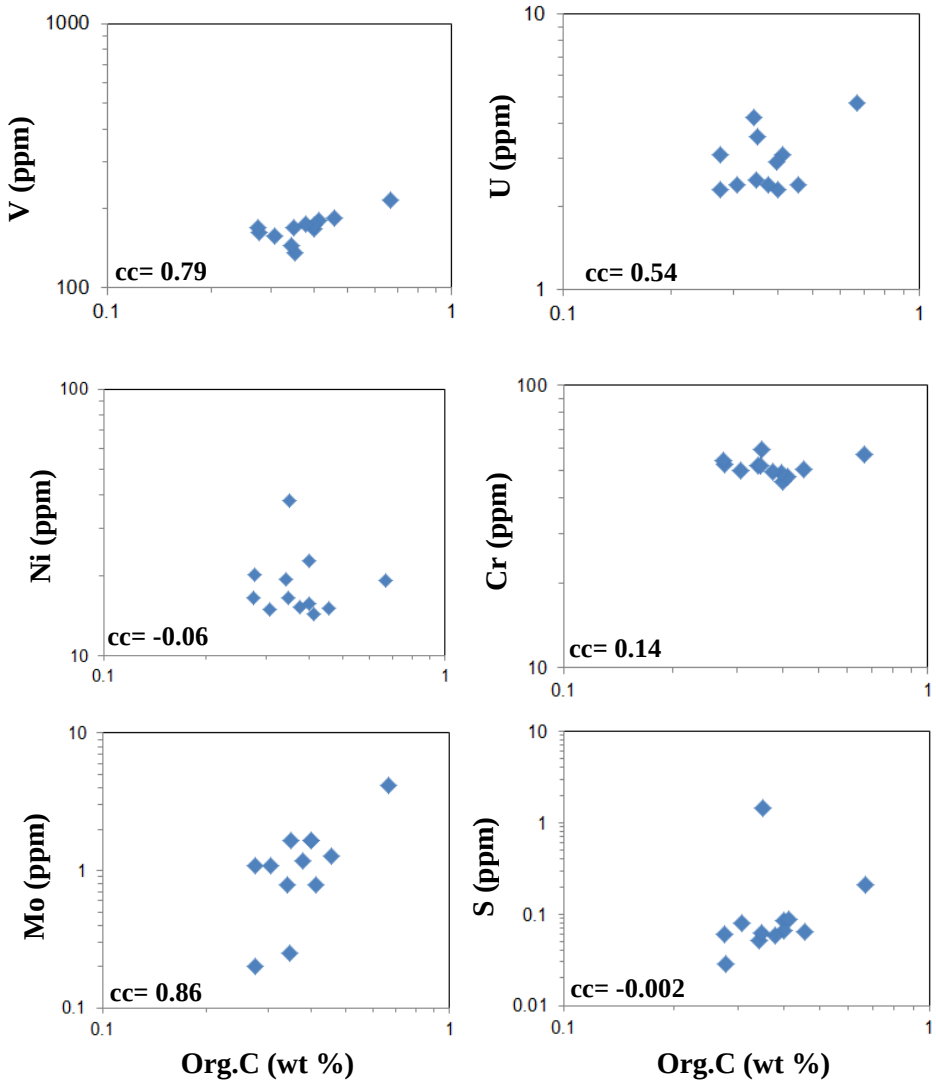

Fig. 4.11. Log-log binary comparison plots showing relationships of organic carbon to V, U, Ni, Cr, Mo, and S in the Semantan Formation (Middle Triassic). Note: cc is the coefficients of correlation as shown in Table 4.5. Organic carbon correlates well with V, U, and Mo.

Table 4.5. Coefficients of correlation of selected trace elements with alumina (Al_2O_3) and organic carbon from the Semantan black shales. In this Table, correlation coefficients (numbers in pink colour) range from 0.5 to 0.9 implying good correlation between two variables.

Correlation	Al_2O_3_wt %	Org.C_wt %	S_wt %	V_ppm	Cr_ppm	Ni_ppm	Cu_ppm	Zn_ppm	As_ppm	Mo_ppm	Sn_ppm	Sb_ppm	U_ppm
Al_2O_3_wt %	1	0.63	0.53	0.63	0.8	0.45	0.3	-0.86	-0.38	0.72	-0.16	0.62	0.67
Org.C_wt %	0.63	1	-0.0027	0.79	0.14	-0.063	-0.37	-0.53	-0.32	0.86	-0.41	0.58	0.54
S_wt %	0.53	-0.0027	1	-0.25	0.44	0.91	0.85	-0.46	-0.68	0.22	-0.16	0.39	0.31
V_ppm	0.63	0.79	-0.25	1	0.55	-0.33	-0.35	-0.67	0.16	0.61	-0.027	0.39	0.37
Cr_ppm	0.8	0.14	0.44	0.55	1	0.4	0.31	-0.93	-0.22	0.42	0.11	0.39	0.61
Ni_ppm	0.45	-0.063	0.91	-0.33	0.4	1	0.81	-0.33	-0.56	0.17	-0.22	0.2	0.34
Cu_ppm	0.3	-0.37	0.85	-0.35	0.31	0.81	1	-0.29	-0.41	-0.15	-0.019	0.064	-0.04
Zn_ppm	-0.86	-0.53	-0.46	-0.67	-0.93	-0.33	-0.29	1	0.29	-0.58	-0.097	-0.56	-0.61
As_ppm	-0.38	-0.32	-0.68	0.16	-0.22	-0.56	-0.41	0.29	1	-0.31	0.33	-0.51	-0.31
Mo_ppm	0.72	0.86	0.22	0.61	0.42	0.17	-0.15	-0.58	-0.31	1	-0.18	0.65	0.66
Sn_ppm	-0.16	-0.41	-0.16	-0.027	0.11	-0.22	-0.019	-0.097	0.33	-0.18	1	-0.42	-0.0012
Sb_ppm	0.62	0.58	0.39	0.39	0.39	0.2	0.064	-0.56	-0.51	0.65	-0.42	1	0.6
U_ppm	0.67	0.54	0.31	0.37	0.61	0.34	-0.04	-0.61	-0.31	0.66	-0.0012	0.6	1

The data indicates that the organic carbon content shows a positive correlation with V, U, Mo, and Sb in the Semantan black shales, and Singa black shales. These correlations suggest that a combination of clays and organic carbon contributed to the concentrations of a range of trace elements in the Semantan shales including V, Cr, Mo, Sb, and U.

4.3.3. Pyrite texture and chemistry

In the Semantan Formation, sedimentary pyrite occurs in the form of elongated clusters of euhedral pyrite micro crystals measuring 20-80 µm across in the black shale (Fig. 4.12A). Some of the pyrite clusters (Fig. 4.12) appear as oxidized pyrite framboids with few unoxidized remains of euhedral pyrite (less than 10 µm across) in their structure. Some euhedral crystals are arranged in a form that they appear as “pyrite rings” (Fig. 4.12B). Pyrite framboids are also common (less than 20 µm across) (Fig. 4.12C). Other clusters are

formed of tiny pyrite crystals of less than 1-2 µm in size (Fig. 4.12D). Relationships among Co, Cu and Ni on one hand and As, Ni, Mo and Se on the other hand are shown in Fig. 4.13.

The Semantan Formation pyrites are characterised by the following ratio values: Co/Ni (0-10), Cu/Ni (0-25), Se/Mo (0.4-73), and As/Ni (0.06-78). The framboid-like texture and chemistry of pyrite (Ag/Au>1; Ni/Co~1) point to a sedimentary origin. The relationships among Au and other trace elements (Fig. 4.14) show four trends consistent with the coefficients of correlation: (1) Au varies positively with Zn and Se; (2) Au varies negatively with As; (3) Au exhibits weak positive correlation with Ag, Ni, and Mo; and (4) Au has no correlation with Te and Sb. Results of spot analyses on sedimentary pyrite are shown in Table 4.6.

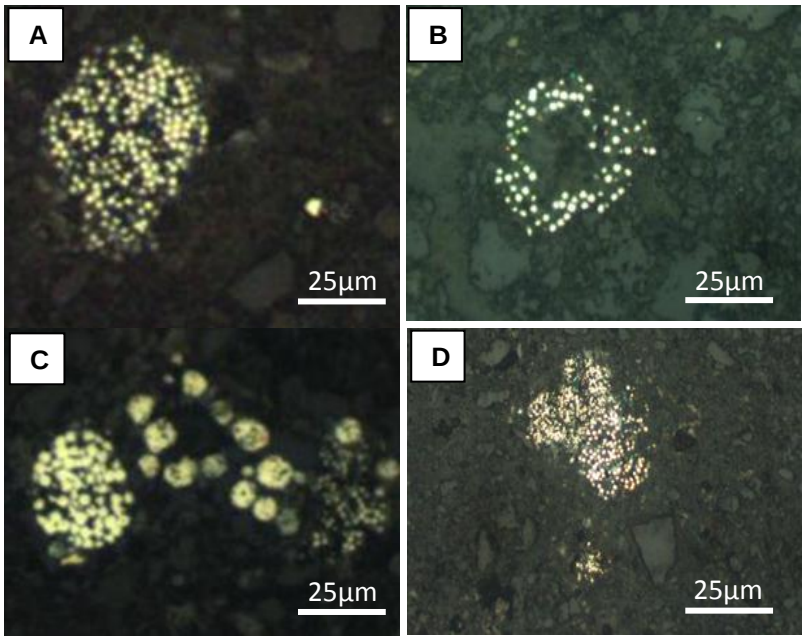

Fig. 4.12. Textural characteristics of pyrite in tuffaceous black shales from the Semantan Formation (Middle Triassic). **A**) Sub-rounded cluster of microcrystal of pyrite. **B**) Ring of microcrystals of euhedral pyrites. **C**) Rounded isolated framboidal pyrites occurring together with smaller scattered pyrite framdoids. **D**) Patches of microcrystal of pyrite mixed with matrix.

Table 4.6. LA ICP-MS analyses (in ppm) of pyrite from the Ladinian Semantan Formation, Malaysia

Analysis No	Co	Ni	Cu	Zn	As	Se	Mo	Ag	Cd	Sb	Te	Au	Tl	Pb	Bi
ME-5912-1	270.78	96.55	246.59	1297.23	826.88	8.48	2.89	20.45	1.35	30.21	8.26	0.17	0.48	302.46	38.21
ME-5912-2	255.89	107.27	98.62	1385.01	1069.42	7.02	2.58	1.48	0.25	7.52	7.68	0.03	2.17	131.80	48.20
ME-5912-3	244.66	64.07	673.40	693.96	4971.81	4.19	4.15	5.60	0.15	16.65	8.76	0.12	7.40	217.37	44.98
ME-5912-4	309.68	113.38	430.01	1131.87	2502.82	2.00	1.97	4.68	0.20	18.51	8.07	0.11	3.67	276.90	37.99
ME-6612B-1	173.42	173.00	1816.55	1882.80	3192.60	5.00	6.09	7.68	0.50	42.16	11.45	0.50	3.29	256.51	65.94
ME-6612B-2	535.71	931.96	510.11	1318.28	134.62	84.95	5.44	3.94	2.50	10.02	7.00	0.30	11.46	368.03	3.12
ME-6612B-3	261.42	255.44	2442.53	1784.64	2523.73	22.44	6.00	3.96	1.86	40.94	8.04	0.70	2.19	201.27	94.38
ME-6612B-4	153.80	166.53	1640.77	1592.18	2768.81	15.43	4.41	3.49	1.03	62.33	17.97	0.08	1.08	226.61	135.08
ME-6612B-5	160.68	123.89	572.02	731.51	2787.11	10.52	2.19	4.65	0.20	19.61	5.84	0.02	1.18	59.96	56.87
ME-6612B-6	106.66	114.80	839.80	1040.51	2271.76	11.20	5.43	12.20	0.66	31.48	6.84	0.02	1.43	131.15	69.36
ME-6612B-8	234.42	124.49	544.23	849.06	2847.30	10.95	2.57	6.38	0.72	25.42	8.01	0.25	0.83	60.27	83.01
ME-6612B-9	113.09	103.01	956.69	922.55	2224.12	20.46	7.27	5.07	0.83	31.45	8.73	0.03	2.70	104.83	52.74
ME-6612A-1	564.39	172.50	1131.82	988.52	4004.70	0.73	1.93	181.00	0.10	22.03	10.54	0.07	2.17	49.29	95.55
ME-6612A-2	1212.20	1793.13	6780.17	6289.31	5675.42	136.10	27.46	18.25	4.50	133.08	43.21	0.50	27.06	935.69	136.42
ME-6612A-3	480.27	180.01	766.14	841.79	3201.11	7.74	2.42	8.84	0.10	13.71	3.51	1.16	1.14	48.39	72.26
ME-6612A-5	117.41	148.00	1136.58	1122.31	1665.71	10.51	4.97	4.56	0.57	13.04	3.96	0.26	1.20	72.21	36.58
ME-6612A-6	145.80	116.92	1856.29	1437.95	4656.51	19.57	2.17	52.01	0.40	23.17	11.65	0.04	4.81	121.57	83.69
ME-5912-4	12.00	482.75	0.00	6989.90	28.47	560.97	8.68	55.68	26.92	27.23	14.84	4.57	4.51	74.84	0.88
ME-5912-5	11.96	487.41	0.00	6896.50	28.04	636.70	8.70	57.26	26.74	27.78	15.34	4.22	4.54	74.37	1.01
ME-5912-7	0.41	0.04	0.99	0.00	1.91	45.02	0.00	0.01	0.04	0.00	58.48	0.00	2.67	47.34	0.66
ME-6612B-2	11.98	479.77		6974.42	27.86	551.79	8.55	55.47	26.52	27.19	14.69	4.27	3.10	2784.03	0.37
Mean	256.03	296.90	1122.17	2198.58	2257.65	103.42	5.52	24.41	4.58	29.69	13.47	0.83	4.24	311.66	55.11
Mean (WDP)	303.00	829.00	436.00	131.00	1360.00	71.00	88.00	9.20	3.00	90.00	4.90	0.10	36.00	387.00	13.00

WDP: worldwide diagenetic pyrite (Gregory et al., 2015)

Table 4.7. Coefficients of correlation of selected trace elements in sedimentary pyrite from the Middle Triassic Semantan Formation. Pink coloured numbers indicate good correlation between two variables.

Correlation	Co_ppm	Ni_ppm	Cu_ppm	Zn_ppm	As_ppm	Se_ppm	Mo_ppm	Ag_ppm	Cd_ppm	Sb_ppm	Te_ppm	Au_ppm	Tl_ppm	Pb_ppm	Bi_ppm
Co_ppm	1														
Ni_ppm	0.73	1													
Cu_ppm	0.76	0.73	1												
Zn_ppm	0.068	0.61	0.33	1											
As_ppm	0.56	0.14	0.65	-0.25	1										
Se_ppm	-0.26	0.33	-0.13	0.9	-0.52	1									
Mo_ppm	0.61	0.9	0.82	0.68	0.25	0.35	1								
Ag_ppm	0.11	0.044	-0.01	0.27	0.09	0.3	-0.0072	1							
Cd_ppm	-0.3	0.29	-0.15	0.9	-0.52	0.99	0.33	0.31	1						
Sb_ppm	0.64	0.73	0.9	0.45	0.48	0.064	0.87	-0.02	0.052	1					
Te_ppm	0.2	0.37	0.36	0.22	-0.038	0.14	0.37	-0.032	0.082	0.36	1				
Au_ppm	-0.3	0.24	-0.18	0.87	-0.5	0.97	0.27	0.29	0.98	0.0051	0.024	1			
Tl_ppm	0.78	0.92	0.78	0.43	0.37	0.13	0.85	-0.03	0.078	0.72	0.46	0.018	1		
Pb_ppm	0.063	0.37	0.82	0.55	-0.16	0.46	0.38	0.11	0.49	0.25	0.14	0.46	0.25	1	
Bi_ppm	0.53	0.16	0.7	-0.22	0.79	-0.52	0.28	0.041	-0.51	0.64	0.0038	-0.51	0.23	-0.17	1

Relationships among Co, Cu and Ni on one hand and As, Ni, Mo and Se on the other hand are important to work out possible proxies to infer the origin of pyrite. For instance, the geochemical ratio Se/Mo > 10 can be used to infer a sedimentary origin for pyrite. The

geochemical ratios such as Co/Ni, Cu/Ni, Se/Mo, and As/Ni in sedimentary pyrite indicate that most values plot within the sedimentary pyrite field (dashed polygon). These proxies (i.e. ratios Co/Ni, Cu/Ni, Se/Mo, As/Ni) are useful to infer the origin of pyrite. Compared to other formation pyrites, the Semantan Formation pyrites data commonly plot close to the Cu/Ni=10 and As/Ni=10 lines (Fig. 4.13).

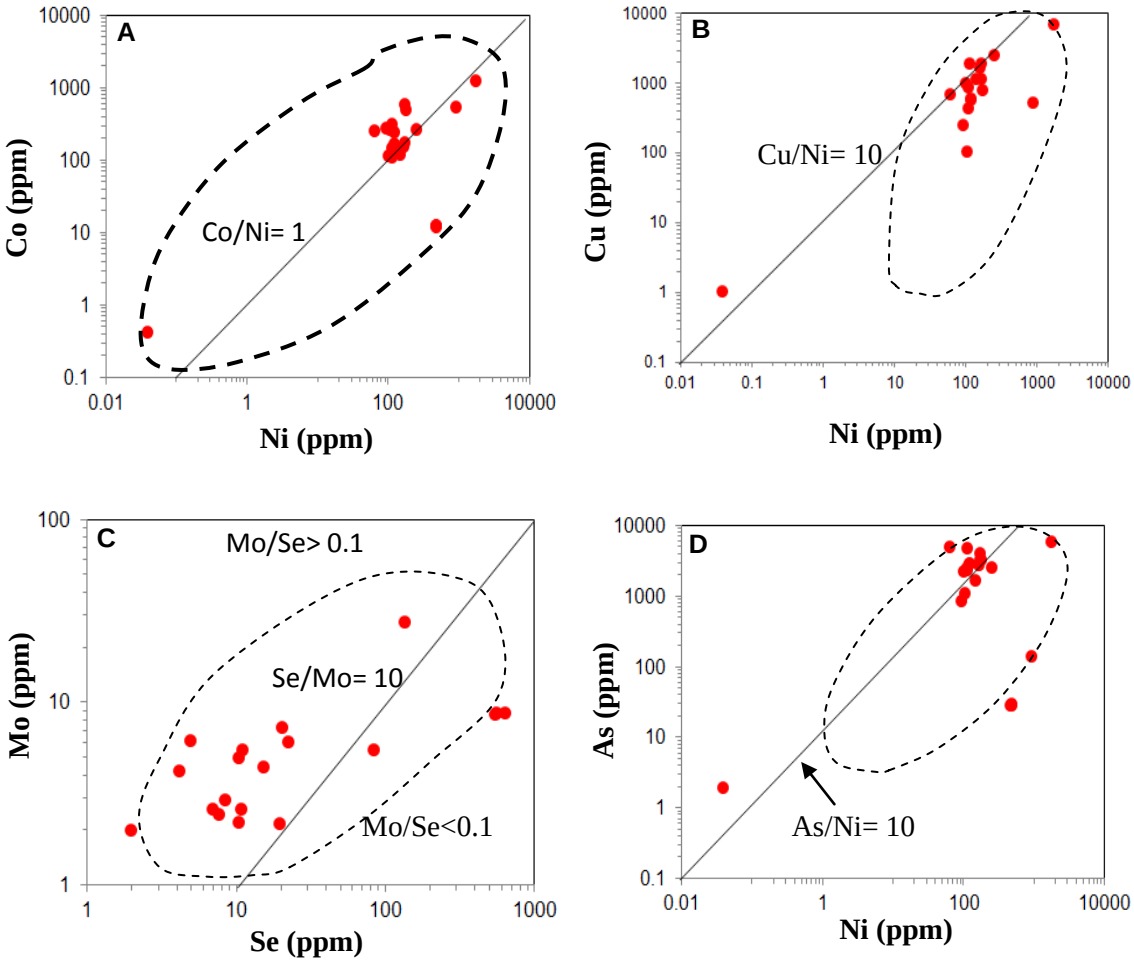

Fig. 4.13. Log-log plots of trace elements in pyrite from the Ladinian Semantan Formation, Malaysia. **A**) Co-Ni plot. **B**) Cu-Ni plot. **C**) Se-Mo plot. **D**) As-Ni plot. Dashed polygon is the field of sedimentary pyrite (Gregory et al., 2015). All analyses of pyrite plot in the sedimentary pyrite field of Gregory et al. (2015) confirming a sedimentary origin.

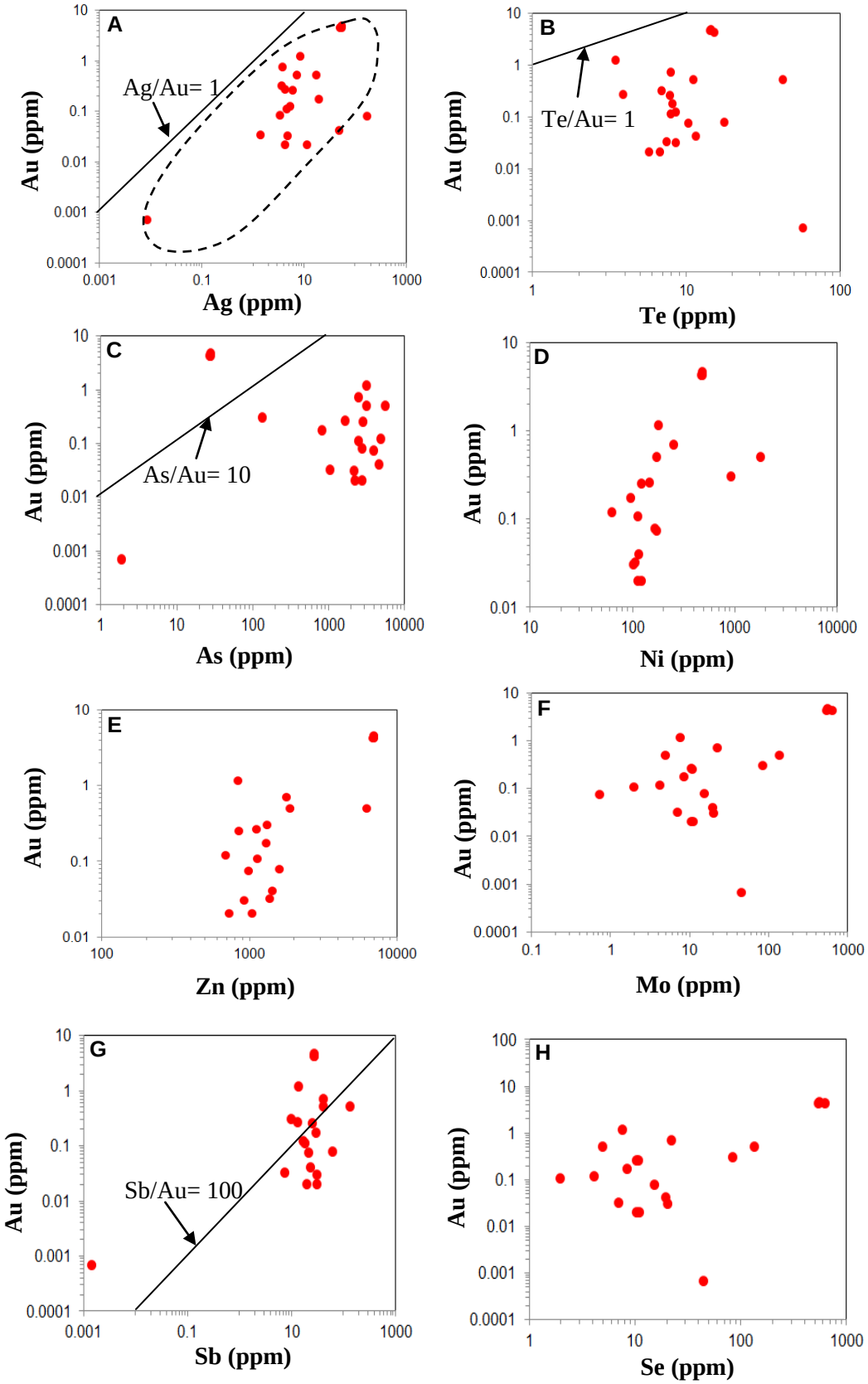

Fig. 4.14. Bivariate log-log plots showing relationships among Au and trace elements from the Ladinian Semantan Formation. **A**) Au-Ag. **B**) Au-Te. **C**) Au-As. **D**) Au-Ni. **E**) Au-V. **F**) Au-Mo. **G**) Au-Sb. and **H**) Au-Se in pyrite for the Semantan Formation, Malaysia. The Ag > Au content of all pyrite analyses arguably indicate a sedimentary origin (Thomas et al., 2011).

Compared with the worldwide diagenetic pyrite (WDP), the Semantan pyrites are strongly enriched in Zn, moderately enriched in Cu, As, Se, Ag, Cd, Te, Au, and Bi but depleted in Mo, Sb, and Tl (Fig. 4.15). Remarkably, from Devonian to Triassic in all studied formation pyrites, the trace elements that are consistently enriched in diagenetic pyrite are Zn and Au and those that are always depleted are Mo, Sb and Tl (Fig. 4.15).

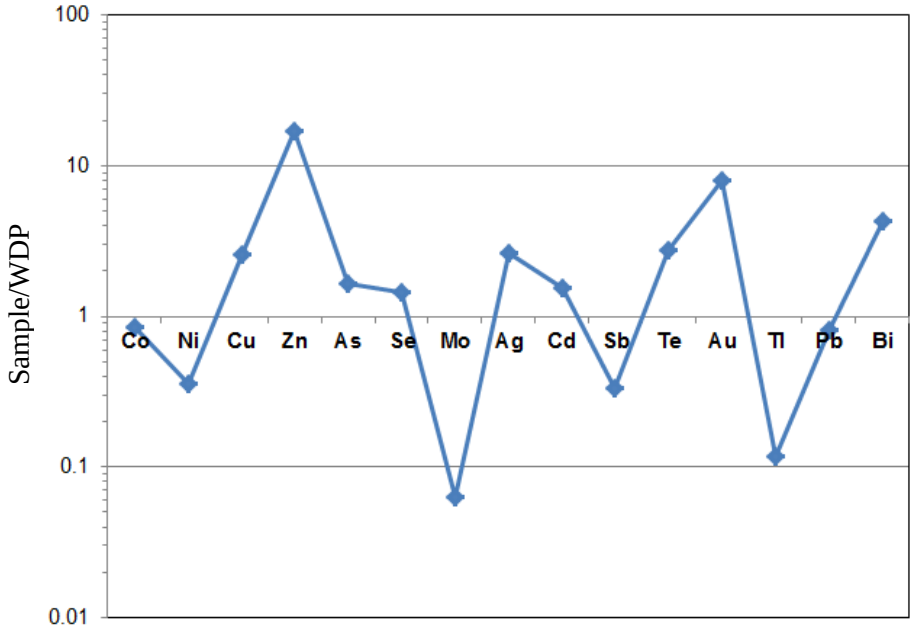

Fig. 4.15. Spider plot of mean values of selected trace elements in sedimentary pyrites normalised to WDP (worldwide diagenetic pyrite, Gregory et al., 2015) from the Semantan Formation, Malaysia. The concentration of manganese is not taken into account in this plot as it was eliminated from the Semantan diagenetic pyrite dataset as part of the matrix composition.

4.3.4. Discussion for the Semantan Formation

The Semantan tuffaceous black shales have a similar major element and trace element composition compared to PAAS. Trace elements in sedimentary pyrite (pyrite 1) are enriched in Cu, Zn, Ag, Au, Te, and Bi and depleted in Ni, Mo, Sb, and Tl compared to worldwide

diagenetic pyrite (WDP). Relationships of Al_2O_3 content with certain trace elements have shown that in the Semantan Formation black shales, Al_2O_3 content varies positively with V, Cr, Mo, Sb, U, and organic carbon whereas it changes negatively with Zn (Table 4.5). The organic carbon content shows positive correlation with V, U, Mo and Sb in the Semantan black shales implying that these elements were introduced into sediments by organic processes. Gold content in sedimentary pyrite from the Semantan Formation varies between 0 and 4.6 ppm (mean 0.8 ppm).

4.4. Gua Musang Formation (Middle Triassic)

4.4.1. Major elements

A total of sixteen black shale and sandstone samples were analysed (Table 4.8) for their major elements (in wt %), trace elements (in ppm), rare earth elements (in ppm), total organic carbon (in wt %) and sulphur content (in wt %) using a combination of XRF (X-ray fluorescence analysis) and ICP-MS techniques at the University of Tasmania. The Gua Musang black shales are depleted in Na_2O and P_2O_5 compared to PAAS (Fig. 4.16). The contents in MnO and CaO are generally below detection limit (0.01 wt %).

The organic carbon content in the Gua Musang black shales varies from 0.05 to 0.6 wt % (mean 0.23 wt %) and in the sandstones ranges from 0.2 to 0.96 wt % (mean 0.6 wt %). Previous research has argued that the values of K_2O/Al_2O_3 for clays are less than 0.3 (Cox et al., 1995). Gua Musang black shales cluster beneath the K_2O/Al_2O_3= 0.3 line implying that the composition of major elements may be controlled by the amount of clay minerals in these formations and the intensity of chemical weathering. The composition of these major elements in the Gua Musang black shales may have been controlled by anorthoclase minerals from the source rocks (Fig. 4.17).

Table 4.8. Comparative mean composition of black shales and sandstones from the Gua Musang Formation (Middle Triassic) with average compositions of PAAS, WAS, NASC, and UCC.

	Black shale (n= 14)	Sandstone (n= 2)	PAAS	WAS	NASC	UCC
(wt %)						
SiO_2	65.65	71.36	62.8	58.9	64.8	61.6
TiO_2	0.72	0.65	1.00	0.8	0.78	0.67
Al_2O_3	19.59	16.87	18.9	16.7	16.9	15.2
Fe_2O_3	3.17	1.98	7.22	6.9	5.7	6.2
MnO	0.03	<0.01	0.11	-	0.06	0.09
MgO	0.93	0.33	2.2	2.6	2.9	3.7
CaO	0.01	0.03	1.3	2.2	3.4	5.5
Na_2O	0.25	0.49	1.2	1.6	1	3.2
K_2O	3.27	2.28	3.7	3.6	3.8	3.4
P_2O_5	0.03	0.05	0.16	-	0.13	0.17
Loss	6.43	5.68	-	-	-	-
Total	99.88	99.71	-	-	-	-
TOC	0.23	0.59	-	-	-	-
S	0.13	0.10	-	-	-	697
(ppm)						
Sc	19.08	19.06	16	-	14.9	16
Ba	527.74	367.65	650	580	636	584
V	125.91	176.70	150	130	-	98
Ni	17.30	5.20	55	68	58	56
Cu	24.87	28.56	50	45	-	25
Zn	54.25	7.38	85	95	-	65
Cr	48.19	58.38	110	90	125	126
Ga	21.79	18.13	20	-	-	15
As	19.96	89.30	-	10	28.4	1.7
Co	14.72	7.36	23	19	-	10
Au (ppb)	28.00	17.00	-	2.3	-	-
Se	0.59	0.85	-	0.5	-	0.12
Rb	144.41	130.73	160	140	125	78
Sr	71.51	129.33	200	300	142	333
Y	29.62	18.89	27	-	-	24
Zr	224.96	184.85	210	160	200	203
Nb	13.05	7.88	19	-	-	19
Mo	1.32	7.98	1	1	-	1.1
Ag	<0.3	<0.2	-	0.07	-	0.07
Cd	7.40	<0.3	-	-	-	-
Sn	3.84	2.55	4	6	-	2.3
Sb	5.29	6.20	-	1.5	2.09	0.3
Te	0.10	0.10	-	-	-	0.005
Tl	1.60	1.92	-	0.68	-	0.52
Pb	32.46	77.34	20	22	-	0.0004
Bi	0.53	0.60	-	0.1	-	0.085
Th	13.40	7.89	14.6	-	12.3	8.5
U	3.98	4.70	3.1	3.7	2.66	1.7

Standards: Post-Archean Australian Shale (PAAS) from Taylor and McLennan (1985), the Wedephol's Average Shale (WAS) from Wedephol (1985), the North American Shale Composite (NASC) from Gromet et al. (1984), and the Upper Continental Crust (UCC) from Taylor and McLennan (1985). –: Not analysed or no data available.

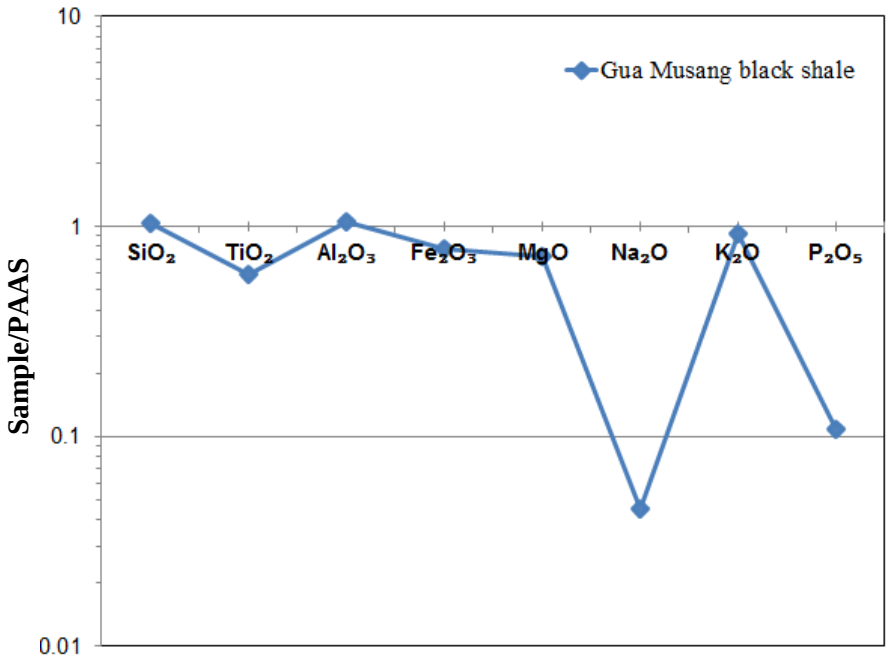

Fig. 4.16. Spider plot of mean concentrations of major elements for the Gua Musang Formation black shales normalized to PAAS.

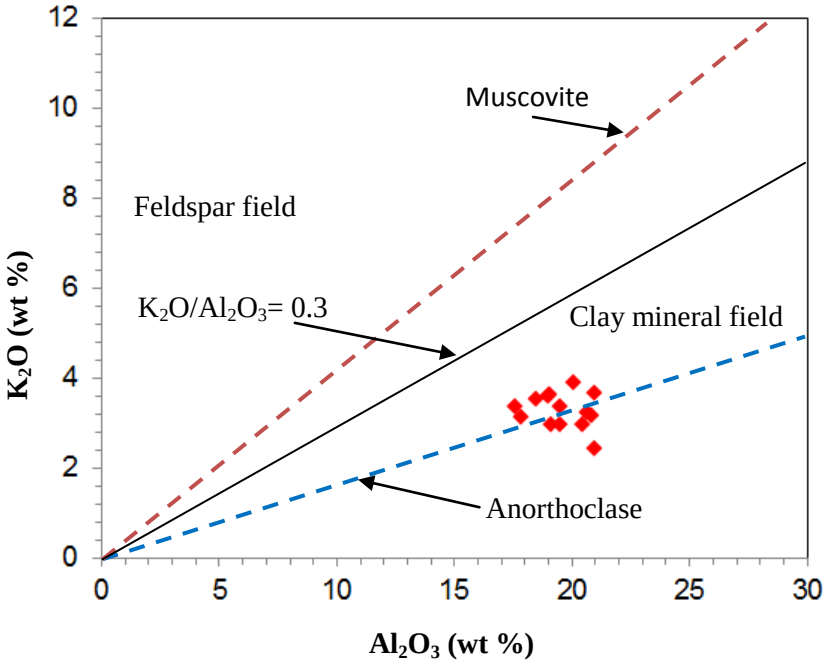

Fig. 4.17. Binary plot of Al_2O_3 against K_2O for the Gua Musang black shales. Blue dashed line represents the anorthoclase composition (data from Deer et al., 1966). The brown dashed line represents muscovite composition.

4.4.2. Trace elements

Enrichment and depletion of some trace elements in the Gua Musang black shales, normalised to PAAS (Post-Archean Australian Shale, Taylor and McLennan, 1985), are presented in Fig. 4.18. The Gua Musang Formation shales are weakly enriched in U, Pb, and Mo and depleted in Ni, Cu, Zn, and Cr relative to PAAS. It turns out that alumina content varies positively with gold content in black shales from the Gua Musang Formation; however, the data is not definitive. Binary plots of alumina and organic carbon to some trace elements are presented in Figs. 19-20.

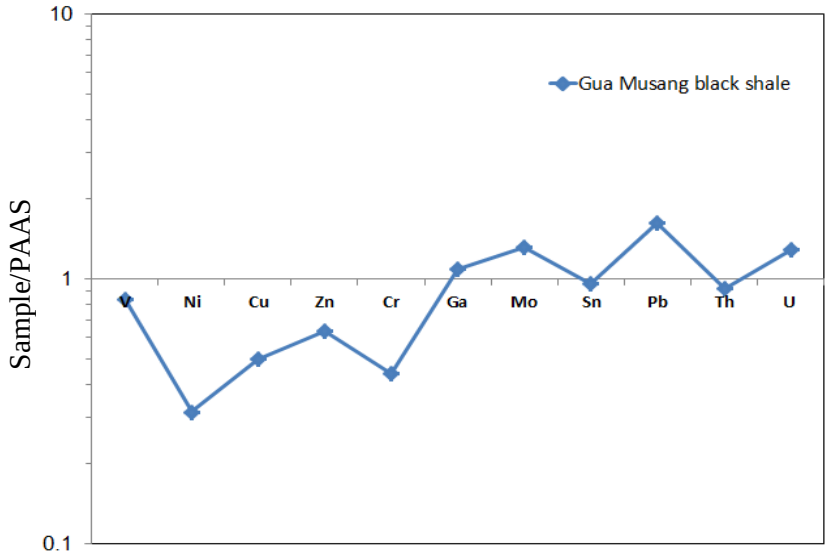

Fig. 4.18. Spider plot showing mean composition of selected trace elements in the Gua Musang Formation normalised to PAAS.

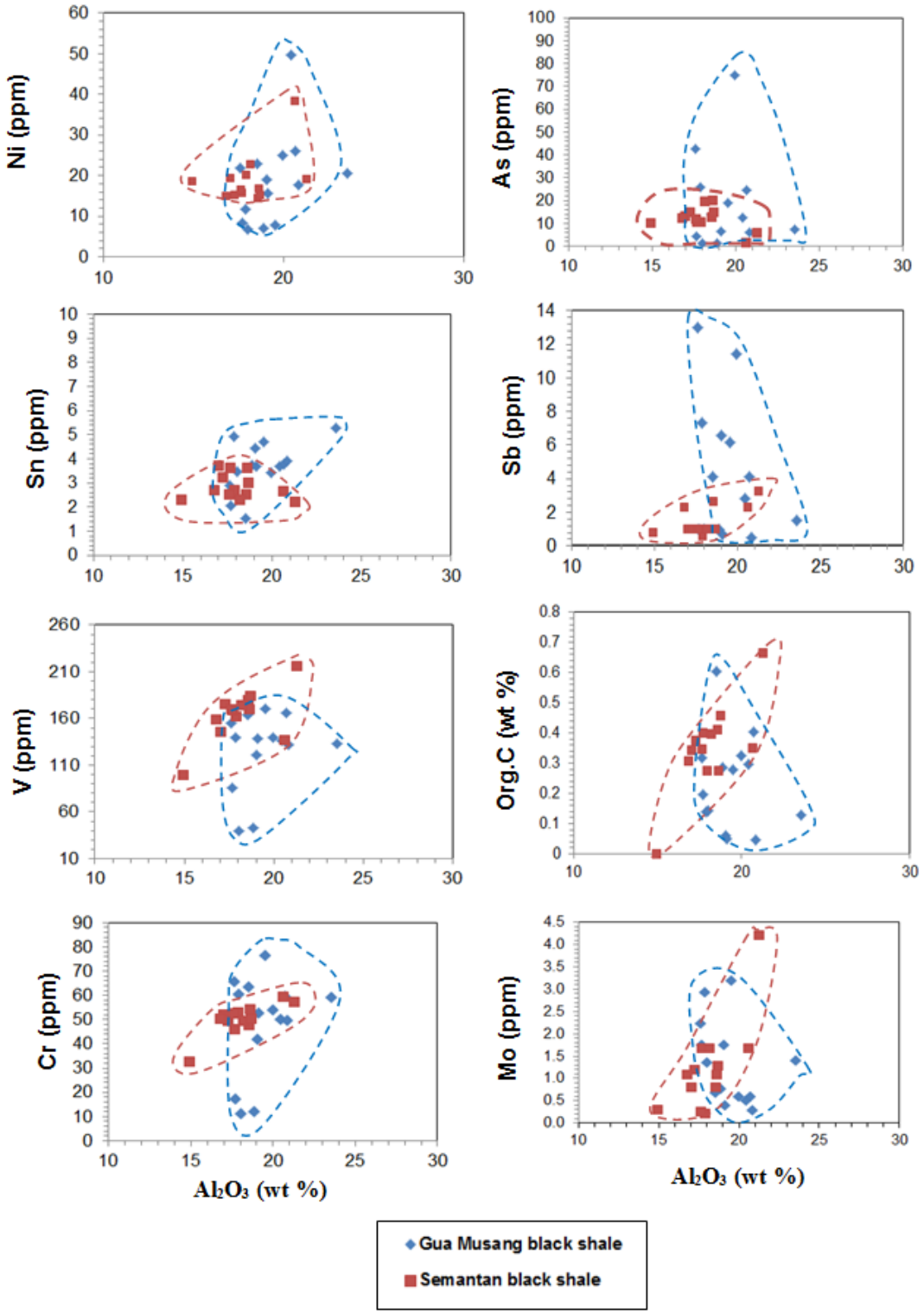

Fig. 4.19. Plots showing Al_2O_3 relationships with selected trace elements and organic carbon in the Gua Musang and Semantan formations. Both formations being of the same age are plotted together to show chemical differences.

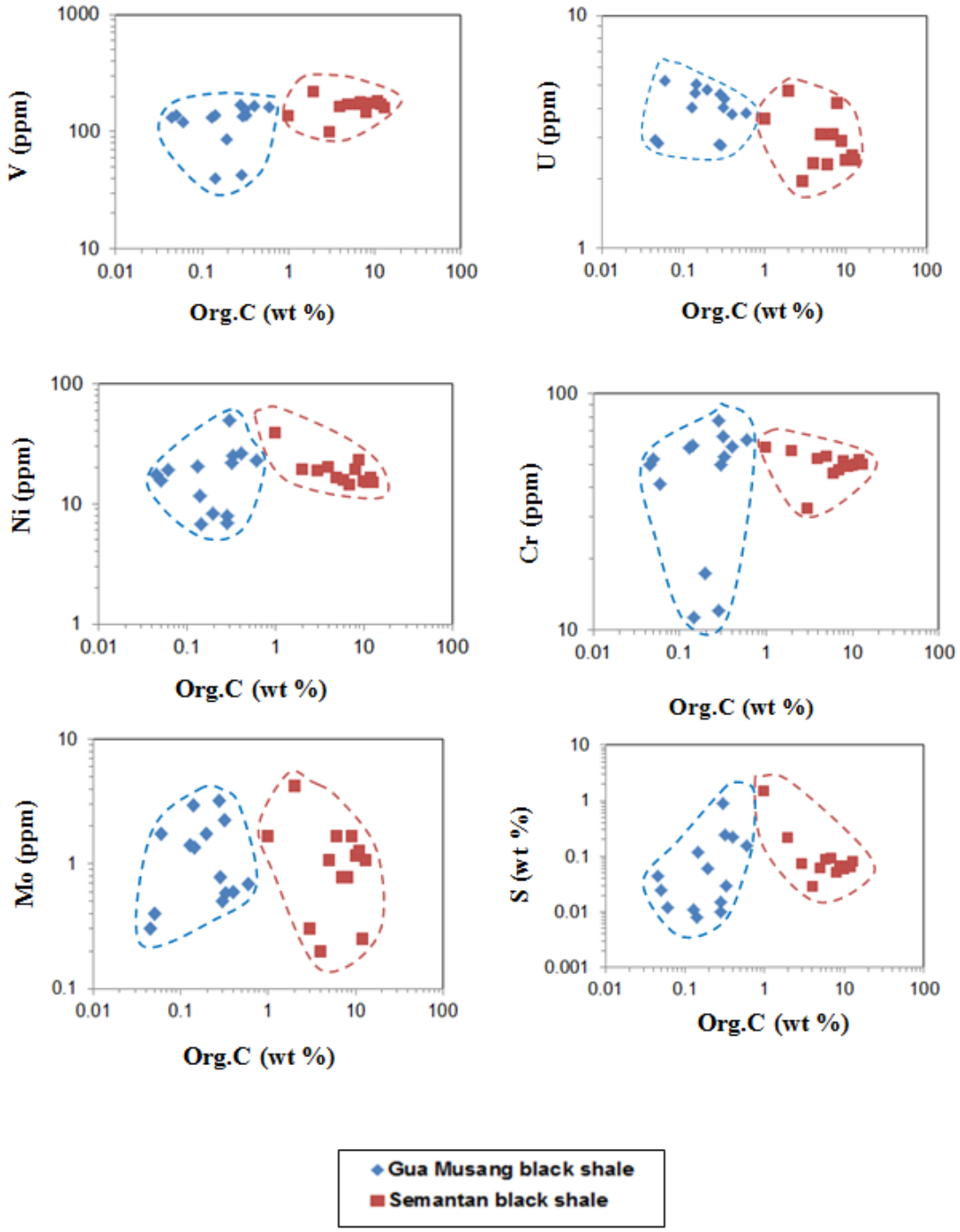

Fig. 4.20. Log-log relationships of alumina and organic carbon to selected trace elements in all shale samples from the Semantan and Gua Musang formations. Except for S, V, Ni none of the trace elements have a positive correlation with organic carbon in the Gua Musang black shales (Table 4.9).

4.4.3. Discussion

Considering the coefficients of correlation (Table 4.9), in the Gua Musang Formation, Al_2O_3 content shows a very weak positive correlation with Au, Ni, Cr, and Sn; whereas other trace elements have no correlation with Al_2O_3. The evidence suggests that Au, Ni, Cr and Sn may have been introduced into sediments attached to clay minerals or contained in the aluminosilicate mineral structure. Overall, organic carbon content is low (up to 0.6 wt %) and has no relationships to the selected trace elements (V, U, Ni, Cr, and Mo). This implies little involvement of organic processes during incorporation of these elements into sediments in the Gua Musang Formation.

Table. 4.9. Coefficients of correlation of selected trace elements with alumina and organic carbon in black shales from the Middle Triassic Gua Musang Formation. Correlation coefficients (Highlighted numbers range from 0.5 to 0.9 implying good correlation between two variables.

Correlation	Al_2O_3_wt %	Org.C_wt %	S_wt %	Au_ppm	V_ppm	Cr_ppm	Ni_ppm	Cu_ppm	Zn_ppm	As_ppm	Mo_ppm	Sn_ppm	Sb_ppm	U_ppm
Al_2O_3_wt %	1	-0.13	0.093	0.37	0.27	0.31	0.39	0.31	0.0092	-0.075	-0.35	0.52	-0.26	-0.39
Org.C_wt %	-0.13	1	0.3	-0.25	0.33	0.27	0.32	0.19	0.048	-0.25	-0.12	-0.57	0.3	-0.098
S_wt %	0.093	0.3	1	-0.22	0.15	0.084	0.84	0.81	0.84	-0.15	-0.27	-0.18	-0.0033	-0.38
Au_ppm	0.37	-0.25	-0.22	1	-0.51	-0.52	-0.11	-0.11	0.095	-0.12	-0.55	0.15	-0.37	0.21
V_ppm	0.27	0.33	0.15	-0.51	1	0.96	0.45	0.28	-0.15	0.062	0.13	0.08	0.47	-0.58
Cr_ppm	0.31	0.27	0.084	-0.52	0.96	1	0.37	0.22	-0.25	0.0068	0.24	0.24	0.51	-0.58
Ni_ppm	0.39	0.32	0.84	-0.11	0.45	0.37	1	0.83	0.65	0.073	-0.44	-0.067	0.18	-0.41
Cu_ppm	0.31	0.19	0.81	-0.11	0.28	0.22	0.83	1	0.68	-0.21	-0.52	-0.24	-0.096	-0.6
Zn_ppm	0.0092	0.048	0.84	0.095	-0.15	-0.25	0.65	0.68	1	-0.21	-0.41	-0.22	-0.13	-0.29
As_ppm	-0.075	-0.25	-0.15	-0.12	0.062	0.0068	0.073	-0.21	-0.21	1	0.15	0.19	0.35	0.43
Mo_ppm	-0.35	-0.12	-0.27	-0.55	0.13	0.24	-0.44	-0.52	-0.41	0.15	1	0.33	0.42	0.24
Sn_ppm	0.52	-0.57	-0.18	0.15	0.08	0.24	-0.067	-0.24	-0.22	0.19	0.33	1	-0.011	-0.081
Sb_ppm	-0.26	0.3	-0.0033	-0.37	0.47	0.51	0.18	-0.096	-0.13	0.35	0.42	-0.011	1	0.16
U_ppm	-0.39	-0.098	-0.38	0.21	-0.58	-0.58	-0.41	-0.6	-0.29	0.43	0.24	-0.081	0.16	1

4.4.4. Pyrite texture and composition

Textural characteristics of pyrite in the Gua Musang Formation are shown in Fig. 4.21 and results are presented in Table 4.10. Two types of pyrite are recognized in this formation: (1) type 1, framboidal pyrites, which are rounded to sub-rounded with size ranging from 20 to 50µm; and (2) type 2, composed of euhedral to subhedral pyrites which contain many inclusions. The pyrite framboids were collected after crushing and milling up to 500 g of black shale rock samples. The framboidal pyrites were then separated, mounted, and polished prior to laser ablation.

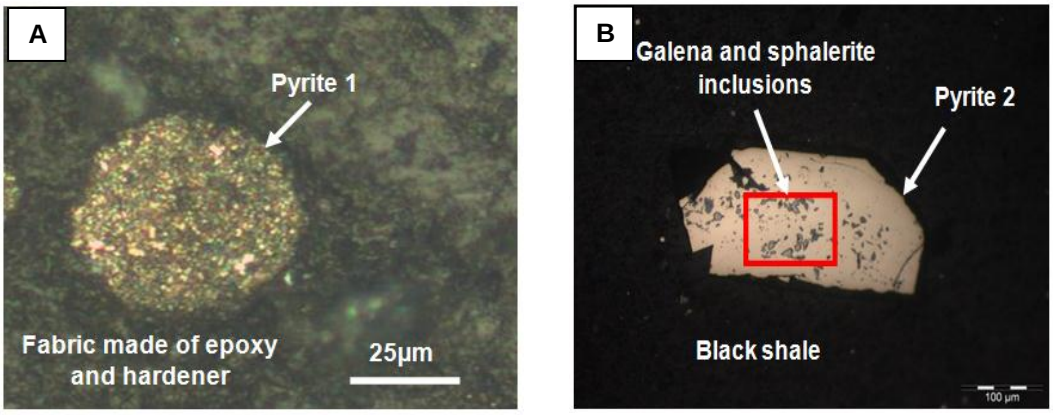

Fig. 4.21. Pyrite textural characteristics of the Ladinian Gua Musang Formation in the Central Gold Belt of Malaysia. **A**) Framboidal pyrite in black shale. **B**) Inclusion-rich subhedral pyrite in black shale.

Table 4.10. LA ICP-MS analyses of pyrite (in ppm) from the Gua Musang Formation.

Analysis no.	Pyrite type	Mn	V	Co	Ni	Cu	Zn	As
GM-1312-1	Pyrite 1	4350.40	1.31	21.98	603.29	427.45	51.01	275.28
GM-1312-2	Pyrite 1	1919.17	2.30	9.40	621.42	379.98	25.37	271.89
GM-1312-3	Pyrite 1	3758.50	1.21	10.91	477.19	776.19	80.77	416.96
GM-1312-4	Pyrite 1	1754.54	2.43	13.73	432.71	380.61	129.00	193.06
GM-1312-5	Pyrite 1	1734.66	1.68	4.38	581.19	396.54	787.62	275.09
GM-1312-6	Pyrite 1	6599.36	1.00	57.51	1321.14	3125.55	479.10	519.25
GM-1312-7	Pyrite 1	1227.36	0.93	9.20	562.26	376.59	24.53	224.97
GM-1312-8	Pyrite 1	1044.00	1.03	5.00	483.76	302.81	22.79	1003.09
GM-1312-9	Pyrite 1	3005.18	2.82	26.90	884.34	866.02	225.44	262.62
GM-1312-10	Pyrite 1	1262.26	1.54	14.31	719.20	417.61	27.51	244.39
GM-1312-11	Pyrite 1	2116.96	1.64	21.10	808.65	436.52	32.91	251.55
GM-1312-12	Pyrite 1	2526.01	2.43	9.22	653.71	384.82	374.08	368.38
GM-1312-13	Pyrite 1	1295.41	1.55	17.12	611.08	458.74	25.79	242.36
GM-1312-14	Pyrite 1	1897.36	1.28	9.02	503.34	335.50	24.86	275.17
GM-1312-15	Pyrite 1	3172.72	1.58	9.65	569.45	329.89	41.53	296.29
GM-1312-16	Pyrite 1	2253.15	1.91	22.15	866.55	481.77	32.98	937.27
GM-1312-17	Pyrite 1	1959.02	1.78	12.96	860.92	515.01	242.67	401.54
GM-1312-18	Pyrite 1	1960.80	1.23	6.45	648.86	405.26	30.23	224.58
GM-1312-19	Pyrite 1	1535.64	1.44	13.45	469.64	471.99	22.16	247.81
GM-1312-20	Pyrite 1	1611.95	0.88	6.12	323.96	290.11	19.91	181.74
GM-1312-21	Pyrite 1	5593.16	1.42	55.27	837.21	533.20	66.81	429.80
GM-1312-22	Pyrite 1	2992.88	1.84	5.18	586.73	1019.84	168.36	171.07
GM-1312-23	Pyrite 1	2139.04	1.65	9.94	654.22	366.20	25.58	782.00
GM-1312-24	Pyrite 1	1414.70	1.07	15.65	535.59	518.62	19.44	434.25
GM-1312-25	Pyrite 1	1189.79	1.16	7.21	399.41	442.00	16.98	214.16
GM-1312-26	Pyrite 1	1286.65	1.05	10.14	466.55	395.07	19.50	189.51
GM-1312-27	Pyrite 1	1405.77	1.58	12.12	402.54	370.40	19.03	176.59
GM-1312-28	Pyrite 1	1634.34	0.72	7.98	340.74	286.14	15.14	150.63
GM-1312-29	Pyrite 1	997.82	1.33	12.94	526.20	489.12	51.45	230.57
GM-1312-30	Pyrite 1	1100.05	1.45	13.35	522.72	416.76	18.37	254.73
GM-1312-31	Pyrite 1	1190.89	1.47	12.93	414.88	460.68	18.15	378.38
GM-1312-32	Pyrite 1	1118.26	1.06	8.73	519.17	333.43	17.37	257.42
GM-1312-33	Pyrite 1	4150.03	0.82	35.00	714.21	609.38	41.62	505.33
GM-1312-34	Pyrite 1	2275.52	1.06	7.20	291.37	354.36	47.05	158.67
GM-1312-35	Pyrite 1	3302.41	2.07	6.54	556.62	289.85	30.64	1191.96
GM-1312-36	Pyrite 1	610.08	1.96	4.49	424.06	370.15	12.99	290.85
GM-1312-37	Pyrite 1	546.94	1.03	10.47	434.45	320.69	12.95	593.74
GM-1312-38	Pyrite 1	1448.44	1.45	7.81	396.50	373.57	17.86	1109.26
GM-1312-39	Pyrite 1	1640.04	2.02	7.02	551.45	409.56	20.28	420.81
GM-1312-40	Pyrite 1	655.53	1.22	14.90	613.26	357.84	14.41	964.07
GM-1312-41	Pyrite 1	919.86	1.52	11.03	390.56	331.54	16.39	236.21
GM-1312-42	Pyrite 1	2118.05	1.76	7.70	465.48	364.55	24.62	253.81
GM-1312-43	Pyrite 1	2682.95	0.31	20.23	588.37	253.85	23.90	305.52
GM-1312-44	Pyrite 1	1055.89	0.54	6.36	303.93	305.46	17.52	1537.56
GM-1312-45	Pyrite 1	1268.56	0.98	4.89	352.88	341.10	19.13	194.90
PJ-1812A-1	Pyrite 2	4.44	0.23	2.67	32.19	11.32	3.01	285.29
PJ-1812A-2	Pyrite 2	2.22	0.18	16.97	114.55	12.35	2.15	336.37
PJ-1812A-3	Pyrite 2	0.01	0.03	12.20	231.48	1.98	0.15	474.26
PJ-1812A-4	Pyrite 2	19.95	2.73	4.33	694.95	1630.29	19078.97	786.09
PJ-1812A-5	Pyrite 2	4.94	3.26	69.38	1904.95	128.44	2677.14	2258.05
PJ-1812A-6	Pyrite 2	0.91	3.69	8.25	440.12	10.49	85.69	685.06
PJ-1812A-7	Pyrite 2	0.34	0.22	2.71	46.84	6.81	16.64	324.73
PJ-1812A-9	Pyrite 2	5.94	16.46	24.65	620.46	75.72	2969.66	735.31
PJ-1812A-10	Pyrite 2	64.97	12.05	11.35	813.19	66.85	56.52	828.29
PJ-1812C-1	Pyrite 2	1.79	0.42	1.44	731.28	12.28	1.18	1051.92
PJ-1812C-2	Pyrite 2	0.02	0.15	0.93	651.37	1.13	0.49	920.65
PJ-1812C-3	Pyrite 2	75.72	6.64	5.70	342.22	4.02	4.06	623.49
PJ-1812B-1	Pyrite 2	2.80	5.75	8.79	155.49	214.66	3.55	295.23
PJ-1812B-2	Pyrite 2	5.27	0.53	4.98	85.12	19.70	4.48	312.92
PJ-1812B-3	Pyrite 2	2.65	0.38	2.95	112.97	12.64	2.74	320.03
Mean (this study)		1531.90	1.95	13.22	537.82	401.35	472.70	479.71
Mean (WDP)		545.00	-	303.00	829.00	436.00	131.00	1368.00

Table 4.10. (continued)

Analysis no.	Pyrite type	Se	Mo	Ag	Cd	Sn	Sb	Te	Au	Tl	Pb	Bi
GM-1312-1	Pyrite 1	99.59	14.41	11.91	2.46	2.18	27.33	27.54	1.70	4.22	83.68	1.04
GM-1312-2	Pyrite 1	74.28	19.01	35.99	2.80	1.56	49.67	10.12	1.23	6.75	89.38	1.03
GM-1312-3	Pyrite 1	69.72	15.92	14.86	2.90	2.25	32.42	20.20	0.70	6.09	91.53	1.13
GM-1312-4	Pyrite 1	60.17	13.06	8.76	3.14	1.89	31.92	9.44	0.72	5.77	71.16	0.84
GM-1312-5	Pyrite 1	64.66	11.12	13.39	10.11	1.97	28.96	12.59	1.44	4.88	82.16	0.30
GM-1312-6	Pyrite 1	69.45	14.95	24.40	5.52	2.27	43.18	29.79	0.75	7.29	193.51	1.89
GM-1312-7	Pyrite 1	53.85	13.01	12.38	3.48	1.98	33.27	15.13	0.84	4.78	93.51	1.64
GM-1312-8	Pyrite 1	57.17	16.22	8.19	2.28	1.67	41.10	9.93	0.73	4.08	60.16	0.68
GM-1312-9	Pyrite 1	107.11	18.93	17.80	5.24	3.24	52.46	23.39	1.83	8.48	154.50	1.41
GM-1312-10	Pyrite 1	51.64	18.79	14.27	3.96	2.64	46.92	13.71	0.96	5.32	95.05	1.69
GM-1312-11	Pyrite 1	54.06	26.43	15.75	4.50	2.74	45.80	23.36	1.13	7.21	125.01	1.00
GM-1312-12	Pyrite 1	88.67	23.51	42.05	7.30	1.89	62.31	17.99	1.35	8.13	119.00	0.35
GM-1312-13	Pyrite 1	50.58	18.88	11.46	2.43	2.22	41.65	13.92	0.77	6.07	98.78	0.91
GM-1312-14	Pyrite 1	58.35	22.13	9.58	2.76	1.98	40.72	21.57	0.67	4.59	64.09	0.85
GM-1312-15	Pyrite 1	55.30	20.60	11.88	2.98	1.89	32.23	33.42	0.72	3.94	59.94	1.35
GM-1312-16	Pyrite 1	69.51	15.27	11.17	3.16	2.20	36.57	19.10	0.99	5.12	83.43	0.85
GM-1312-17	Pyrite 1	81.64	17.65	17.73	4.16	2.08	41.92	13.90	1.68	6.11	131.92	0.69
GM-1312-18	Pyrite 1	56.40	10.82	17.60	3.44	2.34	27.42	15.23	1.01	4.40	93.48	0.12
GM-1312-19	Pyrite 1	50.36	17.02	9.98	2.88	1.94	31.08	8.15	0.62	5.79	78.16	0.26
GM-1312-20	Pyrite 1	43.26	12.06	6.22	2.32	1.16	26.70	7.40	0.50	3.45	43.48	0.71
GM-1312-21	Pyrite 1	103.23	10.21	29.76	1.62	1.67	26.63	44.12	1.18	3.43	105.46	1.95
GM-1312-22	Pyrite 1	131.41	12.58	9.48	3.64	1.67	30.44	17.49	1.51	4.37	54.42	0.54
GM-1312-23	Pyrite 1	68.80	13.40	11.32	2.16	1.65	27.22	20.27	0.74	3.19	53.51	1.78
GM-1312-24	Pyrite 1	54.35	14.51	9.43	2.81	1.76	28.94	10.13	0.63	5.34	82.58	1.01
GM-1312-25	Pyrite 1	52.73	12.23	8.39	2.87	1.58	27.76	8.89	0.65	4.87	62.19	0.59
GM-1312-26	Pyrite 1	54.87	10.05	8.28	2.19	1.32	27.45	10.20	0.60	4.28	60.92	1.25
GM-1312-27	Pyrite 1	105.41	12.02	6.75	2.10	1.01	33.56	8.14	0.69	4.81	51.52	0.60
GM-1312-28	Pyrite 1	43.72	9.35	9.66	2.03	1.24	17.91	12.14	0.35	3.75	48.57	1.78
GM-1312-29	Pyrite 1	73.34	13.60	7.98	2.63	1.49	35.17	8.30	0.45	5.63	51.31	1.47
GM-1312-30	Pyrite 1	89.16	12.66	10.68	2.66	1.60	37.43	9.45	0.69	6.50	67.19	1.99
GM-1312-31	Pyrite 1	60.81	14.88	8.59	3.82	1.75	30.57	6.63	0.53	7.45	74.78	0.41
GM-1312-32	Pyrite 1	77.02	10.42	6.86	2.19	1.19	29.04	8.86	0.47	4.02	48.78	1.55
GM-1312-33	Pyrite 1	60.61	7.11	27.06	1.80	1.49	19.76	29.55	0.46	3.69	88.07	1.96
GM-1312-34	Pyrite 1	37.26	12.99	7.57	2.82	1.43	19.86	9.53	0.34	5.47	50.29	0.74
GM-1312-35	Pyrite 1	78.90	13.24	19.34	2.08	1.50	36.06	20.22	0.61	6.32	82.53	0.69
GM-1312-36	Pyrite 1	52.16	9.56	8.95	2.39	1.47	26.48	4.74	0.33	5.02	67.71	0.20
GM-1312-37	Pyrite 1	44.86	8.22	7.44	2.17	1.70	23.07	6.82	0.42	5.10	53.28	1.60
GM-1312-38	Pyrite 1	45.81	14.67	8.78	2.71	1.91	23.99	10.62	0.37	8.12	63.44	0.33
GM-1312-39	Pyrite 1	81.02	15.44	8.36	2.92	1.49	33.81	9.31	0.54	7.15	50.65	0.76
GM-1312-40	Pyrite 1	50.25	11.29	7.31	1.96	1.32	23.88	7.51	0.43	7.26	52.63	1.22
GM-1312-41	Pyrite 1	56.43	9.33	8.33	2.32	1.54	23.47	7.34	0.58	7.36	49.03	1.30
GM-1312-42	Pyrite 1	87.18	14.95	8.56	3.21	1.63	35.86	11.40	0.51	9.19	50.46	0.76
GM-1312-43	Pyrite 1	81.51	6.12	14.71	1.49	1.31	21.70	29.09	1.22	5.07	75.01	1.27
GM-1312-44	Pyrite 1	33.52	5.04	5.96	1.52	0.84	12.91	5.76	0.25	7.76	38.15	0.55
GM-1312-45	Pyrite 1	46.18	10.21	10.92	2.54	1.82	19.44	10.36	0.34	8.79	57.36	0.94
PJ-1812A-1	Pyrite 2	42.39	0.02	0.32	0.01	0.22	8.94	0.76	0.01	0.01	65.28	6.53
PJ-1812A-2	Pyrite 2	49.64	0.15	0.29	0.05	0.86	8.84	0.82	0.01	0.01	48.60	5.31
PJ-1812A-3	Pyrite 2	53.45	0.00	0.07	0.01	0.11	1.78	1.10	0.00	0.00	11.53	1.44
PJ-1812A-4	Pyrite 2	164.87	0.21	113.19	57.47	1.41	28.72	4.54	0.12	0.06	79469.21	199.97
PJ-1812A-5	Pyrite 2	54.69	0.88	2.33	9.87	0.96	15.45	1.59	0.02	0.00	1508.61	17.19
PJ-1812A-6	Pyrite 2	45.66	0.16	1.03	0.13	0.70	7.81	0.53	0.00	0.00	267.10	6.06
PJ-1812A-7	Pyrite 2	48.89	0.02	0.28	0.05	0.19	5.64	0.74	0.00	0.00	70.54	4.52
PJ-1812A-9	Pyrite 2	67.24	0.09	9.10	10.39	2.45	10.04	1.04	0.01	0.01	8416.59	27.82
PJ-1812A-10	Pyrite 2	98.54	0.25	11.85	0.47	2.04	10.22	1.12	0.02	0.01	11042.44	32.32
PJ-1812C-1	Pyrite 2	36.92	0.10	0.70	0.01	0.23	12.34	0.49	0.01	0.01	82.63	9.53
PJ-1812C-2	Pyrite 2	37.09	0.00	0.04	0.00	0.18	1.52	0.30	0.00	0.00	9.91	1.09
PJ-1812C-3	Pyrite 2	53.16	0.02	0.11	0.01	1.18	3.88	0.54	0.00	0.01	27.85	3.21
PJ-1812B-1	Pyrite 2	35.25	3.49	0.65	0.08	0.85	6.13	0.43	0.01	0.00	35.97	4.95
PJ-1812B-2	Pyrite 2	38.82	0.06	0.39	0.03	0.25	11.83	0.80	0.01	0.00	87.94	9.71
PJ-1812B-3	Pyrite 2	36.15	0.09	0.36	0.00	0.27	10.38	0.78	0.01	0.00	73.37	8.46
Mean (this study)		64.15	10.49	12.11	3.62	1.52	26.49	11.47	0.59	4.28	1744.49	6.40
Mean (WDP)		71.00	88.00	9.20	3.00	-	90.00	4.90	0.10	36.00	387.00	13.00

In pyrite 1, gold correlates well with Se, Ni, Pb, and Sb. However, in pyrite 2, Au strongly correlates with Se, Cu, Zn, Ag, Sb, Te, Ag, Tl, Pb, and Bi. Overall, pyrite 2 shows more trace elements correlating with Au than pyrite 1 (Tables 4.11 and 4.12).

Table 4.11. Coefficients of correlation in framboidal pyrite (pyrite 1) from the Middle Triassic Gua Musang Formation. Highlighted numbers represents coefficients of correlation between two variables.

Correlation	Mo_ppm	Se_ppm	V_ppm	Cr_ppm	Mn_ppm	Co_ppm	Ni_ppm	Cu_ppm	Zn_ppm
Mo_ppm	1	0.13	0.54	-0.067	0.11	0.017	0.35	0.094	0.13
Se_ppm	0.13	1	0.46	0.082	0.44	0.27	0.38	0.21	0.23
V_ppm	0.54	0.46	1	0.26	0.048	-0.051	0.26	-0.0085	0.26
Cr_ppm	-0.067	0.082	0.26	1	-0.2	-0.061	-0.12	-0.2	0.11
Mn_ppm	0.11	0.44	0.048	-0.2	1	0.76	0.65	0.64	0.34
Co_ppm	0.017	0.27	-0.051	-0.061	0.76	1	0.75	0.64	0.21
Ni_ppm	0.35	0.38	0.26	-0.12	0.65	0.75	1	0.68	0.44
Cu_ppm	0.094	0.21	-0.0085	-0.2	0.64	0.64	0.68	1	0.47
Zn_ppm	0.13	0.23	0.26	0.11	0.34	0.21	0.44	0.47	1
As_ppm	-0.17	-0.19	-0.095	-0.11	0.0067	0.013	0.047	-0.013	-0.087
Ag_ppm	0.31	0.32	0.33	-0.033	0.56	0.45	0.56	0.27	0.37
Sb_ppm	0.82	0.38	0.65	0.042	0.15	0.14	0.53	0.24	0.31
Te_ppm	0.19	0.4	0.0092	-0.14	0.85	0.7	0.63	0.33	0.19
Au_ppm	0.38	0.64	0.45	0.11	0.4	0.25	0.56	0.15	0.48
Tl_ppm	0.25	0.0023	0.33	-0.11	-0.1	-0.035	0.049	0.16	0.12
Pb_ppm	0.45	0.25	0.3	-0.11	0.6	0.66	0.85	0.66	0.51
Bi_ppm	-0.15	0.086	-0.26	-0.27	0.31	0.53	0.35	0.25	-0.12

Correlation	As_ppm	Ag_ppm	Sb_ppm	Te_ppm	Au_ppm	Tl_ppm	Pb_ppm	Bi_ppm
Mo_ppm	-0.17	0.31	0.82	0.19	0.38	0.25	0.45	-0.15
Se_ppm	-0.19	0.32	0.38	0.4	0.64	0.0023	0.25	0.086
V_ppm	-0.095	0.33	0.65	0.0092	0.45	0.33	0.3	-0.26
Cr_ppm	-0.11	-0.033	0.042	-0.14	0.11	-0.11	-0.11	-0.27
Mn_ppm	0.0067	0.56	0.15	0.85	0.4	-0.1	0.6	0.31
Co_ppm	0.013	0.45	0.14	0.7	0.25	-0.035	0.66	0.53
Ni_ppm	0.047	0.56	0.53	0.63	0.56	0.049	0.85	0.35
Cu_ppm	-0.013	0.27	0.24	0.33	0.15	0.16	0.66	0.25
Zn_ppm	-0.087	0.37	0.31	0.19	0.48	0.12	0.51	-0.12
As_ppm	1	-0.03	-0.16	-0.0098	-0.23	0.18	-0.083	-0.097
Ag_ppm	-0.03	1	0.53	0.53	0.48	0.12	0.64	0.14
Sb_ppm	-0.16	0.53	1	0.16	0.53	0.29	0.61	-0.034
Te_ppm	-0.0098	0.53	0.16	1	0.47	-0.25	0.52	0.42
Au_ppm	-0.23	0.48	0.53	0.47	1	-0.039	0.58	-0.042
Tl_ppm	0.18	0.12	0.29	-0.25	-0.039	1	0.23	-0.24
Pb_ppm	-0.083	0.64	0.61	0.52	0.58	0.23	1	0.16
Bi_ppm	-0.097	0.14	-0.034	0.42	-0.042	-0.24	0.16	1

Table 4.12. Coefficients of correlation in pyrite 2 from the Middle Triassic Gua Musang Formation. Highlighted numbers indicate good correlation between two variables.

Correlation	Mo_ppm	Se_ppm	V_ppm	Cr_ppm	Mn_ppm	Co_ppm	Ni_ppm	Cu_ppm
Mo_ppm	1	-0.13	0.15	-0.045	-0.11	0.17	0.039	0.082
Se_ppm	-0.13	1	0.3	0.32	0.37	0.025	0.28	0.88
V_ppm	0.15	0.3	1	0.83	0.49	0.24	0.27	0.017
Cr_ppm	-0.045	0.32	0.83	1	0.55	0.12	0.06	0.12
Mn_ppm	-0.11	0.37	0.49	0.55	1	-0.07	0.12	0.078
Co_ppm	0.17	0.025	0.24	0.12	-0.07	1	0.78	-0.051
Ni_ppm	0.039	0.28	0.27	0.06	0.12	0.78	1	0.18
Cu_ppm	0.082	0.88	0.017	0.12	0.078	-0.051	0.18	1
Zn_ppm	-0.041	0.89	0.068	0.18	0.059	0.041	0.26	0.98
As_ppm	0.0023	0.15	0.14	-0.023	0.054	0.79	0.98	0.096
Ag_ppm	-0.054	0.92	0.062	0.16	0.14	-0.09	0.17	0.99
Sb_ppm	-0.033	0.75	0.051	0.11	0.012	0.2	0.38	0.82
Te_ppm	-0.086	0.92	0.042	0.14	0.096	0.14	0.3	0.95
Au_ppm	-0.048	0.9	0.01	0.11	0.11	-0.041	0.23	0.98
Tl_ppm	-0.05	0.91	0.09	0.22	0.17	-0.11	0.11	0.96
Pb_ppm	-0.061	0.94	0.099	0.19	0.16	-0.084	0.18	0.98
Bi_ppm	-0.057	0.93	0.1	0.19	0.14	-0.046	0.22	0.98

Correlation	Zn_ppm	As_ppm	Ag_ppm	Sb_ppm	Te_ppm	Au_ppm	Tl_ppm	Pb_ppm	Bi_ppm
Mo_ppm	-0.041	0.0023	-0.054	-0.033	-0.086	-0.048	-0.05	-0.061	-0.057
Se_ppm	0.89	0.15	0.92	0.75	0.92	0.9	0.91	0.94	0.93
V_ppm	0.068	0.14	0.062	0.051	0.042	0.01	0.09	0.099	0.1
Cr_ppm	0.18	-0.023	0.16	0.11	0.14	0.11	0.22	0.19	0.19
Mn_ppm	0.059	0.054	0.14	0.012	0.096	0.11	0.17	0.16	0.14
Co_ppm	0.041	0.79	-0.09	0.2	0.14	-0.041	-0.11	-0.084	-0.046
Ni_ppm	0.26	0.98	0.17	0.38	0.3	0.23	0.11	0.18	0.22
Cu_ppm	0.98	0.096	0.99	0.82	0.95	0.98	0.96	0.98	0.98
Zn_ppm	1	0.18	0.98	0.84	0.97	0.97	0.95	0.98	0.98
As_ppm	0.18	1	0.083	0.31	0.22	0.15	0.019	0.087	0.12
Ag_ppm	0.98	0.083	1	0.82	0.96	0.99	0.97	1	1
Sb_ppm	0.84	0.31	0.82	1	0.86	0.89	0.85	0.82	0.86
Te_ppm	0.97	0.22	0.96	0.86	1	0.96	0.93	0.96	0.97
Au_ppm	0.97	0.15	0.99	0.89	0.96	1	0.97	0.98	0.99
Tl_ppm	0.95	0.019	0.97	0.85	0.93	0.97	1	0.97	0.97
Pb_ppm	0.98	0.087	1	0.82	0.96	0.98	0.97	1	1
Bi_ppm	0.98	0.12	1	0.86	0.97	0.99	0.97	1	1

Plots of selected trace elements are presented in Figs. 4.22-4.23. The Cu, Mo, and Ni contents show clear depletion in pyrite 2 compared to pyrite 1, whereas the Se content is the same in both pyrites. This is good evidence for loss of trace elements by recrystallisation from the conversion of pyrite 1 to pyrite 2 (Large et al., 2007). The Au, Ag, Te, and Sb contents show the same depletion effect (Fig. 4.23). The weak depletion effect for As, Ni, V, and Se may be

explained by the fact that these elements are tightly held in the pyrite structure compared to others. The loss of such trace elements (e.g. As, Ni, V, and Se) to the metamorphic fluids is less effective during formation of pyrite 2. The trace element pattern and textures indicate that pyrite 2 is metamorphic after pyrite 1. Most gold in pyrite 2 is low as shown in Fig. 4.23. Gold values are commonly below 0.1 ppm.

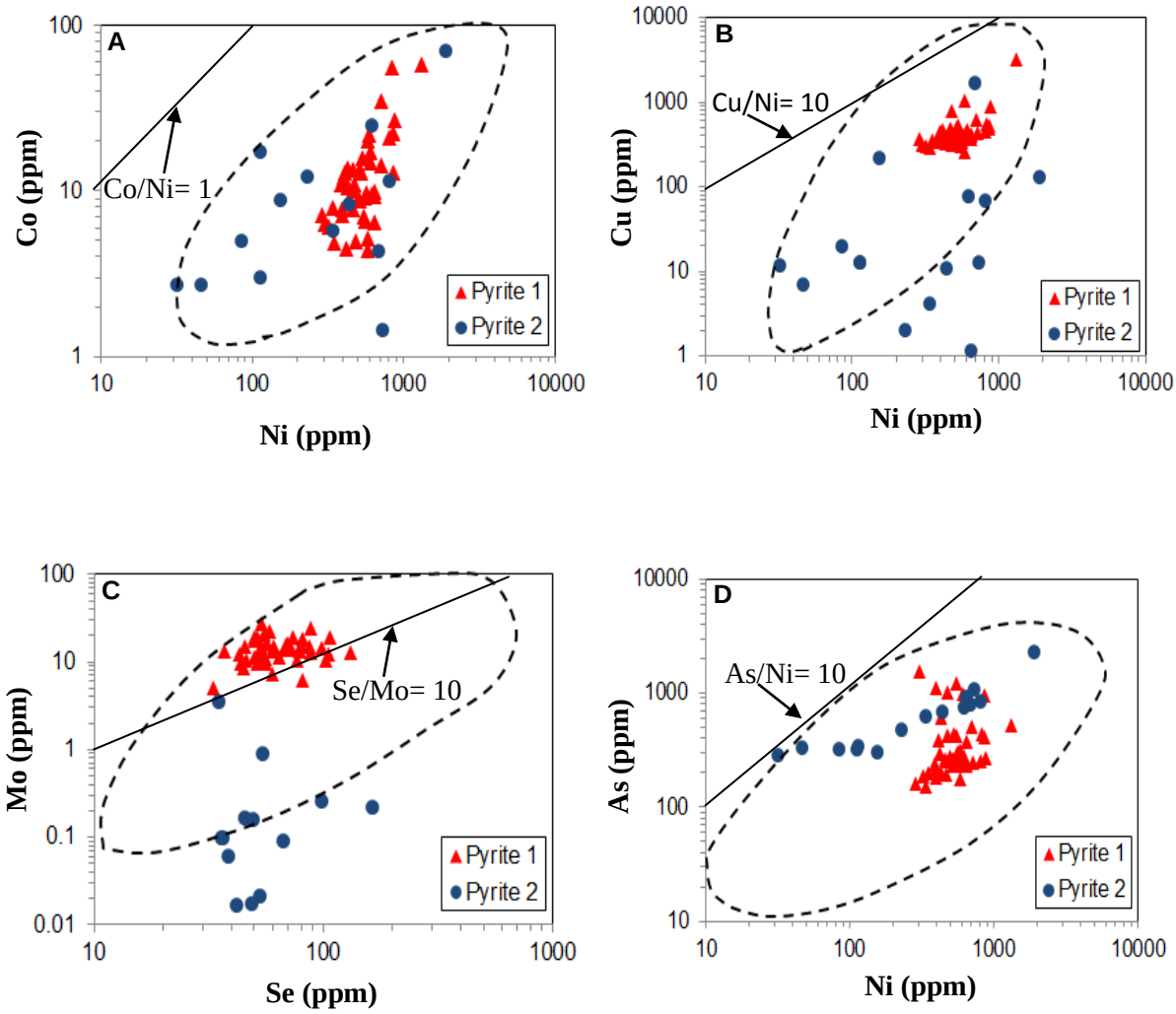

Fig. 4.22. Binary log-log plot of the Gua Musang pyrites, Malaysia. **A**) Co-Ni plot. **B**) Cu-Ni plot. **C**) Mo-Se plot. **D**) As-Ni plot. Dashed polygon is the outline for sedimentary pyrite (Gregory et al., 2015).

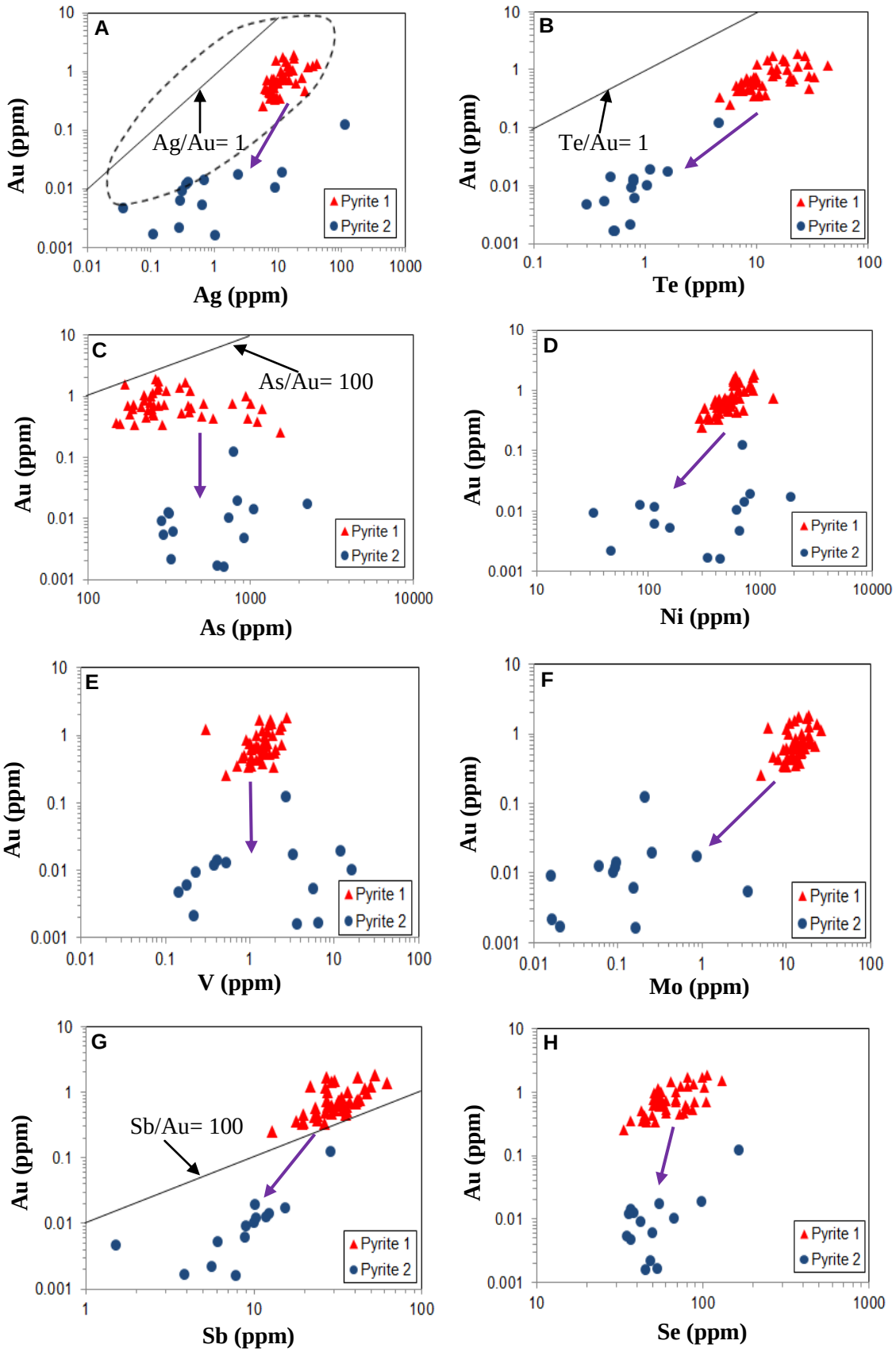

Fig. 4.23. Geochemical bivariate plots for the Gua Musang Formation pyrites. **A**) Au-Ag. **B**) Au-Te. **C**) Au-As. **D**) Au-Ni. **E**) Au-V. **F**) Au-Mo. **G**) Au-Sb. **H**) Au-Se. The dashed polygon in plot A represents the sedimentary pyrite field (Gregory et al., 2015). The purple arrow indicates the depletion effect in trace elements.

The above plots (Figs. 4.22-4.23) show that all data for pyrite 1 are confined to the field of sedimentary pyrite indicating a sedimentary origin for the pyrite framboids. All plots show loss in trace elements from pyrite 1 to pyrite 2 (Fig. 4.23). The sedimentary pyrites (pyrite 1) are also characterised by the following ratios: Ag/Au>1, Te/Au> 1, As/Au>100 and Sb/Au>100 which confirm a sedimentary origin. Pyrite 2 has the following trace element ranges: 0<Mo<3.5 ppm; 32<Ni<1905 ppm; 0.03<V<16 ppm; 0.04<Ag<113 ppm; 285<As<2258 ppm; and 0<Au<0.12 ppm. Compared to worldwide diagenetic pyrite (Fig. 4.24), the Gua Musang sedimentary pyrite (pyrite 1) is enriched in Au and Te and depleted in Co, As, Mo, Sb, Tl, Pb and Bi. There is clearly loss in Au, Te, Mo, Sb, and Se contents from pyrite 1 to pyrite 2 indicating that during recrystallization from pyrite 1 to metamorphic pyrite (pyrite 2) certain trace elements are lost.

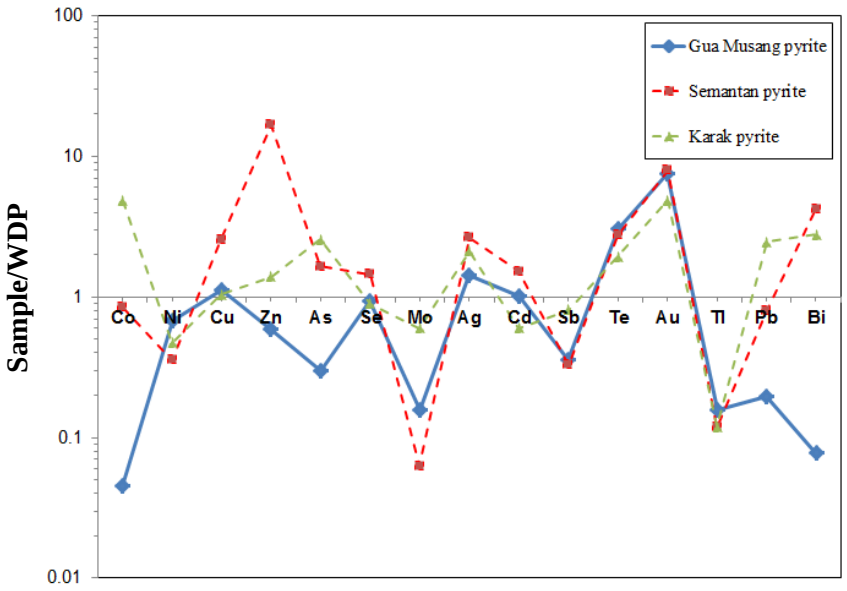

Fig. 4.24. Comparative spider plot of mean values of selected trace elements in sedimentary pyrites from the Gua Musang Formation normalised to WDP (worldwide diagenetic pyrite, Gregory et al., 2015). Plots of the Middle Triassic Karak and Semantan Formation pyrites are shown on Fig. 4.24 for comparison.

The high levels of Ag, and Te in pyrite 1 and positive correlation between Au-Te and Au-Ag suggest the Au may be present in pyrite 1 as Au-Ag-telluride inclusions. A similar feature has been recorded for sedimentary pyrites at the Kumtor deposit, one of the highest gold deposit in the world situated in Central Asia (Large et al., 2010; Porter and Ripley, 1985) and is a common feature of many hydrothermal pyrites in gold ores. The low levels of organic carbon and V in the Gua Musang black shales coupled with the moderate Au-Al_2O_3 correlation in the whole rocks suggests Au may have been introduced into the basin attached to clay minerals.

4.4.5. Discussion for the Gua Musang Formation

The Gua Musang black shales are depleted in Na_2O and P_2O_5 compared to PAAS. The black shales are weakly enriched in U, Pb, and Mo and depleted in V, Ni, Cu, Zn, and Cr relative to PAAS. In diagenetic pyrite 1, Au content varies positively with Ag, Te, Ni, V, Sb, Se, Zn and Pb; however, Au has no correlation with As. The diagenetic pyrites are characterised by Au-Ag-Te microinclusions. The gold content in framboidal pyrite (pyrite 1) varies from 0.2 to 1.8 ppm (mean 0.8 ppm) whereas in metamorphic pyrite (pyrite 2), Au content is low ranging up to 0.1 ppm. Compared to worldwide diagenetic pyrite (Gregory et al., 2015), the Gua Musang framboidal pyrite is enriched in Au, Te, and midly in Ag, and depleted in Co, As, Mo, Sb, Tl, Pb, and Bi. Geochemical bivariate plots indicate loss of some trace elements from pyrite 1 to pyrite 2 strongly implying effects of metamorphism or loss of trace elements to metamorphic fluids. Composition of pyrite 1 in Au, Ag, Te, As, Ni, V, Mo, Sb and Se shows two order of magnitude higher than that of pyrite 2 (Fig. 4.23).

4.5. BRSZ Unit 2 (Late Triassic)

Results of major and trace element contents in cherts from the BRSZ Unit 2 with average contents of Post-Archean Australian Shale (PAAS) from Taylor and McLennan (1985), the Wedephol's Average Shale (WAS) from Wedephol (1985), the North American Shale Composite (NASC) from Gromet et al. (1984), and the Upper Continental Crust (UCC) from Taylor and McLennan (1985) are presented in Table 4.13. Knowing the geochemistry of these Late Triassic cherts is important as they are reported to be widely distributed in orogenic belts in the world and potentially hosting ore minerals and being source rocks for several deposits (Chunlong, 2001; Feng and Liu, 2001).

4.5.1. Major and trace elements

The comparative plots of major and trace elements for the cherts with those of formation shales (this study) normalised to PAAS are shown in Figs. 4.25-4.26 The BRSZ Unit 2 cherts are enriched in SiO_2 (mean 87 wt %) and S (mean 1.38 wt %), and depleted in other major elements relative to PAAS (Fig. 4.25 Fig. 4.25). Compared to the Gua Musang and Semantan formations, the BRSZ Unit 2 Mo content is enriched by one order of magnitude as shown in Fig. 4.26 Fig. 4.26. Compared to PAAS, the BRSZ Unit 2 cherts are enriched in Cu, and Mo, and U and depleted in Cr, Zn, Ga, and Th (Fig. 4.26 Fig. 4.26).

Table 4.13. Major (wt %) and trace element (ppm) mean values for the BRSZ Unit 2 compared to PAAS, WAS, NASC, and UCC.

	Chert (n=13)	PAAS	WAS	NASC	UCC
SiO_2	87.06	62.80	58.90	64.80	61.60
TiO_2	0.18	1.00	0.80	0.78	0.67
Al_2O_3	3.66	18.90	16.70	16.90	15.20
Fe_2O_3	1.87	7.20	6.90	5.70	6.20
MnO	0.01	0.11	-	0.06	0.09
MgO	0.30	2.20	2.60	2.90	3.70
CaO	0.02	1.30	2.20	3.40	5.50
Na_2O	0.05	1.20	1.60	1.00	3.20
K_2O	0.98	3.70	3.60	3.80	3.40
P_2O_5	0.03	0.16	-	0.13	0.17
Loss	5.75	6.00	-	-	-
Total	99.89	104.59	-	-	-
S (wt %)	1.38	-	0.20	-	0.70
TOC (wt %)	1.88	-	-	-	-
Sc	6.99	16.00	-	14.90	16.00
Ba	195.87	650.00	580.00	636.00	584.00
V	135.78	150.00	130.00	-	98.00
Cr	37.12	110.00	90.00	125.00	126.00
Ni	42.43	55.00	68.00	58.00	56.00
Cu	138.40	50.00	45.00	-	25.00
Zn	20.56	85.00	95.00	-	65.00
Ga	7.90	20.00	-	-	15.00
As	21.73	-	10.00	28.40	1.70
Se	5.35	-	0.50	-	0.12
Rb	47.22	160.00	140.00	125.00	78.00
Sr	35.26	200.00	300.00	142.00	333.00
Y	21.56	27.00	-	-	24.00
Zr	43.49	210.00	160.00	200.00	203.00
Nb	5.15	19.00	-	-	19.00
Mo	22.42	1.00	1.00	-	1.10
Ag	-	-	0.07	-	0.07
Sn	2.54	4.00	6.00	-	2.30
Sb	24.99	-	1.50	2.09	0.30
Te	-	-	-	-	0.01
Tl	-	-	0.68	-	0.52
Pb	23.81	20.00	22.00	-	0.00
Bi	-	-	0.10	-	0.09
U	4.18	3.10	3.70	2.66	1.70
Th	5.11	14.60	-	12.30	8.50

- : data not analysed or unavailable

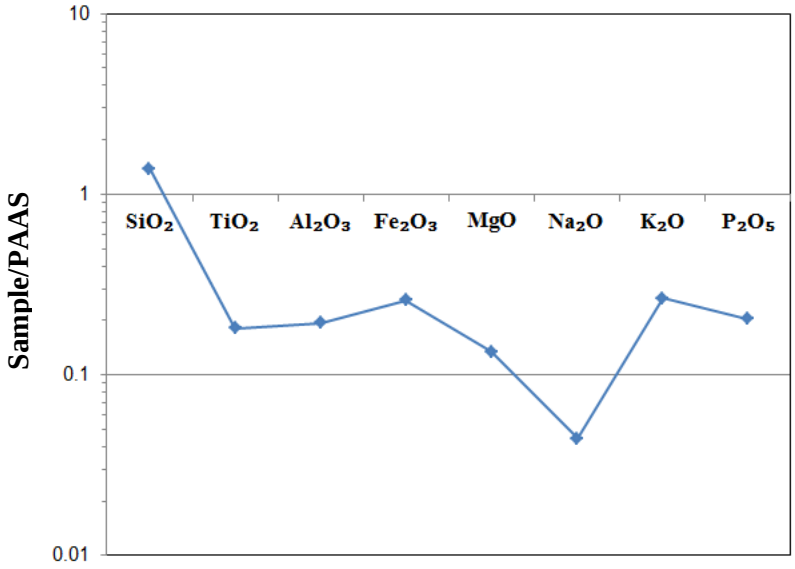

Fig. 4.25. Comparative spider plot of mean concentrations of major elements highlighting the BRSZ Unit 2 chert (plain blue line) normalised to PAAS. In this plot, the SiO_2 enrichment in chert was expected.

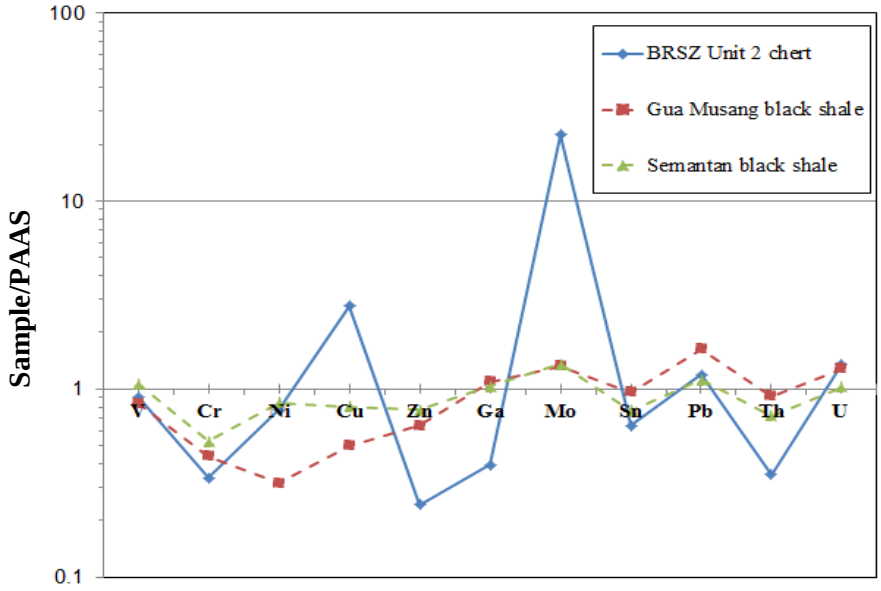

Fig. 4.26. Comparative spider plot of mean concentrations of trace elements for the BRSZ Unit 2 chert (plain blue line) with other formation shales (dashed lines) normalised to PAAS.

However, in the BRSZ Unit 2 black cherts, the organic carbon varies from 0.3 to 5.1 wt % (mean 1.88 wt%; Table 4.13). The ratio organic carbon versus sulphur for the cherts is below 10 and that of black shale in other formations is above 10. In addition, the grey shales show the lowest organic carbon and sulphur contents compared to the BRSZ Unit 2 cherts and other formation black shales (Tables 3.1 and 4.13).

Both the BRSZ Unit 1 and BRSZ Unit 2 have elevated Mo content. Previous research work has demonstrated the use of some major elements such as SiO_2, Fe_2O_3, MnO, and Al_2O_3 to discuss the sedimentary environment of the chert (Haisheng et al., 2003). Some researchers used discriminating diagrams to decipher environment of deposition of cherts (Murray, 1994; Sugitani et al., 1996; Junguo et al., 2011; Wen et al., 2014). Plots of depositional setting for the BRSZ Unit 2 are shown below (Fig. 27). The cherts are enriched in sulphur (mean 1.38 wt%, Table 4.13) compared to the black shales in the district (mean range: 0.13 to 0.23 wt%; Tables 4.4 and 4.8).

The evidence indicates that the BRSZ Unit 2 cherts likely deposited in a continental margin environment. The BRSZ Unit 2 cherts have SiO2 concentrations up to 98.4 wt % that indicates a quite high influx of silica into the ocean. Boström (1983) suggested that hydrothermally-derived cherts yield Fe/Ti ≥20. In the BRSZ Unit 2 cherts, the ratio Fe/Ti shows 38 % of the dataset above 20 (from 30 to 77), and 62 % of the dataset below 20 (from 4 to 14). The results suggest the possibility of hydrothermal discharges on a passive continental margin during formation of the BRSZ Unit 2 cherts but are not conclusive. Based on the ratio of Fe/Ti, the cherts have not formed by hydrothermal processes as siliceous precipitates on the sea floor. Therefore, an organic origin of the cherts is implied.

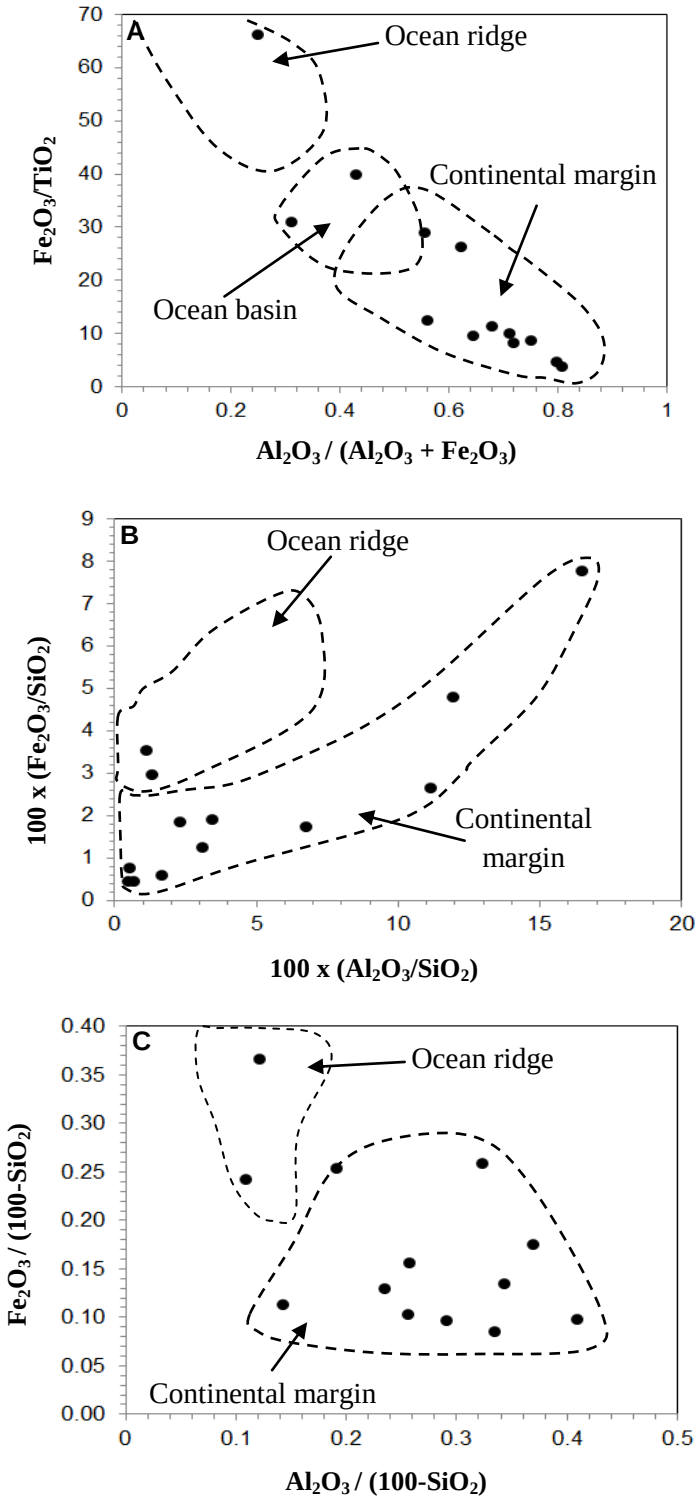

Fig. 4.27. Major element discriminating diagrams for the depositional environment of the BRSZ Unit 2 cherts, Malaysia. Fields of continental margin, ocean basin, and ocean ridge are from Murray (1994).

4.5.2. Pyrite textures

Four pyrite types were recognized in the BRSZ Unit 2 chert as shown below (Fig. 4.28). Pyrite 1 has framboidal textures that are rounded crystals or half-broken. The size of pyrite 1 varies from 5 to 50 µm (Fig. 4.28Aand B). Pyrite 1 also appears as large aggregates of micro-crystals that size varies from 2 to 10 µm (Fig. 4.28C). Pyrite 2 shows concentric growth zones that give an impression of a colloform texture (Fig. 4.28D). Pyrite 3 is massive, dirty with internal growth zones (Fig. 4.28E). Pyrite 3 also occurs overgrown by pyrite 1 (Fig. 4.28B). Pyrite 4 is vein-like pyrite that cross-cuts the chert laminations and has thickness up to 1 mm thickness (Fig. 4.28F).

4.5.3. Pyrite trace element composition

Composition of trace elements in pyrite from the BRSZ Unit 2 is documented in Table 4.14. By comparing the chemistry of the four pyrite generations, pyrite 1 is weakly enriched in V, Mn, Co, Cu, Zn, As, Se, Ag, Cd, Sb, Te, Au, and Bi, compared to the mean of all pyrites (Fig. 4.29). Both pyrite 1 and pyrite 4 are depleted in Mo compared to pyrites 2 and 3. Pyrite 4 is enriched in As and Se compared to other pyrite generations (pyrites 1, 2, 3). The high Ag/Au content coupled with elevated V, Mn, Zn, As, Te, and Bi is indicative of a diagenetic origin for pyrite 1. Pyrites 2 has an Ag/Au ratio similar to pyrite 1 suggesting a late diagenetic origin for pyrite 2.

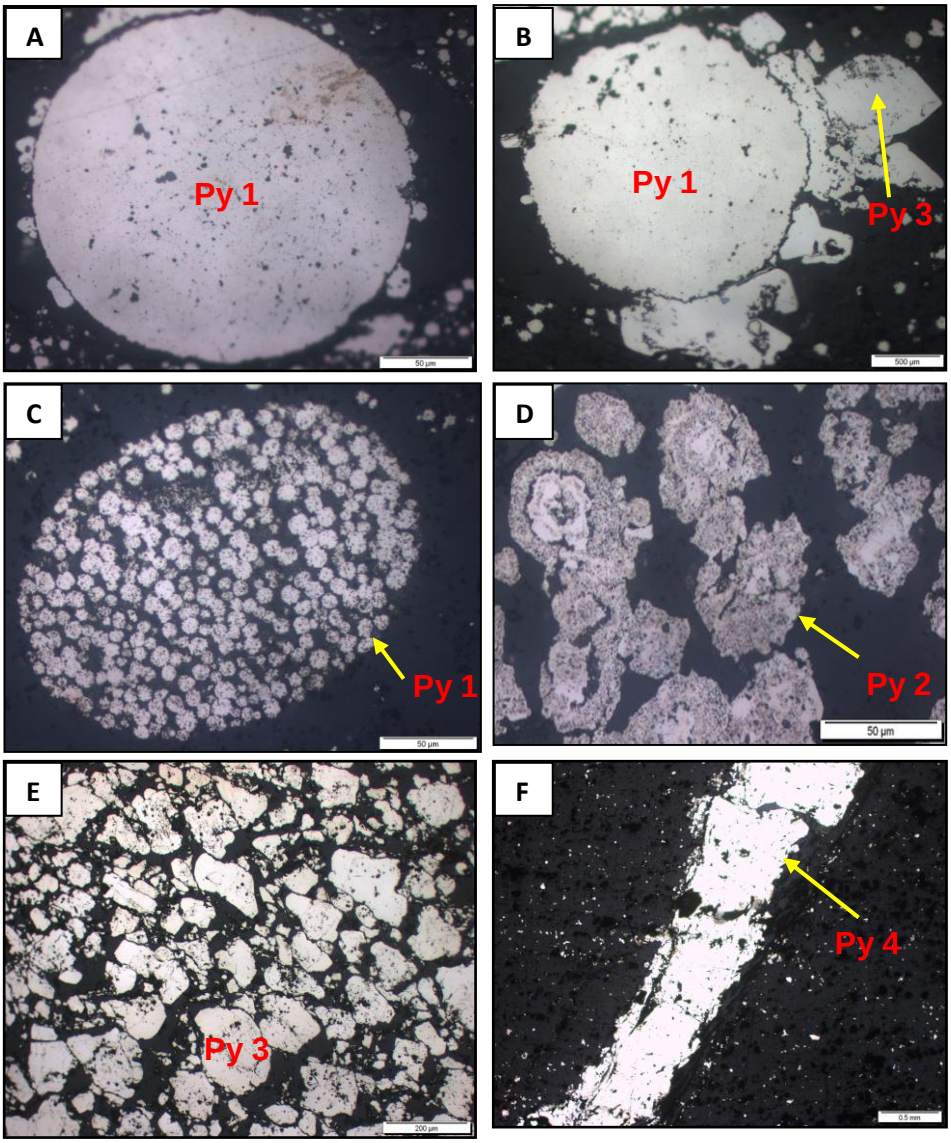

Fig. 4.28. Pyrite textural characteristics in the black cherts from the BRZS Unit 2, Malaysia. **A**) Framboidal pyrite (pyrite 1). **B**) Framboidal pyrite (pyrite 1) and subhedral pyrite (pyrite 3). **C**) Aggregate of framboidal pyrites (pyrite 1). **D**) Cloudy, growth zoned pyrite with a colloform texture (pyrite 2). **E**) Massive pyrite composed of micro-crystals of euhedral and subhedral pyrite embedded in carbonaceous matrix (dark space between crystals). **F**) Vein-like pyrite (pyrite 4) which cross-cuts chert laminations. Note: py= pyrite.

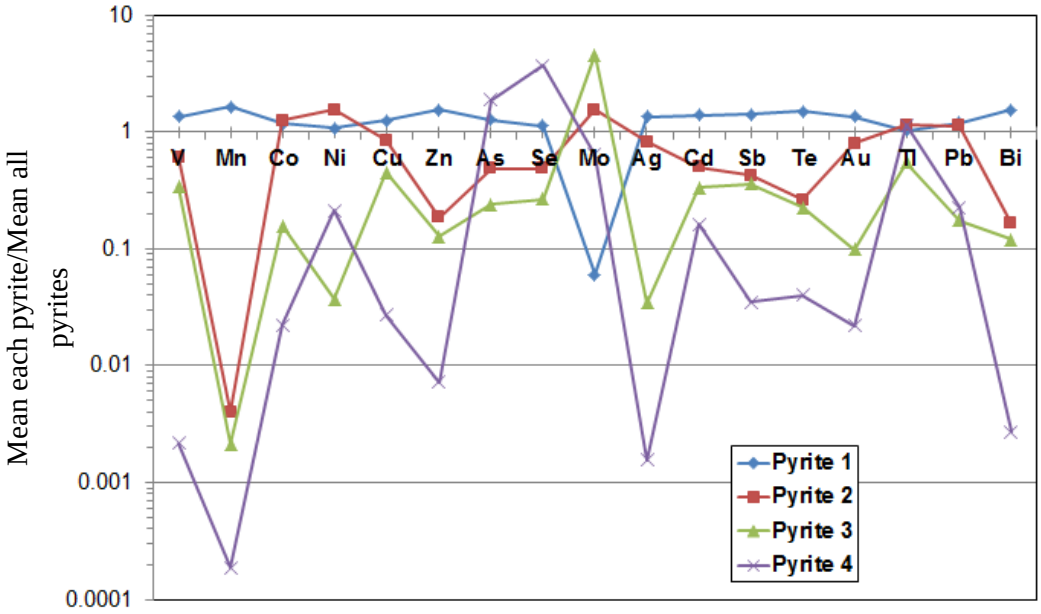

Fig. 4.29. Normalised plot showing comparative chemistry of the pyrite generations in cherts in the BRSZ Unit 2, Malaysia.

Table 4.14. LA ICP-MS analyses of pyrite in ppm for the BRSZ Unit 2, Malaysia.

Analysis no.	Pyrite type	V	Mn	Co	Ni	Cu	Zn	As	Se
BE-5413_1	Pyrite 1	3.38	462.40	5.87	245.87	306.70	29.40	176.32	57.70
BE-5413_2	Pyrite 1	1.21	816.51	2.21	125.20	228.19	16.78	144.77	39.98
BE-5413_3	Pyrite 1	1.90	1820.93	6.07	259.64	344.22	23.99	401.30	85.87
BE-5413_4	Pyrite 1	1.10	370.07	2.45	166.65	283.21	8.93	149.88	21.90
BE-5413_5	Pyrite 1	1.12	192.92	3.28	166.35	274.47	10.25	166.23	26.94
BE-5413_6	Pyrite 1	1.28	1264.09	6.39	175.56	227.96	20.09	1185.52	54.50
BE-5413_7	Pyrite 1	109.48	3019.06	13.86	320.56	385.72	135.83	727.09	76.56
BE-5413_8	Pyrite 1	2.68	2410.19	3.24	225.92	344.58	87.94	244.16	75.77
BE-5413_9	Pyrite 1	1.47	242.98	4.52	234.63	304.33	11.64	210.37	54.53
BE-5413_10	Pyrite 1	43.54	673.65	10.95	304.06	355.43	57.79	1188.65	55.05
BE-5413_11	Pyrite 1	1.82	2589.43	2.48	154.91	271.86	86.06	224.33	137.39
BE-5413_12	Pyrite 1	1.84	859.95	7.33	387.63	343.70	55.04	598.17	86.11
BE-5413_13	Pyrite 1	1.57	258.63	4.03	254.95	309.00	102.78	201.59	59.49
BE-5413_14	Pyrite 1	2.04	2069.30	5.15	245.65	323.98	52.93	294.01	103.90
BE-5413_15	Pyrite 1	1.39	1174.15	3.15	225.17	306.72	206.72	197.01	63.29
BE-5413_16	Pyrite 1	5.65	1629.62	7.87	371.25	387.42	71.51	705.93	80.77
BE-5413_17	Pyrite 1	2.06	1227.43	9.41	368.64	309.01	59.07	1024.20	96.69
BE-5413_18	Pyrite 1	4.07	5768.31	12.39	391.10	267.72	93.76	298.85	191.03
BE-5413_19	Pyrite 1	1.87	2221.01	6.18	273.86	312.53	192.39	225.62	120.20
BE-5413_20	Pyrite 1	1431.39	1551.99	46.05	597.02	401.11	383.20	316.02	107.87
BE-5413_21	Pyrite 1	2.38	5658.06	40.44	538.59	368.28	2365.98	406.10	79.53
BE-5413_22	Pyrite 1	1.63	1427.36	6.38	336.30	281.69	834.37	343.91	112.35
BE-5413_23	Pyrite 1	2.63	2571.15	6.01	268.99	185.75	61.92	301.00	143.04
BE-5413_24	Pyrite 1	27.66	888.86	5.80	614.24	376.94	654.24	345.50	101.70
BE-5413_25	Pyrite 1	3.71	406.64	3.55	337.93	271.01	25.41	1029.12	184.81
BE-5413_27	Pyrite 1	27.70	2729.02	3.69	205.39	301.35	82.47	212.87	85.68
BE-5413_28	Pyrite 1	1.08	585.57	3.37	178.62	292.84	13.32	179.80	41.08
BE-5413_29	Pyrite 1	2.02	1249.48	1.94	175.05	299.66	32.83	200.96	59.77
BE-5413_30	Pyrite 1	1.48	303.02	23.58	368.01	310.42	14.66	491.68	29.36
BE-5413_31	Pyrite 1	11.54	1543.57	9.36	514.63	406.90	108.55	239.95	56.96
BE-5413_32	Pyrite 1	1.16	497.71	32.37	454.29	341.22	116.72	388.28	46.27
BE-5413_33	Pyrite 1	2.22	2307.20	9.27	321.19	343.00	122.65	264.03	83.25
BE-5413_34	Pyrite 1	2.08	421.98	5.72	358.70	383.62	78.71	244.89	40.96
BE-5413_35	Pyrite 1	2.53	222.02	35.20	394.26	347.18	534.17	298.99	72.16
BE-5413_36	Pyrite 1	2.16	126.77	21.11	347.06	303.26	12.48	625.74	32.89
BE-5413_37	Pyrite 1	3.24	2055.38	5.25	357.00	270.78	91.06	847.55	157.71
BE-5413_38	Pyrite 1	34.66	1389.02	16.85	438.79	359.00	231.61	333.83	46.60
BE-5413_40	Pyrite 1	1.75	2871.71	4.78	334.64	271.54	197.06	186.83	80.18
BE-5413_43	Pyrite 1	1.67	1501.27	12.58	380.88	318.49	347.80	230.14	103.84
BE-5413_44	Pyrite 1	1.14	257.89	40.09	519.82	335.08	17.29	331.45	62.51
BE-5413_45	Pyrite 1	1.55	3056.89	4.14	229.48	312.53	249.46	236.90	103.52

Table 4.14 (continued)

Analysis no.	Pyrite type	V	Mn	Co	Ni	Cu	Zn	As	Se
BE-5413_48	Pyrite 1	1.79	1873.91	4.90	288.61	369.74	219.90	293.98	115.94
BE-5413_49	Pyrite 1	2.99	886.65	3.96	384.87	290.43	153.74	297.92	101.68
BE-5413_50	Pyrite 1	1.49	312.07	5.47	435.74	319.73	1604.87	270.25	89.55
BE-5413_55	Pyrite 1	7.94	462.75	39.56	490.88	361.76	602.47	320.16	72.85
BE-5413_56	Pyrite 1	2.27	1699.91	4.95	277.05	318.82	43.69	163.87	54.22
BE-5413_26	Pyrite 1	5.03	2625.28	6.36	395.90	271.26	95.81	414.14	209.79
BE-5413_46	Pyrite 1	2.90	1255.47	6.46	376.90	231.85	157.92	1472.83	79.28
BE-5413_47	Pyrite 1	5.45	277.64	3.91	416.17	293.50	12.13	300.60	124.31
BE-6313-1	Pyrite 2	3.30	7.93	0.83	170.18	115.53	8.65	58.43	21.50
BE-6313-2	Pyrite 2	22.09	0.86	17.31	922.23	279.44	13.71	325.02	65.96
BE-6313-3	Pyrite 2	3.42	0.63	69.24	975.00	311.27	18.63	224.77	92.16
BE-6313-4	Pyrite 2	13.48	2.04	17.60	599.62	253.68	20.69	178.25	50.85
BE-6313-5	Pyrite 2	4.64	0.98	21.10	847.61	287.76	13.21	309.26	62.03
BE-6313-6	Pyrite 2	13.11	1.21	11.39	507.63	210.70	8.50	253.11	29.34
BE-6313-7	Pyrite 2	2.58	0.89	5.98	371.07	203.51	5.04	84.21	26.57
BE-6313-8	Pyrite 2	33.81	1.86	8.00	422.10	166.81	20.24	166.03	29.69
BE-6313-9	Pyrite 2	16.42	2.54	6.64	482.46	185.82	5.64	111.65	39.52
BE-6313-10	Pyrite 2	12.58	2.03	3.85	399.19	204.99	12.69	106.83	26.34
BE-6313-11	Pyrite 2	7.06	2.04	4.62	371.77	197.51	17.81	108.37	26.56
BE-6313-12	Pyrite 2	9.16	2.37	4.23	367.48	219.53	72.09	116.90	28.29
BE-6313-13	Pyrite 2	11.68	6.04	3.03	297.89	211.82	161.25	188.80	25.61
BE-6313-14	Pyrite 2	25.73	12.16	3.48	292.17	216.89	10.25	86.55	22.99
BE-6313-15	Pyrite 2	26.57	10.81	2.88	275.18	183.65	7.73	75.74	17.54
BE-6313-16	Pyrite 2	56.79	3.25	3.14	286.61	175.33	29.76	89.01	24.05
BE-6613_A	Pyrite 3	1.39	1.19	1.01	12.12	162.73	46.64	116.64	19.36
BE-6613_B	Pyrite 3	0.94	2.49	0.45	3.95	664.06	4.41	66.79	11.50
BE-6613_C	Pyrite 3	17.65	4.35	2.81	16.70	67.31	14.77	87.64	31.56
BE-6613_D	Pyrite 3	8.49	3.09	2.57	34.27	45.82	5.69	74.86	20.85
BE-6613_E	Pyrite 3	0.11	0.12	0.19	0.85	3.42	0.42	24.60	25.32
BE-6613_F	Pyrite 3	61.52	2.07	4.13	19.33	107.71	7.24	44.47	19.44
BE-6613_G	Pyrite 3	0.88	1.79	2.78	24.35	60.88	101.25	328.88	30.30
BE-6613_H	Pyrite 3	0.14	0.08	0.03	0.48	6.40	0.50	7.12	17.47
BE-6613_I	Pyrite 3	0.40	3.75	0.33	0.91	8.06	1.10	6.08	14.48
BE-6613_J	Pyrite 3	0.04	0.13	0.05	0.35	1.39	0.28	8.89	12.57
BE-5413_51	Pyrite 4	0.04	0.02	0.11	30.39	2.19	0.66	639.98	161.14
BE-5413_52	Pyrite 4	0.04	0.19	0.18	37.15	1.06	0.72	680.05	231.38
BE-5413_53	Pyrite 4	0.11	0.20	0.16	49.89	1.37	0.83	564.47	300.31
BE-5413_54	Pyrite 4	0.03	0.26	0.38	140.57	22.52	1.90	533.52	429.68
Mean		27.10	913.47	9.22	306.25	253.22	144.32	324.31	76.98
Mean (WDP)		-	545.00	303.00	829.00	436.00	131.00	1360.00	71.00

WDP= Worldwide diagenetic pyrite (Gregory et al., 2015); - : no data available.

Table 4.14 (continued)

Analysis no.	Pyrite type	Mo	Ag	Cd	Sb	Te	Au	Tl	Pb	Bi
BE-5413_1	Pyrite 1	3.35	6.56	2.12	108.92	0.90	0.14	1.66	28.06	0.27
BE-5413_2	Pyrite 1	4.53	6.03	2.17	108.37	0.93	0.12	1.41	29.26	0.11
BE-5413_3	Pyrite 1	7.24	6.87	2.44	128.91	1.28	0.20	1.75	32.60	0.12
BE-5413_4	Pyrite 1	2.58	7.08	2.70	128.40	0.99	0.11	1.83	33.74	0.13
BE-5413_5	Pyrite 1	2.52	6.79	2.41	120.78	1.05	0.11	1.73	33.92	0.15
BE-5413_6	Pyrite 1	4.53	4.71	1.68	88.42	0.95	0.11	1.20	23.14	0.12
BE-5413_7	Pyrite 1	9.05	8.81	2.71	164.67	2.89	0.21	3.18	49.72	0.52
BE-5413_8	Pyrite 1	8.55	6.57	2.62	128.59	1.26	0.16	2.35	31.55	0.16
BE-5413_9	Pyrite 1	3.03	7.29	2.74	140.41	1.18	0.16	2.24	34.57	0.17
BE-5413_10	Pyrite 1	13.79	10.83	2.75	168.86	2.27	0.26	3.59	49.46	0.31
BE-5413_11	Pyrite 1	9.34	5.02	2.14	101.52	1.09	0.12	2.45	27.17	0.17
BE-5413_12	Pyrite 1	4.88	9.68	3.88	184.64	1.60	0.28	3.61	46.59	0.23
BE-5413_13	Pyrite 1	2.86	8.14	3.24	149.01	1.31	0.18	3.50	39.81	0.18
BE-5413_14	Pyrite 1	7.31	6.96	2.67	128.41	1.28	0.18	2.80	32.06	0.14
BE-5413_15	Pyrite 1	4.34	7.02	4.25	128.45	0.98	0.14	2.15	31.66	0.14
BE-5413_16	Pyrite 1	4.79	13.60	3.55	196.76	2.17	0.28	5.64	58.19	0.30
BE-5413_17	Pyrite 1	5.02	7.89	3.36	151.51	2.00	0.26	4.68	38.94	0.22
BE-5413_18	Pyrite 1	26.43	8.24	2.77	137.86	2.11	0.13	5.65	36.69	0.23
BE-5413_19	Pyrite 1	6.99	4.13	2.88	88.50	1.47	0.14	2.72	22.26	0.19
BE-5413_20	Pyrite 1	24.64	14.09	6.18	193.68	6.37	0.66	6.70	56.80	2.72
BE-5413_21	Pyrite 1	10.54	8.46	28.18	174.63	5.12	0.43	4.60	46.03	2.21
BE-5413_22	Pyrite 1	6.41	8.91	11.07	160.71	1.55	0.19	3.72	40.76	0.26
BE-5413_23	Pyrite 1	15.16	6.58	2.37	108.12	1.32	0.11	2.81	27.78	0.17
BE-5413_24	Pyrite 1	3.32	14.72	10.69	245.30	1.75	0.30	5.71	57.80	0.35
BE-5413_25	Pyrite 1	2.19	14.37	2.37	172.27	1.89	0.38	2.93	44.74	0.30
BE-5413_27	Pyrite 1	7.45	7.39	2.27	122.90	1.19	0.17	2.45	31.42	0.14
BE-5413_28	Pyrite 1	4.63	8.82	3.02	145.90	0.92	0.14	2.22	39.04	0.15
BE-5413_29	Pyrite 1	4.19	7.29	2.47	133.38	1.06	0.24	2.19	32.63	0.15
BE-5413_30	Pyrite 1	1.16	6.98	2.64	134.84	1.12	0.15	1.69	31.24	0.43
BE-5413_31	Pyrite 1	2.29	9.21	3.62	174.63	1.87	0.21	2.42	40.41	0.57
BE-5413_32	Pyrite 1	5.03	9.64	3.76	172.87	2.32	0.18	2.15	46.81	0.83
BE-5413_33	Pyrite 1	6.33	7.61	3.72	135.02	2.18	0.19	2.32	36.53	0.44
BE-5413_34	Pyrite 1	0.94	8.03	3.73	161.92	1.36	0.24	2.13	39.07	0.20
BE-5413_35	Pyrite 1	3.84	9.61	7.82	180.83	1.77	0.15	2.28	48.49	0.47
BE-5413_36	Pyrite 1	0.88	6.78	2.35	125.95	1.40	0.23	1.53	32.09	0.26
BE-5413_37	Pyrite 1	9.60	6.76	2.70	138.42	1.41	0.22	2.59	30.56	0.18
BE-5413_38	Pyrite 1	9.88	8.10	4.28	146.46	2.54	0.26	2.10	41.13	0.86
BE-5413_40	Pyrite 1	7.48	5.79	3.23	110.38	1.87	0.19	2.10	30.15	0.50
BE-5413_43	Pyrite 1	6.59	5.80	4.99	126.67	1.14	0.14	2.63	27.47	0.45
BE-5413_44	Pyrite 1	4.75	9.57	3.10	180.36	1.58	0.16	2.68	39.71	0.76
BE-5413_45	Pyrite 1	7.92	7.23	4.50	134.98	1.46	0.17	2.90	32.52	0.33

Table 4.14 (continued)

Analysis no.	Pyrite type	Mo	Ag	Cd	Sb	Te	Au	Tl	Pb	Bi
BE-5413_48	Pyrite 1	7.19	7.68	4.39	165.03	1.22	0.20	3.56	37.14	0.37
BE-5413_49	Pyrite 1	4.12	9.69	4.63	211.70	1.15	0.32	4.43	47.23	0.26
BE-5413_50	Pyrite 1	4.48	10.48	20.02	187.17	0.97	0.21	3.08	44.67	0.23
BE-5413_55	Pyrite 1	7.08	11.61	8.96	206.24	2.51	0.20	5.52	60.21	0.75
BE-5413_56	Pyrite 1	3.83	7.66	2.30	132.58	1.79	0.21	3.11	35.05	0.66
BE-5413_26	Pyrite 1	25.25	11.43	3.55	183.51	2.75	0.24	3.20	41.34	0.26
BE-5413_46	Pyrite 1	5.95	8.13	3.64	136.93	1.51	0.29	2.65	31.03	0.32
BE-5413_47	Pyrite 1	2.24	16.83	2.76	170.12	1.21	0.33	3.18	45.89	0.39
BE-6313-1	Pyrite 2	208.74	3.26	0.52	15.43	0.28	0.10	2.22	13.64	0.02
BE-6313-2	Pyrite 2	193.99	8.45	1.74	99.66	0.55	0.18	4.23	60.98	0.11
BE-6313-3	Pyrite 2	185.36	6.09	1.62	87.74	0.60	0.13	4.99	54.69	0.08
BE-6313-4	Pyrite 2	127.37	6.46	1.27	62.55	0.38	0.15	3.71	48.76	0.03
BE-6313-5	Pyrite 2	169.78	7.88	1.24	81.28	0.50	0.20	4.29	65.54	0.05
BE-6313-6	Pyrite 2	179.92	5.76	1.78	46.27	0.21	0.11	3.72	31.47	0.02
BE-6313-7	Pyrite 2	120.00	3.59	1.36	25.49	0.13	0.09	3.24	21.45	0.01
BE-6313-8	Pyrite 2	168.48	4.64	1.59	37.59	0.30	0.11	2.56	36.72	0.07
BE-6313-9	Pyrite 2	231.43	3.99	1.05	38.05	0.35	0.09	3.03	31.76	0.03
BE-6313-10	Pyrite 2	181.78	4.57	1.65	35.40	0.19	0.11	3.26	30.87	0.03
BE-6313-11	Pyrite 2	199.75	4.86	1.09	35.09	0.18	0.13	2.82	35.33	0.02
BE-6313-12	Pyrite 2	165.70	5.46	2.71	44.03	0.27	0.15	3.15	37.03	0.05
BE-6313-13	Pyrite 2	172.99	5.83	3.57	36.73	0.28	0.15	3.04	40.51	0.05
BE-6313-14	Pyrite 2	167.11	4.12	1.82	28.59	0.16	0.12	2.88	19.26	0.03
BE-6313-15	Pyrite 2	135.37	3.83	1.23	22.94	0.22	0.12	2.89	18.43	0.05
BE-6313-16	Pyrite 2	207.46	3.73	2.16	28.02	0.20	0.09	2.55	26.39	0.03
BE-6613_A	Pyrite 3	394.93	0.23	2.45	53.09	0.19	0.02	0.80	5.00	0.04
BE-6613_B	Pyrite 3	371.19	0.17	1.79	29.12	0.04	0.00	4.40	0.93	0.01
BE-6613_C	Pyrite 3	407.63	0.72	0.64	82.00	1.01	0.05	2.04	12.92	0.09
BE-6613_D	Pyrite 3	383.70	0.52	1.14	50.36	0.47	0.05	2.77	19.75	0.07
BE-6613_E	Pyrite 3	934.97	0.00	0.51	28.34	0.07	0.00	1.16	0.65	0.00
BE-6613_F	Pyrite 3	571.89	0.28	0.48	69.92	0.40	0.02	1.26	8.72	0.06
BE-6613_G	Pyrite 3	196.88	0.20	2.62	22.97	0.26	0.02	0.55	6.63	0.03
BE-6613_H	Pyrite 3	567.35	0.01	0.61	15.51	0.06	0.00	0.67	0.11	0.00
BE-6613_I	Pyrite 3	796.44	0.02	0.21	10.82	0.00	0.00	1.22	0.79	0.00
BE-6613_J	Pyrite 3	580.48	0.01	0.53	21.18	0.08	0.00	0.91	0.19	0.00
BE-5413_51	Pyrite 4	57.20	0.01	0.46	2.68	0.05	0.00	2.32	2.31	0.00
BE-5413_52	Pyrite 4	60.46	0.01	0.54	2.76	0.00	0.00	2.22	3.13	0.00
BE-5413_53	Pyrite 4	83.36	0.01	0.55	4.60	0.05	0.01	4.31	5.75	0.00
BE-5413_54	Pyrite 4	87.75	0.02	0.58	4.75	0.08	0.00	4.34	17.65	0.00
Mean		109.44	6.36	3.31	106.96	1.16	0.16	2.88	32.06	0.26
Mean (WDP)		88.00	9.20	3.00	90.00	4.90	0.10	36.00	387.00	13.00

WDP= Worldwide diagenetic pyrite (Gregory et al., 2015); - : no data available.

The plots of Co-Ni, Cu-Ni, Mo-Se, As-Ni including Au relations to selected trace elements are shown in Figs. 4.30 and 4.31. Data for pyrite 1 is mostly confirned to the field of

sedimentary pyrite (plots A, C, and D). Pyrite 2 and 3 data expand outside the field of sedimentary pyrite. In the four plots, pyrite 3 shows a more scattered pattern (plots B and D). All pyrites show a Co/Ni ratio >1 (Fig. 4.30A). In the plot Cu-Ni, pyrites 2, 3, and 4 data plots below the line Cu/Ni= 10 (Fig. 4.30B).

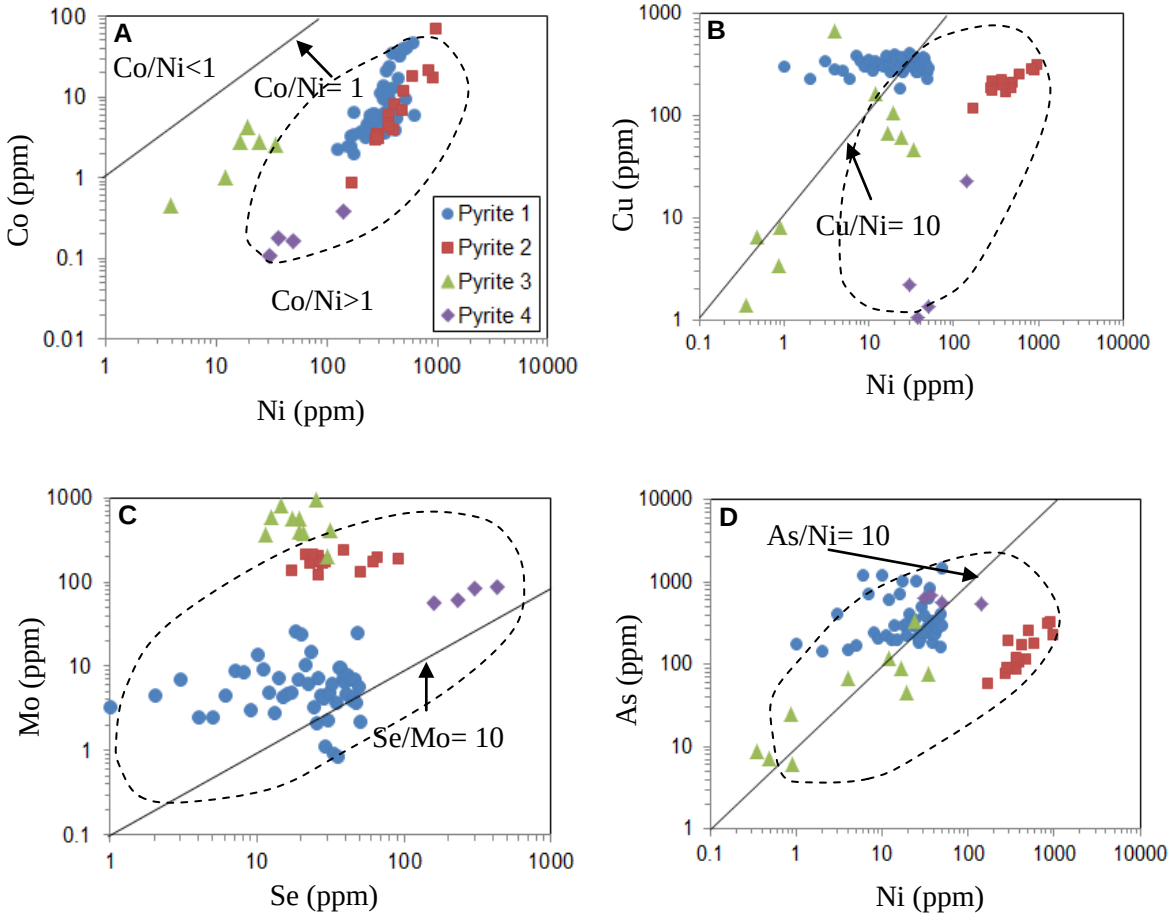

Fig. 4.30 Binary log-log plots of pyrite geochemistry from the BRSZ Unit 2, Malaysia. **A**) Scatter plot of Co-Ni. **B**) Scatter plot of Cu-Ni. **C**). Scatter plot of Se-Mo. **D**) Plot displaying As and Ni values. Dashed polygon represents the field of sedimentary pyrite (Gregory et al., 2015).

However, framboidal pyrites (pyrite 1) plot across the line Cu/Ni= 10. On the plot Mo-Se, pyrite 1 data scatter across the line Se/Mo= 10 (Fig. 4.30C). But pyrites 2, 3, and 4 dataset

plots above the line Se/Mo= 10. The As-Ni plot shows that pyrite 1, 2, and 3 data plot across the As/Ni= 10 line; however, pyrite 4 plots below this line. Correlation coefficients for pyrite 1 and pyrite 2 are summarised in Tables 4.15 and 4.16. Geochemical plots of Au versus Ag, Te, As, Ni, V, Mo, Sb, and Se are shown in Fig. 4.31.

Table 4.15. Coefficients of correlation for early diagenetic pyrite (pyrite 1) from the Late Triassic BRSZ Unit 2. Numbers that are highlighted are equal to or greater than 0.5.

Correlation	Mo_ppm	Se_ppm	V_ppm	Mn_ppm	Co_ppm	Ni_ppm	Cu_ppm	Zn_ppm
Mo_ppm	1	0.61	0.47	0.63	0.23	0.21	-0.051	0.088
Se_ppm	0.61	1	0.074	0.49	-0.13	0.19	-0.24	0.059
V_ppm	0.47	0.074	1	0.022	0.45	0.34	0.29	0.055
Mn_ppm	0.63	0.49	0.022	1	0.023	0.045	-0.023	0.31
Co_ppm	0.23	-0.13	0.45	0.023	1	0.65	0.43	0.38
Ni_ppm	0.21	0.19	0.34	0.045	0.65	1	0.53	0.45
Cu_ppm	-0.051	-0.24	0.29	-0.023	0.43	0.53	1	0.25
Zn_ppm	0.088	0.059	0.055	0.31	0.38	0.45	0.25	1
As_ppm	0.035	0.13	-0.024	-0.057	0.029	0.13	-0.14	-0.085
Ag_ppm	0.11	0.26	0.32	-0.22	0.26	0.62	0.37	0.16
Cd_ppm	0.054	0.033	0.048	0.25	0.39	0.49	0.28	0.99
Sb_ppm	0.057	0.14	0.21	-0.18	0.39	0.75	0.57	0.35
Te_ppm	0.57	0.17	0.7	0.39	0.68	0.62	0.47	0.44
Au_ppm	0.28	0.22	0.68	0.074	0.39	0.62	0.41	0.33
Tl_ppm	0.46	0.41	0.44	0.29	0.34	0.6	0.38	0.34
Pb_ppm	0.12	0.045	0.32	-0.15	0.47	0.67	0.61	0.32
Bi_ppm	0.37	-0.02	0.72	0.25	0.77	0.62	0.46	0.51

Correlation	As_ppm	Ag_ppm	Cd_ppm	Sb_ppm	Te_ppm	Au_ppm	Tl_ppm	Pb_ppm	Bi_ppm
Mo_ppm	0.035	0.11	0.054	0.057	0.57	0.28	0.46	0.12	0.37
Se_ppm	0.13	0.26	0.033	0.14	0.17	0.22	0.41	0.045	-0.02
V_ppm	-0.024	0.32	0.048	0.21	0.7	0.68	0.44	0.32	0.72
Mn_ppm	-0.057	-0.22	0.25	-0.18	0.39	0.074	0.29	-0.15	0.25
Co_ppm	0.029	0.26	0.39	0.39	0.68	0.39	0.34	0.47	0.77
Ni_ppm	0.13	0.62	0.49	0.75	0.62	0.62	0.6	0.67	0.62
Cu_ppm	-0.14	0.37	0.28	0.57	0.47	0.41	0.38	0.61	0.46
Zn_ppm	-0.085	0.16	0.99	0.35	0.44	0.33	0.34	0.32	0.51
As_ppm	1	0.16	-0.083	0.084	0.12	0.26	0.098	0.11	-0.045
Ag_ppm	0.16	1	0.23	0.82	0.41	0.65	0.61	0.85	0.33
Cd_ppm	-0.083	0.23	1	0.43	0.43	0.35	0.37	0.39	0.5
Sb_ppm	0.084	0.82	0.43	1	0.41	0.58	0.67	0.92	0.35
Te_ppm	0.12	0.41	0.43	0.41	1	0.77	0.6	0.55	0.91
Au_ppm	0.26	0.65	0.35	0.58	0.77	1	0.61	0.6	0.73
Tl_ppm	0.098	0.61	0.37	0.67	0.6	0.61	1	0.71	0.47
Pb_ppm	0.11	0.85	0.39	0.92	0.55	0.6	0.71	1	0.45
Bi_ppm	-0.045	0.33	0.5	0.35	0.91	0.73	0.47	0.45	1

Patterns in Fig. 4.31 indicate a loss in Au, Te, As, Ni, and Sb from diagenetic pyrite 1 to hydrothemal pyrite 4.

Table 4.16. Coefficients of correlation for late diagenetic pyrite (pyrite 2) from the Late Triassic BRSZ Unit 2. Numbers that are highlighted are equal to or greater than 0.5.

Correlation	Mo_ppm	Se_ppm	V_ppm	Mn_ppm	Co_ppm	Ni_ppm	Cu_ppm	Zn_ppm
Mo_ppm	1	0.083	0.16	-0.1	0.0076	0.034	-0.21	-0.037
Se_ppm	0.083	1	-0.28	-0.52	0.9	0.95	0.85	-0.14
V_ppm	0.16	-0.28	1	0.22	-0.29	-0.25	-0.28	-0.043
Mn_ppm	-0.1	-0.52	0.22	1	-0.4	-0.59	-0.43	0.089
Co_ppm	0.0076	0.9	-0.29	-0.4	1	0.8	0.74	-0.13
Ni_ppm	0.034	0.95	-0.25	-0.59	0.8	1	0.89	-0.2
Cu_ppm	-0.21	0.85	-0.28	-0.43	0.74	0.89	1	0.025
Zn_ppm	-0.037	-0.14	-0.043	0.089	-0.13	-0.2	0.025	1
As_ppm	0.026	0.71	-0.17	-0.52	0.51	0.84	0.75	0.074
Ag_ppm	-0.061	0.71	-0.23	-0.47	0.46	0.82	0.82	0.16
Cd_ppm	-0.09	-0.1	0.2	0.0089	-0.073	-0.091	0.18	0.86
Sb_ppm	0.032	0.92	-0.21	-0.55	0.72	0.97	0.9	-0.056
Te_ppm	0.18	0.93	-0.21	-0.39	0.76	0.88	0.71	-0.033
Au_ppb	-0.16	0.54	-0.25	-0.23	0.28	0.63	0.71	0.3
Tl_ppm	-0.14	0.9	-0.38	-0.52	0.83	0.93	0.94	-0.097
Pb_ppm	0.02	0.83	-0.21	-0.61	0.6	0.89	0.84	0.14
Bi_ppm	0.098	0.6	0.16	-0.21	0.46	0.62	0.5	0.17

Correlation	As_ppm	Ag_ppm	Cd_ppm	Sb_ppm	Te_ppm	Au_ppb	Tl_ppm	Pb_ppm	Bi_ppm
Mo_ppm	0.026	-0.061	-0.09	0.032	0.18	-0.16	-0.14	0.02	0.098
Se_ppm	0.71	0.71	-0.1	0.92	0.93	0.54	0.9	0.83	0.6
V_ppm	-0.17	-0.23	0.2	-0.21	-0.21	-0.25	-0.38	-0.21	0.16
Mn_ppm	-0.52	-0.47	0.0089	-0.55	-0.39	-0.23	-0.52	-0.61	-0.21
Co_ppm	0.51	0.46	-0.073	0.72	0.76	0.28	0.83	0.6	0.46
Ni_ppm	0.84	0.82	-0.091	0.97	0.88	0.63	0.93	0.89	0.62
Cu_ppm	0.75	0.82	0.18	0.9	0.71	0.71	0.94	0.84	0.5
Zn_ppm	0.074	0.16	0.86	-0.056	-0.033	0.3	-0.097	0.14	0.17
As_ppm	1	0.93	0.16	0.88	0.74	0.75	0.78	0.88	0.62
Ag_ppm	0.93	1	0.22	0.91	0.74	0.9	0.77	0.93	0.64
Cd_ppm	0.16	0.22	1	0.047	-0.078	0.27	0.04	0.16	0.26
Sb_ppm	0.88	0.91	0.047	1	0.89	0.75	0.9	0.93	0.71
Te_ppm	0.74	0.74	-0.078	0.89	1	0.64	0.76	0.83	0.73
Au_ppb	0.75	0.9	0.27	0.75	0.64	1	0.58	0.84	0.6
Tl_ppm	0.78	0.77	0.04	0.9	0.76	0.58	1	0.8	0.48
Pb_ppm	0.88	0.93	0.16	0.93	0.83	0.84	0.8	1	0.64
Bi_ppm	0.62	0.64	0.26	0.71	0.73	0.6	0.48	0.64	1

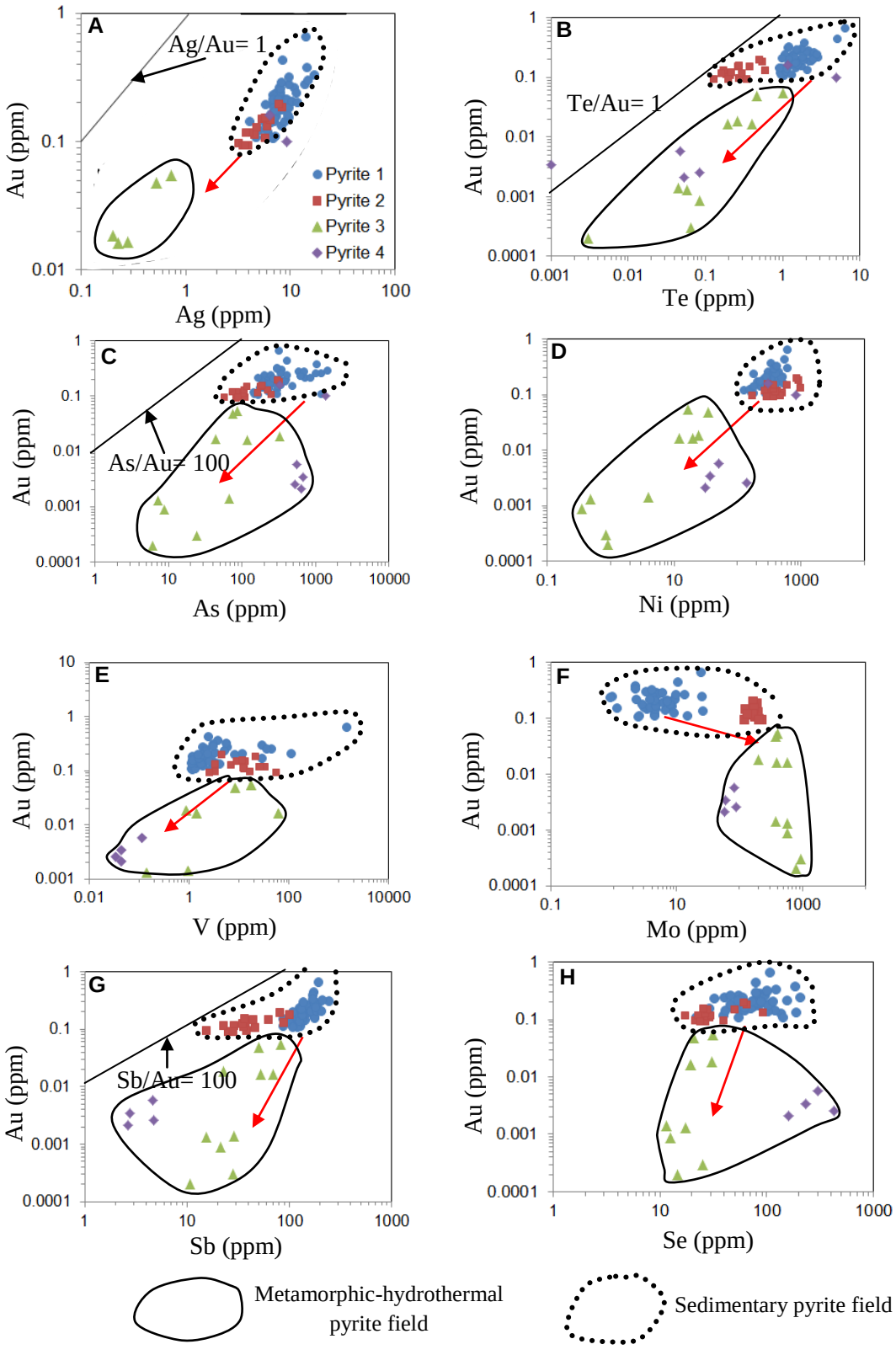

Fig. 4.31. Geochemical bivariate plots for the BRSZ Unit 2 pyrites. **A**) Au-Ag. **B**) Au-Te. **C**) Au-As. **D**) Au-Ni. **E**) Au-V. **F**) Au-Mo. **G**) Au-Sb. **H**) Au-Se. Note: the red arrow indicates loss of some trace elements. The green dashed polygon in Fig. 6.53A represents the field of metamorphic-hydrothermal vein pyrite (pyrite 3).

There is a good correlation among Au, Ag, Te, Ni, V, Sb, Tl, Pb, and Bi in pyrite framboids (pyrite 1) as shown in the correlation of coefficient Table 4.15. Correlation between Au and V is lost in pyrite 2 but improved with Cu, As, Ag, Sb, and Pb. Pyrite 2 is modified from pyrite 1 but with added Mo (Fig. 4.31F). Additionally, the red arrow shows pyrite 3 extends from the pyrite 1 and pyrite 2 field to much lower levels of trace elements. This strongly suggests that pyrite 3 formed by recrystallisation and trace element loss from pyrite 1 and pyrite 2. Therefore, pyrite 3 is interpreted as metamorphic pyrite. Pyrite 4 lies off trend and looks hydrothermal, both in texture and chemistry. Compared to the world average diagenetic pyrites (Fig. 4.32), pyrite 1 is slightly enriched in Zn, Cd, Sb, and Au, depleted in Ni, As, Te and strongly depleted in Co, Mo, Tl, Pb, and Bi.

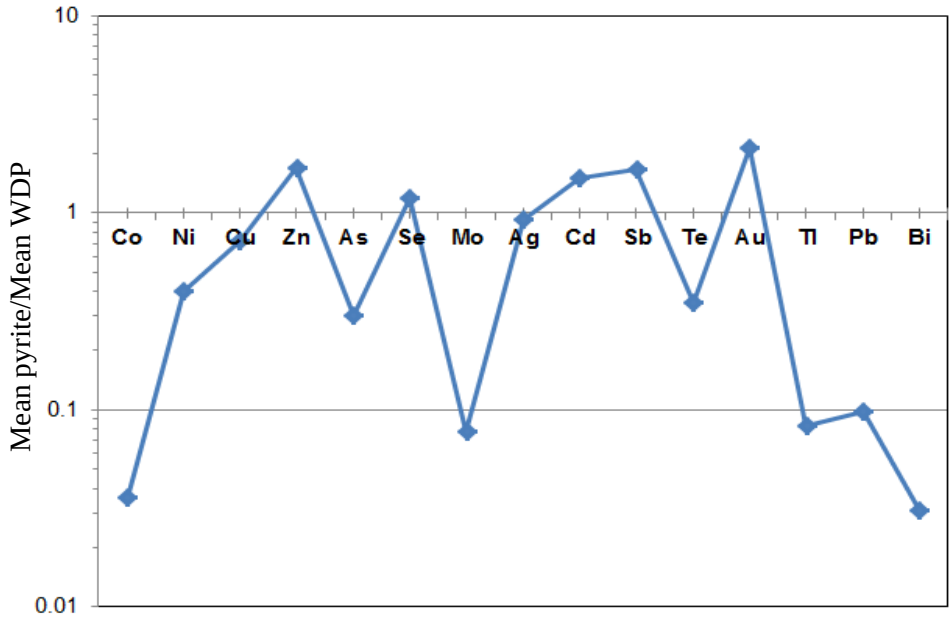

Fig. 4.32. Spider plot of trace element content in diagenetic pyrite 1 of BRSZ Unit 2 normalised to worldwide diagenetic pyrite (Gregory et al., 2015).

4.5.4. Discussion for the BRSZ Unit 2

The BRSZ Unit 2 cherts have elevated contents of SiO_2 and S and consequently have low contents of TiO_2, Al_2O_3, Fe_2O_3, MnO, MgO, CaO, Na_2O, K_2O, and P_2O_5 compared to PAAS. In terms of trace element concentration, the BRSZ Unit 2 cherts are enriched in Cu, Mo, and U and depleted in Cr, Ni, Zn, Ga, and Th. In early diagenetic pyrite 1, V content varies positively with Mo, Co, Te, Au, Tl and Bi (Table 4.15) suggesting that organic matter may have contributed to the nucleation of framboidal pyrite 1. Compared to worldwide diagenetic pyrites, the BRSZ Unit 2 chert framboidal pyrites (pyrite 1) are enriched in Au, Zn, Cd, Sb and depleted in Ni, Cu, Te and strongly depleted in Bi, Tl, Pb, Mo, Co. The fact that the whole rock analyses show enrichment of Mo and U, whereas the pyrite analyses show depletion of Mo, strongly suggests the Mo is concentrated in the organic matrix of the cherts rather than the pyrite.

The late diagenetic pyrite 2 shows an order of magnitude increase in Mo compared with pyrite 1, which may be explained by release of Mo from matrix organics and incorporation in pyrite associated with maturation during late diagenesis. Pyrite 3 is enriched in Mo, and depleted in Co, Ni, Cu, Zn, As, Se, Ag, Cd, Sb, Te, Au, Tl, Pb, and Bi compared to sedimentary pyrites 1 and 2. Typical euhedral texture and presence of zoning patterns in pyrite is interpreted of having a metamorphic-hydrothermal origin (Makoundi, 2012). Pyrite 4 which is vein-like cuts across laminations and is enriched in As and Se relative to pyrite 1, 2, and 3. Similar texture for pyrite 4 has been interpreted as having a hydrothermal origin (Makoundi, 2012).

CHAPTER 5
RARE EARTH ELEMENT COMPOSITION, PROVENANCE, TECTONIC SETTING AND PALEOREDOX CONDITIONS

5.1. Introduction

This chapter documents the rare earth element (REE) compositions of Machinchang (Late Cambrian-Early Ordovician), Setul (Early Ordovician-Silurian), Singa (Pennsylvanian-Early Permian), BRSZ Unit 1 (Late Devonian), Semantan (Middle Triassic), and Gua Musang (Middle Triassic) formations. It also covers provenance and tectonic studies of selected formations including an interpretation of paleoredox conditions on the seafloor during the Phanerozoic in Malaysia. This Chapter combines results of lithogeochemical analyses of shales with redox conditions to discuss whether changes of redox conditions in sea water affected the trace element compositions both of whole rocks and sedimentary pyrites. Relationships between provenance of sedimentary rocks and sedimentary pyrite trace element composition are discussed.

5.2. REE composition

Compositions of REE from sedimentary rocks were determined at the University of Tasmania using the ICP-MS solution method (see appendix for description of method).

5.2.1. Significance of REE in sedimentary rocks

REE studies have been extensively undertaken to determine the provenance of sedimentary rocks (Cullers et al., 1988; Cullers, 1994a, 2000; Cullers and Podkovyrov, 2000; Rahman and Suzuki, 2007; Hinchey, 2012) and verify the REE content relative to world standards such as PAAS and UCC. REE compositions in sedimentary rocks are related to

their parental rocks; however, their chemistry is commonly controlled by chemical weathering and grain size (Mishra and Sen, 2012; Clift, 2015).

Proportions of LREE relative to HREE may be used to suggest felsic or mafic source rocks for the REE. Wronkiewicz and Condie (1987) documented that felsic source rocks will have a high ratio (LREE/HREE>1) whereas mafic source rocks show a low ratio (LREE/HREE<1). Research work by Belousova et al. (2002) documented depletion of LREE relative to HREE in basalts whereas LREE contents were higher than HREE contents in granites.

5.2.2. Machinchang Formation (Late Cambrian-Early Ordovician)

REE compositions of the sandstone and grey shale samples from the Late Cambrian-Early Ordovician Machinchang Formation are given in Table 5.1. There is an increasing trend of light rare earth elements (LREE) (La, Ce, Pr, Nd, Sm, and Eu) with a decreasing pattern of heavy rare earth elements (HREE) (Gd, Tb, Dy, Ho, Er, Tm, Yb and Lu) as shown in Fig. 5.1. Compared with PAAS, the grey shales are enriched in both LREE and HREE which may be related to dilution effects. The La/Sm ratio ranges from 4 to 6 whereas the La/Yb ratio is between 15 and 19. Additionally, the grey shales and sandstones display a weak negative Ce anomaly. The Ce anomaly is indicative of a marine depositional environment (Antonina et al., 2013). The contents of REE in grey shales are higher than in sandstones implying that the grain size has control on the REE chemistry in siliciclastic rocks. The Machinchang sandstones are also enriched in all REE compared to PAAS.

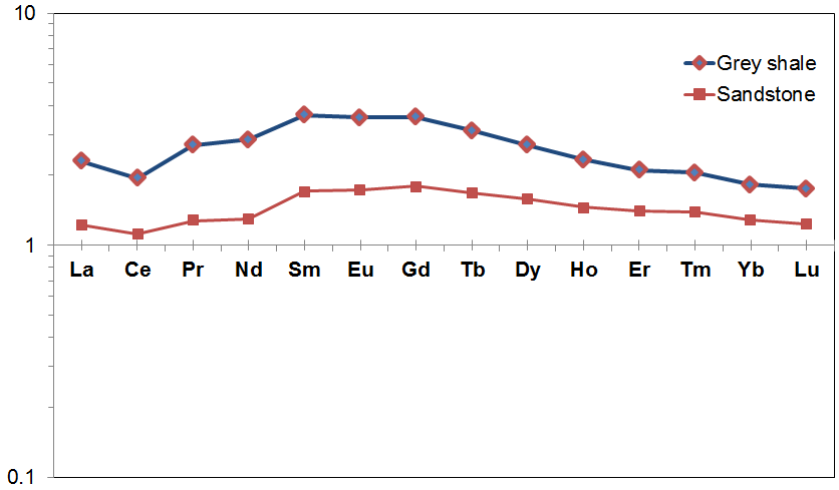

Fig 5.1. Rare Earth Element mean composition of the Machinchang Formation grey shales and sandstones normalised to PAAS (Post-Archean Australian Shale, McLennan, 1989).

Table 5.1. REE composition (ppm) in sandstone and grey shale compared with PAAS for the Late Cambrian-Early Ordovician Machinchang Formation.

	Sandstone (LA-2812) Lower sequence (F5)	Sandstone (LA-3112) Upper sequence (F6)	Mean (ppm)	Grey shale (LA-2912) Lower sequence (F5)	Grey shale (LA-3212) Upper sequence (F6)	Mean (ppm)	PAAS
La	57.7	35.9	46.8	102.7	72.8	87.7	38
Ce	120.5	57.7	89.0	159.0	150.8	154.9	80
Pr	14.3	8.2	11.3	29.5	18.1	23.8	8.9
Nd	57.5	30.0	43.7	126.8	66.1	96.5	32
Sm	12.9	6.0	9.5	28.0	12.2	20.1	5.6
Eu	2.6	1.1	1.8	5.6	2.1	3.8	1.1
Gd	11.6	5.0	8.3	24.3	8.9	16.6	4.7
Tb	1.7	0.8	1.3	3.4	1.4	2.4	0.8
Dy	9.5	5.3	7.4	16.7	8.5	12.6	4.4
Ho	1.7	1.1	1.4	2.8	1.8	2.3	1
Er	4.5	3.4	3.9	6.8	5.1	5.9	2.9
Tm	0.6	0.5	0.5	0.9	0.7	0.8	0.4
Yb	3.8	3.3	3.6	5.4	4.8	5.13	2.8
Lu	0.6	0.5	0.5	0.8	0.7	0.7	0.4

5.2.3. Setul Formation (Early Ordovician-Silurian)

The REE compositions of sandstone samples from the Early Ordovician-Silurian Setul Formation were determined and are presented in Table 5.2. Compared with UCC (Upper

Continental Crust), the Setul Formation sandstones are depleted in both the LREE and HREE (Fig. 5.2). In addition, the sandstones do not show a significant negative Eu anomaly. The pevidence shows that the sandstones of the Machinchang Formation (Fig. 5.1) are enriched in all REE compared with the Setul sandstones (Fig. 5.2A) possibly due to the higher clay content of the former (Mean Al_2O_3 = 16.55 wt% for Machinchang in Table 3.1; Mean Al_2O_3 = 3.19 wt% for Setul in Table 3.5). Similarly, compared to PAAS (Post-Archean Australian shales), the Setul sandstones have a similar trend but are depleted in all REE.

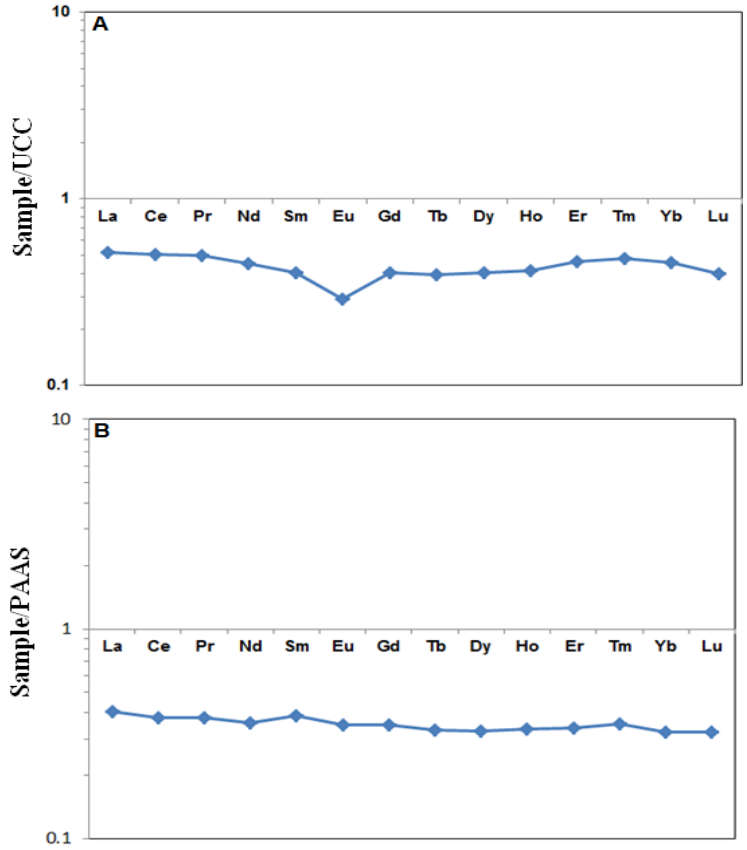

Fig. 5.2. Comparative spider plots of mean values of rare earth elements (REE) in sandstones of the Early Ordovician-Silurian Setul Formation. **A**) Normalised plot to UCC and **B**) Normalised plot to PAAS (Taylor and McLennan, 1985).

The plot normalised to PAAS (Fig. 5.2B) does not display a significant Eu anomaly whereas that normalised to UCC (Fig. 5.2A) shows an Eu anomaly.

Table 5.2. REE composition (ppm) of the Setul Formation sandstones.

	LA-4612	**LA-4712**	**LA-4812**	**LA-4912**	**LA-5012**
La	16.3	11.46	11.22	14.67	14.15
Ce	30.3	22.39	22.65	29.83	27.87
Pr	3.2	2.58	2.56	3.40	2.98
Nd	11.4	9.46	9.41	12.79	10.73
Sm	1.8	1.67	1.88	2.40	1.85
Eu	0.3	0.30	0.38	0.43	0.33
Gd	1.3	1.40	1.58	1.95	1.30
Tb	0.2	0.22	0.28	0.31	0.19
Dy	1.2	1.38	1.41	1.84	1.16
Ho	0.2	0.30	0.31	0.39	0.25
Er	0.8	0.87	0.84	1.10	0.77
Tm	0.13	0.12	0.13	0.16	0.12
Yb	0.87	0.78	0.73	0.96	0.78
Lu	0.13	0.11	0.12	0.15	0.12

5.2.4. Singa Formation (Pennsylvanian-Early Permian)

The REE composition of selected Pennsylvanian-Early Permian Singa Formation shales was determined and results are presented in Table 5.3. The data indicate that the Singa

Formation black shales have a similar trend but are slightly enriched in La, Ce, Pr, Nd, Sm, Eu, Gd, Tb, Dy, Ho, Er, and Tm compared to PAAS (Fig. 5.3). In comparison, the Machinchang Formation grey shales contain higher amounts of LREE and HREE relative to the Singa Formation black shales.

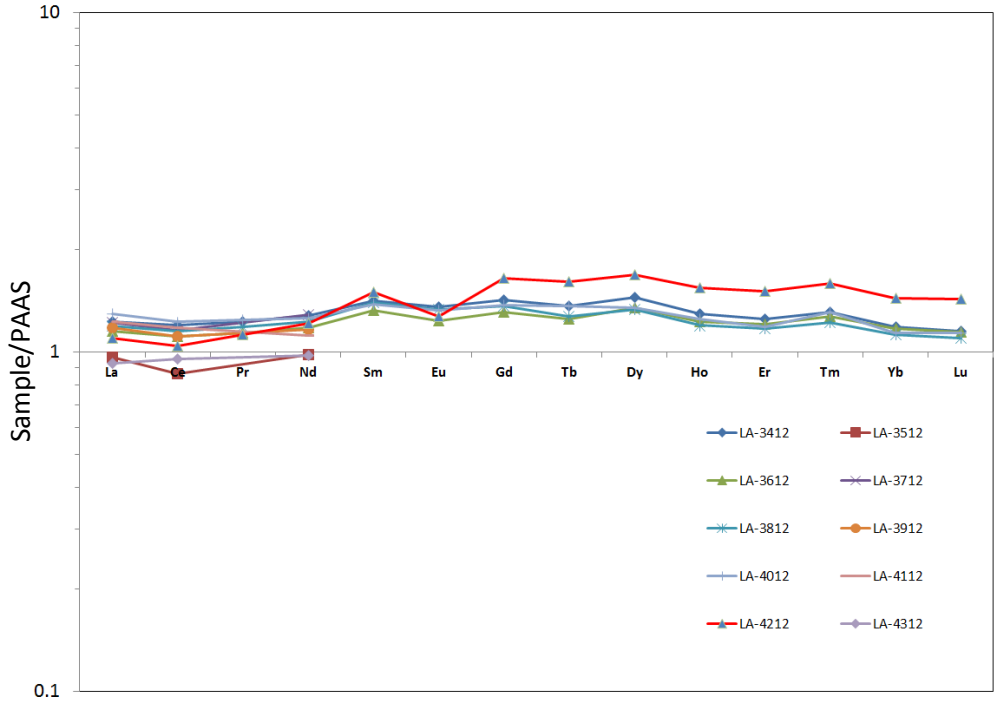

Fig. 5.3. Spider diagram of rare earth elements (REE) in the black shales of the Pennsylvanian-Early Permian Singa Formation, Langkawi Islands normalised to PAAS (Taylor and McLennan, 1985). Most black shale samples are enriched in REE elements except two samples that are depleted in REE elements (i.e. LA-3512 and LA-4312) compared to PAAS.

Table 5.3. REE composition (ppm) of the black shale samples in the Pennsylvanian-Early Permian Singa Formation. Full rare earths are provided for samples analysed with the solution ICPMS. Some samples were also analysed with the XRF technique - Dashes represent concentrations below the limit of the XRF technique.

Sample	LA-3412	LA 3512	LA-3612	LA 3712	LA-3812	LA 3912	LA-4012	LA 4112	LA 4312	LA-4212
La	46.6	36.6	43.7	46.3	45.2	44.9	49.3	46.8	35.2	41.7
Ce	96.2	69.1	88.7	92.5	91.9	88.8	98.0	94.1	76.2	83.5
Pr	11.0	-	10.1	-	10.5	-	11.0	-	-	10
Nd	41.0	31.4	37.7	41.2	39.4	37.3	40.1	35.7	31.3	38.9
Sm	7.9	-	7.4	-	7.8	-	7.7	-	-	8.4
Eu	1.5	-	1.3	-	1.5	-	1.4	-	-	1.4
Gd	6.7	-	6.2	-	6.4	-	6.4	-	-	7.7
Tb	1.1	-	1.0	-	1.0	-	1.0	-	-	1.3
Dy	6.4	-	5.9	-	5.9	-	5.9	-	-	7.4
Ho	1.3	-	1.2	-	1.2	-	1.2	-	-	1.5
Er	3.6	-	3.5	-	3.4	-	3.4	-	-	4.4
Tm	0.5	-	0.5	-	0.5	-	0.5	-	-	0.6
Yb	3.3	-	3.3	-	3.1	-	3.2	-	-	4.0
Lu	0.5	-	0.5	-	0.5	-	0.5	-	-	0.6

5.2.5. BRSZ Unit 1 (Late Devonian)

The results of REE analyses in sandstones are summarized in Table 5.4. The REE composition of the selected sandstone samples from the other formations shows a similar pattern to that of BRSZ Unit 1 (Fig. 5.4). The sandstones are slightly enriched in rare earth elements except in Eu. Comparatively, across selected formations including BRSZ Unit 1, all sandstone samples yield a negative Eu anomaly suggesting they have the signature of felsic rock provenance (Mishra and Sen, 2012).

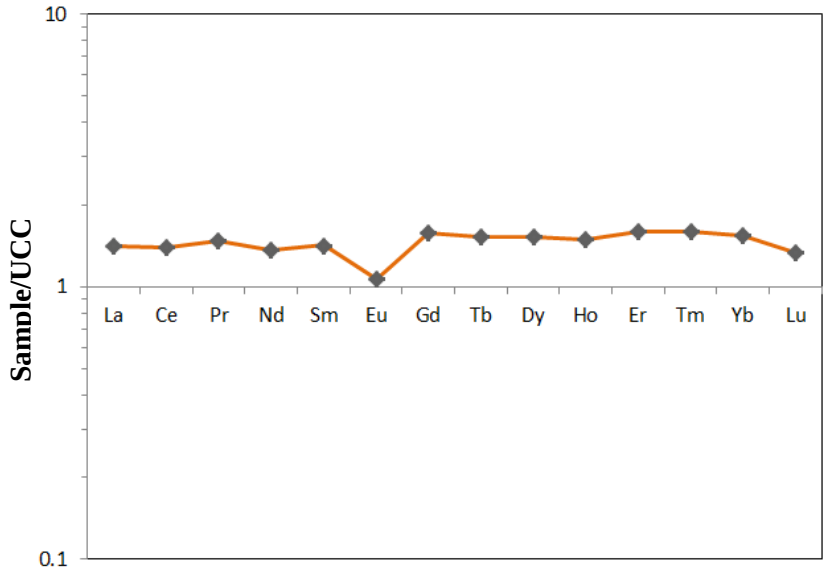

Fig. 5.4. Comparative Rare Earth Element (REE) composition of sandstones in the BRSZ Unit 1 normalised to UCC (Upper Continental Crust, data from Taylor and McLennan, 1985).

The plot (Fig. 5.4) shows a low Eu concentration compared to other REEs indicating a Eu negative anomaly. In addition, the Eu anomaly (plot 5.4) coincides with a decrease of Na_2O (mean 0.1 wt %) and CaO (mean 0.005 wt %) contents in the BRSZ Unit 1 sandstones. This suggests that the Eu anomaly may be related to the presence of feldspar minerals which weathered to hydromuscovite (section 3.5.1; Fig. 3.29) in the BRSZ Unit 1 sandstones. The feldspar minerals may have derived from the weathering of felsic igneous rocks. Miller and Mittlefehldt (1982) documented a depletion of light rare earth elements (i.e. La, Ce, Pr, Nd, Sm and Eu) with a strong Eu anomaly in the felsic igneous rocks belonging to the granite Mountains pluton of southern California. Similarly, calc-alkaline granitoids had shown increasingly negative Eu anomaly in which a loss of an exsolved LREE-rich vapour phase could account for depletion of LREE during fractionation of felsic magmas (Hon and Noyes, 1977). The plot (Fig. 5.4) shows a flat line which indicates that in most REE except Eu, there

is a very small range of variation in concentration. Hence, it appears that the ratio HREE/LREE is close to 1.

Table 5.4. REE composition (ppm) of selected sandstone samples from the BRSZ Unit 1 compared to PAAS, NASC, and UCC

	BE-2212	BE-2312	PAAS	NASC	UCC
La	42.3	41.4	38	31.1	30
Ce	83.8	85.7	80	66.7	60
Pr	9.8	9.8	8.9	-	6.7
Nd	36.9	36.3	32	27.4	27
Sm	7.5	7.3	5.6	5.59	5.3
Eu	1.4	1.3	1.1	1.18	1.3
Gd	6.3	6.2	4.7	-	4
Tb	0.9	1.0	0.8	0.85	0.65
Dy	5.7	5.8	4.4	-	3.8
Ho	1.1	1.2	1	-	0.8
Er	3.3	3.4	2.9	-	2.1
Tm	0.5	0.5	0.4	-	0.3
Yb	3.0	3.2	2.8	3.06	2
Lu	0.4	0.5	0.43	0.46	0.35

5.2.6. Semantan Formation (Middle Triassic)

The REE composition of the black shale samples of the Middle Triassic Semantan Formation is shown in Table 5.5. Results indicate that the Semantan Formation black shales are depleted in REE relative to PAAS (Post-Archean Australian Shales) (Fig. 5.5). The Machinchang Formation grey shales (Late Cambrian-Early Ordovician) have higher REE values compared to the Semantan and Singa Formation black shales (Fig. 5.5). Comparatively, the Machinchang Formation has higher REE content than the Singa and Semantan formations due to a higher Al_2O_3 content and grain size variation.

The elevated Al_2O_3 concentration is due to significant clay content. In addition, the Machinchang Formation grey shales which have elevated REE contents also have low organic carbon content. However, the Singa and Semantan formation black shales have elevated organic carbon content. The REE content in these formations appears to be controlled by the grain size and clay content.

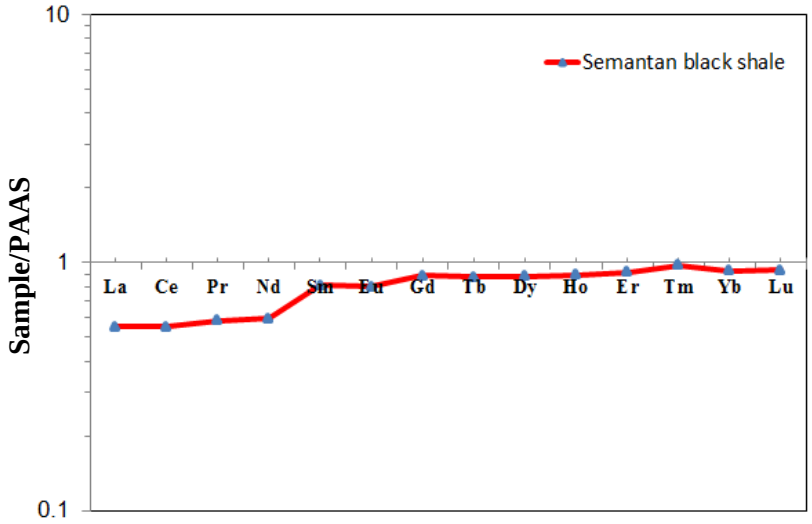

Fig. 5.5. Comparative spider diagram of REE composition in the black shales of the Semantan Formation normalised to PAAS (Post-Archean Australian Shales).

Table 5.5. Comparison of REE compositions (ppm) of the Semantan Formation black shale, Singa Formation black shale, and the Machinchang Formation grey shale, Malaysia.

	Semantan		Singa		Machinchang		PAAS
	Mean	Normalised	Mean	Normalised	Mean	Normalised	
La	21.0	0.55	45.2	1.18	87.7	2.30	38
Ce	43.8	0.55	92.4	1.16	154.9	1.95	80
Pr	5.1	0.58	10.5	1.20	23.8	2.70	8.9
Nd	20.1	0.59	39.4	1.16	96.4	2.85	32
Sm	4.5	0.81	7.7	1.38	20.1	3.63	5.6
Eu	0.8	0.80	1.4	1.32	3.8	3.55	1.1
Gd	4.1	0.89	6.4	1.38	16.6	3.57	4.7
Tb	0.7	0.88	1.0	1.35	2.4	3.12	0.8
Dy	4.1	0.88	6.1	1.31	12.6	2.70	4.4
Ho	0.8	0.90	1.3	1.27	2.3	2.33	1
Er	2.6	0.92	3.5	1.25	5.9	2.10	2.9
Tm	0.4	0.98	0.5	1.28	0.8	2.05	0.4
Yb	2.6	0.93	3.3	1.17	5.1	1.82	2.8
Lu	0.4	0.94	0.5	1.14	0.7	1.75	0.43

PAAS= Post-Archean Australian Shales (data from Taylor and McLennan, 1985).

5.2.7. Gua Musang Formation (Middle Triassic)

In this section, the REE compositions of black shale from the Gua Musang Formation are combined with data from the Semantan, Singa, and Machinchang formations and then normalised to PAAS. The REE contents in the Gua Musang Formation are given in Table 5.6. Compared to PAAS, the Gua Musang Formation black shales are slightly enriched in Sm, Eu, Gd, Tb, Dy, Ho, Er, Tm, Yb, and Lu and depleted in La, Ce, Pr, and Nd (Fig. 5.6). Comparatively, the Gua Musang Formation black shales and Singa black shales show an intermediate REE composition compared to Machinchang Formation grey shales and Semantan Formation black shales (Figs. 5.1, 5.3, and 5.5).

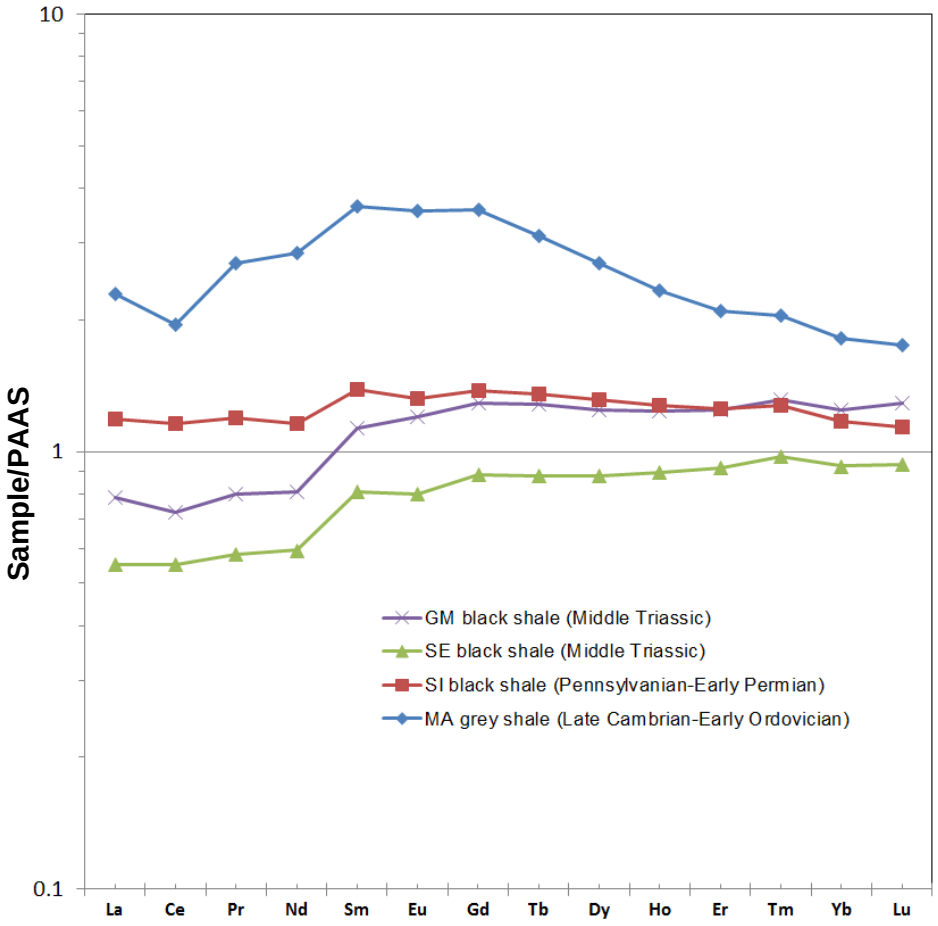

Fig. 5.6. Comparative spider diagram of REE composition in the Gua Musang (Middle Triassic) Formation black shales normalised to PAAS (Post-Archean Australian Shales) compared to other formation shales such as the Machinchang (Late Cambrian-Early Ordovician) Formation, the Singa (Pennsylvanian-Early Permian) Formation, the Semantan Formation (Middle Triassic), and the Gua Musang (Middle Triassic) Formation. The Setul Formation is not shown in this chart as it is composed of sandstones. Abbreviations used: Ma= Machinchang; SI= Singa; SE= Semantan; GM= Gua Musang.

Table 5.6. REE composition (in ppm) of selected Gua Musang Formation black shale samples, Malaysia.

	GM-0912	GM-1012	KL-0112	KL-0212	KL-0312	KL-0412	Mean	PAAS
La	34.23	23.93	16.11	33.99	33.28	38.09	29.94	38
Ce	54.68	47.64	34.77	67.29	66.59	76.71	57.95	80
Pr	5.70	6.49	4.45	8.13	8.23	9.33	7.05	8.9
Nd	18.88	26.02	19.00	31.40	32.20	36.72	27.37	32
Sm	3.26	5.89	5.73	6.30	7.18	9.29	6.27	5.6
Eu	0.53	1.13	1.40	1.19	1.46	2.10	1.30	1.1
Gd	2.53	3.81	7.46	5.12	6.38	10.75	6.01	4.7
Tb	0.42	0.53	1.25	0.85	1.06	1.84	0.99	0.8
Dy	2.48	2.63	7.38	5.14	6.38	10.90	5.82	4.4
Ho	0.55	0.48	1.53	1.15	1.38	2.29	1.23	1
Er	1.82	1.40	4.21	3.38	4.06	6.39	3.54	2.9
Tm	0.32	0.22	0.59	0.53	0.61	0.92	0.53	0.4
Yb	2.54	1.59	3.75	3.41	4.01	5.82	3.52	2.8
Lu	0.47	0.28	0.57	0.54	0.62	0.89	0.56	0.43

PAAS= Post-Archean Australian Shales (data from Taylor and McLennan, 1985)

5.2.8. Summary of REE content

- The Machinchang and Setul formations are characterised by a ratio LREE/HREE>1 suggesting that the source rocks for such sediments are enriched in La, Ce, Pr, Nd, Sm and Eu.

- The Eu anomaly recorded in the sandstones belonging to the Machinchang, Setul, Singa, and BRSZ Unit 1 formations suggests that the sediments may have been derived from a felsic source rock (Taylor and McLennan, 1985). The granitic term was replaced by felsic. And again, no rhyolite exposures were mapped in the area. Everywhere, it is only granite that crops out.

- The Machinchang Formation is the only sedimentary unit that has elevated REE contents compared to other studied formations in this study. The Setul Formation is highly depleted in all REE relative to other formations.

5.3. Provenance and tectonic setting

Chemical compositions of sandstones and shales have been used to suggest sediment source area and their tectonic settings (Drost et al., 2003; Cingolani et al., 2003; Jafarzadeh and Hosseini-Bazri, 2008; Mishra and Sen, 2012; Hinchey, 2012). The source rock composition is an important parameter that controls the composition of the forming sedimentary rocks (Taylor and McLennan, 1985).

In this study, trace elements and some rare earth elements (REE) including La, Zr, Th, Sc are also used for provenance determination due to their low mobility during weathering, transport, diagenesis and metamorphism (Nyakairu and Koeberl, 2001). The ratio of some immobile elements such as La and Th (evidence for felsic provenance) over compatible elements such as Sc and Cr (evidence for mafic provenance) is also used to distinguish between felsic and mafic parent rocks (McLennan, 1989; McLennan and Taylor, 1991; McLennan et al., 1980; Wronkiewicz and Condie, 1990).

It is argued that the Al_2O_3/TiO_2 ratio for mafic rocks varies from 3 to 8, for intermediate rocks from 8 to 21 and for felsic igneous rocks between 21 and 70 (Noori and Rais, 2014). However, the Al_2O_3/TiO_2 ratio is not entirely reliable unless combined with grain size variation data which is lacking in this thesis. The discriminant function diagram of Roser and Korsch (1988) use the major elements Al_2O_3, TiO_2, Fe_2O_3, MgO, CaO, Na_2O, and K_2O contents as variables for provenance interpretation. The La-Th-Sc plot also helps discriminate between felsic and mafic source rocks (Taylor and McLennan, 1985; Bhatia and Crook, 1986).

5.3.1. Provenance and tectonic setting of the Machinchang Formation

Provenance and tectonic setting of the Late Cambrian-Early Ordovician Machinchang Formation sandstones is discussed in this section using Th-Sc, discrimination functions, La-Th-Sc, and Q-F-L plots. The plots of Th versus Sc (Fig. 5.7A) and La versus Th also indicate a felsic provenance for the Machinchang sandstones (Taylor and McLennan, 1985). The two discriminant functions of Roser and Korsch (1988) are (1) Discriminant function 1= -1.773 TiO_2 + 0.607 Al_2O_3 + 0.76 Fe_2O_3 – 1.5 MgO + 0.616 CaO + 0.509 Na_2O – 1.224 K_2O – 9.09; and (2) Discriminant function 2= 0.445 TiO_2 + 0.07 Al_2O_3 – 0.25 Fe_2O_3 – 1.142 MgO + 0.438 CaO + 1.475 Na_2O + 1.426 K_2O – 6.861.

Roser and Korsch (1988) defined four fields to discriminate sediment provenance. The four fields or sources are felsic igneous, quartzose sedimentary, intermediate igneous and mafic igneous. Ryan and Williams (2007) stressed that using the discriminant diagram based on major elements appears more representative than the Th versus Sc plot of the source rock lithology.

The Machinchang Formation shales plot in the felsic source field and the Machinchang Formation sandstones are on the boundary of the quartzose sedimentary source field. The La-Th-Sc plot (Fig. 5.7C) suggests a mixed source. Additionally, the geochemical and point count data of quartz, feldspar and rock fragment abundance are used to plot the QFL ternary diagram to discuss tectonic setting (e.g. Dickinson et al., 1983). The QFL diagram is plotted based on estimated percentage (using visual estimate) of quartz (Q), feldspar (F) and rock fragments (L) contained in thin sections made from the sandstones (Fig. 5.7D).

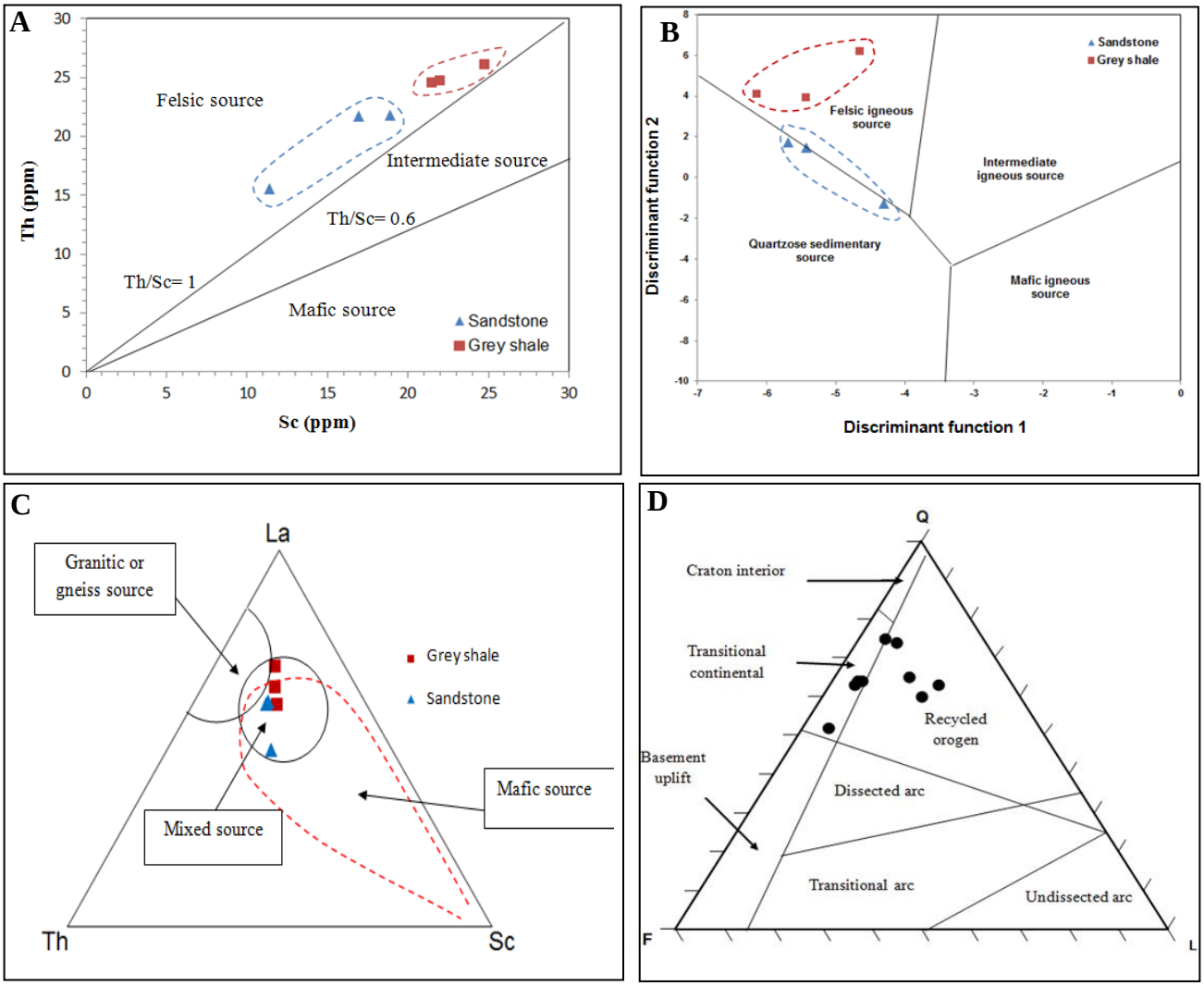

Fig. 5.7. Provenance and tectonic setting plots for the Late Cambrian-Early Ordovician Machinchang Formation. **A**) Th-Sc plot. **B**) Discriminant diagram (adapted from Roser and Korsch, 1988). **C**) La-Th-Sc plot (adapted from Taylor and McLennan, 1985; Bhatia and Crook, 1986; Hinchey, 2012). **D**) Quartz (Q)-Feldspar (F)-Lithics (L) plot (adapted from Dickinson et al., 1983).

Cullers et al. (1987) argued that secondary processes such as weathering, transport and diagenesis may have an effect on the rock composition. The diagram (Fig. 5.7D) shows that most sandstone samples cluster in both the transitional continental and recycled orogen fields. Provenance and tectonic studies have revealed that most sediments of the Machinchang

Formation were derived from a felsic source and that the tectonic setting was likely to be an active continental margin (Fig. 5.8) within the Sibumasu Terrane.

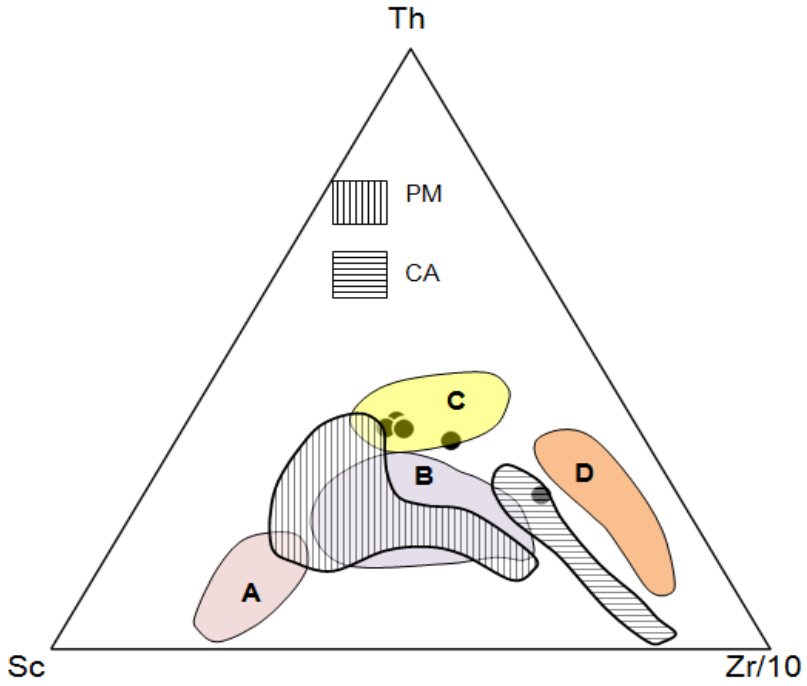

Fig. 5.8. Ternary diagram Th-Sc-Zr/10 of the Machinchang Formation sandstones Langkawi Island, Malaysia. Discrimination plot of tectonic setting after Bhatia and Crook (1986). A= ocean island arc; B= continental island arc; C= active continental margin; D= passive margin; PM= recent deep-sea turbidites derived from and deposited at a passive margin; CA= recent deep-sea turbidites derived from and deposited at a continental arc margin. The dataset indicates derivation from an active continental margin.

The high ratio of LREE over HREE (LREE/HREE = 6.9) points to a felsic source for the Machinchang Formation black shales.

5.3.2. Provenance and tectonic setting of Setul Formation sandstones

Provenance plots for the Setul Formation are shown in Fig. 5.9. The Th/Sc ratio varies from 1.57 to 3.21 (mean 2.38). The La/Th ratio ranges from 2.6 to 3 (mean 2.8). The data

clearly indicate a dominantly felsic source rock for the Early Ordovician-Silurian Setul Formation (Taylor and McLennan, 1985) and an active continental margin setting.

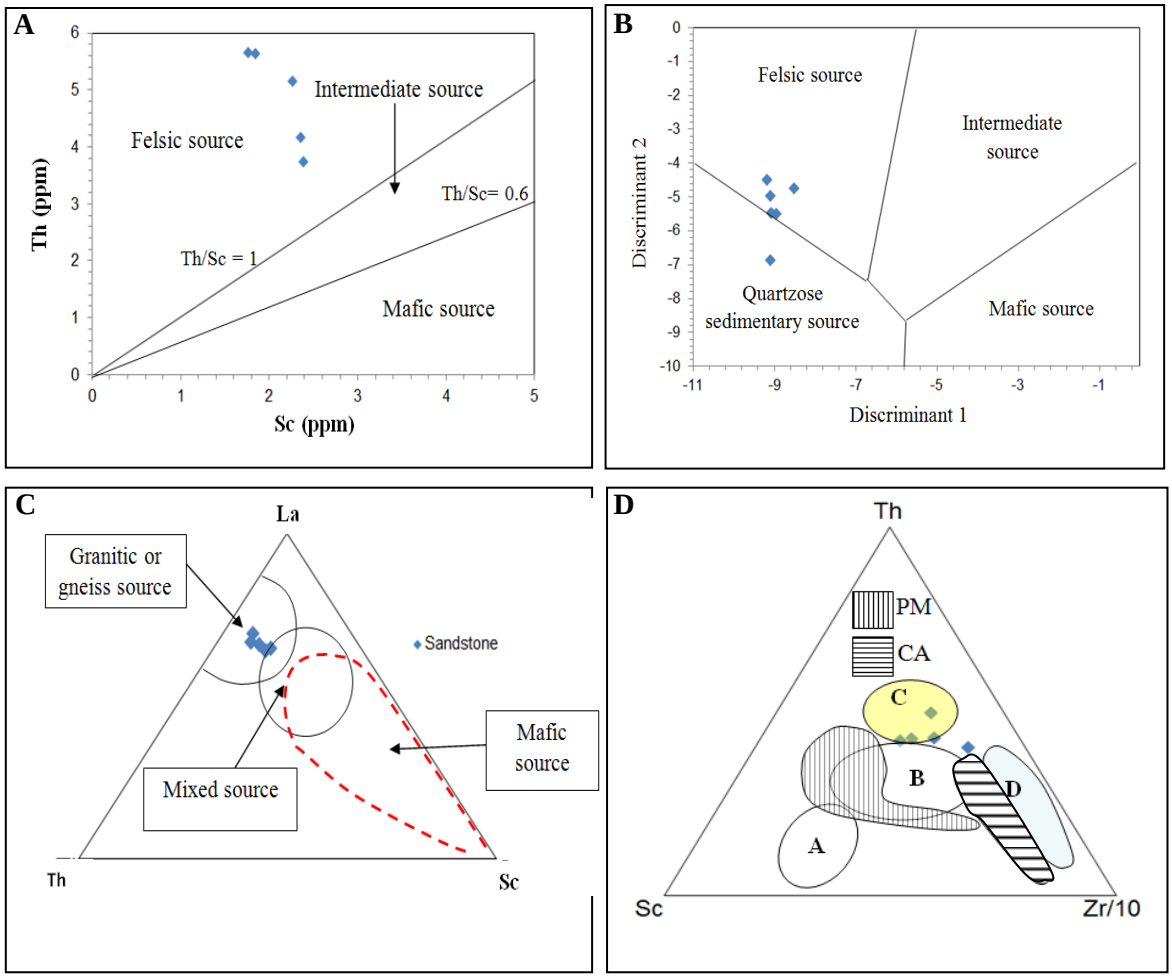

Fig. 5.9. Provenance and tectonic setting plots for the Early Ordovician-Silurian Setul Formation. **A**) Th-Sc plot (adapted from Taylor and McLennan, 1985). All samples plot above the Th/Sc = 1 line in the felsic source field. **B**) Discriminant diagram. Samples plots preferentially in the felsic source field. **C**) La-Th-Sc plot (adapted Taylor and McLennan, 1985; Bhatia and Crook, 1986). Most samples plot in the granitic/gneiss field. **D**) Th-Sc-Zr/10 plot. Analyses indicate that samples mostly cluster in the active continental margin area. Abbreviation used: PM= recent deep-sea turbidites derived from and deposited at a passive margin; CA= recent deep-sea turbidites derived from and deposited at a continental arc margin (data from McLennan at al., 1990). A= ocean island arc; B= continental island arc; C= active continental margin; D= passive margin. The likely tectonic setting is the Sibumasu Terrane as discussed in Chapter 2.

5.3.3. Provenance and tectonic setting of the Singa Formation

Provenance and tectonic setting of the Pennsylvanian-Early Permian Singa Formation is documented below. The first approach that has been used is to plot the Th-Sc diagram as shown below (Fig. 5.10A). The plot indicates a predominantly felsic provenance. The La-Th-Sc plot (Fig. 5.10C) is used to discriminate between felsic and mafic source rocks for sedimentary rocks (Taylor and McLennan, 1985; Bhatia and Crook, 1986). The plot shows a mixed provenance for the Singa Formation. The discriminant functions (Fig. 5.10B) of Roser and Korsch (1988) use the major elements Al_2O_3, TiO_2, Fe_2O_3, MgO, CaO, Na_2O, and K_2O contents as variables. This plot suggests that there are three possible sources, including felsic, intermediate igneous and quartzose sedimentary rocks for the Singa Formation.

The QFL (quartz-feldspar-lithics) diagram displays two possible tectonic settings for the Singa Formation sandstones (Fig. 5.10D): transitional continental or recycled orogen Bhatia and Crook (1986) suggested that low-mobility trace elements such as La, Th, Y, Zr, Ti, Co and Ni are useful for provenance discrimination. In this study, the data indicate that the sandstones and black shales of the Singa Formation may have derived from an active continental margin and/or continental island arc (Fig. 5.11). Samples that cluster closer and in the “C” field (Fig. 5.11) imply an active continental margin. The REE data show a slightly high LREE/HREE (LREE/HREE = 8.7) ratio suggesting a felsic provenance signature for the Singa Formation. The fact that sandstones and black shales do not always plot in the same place may well suggests different parent rocks. The black shales may have derived from an intermediate-felsic source. Conclusively, sandstones and shales derived from two different sources. Shales likely derived from felsic parent rocks whereas sandstones from a mixed source (Fig. 5.10B).

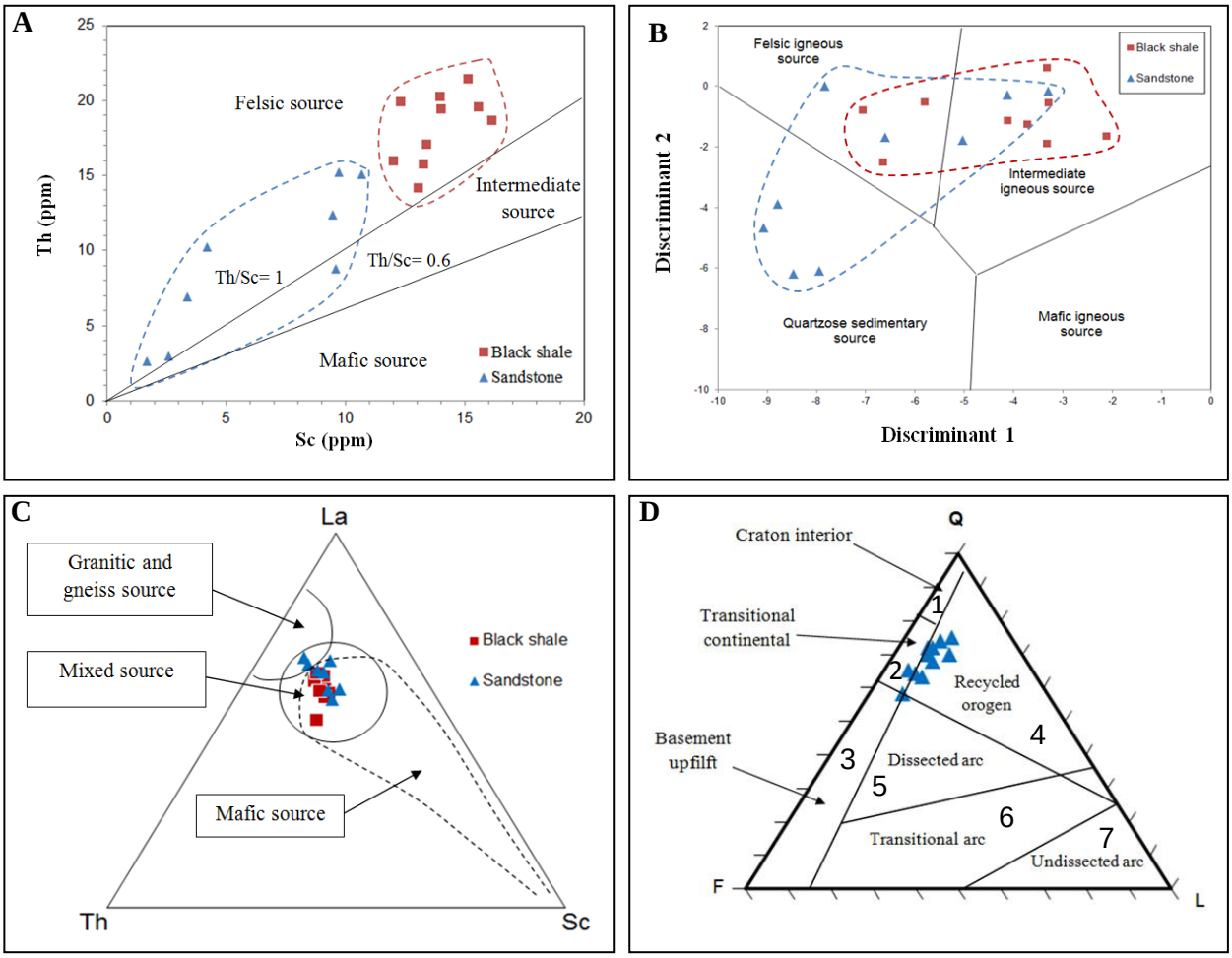

Fig. 5.10. Provenance and tectonic setting plots for the Pennsylvanian-Early Permian Singa Formation. **A**) Th-Sc plot. The black shales and sandstones show two populations although plotting above the Th/Sc = 1 line strictly in the felsic source field. This suggests they may not have derived from the same felsic parent rock. Black shale sample composition in Th and Sc appear grouped whereas the sandstones samples are spread along the line Th/Sc = 1. **B**) Discriminant diagram (adapted from Roser and Korsch, 1988).The black shales samples plot within the felsic and intermediate igneous source fields. However, the sandstone samples are scattered across the quartzose sedimentary, felsic-intermediate source fields. **C**) La-Th-Sc plot (adapted from Taylor and McLennan, 1985; Bhatia and Crook, 1986; Hinchey, 2012). Most samples plot in the mixed source field regardless of whether they are black shales or sandstones. **D**) Quartz (Q)-Feldspar (F)-Lithics (L) plot (adapted from Dickinson et al., 1983). Fields: 1- Craton interior; 2 - Transitional continent; 3 - Basement uplift; 4 – Recycled orogen; 5 – Dissected arc; 6 – Transitional arc; 7 – Undissected arc. Note: Q= quartz; F= feldspar; L= lithics or rock fragments. In this plot, the majority of sandstone samples plot in the recycled orogen field but also touching the boundary with the transitional continental field.

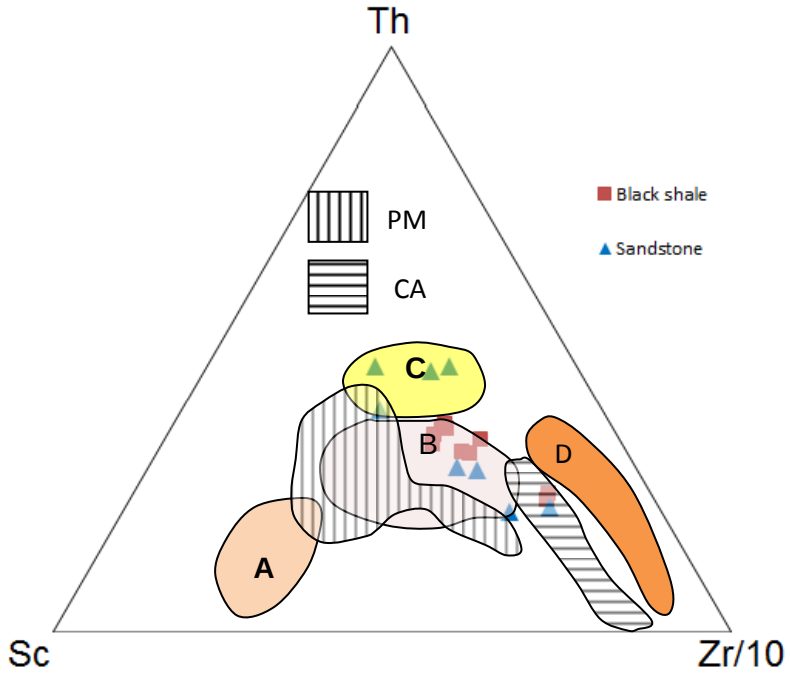

Fig. 5.11. Ternary diagram Th-Sc-Zr/10 of the Singa Formation sandstone and black shale, Langkawi Island, Malaysia. Discrimination plot of tectonic setting after Bhatia and Crook (1986). A= ocean island arc; B= continental island arc; C= active continental margin; D= passive margin; PM= recent deep-sea turbidites derived from and deposited at a passive margin; CA= recent deep-sea turbidites derived from and deposited at a continental arc margin (data from McLennan at al., 1990). The data infer derivation from broadly two sources: an active continental margin and/or a continental island arc.

5.3.4. Provenance and tectonic setting of BRSZ Unit 1

Provenance and tectonic setting plots of the BRSZ Unit 1 are shown in Fig. 5.12. The Th versus Sc plot displays data that cluster along, above, and below the Th/Sc= 1 line for the sandstones whereas for the black shales all scatter above the Th/Sc= 0.6 line. In these plots, the Th/Sc= 1 is for the upper continental crust (UCC). The plot (Fig. 5.12A) indicates a dominantly intermediate source for the sandstones and black shales.

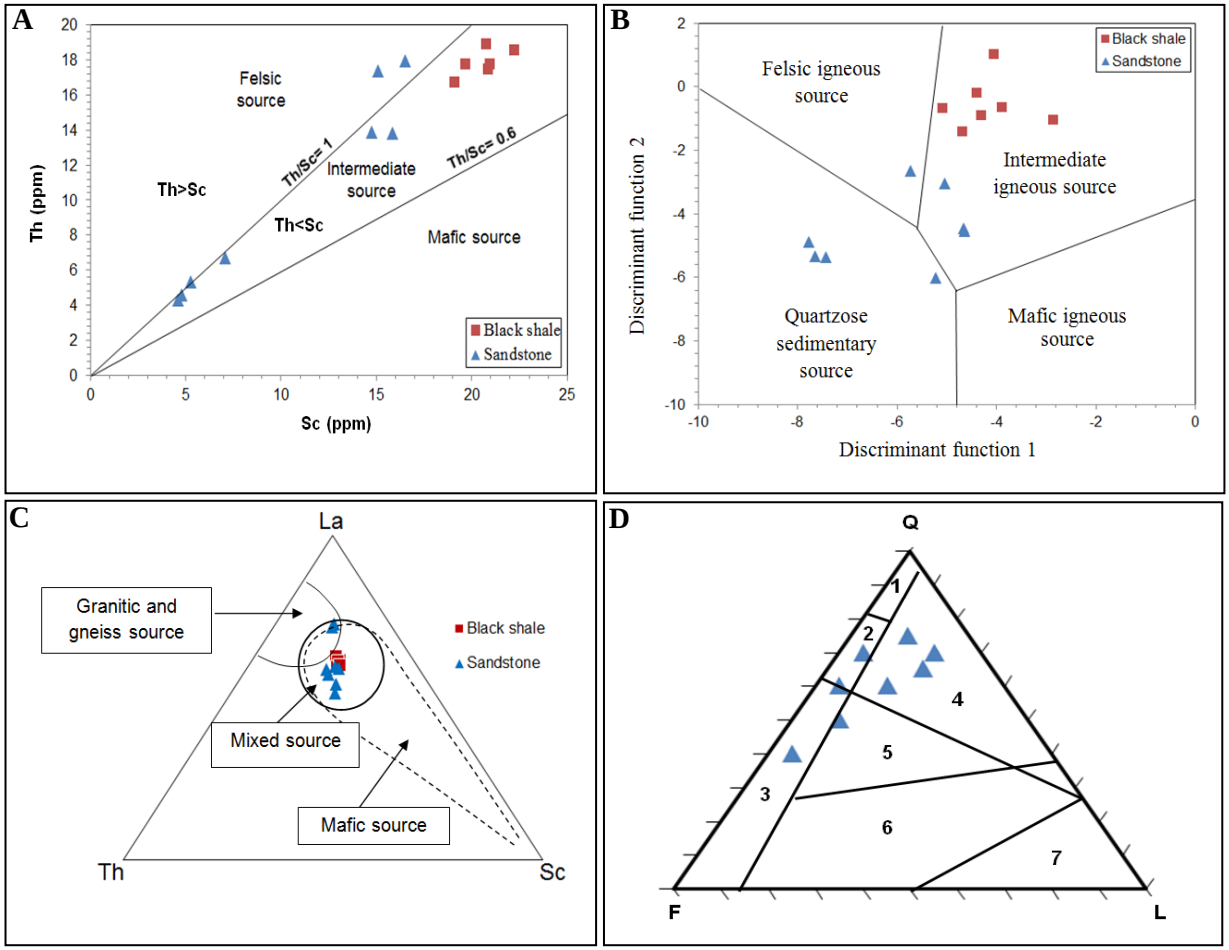

Fig. 5.12. Provenance and tectonic setting plots for the Late Devonian BRSZ Unit 1. **A**) Th-Sc plot. Sandstone samples preferably plot in both the felsic and intermediate source fields. **B**) Discriminant diagram (adapted from Roser and Korsch, 1988). Black shale samples stand alone and plot in the intermediate source filed whereas sandstone samples are scattered. **C**) La-Th-Sc plot (adapted from Taylor and McLennan, 1985; Bhatia and Crook, 1986; Hinchey, 2012). All samples plot in the mixed source field. **D**) Quartz (Q)-Feldspar (F)-Lithics (L) plot (adapted from Dickinson et al., 1983). Fields: 1- Craton interior; 2 - Transitional continent; 3 - Basement uplift; 4 – Recycled orogen; 5 – Dissected arc; 6 – Transitional arc; 7 – Undissected arc. Note: Q= quartz; F= feldspar; L= lithics or rock fragments. The sandstone samples are spread across the transitional continent, basement and recycled orogen fields. Black shale data indicate a felsic provenance wheares the sandstone data suggests a mixed source.

In order to confidently constrain the source rocks for the BRSZ Unit 1, the discriminant diagram using only major elements is also proposed (Fig. 5.12B). The plot (Fig. 5.12.B) suggests an intermediate and quartzose sedimentary source provenance for the sandstones. However, the black shales also indicate intermediate parent rocks (Fig. 5.12A and B). The La-Th-Sc plot (Fig. 5.12C) indicates a mixed source for the BRSZ Unit 1. A similar approach has been used to determine the nature of the source rocks in most recent research (Jafarzadeh and Hosseini-Bazri, 2008; Hinchey, 2012).

Considering all the plots, the sandstones are not consistently related to a single provenance, indicating a possible mixing of sources. In contrast, the black shales cluster together and have an intermediate source rock signature. The evidence indicates that none of the analysed samples have a mafic provenance. The low concentration in MgO supports the conclusion that source rocks of the BRSZ Unit 1 were not mafic as Mg is essentially enriched in ferromagnesian minerals such as olivine, pyroxene, and amphibole.

The low MgO may be related to chemical weathering and leaching of magnesium from the bedrock. The REE patterns can also be used to infer sources of siliciclastic rocks. It is known that lower LREE/HREE ratios and no Eu anomalies points to a mafic source; however, higher LREE/HREE ratios and negative Eu anomalies indicates a felsic provenance (e.g. Wronkiewicz and Condie, 1987).

Comparatively, the REE plot of sandstone samples show an Eu negative anomaly for the BRSZ Unit 1 (Fig. 5.4), and the Setul Formation (Fig. 5.2) sandstones consistent with a felsic source for the sediments. The quartz, feldspar and lithic fragments were estimated in order to produce a QFL diagram, which usually discriminates tectonic settings of sandstones (Table 5.7). The plot (Fig. 5.12D) shows that the sandstones of BRSZ Unit 1 have the signature of a recycled orogen and basement uplift.

Table 5.7. Estimated amounts of quartz, feldspar and rock fragments (lithics) in sandstone for the BRSZ Unit 1, Malaysia.

Sample no.	Sorting	Monocrystalline qtz (%)	Polycrystalline qtz (%)	Feldspar (%)	Mica (%)	Calcite (%)	Lithics (%)
BE-2312	P	55	5	25			>15
BE-4713-A	P	55	-	>20			>5
BE-4713-B	P	50	-	24			20
BE-4713-C	M	65	-	15			20
BE-3313-A	P	60	-	33			5
BE-3313-B	P	70	-	20			12
BE-3213-A	P	70	-	25			5
BE-3213-B	P	65	-	18			20

Keys for sorting: P for poorly sorted; M for moderately sorted.

The sample location of the BRSZ Unit 1 (latitude 3°35'26.77''N; longitude 101°54'4.03''E) indicates close proximity to the Bentong-Raub Suture Zone of the Malay Peninsula. The suture zone represents the Palaeo-Tethys ocean basin, which forms the boundary between the Sibumasu Terrane in the west and the Sukhothai Arc in the east (Makoundi et al., 2014). The active continental margin setting interpretation of the BRSZ Unit 1 can be explained by the dynamics of the closure of the Palaeo-Tethys Ocean during the collision of the Sibumasu Terrane and the Sukhotai Arc in Peninsular Malaysia (Makoundi et al., 2014).

There is evidence that the accretionary wedge was developed during the collision of the Sibumasu and Indochina terranes and the intrusion of granitoids in the Late Triassic (e.g. Metcalfe, 2000). The accretionary wedge was developed during the collision of the Sibumasu and Indochina terranes and the intrusion of granitoids in the Late Triassic. The evidence also

suggests that the BRSZ Unit 1 sandstones record a recycled orogen and basement uplift signature implying that the BRSZ Unit 1 sediments may have derived from the East Malaya terrane not the accretionary complex. The Th-Sc-Zr plot points to a continental island arc (B field) for the BRSZ Unit 1 (Fig. 5.13).

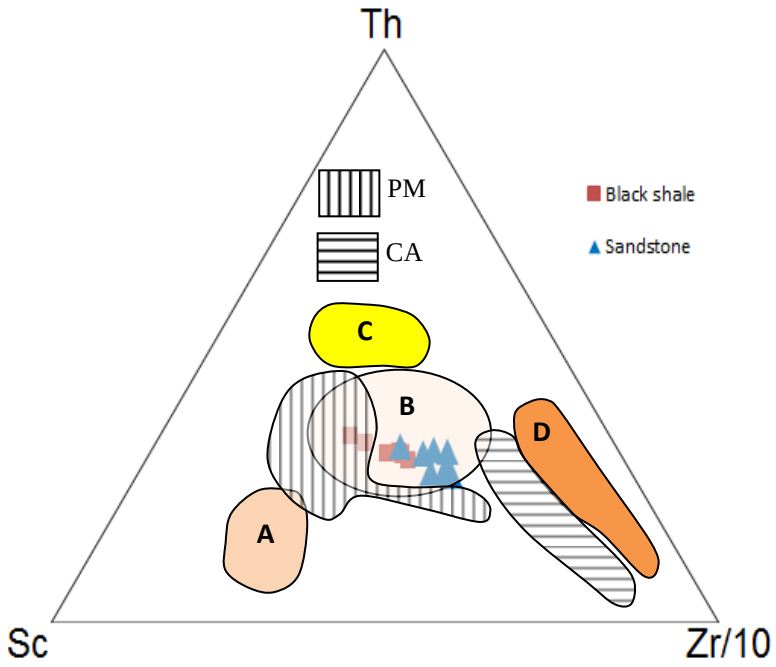

Fig. 5.13. Ternary Th-Sc-Zr/10 discrimination plot of the BRSZ Unit 1 (Late Devonian) sandstones and black shales, Malaysia after Bhatia and Crook (1986). Discrimination plot of tectonic setting after Bhatia and Crook (1986). A= ocean island arc; B= continental island arc; C= active continental margin; D= passive margin; PM= recent deep-sea turbidites derived from and deposited at a passive margin; CA= recent deep-sea turbidites derived from and deposited at a continental arc margin.

5.3.5. Provenance and tectonic setting of Semantan Formation

Provenance and tectonic diagrams are given below for source rocks of the Semantan Formation black shales (Fig. 5.14). The plot Th-Sc (Fig. 5.14A) indicates a predominantly mafic source for the black shales in the Semantan Formation. The discriminant diagram (Fig.

5.14B) also shows a mafic source. The La-Th-Sc plot (Fig. 5.14C) displays mixed and mafic sources. Overall, the Semantan sedimentary rocks have a mafic source. The tectonic setting diagram indicates an oceanic island arc environment for the Semantan Formation (Fig. 5.14D). The mafic provenance of the Semantan Formation may be inherited from the mafic plutonic rocks such as gabbro present in the Gunong Benon area and basaltic flows that crop out in Segamat, south of the Semantan basin.

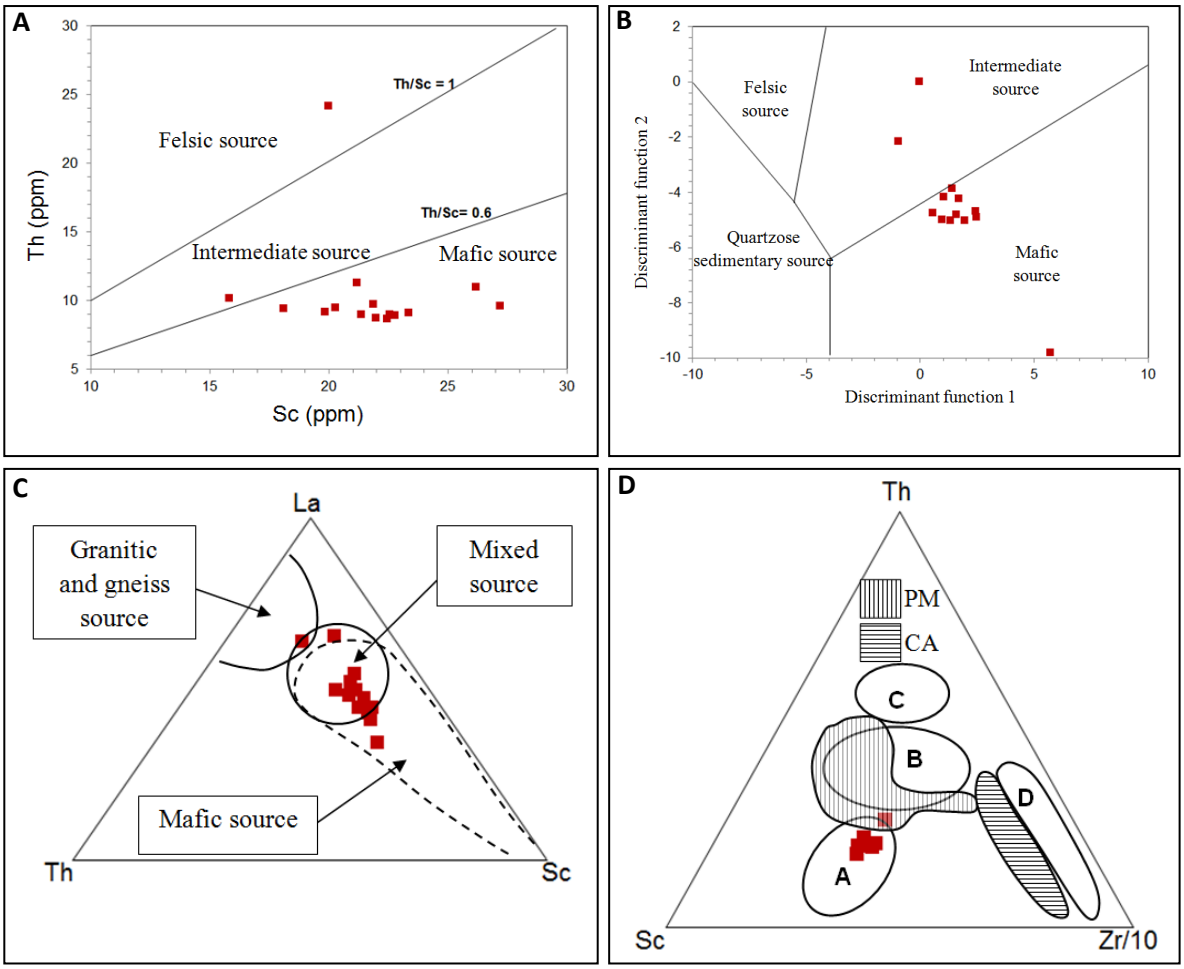

Fig. 5.14. Provenance and tectonic setting plots for the Semantan Formation. **A**) Th-Sc plot (adapted from Taylor and McLennan, 1985). Data for the black shales indicate a predominantly mafic source. **B**) Discriminant diagram (adapted from Roser and Korsch, 1988). Data suggests a mafic source for the most part. **C**) La-Th-Sc plot (adapted Taylor and McLennan, 1985; Bhatia and Crook, 1986). Samples plot in the mixed and mafic provenance fileds. **D**) Th-Sc-Zr/10 plot. PM= recent deep-sea turbidites derived from and deposited at a passive margin; CA= recent deep-sea turbidites derived from and deposited at a continental arc margin (data from McLennan et al., 1990). A= Ocean island arc; B= Continental island arc; C= Active continental margin; D= Passive margin. Samples plot in the oceanic island arc field.

5.3.6. Provenance and tectonic setting of Gua Musang Formation

Provenance and tectonic setting plots for the Gua Musang Formation shales are shown below (Fig. 5.15).

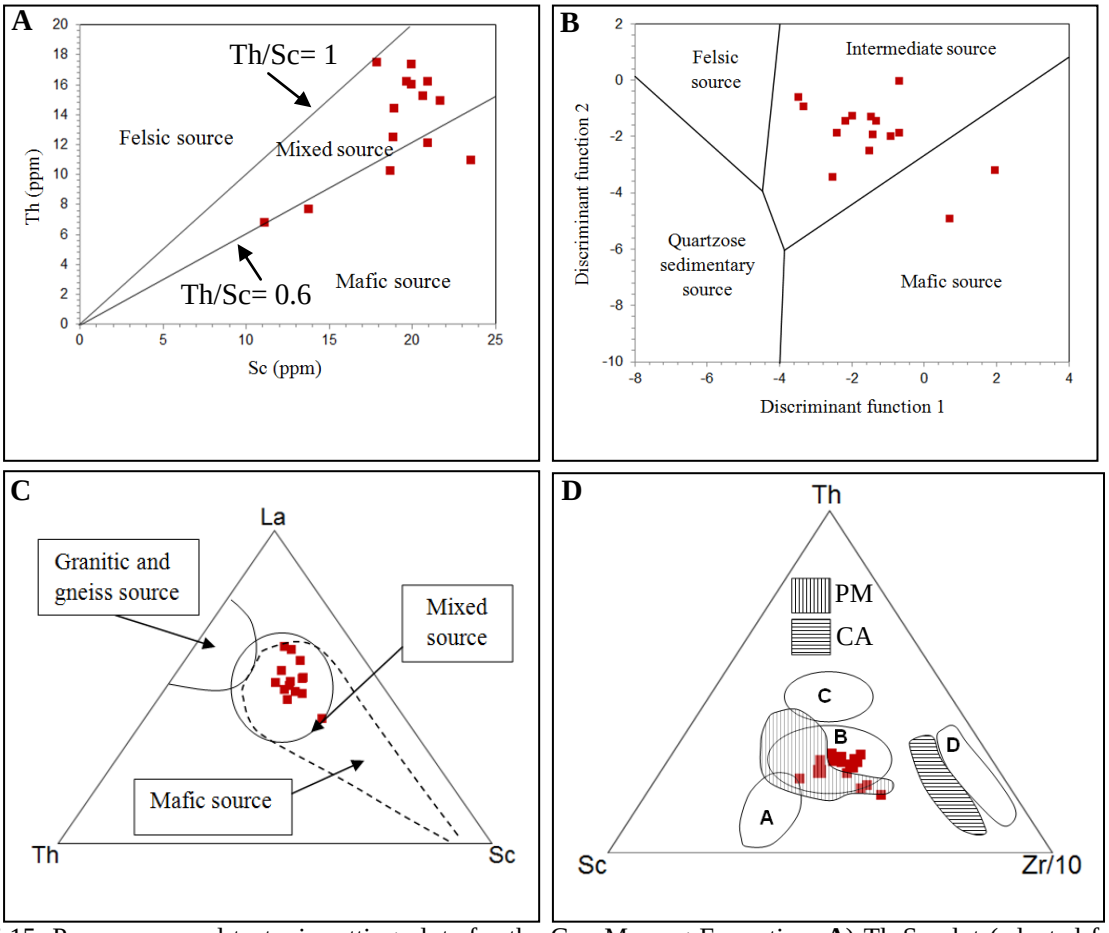

Fig. 5.15. Provenance and tectonic setting plots for the Gua Musang Formation. **A**) Th-Sc plot (adapted from Taylor and McLennan, 1985). Samples indicate a mixed source with possibly mafic contribution. **B**) Discriminant diagram (adapted from Roser and Korsch, 1988). Consistently, this plot shows intermediate or mixed source plus mafic input. **C**) La-Th-Sc plot (adapted Taylor and McLennan, 1985; Bhatia and Crook, 1986). Samples plot in the mixed source field. **D**) Th-Sc-Zr/10 plot. PM= recent deep-sea turbidites derived from and deposited at a passive margin; CA= recent deep-sea turbidites derived from and deposited at a continental arc margin. A= Ocean island arc; B= Continental island arc; C= Active continental margin; D= Passive margin. A continental island arc is a preferred tectonic setting.

The Th versus Sc plot (Fig. 5.15A) shows that most Gua Musang black shale data cluster above the Th/Sc= 0.6 line and few data points are below this line, indicating a minor contribution from mafic rocks (plots A and B) and a major contribution from intermediate parent rocks (plot C) rocks. Most sediment may have derived from the plutonic complexes such as the Benta complex (intermediate to mafic rocks) and the Benom granite of calc alkali affinity, complexes which are exposed south of the Gua Musang basin in the central gold belt of Peninsular Malaysia. The discriminant function diagram shows a mixed source for the Gua Musang Formation (Fig. 5.15B). The La-Th-Sc plot (Fig. 5.15C) indicates a mainly mixed source for the black shales in the Gua Musang Formation. In addition, the Th-Sc-Zr plot suggests a continental island arc setting (Fig. 5.15D). The evidence strongly indicates an intermediate source rock for the Gua Musang Formation and a continental island arc tectonic setting (Figs. 5.15A and B). Provenance and tectonic setting for the selected Phanerozoic formations is summarized in Table 5.8.

Table 5.8. Provenance and tectonic settings of the selected Phanerozoic formations (this study) in Malaysia

Formation	Age	Provenance	Tectonic setting
Gua Musang	Middle Triassic	Intermediate	Continental island arc
Semantan	Middle Triassic	Mafic	Oceanic island arc
BRSZ Unit 1	Late Devonian	Intermediate	Recycled orogen
Singa	Pennsylvanian-Early Permian	Felsic-intermediate	Continental island arc
Setul	Early Ordovician-Silurian	Felsic	Continental margin
Machinchang	Late Cambrian-Early Ordovician	Felsic	Continental margin

5.4. Relationship between provenance and sedimentary pyrite TE composition

The aim of this section is to determine whether the provenance of sedimentary rocks has an effect on the trace element (TE) composition of sedimentary pyrite. Commonly, the trace elements more abundant in felsic rocks are Bi and Tl whereas those that are abundant in mafic rocks include Cr, Co, Cu and Ni. The mean concentration (in ppm) of elements such as Cr, Co, Cu, Ni, Bi and Tl in sedimentary pyrites compared with the provenance signature of each formation is summarised in Table 5.9 below.

Table 5.9. Mean composition (ppm) of Ni, Co, Cu, Bi, and Tl in sedimentary pyrite relative to provenance (this study). Note: - no data or concentration unknown.

Number of analyses (n = 185)	Mean Ni	Mean Co	Mean Cr	Mean Cu	Mean Bi	Mean Tl	Ni/Co	Ni/Tl
Gua Musang Intermediate (**East Malaya Terrane**)	562	14	-	486	1	6	40 Ni/Co>1	94 Ni/Tl<100
Semantan mafic **(East Malaya Terrane)**	297	256	-	1122	55	4	1.2 Ni/Co>1	74 Ni/Tl<100
BRSZ Unit 1 Intermediate **(East Malaya Terrane)**	1047	15	-	596	0.9	4	0.9 Ni/Co<1	262 Ni/Tl>100
Singa felsic-intermediate **(Sibumasu Terrane)**	2245	2307	-	1245	120	1	0.97 Ni/Co<1	2245 Ni/Tl>100
Setul-felsic	-	-	-	-	-	-	-	-
Machinchang-felsic	-	-	-	-	-	-	-	-

Data in Table 5.9 summarizes trace element concentrations in sedimentary pyrite for selected formations with their provenance interpretation (i.e. intermediate, mafic or intermediate-mafic). The evidence indicates that Co and Cu have elevated contents in sedimentary pyrite belonging to the Semantan Formation which has a mafic provenance. Such higher Co and Cu concentrations in sedimentary pyrite may be used as proxies for provenance of sedimentary rocks on the East Malaya Terrane (this study). Other proxies such as Ni/Co and Ni/Tl in sedimentary pyrite can also be used for provenance. This interpretation on provenance using Co and Cu contents in sedimentary pyrite is not conclusive. Despite a low number of analyses (n= 185), this study has demonstrated that in sedimentary pyrite (e.g. Semantan Formation) sediments of mafic provenance yield Ni/Co ratio greater than 1 and Ni/Tl less than 100.

In contrast, the composition of sedimentary pyrites in black shales of intermediate provenance (i.e. BRSZ Unit 1) displays Ni/Co ratios less than 1 and Ni/Tl ratios greater than 100. Comparatively, the Bi content in sedimentary pyrite from the Singa Formation (felsic-intermediate) which lies in the Sibumasu Terrane is higher than that from other formations of intermediate-mafic provenance, found on the East Malaya Terrane, indicating that Bi content may be used as a provenance proxy. Again, this interpretation is not conclusive and needs a robust dataset in future research. In future research, grain size will account when dealing with chemistry of sedimentary pyrite. Nevertheless, it is essential to know that the amount of sedimentary pyrite is commonly related to the fraction of mud (<1/16 mm in grain size) in the sediments. Sedimentary pyrites grow either in the water column or in the mud. Therefore, when this study refers to shales and sandstones and cherts, it is clear that the grains size vary across these lithologies. Therefore from a sedimentological point of view, there is no confusion

in grain size between shales, sandstones and cherts as they have been described in this thesis (chapter 2).

5.5. Seafloor redox conditions

A number of redox proxies have been used to imply the palaeo-oxygenation of the seawater environment. Ratios such as U/Th, V/Cr, Ni/Co, and V/V+Ni are used to discuss paleo-oxygenation conditions (e.g. Dypvik, 1984; Dill, 1986; Dill et al., 1988; Hatch and Leventhal, 1992; Jones and Manning, 1994; Rimmer, 2004; Riquier et al., 2005). Recent studies have revealed that low content of Mo in black shales implies restriction of H_2S consistent with suboxic bottom waters in the ocean (Meyers et al., 2005; Dumoulin et al., 2011). A summary of palaeoredox proxies are given in Tables 5.11-5.13. The U/Th ratio is sensitive to the relative input of Th-bearing clay minerals and U that is fixed in sediments during diagenesis in euxinic environments (Athur and Sagenan, 1994). Increasing V content over Ni may indicate sulfidic (euxinic) conditions and variation in the V/V+Ni ratio may imply relative changes in oxygenation in the water column. Cobalt behaves differently in oxic and anoxic conditions.

In oxic environment, Co is present in the form of dissolved cation Co^{2+} or is complexed with humic/fulvic acid (Saito et al., 2002). In oxygenated water, chromium is in the form of a cation Cr (VI) in the chromate anion CrO_4^{2-}. In normal seawater conditions, this anion is soluble but in anoxic conditions of a cation Cr (IV) which is reduced to a cation Cr (III). It is during the anoxic conditions that Cr^{3+} forms aquahydroxyl and hydroxyl cations ($Cr(OH)_2^+$, $Cr(OH)_3$, $(Cr,Fe)(OH)_3$) which can complex with humic and fulvic acid or adsorb to Fe- and Mn-oxyhydroxides (Algeo and Maynard, 2004).

Table 5.10. Selected trace elements from shale samples for paleoredox proxy estimation

Sample No.	Formation	V	Cr	Ni	Cu	Zn	U
GM-0912	Gua Musang	132.60	59.25	20.47	25.42	14.94	4.02
GM-1012	Gua Musang	170.90	76.65	7.88	8.39	12.98	2.80
GM 1212	Gua Musang	120.90	41.70	19.09	11.78	19.07	5.24
GM 1312	Gua Musang	139.30	60.30	11.68	6.76	15.44	4.67
KL 0512	Gua Musang	139.90	54.20	25.08	22.33	66.74	4.38
KL-0112	Gua Musang	135.80	50.15	49.58	74.54	194.37	2.78
KL-0212	Gua Musang	166.30	59.80	26.10	18.38	55.24	3.75
KL-0312	Gua Musang	138.70	52.75	15.51	26.14	68.33	2.84
KL-0412	Gua Musang	131.70	49.90	17.70	45.61	43.19	2.93
TP-1512	Gua Musang	163.80	63.50	22.95	37.38	8.91	3.81
TP-1612	Gua Musang	154.50	65.70	21.83	33.90	62.49	4.02
PJ 1812	Gua Musang	39.80	11.30	6.70	12.70	56.58	5.10
PJ 1912	Gua Musang	42.60	12.10	7.01	9.73	58.66	4.60
PJ 2112	Gua Musang	85.90	17.40	8.22	15.06	82.60	4.81
ME-5912	Semantan	135.80	59.20	38.28	86.85	13.37	3.59
ME-6612	Semantan	215.50	57.00	19.09	6.25	15.44	4.74
ME-10013	Semantan	98.70	32.60	18.61	21.50	196.85	1.95
ME-10113	Semantan	161.60	52.80	20.09	40.22	84.24	2.32
ME-10213	Semantan	169.28	54.14	16.54	24.90	66.27	3.10
ME-9413	Semantan	168.04	45.62	15.65	33.62	75.01	2.30
ME-9513	Semantan	179.45	47.58	14.25	34.70	71.15	3.10
ME-9613	Semantan	145.02	51.79	19.33	23.93	76.03	4.20
ME-9713	Semantan	173.49	49.05	22.72	35.67	84.16	2.90
ME-9813	Semantan	174.52	49.44	15.15	27.48	68.31	2.40
ME-9913	Semantan	183.67	50.32	15.05	30.50	70.24	2.40
ME-6212	Semantan	169.48	52.28	16.44	22.20	66.48	2.50
ME-6312	Semantan	157.87	50.13	14.95	27.16	71.56	2.40
BE-2813	BRSZ Unit 1	230.74	103.58	23.22	20.80	15.04	7.50
BE-3013	BRSZ Unit 1	345.85	141.27	30.39	37.18	60.89	8.00
BE-3513	BRSZ Unit 1	221.28	121.01	34.68	76.73	25.51	6.90
BE-3613	BRSZ Unit 1	202.68	116.50	38.37	82.01	30.29	6.40
BE-3713	BRSZ Unit 1	166.91	108.28	54.31	77.06	30.49	6.30
BE-3913	BRSZ Unit 1	242.45	117.88	24.31	116.07	18.09	7.50
BE-4013	BRSZ Unit 1	649.87	149.99	54.91	100.44	26.33	8.60
LA-3412	Singa	143.00	84.70	32.18	37.09	97.67	2.23
LA 3512	Singa	142.00	93.60	35.70	21.30	91.90	3.50
LA-3612	Singa	129.00	72.70	27.92	26.40	85.34	2.15
LA 3712	Singa	129.00	90.40	34.90	21.50	97.90	3.20
LA-3812	Singa	118.00	72.90	25.79	21.76	74.57	2.12
LA 3912	Singa	129.00	90.60	36.90	25.10	100.00	3.70
LA-4012	Singa	150.00	80.10	28.07	17.39	59.19	2.22
LA 4112	Singa	149.00	100.40	32.40	30.30	88.20	4.20
LA 4312	Singa	140.00	80.00	33.40	19.60	89.20	2.90
LA-4212	Singa	133.00	80.50	28.10	13.60	85.90	3.50
LA-3212	Machinchang	194.00	133.50	32.80	3.11	24.21	4.81
LA-2912	Machinchang	159.00	105.70	20.35	6.00	24.09	5.39
LA 3012	Machinchang	161.00	117.10	22.10	3.40	42.60	5.80

Table 5.10 (continued)

Sample No.	Formation	Mo	Co	Th	U/Th	V/Cr	(V+Ni)	V/(V+Ni)	Cu/Zn
GM-0912	Gua Musang	1.40	8.08	16.17	0.25	2.24	153.07	0.87	1.70
GM-1012	Gua Musang	3.20	3.95	7.65	0.37	2.23	178.78	0.96	0.65
GM 1212	Gua Musang	1.75	-	10.23	0.51	2.90	139.99	0.86	0.62
GM 1312	Gua Musang	2.92	-	12.46	0.37	2.31	150.98	0.92	0.44
KL 0512	Gua Musang	0.58	-	17.48	0.25	2.58	164.98	0.85	0.33
KL-0112	Gua Musang	0.50	41.53	6.74	0.41	2.71	185.38	0.73	0.38
KL-0212	Gua Musang	0.60	15.09	14.88	0.25	2.78	192.40	0.86	0.33
KL-0312	Gua Musang	0.40	9.81	14.36	0.20	2.63	154.21	0.90	0.38
KL-0412	Gua Musang	0.30	9.88	15.23	0.19	2.64	149.40	0.88	1.06
TP-1512	Gua Musang	0.68	-	10.88	0.35	2.58	186.75	0.88	4.19
TP-1612	Gua Musang	2.24	-	12.09	0.33	2.35	176.33	0.88	0.54
PJ 1812	Gua Musang	1.36	-	17.30	0.29	3.52	46.50	0.86	0.22
PJ 1912	Gua Musang	0.78	-	16.18	0.28	3.52	49.61	0.86	0.17
PJ 2112	Gua Musang	1.75	-	15.99	0.30	4.94	94.12	0.91	0.18
ME-5912	Semantan	1.66	-	9.58	0.38	2.29	174.08	0.78	6.50
ME-6612	Semantan	4.19	-	10.97	0.43	3.78	234.59	0.92	0.40
ME-10013	Semantan	0.30	-	10.13	0.19	3.03	117.31	0.84	0.11
ME-10113	Semantan	0.20	-	9.14	0.25	3.06	181.69	0.89	0.48
ME-10213	Semantan	1.08	-	9.72	0.32	3.13	185.82	0.91	0.38
ME-9413	Semantan	1.67	-	8.72	0.26	3.68	183.69	0.91	0.45
ME-9513	Semantan	0.78	-	8.97	0.35	3.77	193.70	0.93	0.49
ME-9613	Semantan	0.78	-	9.38	0.45	2.80	164.35	0.88	0.31
ME-9713	Semantan	1.67	-	8.64	0.34	3.54	196.21	0.88	0.42
ME-9813	Semantan	1.18	-	9.47	0.25	3.53	189.66	0.92	0.40
ME-9913	Semantan	1.27	-	9.05	0.27	3.65	198.71	0.92	0.43
ME-6212	Semantan	<0.5	-	8.89	0.28	3.24	185.92	0.91	0.33
ME-6312	Semantan	1.08	-	8.97	0.27	3.15	172.82	0.91	0.38
BE-2813	BRSZ Unit 1	7.45	-	17.77	0.42	2.23	253.96	0.91	1.38
BE-3013	BRSZ Unit 1	10.19	-	17.44	0.46	2.45	376.24	0.92	0.61
BE-3513	BRSZ Unit 1	2.55	-	17.69	0.39	1.83	255.96	0.86	3.01
BE-3613	BRSZ Unit 1	3.53	-	18.85	0.34	1.74	241.04	0.84	2.71
BE-3713	BRSZ Unit 1	2.74	-	16.69	0.38	1.54	221.22	0.75	2.53
BE-3913	BRSZ Unit 1	6.66	-	17.69	0.42	2.06	266.77	0.91	6.42
BE-4013	BRSZ Unit 1	16.37	-	18.52	0.46	4.33	704.78	0.92	3.82
LA-3412	Singa	0.80	19.80	19.36	0.12	1.69	175.18	0.82	0.38
LA 3512	Singa	0.25	-	21.40	0.16	1.52	177.70	0.80	0.23
LA-3612	Singa	0.40	18.14	17.01	0.13	1.77	156.92	0.82	0.31
LA 3712	Singa	0.70	-	18.60	0.17	1.43	163.90	0.79	0.22
LA-3812	Singa	1.50	15.55	15.89	0.13	1.62	143.79	0.82	0.29
LA 3912	Singa	0.90	-	19.50	0.19	1.42	165.90	0.78	0.25
LA-4012	Singa	0.40	17.96	19.87	0.11	1.87	178.07	0.84	0.29
LA 4112	Singa	2.00	-	20.20	0.21	1.48	181.40	0.82	0.34
LA 4312	Singa	1.10	-	14.10	0.21	1.75	173.40	0.81	0.22
LA-4212	Singa	0.90	-	15.70	0.22	1.65	161.10	0.83	0.16
LA-3212	Machinchang	0.80	8.23	26.04	0.18	1.45	226.80	0.86	0.13
LA-2912	Machinchang	0.80	4.88	24.51	0.22	1.50	179.35	0.89	0.25
LA 3012	Machinchang	1.30	0.00	24.70	0.23	1.37	183.10	0.88	0.08

Paleoredox plots indicate variable redox conditions in the ocean (Fig. 5.16).

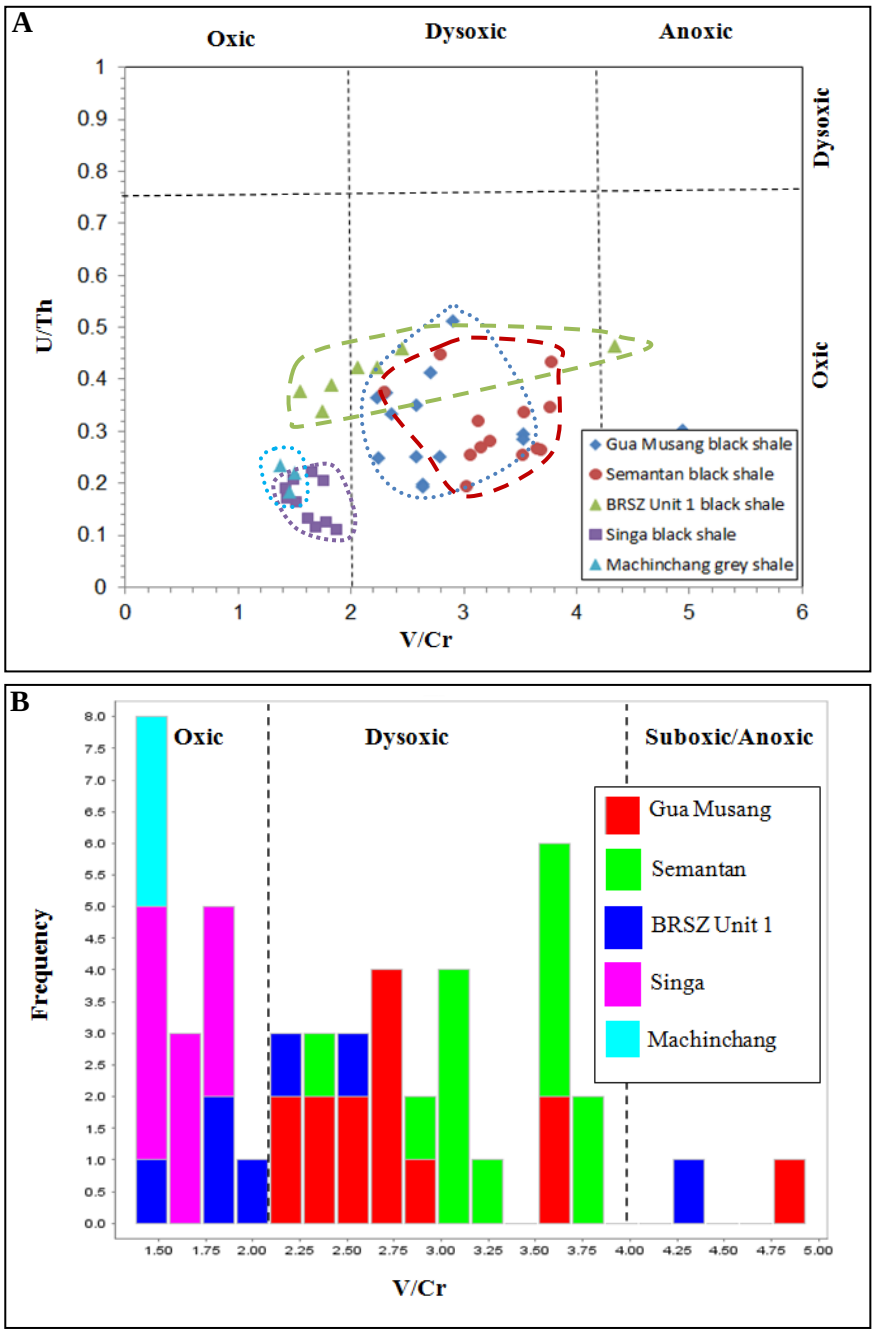

Fig. 5.16. Trace element plots indicating seafloor conditions of the studied shales in Malaysia. **A**) U-Th versus V/Cr scatter plot. **B**) Histogram of frequency versus V/Cr ratio. Ranges for inferred bottom-water conditions are from Hatch and Leventhal (1992).

The paleoredox proxies that were taken into consideration from previous work are indicated in Table 5.11 and the interpreted proxies with framboidal pyrite data in this study are summarized in Table 5.12.

Table 5.11. Summary of paleoredox proxies from previous work

	Oxic	Dysoxic	Anoxic	Euxinic
Ni/Co[1]	< 5	5 – 7	> 7	
V/Cr[2]	< 2	2 – 4.5	>4.5	
V/(V+Ni)[3]	< 0.46	0.46 – 0.60	0.54 – 0.82	> 0.84
U/Th[4]	< 0.75	0.75 – 1.25	> 1.25	

[1,2,4] Jones and Manning (1994)
[2] Dill et al. (1988)
[3] Hatch and Leventhal (1992)

Table 5.12. Interpreted seafloor conditions based on some palaeoredox proxies (this study)

Formation	Ni/Co	V/Cr	V/V+Ni	U/Th	Framboid size	Likely conditions
Semantan	no data	3.08 dysoxic	0.88 euxinic	0.31 oxic	<10 µm anoxic	anoxic to euxinic
BRSZ Unit 1	no data	2.31 dysoxic	0.87 euxinic	0.41 oxic	<10 µm anoxic-euxinic	anoxic to euxinic
Gua Musang	1.8 oxic	2.85 dysoxic	0.87 euxinic	0.31 oxic	>20 µm dysoxic-oxic	dysoxic to oxic
Machinchang	4.1 oxic	1.44 oxic	0.87 euxinic	0.21 oxic	no visible framboidal pyrite	oxic
Singa	1.6 oxic	1.62 oxic	0.81 anoxic	0.17 oxic	>10 µm oxic	oxic

Recent studies argued that the size of framboidal pyrite (<10 µm) points to an anoxic-euxinic sea water environment (Wilkin et al., 1996; Bond and Wignall., 2010; Slack et al., 2015). Larger framboidal pyrites (>10 µm) associated with crystalline pyrite indicates dysoxic-oxic

conditions. It is clear that the different proxies commonly give different indicators of the palaeoredox conditions. The U/Th ratio suggests all shales were deposited under oxic conditions whereas the V/V+Ni ratio suggest all shales were deposited under anoxic to euxinic conditions. The most reliable proxy is framboid size (Meyers and Kump, 2008). Overall, the euxinic environment (e.g. the BRSZ Unit 1 shales) is characterized by relatively high Mo content which strongly correlates positively with total organic carbon and the abundance of framboidal pyrites (<10 μm) in the pyrite fraction. Potter (2005) also documented that euxinic conditions are marked by high content of total organic carbon.

5.6. Relationships between seafloor conditions and TE trends in shale

In this section, the compositions of the five shale-bearing formations including the Machinchang, Singa, BRSZ Unit 1, Semantan and Gua Musang formations are examined. The aim is to discuss whether a change from oxic to anoxic water conditions is reflected in the trace element trends in selected sedimentary basins in Malaysia. The data indicate that the content of organic carbon and sulfur in oxic conditions is relatively low compared to the content of the same components in euxinic/anoxic conditions (Fig. 5.17). Euxinic conditions show consistent high organic carbon, V, Cr, U, Mo, and Se contents. However, in the suboxic environment, the Sb content is elevated. Similarly, the Ni content is elevated in either condition. The sulfur content increases from oxic to euxinic/anoxic conditions in sedimentary basins (Fig. 5.17). The Se content is elevated in the euxinic environment. This study shows that the content in Se, U, V, and Mo help distinguish oxic-suboxic environments from the euxinic-anoxic environments. Remarkably, the elevated total organic carbon (TOC) in the BRSZ Unit 1 shales is accompanied with higher contents in Ni, Cu, V, and U (Fig. 5.17). These elements are commonly supplied to the sediments mixed with organic matter (Tribovillard et al., 2006). This study reiterates the use of redox-sensitive elements such as U,

V, Mo to infer palaeo-oxygenation conditions in the ocean (Pi et al., 2013). The relationship between seafloor conditions and sedimentary pyrite composition is shown in Figs. 5.18-5.20. In every box plot, the open circle represents an outlier, which is the top and bottom 5% of the data. The triangular is a far outlier that indicates a highly anomalous value.

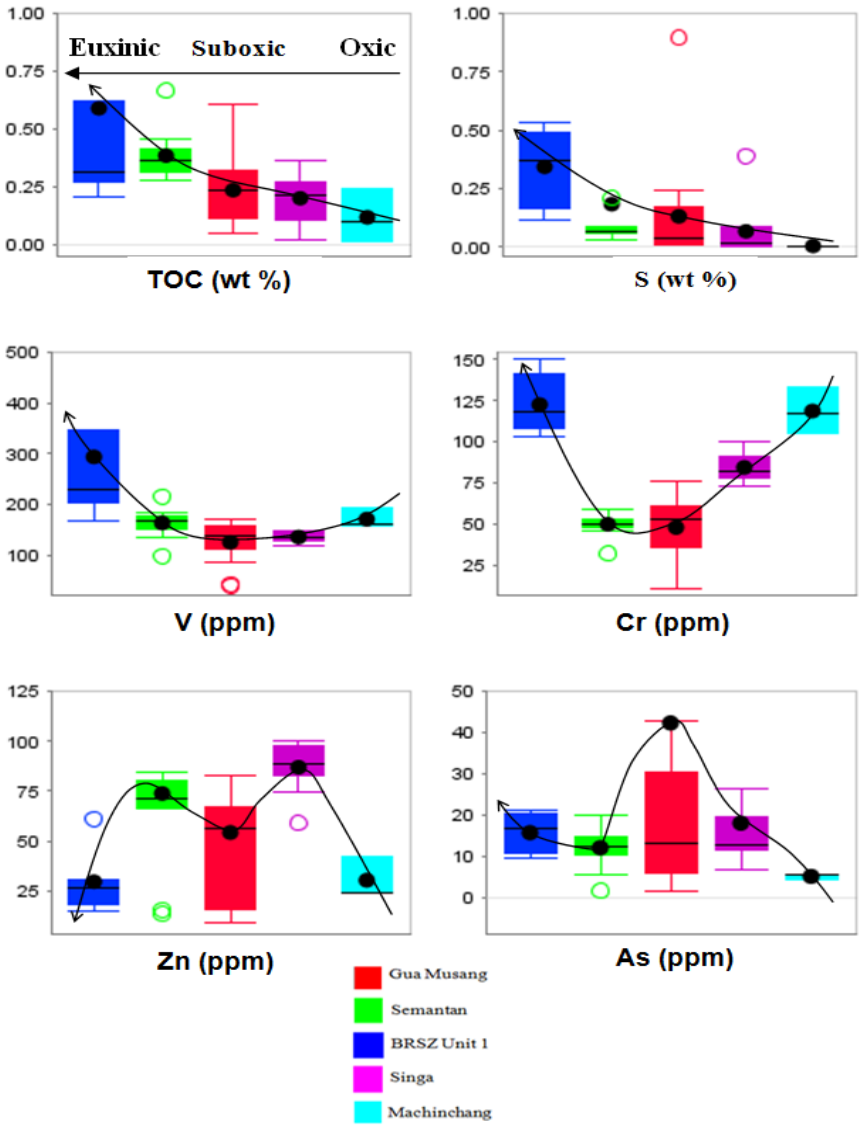

Fig. 5.17. Turkey box plots showing relationships between palaeoredox conditions and selected trace element contents in all studied shale-bearing formations. The black circle is the mean value for each trace element. Euxinic conditions are characterised by elevated organic carbon, sulphur, V, and Cr contents. However, Zn and As are unstable as seawater conditions changed.

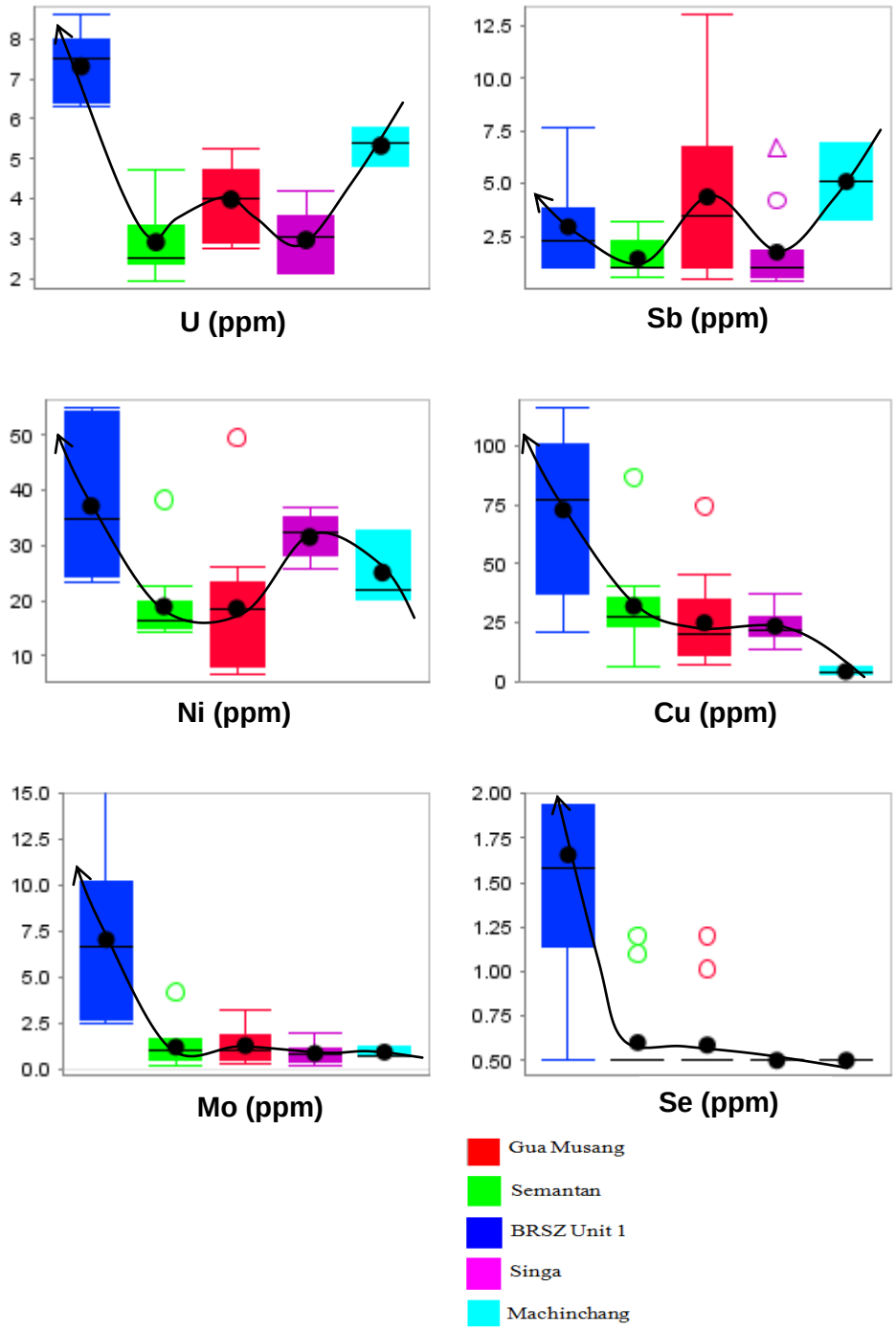

Fig. 5.18. Turkey box plots showing relationships between paleoredox conditions and selected trace element contents in all studied shale-bearing formations. In every box plot, the open circle (green and red in colour) represents an outlier, which is the top and bottom 5% of the data. The triangular is a far outlier that indicates a highly anomalous value. The black circle is the mean value for each trace element. In every box plot, the open circle (green and red in colour) represents an outlier, which is the top and bottom 5% of the data. The triangular is a far outlier that indicates a highly anomalous value. The black circle is the mean value for each trace element. The transition of oxic to euxinic conditions is indicated by increased levels of U, Ni, Cu, Mo and Se in the shales. Importantly, Mo and Se contents show a sudden jump when seawater conditions become euxinic.

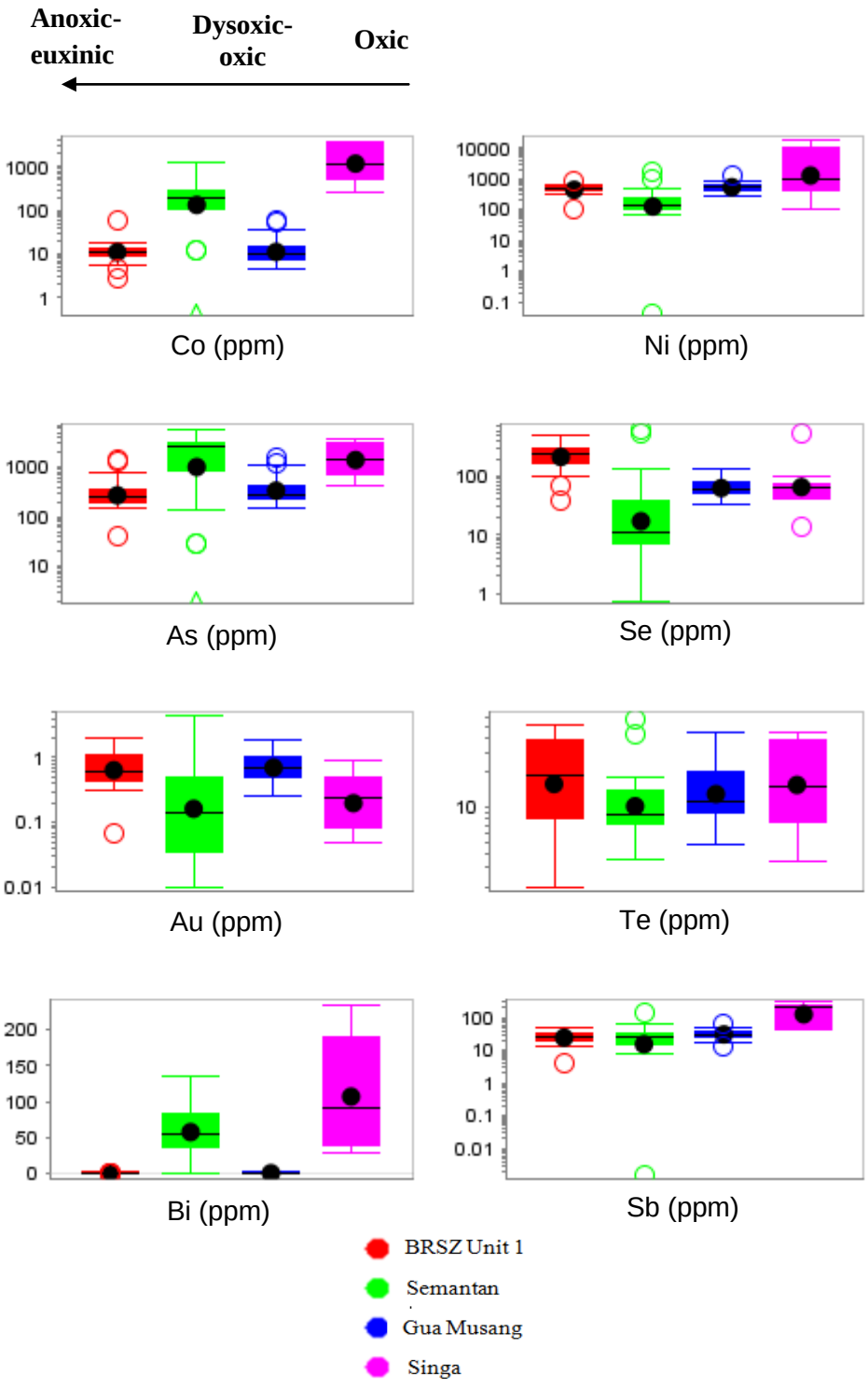

Fig. 5.19. Turkey box plots showing variation of mean composition of Co, Ni, As, Se, Au, Te, Bi and Sb in sedimentary pyrite in relation to seafloor conditions. The Au, Se and Te contents are elevated in anoxic water conditions. Co, As, and Ni contents fluctuate as seafloor conditions changed. Bi content plummeted towards a more anoxic-euxinic water conditions. Selenium content is elevated in both the sedimentary pyrite structure and the sediment matrix.

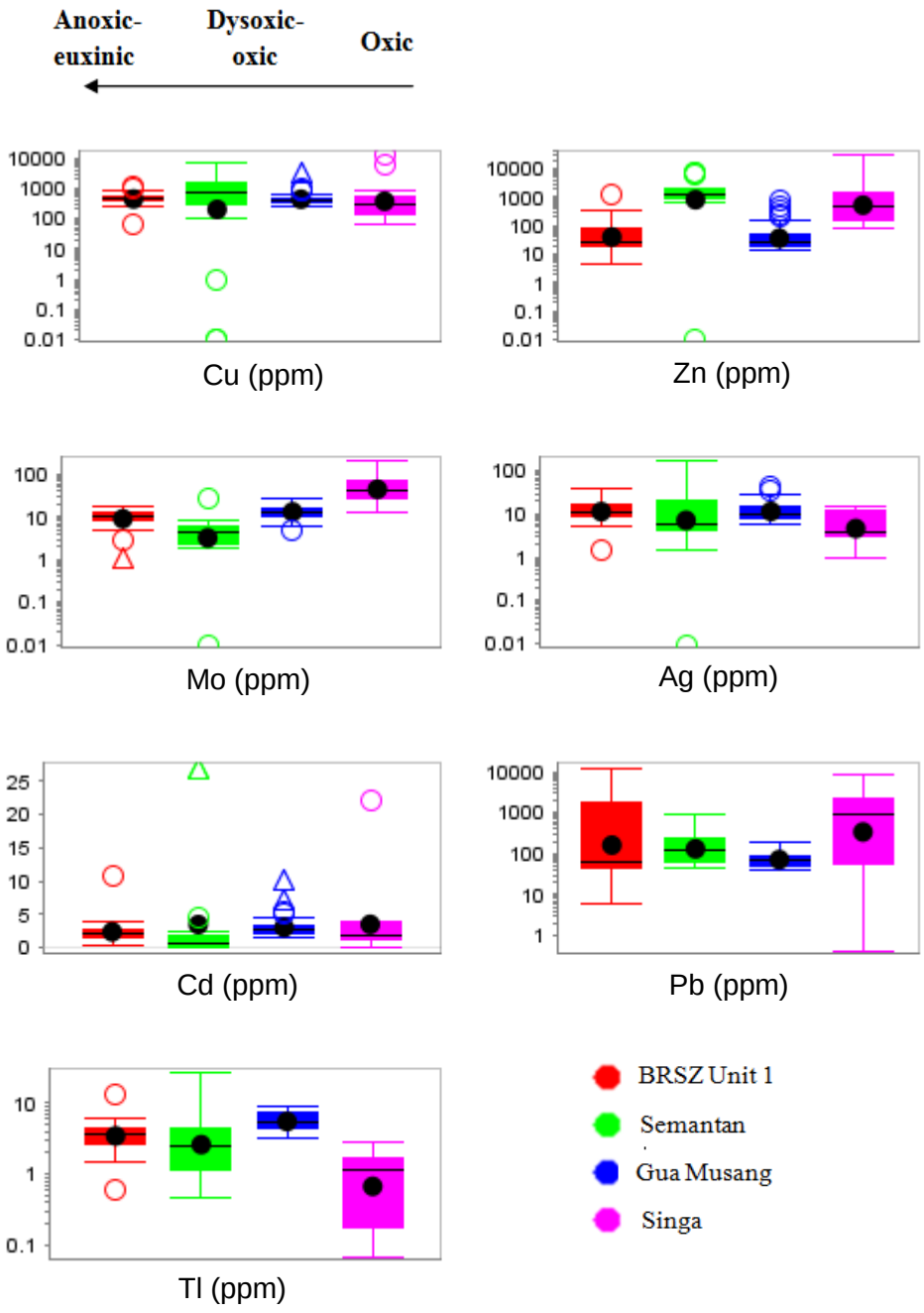

Fig. 5.20. Turkey box plots showing variation of mean composition of Cu, Zn, Mo, Ag, Cd, Pb, and Tl in sedimentary pyrite in relation to seafloor conditions. In every box plot, the open circle (green and red in colour) represents an outlier, which is the top and bottom 5% of the data. The triangular is a far outlier that indicates a highly anomalous value. The black circle is the mean value for each trace element.

It is obvious that TE composition of sedimentary pyrite varies according to the seafloor conditions (Figs. 5.19-5.20). In this study, three main trends of TE in sedimentary pyrite are recognized: 1) In oxic conditions, TE that have elevated concentration are Co, Bi, Ni, Sb, Pb and Mo; 2) In dysoxic-oxic conditions, concentrations of Cu, As, Ag, Cd do not change significantly and are characterised by flat trend lines; and 3) In euxinic-anoxic conditions, sedimentary pyrite contains higher contents of Au, Te, Se, Ag, and Tl. In the context of regional tectonics, sediments for the Machinchang, Setul and Singa formations likely derived from the Sibumasu terrane; however, the sediments for the BRSZ Unit 1 may have derived from the Indochina terrane or Sukhothia Arc (e.g. Metcalfe, 2011).

5.7. Conclusions

The selected Palaeozoic formations that include Machinchang, Setul, Singa and BRSZ Unit 1 have a consistent felsic-intermediate provenance but show different tectonic settings. The Machinchang, Setul, and Singa formations have a continental margin-island arc setting. In the context of regional tectonics, sediments for the Machinchang, Setul and Singa formations likely derived from the Sibumasu terrane; however, the sediments for the BRSZ Unit 1 may have derived from the Indochina terrane or Sukhothai Arc. In whole rocks, under anoxic-euxinic conditions, trace elements that have elevated contents are V, U, Ni, Cu, Mo, Se as well as TOC and S. TE compositions in sedimentary pyrite in oxic-dysoxic conditions, indicate elevated levels of As, Co, Ni, and Bi with appreciable amount of Au in; however, in anoxic-euxinic conditions, Te, Se, Au and Tl contents are elevated.

The selected Mesozoic formations that comprise the Gua Musang and Semantan formations show a consistent intermediate-mafic provenance suggesting provenance from the

East Malaya terrane. In anoxic-euxinic conditions (e.g. the Semantan Formation), TOC, V, Zn contents are elevated whereas in oxic-dysoxic conditions (e.g. the Gua Musang Formation) U, and Sb indicate elevated levels in whole rocks. In sedimentary pyrites, Co, As, and Zn contents are elevated in anoxic-euxinic bottom water whereas Au, Ni, Se, and Tl contents are high in oxic-dysoxic conditions.

CHAPTER 6
RADIOGENIC AND STABLE ISOTOPES OF LEAD, SULPHUR AND ORGANIC CARBON

6.1. Introduction

In this Chapter, the lead, sulphur and carbon isotopic compositions of selected pyritic black shale samples at and away from existing sediment-hosted gold deposits are presented and discussed. Previous research on lead isotope studies was done for the following: (1) determine the age of rocks and minerals, (2) examine geological processes that constrain the source of the metals (Zartman and Stacey, 1971; Zartman and Doe, 1981; Gulson, 1986; Carr et al., 1995; Rollinson, 1996), and (3) provide insights into the ore genesis (Zhao et al., 2006; Large et al., 2007; Meffre et al., 2008; Large et al., 2009). The Pb^{204}, Pb^{206}, Pb^{207} and Pb^{208} of pyrite combined with those of K-feldspar from igneous rocks are used to discuss possible metallogenic links.

6.2. Aims

The aims of the stable and radiogenic isotopic studies are the following:

1) To compare lead isotopic compositions of pyrite using LA ICP-MS technique from selected pyritic black shale samples in sedimentary basins, with those of the Tersang, and Selinsing gold deposits and K-feldspar in the intruding S-type granitoids, in parallel with the zircon ages. In this chapter, care has been taken to check whether there is a temporal relationship between the absolute ages of zircon and the model Pb-Pb ages of K-feldspar in the same granite samples that have been analysed. In case that there is a good match between the two ages, then the calculated Pb-Pb model age of K-feldspar is most reliable.

2) To constrain the age of gold mineralisation.

3) To compare the sulphur isotope compositions of sedimentary rocks far from mining areas with those previously studied at deposit scale (Makoundi, 2012).

4) To investigate whether the carbon in the shales is from a terrestrial or marine environment.

6.3. Lead isotopes

This section gives a detailed comparison of the lead isotopic composition of pyrite from the Selinsing and Tersang gold deposits with those of pyrite from black shales that crop out in the Central Gold Belt. The pyritic black shales were collected from the Gua Musang Formation, Semantan formations, and BRSZ Unit 1 within the East Malaya Block and in the Machinchang and Singa formations from the Sibumasu Terrane on Langkawi Island, Malaysia. Additionally, Pb isotope compositions of K-feldspar from some igneous rocks (e.g. S-type granite and rhyolite) are also examined in detail to check whether there is a magmatic contribution from intruding granites to the ore deposits in the mining district of the Central Gold Belt in Peninsular Malaysia. The methods used to determine the lead isotopic composition in the minerals are outlined in appendix A.

6.3.1. Pb isotopes samples

The results of lead isotope composition of pyrite from the Machinchang, Singa, Semantan, and BRSZ Unit 1 formations and those from the Selinsing and Tersang gold deposits are presented in Tables 6.1 and 6.2. In addition, the lead isotope composition of K-feldspar collected from the S-type granites is presented in Table 6.3. Moreover, some U-Pb zircon dates of the S-type granitoids are discussed in this section to help interpret the K-feldspar analyses. The zircon ages were undertaken to verify consistency between the Pb isotope results of K-feldspar and crystallization ages of the S-type granite that intruded

sedimentary sequences in the Central Gold Belt (e.g. East Malaya Block) and on Langkawi Island (e.g. Sibumasu Terrane). All of the granite samples analysed for lead isotopes in K-feldspar has low magnetic susceptibility (dashed squares in Fig. 6.1) suggesting that these are S-type ilmenite series granites. The magnetic susceptibility of the granitic rocks varies between 0.08 x 10-3 SI to 18.58 x 10-3 SI, corresponding respectively to ilmenite series (< 3x 10^{-3} SI; oxidized type) and magnetite series (> 3x 10^{-3} SI; reduced type) granite (Adi Maulana et al., 2013). The magnetite and ilmenite series granite classification is determined by the magnetite content of granitic rocks which can be characterised by the magnetic susceptibility (MS). The MS reflects the oxygen fugacity of the granitic magma.

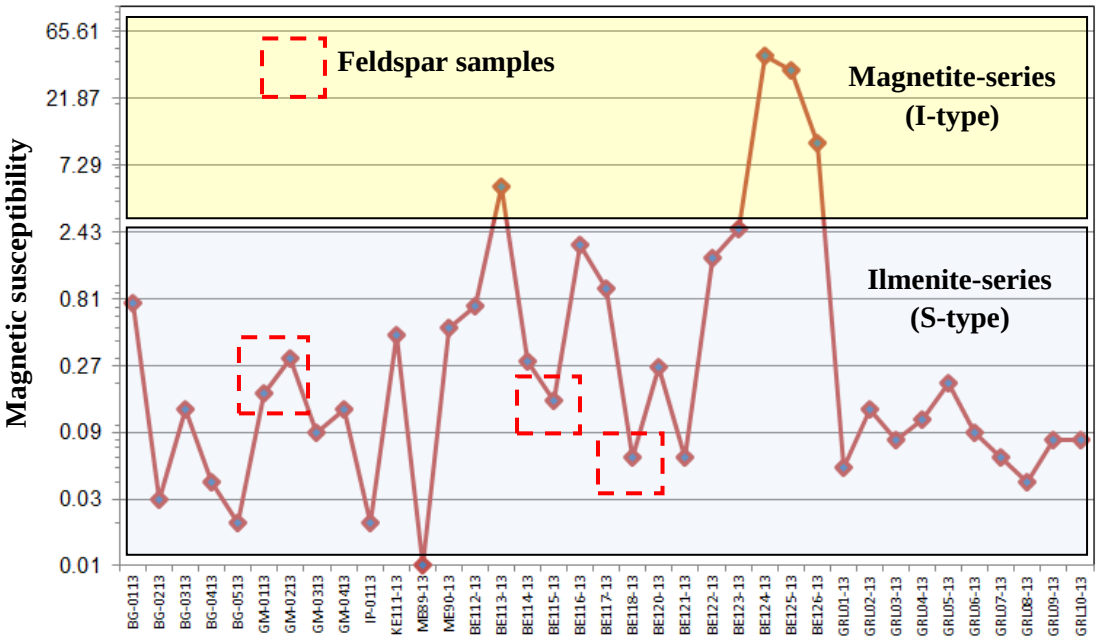

Fig. 6.1. Plot of magnetic susceptibility(MS) measurements for all the igneous rocks collected in the field, Malaysia.

6.3.2. Results

Prior to interpretation, the pyrite Pb isotope compositions were filtered to remove outliers (MSWD >2.5, $^{206}Pb/^{204}Pb$ precision >0.5% and $^{206}Pb/^{238}U$>5). The results (Table 6.1,

Fig. 6.3) show that there is considerable variation in the Pb isotopic composition of the pyrite. Machinchang and Semantan pyrites tend to be less radiogenic (low $^{206}Pb/^{204}Pb$ ratio) than the BRSZ Unit 1 pyrite (high $^{206}Pb/^{204}Pb$ ratio). Part of the variation in each sample is related to the in situ decay of U and Th (Fig. 6.9) but the remainder relates to initial isotopic differences during crystallization of pyrite.

Table 6.1. Lead isotope composition using LA ICP-MS of pyrite from the selected sedimentary units, Malaysia.

Analysis No.	Sample ID	Mineral	206/204	+/-1s	207/204	+/-1s	208/204	+/-1s	206/238	+/-1s	208/232	+/-1s
AU13A033	BE-2412A	Pyrite	18.36	0.42	15.55	0.37	38.04	0.90	517.63	370.98	566.33	1140.83
AU13A032	BE-2412A	Pyrite	19.08	0.10	15.62	0.07	38.85	0.19	10943.45	1752.10	9743.29	6459.56
AU13A034	BE-2412A	Pyrite	19.14	0.10	15.71	0.07	39.08	0.16	6284.36	21198.14	2339.87	2076.13
AU13A031	BE-2412A	Pyrite	19.15	0.15	15.80	0.14	39.22	0.31	7585.00	3045.60	3544.54	2151.00
AU13A030	BE-2412A	Pyrite	19.30	0.21	15.68	0.17	39.05	0.42	5105.74	6483.72	27539.66	33740.93
AU13A069	BE-2412B	Pyrite	18.05	0.13	15.64	0.15	37.83	0.29	12092.44	18846.77	73646.43	14947.81
AU13A070	BE-2412B	Pyrite	18.58	0.20	15.75	0.19	38.44	0.42	3098.45	25894.47	3794.91	985.79
AU13A071	BE-2412B	Pyrite	19.14	0.09	15.78	0.06	39.19	0.15	14354.39	2586.68	8454.02	1181.55
AU13A062	BE-2412B	Pyrite	19.33	0.08	15.85	0.09	39.32	0.19	7691.28	853.16	5767.66	625.57
AU13A061	BE-2412B	Pyrite	19.37	0.34	15.92	0.33	39.39	0.84	3843.95	816.62	8141.29	11423.08
AU13A063	BE-2412B	Pyrite	19.46	0.28	15.74	0.21	39.31	0.58	5875.94	70772.18	3056.42	23285.86
AU13A058	BE-2712B	Pyrite	19.03	0.45	15.67	0.32	38.62	0.88	4100.26	3365.11	3017.70	3601.59
AU13A060	BE-2712B	Pyrite	19.19	0.24	15.93	0.14	38.76	0.51	3899.95	4370.61	2903.61	1391.89
AU13A057	BE-2712B	Pyrite	19.24	0.44	15.75	0.33	39.54	0.83	2823.45	841.31	2313.31	2265.36
AU13A056	BE-2712B	Pyrite	19.76	0.10	16.05	0.12	40.07	0.36	4100.86	2668.24	2174.87	9774.81
AU13A052	LA-3312A	Pyrite	18.86	0.04	15.84	0.04	39.66	0.07	139.05	6.95	80.30	16.07
AU13A051	LA-3312A	Pyrite	19.60	0.18	16.18	0.14	40.33	0.43	173.41	22.59	322.26	142.52
AU13A074	LA-3312B	Pyrite	18.69	0.07	15.75	0.05	39.25	0.14	28.36	13.83	27.44	14.70
AU13A072	LA-3312B	Pyrite	18.75	0.11	15.75	0.08	39.36	0.24	83.63	8.48	30.55	6.53
AU13A076	LA-3312B	Pyrite	18.75	0.10	15.82	0.07	39.43	0.19	53.49	7.58	26.34	7.25
AU13A077	LA-3312B	Pyrite	18.83	0.09	15.87	0.10	39.58	0.20	63.42	5.89	29.68	5.52
AU13A075	LA-3312B	Pyrite	18.84	0.07	15.82	0.06	39.61	0.16	55.15	3.21	22.96	9.27
AU13A024	LA-3812	Pyrite	18.40	0.03	15.57	0.02	38.77	0.07	2488.35	327.90	561.66	214.66
AU13A025	LA-3812	Pyrite	18.55	0.03	15.68	0.03	38.98	0.06	2326.13	373.55	404.55	145.86
AU13A027	LA-3812	Pyrite	18.58	0.06	15.70	0.06	38.94	0.10	579.14	37.63	249.82	27.55
AU13A028	LA-3812	Pyrite	18.60	0.06	15.72	0.05	38.73	0.13	300.10	58.01	103.15	10.57
AU13A023	LA-3812	Pyrite	18.60	0.06	15.82	0.09	39.08	0.15	152.40	28.62	53.76	33.61
AU13A026	LA-3812	Pyrite	19.15	0.27	16.18	0.18	39.76	0.49	334.97	23.39	1898.97	851.27
AU13A036	LA-4112A	Pyrite	18.77	0.03	15.68	0.03	39.63	0.10	18336.49	10039.24	2249.60	2325.69
AU13A035	LA-4112A	Pyrite	18.81	0.04	15.70	0.03	39.75	0.07	1292.82	634.77	331.11	114.07
AU13A040	LA-4112A	Pyrite	18.81	0.03	15.67	0.03	39.60	0.07	11538.42	1139.14	305.07	28.22
AU13A039	LA-4112A	Pyrite	18.82	0.03	15.74	0.02	39.66	0.07	4221.68	298.86	1561.66	140.07
AU13A037	LA-4112A	Pyrite	18.84	0.05	15.82	0.06	39.69	0.17	6144.17	965.62	796.42	110.96
AU13A038	LA-4112A	Pyrite	18.85	0.05	15.82	0.05	39.64	0.09	1301.94	348.46	539.58	59.62
AU13A008	LA-4112B	Pyrite	18.73	0.06	15.64	0.05	39.37	0.13	558.04	72.03	231.15	83.03
AU13A010	LA-4112B	Pyrite	18.73	0.04	15.66	0.05	39.42	0.10	9851.50	1985.16	2976.22	2445.01
AU13A009	LA-4112B	Pyrite	18.79	0.05	15.68	0.04	39.43	0.10	3860.93	1419.21	272.80	126.06
AU13A007	LA-4112B	Pyrite	18.83	0.13	15.79	0.11	39.34	0.18	2356.53	3532.71	485.58	360.63
AU13A012	LA-4112B	Pyrite	18.85	0.07	15.76	0.05	39.80	0.11	4279.44	453.37	303.66	246.61
AU13A011	LA-4112B	Pyrite	18.85	0.05	15.76	0.04	39.67	0.06	5923.58	381.57	484.43	98.22
AU13A016	LA-5312B	Pyrite	20.75	0.10	15.80	0.08	38.78	0.19	11.06	1.63	49.58	10.14
AU13A018	LA-5312B	Pyrite	20.76	0.15	16.01	0.09	39.26	0.27	24.74	2.12	131.01	25.37
AU13A014	LA-5312B	Pyrite	20.92	0.08	15.86	0.11	38.98	0.25	6.18	0.65	19.89	4.91
AU13A017	LA-5312B	Pyrite	21.07	0.26	16.12	0.20	39.54	0.41	14.70	1.48	67.85	23.91
AU13A013	LA-5312B	Pyrite	21.20	0.25	16.30	0.19	40.22	0.40	9373.57	3523.57	15589.23	14745.59
AU13A046	ME-5912	Pyrite	18.89	0.24	15.82	0.22	38.79	0.33	212.12	48.70	221.70	55.78
AU13A045	ME-5913	Pyrite	18.52	0.21	15.57	0.20	38.94	0.57	516.69	50.65	1686.31	295.22
AU13A048	ME-5913	Pyrite	19.01	0.26	15.57	0.24	38.23	0.45	98.25	10.46	352.45	59.01
AU13A047	ME-5913	Pyrite	19.41	0.47	16.28	0.24	40.69	0.75	50.29	9.68	56.32	5.94

Note: 206/204= Pb^{206}/Pb^{204}; +/-s= error. Late Devonian BRSZ Unit 1 samples: BE-2412A and B, and BE-2712B. Late Cambrian-Early Ordovician Machinchang Formation samples: LA-3312A and B. Pennsylvanian-Early Permian Singa Formation samples: LA-3812, LA-4112A and B and LA-5312B. Middle Triassic Formation samples: ME-5912 and ME-5913.

The Singa Formation contains pyrites with two different compositions: one is similar to the Machinchang and Semantan but slightly lower in $^{207}Pb/^{204}Pb$, and the other is much more radiogenic that the BRSZ Unit 1 pyrite (Table 6.1; Fig. 6.2). The Pb isotope compositions of K-feldspar from granitoids are given in Table 6.2. The ages of zircon from the granitoids vary from 204.1 ± 4.7 to 223.7 ± 3.2 Ma (Fig. 6.3). These ages conform to the 200-250 Ma model ages (Fig. 6.2) from the Pb isotopic composition of the feldspars (on the growth curve of Cumming and Richards, 1975).

Table 6.2. Lead isotope composition of K-feldspar in S-type granitoids, Malaysia.

Analysis No	Sample ID	Mineral	207/206	+/-1s	208/206	+/-1s	206/204	+/-1s	207/204	+/-1s	208/204	+/-1s	206/238	+/-1s
FE17a056	BE11513-9	Feldspar	0.84	0.01	2.07	0.02	18.77	0.48	15.83	0.49	38.94	0.78	5.14	-
FE17a050	BE11513-4	Feldspar	0.84	0.01	2.10	0.01	18.75	0.29	15.83	0.23	39.33	0.53	204.26	-
FE17a057	BE11513-10	Feldspar	0.85	0.01	2.11	0.02	18.11	0.44	15.33	0.38	38.24	0.78	139.70	-
FE17a055	BE11513-8	Feldspar	0.85	0.01	2.10	0.01	18.48	0.28	15.69	0.31	38.81	0.51	255.16	-
FE17a054	BE11513-7	Feldspar	0.85	0.01	2.09	0.01	18.52	0.23	15.73	0.29	38.68	0.52	65.64	-
FE17a051	BE11513-4	Feldspar	0.85	0.01	2.10	0.00	18.63	0.11	15.86	0.13	39.04	0.24	482.80	-
FE17a052	BE11513-5	Feldspar	0.85	0.00	2.09	0.01	18.18	0.10	15.50	0.13	38.09	0.25	693.51	-
FE17a048	BE11513-2	Feldspar	0.85	0.01	2.11	0.01	18.32	0.11	15.62	0.10	38.66	0.15	51.04	-
FE17a049	BE11513-3	Feldspar	0.85	0.01	2.11	0.02	18.74	0.34	15.98	0.40	39.52	0.74	40.61	-
FE17a047	BE11513-1	Feldspar	0.85	0.01	2.11	0.01	18.18	0.22	15.55	0.29	38.31	0.50	8.20	-
FE17a053	BE11513-6	Feldspar	0.85	0.02	2.10	0.05	18.60	0.29	15.93	0.40	39.03	0.55	203.91	-
FE17a009	BE-11813-5	Feldspar	0.81	0.03	2.04	0.06	18.46	1.12	14.99	1.02	37.65	2.39	83.54	-
FE17a013	BE-11813-9	Feldspar	0.83	0.01	2.07	0.02	18.65	0.58	15.54	0.60	38.62	1.09	19.58	-
FE17a008	BE-11813-4	Feldspar	0.83	0.01	2.13	0.02	18.71	0.49	15.64	0.50	39.80	0.96	511.88	-
FE17a012	BE-11813-8	Feldspar	0.84	0.02	2.09	0.04	19.32	0.62	16.29	0.70	40.31	1.21	130.73	-
FE17a005	BE-11813-1	Feldspar	0.86	0.02	2.14	0.03	17.73	0.28	15.28	0.44	37.99	0.58	199.22	-
FE17a014	BE-11813-10	Feldspar	0.88	0.04	2.12	0.08	19.52	1.81	17.14	2.26	41.37	3.87	31.22	-
FE17a021	GM-0113-C	Feldspar	0.84	0.01	2.10	0.02	19.21	0.52	16.09	0.60	40.36	1.08	42.93	-
FE17a023	GM-0113-E	Feldspar	0.84	0.02	2.08	0.06	18.67	0.93	15.64	0.92	38.75	2.09	3.30	-
FE17a027	GM-0113-H	Feldspar	0.84	0.01	2.09	0.02	18.81	0.25	15.81	0.22	39.37	0.35	383.21	-
FE17a024	GM-0113-F	Feldspar	0.84	0.01	2.09	0.03	18.80	0.47	15.81	0.39	39.22	0.84	230.31	-
FE17a022	GM-0113-D	Feldspar	0.84	0.01	2.09	0.01	18.64	0.16	15.70	0.15	38.99	0.23	107.43	-
FE17a020	GM-0113-B	Feldspar	0.84	0.00	2.08	0.01	18.76	0.11	15.81	0.15	39.08	0.24	191.83	-
FE17a019	GM-0113-A	Feldspar	0.84	0.00	2.09	0.01	18.68	0.08	15.75	0.08	39.13	0.14	4.89	-
FE17a025	GM-0113-G	Feldspar	0.85	0.01	2.14	0.02	18.53	0.13	15.72	0.12	39.62	0.32	103.18	-
FE17a026	GM-0113-I	Feldspar	0.85	0.00	2.10	0.01	18.60	0.13	15.78	0.12	39.05	0.27	667.85	-
FE17a028	GM-0113-J	Feldspar	0.85	0.01	2.09	0.02	18.72	0.10	15.92	0.16	39.17	0.25	261.08	-
FE17a034	GM0213-2	Feldspar	0.82	0.01	2.07	0.02	19.03	0.37	15.66	0.37	39.38	0.85	14.94	4.27
FE17a040	GM0213-8	Feldspar	0.82	0.01	2.11	0.03	18.65	0.59	15.39	0.63	39.26	1.34	14.31	1.99
FE17a039	GM0213-7	Feldspar	0.83	0.01	2.07	0.02	18.99	0.34	15.84	0.35	39.26	0.58	29.15	9.24
FE17a033	GM0213-1	Feldspar	0.83	0.02	2.11	0.03	18.69	0.63	15.63	0.67	39.48	1.32	7.66	2.23
FE17a037	GM0213-5	Feldspar	0.84	0.01	2.08	0.01	18.86	0.26	15.79	0.28	39.20	0.58	37.75	30.87
FE17a042	GM0213-10	Feldspar	0.84	0.00	2.09	0.01	18.94	0.17	15.91	0.24	39.62	0.44	924.56	418.18
FE17a038	GM0213-6	Feldspar	0.84	0.00	2.10	0.01	18.69	0.17	15.75	0.16	39.22	0.34	403.25	199.95
FE17a041	GM0213-9	Feldspar	0.84	0.00	2.08	0.01	18.77	0.20	15.85	0.19	39.02	0.36	519.33	1432.03
FE17a035	GM0213-3	Feldspar	0.84	0.00	2.10	0.01	18.61	0.12	15.73	0.12	39.02	0.18	2755.42	-

Note: - = no data.

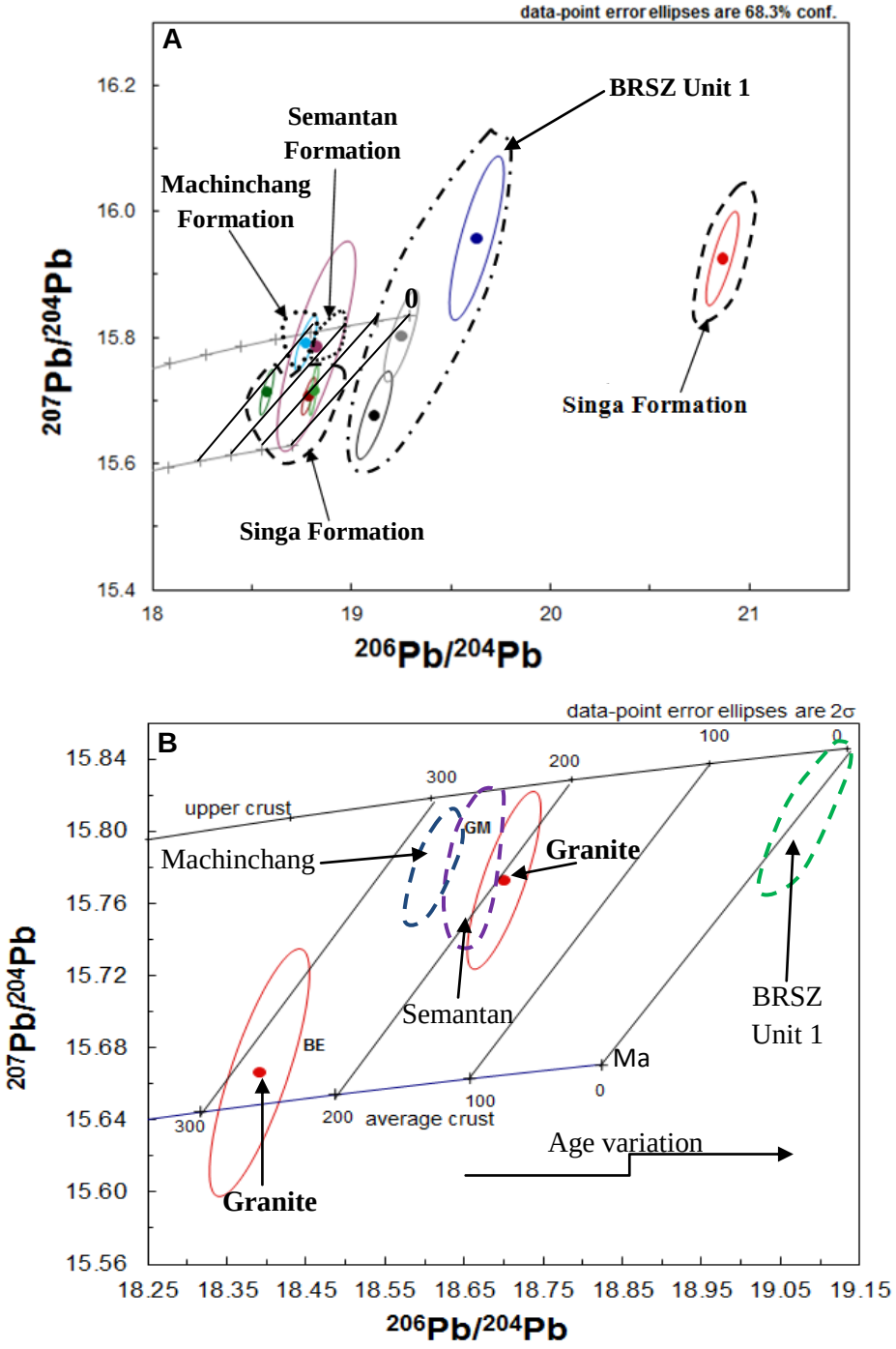

Fig. 6.2. Pb isotope compositions in sedimentary rocks and granitoids. **A**) Pb^{206}/Pb^{204} vs Pb^{207}/Pb^{204} in pyrite from sedimentary rocks. **B**) Pb^{206}/Pb^{204} vs Pb^{207}/Pb^{204} in feldspar from granitoids. Note: GM red field represents ellipsoids for the analysed granite that intruded the Gua Musang Formation whereas the other BE ellipsoid corresponds to the megacrystic granite that is found in patches and in zones sub-parallel to rhyolite bodies in the vicinity of the Tersang gold deposit. In addition, the blue, purple, and green ellipsoids are the three Phanerozoic formations.

There is a temporal relationship between the model age of K-feldspar and the crystallisation age of the granites. This implies conformity to the 200-250 Ma model age (Fig. 6.2).

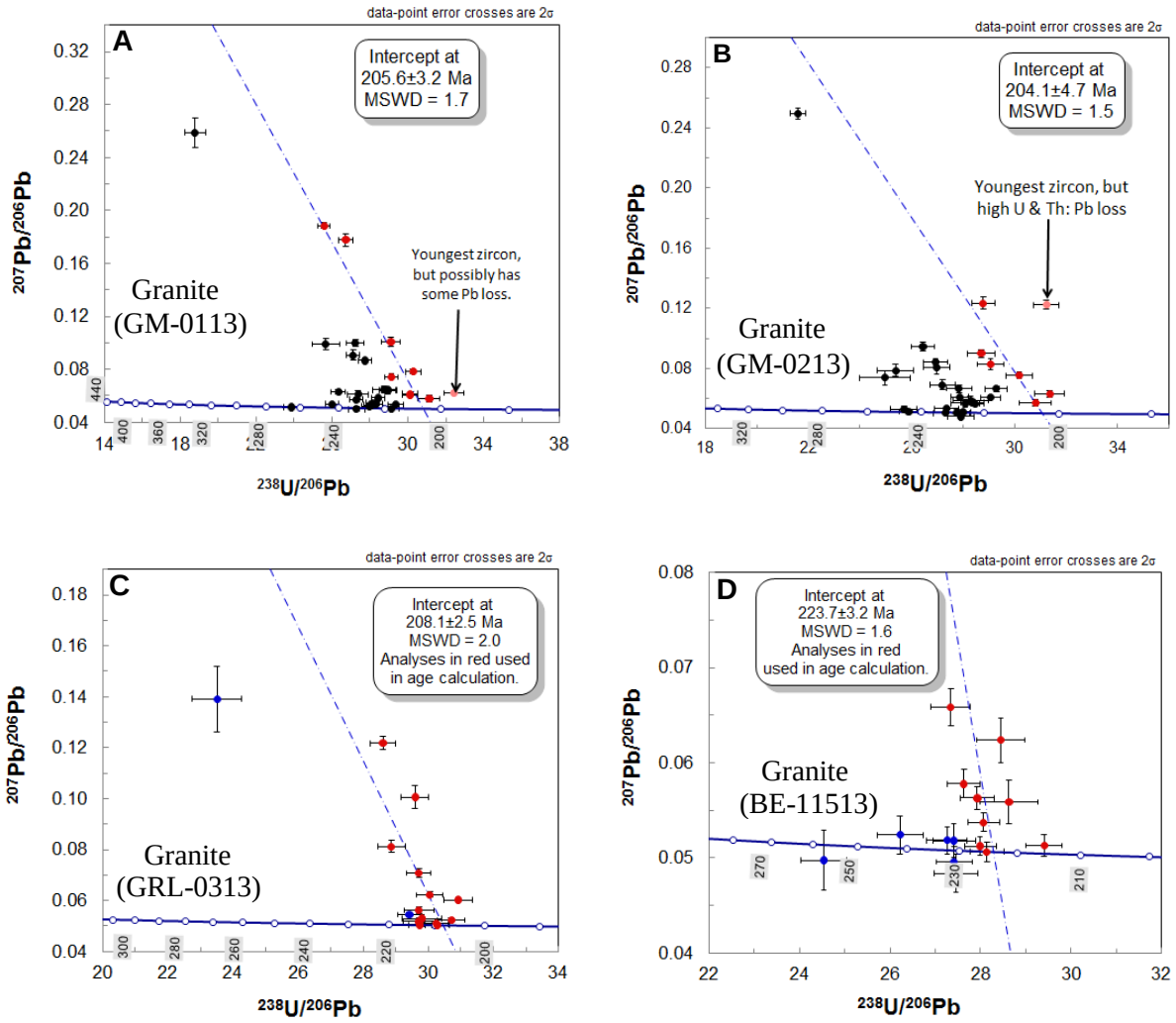

Fig. 6.3. U-Pb zircon Tera-Wasserburg diagrams (reverse Concordia) of selected S-type granitoids from Malaysia. These four S-type granitoid samples are the same specimens which were studied for their Pb isotope composition of K-feldspar (Table 6.2, Fig. 6.2). **A**) Granite. **B**) Granite. **C**) Granite. **D**) Granite.

Makoundi (2012) documented that there is a strong correlation between Au and Pb in the cores of pyrite based on pyrite trace element chemistry. In this study, a number of pyrite grains with core and rim zones from gold deposits were selected to determine the Pb isotope composition and infer the age of Au mineralisation. The core and rim of the pyrite grains

were analysed for their Pb isotope compositions. Results of the Pb isotopes in pyrite from the selected gold deposits are presented in Table 6.3 below. The Pb isotope plots for the ratio $^{206}Pb/^{204}Pb$ versus $^{207}Pb/^{204}Pb$ for pyrite from both the Selinsing and Tersang gold deposits are presented in Figs. 6.4-6.7. The Selinsing pyrite core and rim results indicate variable Pb isotope compositions. The Selinsing pyrite rims are more radiogenic than the Selinsing pyrite cores. The Tersang pyrite core and rims have consistent values that are similar to the least radiogenic of the Selinsing pyrite cores (Figs. 6.4-6.7).

Table 6.3. Pb isotope analyses in pyrite from the Selinsing (SEL) and Tersang (TER) gold deposits, Malaysia.

Sample ID	Mineral	Analysis no	Description	207/206	+/-1s	208/206	+/-1s	206/204	+/-1s	207/204	+/-1s	208/204	+/-1s
SEL-R013	pyrite	43	rim	0.827863	0.002608	2.074741	0.00539	19.06674	0.122914	15.78454	0.118466	39.55843	0.228744
SEL-R013	pyrite	44	rim	0.828023	0.006897	2.07444	0.017489	19.01887	0.159174	15.74796	0.213602	39.45339	0.504404
SEL-R013	pyrite	42	core	0.828973	0.001375	2.064691	0.003961	18.72547	0.067605	15.52281	0.054664	38.66219	0.129974
SEL-R013	pyrite	40	core	0.829446	0.002227	2.084146	0.007326	18.7154	0.115062	15.52332	0.11927	39.00551	0.301137
SEL-R013	pyrite	39	core	0.829788	0.001042	2.078157	0.003487	18.90994	0.058691	15.69114	0.06469	39.29771	0.143188
SEL-R013	pyrite	41	rim	0.832539	0.006405	2.070347	0.00723	19.13943	0.09965	15.93421	0.115662	39.62514	0.25831
SEL-R013	pyrite	38	rim	0.83922	0.002374	2.111481	0.008412	18.58452	0.121106	15.5964	0.089099	39.24073	0.283383
SEL-R013	pyrite	37	rim	0.830227	0.013169	2.116962	0.031036	20.52912	0.704319	17.04372	0.530961	43.45924	1.553684
SEL-R015	pyrite	60	rim	0.809948	0.006249	2.028707	0.01439	19.38371	0.181386	15.6997	0.116209	39.32378	0.314738
SEL-R015	pyrite	61	rim	0.812422	0.006424	2.052934	0.017939	19.43945	0.28906	15.79295	0.226968	39.90782	0.474385
SEL-R015	pyrite	58	rim	0.826839	0.01131	2.075057	0.023932	19.10773	0.467598	15.79892	0.435332	39.64954	0.918958
SEL-R015	pyrite	56	rim	0.828769	0.002518	2.057873	0.013008	19.11265	0.264931	15.83986	0.213687	39.33132	0.690204
SEL-R015	pyrite	59	rim	0.837725	0.002526	2.071289	0.005543	18.79919	0.234434	15.74846	0.207407	38.93846	0.432981
SEL-R685	pyrite	49	rim	0.819103	0.004393	2.054947	0.007833	18.99048	0.159595	15.55505	0.165432	39.02432	0.348619
SEL-R685	pyrite	53	core	0.825835	0.004187	2.066448	0.007552	18.88962	0.291214	15.5996	0.209829	39.03431	0.521542
SEL-R685	pyrite	48	core	0.832189	0.005192	2.073127	0.009036	18.8819	0.238059	15.7132	0.230569	39.14447	0.539919
SEL-R685	pyrite	55	core	0.832374	0.002487	2.074568	0.006847	18.79397	0.088222	15.64351	0.052231	38.98926	0.174284
SEL-R685	pyrite	50	rim	0.834148	0.001085	2.080312	0.002291	18.80882	0.046488	15.68923	0.037333	39.1281	0.102036
SEL-R685	pyrite	47	core	0.839018	0.001829	2.085598	0.003237	18.67545	0.095228	15.66893	0.078044	38.94936	0.203873
SEL-R685	pyrite	46	core	0.842462	0.002086	2.083263	0.00262	18.49993	0.041224	15.58538	0.051235	38.54011	0.096437
SEL-R685	pyrite	51	rim	0.842803	0.001276	2.091905	0.002679	18.52998	0.082361	15.61701	0.071285	38.76284	0.174716
SEL-R685	pyrite	52	core	0.843383	0.001162	2.08963	0.003865	18.55586	0.054779	15.6496	0.049622	38.77479	0.124817
SEL-R685	pyrite	45	core	0.844196	0.001757	2.090879	0.003204	18.55549	0.060095	15.66436	0.031706	38.79717	0.108639
SEL-R685	pyrite	54	rim	0.844803	0.001605	2.094648	0.00215	18.51033	0.097245	15.63747	0.096497	38.77252	0.188595
TER-R016	pyrite	78	core	0.831371	0.006912	2.077991	0.013013	18.66704	0.328898	15.51918	0.366112	38.78992	0.805899
TER-R016	pyrite	76	core	0.83394	0.001384	2.083718	0.004932	18.74319	0.040431	15.63063	0.047117	39.05548	0.136554
TER-R016	pyrite	68	core	0.839852	0.002854	2.079681	0.006481	18.59804	0.088168	15.61952	0.043474	38.67793	0.128032
TER-R016	pyrite	67	core	0.840445	0.002564	2.083018	0.004375	18.71596	0.057382	15.72965	0.086196	38.9856	0.155009
TER-R016	pyrite	79	core	0.841223	0.001058	2.08753	0.00582	18.61536	0.165731	15.65961	0.130573	38.86009	0.293069
TER-R016	pyrite	75	core	0.841404	0.002302	2.087889	0.009056	18.486	0.15054	15.55414	0.141396	38.59667	0.339742
TER-R016	pyrite	70	core	0.843374	0.002081	2.077655	0.003485	18.74288	0.061495	15.80718	0.050452	38.94119	0.124203
TER-R016	pyrite	72	core	0.843514	0.003043	2.083809	0.008954	18.65007	0.124391	15.73151	0.094051	38.86312	0.290491
TER-R016	pyrite	69	core	0.843737	0.003718	2.086161	0.011102	18.95962	0.069671	15.99684	0.09866	39.55275	0.291622
TER-R016	pyrite	71	core	0.845286	0.006902	2.074145	0.011507	18.71893	0.0956	15.82277	0.128439	38.82573	0.226738
TER-R016	pyrite	73	core	0.845425	0.003479	2.088233	0.0071	18.58883	0.103104	15.71538	0.092244	38.81775	0.210653
TER-R016	pyrite	74	core	0.845554	0.002696	2.09296	0.006277	18.74265	0.08671	15.84784	0.078551	39.22756	0.201692
TER-R016	pyrite	77	core	0.849764	0.005523	2.083934	0.01002	18.69884	0.141548	15.88953	0.141514	38.9671	0.254815

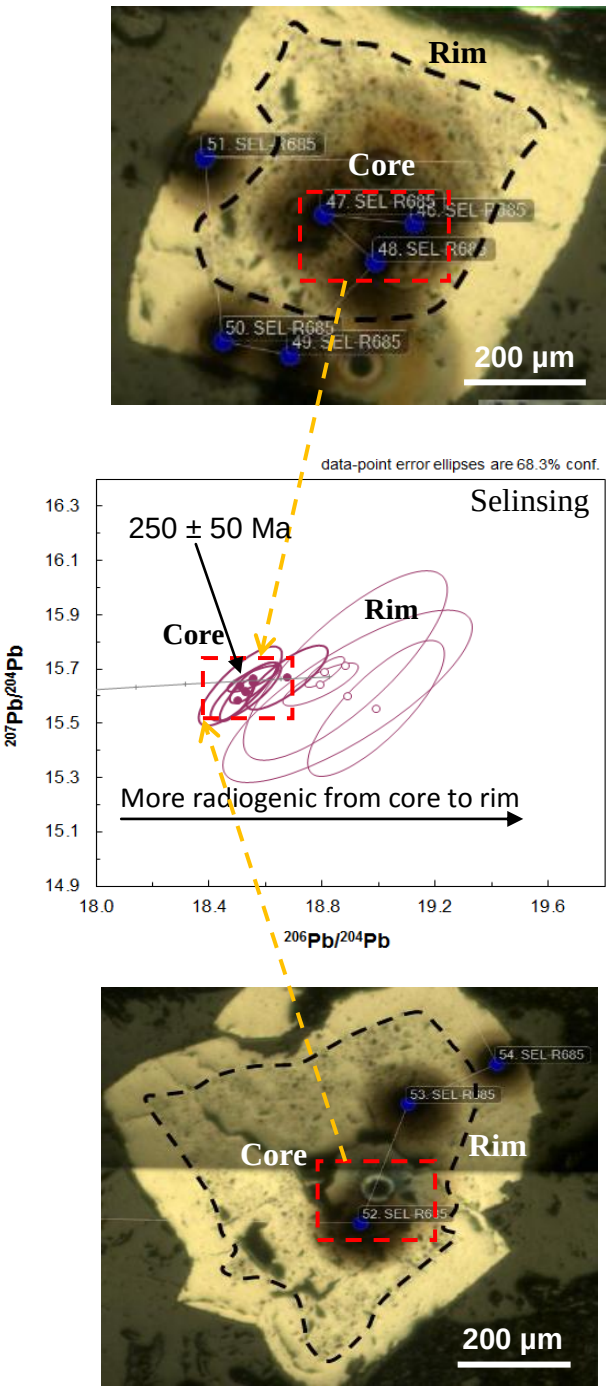

Fig. 6.4. Pb isotope analyses (sample SEL-R685) of pyrite highlighting the position of the pyrite core and the corresponding analyses in the ellipses from the Selinsing gold deposit, Malaysia. The age of gold mineralisation is deduced from this figure. The core of pyrite has a Pb-Pb model age around 250 ± 50 Ma (concentric ellipses). The pyrite rims are more radiogenic and do not help in the deduction of the age with more spreading ellipses.

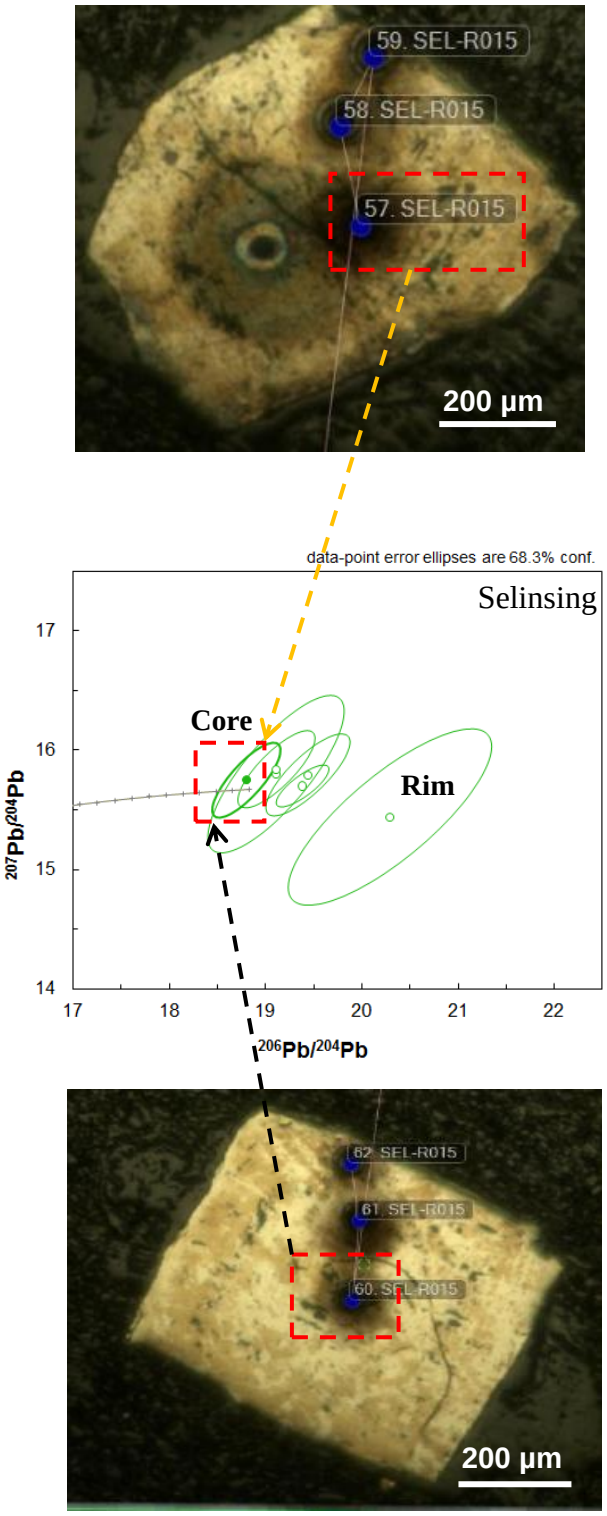

Fig. 6.5. Pb isotope analyses (sample SEL-R015) of pyrite from the Selinsing gold deposit, Malaysia. Pyrite rims are more radiogenic than their cores.

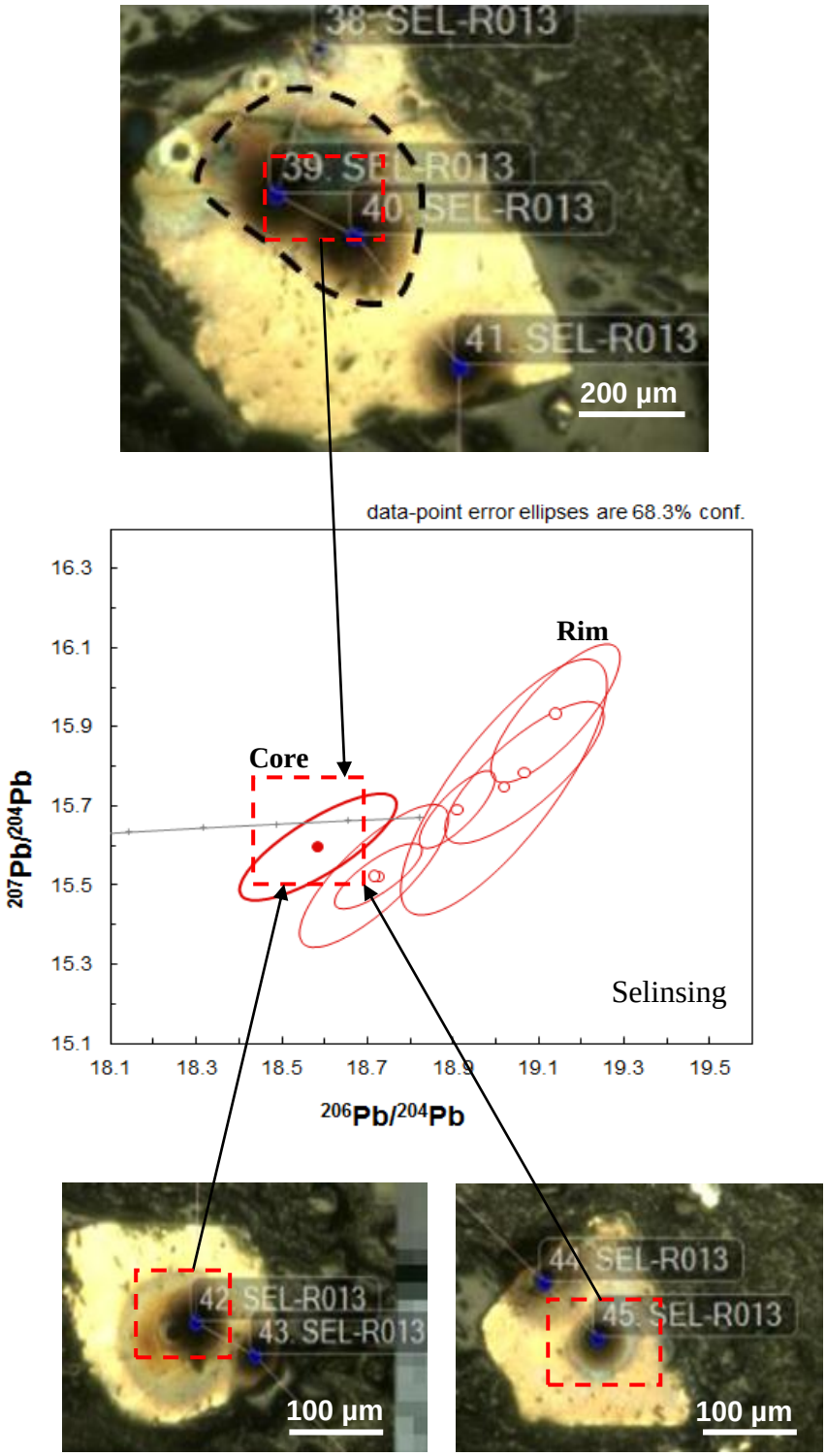

Fig. 6.6. Pb isotope analyses (sample SEL-R013) of pyrite from the Selinsing gold deposit, Malaysia. The pyrite cores are less radiogenic than the rims.

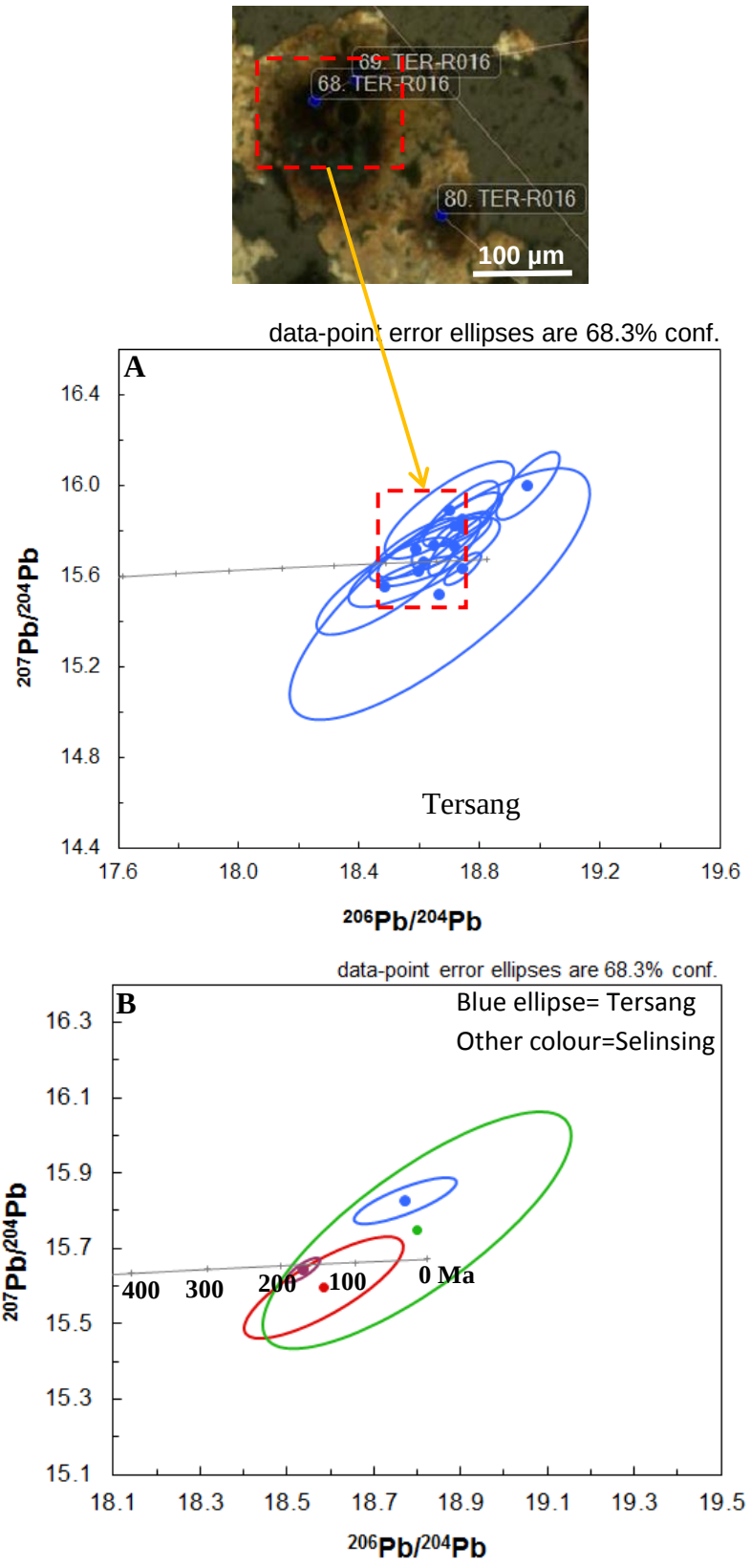

Fig. 6.7. Comparative Pb isotope composition from the gold deposits, Malaysia. A) The ratio $^{206}Pb/^{204}Pb$ versus $^{207}Pb/^{204}Pb$ in pyrite from the Tersang gold deposit. **B**) The ratio $^{206}Pb/^{204}Pb$ versus $^{207}Pb/^{204}Pb$ for all pyrite core analyses from the Selinsing and Tersang gold deposits. Note: Ma= million years.

6.3.3. Discussion

Early researchers speculated that the gold mineralisation in central mainland Malaysia may be associated with granitoids (Scrivenor, 1928; Willbourn, 1933; Ingham, 1938; Richardson, 1939). Later studies such as Yeap (1993) documented that in the Central Gold Belt gold mineralisation may be associated with volcanism in the area. In this study, field observation has shown that the Semantan black shales (Chapter 2) are associated with tuffs which strongly indicate that volcanism in the area occurred during deposition of the shales. The age of the tuff is 233.1 ± 1.6 Ma indicating a Middle Triassic age (Ladinian) for the volcanism. The Pb isotope composition of pyrite from the Semantan tuffaceous black shales (Fig. 6.2A) is slightly less radiogenic than that of K-feldspar (Fig. 6.2B) from S-type granites that crop out in the Central Gold Belt. Similarly, the Pb-Pb isotopic model age of feldspar is similar to the crystallisation age of zircon from granites (Fig. 6.3). The Pb isotope compositions of pyrite cores at the Selinsing and Tersang gold deposits indicate an approximate age of gold mineralisation around 200 Ma (Early Jurassic). This age coincides with that of gold mineralisation at the Penjom gold deposit where K-Ar age of sericite from gold-hosted tonalite intrusion thought to be coeval with the timing of mineralisation gave 197-199 Ma (Early Jurassic) (Makoundi, 2012).

Although the age of the granites and ores may be similar there are small differences in the Pb isotopic composition of the ores and that of the granite and sedimentary pyrite. The sedimentary pyrite and granite K-feldspars plot on a high μ (high U/Pb) growth curve typical of S-type granites and sediments but the ores tend to plot on the bulk crustal growth curve (Figs. 6.4-6.7) suggesting a greater proportion of mantle Pb relative to upper crustal Pb. This mantle Pb could be partly sourced from I-type granitoids, mafic rocks or arc-related volcanic rocks. The present research outcomes show no evidence of temporal relationship between

gold mineralisation and volcanism because of 33 Ma of age difference between the approximate 200 Ma (age of gold mineralisation) and 233 Ma (age of the volcaniclastic rocks). The Pb isotope compositions of K-feldspar from megacrystic granite and their zircon age data (e.g. sample BE-11513) are different from those of granites. Field relationships of the megacrystic granite with adjacent rocks close to the Tersang gold deposit are shown in Fig. 6.8.

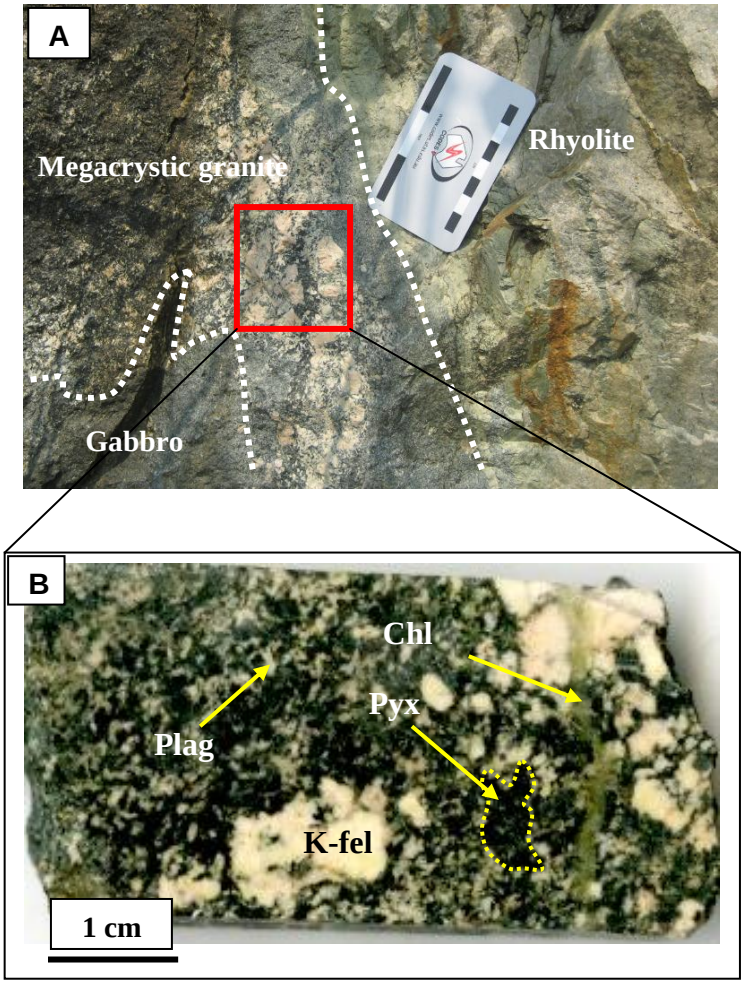

Fig. 6.8. Field relation of the megacrystic granite, rhyolite, and gabbro from an igneous complex, east of the Tersang gold deposit, Malaysia. **A**) Outcrop showing the megacrystic granite, gabbro, and rhyolite. **B**) Close-up of the megacrystic granite hand specimen. Megacrystic granite is composed of large crystals of alkali feldspar (pink colour) with size varying from 1.3 to 2.2 cm, plagioclase, pyroxene and chlorite. Plagioclase and pyroxene are primary phases whereas chlorite may have derived from deuteric or other alteration or metamorphism; not a primary phase.

6.4. Sulphur isotopes

Gold is commonly carried as bisulfide complexes in orogenic terrains (Groves et al., 2003; Goldfarb et al., 2005). Therefore, the source of sulphur is important in deducing the source of gold and ore-forming fluids. Sulphur has four stable isotopes which include: S^{32} (95.02 %), S^{33} (0.75 %), S^{34} (4.21 %), and S^{36} (0.02 %). Among these isotopes, S^{32} and S^{34} differ in mass by 6% with a precision ratio of 0.02 % (Rye and Ohmoto, 1974). The isotopic ratio in a given reservoir is determined by the proportion of heavy isotope over the light isotope, which is the ratio of S^{34}/S^{32}. The isotopic composition is determined by the measurement of the S^{34}/S^{32} with data for each isotope given in parts per thousand or per mil and formulated in the following equation: $\delta^{34}S = [(R\ sample - R\ standard)] \times 10^3$; here $R = S^{34/32}$ (Rollinson, 1996). The Canon Diablo Troilite (CDT) is the standard for $\delta^{34}S$ and has an isotopic ratio of $S^{34}/S^{32} = 0.0450045$ (Ault and Kulp, 1960) and a given value of 0.00 ‰ (Ohmoto and Rye, 1979). Positive per mil deviations point to enrichments of S^{34} relative to the standard (CDT); however negative per mil deviations indicate depletions. The analyses were determined using conventional techniques as summarized in the appendix A. An accuracy of ± 0.15 ‰ is obtained by the conventional method at the Central Science Laboratory, University of Tasmania.

Rye and Ohmoto (1974) reported that sulphur of mantle and magmatic origin is considered to have a $\delta^{34}S$ value close to zero comparable to the standard (CDT). In contrast, $\delta^{34}S$ values of approximately +20 per mil imply that marine evaporates or seawater is likely to be the source of the sulphur. Seawater sulphates can yield variable heavy $\delta^{34}S$ isotopic values ranging from +10 to +35 ‰ from the Cambrian to the present (Rollinson, 1996). Modern seawater sulphates have $\delta^{34}S$ values which range from +18 to 20 ‰ (Rollinson, 1996), whereas sedimentary environments can have variable $\delta^{34}S$ values ranging from -70 to >+20 ‰ (Ohmoto and Rye, 1979). Furthermore, sulphides in hydrothermal systems mostly

yield $\delta^{34}S$ values clustered around 0.0 ‰ with values ranging up to 10‰ when certain conditions of temperature and pH are met and the primary isotopic compositions are preserved (Ohmoto and Rye, 1979). Sulphur can be also introduced by metamorphic fluids from wall rocks (Sangster, 1992; Goldfarb et al., 1997) or from the deep crust during amphibolite-grade and granulite-grade metamorphism (Phillips et al., 1987). Most $\delta^{34}S$ values of sulphides from skarn deposits are between -5 per mil and +8 per mil implying a magmatic origin of the sulphur (Bowman, 1998).

6.4.1. Results and discussion

In this section, sulphur isotope compositions of pyrite in sedimentary rocks and those of pyrite in the gold deposits are documented, compared, and discussed in terms of the source of sulphur. Results of sulphur isotope compositions are given in Table 6.4. The sulfur isotope composition of the Ladinian Gua Musang Formation yield values that range from -27.9 ‰ to – 0.9 ‰ (mean -13.4 ‰). The $\delta^{34}S$ values for the Anisian Karak Formation are between -8.0 ‰ and -10.3 ‰ (mean -9.1 ‰). In contrast, the Late Devonian BRSZ Unit 1 $\delta^{34}S$ values are negative and range from -14.0 ‰ to -32.1 ‰ (mean -26.8) and are much lighter compared to the Anisian Karak pyrites. The $\delta^{34}S$ values for the Pennsylvanian-Early Permian Singa Formation range from -24.6 ‰ to 2.9 ‰ (mean -8.3 ‰). The Early Ordovician-Silurian Setul pyrites have $\delta^{34}S$ values which spread from -14.8 ‰ to -7.9 ‰ (mean -11.3). These values are best fit within the range of the Late Devonian BRSZ Unit 1 isotope values. Histograms of sulphur isotope values in the Phanerozoic formations are shown in Figs. 6.9 and 6.10.

Table 6.4. Results of sulphur isotope analyses of pyrite from selected black shale and sandstone samples in the studied formations, Malaysia.

Samples	Rock type	Formation	Age	$\delta^{34}S_{CDT}$	Mean
CH-0612	Black shale	**Semantan**	**Ladinian**	-3.69	-3.7
PJ-1812	Black shale	**Gua Musang**	**Ladinian**	-9.22	-13.4
PJ-2112	Black shale	**Gua Musang**	**Ladinian**	-13.01	
KL-0112	Black shale	**Gua Musang**	**Ladinian**	-3.53	
GM-0912	Black shale	**Gua Musang**	**Ladinian**	0.91	
GM-1212	Black shale	**Gua Musang**	**Ladinian**	-20.63	
TP-1612	Black shale	**Gua Musang**	**Ladinian**	-27.85	
GM-1312	Black shale	**Gua Musang**	**Ladinian**	-18.41	
KL-0312	Black shale	**Gua Musang**	**Ladinian**	-12.31	
GM-1112	Black shale	**Gua Musang**	**Ladinian**	-16.90	
ME-6312	Black shale	**Karak**	**Anisian**	-10.27	-9.1
ME-6212	Black shale	**Karak**	**Anisian**	-8.02	
BE-2512	Black shale	**BRSZ Unit 1**	**Late Devonian**	-31.85	-26.8
BE-2312	Black shale	**BRSZ Unit 1**	**Late Devonian**	-13.98	
BE-2612	Black shale	**BRSZ Unit 1**	**Late Devonian**	-29.10	
BE-2712	Black shale	**BRSZ Unit 1**	**Late Devonian**	-32.13	
LA-3812	Black shale	**Singa**	**Pennsylvanian-Early Permian**	6.24	-8.3
LA-5712	Black shale	**Singa**	**Pennsylvanian-Early Permian**	-13.86	
LA-3712	Black shale	**Singa**	**Pennsylvanian-Early Permian**	-8.44	
LA-3912	Black shale	**Singa**	**Pennsylvanian-Early Permian**	-4.19	
LA-3612	Black shale	**Singa**	**Pennsylvanian-Early Permian**	-7.47	
LA-4212	Black shale	**Singa**	**Pennsylvanian-Early Permian**	-5.15	
LA-4312	Black shale	**Singa**	**Pennsylvanian-Early Permian**	2.88	
LA-4412	Black shale	**Singa**	**Pennsylvanian-Early Permian**	-2.34	
LA-3512	Black shale	**Singa**	**Pennsylvanian-Early Permian**	-19.69	
LA-4012	Black shale	**Singa**	**Pennsylvanian-Early Permian**	-1.41	
LA-4112	Black shale	**Singa**	**Pennsylvanian-Early Permian**	-24.64	
LA-3412	Black shale	**Singa**	**Pennsylvanian-Early Permian**	-21.61	
LA-4612	Sandstone	**Setul**	**Early Ordovician-Silurian**	-7.90	-11.3
LA-5012	Sandstone	**Setul**	**Early Ordovician-Silurian**	-14.77	

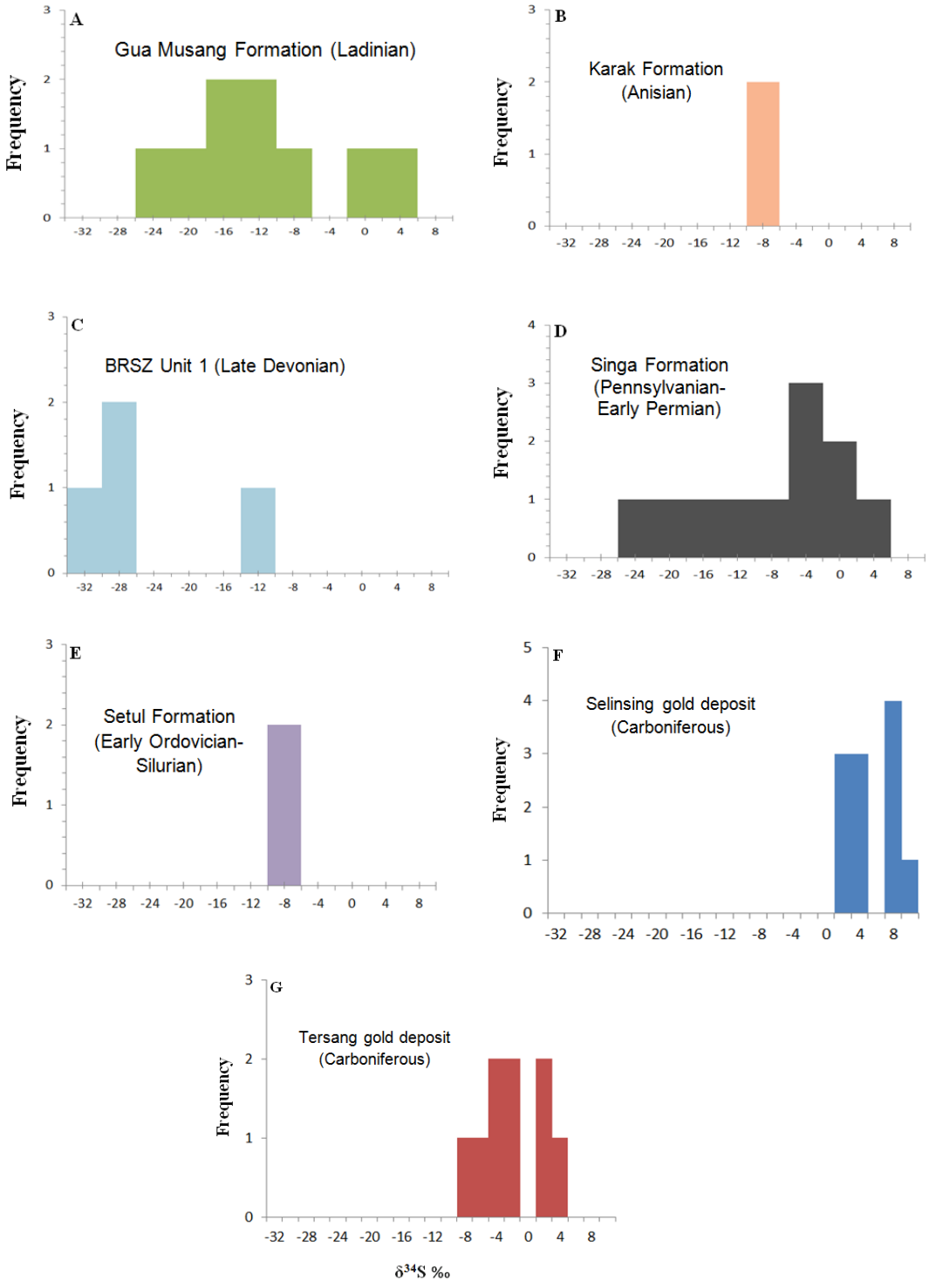

Fig. 6.9. Histograms of sulphur isotope composition of formation pyrite in the selected Phanerozoic sedimentary formations, Malaysia. **A**) Ladinian Gua Musang Formation. **B**) Anisian Karak Formation. **C**) Late Devonian BRSZ Unit 1. **D**) Pennsylvanian-Early Permian Singa Formation. **E**) Early Ordovician-Silurian Setul. **F**) Carboniferous Selinsing gold deposit (data from Makoundi, 2012). **G**) Carboniferous Tersang gold deposit (data from Makoundi, 2012).

Compared to deposit-hosted pyrites (Fig. 6.10), the sulphur isotope compositions of pyrite in black shales have a wider spread of data ranging from -32.1 ‰ to 6.2 ‰ (mean -12.4 ‰). The sulphur isotope composition of pyrite (grey curve to the left, Fig. 6.10) in the sedimentary basins that are composed of the Setul, Singa, BRSZ Unit 1, Karak, and Gua Musang formations, show trend that is broadly parallel (Fig. 6.10) to the seawater sulphate curve (Fig. 6.10, green curve to the right). The evidence suggests that sulphur in the black shales and in host rocks at the gold deposits originated from the reduction of seawater sulphate as the sulphate and pyrite curves vary in a similar fashion.

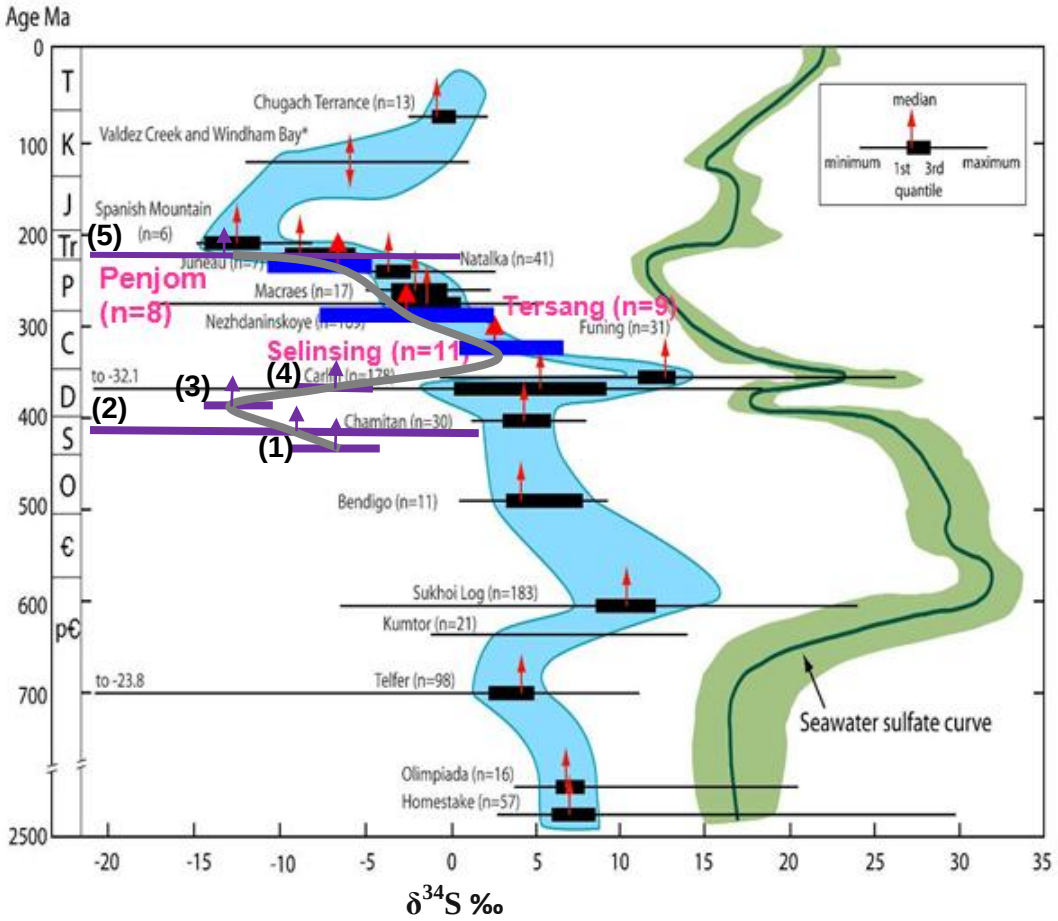

Fig. 6.10 Sulphur isotope composition of the selected Phanerozoic formations (lines in purple colour) combined with data from Khin Zaw et al. (2008) for the Penjom gold deposit and Makoundi (2012) for the Selinsing and Tersang gold deposits. Note the trends of well known sediment-hosted orogenic gold deposits through geologic time (blue curve) and sea water sulfate curve (green curve) (Modified after Chang et al., 2008). Current formations studied are: **1**) Setul Formation (427.4 Ma), **2**) Singa Formation (418.6 Ma), **3**) BRSZ Unit 1 (367.6 Ma), **4**) Karak Formation (236.7 Ma), and **5**) Gua Musang Formation (231 Ma). Red arrows mean the median and the black bars are the gold deposit sulphur ranges.

Similarly, Makoundi (2012) interpreted the sulphur isotope compositions from the Selinsing, and Tersang gold deposits as having originated from seawater sulphate. The $\delta^{34}S$ values in this study are typical of sedimentary pyrite as shown in Fig. 6.11. Compared to the ore $\delta^{34}S$ curve (Fig. 6.10, blue curve), the isotopic composition curve is offset to heavier or more negative values in the Pennsylvanian-Early Permian sediments.

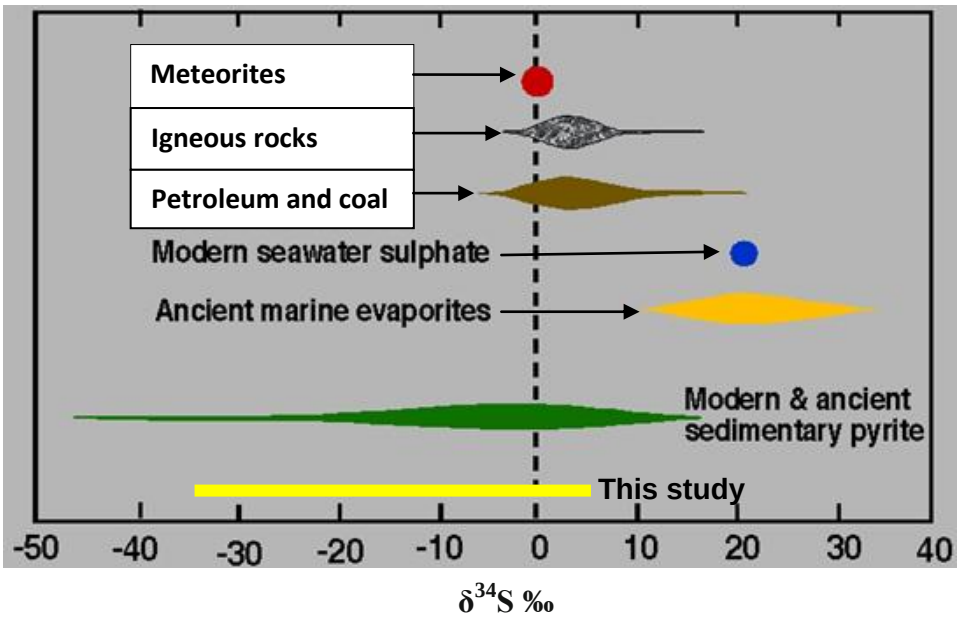

Fig. 6.11. Chart showing $\delta^{34}S$ values from various geological reservoirs (modified from Seal, 2006). Note that the present dataset (the yellow bar) fits within the modern and ancient sedimentary pyrite range.

6.5. Organic carbon isotope

A number of samples (Table 6.5) from the sedimentary formations including the Middle Triassic Gua Musang, Middle Triassic Karak, Late Devonian BRSZ Unit 1, Pennsylvanian-Early Permian Singa, and Early Ordovician-Silurian Setul formations have been analysed to determine their organic carbon isotope compositions at the Central Science Laboratory, University of Tasmania, Australia. Method of analysis is documented in

Appendix A. The aim of this study is to determine whether the sediments originated from marine or terrestrial organic matter.

6.5.1. Results

Organic-rich clastic sequences were analysed for their organic carbon isotope compositions (Table 6.5). The Gua Musang, Karak, BRSZ Unit 1, Singa and the Setul formations were selected because of elevated organic carbon content which varies up to 2.41 wt %. Results indicate that the Ladinian Gua Musang Formation has a range of organic carbon isotope composition from – 29.8 ‰ to – 18.7 ‰ (mean -24.0 ‰). The Anisan Karak Formation has a narrow range of organic carbon composition from -19.5 ‰ to -22.3 ‰ (mean -20.9 ‰). Additionally, the Late Devonian BRSZ Unit 1 also displays a narrow range between -26.6 ‰ and -28.53 ‰ (mean -27.9 ‰). The Pennsylvanian-Early Permian Singa Formation has a wide range from -23.9 ‰ to -5.8 ‰ (mean -14.6 ‰); however, the youngest Early Ordovician-Silurian Setul Formation indicates $\delta^{13}C_{org}$ values ranging from – 29.5 ‰ to -7.0 ‰ (mean -18.3 ‰).

6.5.2. Discussion

Commonly, $\delta^{13}C_{org}$ (organic carbon isotopic composition) for the marine plants varies from -8 ‰ to -17 ‰, whereas for the land plants, it is between -22 ‰ and -29 ‰ (Craig, 1953; Clayton and Degens, 1959; Keith et al., 1964; Sackett, 1964; Keith and Parker, 1965; Degens, 1969; Schidlowski et al., 1983). The Singa and Setul formations have less depleted $\delta^{13}C$ values consistent with elevated organic carbon content (0.1 wt % – 2.4 wt %).

Table 6.5. Results of organic carbon isotope analyses of selected formations, Malaysia. PDB (Peedee Belemnite) refers to the standard used in reporting $\delta^{13}C_{org.}$

Sample ID	Formation	Depositional age	Weight (mg)	^{13}C (org)	Corrected $\delta^{13}C_{PDB}$	Source
PJ-1812	Gua Musang	Ladinian	28.1159	-24.80	-25.36	Terrestrial
PJ-2112	Gua Musang		30.9970	-23.67	-24.21	Terrestrial
CH-0612	Gua Musang		28.8222	-29.19	-29.85	Terrestrial
GM-0912	Gua Musang		20.7203	-26.35	-26.95	Terrestrial
GM-1212	Gua Musang		21.3416	-19.78	-20.24	Terrestrial
TP-1612	Gua Musang		21.6485	-21.14	-21.63	Terrestrial
GM-1312	Gua Musang		13.0203	-19.93	-20.40	Terrestrial
KL-0312	Gua Musang		13.3741	-25.05	-25.63	Terrestrial
GM-1112	Gua Musang		12.6069	-18.23	-18.66	Terrestrial
KL-0112	Gua Musang		7.5474	-26.66	-27.27	Terrestrial
ME-6212	Karak	Anisian	11.5853	-21.79	-22.30	Terrestrial
ME-6312	Karak		6.8541	-19.05	-19.50	Terrestrial
BE-2512	BRSZ Unit 1	Late Devonian	30.3483	-27.44	-28.07	Terrestrial
BE-2312	BRSZ Unit 1		28.3780	-26.05	-26.65	Terrestrial
BE-2612	BRSZ Unit 1		6.4023	-27.69	-28.32	Terrestrial
BE-2712	BRSZ Unit 1		5.3277	-27.90	-28.53	Terrestrial
LA-3412	Singa	Pennsylvanian-Early Permian	30.4930	-23.40	-23.94	Terrestrial
LA-3512	Singa		21.0176	-17.80	-18.21	Terrestrial
LA-3612	Singa		14.8908	-9.22	-9.46	Marine
LA-3712	Singa		11.0084	-11.31	-11.59	Marine
LA-3812	Singa		7.9452	-5.69	-5.85	Marine
LA-3912	Singa		14.1708	-8.17	-8.38	Marine
LA-4012	Singa		24.8003	-21.89	-22.40	Terrestrial
LA-4112	Singa		22.6723	-21.47	-21.97	Terrestrial
LA-4212	Singa		30.0938	-18.19	-18.62	Terrestrial
LA-4312	Singa		29.3079	-17.62	-18.03	Terrestrial
LA-4412	Singa		28.1086	-6.72	-6.90	Marine
LA-5712	Singa		16.7783	-9.20	-9.44	Marine
LA-4612	Setul	Early Ordovician-Silurian	6.4456	-28.92	-29.58	Terrestrial
LA-5012	Setul		21.0246	-6.91	-7.09	Marine

The Singa Formation has $\delta^{13}C_{org}$ values that range from -23.9 ‰ to -5.8 ‰ (mean -14.6 ‰) whereas the Setul Formation has $\delta^{13}C_{org}$ values between -7.0 ‰ and -29.5 ‰ (mean -18.3

‰). These values reflect a mixed terrestrial and marine origin for organic carbon. The source of the organic carbon has effects on the nature of the organic carbon in the sediments. A comparative chart of $\delta^{13}C_{org}$ ‰ values is shown below (Fig. 6.12). The less depleted $\delta^{13}C_{org}$ values (Table 6.5) may be explained by an increase in the proportion of organic carbon in the sediments (Kump and Arthur, 1999).

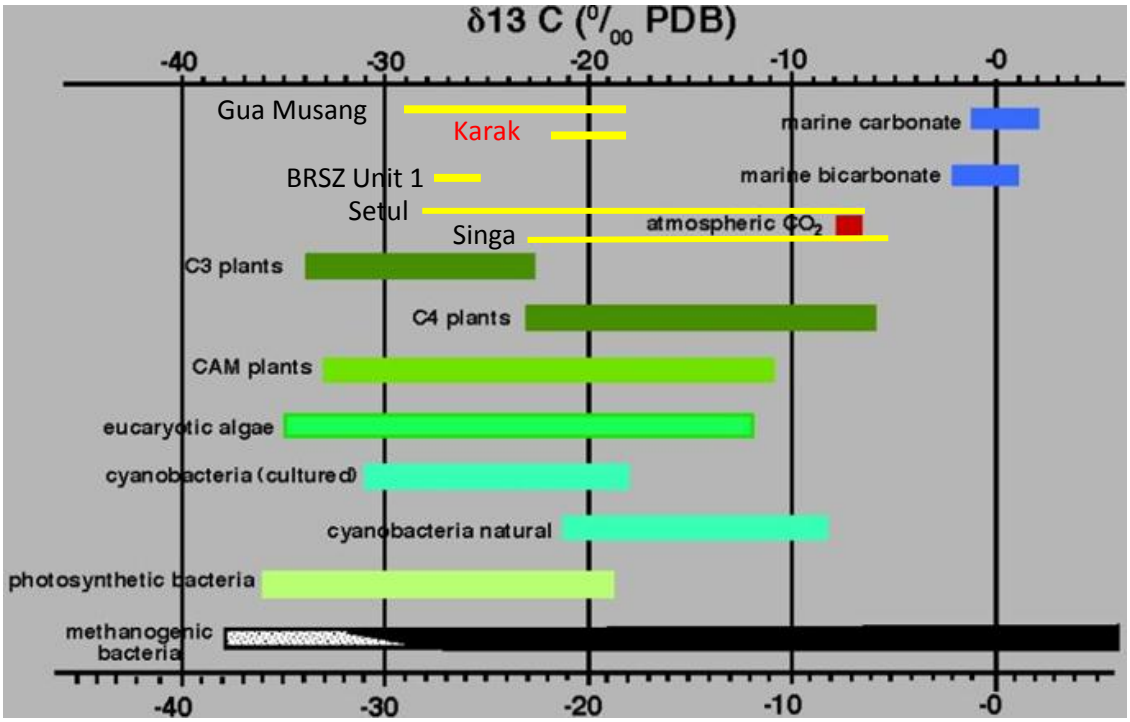

Fig. 6.12. Comparative chart of organic carbon isotope compositions from selected Phanerozoic formations in Malaysia and data from previous work (modified from Schidlowski et al.,1983).

The Late Devonian BRSZ Unit 1 has a narrow range of organic carbon composition ranging from -28.5 ‰ to – 26.6 ‰ indicating terrestrial origin for organic carbon. This sedimentary unit has the strongest depletion in $\delta^{13}C_{org}$ (mean value -27.9 ‰). Xu et al. (1986) argued that pronounced depletion in carbon isotopic compositions may be due to mass extinction across the Devonian/Carboniferous boundary.

The Middle Triassic Gua Musang Formation has a narrow range from -29.8 ‰ to -18.7 ‰ (mean -24 ‰) suggesting a terrestrial origin of organic carbon. Similarly, the Middle Triassic Karak Formation records a range between -22.3 ‰ and -19.5 ‰ (mean -20.9 ‰) indicating a terrestrial origin of organic carbon. Both formations have moderately depleted δ^{13}Corg values. In this study, there is contribution of organic matter from both the marine and land environments. A comparison of organic isotope composition for the Neo-Proterozoic and Phanerozoic organic matter with that of present work is shown below (Fig. 6.13).

Sackett (1989) reported that the sedimentary $\delta^{13}C_{org}$ values are controlled by the relative contributions of marine and terrestrial matter and that the isotopic composition of terrestrially derived organic matter is significantly lighter than that of marine organic matter (Sackett, 1989).The work of Oehlert and Swart (2014) also supported the terrestrial origin of organic matter for δ13Corg values that range from -32 ‰ to -20 ‰ in mangroves and fresh water algae on the Great Bahama Bank, USA. Overall, the evidence indicates that the $\delta^{13}C_{org}$ values for the studied formations likely represents eukaryotic algae (mean -20.2 ‰) and lichens both from the sea and land as shown on Fig. 6.12.

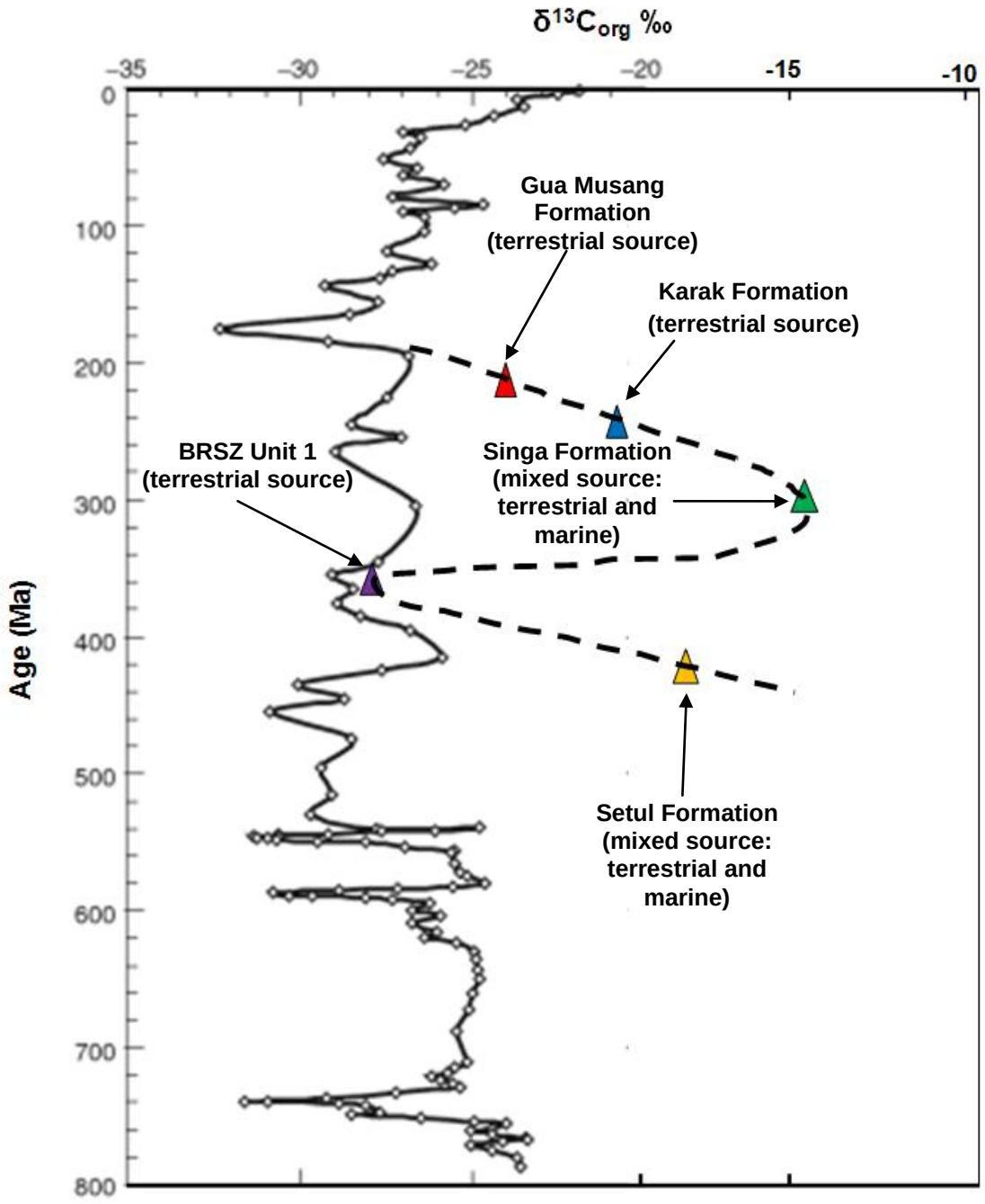

Fig. 6.13. Carbon isotopic composition in Neo Proterozoic age (> 570 Ma) and Phanerozoic time (this study) of sedimentary organic matter (modified from Holland and Turekian, 2011). The dashed line represents variation of the organic carbon isotopic composition (mean values) of the selected formations. There is a trough pointing to a strongly depleted organic carbon isotopic composition in the sediments of terrestrial source for organic carbon. Importantly, the sediments that contain a mixed source of organic carbon (e.g. Singa and Setul formations) have organic carbon isotopic compositions heavier than those of terrestrial origin (e.g. BRSZ Unit 1, Gua Musang and Karak formations).

6.6. Conclusions

The Pb isotope compositions of pyrite in the studied formations do not match the age of volcanism in the district which is around 233.1 Ma. Gold-bearing ore pyrites from the Selinsing and Tersang gold deposits have Pb isotope compositions around 200 Ma. This age may be interpreted as the age of gold mineralisation in the district. The sulphur isotope compositions of pyrite in the sedimentary sequences from the Early Ordovician-Silurian Setul, Pennsylvanian-Early Permian Singa, Late Devonian BRSZ Unit 1, Middle Triassic Karak, and Middle Triassic Gua Musang formations, trend parallel to the seawater sulphate curve strongly suggesting that sulphur in the black shales far from ore zones and in host rocks at the gold deposits may have originated from the reduction of seawater sulphate.

The Palaeozoic formations have shown a mix of terrestrial and marine source for organic carbon; however, the Mesozoic formations point to a terrestrial origin for the organic carbon. In this study, the evidence indicates that the sulphur isotope compositions in the black shales far from mineral deposits and those from the sediment-hosted gold deposits gold deposits originated from the reduction of seawater sulphate. The big shift between the sea water sulphate curve and sediment-hosted orogenic gold deposits is due to isotopic fractionation of sulphur as a result of interaction between magmatic hydrothermal fluids and sediments at the deposit scale.

CHAPTER 7
DISCUSSION AND CONCLUSIONS

7.1. Introduction

This Chapter combines lithogeochemistry, zircon dating, pyrite trace element chemistry, and Pb isotope composition of the formation shales to discuss relationships to gold mineralisation and source rock characteristics. Temporal changes in trace element content in both the whole rocks and pyrite are also documented. Chemical criteria for sedimentary and metamorphic-hydrothermal pyrites (this study) are compared with worldwide diagenetic pyrites (Gregory et al., 2015) for the purpose of contributing to the existing geochemical knowledge on pyrite. The gold content in sedimentary pyrite is compared to that of pyrites contained in some magmatic rocks to assess the likely sources for the gold. Establishing the source of gold is important, not only in guiding exploration, but also for an assessment of the potential occurrences of new gold deposits in the world.

7.2. Trace elements in black shales and geochemical controls

This section summarizes enrichment and depletion against PAAS (Post-Archean Australian Shales) of some trace elements and their relationships with organic carbon and alumina for the Pennsylvanian-Early Permian Singa Formation black shales, the Late Devonian BRSZ Unit 1 black shales, the Middle Triassic Semantan and Gua Musang formation black shales. The Pennsylvanian-Early Permian Singa Formation black shales show a similar trace element composition compared to PAAS. Al_2O_3 content varies positively with Ni, Cu, Zn, As, and Sb implying that these trace elements may have been adsorbed onto clays

or aluminosilicates during deposition. The total organic carbon content (mean 0.2 wt %) is low and shows no correlation with trace elements such as Au, V, Cr, U, and Ni indicating that the deposition of these metals was not controlled by organic processes. Gold has a weak correlation with V (cc= 0.32) pointing to little control of organic processes during deposition of gold into sediment. The Singa black shales were likely deposited under oxic bottom waters consistent with a weak control of organic processes during deposition of trace metals.

Compared to PAAS (Post-Archean Australian Shale), the BRSZ Unit 1 black shales are enriched in V, Cu, Mo, Sn, Pb, U, and Ga and depleted in Ni, and Zn. In the Late Devonian BRSZ Unit 1 black shales, trace elements such as V, Cr, Zn, As, Se, Mo, Sn, Sb, and U have positive correlation with alumina implying some sedimentary (clay) control for these trace elements during their deposition into basin. In these black shales, organic carbon content varies positively with V, Cr, Ni, As, Se, Mo, Sn, Sb, and U suggesting an additional control of organic matter on such elements in the BRSZ Unit 1 black shales. Additionally, the Late Devonian BRSZ Unit 1 black shales record the highest contents of V, Cu, Bi, Mo, Cr, Te, Se, Ag, S, Ni, U, and organic carbon compared to other formation shales in Malaysia. The BRSZ Unit 1 black shales deposited under euxinic/anoxic conditions consistent with elevated total organic carbon, sulphur, Mo and U contents. The Middle Triassic Semantan black shales have similar trace element composition relative to PAAS. Al_2O_3 content varies positively with V, Cr, Mo, Sb, and U and organic carbon whereas it changes negatively with As and Zn. The evidence indicates that V, Cr, Sb, Mo, and Sb were introduced into sediments via clays in the Semantan basin. In the Semantan black shales, organic carbon (TOC) content ranges from 0.3 to 0.7 wt % (mean 0.4 wt %) and shows a positive correlation with V, U, Mo, and Sb suggesting that these elements were introduced into sediments by organic processes in anoxic-euxinic bottom waters.

The Middle Triassic Gua Musang black shales are weakly enriched in U, Pb, and Mo and depleted in Ni, Cu, Zn, and Cr relative to PAAS. Al_2O_3 content displays a weak positive correlation with Au, Ni, Cr, and Sn; however, other trace elements have no correlation with Al_2O_3. The evidence suggests that Au, Ni, Cr and Sn may have been introduced into sediments attached to clay minerals or contained in the aluminosilicate mineral structure. As a whole, organic carbon content is low (up to 0.6 wt %) and displays no clear relationships with V, U, Ni, Cr, and Mo implying little contribution of organic processes during incorporation of these elements into sediments. The evidence suggests that in the Gua Musang Formation gold may have been introduced into sediments attached to clay particles.

From the Late Cambrian to Late Triassic (Norian), changes in concentration of organic carbon, sulphur and selected trace elements in whole rocks are shown in Figs. 7.1-7.3. The corresponding ages for each formation as shown on Y axis represent newly constrained maximum depositional ages of detrital zircons documented in previous chapters. Through time, the total organic carbon and sulphur content trends are almost similar likely reflecting the redox conditions in the ocean (Fig. 7.1). In previous work, positive correlation was observed between organic matter and pyrite implying the covariance of carbon and sulphur at depth in marine sediments (Berner, 1982).

In anoxic-euxinic conditions, the total organic carbon (TOC), S, and V contents are particularly elevated as shown in the BRSZ Unit 1 and 2. The Ni, Cu contents are elevated in euxinic/anoxic conditions, whereas the Zn content had increased in an oxic environment such as the Pennsylvanian-Early Permian Singa Formation. The Mo and U contents are high in the anoxic to euxinic water conditions within the BRSZ unit 2 likely related to a higher productivity and organic carbon content (Fig. 7.3). A summary of the major and trace element characteristics of most formations (Table 7.1) except for the Karak Formation whose whole

rock compositions were not determined. In terms of provenance, the Triassic formation shales (i.e. Gua Musang; Semantan; BRSZ Unit 2) record an intermediate-mafic provenance; however, the Palaeozoic formation shales (i.e. Machinchang; Setul; Singa; BRSZ Unit 1) yield a felsic-intermediate provenance (Table 7.1).

Table 7.1. Major and trace element characteristics of the studied Phanerozoic formations in Malaysia.

Formation	**Machinchang**	**Setul**	**Singa**	**BRSZ Unit 1**	**Gua Musang**	**Semantan**	**BRSZ Unit 2**
Age	Late Cambrian-Early Ordovician	Early Ordovician-Silurian	Pennsylvanian-Early Permian	Late Devonian	Middle Triassic	Middle Triassic	Late Triassic
Mean org. C (wt %)	0.1	1.5	0.2	0.6	0.2	0.4	2
Mean alumina	23.4	3.2	14.5	19.7	19.6	18.3	4
Mean Au In whole rock (ppb)	49	26.5	58	23	28	Not analysed	Not analysed
TE enriched versus PAAS	U, Sn, Th	Co, Mo, U	Similar to PAAS	V, Cu, Mo, Sn, Pb, U	U, Mo, Pb	Similar to PAAS	Mo, Cu
TE depleted versus PAAS	Co, Ni, Cu, Zn	Ni, Cu, Zn, Cr, Sn	Similar to PAAS	Zn, Ni	Ni, Cu, Zn, Cr	Similar to PAAS	Cr, Zn, Th, Ga
TE correlated with Org.C	Cu, Co, Sn	V, Ni, Zn, As, Se, Sb, U, Tl	Au, Zn, Cu, Sn	V, Cr, As, Se, Mo, Sn, Sb, U, Ni	V, Cr, Ni, Sb	V, Mo, Sb, and U	Mo, Cu, Ni, Sb
TE correlated with alumina	Au, V, Cr, Ni, Co, Sn, Sb	Au, Cr, Tl	Zn, Cu, Ni, As, Sb	V, Cr, Zn, As, Se, Mo, Sn, Sb, U	Au, Ni, Cr, Sn	V, Cr, Mo, Sb, and U	Cr, Sn
Redox conditions	Oxic	Anoxic	Oxic	Anoxic-euxinic	Dysoxic-oxic	Anoxic-euxinic	Anoxic - euxinic
Provenance	Felsic	Felsic	Felsic-intermediate	Intermediate	Intermediate	Mafic	-
Comments	Au introduced on clays	Au introduced on clays	Au introduced on organics	-	Au introduced on clays	-	-

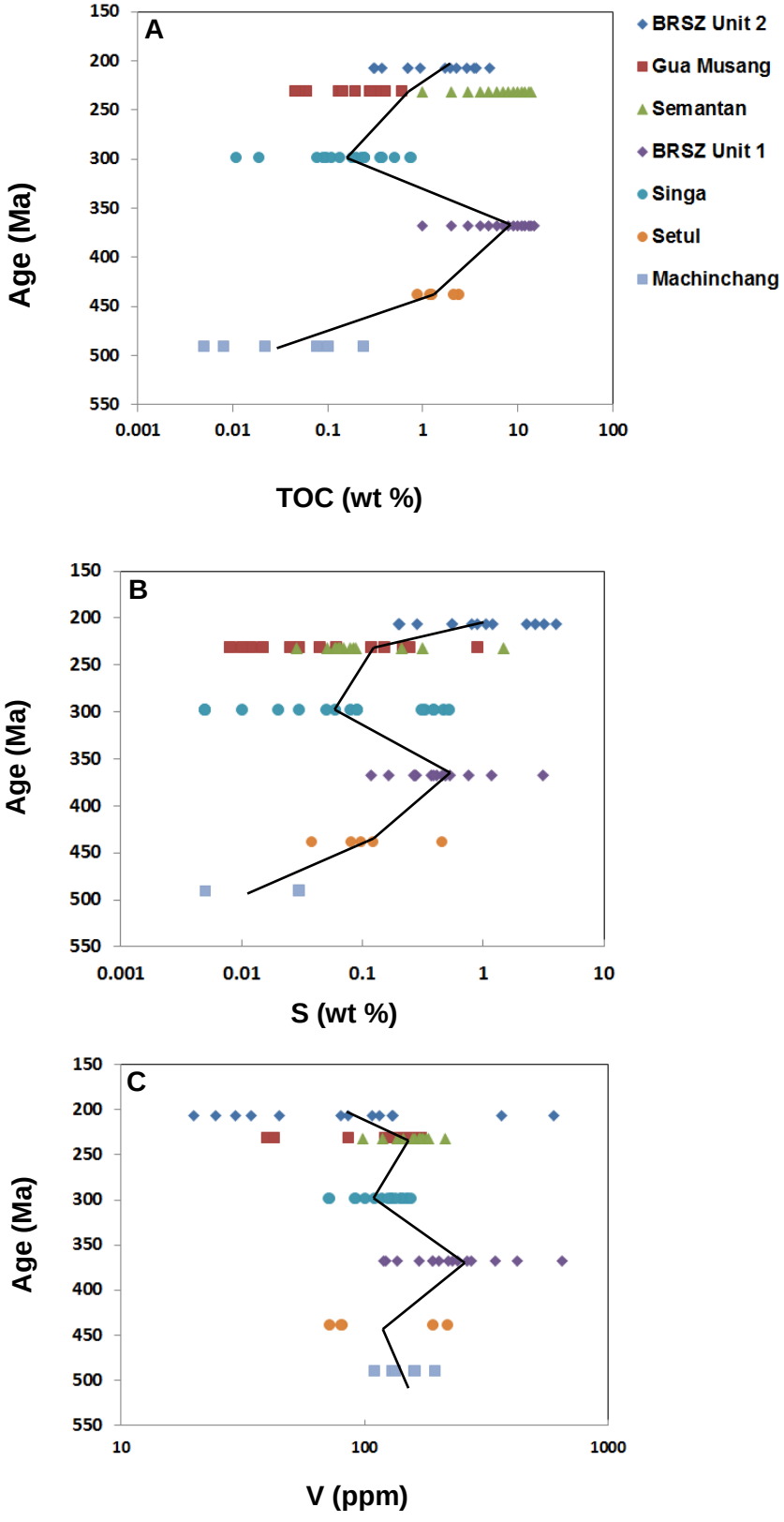

Fig. 7.1. Chemostratigraphy of total organic carbon, sulphur, V and Mo contents in Phanerozoic formations in Malaysia. **A**) Total organic carbon content. **B**) Sulphur content. **C**) Vanadium content. Total organic carbon content varies in the same fashion with the S; however, the V content shows a slightly reverse trend in Cambrian and Late Devonian through time. Overall, the BRSZ Unit 1 and Singa Formation exhibit the same fashion for TOC, S and V contents.

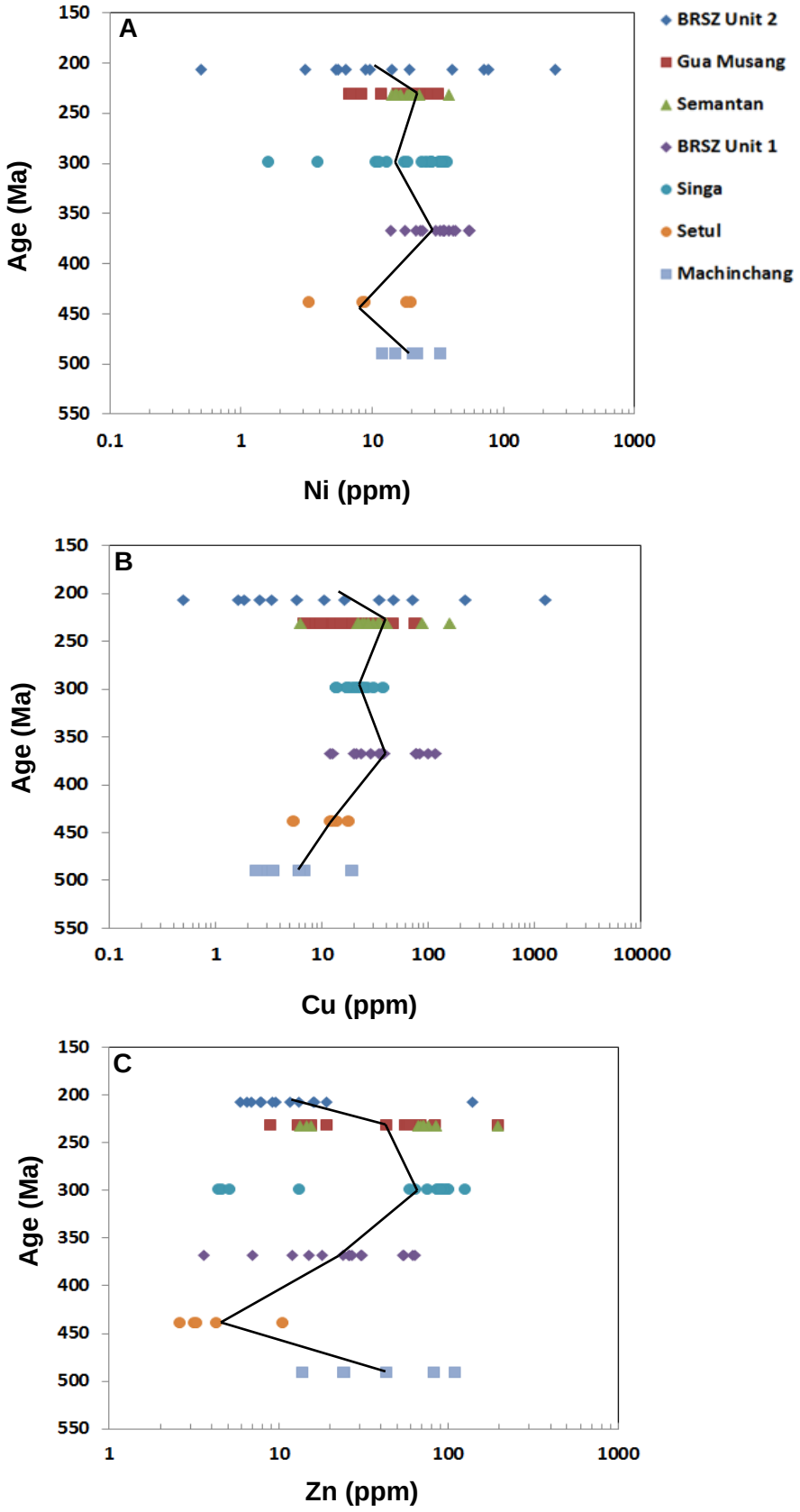

Fig. 7.2. Chemostratigraphy of Ni, Cu, and Zn contents in Phanerozoic formations in Malaysia. The Cu and Ni contents vary in the same fashion though Phanerozoic whereas Zn shows a different trend through Phanerozoic.

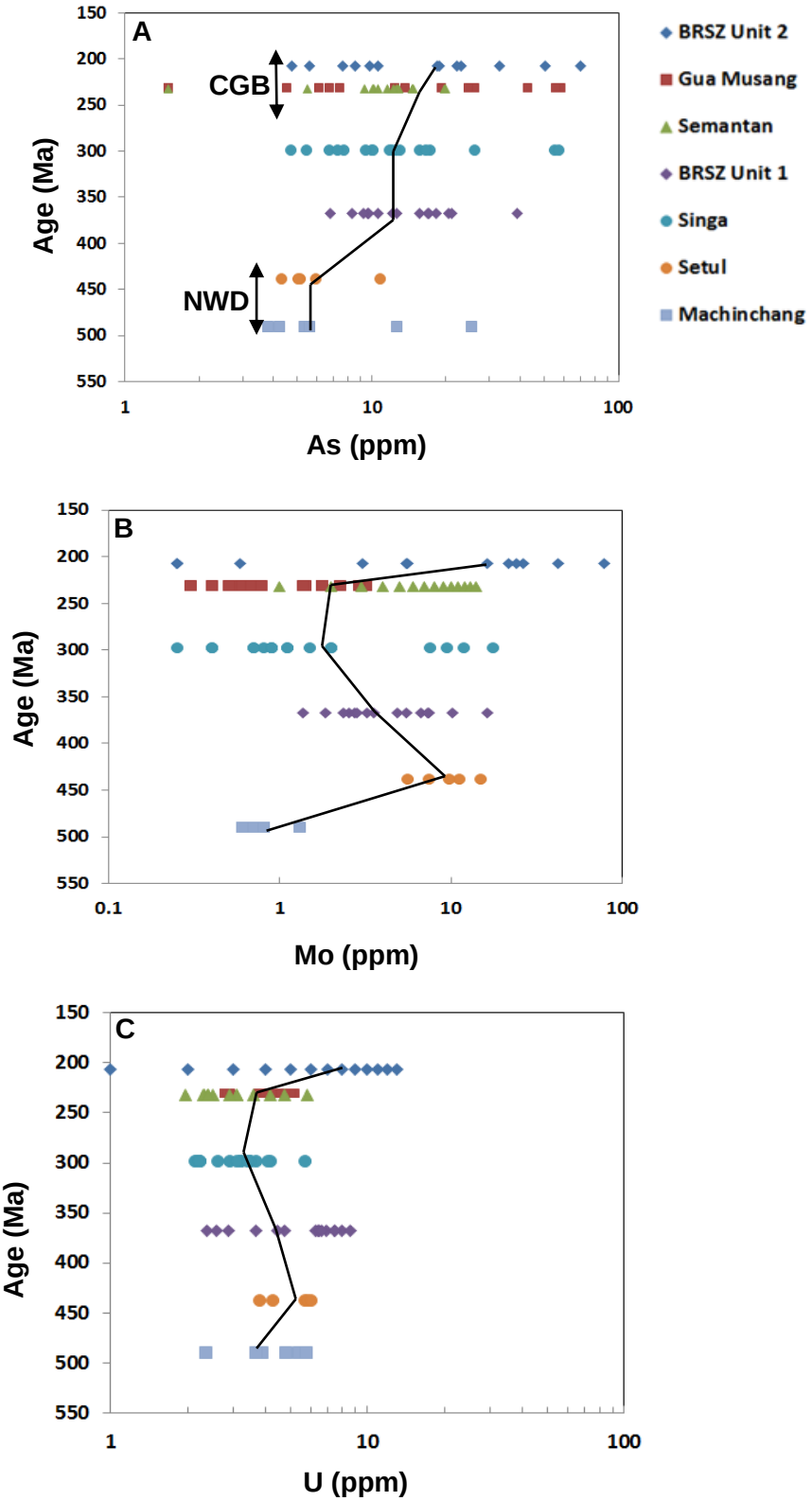

Fig. 7.3. Chemostratigraphy of As, Mo, and U contents in Phanerozoic formations in Malaysia. The U content varies in a similar fashion with Mo and As contents. The As content is elevated in the Central Gold Belt (CGB), slightly lower in the Singa Formation and significantly dropped in the Setul and Machinchang formations (NWD). The whole rocks in the CGB have high As content indicating that this zone is highly prospective for gold.

7.3. Comparisons of trace element content of Malaysia sedimentary pyrites with worldwide diagenetic pyrites

The trace element compositions in sedimentary pyrite have been normalised to WDP (Gregory et al., 2015) to depict enrichment and depletion in the palaeo-ocean (Fig. 7.4). The three trace element trends are: (1) Au is consistently enriched in diagenetic pyrite from Silurian to Triassic; (2) Mo is depleted and Tl is strongly depleted in all formation pyrites relative to the WDP dataset; and (3) Contents of Co, Ni, Cu, Zn, As, Se, Ag, Cd, Sb, Te, Pb and Bi change dramatically through time. The Co content is elevated in the Ladinian Semantan and Anisian Karak formations probably attributable to the association with tuffaceous facies (Fig. 7.4A). Remarkably, the Zn content in the Semantan Formation is one order of magnitude higher than other Triassic shales. The Zn content is commonly elevated in most of the formations except the Ladinian Gua Musang Formation. The Au content also about one order of magnitude higher (compared to WDP) in the Devonian BRSZ Unit 1 that is located in the Central Gold Belt near the suture zone.

Additionally, the Se content is accompanied with high Au along with Ni, Cu, Zn, Ag, and Pb (Fig. 7.4C). The Selinsing and Singa pyrite show similar compositional pattern as they both formed under dysoxic to oxic bottom water conditions (Fig. 7.4B and D). The BRSZ Unit 1, the BRSZ Unit 2, Gua Musang, Semantan, and Karak overly display similar patterns likely due to the same anoxic-euxinic redox conditions that prevailed during the formation of their sedimentary pyrites (Figs. 7.4A and C). Comparatively, the Semantan and Karak pyrites have both elevated Bi content possibly related to the sediments having a mafic provenance. However, other formations (e.g. Gua Musang and BRSZ Unit 2) whose Bi content is low indicate an intermediate provenance (Fig. 7.4A). This study demonstrates that the Bi content in sedimentary pyrite can be used as a proxy for provenance.

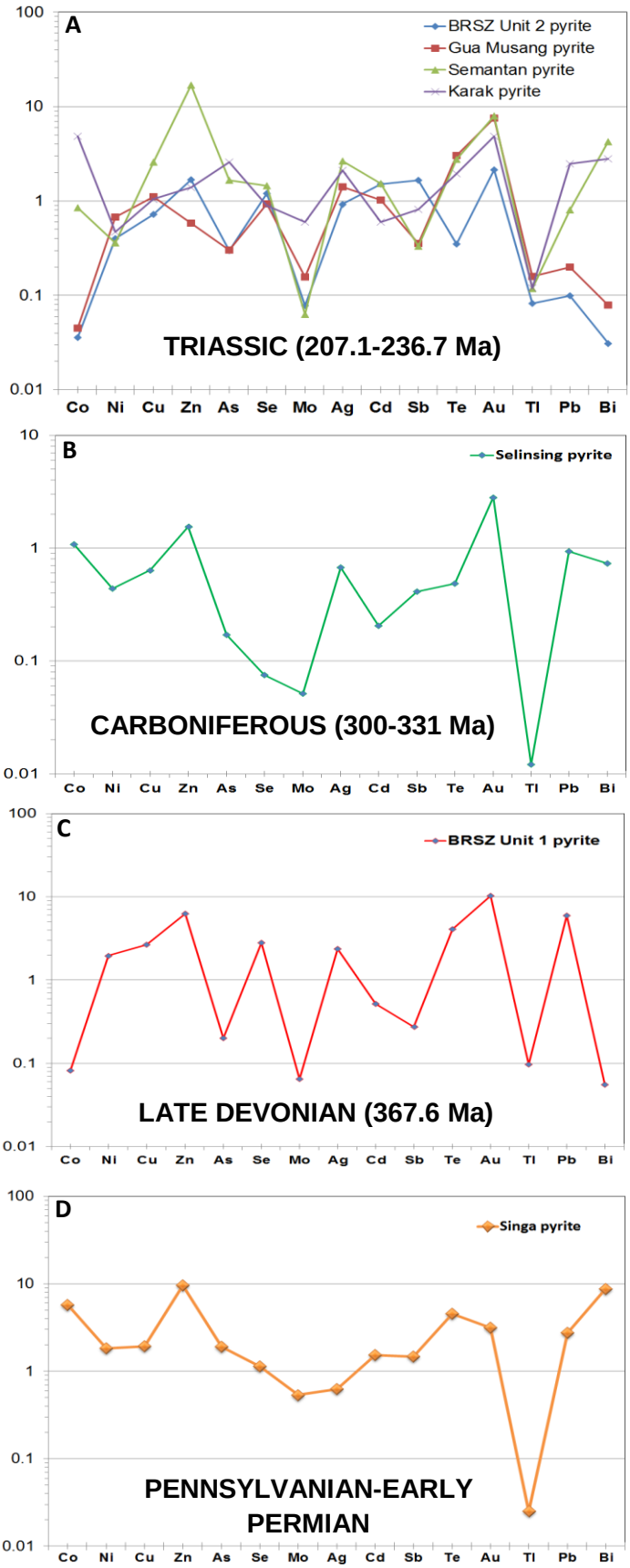

Fig. 7.4. Comparative spider plots of selected trace elements in sedimentary pyrite normalised to worldwide diagenetic pyrite (WDP) from Silurian to Triassic. The ages represent detrital zircon ages determined in this study (plots A, B, and C) including fossil age (plot D).

Some geochemical ratios are useful to infer the sedimentary origin of pyrite. A significant addition to the work of Gregory et al. (2015) is given in Table 7.2. This table summarizes chemical criteria for sedimentary pyrite (Gregory et al., 2015) combined with those of present study. In Table 7.1, numbers in percentage represent the analysis results that best fit in a given ratio range of WDP database (Gregory et al., 2015). Elements such as Ag, As, and Te are held tightly in the pyrite structure that's why their ratios against Au may be reliable to infer the pyrite origin. Among all ratios, only the ratios Ag/Au, As/Au, and Te/Au fall within the WDP identical ratios (Gregory et al., 2015) with an accuracy from 80 to 100%. Proportions of each ratio are presented in pie diagrams (Fig. 7.5). The Semantan pyrites have the lowest ratio numbers (Table 7.2) may be due to the mixing of black shales with tuffaceous facies as enormous amount of Ni was supplied into the basin and deposition into diagenetic pyrites.

Table 7.2. Chemical criteria for sedimentary pyrite (Gregory et al., 2015) compared with current data.

	Co/Ni	Zn/Ni	Cu/Ni	As/Ni
Background sedimentary pyrite (Gregory et al., 2015)	0.01-2	0.01-10	0.01-10	0.1-10
Singa pyrite	0.05-7; **41%**	0.04-31; **94%**	0.02-6; **100%**	0.07-42; **83%**
BRSZ Unit 1 pyrite	0.001-0.4; **74%**	0.02-5; **100%**	0.003-8; **96%**	0.01-4; **72%**
Selinsing pyrite	0.5-2; **100%**	0.2-2; **100%**	0.4-2; **100%**	0.4-3; **100%**
Karak pyrite	3-5; **25%**	0.1-1.5; **100%**	0.4-3; **100%**	1-43; **25%**
Semantan pyrite	0-10.5; **29%**	0-15; **47%**	0-25; **19%**	0.1-78; **67%**
Gua Musang pyrite	0.01-0.07; **100%**	0.02-1; **100%**	0.4-2; **100%**	0.3-5; **100%**
BRSZ Unit 2 pyrite	0.01-0.1; **96%**	0.03-4; **100%**	0.6-2; **100%**	0.5-7; **100%**

Table 7.2 (continued)

	Te/Au	As/Au	Ag/Au	Sb/Au	Bi/Au
Background sedimentary pyrite (Gregory et al., 2015)	1-1000	>200	>2	>100	>1
Singa pyrite	22-500; **100%**	>2184; **100%**	4-65; **100%**	51-2755; **96%**	46-2836; **100%**
BRSZ Unit 1 pyrite	2-165; **100%**	54-2955; **100%**	5-76; **100%**	8-159; **6%**	0.2-14; **51%**
Selinsing pyrite	0.08-34; **90%**	>274; **100%**	9-203; **100%**	45-1192; **75%**	46-2836; **100%**
Karak pyrite	14.5-21.5; **100%**	>1384; **100%**	>30; **100%**	127-171; **100%**	>49; **100%**
Semantan pyrite	3-342; **100%**	>6; **86%**	6-2475; **100%**	2-1574; **57%**	0.1-3468; **86%**
Gua Musang pyrite	8-64; **100%**	>113; **91%**	>6; **100%**	16-80; **100%**	0.1-5; **62%**
BRSZ Unit 2 pyrite	4-16; **100%**	>482; **100%**	19-65; **100%**	>295; **100%**	0.6-5; **73%**

Other ratios such as Te/Au, As/Au, Ag/Au, Sb/Au, and Bi/Au also have ranges completely different from those of worldwide sedimentary pyrite (Gregory et al., 2015). Metamorphic-hydrothermal pyrites commonly show low ratio numbers especially for Co/Ni, Zn/Ni, Cu/Ni and As/Ni (Table 7.3). These ratios may be used to differentiate sedimentary pyrites from metamorphic-hydrothermal pyrites in future research work. Each geochemical ratio percentage indicates a level of confidence on how they can well be used to imply a sedimentary origin of pyrite. For instance, the levels of confidence that are suggested in this thesis are “robust, strong, and weak”. Based on this approach, the Ag/Au, Te/Au, and As/Au are the best geochemical ratios that can be used to indicate a sedimentary origin of pyrite in future research (Fig. 7.5).

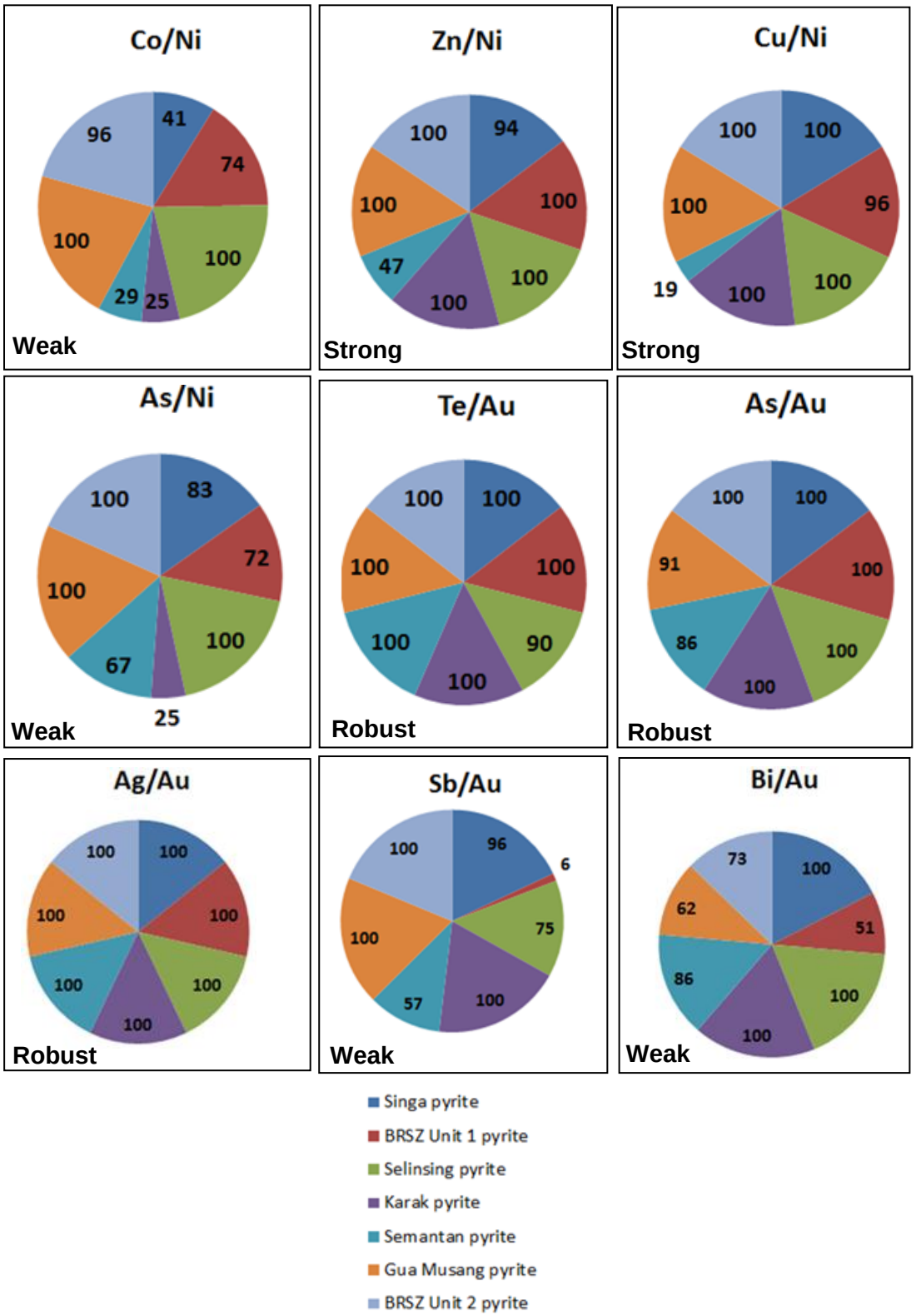

Fig. 7.5. Proportion (in %) of geochemical ratios Ag/Au, Sb/Au, and Bi/Au relative to worldwide diagenetic pyrite (WDP). Numbers in each pie diagram represents percentage of these ratios that fall within the WDP range (Table 7.2) in Gregory et al. (2015). Levels of confidence for each ratio are suggested by the words robust, strong and weak relative to the WDP ratio ranges. Only Ag/Au, Te/Au and As/Au correspond to 86-100 % of the data matching the values of WDP making these ratios the most reliable to imply the sedimentary origin of pyrite.

Table 7.3. Chemical criteria for metamorphic-hydrothermal pyrites (this study) compared with worldwide diagenetic pyrite (Gregory et al., 2015)

	Co/Ni	**Zn/Ni**	**Cu/Ni**	**As/Ni**
Sedimentary pyrite (Gregory et al., 2015)	0.01-2	0.01-10	0.01-10	0.01-10
Singa	0.01-6	0.001-9	0.003-2	0.0004-20
Karak	0.05-7	0.001-7	0.004-2	0.01-26
Gua Musang	0.001-0.1	0.0006-27	0.002-2	1-9
BRSZ Unit 2	0.005-0.4	0.01-4	0.3-168	0.2-29
Machinchang	0.05-1	0.001-46	0.08-9	>1

	Te/Au	**As/Au**	**Ag/Au**	**Sb/Au**	**Bi/Au**
Sedimentary pyrite (Gregory et al., 2015)	1-1000	>200	>2	>100	>1
Singa	3-214	>8	0-308	>58	0-1161
Karak	5-284	>150	3-26	47-244	30-247
Gua Musang	35-346	>6499	8-936	>237	>235
BRSZ Unit 2	1.4-218	>600	4-123	>160	0.08-21
Machinchang	>3	>566	0.06-2	0.6-1270	0.4-794

7.4. Source rock characteristics

In order to evaluate the enrichment of some trace element in black shale, a summary of enrichment factors is given in Table 7.4. Enrichment factor (EF) is defined by the following equation (Özkan, 2012): $EF= (C_x/C_{Al})_{sample}/(C_x/C_{Al})_{background.}$ Aluminium is used as a reference element. In this equation, $(C_x/C_{Al})_{sample}$ is the ratio of metal and Aluminium concentrations of the sample and $(C_x/C_{Al})_{background}$ is the ratio of metal and Aluminium concentrations of background. In this study, the background of metals in the average shales from Wedephol (1995) is used. Recent studies have used this method to estimate the enrichment factor (Özkan, 2012) of heavy metals in the inner Izmir bay located east of the Aegean Sea, Turkey. For the Gua Musang black shales, V, Mo, Sb, U, Se are enriched one to three times compared to Wedephol's Average Shale (Wedephol, 1995). In addition, As is enriched four times and Au 12 times relative to Wedephol's Average Shale. The Semantan black shales do not show any significant enrichment compared to Wedephol's Average Shale.

For the BRSZ Unit 1 black shales, trace elements such as As, Ba, V, Cr, Cu, Se, Sb, and U are enriched one to three times. In addition, Mo is enriched seven times and gold ten times over the WAS average standard shale. The Singa black shales are moderately enriched in V, As, and Sb compared to Wedephol's Average Shale. Gold is enriched 25 times relative to WAS. Based on the geochemical data obtained in this study, the Gua Musang, BRSZ Unit 1, and Singa black shales can be classified as metalliferous black shales because of the gold content and other trace element which have an enrichment factor of greater than two (Table 7.4).

Histograms of gold content from whole rocks are shown in Fig. 7.6. In the Pennsylvanian-Early Permian Singa black shales, gold content in whole rock varies from 0 to

65 ppb (mean 58 ppb). In the Late Devonian BRSZ Unit 1 gold content in whole rock ranges from 1 to 39 ppb (mean 23 ppb). However, in the youngest Middle Triassic Gua Musang, gold content in whole rock is between 3 and 51 ppb (mean 28 ppb) (Table 7.3). Variation of gold content in sedimentary pyrite contained in black shales is shown on Figs. 7.7-7.8 for all the sedimentary sequences through time. Diagenetic pyrites proximal to ore have Au content up to 1 ppm (e.g. Selinsing gold deposit). Other formation diagenetic pyrites have Au contents close to that of Selinsing gold deposit; however, the Middle Triassic Gua Musang Formation, the Late Devonian BRSZ Unit 1 and the Pennsylvanian-Early Permian Singa Formation have diagenetic pyrite Au content as high as 2 ppm but distal from ore. The Gua Musang Formation sampled area is located at about 2 km from the Selinsing gold deposit. The BRSZ Unit 1 is situated around 20 km from the Bukit Koman gold deposit.

Table 7.4. Enrichment factors (EF) for selected trace elements (TE) in the Gua Musang, Semantan, BRSZ Unit 1, and Singa black shales. The numbers coloured in pink indicate EF greater than 2.

	Gua Musang	EF-1	Semantan	EF-2	BRSZ Unit 1	EF-3	Singa	EF-4	WAS
V	125.9	1.0	163.0	1.3	294.3	2.3	136.2	1.0	130
Cr	48.2	0.5	58.8	0.7	122.6	1.4	84.6	0.9	90
Ni	18.6	0.3	48.2	0.7	37.2	0.5	31.5	0.5	68
Cu	24.9	0.6	31.8	0.7	72.9	1.6	23.4	0.5	45
Zn	54.3	0.6	69.6	0.7	29.5	0.3	87.0	0.9	95
As	42.4	4.2	11.8	1.2	15.6	1.6	18.0	1.8	10
Mo	1.3	1.3	1.3	1.3	7.1	7.1	0.9	0.9	1
Sn	3.7	0.6	2.9	0.5	5.7	0.9	3.0	0.5	6
Sb	4.4	2.9	1.5	1.0	3.0	2.0	1.8	1.2	1.5
U	4.0	1.1	3.0	0.8	7.3	2.0	3.0	0.8	3.7
Ag	nd	nd	nd	nd	nd	nd	0.7	9.4	0.07
Cd	7.4	nd	nd	nd	nd	nd	0.2	nd	nd
Co	14.7	0.8	nd	nd	nd	nd	17.9	0.9	19
Se	0.6	1.2	0.6	1.2	1.7	3.3	0.5	1.0	0.5
Te	0.1	nd	1.0	nd	2.4	nd	0.6	nd	nd
Ba	527.7	0.9	306.8	0.5	689.6	1.2	579.1	1.0	580
S_wt %	0.1	nd	0.2	nd	0.3	nd	0.1	nd	nd
TOC _wt %	0.2	nd	0.4	nd	0.6	nd	0.2	nd	nd
Au_ppb	28.0	12.2	nd	nd	23.0	10.0	58.0	25.2	2.3

Note: EF= enrichment factor against Wedephol's Average Shale (WAS, Wedephol, 1995). EF-1 for Gua Musang black shales; EF-2 for Semantan black shales; EF-3 for BRSZ Unit 1 black shales and EF-4 for Singa black shales. nd: no data.

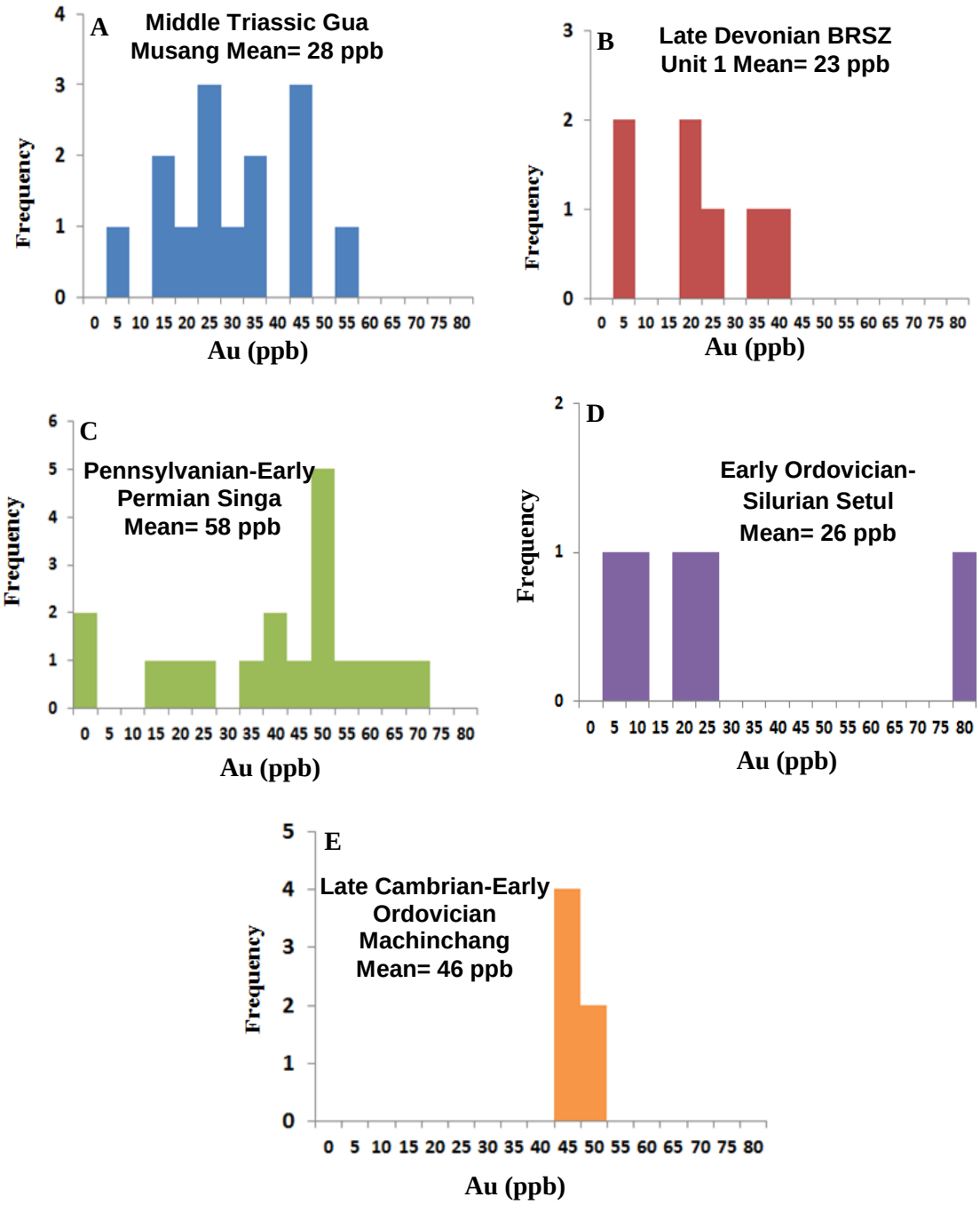

Fig. 7.6. Histograms of gold content in whole rocks for the selected Phanerozoic formations in Malaysia. **A**) Gua Musang black shales. **B**) BRSZ Unit 1 black shales. **C**) Singa black shales and sandstones. **D**) Setul sandstones. **E**) Machinchang grey shales. Machinchang Formation grey shales show a close range for the gold content whereas other formations display wide ranges in gold content. The Setul Formation has record of high gold content (plot D). The Singa Formation has the highest mean value in gold content.

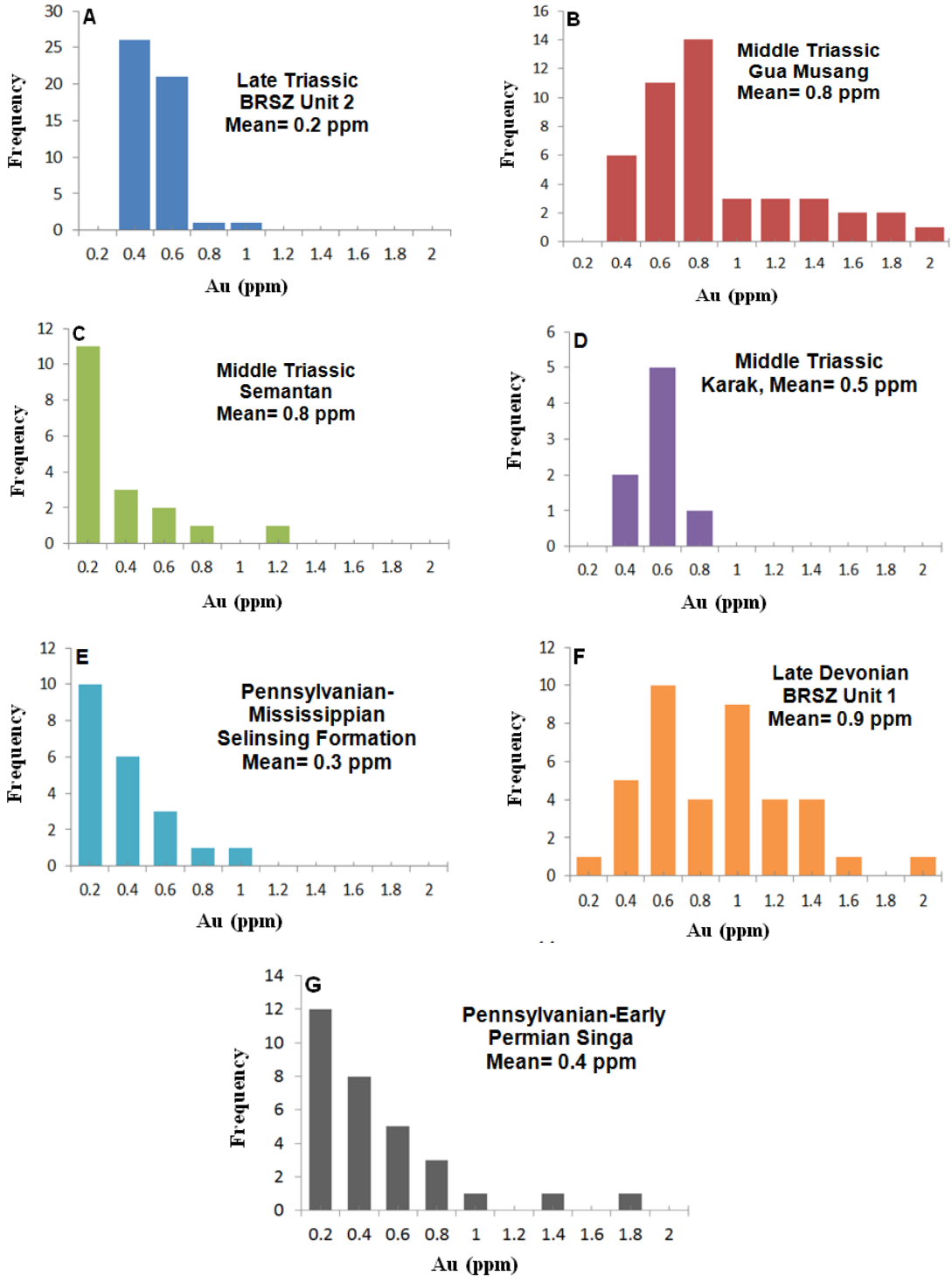

Fig. 7.7. Histograms of gold content in sedimentary pyrites for the selected Phanerozoic formations in Malaysia. **A**) Late Triassic BRSZ Unit 2 (207 ± 3.2 Ma). **B**) Middle Triassic Gua Musang Formation (231 ± 2.9 Ma). **C**) Middle Triassic Semantan Formation (231.6 ± 3.6 Ma). **D**) Middle Triassic Karak Formation. **E**) Carboniferous Selinsing gold deposit. **F**) Late Devonian BRSZ Unit 1. **G**) Pennsylvanian-Early Permian Singa Formation.

Diagenetic pyrites are enriched in both Au and As (Fig. 7.8A), whereas igneous rock-hosted pyrites are commonly depleted in Au and As. Because both Au and As are the two key elements in the local gold deposits (Makoundi, 2012) then the sedimentary pyrites hosted in black shales are the likely gold and As sources in the district. The evidence indicates less likelihood of gold being sourced from magmatic rocks. The S isotope study supports this conclusion as all isotope compositions suggest that sulphur originated from reduction of seawater sulphate. Diagenetic pyrites in black shales that are enriched in Au commonly have Se content higher than Co content ($Au/As > 10^{-4}$; $Se/Co > 1$) as shown in Fig. 7.8B.

The BRSZ Unit 1, BRSZ Unit 2, and Gua Musang pyrite are enriched in gold ($Au/As > 10^{-4}$), and also have a ratio $Se/Co > 1$. Importantly, trace elements such as Se, Mo, Cd, are used as proxies for oxygenation in the atmosphere and ocean (Large et al., 2014). The Se content can be used as a proxy for atmospheric oxygenation. Large et al. (2014) also suggest that elevated Se content in marine sediments is a result of active continental weathering favouring the release of soluble Se with other trace elements (e.g. Au, Mo, U, Tl, Mn, Cd, Ag) to the ocean. In this regard, Se content may be used as an exploration tool to best target metalliferous black shales. This study has shown that there is a good relationship among gold content in sedimentary pyrite, total organic carbon (TOC) (Fig. 7.9A), total sulphur (Fig. 7.9B), and alumina content (Fig. 7.9C) in shales from Cambrian to Triassic. TOC and sulphur contents vary negatively with Au content in sedimentary pyrite for the sedimentary rocks outcropping in the NW Domain (NWD) or the Langkawi Islands. However, both TOC and S contents vary positively with Au content in sedimentary pyrite for the sedimentary rocks occurring in the Central Gold Belt (CGB). The Au content in sedimentary pyrite varies positively with alumina in both NWD and CGB rocks. Overall, the evidence suggests that gold may have been introduced into sedimentary pyrite through organic processes in the whole district.

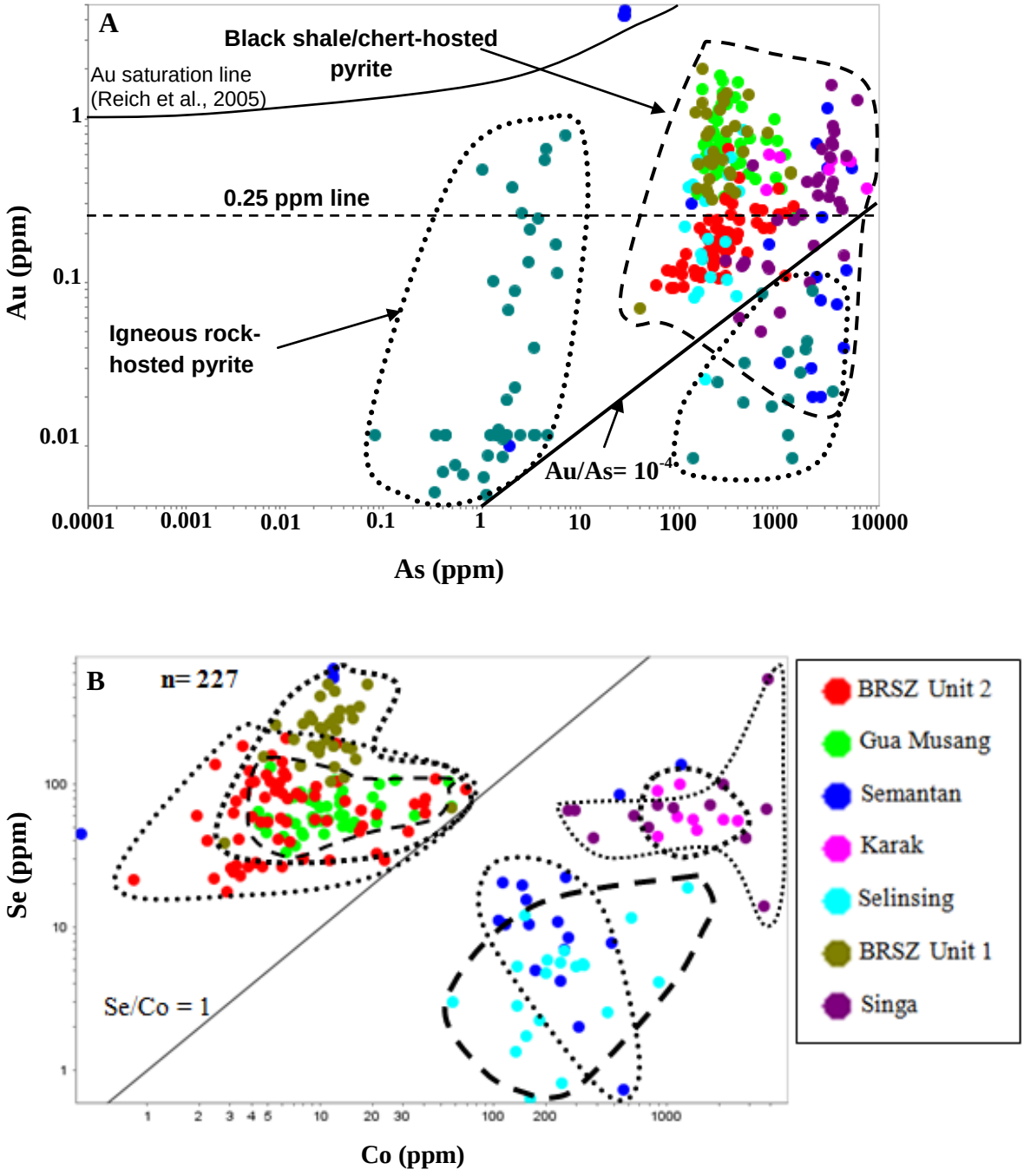

Fig. 7. 8. Plots showing Au and As relationship in pyrite from black shales and igneous rocks with Se and Co relationship in black shales. **A**) Log-log plot of Au-As relations in black shale hosted diagenetic pyrites and igneous rock hosted pyrites. Diagenetic pyrites in carbonaceous black shales show elevated Au and As contents compared to igneous rocks making them ideal source. The Middle Triassic (Ladinian) Semantan diagenetic pyrites contain gold in inclusions as shown by the presence of some analyses plotted above the Au saturation line. **B**) Log-log plot of Se-Co relations in black shale hosted diagenetic pyrites.

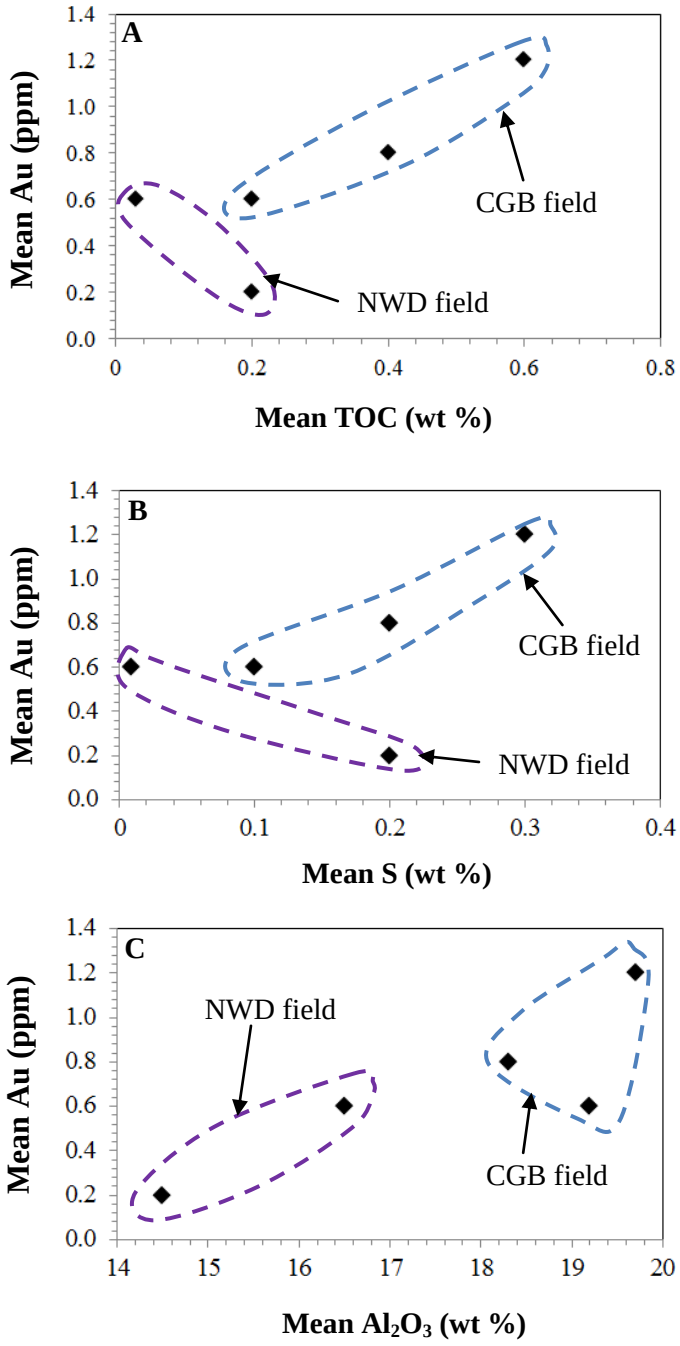

Fig. 7.9. Scatter plots of mean Au in sedimentary pyrite versus mean alumina (Al_2O_3), S and TOC contents in all shale samples from Gua Musang, Semantan, BRSZ Unit 1, Singa and Machinchang formations. Note: NWD= Northwest Domain; CGB= Central Gold Belt. Mean Au in sedimentary pyrite in ppm (part per million).

In this study, it is demonstrated that diagenetic pyrites from black shales located far from gold deposits are enriched in gold. The gold content ranges from 0.01 to 5 ppm (mean 1 ppm). The mean value of 1 ppm (1000 ppb) is far above the value of 250 ppb documented by Large et al.

(2011) in diagenetic pyrite indicative of carbonaceous shale source rocks with the potential to produce economic gold deposits. Previous researchers demonstrated that an amount of 10 ppb Au in whole rocks combined with 10 km^3 of the rock can produce a gold deposit containing 10^6 ounces (Burge, 1982; Romberger, 1988). In the current study, mean range of gold content varies from 19 to 38 ppb in whole rocks, making the Gua Musang black shales, the BRSZ Unit 1 black shales and the Singa black shales gold source rocks in the district. As for Fig. 3.8A, the proportions of gold content in sedimentary pyrites relative to the 0.25 ppm Au line are given in Table 7.5 below. The igneous rocks have the lowest Au content in pyrite. At the Selinsing gold deposit in the vicinity of the orebody, twenty one analyses of gold content in diagenetic pyrites (which represents 100% of the population) were carried out. However, only 45% of the population have gold content greater than 250 ppb (Table 7.5).

Table 7.5. Proportion (%) of Au content higher than 0.25 ppm determined in pyrite from sedimentary and igneous rocks.

	Gua Musang	BRSZ Unit 1	Singa	BRSZ Unit 2	Selinsing	Semantan	Karak	Igneous rocks
Proportion of gold content in pyrite in excess of 250 ppb	100 %	100 %	59 %	17 %	45 %	43 %	100 %	11 %

Table 7.5 indicates at least 50 % of Au content in sedimentary pyrites from the Gua Musang, BRSZ Unit 1, Karak formations and Singa Formation is above 250 ppb Au. Igneous rock-hosted pyrites have the lowest percentage of Au content above 250 ppb. These preliminary data confirm that igneous rocks are unlikely gold source rocks in the district. The Au content in the district correlates strongly with Ag and weakly with Se (Fig. 7.10) reiterating the control of organic processes during gold introduction into pyrite. However, Au content in sedimentary pyrite does not correlate with V, U, and Mo in the studied region (Fig. 7.10).

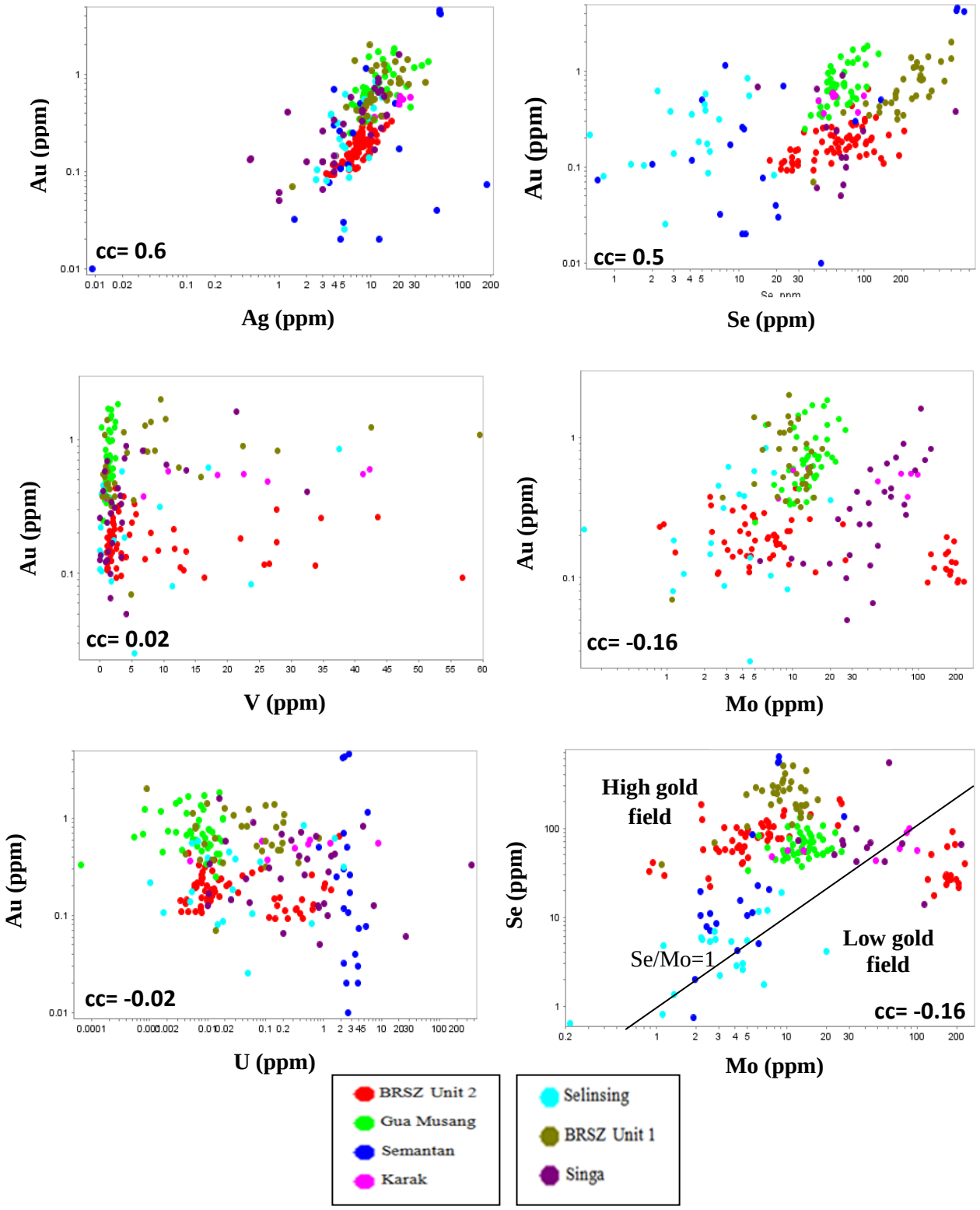

Fig. 7.10. Binary plots of Au versus Ag, Se, V, Mo, and U plus Se-Mo plot from sedimentary pyrites. CC represents coefficients. The plot Se-Mo clearly indicates that Gua Musang and BRSZ Unit 1 have the highest Se content suggesting active continental weathering and transportation and deposition of trace elements into the ocean. The Gua Musang and BRSZ Unit 1 are ideal stratigraphic units to explore for gold and other metals. The Se/Mo=1 line delineates high and low gold fields for all the studied formation pyrites.

7.5. Chemostratigraphy of selected trace elements in sedimentary pyrite

Chemostratigraphy of gold in sedimentary pyrite (Fig. 7.11) indicates that gold content show two maximum levels in the Devonian and Triassic and a minimum level in the Carboniferous. The Au content broadly shows the same trend with those of Se, Cd and Tl in diagenetic pyrite. The existing sediment-hosted gold deposit (e.g. Selinsing gold deposit) does not sit on one of the maxima implying that basinal concentration of gold in sedimentary pyrite is much higher in other areas in the auriferous district. This study has revealed considerable variability in Se content of sedimentary pyrite. The maximum level of Se content is at 368 Ma (Late Devonian) recorded within the BRSZ Unit 1, which crop out in the vicinity of the Bentong-Raub Suture Zone. Another elevated level in Se peaked between 207 and 237 Ma (Middle Triassic). The minimum in Se content in pyrite is at 330 Ma in the Selinsing Formation.

The Selinsing Formation data coincides with the decrease of Se, Cd, Mo, and Tl contents in the Carboniferous suggesting the possibility of lower levels of both Se and Au in the ocean corresponding with a drop in O_2 in the atmosphere (Large et al., 2015). Similarity of trends is also shown by Sb, Ni, and Co. Se in sedimentary pyrite data (this study) shows a good fit except for the BRSZ Unit 1 at 368 Ma (Fig. 7.12A). Mo in sedimentary pyrite data (Fig. 7.12B) from Malaysia (this study) fits well with the global curve of Large et al. (2015). In addition, Co in sedimentary pyrite data from Malaysia (this study) matches with the global curve of Large et al. (2015) excluding the BRSZ Unit 1 at 368 Ma (Fig. 7.12C). However, Au in sedimentary pyrite data from Malaysian black shales is generally more elevated than the global curve of Large et al. (2015) as shown in Fig. 7.12D. Overall, among all formations, gold content in pyrite correlates strongly with V, Se, U but weakly with alumina (Al_2O_3) strongly suggesting a control of organic processes on Au introduction into pyrite (Table 7.6).

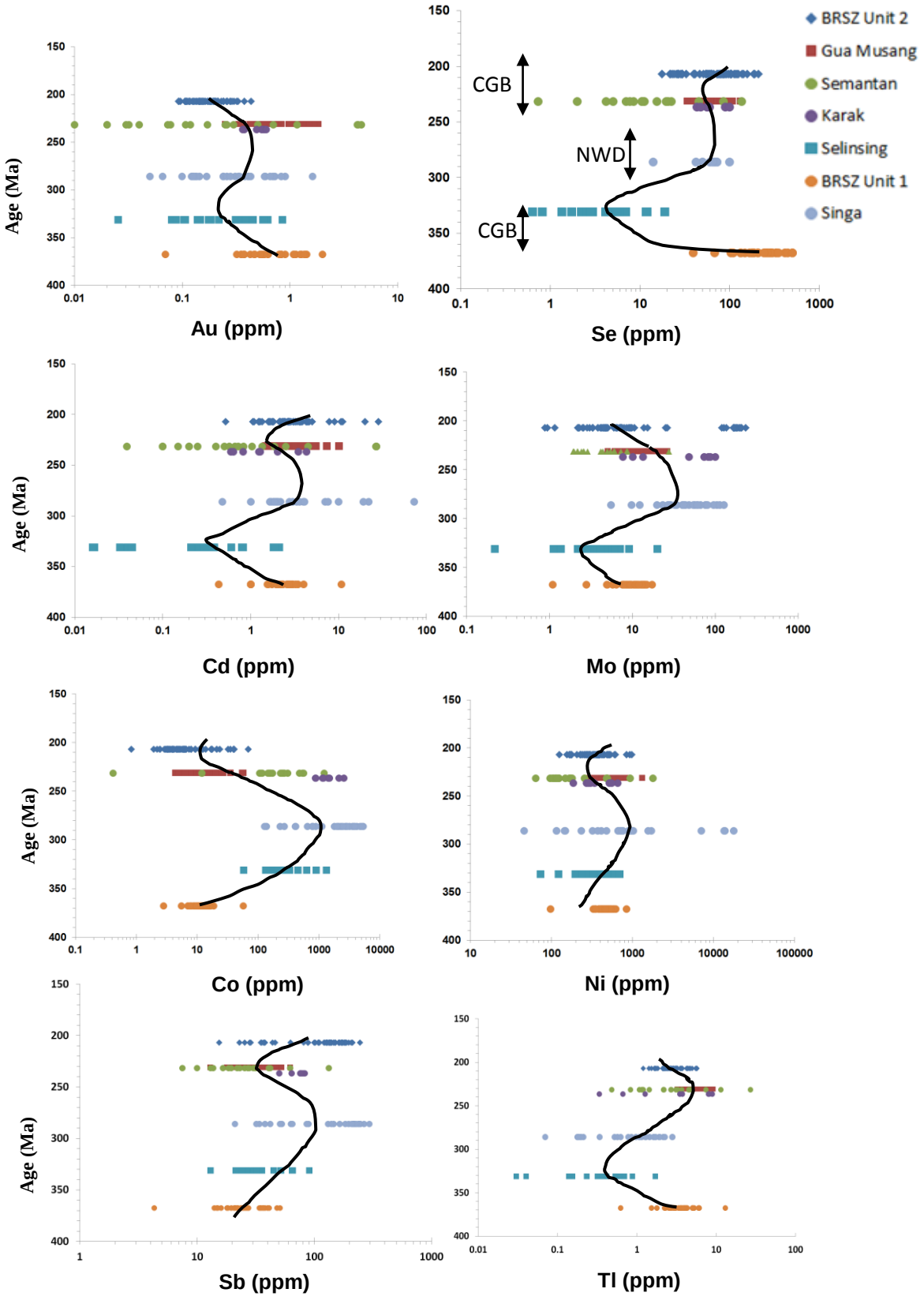

Fig. 7.11. Plots showing variation of Au, Se, Cd, Mo, Co, Ni, Sb, and Tl contents in sedimentary pyrite for the Phanerozoic formations in Malaysia. The curve black line crosses each dataset at the median value. The Au, Se, Cd, Mo, and Tl contents vary in a similar fashion which was expected. However, the Co, Sb, and Ni contents consistently show a reverse trend through time. The BRSZ Unit 1, BRSZ Unit 2, and the Gua Musang Formation have elevated Se content relative to other formation pyrites.

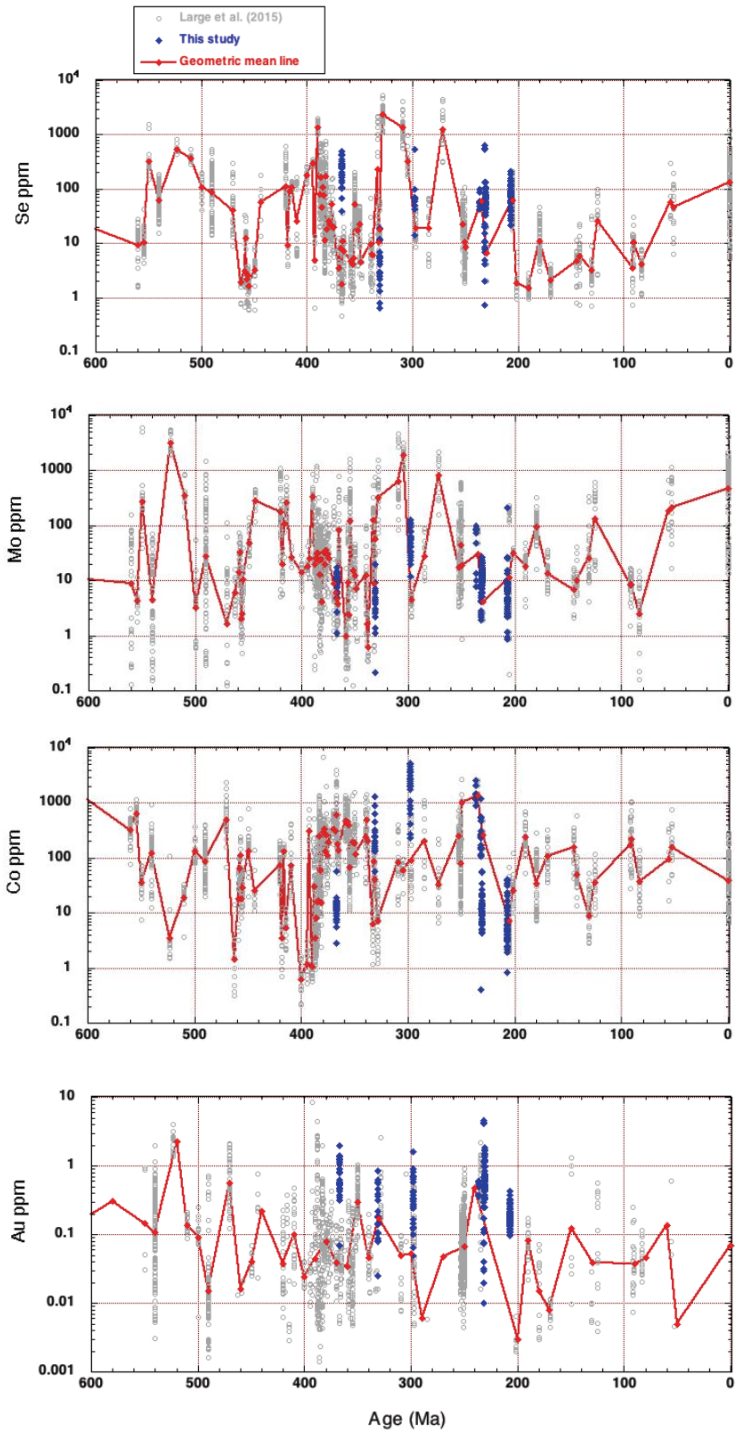

Fig. 7.12. Plots show the global curves of Se (plot A), Mo (plot B), Co (plot C), and Au (plot D) in red line from sedimentary pyrite together with data from this study in blue dots. The global curve is from Large et al. (2015). On the global curve, Se, Mo and Au show a similar trend whereas Co shows a reverse trend. Overall, the Malaysian sedimentary pyrites indicate higher Au contents compared to the global mean. Note: 0-100 Ma: Quaternary-Late Cretaceous; 100-200 Ma: Late Cretaceous-Early Jurassic; 200-300 Ma: Early Jurassic-Late Carboniferous; 300-400 Ma: Late Carboniferous-Early Devonian; 400-500 Ma: Early Devonian-Late Cambrian; 500-600 Ma: Late Cambrian-Neoproterozoic.

Table 7.6. Correlation coefficients of mean Au in pyrite with mean of major and trace elements including total organic carbon and total sulphur from whole rock compositions for all formations (this study). Numbers in pink colour are equal to or greater than 0.5.

Correlation	SiO_2	TiO_2	Al_2O_3	Fe_2O_3	MgO	Na_2O	K_2O	P_2O_5	TOC	S
SiO_2	1	-0.93	-0.97	-0.75	-0.77	-0.22	-0.64	-0.33	0.91	0.9
TiO_2	-0.93	1	0.93	0.5	0.63	0.076	0.77	0.24	-0.87	-0.85
Al_2O_3	-0.97	0.93	1	0.61	0.59	0.023	0.68	0.14	-0.84	-0.84
Fe_2O_3	-0.75	0.5	0.61	1	0.87	0.48	0.25	0.51	-0.64	-0.65
MgO	-0.77	0.63	0.59	0.87	1	0.71	0.33	0.74	-0.82	-0.81
Na_2O	-0.22	0.076	0.023	0.48	0.71	1	-0.13	0.88	-0.52	-0.53
K_2O	-0.64	0.77	0.68	0.25	0.33	-0.13	1	0.28	-0.61	-0.59
P_2O_5	-0.33	0.24	0.14	0.51	0.74	0.88	0.28	1	-0.61	-0.61
TOC	0.91	-0.87	-0.84	-0.64	-0.82	-0.52	-0.61	-0.61	1	1
S	0.9	-0.85	-0.84	-0.65	-0.81	-0.53	-0.59	-0.61	1	1
Ba	-0.61	0.76	0.6	0.19	0.44	0.17	0.92	0.53	-0.73	-0.71
V	-0.054	0.25	0.14	-0.15	-0.18	-0.67	0.12	-0.63	0.22	0.28
Ni	0.38	-0.53	-0.46	0.19	-0.079	-0.12	-0.59	-0.27	0.6	0.6
Cu	0.92	-0.94	-0.88	-0.57	-0.76	-0.38	-0.7	-0.51	0.98	0.97
Zn	-0.52	0.34	0.35	0.67	0.85	0.94	0.069	0.86	-0.74	-0.76
Ga	-0.88	0.91	0.95	0.49	0.43	-0.23	0.81	-0.0029	-0.69	-0.68
As	0.19	-0.21	-0.3	-0.13	0.19	0.79	-0.35	0.58	-0.21	-0.22
Se	0.48	-0.22	-0.43	-0.58	-0.45	-0.5	-0.23	-0.54	0.56	0.62
Rb	-0.63	0.79	0.71	0.17	0.22	-0.32	0.97	0.064	-0.53	-0.51
Sr	-0.077	-5.80E-04	-0.087	0.22	0.53	0.95	-0.18	0.81	-0.45	-0.46
Y	-0.72	0.78	0.74	0.42	0.4	-0.16	0.97	0.24	-0.6	-0.59
Zr	-0.78	0.85	0.73	0.39	0.69	0.49	0.6	0.57	-0.95	-0.93
Nb	-0.61	0.85	0.61	0.13	0.43	0.0049	0.81	0.27	-0.66	-0.61
Mo	0.94	-0.91	-0.88	-0.67	-0.84	-0.45	-0.56	-0.5	0.98	0.97
Sn	-0.0043	-0.015	-0.17	0.13	0.49	0.92	-0.087	0.85	-0.4	-0.39
Sb	0.87	-0.87	-0.78	-0.66	-0.87	-0.49	-0.44	-0.49	0.92	0.89
Pb	-0.4	0.56	0.54	-0.051	-0.12	-0.62	0.86	-0.24	-0.22	-0.21
Th	-0.7	0.84	0.76	0.28	0.33	-0.23	0.98	0.15	-0.61	-0.59
U	0.082	0.2	0.078	-0.48	-0.48	-0.86	0.28	-0.71	0.3	0.34
Au	-0.45	0.59	0.5	0.17	0.19	-0.43	0.26	-0.42	-0.19	-0.14

Correlation	Ba	V	Ni	Cu	Zn	Ga	As	Se	Rb	Sr
SiO_2	-0.61	-0.054	0.38	0.92	-0.52	-0.88	0.19	0.48	-0.63	-0.077
TiO_2	0.76	0.25	-0.53	-0.94	0.34	0.91	-0.21	-0.22	0.79	-5.80E-04
Al_2O_3	0.6	0.14	-0.46	-0.88	0.35	0.95	-0.3	-0.43	0.71	-0.087
Fe_2O_3	0.19	-0.15	0.19	-0.57	0.67	0.49	-0.13	-0.58	0.17	0.22
MgO	0.44	-0.18	-0.079	-0.76	0.85	0.43	0.19	-0.45	0.22	0.53
Na_2O	0.17	-0.67	-0.12	-0.38	0.94	-0.23	0.79	-0.5	-0.32	0.95
K_2O	0.92	0.12	-0.59	-0.7	0.069	0.81	-0.35	-0.23	0.97	-0.18
P_2O_5	0.53	-0.63	-0.27	-0.51	0.86	-0.0029	0.58	-0.54	0.064	0.81
TOC	-0.73	0.22	0.6	0.98	-0.74	-0.69	-0.21	0.56	-0.53	-0.45
S	-0.71	0.28	0.6	0.97	-0.76	-0.68	-0.22	0.62	-0.51	-0.46
Ba	1	-0.081	-0.76	-0.79	0.31	0.64	0.035	-0.27	0.84	0.19
V	-0.081	1	0.3	0.074	-0.63	0.33	-0.71	0.79	0.34	-0.71
Ni	-0.76	0.3	1	0.63	-0.24	-0.4	-0.35	0.34	-0.54	-0.29
Cu	-0.79	0.074	0.63	1	-0.62	-0.77	-0.094	0.45	-0.65	-0.32
Zn	0.31	-0.63	-0.24	-0.62	1	0.085	0.63	-0.67	-0.1	0.85
Ga	0.64	0.33	-0.4	-0.77	0.085	1	-0.54	-0.25	0.87	-0.34
As	0.035	-0.71	-0.35	-0.094	0.63	-0.54	1	-0.28	-0.5	0.93
Se	-0.27	0.79	0.34	0.45	-0.67	-0.25	-0.28	1	-0.068	-0.42
Rb	0.84	0.34	-0.54	-0.65	-0.1	0.87	-0.5	-0.068	1	-0.36
Sr	0.19	-0.71	-0.29	-0.32	0.85	-0.34	0.93	-0.42	-0.36	1
Y	0.82	0.18	-0.41	-0.68	0.076	0.87	-0.49	-0.28	0.95	-0.27
Zr	0.79	-0.16	-0.74	-0.96	0.66	0.6	0.33	-0.38	0.53	0.5
Nb	0.86	0.37	-0.58	-0.76	0.14	0.69	-0.13	0.14	0.83	0.012
Mo	-0.66	0.049	0.49	0.98	-0.69	-0.73	-0.1	0.44	-0.52	-0.35
Sn	0.28	-0.65	-0.3	-0.29	0.78	-0.37	0.9	-0.31	-0.28	0.97
Sb	-0.56	-0.06	0.36	0.92	-0.68	-0.63	-0.14	0.27	-0.42	-0.39
Pb	0.63	0.4	-0.43	-0.36	-0.42	0.76	-0.67	0.024	0.93	-0.63
Th	0.86	0.29	-0.53	-0.71	0.0011	0.89	-0.46	-0.14	0.99	-0.29
U	0.081	0.88	-0.0086	0.12	-0.82	0.33	-0.68	0.75	0.48	-0.79
Au	0.11	0.9	0.13	-0.32	-0.28	0.59	-0.6	0.53	0.45	-0.51

Table 7.6 (continued). Correlation coefficients of mean Au in pyrite with mean of major and trace elements including total organic carbon and total sulphur from whole rock compositions for all formations (this study). Numbers in pink colour are equal to or greater than 0.5.

Correlation	Y	Zr	Nb	Mo	Sn	Sb	Pb	Th	U	Au
SiO_2	-0.72	-0.78	-0.61	0.94	-0.0043	0.87	-0.4	-0.7	0.082	-0.45
TiO_2	0.78	0.85	0.85	-0.91	-0.015	-0.87	0.56	0.84	0.2	0.59
Al_2O_3	0.74	0.73	0.61	-0.88	-0.17	-0.78	0.54	0.76	0.078	0.5
Fe_2O_3	0.42	0.39	0.13	-0.67	0.13	-0.66	-0.051	0.28	-0.48	0.17
MgO	0.4	0.69	0.43	-0.84	0.49	-0.87	-0.12	0.33	-0.48	0.19
Na_2O	-0.16	0.49	0.0049	-0.45	0.92	-0.49	-0.62	-0.23	-0.86	-0.43
K_2O	0.97	0.6	0.81	-0.56	-0.087	-0.44	0.86	0.98	0.28	0.26
P_2O_5	0.24	0.57	0.27	-0.5	0.85	-0.49	-0.24	0.15	-0.71	-0.42
TOC	-0.6	-0.95	-0.66	0.98	-0.4	0.92	-0.22	-0.61	0.3	-0.19
S	-0.59	-0.93	-0.61	0.97	-0.39	0.89	-0.21	-0.59	0.34	-0.14
Ba	0.82	0.79	0.86	-0.66	0.28	-0.56	0.63	0.86	0.081	0.11
V	0.18	-0.16	0.37	0.049	-0.65	-0.06	0.4	0.29	0.88	0.9
Ni	-0.41	-0.74	-0.58	0.49	-0.3	0.36	-0.43	-0.53	-0.0086	0.13
Cu	-0.68	-0.96	-0.76	0.98	-0.29	0.92	-0.36	-0.71	0.12	-0.32
Zn	0.076	0.66	0.14	-0.69	0.78	-0.68	-0.42	0.0011	-0.82	-0.28
Ga	0.87	0.6	0.69	-0.73	-0.37	-0.63	0.76	0.89	0.33	0.59
As	-0.49	0.33	-0.13	-0.1	0.9	-0.14	-0.67	-0.46	-0.68	-0.6
Se	-0.28	-0.38	0.14	0.44	-0.31	0.27	0.024	-0.14	0.75	0.53
Rb	0.95	0.53	0.83	-0.52	-0.28	-0.42	0.93	0.99	0.48	0.45
Sr	-0.27	0.5	0.012	-0.35	0.97	-0.39	-0.63	-0.29	-0.79	-0.51
Y	1	0.52	0.73	-0.58	-0.2	-0.46	0.84	0.97	0.26	0.33
Zr	0.52	1	0.76	-0.92	0.48	-0.89	0.22	0.59	-0.17	0.21
Nb	0.73	0.76	1	-0.68	0.11	-0.68	0.61	0.84	0.41	0.55
Mo	-0.58	-0.92	-0.68	1	-0.29	0.97	-0.21	-0.6	0.19	-0.37
Sn	-0.2	0.48	0.11	-0.29	1	-0.34	-0.55	-0.21	-0.7	-0.5
Sb	-0.46	-0.89	-0.68	0.97	-0.34	1	-0.08	-0.5	0.16	-0.46
Pb	0.84	0.22	0.61	-0.21	-0.55	-0.08	1	0.89	0.63	0.38
Th	0.97	0.59	0.84	-0.6	-0.21	-0.5	0.89	1	0.4	0.44
U	0.26	-0.17	0.41	0.19	-0.7	0.16	0.63	0.4	1	0.71
Au	0.33	0.21	0.55	-0.37	-0.5	-0.46	0.38	0.44	0.71	1

7.6. Conclusion

The elevated concentration of gold in diagenetic pyrite coupled with higher levels of gold in whole rock from the Pennsylvanian-Early Permian Singa Formation (in the NW Domain), the Late Devonian BRSZ Unit 1, and the Middle Triassic Gua Musang Formation (in the Central Gold belt) make these formations good source rocks for sediment-hosted gold deposits in Malaysia. The Se contents in the BRSZ Unit 1, Gua Musang Formation and Singa Formation sedimentary pyrites is elevated compared to other studied formation pyrite. Recent research (Large et al., 2015; Gregory et al., 2015) argued that the periods of elevated Se contents in sedimentary pyrites coincide with periods of increased atmospheric oxygenation

in the Earth's history. Therefore, the Se content can be used as a proxy for atmospheric oxygenation. The Se content is significant based on the fact that much weathering of gold enriched-rocks and minerals on land occurred during the periods of increased oxygen in the atmosphere (as inferred in Se content in pyrite) (Gregory et al., 2015). A positive correlation between Se in sedimentary pyrite and organic carbon (Table 7.6) in sedimentary rocks (correlation coefficient of 0.6) also implies that organic processes were involved during introduction of Se into pyrite with other trace metals.

Consequently, based on current models for formation of sediment-hosted gold deposits (Makoundi et al., 2014; Gregory et al., 2015), it is implied that gold may have been adsorbed onto clay minerals, transported and deposited into basin and then may have been introduced into pyrite through organic processes (as commented in Table 7.1). To date, the Pennsylvanian-Early Permian Singa Formation that crops out on the Langkawi Island has never been the subject of grass root exploration. However, the gold content of sedimentary pyrites that is contained in the Singa Formation warrants future exploration.

In addition, areas of exploration interest would be sections of the district-scale stratigraphy (Figs. 7.13 and 7.14) which are deformed or tectonized/sheared as a prerequisite for metamorphic or magmatic fluids as having circulated and leached trace metals from sedimentary pyrite and deposited them in structural traps forming gold deposits. This research shows no evidence of a link between Au mineralisation and volcanism in the southern part of the Central Gold Belt notably in the Semantan Formation. The Pb isotope composition in sedimentary pyrite of the tuff-bearing Semantan Formation is close to that of ore pyrites (as documented in chapter 6). The BRSZ Unit 1 represents carbonaceous black shales interbedded with sandstones of Late Devonian age that crop out in the Bentong-Raub Suture Zone. The BRSZ Unit 1 contains elevated Au content in whole rock and sedimentary pyrite.

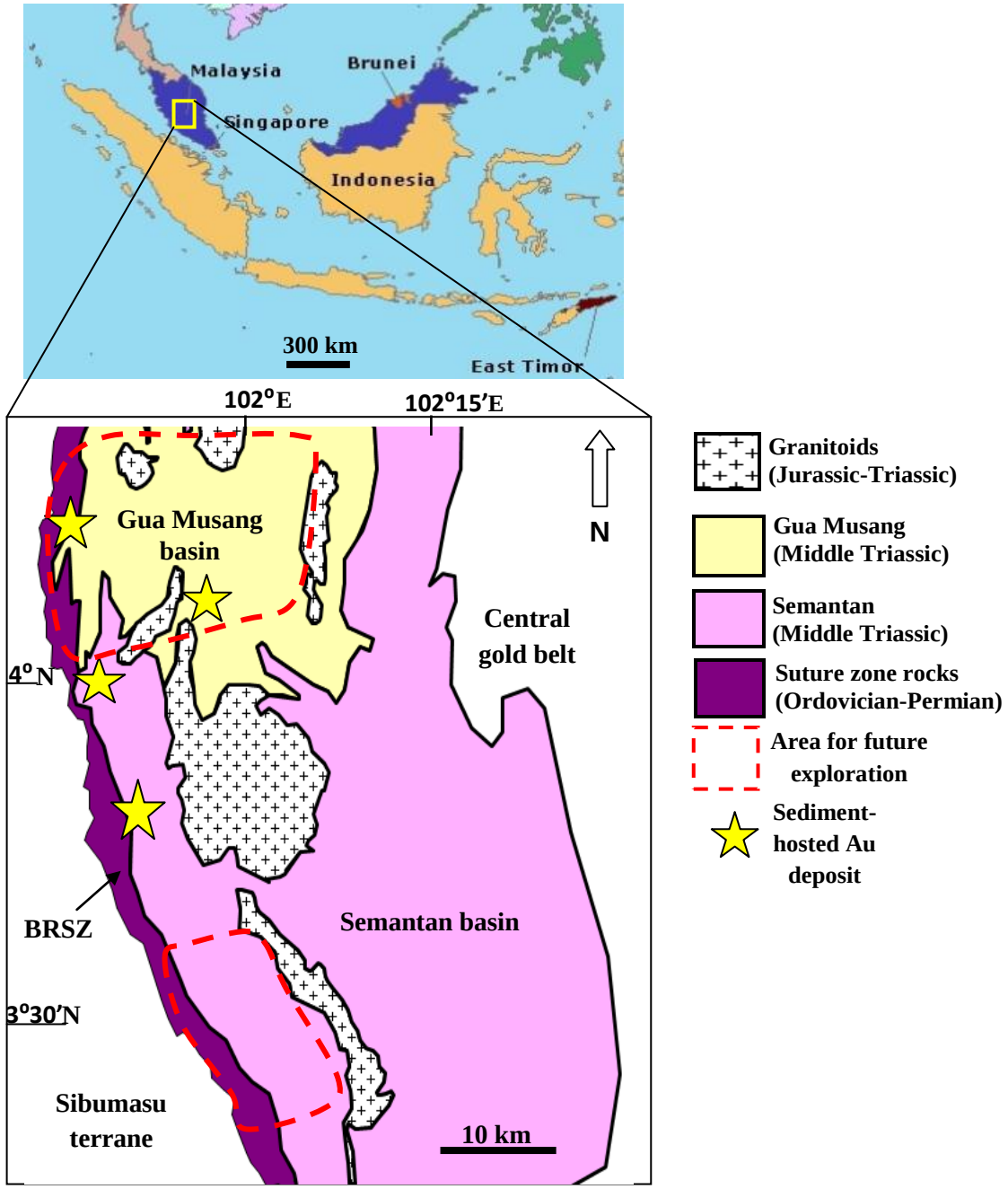

Fig. 7.13. Simplified geological map showing the proposed areas for future exploration on mainland Peninsular Malaysia. The Semantan basin is the largest basin compared to the Gua Musang basin.

The BRSZ Unit 1 was also a subject of much deformation and the shales are crosscut by quartz veins. Exploration along the Bentong Raub Suture Zone (BRSZ) should be enhanced to target possible haloes of gold concentration that may lead to new discoveries of sediment-hosted gold deposits.

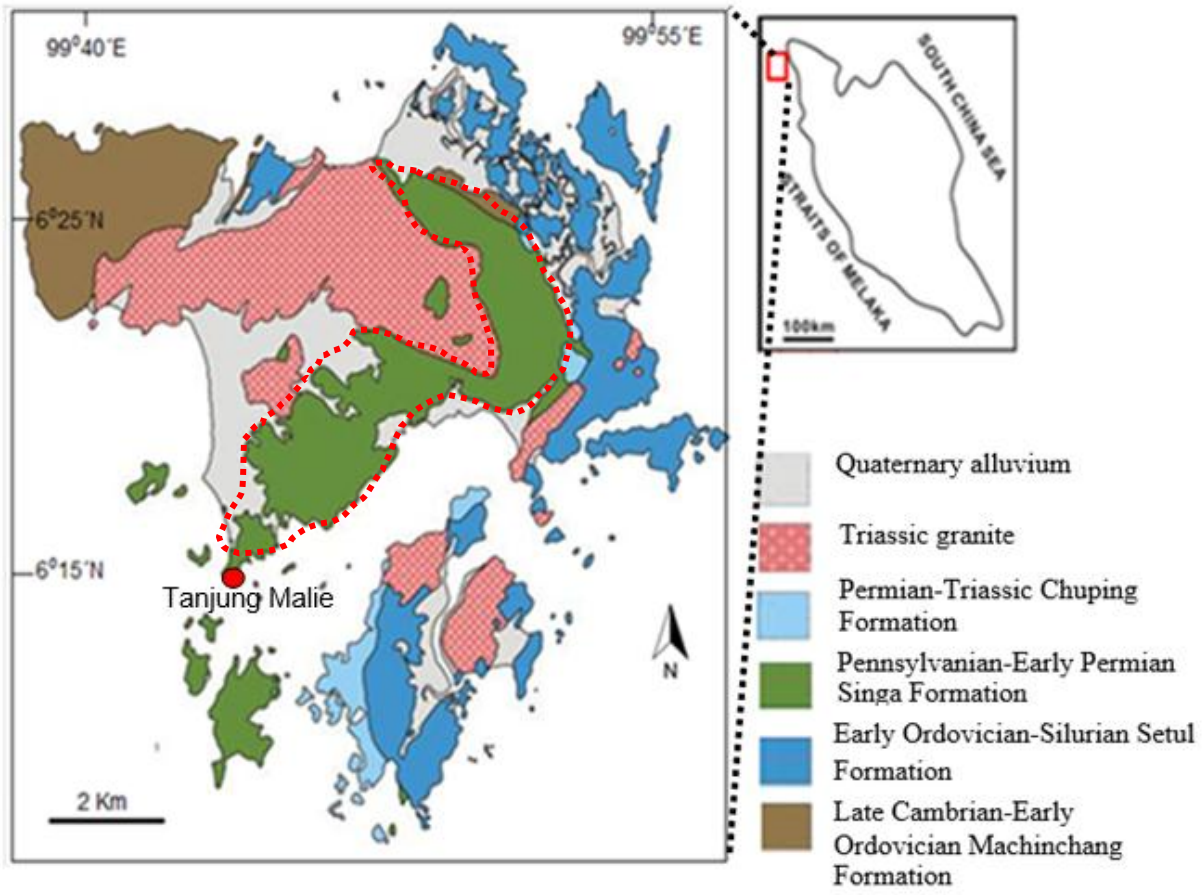

Fig. 7.14. Geological map of the Langkawi Island that shows the proposed areas (red dashed polygon) to explore for gold exploration. The square dot polygon is the proposed area for gold exploration in the Singa Formation.

Mapping should be enhanced to the north and south of the Bentong-Raub Suture Zone as formations enriched in gold-bearing sedimentary pyrites may well be identified as the BRSZ Unit 1 crops out along the suture trend. It is simply explained by the fact that most existing

gold deposits were discovered immediately east of the Bentong-Raub Suture Zone in the BRSZ Unit 1. Although, the suture zone is mountainous, more efforts are needed to target stratigraphic units that strike within the suture zone. The Gua Musang Formation is found within the second largest sedimentary basin in the Central Gold Belt. Gold deposits such as Tersang, Penjom, and Selinsing have been discovered in this basin. Fig. 7.13 (in the Central Gold Belt) and Fig. 7.14 (at Langkawi Islands) show proposed areas for future gold exploration. This study reveals that there are still potential areas for gold exploration and simplified geologic maps (Figs. 7.13 and 7.14) with emphasis on gold are provided for mineral exploration projects in Peninsular Malaysia and Langkawi Islands. In this study, the Middle Triassic Gua Musang Formation shows that 100% of its invisible gold content in sedimentary pyrites is above 250 ppb.

Similarly, the Late Devonian BRSZ Unit 1 and the Middle Triassic Karak Formation also have 100 % of invisible content in pyrite above 250 ppb. Both the Gua Musang and BRSZ Unit 1 are best targets for further discovery of sediment-hosted gold deposits. In addition, the Singa Formation sedimentary pyrites contain 59% of gold in excess of 250 ppb making another target to discover sediment-hosted gold deposits at the Langkawi Islands. Although, current exploration activities are still focussed on the Carboniferous (319-337 Ma) and Permian (259-264 Ma) host rocks (Makoundi, 2012). This thesis arguably concludes that gold exploration should be extended to new stratigraphic horizons of Pennsylvanian-Early Permian (i.e. Singa Formation), Late Devonian (i.e. BRSZ Unit 1) and Middle Triassic (i.e. Gua Musang) in age that contain high Se and Au contents in sedimentary pyrites (this study) in order to discover new sediment-hosted gold deposits. Delineating stratigraphic horizons enriched in Se and Au within sedimentary pyrites in black shales would significantly enhance gold prospectivity in sedimentary basins.

References

Adi Maulana., Koichiro Watanabe, Akira Imai, Kotaro Yonezu., 2013. Origin of Magnetite- and Ilmenite-series Granitic Rocks in Sulawesi, Indonesia: Magma Genesis and Regional Metallogenic Constraint. Procedia Earth and Planetary Science (Elsevier). vol. 6, pp. 50-57.

Agangi, A., Hofmann, A., Wohlgemuth-Ueberwasser, C.C., 2013. Pyrite zoning as a record of mineralization in the Ventersdorp Contact Reef, Witwatersrand Basin, South Africa. Econ. Geol. 108, pp. 1243–1272.

Agematsu, S., Sashida, K., Ibrahim, A., 2008. Biostratigraphy and paleobiogeography of Middle and Late Ordovician conodonts from the Langkawi Islands, northern peninsular Malaysia. Journal of Paleontology 82, 957–973. http://dx.doi.org/10.1666/07-058.1.

Ahmad Jantan, Kamal Roslan Mohamed, Che Aziz Ali, Ibrahim Abdullah, Uyop Said and Abd. Rahim Samsudin., 1991. Relationship and depositional setting of the Lanis conglomerate, Mangkin sandstone and Termus shale of the Tembeling Group in Tekai valley, Pahang. Geological Society of Malaysia, Warta Geologi, 17, 158p.

Allen, R.L., Weihed, P., Blandell, D., Crawford, T., Davidson, G., 2002. Global comparison of volcanic-associated massive sulphide districts, Geol. Soc. Spec. Publ., 2001, vol. 204, pp. 13-37.

Allen, C., and I. Campbell., 2012. Identification and elimination of a matrix-induced systematic error in LA-ICP-MS $^{206}Pb/^{238}U$ dating of zircon; Chem. Geol., 332, pp. 157– 165.

Alonso-Azcarate, J., Rodas, M., Bottrell, S.H., Raiswell, R., Velasco, F and Mas, J.R., 1999. Pathways and distances of fluid flow during low-grade metamorphism: evidence from pyrite deposits of the Cameros Basin, Spain, Journal of Metamorphic petrology, 17, pp. 339-348.

Algeo, T.J., Maynard, J.B., 2004. Trace element behaviour and redox facies in the core shales of upper Pennsylvanian Kansas-type cyclotherms. Chem. Geol. 206, pp. 289-318.

Amato, J. M., and T. L. Pavlis., 2010. Detrital zircon ages from the Chugach Terrane, southern Alaska, reveal multiple episodes of accretion and erosion in a subduction complex, Geology, 38(5), 459-462, doi: 10.1130/G30719.1.

Antonina, A.N., Shazili, N.A.M., Kamaruzzaman, B. Y., Ong, M. C. Rosnan, Y., Sharifah. F. N., 2013. Geochemistry of the Rare Earth Elements (REE) Distribution in Terengganu Coastal Waters: A Study Case from Redang Island Marine Sediment. Open Journal of Marine Science, 2013, 3, pp. 154-159.

Arthur, M.A. and Sageman, B.B., 1994. Marine black shales: a review of depositional mechanisms and environments of ancient deposits. Ann. Rev. Earth Planet. Sci. 22, pp. 499-551.

Ault, W.V., and Kulp, J.L., 1960. Sulphur isotopes and ore deposits: Economic Geology, vol. 55, pp. 73-100.

Barber, A. J., and M. J. Crow., 2009. Structure of Sumatra and its implications for the tectonic assembly of Southeast Asia and the destruction of Palaeo-tethys, Island Arc, 18 (1), 3-20.

Baker, J., Peate, D., Waight, T., and Meyzen, C., 2004, Pb isotopic analysis of standards and samples using a Pb207/Pb204 double spike and thallium to correct for mass bias with a double-focusing MC-ICP-MS. Chemical Geology, 211, pp. 275 - 303.

Barker, S.L.L., Hickey, K.A., Cline, J.S., Dipple, G.M., Kilburn, M.R., Vaughan, J.R. and Longo, A.A., 2009. Uncloaking invisible gold; use of NanoSIMS to evaluate gold, trace elements, and sulfur isotopes in pyrite from carlin-type gold deposits. Econ. Geol. Bull. Soc. Econ. Geol, 104, pp. 897–904.

Barton, E.S. and Hallbauer, D.K., 1996. Trace-element and U-Pb isotope composition of pyrite types in the Proterozoic Black Reef, Transvaal Sequence, South Africa: Implications on genesis and age. Chem. Geol., 133, pp. 173–199.

Basir Jasin, Zaiton Harun, and Siti Norhajar Hassan., 2003. Black siliceous deposits in Peninsular Malaysia: their occurrence and significance. Geological Society of Malaysia, 64, pp. 149-154.

Basir Jasin., 2013. Chert blocks in Bentong-Raub Suture Zone: A heritage of Palaeo-Tethys. Bulletin of the Geological Society of Malaysia, vol. 59, November 2013, pp. 85 – 91.

Belousova, E.A., Griffin, W.L., O'Reilly, S.Y., Fisher, N.I., 2002. Igneous zircon: trace element composition as an indicator of source rock type. Contrib. Mineral Petrol (2002); Springer-Verlag 143: pp. 602-622.

Benning, L.G., Wilkin, R.T., and Barbes, H.L., 2000. Reaction pathways in the Fe-S system below 100° C, Chem. Geol. vol. 167, pp. 25-51.

Berner, Z.A., Puchelt, H., Nöltner, T., Kramar, U., 2013. Pyrite geochemistry in the Toarcian Posidonia Shale of southwest Germany: Evidence for contrasting trace-element patterns of diagenetic and syngenetic pyrites. Sedimentology (2013) 60, 548–573. doi: 10.1111/j.1365-3091.2012.01350.x.

Berner, R.A., 1970. Sedimentary pyrite formation. Am. J. Sci., 268, pp. 1–23.

Berner, R.A., 1982. Burial of organic carbon and pyrite sulfur in the modern ocean: its geochemical and environmental significance. American Journal of Science, vol. 282, April 1982, pp. 451-473.

Berner, R.A., 1984. Sedimentary pyrite formation: an update. Geochim. Cosmochim. Acta, 48, 605–615.

Bhatia, M.R., Crook, K.A.W., 1986. Trace element characteristics of greywackes and tectonic setting discrimination of sedimentary basins. Contributions to Mineralogy and Petrology, vol. 92, pp. 181-193.

Bignell, J.D., and Snelling, N.J., 1977. K-Ar ages on some basic igneous rocks from Peninsular Malaysia and Thailand, Bulletin of the Geological Society of Malaysia, vol. 8, pp. 89 - 93.

Black, L.P., and Gulson B.L., 1978, The age of the Mud tank Carbonatite, Strangways Range, Northern Territory. BMR Journal of Australian Geology and Geophysics 3, pp. 227 - 232.

Black, L.P., Kamos, L., Allen., C.M., Aleinikoff, J.N., Davis, D.W., Korsch, R.J., Foudoulis, C., 2003, TEMORA 1: a new zircon standard for Phanerozoic U–Pb geochronology. Chemical Geology 200, pp. 155 – 170.

Black, L.P., Kamo, S.L., Allen, C.M., Davis, D.W., Aleninikoff, J.N., Valley, J.W., Mundil, R., Campbell, I. H., Korsch, R. J., Williams, I. S., and Foudoulis, C., 2004. Improved $^{206}Pb/^{238}U$ microprobe geochronology by the monitoring of a trace-element related matrix effect; SHRIMP, ID-TIMS, ELA-ICP-MS, and oxygen isotope documentation for a series of zircon standards. Chemical Geology 205, pp. 115 -140.

Bowman, J.R., 1998. Stable-isotope systematics of skarns, in Lentz, D. R (Eds), Mineralised intrusion-related skarn systems: Mineralogical Association of Canada Short Course Series, v. 26, pp. 359 - 414.

Bond, D., and Wignall, P.B., 2010. Pyrite framboid study of marine Permian-Triassic boundary sections: a complex anoxic event and its relationship to contemporaneous mass extinction.

Böning, P., Brumsack, H.J., Böttcher, M.E., Schnetger, B., Kriete, C., Kallmeyer, J., Borchers, S.L., 2004. Geochemistry of Peruvian near-surface sediments. Geochim. Cosmochim. Acta 68, pp. 4429-4451.

Boström, K., 1983. Genesis of ferromanganese deposits-diagnostic criteria for recent and old deposits. In: hydrothermal processes at seafloor spreading centers (Eds). P.A. Rona, K.Bostrom., L. Laubier., and K.L. Smith, pp. 473-483. Plenum Press, New York.

Bralia, A., Sabatini, G. and Troja, F., 1979. A revaluation of the Co/Ni ratio in pyrite as geochemical tool in ore genesis problems. Mineral. Deposita, 14, pp. 353-374.

Brumsack, H.J., 1989. Geochemistry of recent TOC-rich sediments from the Gulf of California and Black Sea. Geol. Rundsch. 78, pp. 851-882.

Bull, S.W and Large, R.R., 2014. Setting the stage for the genesis of the giant Bendigo ore system. V.3993. doi: 10.1144/sp393.10. The Geological Society of London Special Publication.

Burge, S., 1982. Trace element distribution around precious and base metal veins, Idaho Springs district, Colorado: Golden, Colorado School of Mines, MSc thesis, 112p.

Clive Burrett, Khin Zaw, Sebastien Meffre, Chun Kit Lai, Somboon Khositanont, Pol Chaodumrong, Mongkol Udchachon, Samuel Ekins, Jacqueline Halpin., 2014. The configuration of Greater Gondwana—Evidence from LA ICPMS, U–Pb geochronology of detrital zircons from the Palaeozoic and Mesozoic of Southeast Asia and China. Gondwana Research vol. 26, pp. 31-51.

Calvert, S.E., Pedersen, T.F., 1993. Geochemistry of recent oxic and anoxic sediments: implications for the geological record. Mar. Geol. 113, pp. 67-88.

Canet, C., Prol-Ledesma, R.M., Melgareso, J.C., and Reyes, A., 2003. Methane related carbonates formed at submarine hydrothermal springs: a new setting for microbially-derived carbonates, Marine Geology, 199, pp. 245-261.

Canfield, D. E., and Raiswell, R., 1991, Pyrite formation and fossil preservation, *in* Allison, P. A. and Briggs, D. E. G., editors, Topics in Geobiology: New York, Plenum Press, p. 337–387.

Carr, G.R., Dean, J.A., Suppel, D.W., and Heithersay, P.S., 1995. Precise lead isotope fingerprinting of hydrothermal activity associated with Ordovician to Carboniferous metallogenetic events in the Lachlan Foldbelt of New South Wales: Economic Geology, v. 90, pp. 1467-1505.

Chang, Z., Large R.R. and Maslennikov V., 2008. Sulphur isotope in sediment-hosted orogenic gold deposits: Evidence for an early timing and a seawater sulphur source. Geology, v. 36, pp. 971 - 974.

Che Aziz Ali, Kamal Roslan Mohamed, Mohd Shafeea Leman, Ibrahim Komoo, and Tanot Unjah., 2008. Field guide to geology of Langkawi geopark. Cataloguing-in-publication data, 82p.

Chunlong, C., 2001. Some problems in the study of siliceous Rocks. *Journal of Mineralogy and Petrology*, 21 (3), 100-104.

Cingolani, C.A., Manassero, M., Abre, P., 2003. Composition, provenance, and tectonic setting of Ordovician siliciclastic rocks in the San Rafael block: Southern extension of the Precordillera crustal fragment, Argentina, Journal of South American earth Sciences, vol. 16, pp. 91-106.

Clark, Ch., Grguric, B. and Schmidt Mumm, A., 2004. Genetic implications of pyrite chemistry from the Palaeoproterozoic Olary Domain and overlying Neoproterozoic Adelaidean sequences, northeastern South Australia. Ore Geol. Rev., 25, pp. 237-257.

Clift, P. D. (2015), Assessing effective provenance methods for fluvial sediment in the South China Sea, in River-dominated shelf sediments of East Asian seas, edited by P. D. Clift, J. Harff, J. Wu and Q. Yan, Geological Society of London, London, doi:10.1144/SP429.3.

Cobbing, E.J., Mallick, D.I.J., Pitfield, P.E.J., and Teoh, L.H., 1986. The granites of Southeast Asia. Journal of Geological Society of London, 143, pp. 537-550.

Cobbing, E.J., Pitfield, P.E.J., Darbyshire, D.P.F. and Mallick, D.I.J., 1992. The granites of the South-East Asian Tin Belt. British Geological Survey, Overseas Memoir, 10.

Cocks, L.R.M., Fortey, R.A., and Lee, C.P., 2005. A review of Lower and Middle Paleozoic biostratigraphy in west Peninsular Malaysia and southern Thailand in its context within the Sibumasu Terrane. Journal of Asian Earth Sciences, 24, pp. 703-717.

Coleman, M., Raiswell, R., 1995. Source of carbonate and origin of zonation in pyritiferous carbonate concretions: evaluation of a dynamic model. Am. J. Sci. 295, pp. 282–308.

Cox, R., Lowe, D.R., and Cullers, R.L., 1995. The influence of sediment recycling and basement composition on evolution of mudrock chemistry in the south-western United States. Geochim. Cosmochim. Acta 59, pp. 2919-2940.

Craig, H., 1953. The geochemistry of the stable carbon isotopes. Geochim. Cosmochim. Acta, 3: 53-92.

Craig, J.R., Vokes, F.M. and Solberg, T.N., 1998. Pyrite: physical and chemical textures. Mineralium Deposita, 34: 82-101.

Cullers, R.L., Barrett, T., Carlson, R. and Robinson, B., 1987. Rare-Earth element and mineralogical changes in Holocene soil and stream sediment: a case study in the wet mountains region, Colorado, USA. Chem. Geol. 63, pp. 275-297.

Cullers, R.L., Basu, A., and Suttner, L., 1988. Geochemical signature of provenance in sand-size material in soils and stream sediments near the Tobacco Root batholith, Montana, USA. Chem. Geol. 70, pp. 335-348.

Cullers, R.L., 1994a. The controls on the major and trace element variations of shales, siltstones, and sandstones of Pennsylvanian-Permian age from uplifted continental blocks in Colorado to platform sediment in Kansas, USA. Geochimica Cosmochimica Acta, 58, 4955-4972.

Cullers, R. L., 2000. The geochemistry of shales, siltstones and sandstones of Pennsylvian-Permian age, Colorado, USA: implications for provenance and metamorphic studies. Lithos 51, 181–203.

Cullers, R.L., Podkovyrov, V.M., 2000. Geochemistry of the Mesoproterozoic Lakhanda shales in southeastern Yakutia, Russia: implications for mineralogy, provenance, and recycling. Precambrian Research, 104, pp. 77-93.

Cumming, G.L. and Richards, I.R., 1975. Ore lead isotope ratios in a continuously changing Earth. *Earth and Planetary Science Letters*, 28, 155-171.

Danyushevsky, L.V., Robinson, P., Gilbert, S., Norman, M., Large, R.R, McGoldrick, P., and Shelley, J. M. G., 2011. Routine quantitative multi-element analysis of sulfide minerals by laser ablation ICP-MS: Standard development and consideration of matrix effects. Geochemistry: Exploration, Environment, Analysis 11, pp. 51-60.

Darbyshire, D.P.F., 1988. Geochronology of Malaysian Granites. NERC Isotope Geological Report, British Geological Survey, vol. 3, 60p.

Deer, W. A., Howie, R. A., and Zussman, J., 1966. An Introduction to the Rock Forming Minerals. Wiley, New York.

Degens, E.T., 1969. Biogeochemistry of stable carbon isotopes. In Eglinton, G., and Murphy, M.T.J. (Eds), Organic geochemistry methods and results: Berlin Springer-Verlag, pp. 304-329.

Dickinson, W.R., Beard, I.S., Brakenridge, G.R., Erjavee, J.L., Ferguson, R.C., Inman, K.F., Knep, R.A., Lindberg, F.A., Ryberg, P.T., 1983. Provenance of North American Phanerozoic sandstones in relation to tectonic setting: Geological Society of America bulletin, 94, pp. 222-235.

Dill, H., 1986. Metallogenesis of early Paleozoic graptolite shales from the Graefenthal Horst (Northern Bavaria-Federal Republic of Germany). Econ. Geol. 81, pp. 889–903.

Dill, H., Teschner, M. and Wehner, H., 1988. Petrography, inorganic and organic geochemistry of Lower Permian carbonaceous fan sequences ("Brandschiefer Series")—Federal Republic of Germany: constraints to their paleogeography and assessment of their source rock potential. *Chem. Geol*. 67, pp. 307–325.

Donohue, C.L. and Essene, E.J., 2005. Granulite-facies conditions preserved in vanadium- and chromium-rich metapelites from the Paradise Basin, Wind River Range, Wyoming, U.S.A. Canadian Mineralogist, 41, 495–511.

Drost, K., Linnemann, U., Wemmer, K., Budil, P., Kraft, Fatka, O., Marek, J., 2003. Provenance and early diagenetic processes of the Ordovician Sarka Formation at Praha-Cerveny vrch Hill (Barrandian, Czech Republic); vol. 78, No. 2, Czech Geological Survey, pp. 147-156.

Dumoulin, J.A and Till, A.B., 2011. Reconstruction of a Late Proterozoic to Devonian continental Margin sequence, Northern Alaska: its paleogeographic significance, and contained based metal sulfide deposits. Special paper 506. The geological Society of America.

Dypvik, H., 1984. Geochemical compositions and depositional conditions of Upper Jurassic and Lower Cretaceous Yorkshire clays, England: Geological Magazine, 121(5), pp. 489-504.

Feng, Caixia and Liu, Jiajun., 2001. The Investive Actuslity and Mineralization Significance of Cherts. World geology, 20(2), 119-123.

Foo, K.Y., 1964. Geology of the north central region Pulau Langkawi. Unpublished B.Sc. (Hons) thesis. Department of geology, University of Malaya.

Foo, K.Y., 1983. The Paleozoic sedimentary rocks of Peninsular Malaysia- stratigraphy and correlation. Proceedings of the workshop on stratigraphic correlation of Thailand and Malaysia, 1, technical papers, 1-19.

Fontaine, H., Khoo, H.P., Vachard, D., 1988. Discovery of Triassic fossils at Bukit Chuping, Gunung Sinyum and Kota Jin, Peninsular Malaysia. J. SE Asian Earth Science, 2, pp. 145-162.

Fontaine, H., Ibrahim Amnan, Khoo, H.P., Nguyen, D.T and Vachard, D., 1994. Discovery of Upper Permian to Triassic limestone in the lower basin of Sungai Kenong, Kuala Lipis area, Pahang. Geological Survey of Malaysia. Geological papers, 4, pp. 45-55.

Ghandour, I.M., Masuda, H., and Maejima, W., 2003. Mineralogical and chemical characteristics of Bajocian-Bathonian shales, G. Al-Maghara, North Sinai, Egypt: Climatic and environmental significance. Geochemical Journal, 37, pp. 87-108.

Gobbett, D.J and Hutchison, C.S (Eds)., 1973. Geology of the Malay Peninsular: West Malaysia and Singapore. New York: Wiley-Interscience, 438p.

Goh, S. H., 2005. Gold mineralization in the Eastern Gold Belt of Peninsular Malaysia with emphasis on the Mengapor skarn deposit. Ph.D. thesis. University of Malaya (Unpublished).

Goldfarb, R.J., Miller, L.D., Leach, D.L., and Snee, L.W., 1997. Gold deposits in metamorphic rocks of Alaska: Economic Geology Monograph 9, pp. 151 - 190.

Goldfarb, R.J., Baker, T., Dube, B., Groves, D.I., Hart, C.J.R., and Gosselin, P., 2005. Distribution, character and genesis of gold deposits in metamorphic terranes: Economic Geology 100th Anniversary Volume, pp. 407 - 450.

Greensmith, J. T., Hatch, F. H., and Rastall, R. H., 1971. Petrology of the Sedimentary Rocks. Thomas Murby and Company, London.

Gregory, D., Meffre, S., and Large, R.R., 2014. Comparison of metal enrichment in pyrite framboids from a metal-enriched and metal-poor estuary. American Mineralogist, Volume 99, pp. 633–644.

Gregory, D.D., Large, R.R., Halpin, J.A., Steadman, J.A., Hickman, A.H., Ireland, T.R., Holden, P., 2015. The chemical conditions of the late Archean Hamersley basin inferred from whole rock and pyrite geochemistry with Δ33S and δ34S isotope analyses. Geochimica et Cosmochimica Acta 149, 223-250.

Gregory, D., Large, R.R., Halpin, J.A., Baturina, E.L., Lyons, T.W., Wu, S., Sack, P.J., Chappaz, A., Maslennikov, V.V., and Bull, S.W., 2015. Trace element content of background sedimentary pyrite in black shales; Economic Geology.

Gromet, L. P., Dymek, R. F., Haskin, L. A. and Korotev, R. L., 1984. The 'North American shale composite' – its compilation, major and trace element characteristics. Geochimica et Cosmochimica Acta, pp. 2469–2482.

Groves, D.I., Goldfarb, R.J., Robert, F., and Hart, C.J.R., 2003. Gold deposits in metamorphic belts: overview of current understanding, outstanding problems, future research, and significance: Economic Geology, v. 98, pp. 1 - 29.

Gulson, B.L., 1986. Lead isotopes in mineral exploration: Development in Economic Geology, v. 23, pp. 1 - 245.

Guy, B.M., Beukes, N.J., Gutzmer, J., 2010. Paleoenvironmental controls on the texture and chemical composition of pyrite from non-conglomeratic sedimentary rocks of the Mesoarchean Witwatersrand Supergroup, South Africa. S.Afr. J. Geol.113, pp.195–228.

Guy, B.M., Ono, S., Gutzmer, J., Kaufman, A.J., Lin, Y., Fogel, M.L., Beukes, N.J., 2012. A multiple sulfur and organic carbon isotope record from non-conglomeratic sedimentary rocks of the MesoArchaean Witwatersrand Supergroup, South Africa. Precambrian Res. 216–219, pp. 208–231.

Hallberg, R.O., 1976. A geochemical method for investigation of palaeoredox conditions in sediments: Ambio, Special Report, 4, pp.139-147.

Hanlie, Hong., Wang Qinyan., and Chang, Jiamping., 1999. Occurrence and distribution of invisible gold in the Shewushan supergene gold deposit, southeastern Hubei, China. The Canadian Mineralogist, vol. 37, pp. 1525-1531.

Hasnol Hady Ismail, Mazlan Madon, and Zainol Affendi Abu Bakar., 2007. Sedimentology of the Semantan Formation (Middle - Upper Triassic) along the Karak-Kuantan Highway, central Pahang. Geological Society of Malaysia, Bulletin 53, June 2007, pp. 27 – 34.

Hatch, J.R., Leventhal, J.S., 1992. Relationship between inferred redox potential of the depositional environment and geochemistry of the Upper Pennsylvanian (Missourian) stark shale member of the Dennis Li Wabaunsee County, Kansas, USA. Chem. Geol. 99, pp. 65-82.

Harbury, N.A., Jones, M.E., Audley-Charles, M.G., Metcalfe, I., and Mohamed, K.R., 1990. Structural evolution of Mesozoic Peninsular Malaysia. Journal of Geological Society of London, 147, pp. 11-26.

Junguo, H., Yongzhang, Z., Hongzhong, L., 2011. Study on Geochemical Characteristics and Depositional Environment of Pengcuolin Chert, Southern Tibet. Journal of Geography and Geology, vol. 3, No. 1. doi:10.5539/jgg.v3n1p178.

Hild, E., Brumsack, H.J., 1998. Major and minor element geochemistry of Lower Aptian sediments from the NW German Basin (core Hoheneggelsen KB 40). Cretac. Res. 19, pp. 615–633.

Hinchey, J., 2012. Preliminary insights into lithogeochemical signatures and possible provenance of reduced sedimentary units associated with copper mineralisation – western Avalon Zone, Newfoundland. Newfoundland and Labrador Dept of Natural Resources, Geological Survey, report 12-1, pp. 1-20.

Holland, H.D., and Turekian, K.K., 2011 (Eds). Isotope Geochemistry from the Treatise on Geochemistry. In: Lerman, A., and Clauer, N. Stable isotopes in the sedimentary record. pp. 285-336. Elsevier.

Hon, R., and Noyes, H. J., 1977, REE and other trace elements during fractionation of granitic aplites of Sierra Nevada Batholith, CA and Katahdin pluton, ME: Geological Society of America Abstracts with Programs, vol. 9, p. 1023.

Huerta-Diaz, M.A., and Morse, J.W., 1990. A quantitative method for determination of trace metal concentrations in sedimentary pyrite. Marine Chemistry, 29, pp. 119–144.

Huerta-diaz M.A. and Morse J.W., 1992. Pyritization of trace-metals in anoxic marine sediments. Geochim. Cosmochim. Acta 56, 2681-2702.

Huston, D.L., Sie, S.H., Suter, G.F., Cooke, D.R. and Both, R.A., 1995. Trace-elements in sulfide minerals from eastern Australian volcanic-hosted massive sulfide deposits. 1. Proton microprobe analyses of pyrite, chalcopyrite, and sphalerite, and 2. selenium levels in pyrite – comparison with delta-s-34 values and implications for the source of sulfur in volcanogenic hydrothermal systems. Econ. Geol., 90, pp. 1167–1196.

Hutchison, C., 1977. Granite emplacement and tectonic subdivision of Peninsular Malaysia. Geological Society of Malaysia Bulletin 9, pp. 187-207.

Hutchison, C.S., 1989. Geological evolution of South-east Asia. Oxford Monographs on Geology and Geophysics, 13, Oxford University Press, p: 368.

Hu Kai., 2000. Genesis and organic geochemical characteristics. Science in China. vol. 43, no. 5.

Ingham, F.T., 1938. The geology of the neighbourhood of Tapah and Telok Anson, Perak, F.M.S with accounts of mineral deposits. Geological Survey Department Federation of Malaya Memoir, 2, 72p.

Jaafar, B.A., 1976. Geology and mineral resources of the Karak and Temerloh areas, Pahang, Geological Society of Malaysia, Memoir 15, 138p.

Jaafar, B.A., 1979. The petrology of the Benom igneous complex. Geological Survey of Malaysia, special paper 2, 141p.

Jaafar, B.A., 1980. Geology and mineral resources of the Teris area, Pahang. Geological Survey of Malaysia, District memoir, 18, 148p.

Jackson, S.E., Pearson, N.J., Griffin, W.L., Belousova, E.A., 2004, The application of laser ablation-inductively coupled plasma-mass spectrometry to in situ U–Pb zircon geochronology: Chemical Geology 211, pp. 47 - 69.

Jafarzadeh, Mahdi and Mahboobeh Hosseini-Barzi., 2008. Petrography and geochemistry of Ahwaz sandstone Member of Asmari Formation, Zagros, Iran: implications on provenance and tectonic setting. Vol. 25, num 2, Revista Mexicana de ciencias Geologicas, pp. 247-260.

Jones, B., and Manning, D.A.C., 1994. Comparison of geochemical indices used for the interpretation of paleoredox conditions in ancient mudstones. Chem. Geol. 114, pp. 111-129.

Jones, C.R., 1961. A revision of the stratigraphical sequence of the Langkawi Islands, Federation of Malaya. Proceedings 9th Pacific Science Congress, 12, pp. 287-300.

Jones, C.R., 1968. Lower Paleozoic rocks of the Malay Peninsula. American Association of Petroleum Geologists Bulletin, 52, pp. 1259-1278.

Jones, C.R., 1970a. On a Lower Devonian fauna from Pahang, West Malaysia. Geological Society of Malaysia Bulletin, 3, pp. 63-75.

Kamar, S.A., Sinjeng, P.P., Mian, K.H., 1994. Mineralogy and petrology of the Penjom gold prospect, Kuala Lipis, Pahang, Proceedings International conference on recent advances in material and mineral resources (1994), 3-5 May 1994, USM, pp. 389-401.

Khin Zaw, Rodmanee, T., Khositanont, S., Ruamkid, S., 2008. Geology, mineralogy and genesis of Phu Thap Fah gold skarn deposit, Northeast Thailand. Implications for reduced gold skarn formation. 33rd International Geological Congress (IGC), 5–14 August, 2008, Oslo, Norway, CD-ROM.

Khin Zaw, Meffre, S., Lai, C.K., Burrett, C., Santosh, M., Graham, I.T., Manaka, T., Salam, A., Kamvong, T., Cromie, P.W., 2014. Tectonics and metallogeny of mainland Southeast Asia — A review and contribution. Gondwana Research, v. 26, 5-30.

Khoo, H.P., 1977. The geology of the Sungai Tekai area. Geological Survey of Malaysia, Annual Report, 1977, pp. 93-103.

Khoo, S.C., 1988. Geology and mineralisation of the Cheroh-Tersang area, Pahang Darul Makmur. Unpubl. B.Sc. Hons. Thesis, University of Malaya, 98p.

Khoo, H. P., 1983. Mesozoic stratigraphy in Peninsular Malaysia. Proceedings Workshop on "Stratigraphic correlation of Thailand and Malaysia" Hatyai Thailand, pp. 253-90.

Khoo, H.P and Tan, B.K., 1983. Geological Evolution of Peninsular Malaysia. Proceedings of worshop on stratigraphic correlation of Thailand and Malaysia, 1: Technical papers, Geological Society of Thailand and Geological Society of Malaysia, pp. 253-290.

Klötzli U., Klötzli E., Günes Z. and Košler J., 2009. External accuracy of laser ablation U-Pb zircon dating: results from a test using five different reference zircons. Geostand. Geoanal. Res. 33, 1, pp. 5-15.

Kobayashi, T., and Tamura, M., 1968. Myophoria in Malaya with a note on the Triassic Trigoniacea. In: Kobayashi, T and Toriyama, R. (Eds) Geology and Paleontology of Southeast Asia, vol. 5. Tokyo: University of Tokyo Press, pp. 88-137.

Koeberl, C., Nyakairu, G.W.A., 2001. Mineralogical and chemical composition and distribution of rare earth elements in clay-rich sediments from central Uganda. Geochemical Journal, v. 35, pp. 13-28.

Kosler, J., 2001. Laser-ablation ICPMS study of metamorphic minerals and processes. In: Sylvester, P. J. (Ed). Laser-ablation-ICPMS in the earth sciences; principles and applications: Mineralogical Association of Canada Short Course Handbook 29, pp. 185 - 202.

Krom, M.D., and Berner, R.A., 1983. A rapid method for the determination of organic and carbonate carbon in geological samples. Journal of sedimentary research, 53 (2), pp. 600-663.

Kump, L.R., Arthur, M.A., 1999. Interpreting carbon-isotope excursions; carbonates and organic matter. Chem. Geol. 161, pp. 181– 198.

Large, R.R., Maslennikov, V.V., Robert, F., Danyushevsky, L.V., Chang, Z., 2007. Multistage sedimentary and metamorphic origin of pyrite and gold in the Giant Sukhoi log deposit, Lena Gold Province, Russia. Econ. Geol. 102, 1233–1267.

Large, R.R., Danyushevsky, L., Hollit, C., Maslennikov, V., Meffre, S., Gilbert, S., Bull, S., Bull, S., Scott, R., Emsbo, P., Thomas, H., Singh, B., and Foster, J., 2009. Gold and Trace element zonation in pyrite using a laser imaging technique: Implications for the timing of gold in orogenic and Carlin-style sediment-hosted deposits. Economic Geology 104, pp. 635-668.

Large, R.R., 2010. Evidence for a two-stage process in the genesis of sediment-hosted gold-arsenic deposits, Deb, M., and Goldfarb, R., Eds., Gold Metallogeny India and Beyond, Alpha Science International Ltd., Oxford, U.K., pp. 30-47.

Large, R.R., Bull, S.W., and Maslennikov, V.V., 2011. A carbonaceous sedimentary source-rock model for Carlin-type and orogenic gold deposits: Society of Economic Geologists, v. 106, pp. 331-358.

Large, R.R., Halpin, J.A., Danyushevsky, L.V., Maslennikov, V.V., Bull, S.W., Long, J.A., Gregory, D.D., Elena Lounejeva, Lyons, T.W., Sack, P.J., McGoldrick, P.J., Calver, C.R., 2014. Trace element content of sedimentary pyrite as a new proxy for deep-time ocean–atmosphere evolution. Earth and Planetary Science Letters 389 (2014) 209–220.

Large, R.R., Halpin, Jacqueline A., Lounejeva, Elena, Danyushevsky, L.V., Maslennikov, V.V., Gregory, D., Sack, Patrick J., Haines, P.W., Long, J.A., Makoundi, C., Stepanov, Sasha., 2015. Cycles of nutrient trace elements in the Phanerozoic ocean, Gondwana Research (2015); doi: 10.1016/j.gr.2015.06.004.

Laurie, J., Burrett, C., 1992. Biogeographic significance of Ordovician brachiopods from Thailand and Malaysia. Journal of Paleontology 66, 16–23.

Lee, C.P., 1983. Stratigraphy of the Tarutao and Machinchang Formations. In: Nutalaya, P. (Ed.), Stratigraphic correlation of Thailand and Malaysia. Geological Societies of Thailand and Malaysia, Bangkok, pp. 20–38.

Lee, C.P., 2006. The Cambrian of Malaysia. Palaeoworld, 15, pp. 242-255.

Lee, C.P., 2009. Palaeozoic Stratigraphy. In: Hutchison, C,R., Tan, D.N.K. (Eds.), Geology of Peninsular Malaysia. University of Malaya and Geological Society of Malaysia, Kuala Lumpur, pp. 55–86.

Leman, M.S., 1994. The significance of Upper Permian Brachiopods from Merapoh area, northwest Pahang. Geological Society of Malaysia. Bulletin 35, pp.113 -121.

Lennie, A.R., England, K.E., and Vaughan, D.J., 1995. Transformation of synthetic mackinawite to hexagonal pyrrhotite: A kinematic study. American mineralogist, 80, pp. 960-967.

Lennie, A.R., Redfern, S.A.T., Champness, P.E., Stoddart, C.P., Schofield, P.F., Vaughan, D.J., 1997. Transformation of mackinawite to greigite: an in situ X-ray powder diffraction and transmission electron microscopy study. Am. Mineral. 82, pp. 302–309.

Liew, T.C., 1983. Petrogenesis of Peninsular Malaysia granitoids batholiths. Unpubl. PhD thesis, Australian National University.

Loftus-Hills, G. and Solomon, M., 1967. Cobalt, nickel, and selenium in sulfides as indicators of ore genesis. Mineral. Depos, 2, pp. 228–242.

Love, L. G. and Amstutz, C. G., 1966. Review of microscopic pyrite. Fortshcritte der Mineralogie, 43, pp. 273-309.

Mahdi Jafarzadeh and Mahboobeh Hosseini-Bazri., 2008. Petrography and geochemistry of Ahwaz Sandstone Member of Asmari Formation, Zagros, Iran: implications on provenance and tectonic setting. Revista Mexicana de Ciencias Geológicas, v. 25, núm. 2, 2008, pp. 247-260.

Makoundi, C., 2004. Facies analysis of the Triassic Jelai Formation in the Central Basin of Peninsular Malaysia: implications on paleogeography and tectonics. M.Sc. thesis, University of Malaya, 140p.

Makoundi, C., 2012. Geology, Geochemistry and Metallogenesis of Selected Sediment-hosted Gold deposits in the Central Gold Belt, Peninsular Malaysia. M.Sc. thesis, University of Tasmania, 212p.

Makoundi, C., Khin Zaw, Large, R.R., Meffre, S, Lai Chun-Kit., Hoe Teh Guan., 2014. Geology, geochemistry and metallogenesis of the Selinsing gold deposit, Central Malaysia, Gondwana Research, v. 26, pp. 241-261.

Mann, S., Sparks, N.H.C., Frankel, R.B., Bazylinski, D.A., and Jannasch, H.W., 1990. Biomineralisation of ferromagnetic greigite (Fe_3S_4) and iron pyrite (FeS_2) in a magnetotactic bacterium: Nature, v. 343, pp. 258–242.

McLennan, S.M., W.B. Nance and S.R. Taylor., 1980. Rare earth element-thorium correlations in sedimentary rocks and the composition of the continental crust. Geochim. Cosmochim. Acta, 44: pp. 1833-1839.

McLennan, S.M., 1989. Rare earth elements in sedimentary rocks: influence of provenance and sedimentary processes. In: Lipin, B.R., McKay, G.A. (Eds). Geochemistry and Mineralogy of Rare Earth Elements. Reviews in Mineralogy and Geochemistry, vol. 21, pp. 169-200.

McLennan, S.M., Taylor, S.R., McCulloch, M.T., Maynard, J.B., 1990. Geochemical and Nd-Sr isotopic composition of deep-sea turbidites: crustal evolution and plate tectonics associations. Geochimica and Cosmochimica Acta 54, pp. 2015-2050.

McLennan, S.M., and Taylor, S.R., 1991. Sedimentary rocks and crustal evolution: tectonic setting and secular trends. J. Geol, 99, pp. 1-21.

McClay, K.R., and Ellis, P.G., 1983. Deformation and recrystallization of pyrite. Mineralogical Magazine, December 1983, vol. 47, pp. 527-38

Meffre, S., Large, R.R., Scott, R., Woodhead, J., Chang, Z., Gilbert, S.E., Danyushevsky, L.V., Maslennikov,V., Hergt, J.M., 2008. Age and pyrite Pb-isotopic composition of the giant Sukhoi Log sediment-hosted gold deposit, Russia. Geochim. Cos-mochim.Acta72, pp. 2377–2391.

Metcalfe, I., 1985. Lower Permian conodonts from the Terbat Formation, Sarawak. Warta Geologi 11, 1–4.

Metcalfe., I. 2000. The Bentong-Raub Suture Zone. Journal of Asian Earth Sciences. 18 , pp. 691 – 712 .

Metcalfe, I. 2002. Permian tectonic framework and palaeogeography of SE Asia. Journal of Asian Earth Sciences, 20, 551–566.

Metcalfe, I., 2011. Tectonic framework and Phanerozoic evolution of Sundaland. Gondwana Research 19 (2011) 3–21.

Metcalfe, I., 2013. Tectonic evolution of the Malay Peninsula. Journal of Asian Earth Sciences. doi:10.1016/j.jseaes.2012.12.011.

Meyers, S. R., B. B. Sageman, and Lyons, T. W., 2005. Organic carbon burial rate and the molybdenum proxy: Theoretical framework and application to Cenomanian-Turonian oceanic anoxic event 2, Paleoceanography, 20, PA2002, doi:10.1029/2004PA001068.

Meyer, K.M, Kump L.R, Ridgwell, A., 2008. The biogeochemical controls on photic-zone euxinia during the end-Permian mass extinction. Geology 36:747–750.

McClay, K.R., and Ellis, P.G., 1983. Deformation and recrystallization of pyrite. Mineralogical Magazine, December 1983, vol. 47, pp. 527-538.

Miller, C.F., and Mittlefehdt, D., 1982. Depletion of light rare-earth elements in felsic magmas. GEOLOGY, vol. 10, pp. 129-133, March 1982.

Milner, H. B., 1962. Sedimentary Petrology. The MacMillan, Company, New York.

Mishra, M., and Sen, S., 2012. Provenance, tectonic setting and source area weathering of the Mesoproterozoic Kaimur Group, Vindhyan Supergroup, Central India. vol. 10; no. 3; Geologica Acta.

Mitchell, A.H.G., Young, B and Jataranipa, W., 1970. The Phuket Group, Peninsular Thailand: A Paleozoic geosynclinals deposit – Geol. Mag, vol. 107, No. 4, pp. 411-428.

Mitchell, A.H.G., 1981. Phanerozoic plate boundaries in mainland SE Asia, the Hymalayas and Tibet: Journal of the Geological Society of London 138, pp. 109-122.

Mohd Shafeea Leman and Sone, M., 2001. Conglomerate from setia Jasa near Temerloh, Pahang, Peninsular Malaysia: its stratigraphic position and depositional environment. Proceedings of Geological Society of Malaysia Annual Conference 2001, pp. 115-119.

Mohd Shafeea Leman and Azmaniza Yop., 2002. Early Permian sequence from Sungai Itau quarry, Langkawi: its age, depositional environment and paleoclimatic implication. Geological Society of Malaysia Bulletin, 46, pp. 163-170.

Morford,J.L., Emerson, S., 1999. The geochemistry of redox sensitive trace metals in sediments. Geochim, Cosmochim. Acta 63, pp. 1735-1750.

Morse, J., Millero, F., Cornwell, J. and Rickard, D., 1987. The chemistry of the hydrogen-sulphide and iron sulphide systems in natural-waters. Earth Sci. Rev., 24, pp. 1-42.

Morse, J.W., and Arakaki, T., 1993. Adsorption and coprecipitation of divalent metals with mackinawite (FeS). Geochimica et Cosmochimica Acta, 57, pp. 3635-3640.

Murray, R.W., 1994. Chemical criteria to identity the depositional environment of chert: general principles and applications. Sed. Geol., 90, pp. 213-232.

Mustaffa Kamal Shuib, 2000a. The olistostrome in the Bentong area, Pahang and their tectonic implications. Proceedings of the Geol. Soc. Malaysia Ann. Conf, 2000, pp. 51-55.

Mustaffa Kamal, S., 2000. The Mesozoic tectonics of Peninsular Malaysia- An overview. Dynamic stratigraphy and tectonics of P. Malaysia, J'd. seminar -The Mesozoic of Peninsular Malaysia, pp.106-126.

Mustaffa Kamal Shuib, and Abdul Hadi, 2000. The Mesozoic of the Central Belt of the Malay Peninsula: Basin configuration and tectonics. Warta Geologi, vol. 26, 3, pp. 77-80.

Neumann, T., Rausch, N., Leipe, T., Dellwig, O., Berner, Z., and Böttcher, M.E., 2005. Intense pyrite formation under low-sulfate conditions in the Achterwasser lagoon, SW Baltic Sea. Geochimica et Cosmochimica Acta, 69, pp. 3619-3630.

Ng, T.F., 1986. Geology and mineralisation of the Pahang Tengku area, Pahang Darul Makmur, Unpublished B.Sc. (Hons) thesis, Department of geology, University of Malaya.

Noori, A., and Rais, S., 2014. Geochemistry and detrital modes of sandstone from Barakar Formation in Mand Valley Basin, Chhattisgarh, India: Implications for Provenance, Tectonic Setting and Paleoweathering.

Nyakairu, W.A.G., Koebel, C., 2001. Mineralogical and chemical composition and distribution of rare earth elements in clay-rich sediments from central Uganda; v. 35, pp. 13-28.

Oehlert, A.M., and Peter K. Swart., 2014. Interpreting carbonate and organic carbon isotope covariance in the sedimentary record. DOI: 10.1038/ncomms5672. 2014 Macmillan Publishers Limited.

Ohmoto, H., and Rye, R.O., 1979. Isotopes of sulphur and carbon. In: Barnes H.L. (Ed) Geochemistry of hydrothermal ore deposits. Wiley, New York, pp. 509-567.

Oliver, G., Khin Zaw., Hotson, M., Meffre, S., Takayuki Manaka., 2014. U-Pb zircon geochronology of Early Permian to Late Triassic rocks from Singapore and Johor: A plate tectonic reinterpretation; Gondwana Research 26, pp. 132-143.

Ong, S.S., 1969. Geology of the Muda Dam Area, Kedah, West Malaysia. Unpublished B.Sc. (Hons) thesis, Dept of Geology, University of Malaya.

Özkan, E.Y., 2012. A New Assessment of Heavy Metal Contaminations in a Eutrophicated Bay (Inner Izmir Bay, Turkey). Turkish Journal of Fisheries and Aquatic Sciences 12: 135-147 (2012); doi: 10.4194/1303-2712-v12_1_16.

Pašava, J., Sulovsky, P., Kovalova, M., 1993. Geochemistry and mineralogy of Proterozoic metal-rich black shales from the Bohemian massif Czech Republic with a description of possible new Molybdenum selenide and Telluride phases. The Canadian Mineralogist, v. 31, pp.745-754.

Passier, H.F., Middelburg, J.J., De Lange, G.J., Böttcher, M.E., 1997. Pyrite contents, microtextures, and sulfur isotopes in relation to formation of the youngest eastern Mediterranean sap, Geology; June 1997; v. 25; no. 6; pp. 519–522.

Paton, C., Woodhead, J.D., Hellstrom, J.C., Hergt, J.M., Greig, A., and Maas, R., 2010. Improved laser ablation U-Pb zircon geochronology through robust downhole fractionation correction. Geochemistry, Geophysics, Geosystems 11, pp.1,525-2,027.

Pereira, J.J., 1996. The geology and mining of gold deposits, their tailings disposal and subsequent impact on the physical environment in selected areas of Peninsular Malaysia. Unpublished PhD thesis, Dept of geology, University of Malaya.

Phillips, G. N., Groves, D.I., and Brown, I.J., 1987, Source requirements for the Golden Mile, Kalgoorie: Significance to the metamorphic replacement model for Archean gold deposits: Canadian Journal of Earth Sciences, v. 24, pp. 1,643-1,651.

Pi, D.H., L. Cong-Qiang, A.G. Shields-Zhoud and J. Shao-Yong., 2013. Trace and rare earth element geochemistry of black shale and kerogen in the early Cambrian Niutitang Formation in Guizhou province, South China: Constraints for redox environments and origin of metal enrichments, Precambrian Research, 225: 218- 229.

Piper, D.Z., Perkins, R.B., 2004. A modern vs. Permian black shales-the hydrography, primary productivity and water-column chemistry of deposition. Chem. Geol. 206, pp.177-197.

Pisarzowska A, Berner, Z.A., Racki, G., 2014. Geochemistry of Early Frasnian (Late Devonian) pyrite-ammonoid level in the Kostomłoty Basin, Poland, and a new proxy parameter for assessing the relative amount of syngenetic and diagenetic pyrite. Sedimentary Geology 308 (2014), pp.18–31.

Pitcairn, I.K., Teagle, D.A.H., Craw, D., Olivo, G.R., Kerich, R., and Brewer, T.S., 2006. Source of metals and fluids in orogenic gold deposits: Insights from the Otago and Alpine schists, new Zealand: ECONOMIC GEOLOGY, v. 101, pp. 1525-1546.

Plank, T. and Langmuir, C. H. 1998. The chemical composition of subducting sediment and its consequences for the crust mantle. Chemical Geology, 145, pp. 325–394.

Porter, E. W., and Ripley, E., 1985. Petrologic and stable isotope study of the gold-bearing breccia pipe at the Golden Sunlight deposit, Montana: Econ. Geol., v. 80, pp. 1189-1706.

Potter, P.E; Maynard, J.B., Depetris, P.J., 2005. Mud and mudstones: introduction and overview. Springer Berlin Heidelberg.

Rahman, J.J.M., and Suzuki S, 2007. Geochemistry of sandstones from the Miocene Surma Group, Bengal Basin, Bangladesh: Implications for Provenance, tectonic setting and weathering. Geochemical Journal, Vol. 41, pp. 415-428. The Geochemical Society of Japan.

Raiswell, R., 1982. Pyrite texture, isotopic composition and the availability of iron: American Journal of Science, v. 82, pp. 1244–1263.

Raiswell, R., Bottrell, S.H., Al-Biatty, H.J and Tan, M.M.D., 1993. The influence of bottom water oxygenation and reactive iron content on sulfur incorporation into bitumens from Jurassic marine shales. Am. J. Sci. 293, pp. 569-596.

Raiswell, R., Canfield, D.E., 2012. The iron biogeochemical cycle Past and Present. v. 1, number 1, Geochemical Perspectives. 232p.

Ramdohr, P., 1958. New observation of the Ores of the Witwatersand in South Africa and their genetic significance. Transactions of the Geological Society of South Africa, 61, pp. 1-50.

Raymond, O.L., 1996. Pyrite composition and ore genesis in the Prince Lyell copper deposit, Mt Lyell mineral field, western Tasmania, Australia. In: The Conjunction of Processes Resulting in the Formation of Orebodies (Eds R.M. Vielreicher, D.I. Groves, C.A. Heinrich and J.L. Walshe), Ore Geol. Rev., v. 10, pp. 231–250.

Reich, M., Kesler, S.E., Utsunomiya, S., Palenik, C.S., Chryssoulis, S.L., and Ewing, R., 2005. Solubility of gold in arsenian pyrite: Geochimica et Cosmochimica Acta, v. 69, pp. 2,781-2,796.

Reid, I., and Frostick, L.L., 1985. Role of settling, entrainment and dispersive equivalence and of interstice trapping in placer formation. Journal of Geological Society of London, 142, pp. 739-746.

René, M., 2012. Distribution and Origin of Clay Minerals during Hydrothermal Alteration of Ore Deposits. http://dx.doi.org/10.5772/48312.

Richardson, J.A., 1939. The Geology and mineral resources of the neighbourhood of Raub, Pahang with an account of the Geology of the Raub Australian Gold Mine. Geological Survey of Malaysia, Kuala Lumpur, 3, 166p.

Rickard, D., and Luther, G.W. III., 2007. Chemistry of iron sulfides. Chem. Rev., 2007, vol. 107, pp. 514-562.

Rimmer, S.M., 2004. Geochemical paleoredox indicators in Devonian–Mississippian black shales, Central Appalachian Basin (USA) Department of Geological Sciences, University of Kentucky, Lexington, KY 40506-0053, USA. Chemical Geology 206 (2004), pp. 373– 391.

Riquier, L., Tribovillard, N., Averbuch, O., Joachimski, M.M., Racki, G., Devleeschouwer, X., El Albani, A., Riboulleau, A., 2005. Productivity and bottom water redox conditions at the Frasnian–Famennian boundary on the both sides of the Eovariscan Belt constraints from trace element geochemistry. In: Over, D.J., Morrow, J.R., Wignall, P.B. (Eds), Understanding Late Devonian and Permian–Triassic Biotic and Climatic Events: Towards an Integrated Approach: Developments in Palaeontology and Stratigraphy, v. 20, pp. 199–224.

Roberts, F.I., 1982. Trace-element chemistry of pyrite: a useful guide to the occurrence of sulfide base metal mineralization. J. Geoch. Explor. v.17, pp. 49–62.

Rollinson, H.R., 1996. Using geochemical data: evaluation, presentation, interpretation, Longman, Singapore, pp. 1 – 314.

Romberger, S.B., 1988. Geochemistry of gold in hydrothermal deposits. US Geological Survey Bulletin, v. 1857, Library of congress cataloguing-in-publication data, pp. 1-25.

Roser, B.P., Korsch, R.J., 1988. Provenance signatures of sandstone-mudstone suites determined using discriminant function analysis of major-element data. Chem. Geol. v. 67, pp. 119-139.

Ryan, K.M., and Williams, D.M., 2007. Testing the reliability of discrimination diagrams for determining the tectonic depositional environment of ancient sedimentary basins. Chemical Geology, vol. 242, pp. 103-125.

Rye, R. O., and Ohmoto, H., 1974. Sulphur and carbon isotopes and ore genesis: A review: Economic Geology, v. 69, pp. 826 - 842.

Sack, P.J., Danyushevsky, L.V., Large, R.R., Gilbert, S., and Gregory, D., 2014. Sedimentary pyrite as a gold-source in sediment-hosted gold occurrences in the Selwyn basin area, eastern Yukon. In: Yukon Exploration and Geology 2013, K.E. MacFarlane, M.G. Nordling, and P.J. Sack (Eds.), Yukon Geological Survey, pp. 195-220.

Sackett, W.M., 1964. The depositional history and isotopic organic carbon composition of marine sediments. Mar. Geol., 2: 173-185.

Sackett, W.M., 1989. Stable carbon isotope studies on organic matter in the marine environment. *In* Fritz, P., and Fontes, J.C. (Eds.), *Handbook of Environmental Isotope Geochemistry* (Vol. 3): *The Marine Environment, A:* Amsterdam (Elsevier), 139-169.

Sangster, A.L., 1992. Light stable isotope evidence for a metamorphogenic orogen for bedding-parallel, gold-bearing veins in Cambrian flysch, Meguma Group, Nova Scotia: Exploration and Mining Geology, v. 1, pp. 69 - 79.

Saito, M.A., Moffett, J.W., Chisholm, S.W., Waterbury, J.B., 2002. Cobalt uptake in Prochlococcus. Limnol. Oceanogr. 47, pp. 1629-1636.

Schidlowski, M., Hayes, J.M. and Kaplan, I, R., 1983. Isotopic inferences of ancient biochemistries: carbon, sulphur, hydrogen, and nitrogen, in Schopf, J.W., ed., Earth's Earliest Biosphere: its origin and evolution: Princeton, University Press, Princeton, pp.149-187.

Schieber, J., 2011. Iron sulfide formation. Encyclopedia of Geobiology, Springer Verlag, J. Reitner and V. Thiel (Eds), pp. 486-502.

Schoonen, M., and Barnes, H., 1991. Reactions forming pyrite and marcasite from solution: II. Via FeS precursors below 100 °C. Geochimica et Cosmochimica Acta, 55, pp. 1505–1514.

Schwartz, M.O., Rajah, S.S., Askury, A.K., Putthapiban, P., Djaswadi, S., 1995. The Southeast Asian Tin Belt. Earth Science Reviews 38, pp. 95-293.

Scott, R.J., Meffre, S., Woodhead, J., Gilbert, S.E., Berry, R.F., and Emsbo, P., 2009. Development of framboidal pyrite during diagenesis, low-grade regional metamorphism, and hydrothermal alteration, Economic Geology, 104, pp. 1143-1168.

Scrivenor, J.B., 1928. The Geology of Malayan Ore Deposits. Macmillan, London, 216p.

Seal, R.R. II, 2006. Sulfur Isotope Geochemistry of Sulfide Minerals. Reviews in Mineralogy and Geochemistry, v. 61, pp. 633-677.

Şengör, A.M.C., 1984. The Cimmeride orogenic system and the tectonics of Eurasia. The Geological Society of American, special paper 195, 82p.

Şengör, A.M.C., 1986. The dual nature of the Alpine-Himalayan system; progress, problems and prospects. Tectonophysics, 127, pp. 177-195.

Shergold, J., Burrett, C., Akerman, T., Stait, B., 1988. Late Cambrian trilobites from Tarutao Island, Thailand. New Mexico Bureau of Mines and Mineral Resources Memoir 44, pp. 303–320.

Slack, J.F., Selby, D., Dumoulin, J.A., 2015. Hydrothermal, biogenic, and seawater components in metalliferous black shales of the Brooks Range, Alaska: synsedimentary metal enrichment in a carbonate ramp setting. Economic Geology, 110, pp. 653-675.

Slingerland, R., and Smith, N., 1986. Occurrence and formation of water-laid placers. Annual Review of Earth and Planetary Science, v.14, pp. 113-147.

Sone, M., Metcalfe, I., Leman, M.S., 2008. Search for the Permian–Triassic boundary in central Peninsular Malaysia: Preliminary report. Permophiles No. 51, pp. 32-33.

Stauffer, P.H., and Lee, C.P., 1986. Late Palaeozoic glacial marine facies in Southeast Asia and its implications. GEOSEA V Proceedings, Geological Society of Malaysia Bulletin, 20, pp. 363-397.

Stait, B., Burrett, C., Wongwanich, T., 1984. Ordovician trilobites from the Tarutao Formation Southern Thailand. Neues Jahrbuch fur Geologie und Palaeontologie Monatschefte 1984 (1), 53–64.

Stait, B., Wyatt, D., Burrett, C., 1987. Ordovician nautiloid faunas of Langkawi Islands, Malaysia and Tarutao Island, Thailand. Neues Jahrbuch fur Palaeontologie Abh 174, pp. 373-391.

Stumm, W and Morgan, J.J., 1981. Aquatic chemistry: an introduction emphasizing chemical equilibria in natural waters, 2nd edition: Wiley-Interscience, New York, 780p.

Sugitani, K., Horiuchi, Y., Adachi, M., Sugisaki, R., 1996. Anomalously low Al2O3/TiO2 values for Archean cherts from the Pilbara Block, Western Australia-possible evidence for extensive chemical weathering on the early earth. Precambrian Res. 80, pp. 49-76.

Suits, N.S., and Wilkin, R.T., 1998. Pyrite formation in the water column and sediment of a meromictic lake: Geology, v. 26, pp. 1099-1102.

Taylor, K.G., Macquaker, J.H.S., 2000. Early diagenetic pyrite morphology in a mudstone-dominated succession: the Lower Jurassic Cleveland Ironstone Formation, eastern England. Sedimentary Geology 131 (2000), pp. 77-86.

Taylor, K.G. and Macquaker, J.H.S., 2011. Iron in marine sediments: minerals as records of chemical environments. DOI:10.2113/gselements.7.2.113.

Taylor, S.R., and McLennan, S.M., 1985. The continental crust: its composition and evolution. Oxford: Blackwell, 312p.

Thomas, H.V., Large, R.R., Bull, S.W., Maslennikov, V., Berry, R.F., Fraser, R., and Froud, S., Moye, R., 2011. Pyrite and pyrrhotite textures and composition in sediments, laminated quartz veins and reefs, at Bendigo Gold Mine, Australia; Insights for orogenesis: Economic Geology, v. 106, pp. 1-31.

Tomkins, A.G., 2010. Windows of metamorphic sulfur liberation in the crust: Implications for gold deposit genesis: Geochimica et Cosmochimica Acta, v. 74, pp. 3246-3259.

Tomkins, A.G., 2013. A biogeochemical influence on the secular distribution of orogenic gold. Express letter, Economic Geology v. 108, pp. 193-197.

Totten, M.W and Hanan, M.A., 2007. Heavy minerals in shales. Developments in Sedimentology, v. 58, pp. 323–341. Elsevier. ISSN: 0070-4571/doi:10.1016/S0070-4571 (07)58012-X.

Tribovillard, N., Desprairies, A., Lallier-Vergès, E., Moureau, N., Ramdani, A., Ramanampisoa, L., 1994. Geochemical study of organic-rich cycles from the Kimmeridge Clay Formation of Yorkshire (G.B.): productivity vs. anoxia. Palaeogeogr. Palaeoclimatol. Palaeoecol. 108, pp. 165–181.

Tribovillard, N., Algeo, T.J., Lyons, T., Riboulleau, A., 2006. Trace metals as paleoredox and paleoproductivity proxies: An update. Chemical Geology 232 (2006) 12–32. Elsevier.

Ulrich, Th., Long, D.G.F., Kamber, B.S. and Whitehouse, M.J., 2011. In situ trace element and sulfur isotope analysis of pyrite in a Paleoproterozoic gold placer deposit, Pardo and Clement Townships, Ontario, Canada. Econ. Geol. Bull. Soc. Econ. Geol., v. 106, pp. 667-686.

Uyop, S, Malihan, M and Konjing, Z 2007. Neocomian palynomorph assemblage from Central Pahang, Malaysia. Geological Society of Malaysia, bulletin 53, pp. 21-25.

Vallentyne, J. R., 1963. Isolation of pyritic spherules from recent sediments. Limnology and Oceanography 8, 1G30.

Volkov, I.I and Fomina, L.S., 1974. Influence of organic material and processes of sulfide formation on distribution of some trace elements in deep water sediments of the black sea. In: D.A. Ross and E.T. Degens (Eds), The black sea-geology, chemistry, and biology. American Association of Petroleum Geologists, Memoir 20, pp. 456-476.

Wagner, T and Boyce, A.J., 2006. Pyrite metamorphism in the Devonian Hunsrück slate of Germany: insights from laser microprobe sulfur isotope analysis and thermodynamic modelling. American Journal of Science, 306, pp. 525-552.

Wan Fuad, W.H., and Purwanto, H.S., 2002. Type deposits of Primary Gold Mineralisation in the Central Belt, Peninsular Malaysia. Buletin Persatuan Geologi Malaysia, 45, pp. 111-116.

Waterhouse, J.B., 1982. An early Permian cool-water fauna from pebbly mudstone in south Thailand. Geological Magazine, vol. 119, No. 4, July 1982, pp. 337-432.

Wedepohl, K.H., 1985. Origin of the Tertiary basaltic volcanism in the northern Hessian depression. Contrib. Mineral. Petrol., 89: 122-143.

Wedephol, K. H. 1995. The composition of the continental crust. Geochimica et Cosmochimica Acta, v. 59, pp. 1217-1232.

Wen, L., LÜ Xinbiao., WU Chunming., and YANG Enlin., 2014. Geochemical Characteristics and Depositional Environment of Early Cambrian Cherts of the Black Shale-Hosted Ag-V Deposit in Kuruktag, Xinjiang, West China. Acta Geologica Sinica (English Edition), 88 (supp. 2), pp. 260-261.

Wiendenbeck, M., Alle, P., Corfu, F., Griffin, W.L., Meier, M., Oberli, F., Vonquadt, A., Roddick, J.C., and Speigel, W., 1995, 3 Natural Zircon Standards for U-Th-Pb, Lu-Hf, Trace-Element and REE Analyses. Geostandards Newsletter 19, pp. 1 - 23.

Wilkin, R.T., Barnes, H.L., Brantley, S.L., 1996. The size distribution of framboidal pyrite in modern sediments: an indicator of redox conditions. Geochim. Cosmochim. Acta 60, pp. 3897–3912.

Willbourn, E.S and Ingham, F.T., 1933. Geology of the scheelite mine, Kramat Pulai, F.M.S. Quarterly. Journal of the Geological Society of London, v. 89, pp. 449-479.

Wood, S.A., 1996. The role of humic substances in the transport and fixation of metals of economic interest (Au, Pt, Pd, U, V): Ore Geology Reviews, v.11, pp. 1–33.

Wongwanich, T., 2001. Lower Palaeozoic. In: Bunopas, S., Piyasin, S., Nutasari, N. (Eds.), Toraniwitayapratetthai (Geology of Thailand). Department of Mineral Resources, Bangkok, Thailand. ISBN: 9747733633, pp. 53–110 (in Thai).

Wronkiewicz, D.J and Condie, K.C., 1987. Geochemistry of Archean shales from the Witwatersand Supergroup, South Africa: source-area weathering and provenance. Geochem. Cosmochim. Acta 51, pp. 2401-2416.

Wronkiewicz, D.J and Condie, K.C., 1990. Geochemistry and mineralogy of sediments from the Ventersdorp and Transvaal Supergroups, South Africa: cratonic evolution during the early Proterozoic. Geochim. Cosmochim. Acta, 54, pp. 343-354.

Xu, D.-., Yan, Z., Zhang, Q. W., Shen, Z. D., Sun, Y. Y., Ye, L. F., 1986. Significance of a δ13C anomaly near the Devonian/Carboniferous boundary at the Muhua section, South China. Nature 321, pp. 854–855.

Yamamoto, K., Sugisaki, R., and Arai, F., 1986. Chemical aspect of alteration of acidic tuff and their application to siliceous deposits. Chem. Geol. 55, pp. 61-76.

Haisheng, Y., Yongzhang. Z and Zhijun, Y., 2003. REE Geochemical Characteristics of Hydrothermal Cherts from South China. *Bulletin of Mineralogy, Petrology and Geochemistry*, 22(1), 61-64.

Yeap, E.B., 1993. Tin and gold mineralization in Peninsular Malaysia and their relationships to the tectonic development: Journal of Southeast Asian Earth Sciences, v. 8, pp. 329-348.

Young, G.M. and Nesbitt, H.W., 1998. Processes controlling the distribution of Ti and AI in weathering profiles. Siliciclastic sediments and sedimentary rocks. J. Sed. Research, 68(3). 448-455.

Zatman, R.E., and Stacey, J.S., 1971. Lead isotope and mineralisation ages in belt supergroup rocks, Northwestern Montana and Northern Idaho, v. 66, pp. 849 -860.

Zatman, R.E., and Doe, B.R., 1981. Plumbotectonics – the model: Tectonophysics, v. 75, pp. 135 - 162.

Zhao, K.D., Jiang, S.Y., Ni, P., Ling, H.F., and Y.-H. Jiang., 2006. Sulfur, lead and helium isotopic compositions of sulfide minerals from the Dachang Sn-polymetallic ore district in South China: implication for ore genesis. Mineralogy and Petrology (2006), Doi: 10.1007/s00710-006-0148-2.

APPENDIX A

METHODS OF STUDY

A1. Fieldwork

Lithologic logs were completed from field observations to place all samples into geological context. A global positioning System device (GPS) was used to record latitude and longitude of each sample. In this study, coordinate systems are in UTM (Universal Transverse Mercator), zone 47, northern hemisphere (Map datum-WGS 84), latitude-longitude (Map datum-Kertau 1948) system. If UTM and RSO systems were used, the coordinates were shown as northing and easting, typically in meters.

A2. Laboratory methods

The laboratory studies include U-Pb zircon dating, petrographic analysis, whole-rock geochemistry and Laser Ablation Inductively Coupled Plasma Mass-Spectrometry (ICP-MS) on pyrite (Large et al., 2009; Danyushevsky et al., 2011). The details of each method are provided below.

A2.1. U-Pb zircon dating

The following procedure was applied for U-Pb dating. Approximately 100 g of rock was repeatedly sieved and crushed in a Cr-steel ring mill to a grain size <400 micron. Non-magnetic heavy minerals were then separated using a gold pan and a Fe-B-Nd hand magnet. The zircons were handpicked from the heavy mineral concentrate under the microscope in cross-polarised transmitted light. The selected crystals were placed on double sided sticky tape and epoxy glue was then poured into a 2.5 cm diameter mould on top of the zircons. The mount was dried for 12 hours and polished using clean sandpaper and a clean polishing lap. The samples were then washed in distilled water in an ultrasonic bath. The standard procedure for the Laser ICP-MS zircon dating is performed on an Agilent 7500cs quadrupole ICPMS with a 193 nm Coherent Ar-F gas laser and the Resonetics M50 ablation cell at

CODES, University of Tasmania. The downhole fractionation, instrument drift and mass bias correction factors for Pb/U ratios on zircons were calculated using two analyses on the primary (91500 standard of Wiendenbeck et al. 1995) and one analysis on each of the secondary standard zircons (Temora standard of Black et al., 2003 and Jackson et al., 2004) analysed at the beginning of the session and every 12 unknown zircons (roughly every 1/2 hour) using the same spot size and conditions as used on the samples. Additional secondary standards (The Mud Tank Zircon of Black and Gulson 1978) were also analysed. The correction factor for the $^{207}Pb/^{206}Pb$ ratio was calculated using 3 large spot of NIST610 analysed at the beginning and end of the day and corrected using the values recommended by Baker et al. (2004). Each analysis on the zircons began with a 30 second blank gas measurement followed by a further 30 seconds of analysis time when the laser was switched on. Zircons were sampled on 32 micron spots using the laser at 5 Hz and a density of approximately 1.5 J/cm^2. A flow of He carrier gas at a rate of 0.6 litres/minute carried particles ablated by the laser out of the chamber to be mixed with Ar gas and carried to the plasma torch. Elements measured include ^{49}Ti, ^{96}Zr, ^{146}Nd, ^{178}Hf, ^{202}Hg, ^{204}Pb, ^{206}Pb, ^{207}Pb, ^{208}Pb, ^{232}Th and ^{238}U with each element being measured sequentially every 0.16 s with longer counting time on the Pb isotopes compared to the other elements. The data reduction used was based on the method outlined in detail in Meffre et al. (2008) similar to that outlined in Black et al. (2004) and Paton et al. (2010). Element abundances on zircons were calculated using the method outlined by Kosler (2001) using Zr as the internal standard element, assuming stoichiometric proportions and using the 91500 to standard correct for mass bias.

The interpretation of the U-Pb detrital zircon was based on considering the approach of the work of Amato and Pavlis (2010).

A2.2. Whole-rock geochemical analysis (XRF)

Fresh and weakly weathered outcrop samples were analysed by X-ray fluorescence analysis to obtain the whole rock major and trace element composition. The instrument used for this analysis is PANalytical Axios Advanced X-Ray Spectrometer. It is equipped with X-Ray Tubes of 4KW maximum and a Rh anode end window. The element that are routinely analysed are: F, Na, Mg, Al, Si, P, S, K, Ca, Ti, Mn, Fe and trace elements Sc, V, Cr, Co, Ni, Cu, Zn, Ga, Ge, As, Se, Br, Rb, Sr, Y, Zr, Nb, Mo, Ag, Cd, Sn, Sb, Te, I, Ba, La, Ce, Nd, W, Tl, Pb, Bi, Th and U. The instrument also has the following parts: Crystals: PX-10, LiF 220, PX-1 (for F, Na and Mg), curved PE002, and curved Ge111. The collimators are coarse (0.7mm), fine (0.3mm) with high resolution (0.15mm). The detectors are Gas flow proportional counters with P10 gas (10% methane argon), a sealed Xe Duplex and Scintillation Counter. The sample changer is PANalytical X-Y sample changer with capacity for 96 fusion discs and 64 pills.

In sample preparation for the major elements, 32mm fusion discs were prepared at 1100 degrees C in 5%Au/95%Pt crucibles 0.500g sample, 4.500g 12-22 Flux (Lithium Tetraborate-Metaborate mix), 0.0606g LiNO3 for silicates. Platinum/5% gold moulds were used for cooling. Sulphide bearing samples had a different mix with more LiNO3 as oxidising agent and the mix is pre-ignited at 700 degrees C for 10 minutes. Ore samples and ironstones used 12/22 flux and a higher flux/sample ratio. Dolomites and limestones needed pure lithium tetraborate as a flux. Iodine vapour was used as a releasing agent to remove discs from the mould. For the trace elements, 32mm diameter pressed powder pills (10g, 3.5 tons/cm-2) were used and a sample Binder PVP-MC. Corrections for mass absorption were calculated using PANalytical Super-Q software with its Classic calibration model and alpha coefficients. In house inter-element corrections were also applied. Calibration was done on

pure element oxide mixed in pure silica, along with International and Tasmanian reference rocks.

A2.3. Laser ablation ICP-MS (LA ICP-MS)

Trace element geochemistry on pyrite grains was undertaken using the Laser ablation ICP-MS facility at CODES, University of Tasmania, Australia. Analyses were done using a Newwave UP213 laser ablation microprobe coupled with an Agilent 7500 or 7700 ICP-MS. Samples were ablated in He and mixed with Ar before reaching the ICP-MS. Calibration was carried out with the in-house standard (STDGL2b2), which is a lithium borate fused glass disk, with known concentrations of trace elements (Danyvshevsky et al., 2011). The standard was analysed at regular intervals to correct for drift and mass bias. To minimize surface contamination, sulphides were pre-ablated with laser pulses.

The background gas levels were monitored for 30 s before analysis. The laser shutter was then opened and the sulphides were ablated for about 60-70 s at a firing rate of 5 Hz with laser energy of 3.5 J/cm^2. The spot sizes used were 10, 15, 20 and 50 µm depending on the size of the pyrite grains. The backgrounds were recorded before each image and subtracted from each analysis line (Large et al., 2009). Three standards STGDL2b2, GSD-1G, and PERU Pyrite were set up at the beginning and the end of each set of analysis (Danyvshevsky et al., 2011). Fe was used as the internal standard (465x10^{3}ppm). The elements that are analysed by spot analyses include Na, C, Mg, Al, Si, S, K, Ca, Ti, V, Cr, Mn, Fe, Co, Ni, Cu, Zn, As, Se, Rb, Sr, Zr, Mo, Ag, Cd, Sn, Sb, Te, Ba, Gd, Hf, Ta, W, Pt, Au, Hg, Tl, Pb, Th, Bi, and U. Trace element map was made and comprised of the following elements Ti, V, Cr, Mn, Fe, Co, Ni, Cu, Zn, As, Mo, Ag, Sb, Au, Tl, Pb, and Bi. The technique of LA-ICPMS pyrite mapping is as follows: (1) Firstly, the trace element maps were converted from count per second into part per millions (ppm) in order to get a robust representation of element

concentration for each pyrite type; (2) Secondly, the csv files were imported into ioGAS which is an advanced geochemical exploratory data analysis software package; (3) Thirdly, each pyrite types for each gold deposit were classified and examined in x and y coordinates for visualization and presentation; (4) Fourthly, statistical analysis of all trace elements within each pyrite type were exported into excel for data processing (e.g. Makoundi et al., 2013).

A2.4. Determination of total organic carbon (TOC)

The procedure of total carbon determination is done in two stages. Firstly, samples are crushed and milled using a tungsten-carbide mil. One half (about 10g) of the samples is then weighted with a crucible. The samples and crucible are left in an oven overnight to be ashed in a heat up to 450°C. The combustion of the sample is used to remove the organic carbon component and preserve the inorganic carbon component as tested by Krom and Berner (1983). Secondly, the unashed half is processed separately by measuring the total carbon which makes up the organic and inorganic carbon (calcium carbonate) contents in a given sample. Finally, the Total organic carbon is calculated as the difference between total carbon and inorganic carbon (Riquier et al., 2005).

A2.5. Sulphur isotope analysis

Selected samples from sedimentary rocks were analysed by the conventional method at the Central Science Laboratory (CSL), University of Tasmania. Results of this analysis were combined with those of previous data from the Penjom deposit (Khin Zaw et al., 2008). For the conventional technique, sulphides such as pyrite, galena and arsenopyrite from the Tersang and Selinsing deposits were drilled out of the samples using a dentist's drill to

produce a powdered sample of about 10-25 mg. The powdered sulphide samples were submitted to the Central Science Laboratory for analysis. The isotopic compositions for S^{34}/S^{32} were obtained by combustion with cuprous oxide method (Robinson and Kasakabe, 1975). The Canon Diablo Troilite (CDT) international standard was used to monitor the raw sulphur isotopic data. An accuracy of ± 0.15 ‰ is obtained by the conventional method at the CSL.

A2.6. Lead Isotope Analysis

Analyses were conducted at the University of Tasmania using LA ICP-MS method on feldspar and pyrite from sedimentary rocks and granites. The analyses were performed on an Agilent 4500 ICPMS coupled to a New Wave 213 nm solid state laser in a custom made, low volume (3.4 cm^3), barrel-shaped chamber in a He atmosphere. The laser was operated at 5 or 10 Hz using spot sizes between 15 and 110 μm. Data were collected in time-resolved mode with 30s gas blank measurement followed by 60s analysis time typically drilling at around ~1 μm s−1. Data deconvolution was performed using custom made excel-based spreadsheets.

A2.7. Organic carbon isotope determination

NCS combustion, to analyse $\delta^{13}C$ and $\delta^{34}S$, is a capability of the vario MICRO, ISOTOPE and PYRO cubes. The vario PYRO cube has the following setup for NCS mode: two packed reactor tubes (combustion and reduction), two 'purge and trap' desorption columns (for SO_2 and CO_2) and an inlet for both the sample and reference gas to enter the IsoPrime100 IRMS. After combustion the bulk sample gas passes through the system and columns and is stripped of H_2O, in the water traps, as well as SO_2 and CO_2, in the 'Purge and Trap' Columns. The N_2 component gas is not trapped in a column and is the first to enter the IRMS. After the N_2 reference and sample peaks have been collected the CO_2 desorption column is heated to

110°C and the CO_2 sample gas is released, passing through a second water trap and into the IRMS. The final gas to be released is SO_2 which occurs when the desorption column is heated to 220°C, this sample gas then bypasses the CO_2 column (where it could potentially be retained), passes through a second water trap and enters the IRMS. The dilutor can be used to lower the gas loads entering the IRMS source. This 'Purge and Trap' technique of gas release on the vario PYRO is superior to standard GC separation methods, on other EA systems, and allows user control over timing, without peak broadening due to slow release times between different gas species.

APPENDIX B

U-Pb ZIRCON DATING DATA AND LA ICP-MS GOLD DATA

SEDIMENTARY ROCKS

Machinchang Formation	207 cor 206Pb/ 238U age	+/-1 ster	206Pb/ 238U ratio	+/-1 RSE	208Pb/ 232Th ratio	+/-1 RSE	207Pb/ 206Pb ratio	+/-1 RSE	Pb204 ppm	Pb206 ppm	Pb207 ppm	Pb208 ppm
LA-3312												
JL01A471	421	9	0.0691	2.2%	0.0230	2.8%	0.0732	5.2%	0.01	15	1	5
JL01A497	425	9	0.0695	2.1%	0.0229	2.6%	0.0708	3.3%	0.04	35	2	16
JL01A495	426	5	0.0688	1.3%	0.0200	2.0%	0.0612	1.2%	0.04	111	7	40
JL01A480	429	9	0.0701	2.0%	0.0271	2.4%	0.0704	3.9%	0.02	13	1	3
JL01A487	430	9	0.0694	2.1%	0.0231	2.6%	0.0598	3.8%	0.00	19	1	5
JL01A490	438	11	0.0711	2.5%	0.0241	2.6%	0.0643	4.6%	0.03	17	1	7
JL01A482	446	5	0.0728	1.1%	0.0223	1.5%	0.0689	1.3%	0.05	74	5	19
JL01A481	450	7	0.0729	1.7%	0.0250	2.4%	0.0624	3.5%	0.01	15	1	5
JL01A496	453	9	0.0752	1.9%	0.0282	6.7%	0.0820	4.1%	0.00	22	2	11
JL01A479	456	7	0.0737	1.5%	0.0231	1.5%	0.0595	2.4%	0.03	27	2	11
JL01A473	465	6	0.0750	1.4%	0.0238	1.7%	0.0585	2.3%	0.01	44	3	18
JL01A486	474	6	0.0762	1.3%	0.0230	1.5%	0.0566	2.0%	0.00	29	2	10
JL01A492	594	8	0.0965	1.4%	0.0291	2.0%	0.0590	2.4%	0.00	23	1	10
JL01A491	645	12	0.1063	1.8%	0.0200	2.8%	0.0691	4.6%	0.00	61	4	19
JL01A483	713	7	0.1196	1.1%	0.0313	1.3%	0.0819	0.7%	0.02	266	22	31
JL01A478	723	8	0.1190	1.1%	0.0366	1.6%	0.0661	1.3%	0.03	58	4	11
JL01A474	787	9	0.1309	1.2%	0.0378	1.4%	0.0719	1.2%	0.05	151	11	36
JL01A493	819	12	0.1372	1.4%	0.0482	2.7%	0.0773	3.0%	0.17	106	8	20
JL01A476	912	9	0.1523	1.0%	0.0533	1.8%	0.0707	0.8%	0.00	202	14	21
JL01A494	917	17	0.1552	1.9%	0.0399	2.3%	0.0823	3.0%	0.00	57	5	15
JL01A477	976	74	0.1663	7.8%	0.0323	4.6%	0.0853	4.1%	0.00	32	3	2
JL01A489	987	18	0.1667	1.9%	0.0486	2.1%	0.0782	2.2%	0.00	58	5	25
JL01A484	1020	11	0.1731	1.1%	0.0346	2.8%	0.0817	1.3%	0.02	189	15	7
JL01A488	1047	18	0.1813	1.8%	0.0769	2.1%	0.0969	1.8%	0.04	79	8	18
JL01A485	1166	16	0.2024	1.4%	0.0601	1.7%	0.0959	1.6%	0.00	54	5	17
JL01A472	1769	27	0.3286	1.5%	0.0918	2.8%	0.1422	1.6%	0.00	288	41	24
JL01A475	1873	26	0.3427	1.4%	0.0874	1.5%	0.1289	1.1%	0.04	159	20	28

Machinchang Formation

	Th232 ppm	U238 ppm	Ti49 ppm	Fe56 ppm	Hf178 ppm	238U/206Pb ratio	+/-1 std err	207Pb/ 206Pb ratio	+/-1 std err	common Pb at age of zirc	206Pb/ 238U age	208Pb/ 232Th age
JL01A471	234	246	59	44	11561	14.47	0.33	0.0732	0.0038	0.865	431	460
JL01A497	801	530	70	154	12238	14.38	0.30	0.0708	0.0024	0.865	433	458
JL01A495	1835	1517	19	666	13172	14.53	0.19	0.0612	0.0008	0.865	429	401
JL01A480	123	180	10	139	11510	14.27	0.29	0.0704	0.0027	0.865	437	540
JL01A487	222	283	9	23	12570	14.41	0.30	0.0598	0.0023	0.865	432	461
JL01A490	291	252	48	32	10339	14.07	0.35	0.0643	0.0029	0.866	443	481
JL01A482	814	1018	33	236	11534	13.74	0.16	0.0689	0.0009	0.866	453	445
JL01A481	181	214	7	66	10522	13.72	0.23	0.0624	0.0022	0.866	453	499
JL01A496	401	296	92	1289	10831	13.30	0.25	0.0820	0.0034	0.867	467	561
JL01A479	454	363	17	74	11049	13.57	0.20	0.0595	0.0014	0.867	458	461
JL01A473	766	613	40	26	12354	13.34	0.18	0.0585	0.0013	0.867	466	475
JL01A486	417	372	11	14	10857	13.12	0.17	0.0566	0.0012	0.868	474	459
JL01A492	344	238	2	3	11344	10.36	0.14	0.0590	0.0014	0.877	594	579
JL01A491	951	542	77	218	12761	9.41	0.17	0.0691	0.0032	0.881	651	400
JL01A483	970	2213	58	2446	16714	8.36	0.09	0.0819	0.0005	0.887	729	623
JL01A478	307	489	21	23	12584	8.40	0.10	0.0661	0.0008	0.887	725	726
JL01A474	948	1190	103	636	11746	7.64	0.09	0.0719	0.0009	0.892	793	750
JL01A493	371	716	626	179	13319	7.29	0.10	0.0773	0.0023	0.895	829	951
JL01A476	403	1327	6	401	14353	6.57	0.07	0.0707	0.0006	0.902	914	1049
JL01A494	398	394	14	66	11854	6.44	0.12	0.0823	0.0025	0.903	930	790
JL01A477	80	204	30	71	13887	6.01	0.47	0.0853	0.0035	0.908	991	643
JL01A489	553	365	5	55	10905	6.00	0.11	0.0782	0.0017	0.908	994	958
JL01A484	212	1076	11	241	22477	5.78	0.07	0.0817	0.0011	0.911	1029	688
JL01A488	241	485	61	1343	13270	5.52	0.10	0.0969	0.0017	0.915	1074	1497
JL01A485	276	262	9	62	11144	4.94	0.07	0.0959	0.0015	0.925	1188	1179
JL01A472	225	821	9	182	12287	3.04	0.05	0.1422	0.0022	0.985	1832	1776
JL01A475	336	495	57	187	11181	2.92	0.04	0.1289	0.0014	0.992	1899	1694

Machinchang Formation

		207Pb/206Pb		Hg202	Pb204	Pb206	Pb207	Pb208	Th232	U238	Ti49	Fe56	Zr90	Hf178
	+/-1 ster	age	+/-1 ster											
JL01A471	13	1020	53	89	6	7830	574	2589	106428	118846	255	4010	71967403	2341055
JL01A497	12	953	34	0	14	12024	808	5364	240955	169131	201	9213	47709237	1643133
JL01A495	8	646	13	0	16	49102	2965	17166	720656	631672	72	51921	62248599	2307586
JL01A480	13	940	40	6	9	6220	419	1578	53943	83967	40	12117	69502982	2251102
JL01A487	12	598	41	70	0	8935	525	2354	94393	127519	36	1911	67317936	2381170
JL01A490	13	753	48	47	14	7219	449	2774	109562	100924	172	2387	59713343	1737334
JL01A482	7	895	13	39	22	35509	2433	8734	346326	459345	134	19849	67283459	2183764
JL01A481	12	689	38	7	3	7109	433	2040	74701	93356	29	5413	65126903	1928228
JL01A496	38	1245	40	34	0	5433	441	2711	88565	69347	193	56518	35049703	1068329
JL01A479	7	585	26	19	13	11677	678	4664	175536	149135	63	5668	61199024	1902628
JL01A473	8	548	25	39	6	24332	1414	9618	380990	323390	187	2521	78531442	2729788
JL01A486	7	474	23	39	0	14668	820	4984	189014	178776	47	1229	71784163	2193242
JL01A492	12	566	26	30	1	12244	709	5285	165750	121356	10	320	76320271	2436527
JL01A491	11	903	48	32	0	28676	1981	8840	394781	238621	305	17941	65801150	2363028
JL01A483	8	1244	6	89	8	124515	10084	14299	403688	976544	228	201657	65831147	3096188
JL01A478	11	809	13	0	17	30478	1997	5793	143350	242308	91	2099	73805839	2613487
JL01A474	10	983	13	0	23	72642	5133	16668	404892	539358	419	53754	67462920	2229633
JL01A493	25	1129	30	22	26	16529	1259	3065	51290	105029	823	4904	21923998	821752
JL01A476	19	950	8	65	0	104927	7324	10772	186188	650130	25	36675	72973722	2947035
JL01A494	18	1252	29	29	0	21091	1700	5560	131443	137748	43	4325	52295566	1744589
JL01A477	29	1322	40	103	0	14034	1147	1058	31028	84307	110	5469	61624626	2408017
JL01A489	20	1152	22	82	0	13792	1070	5935	117467	82326	9	2317	33653527	1032712
JL01A484	19	1239	13	13	9	75015	6032	2840	74744	401955	38	16838	55750310	3526214
JL01A488	31	1566	16	0	18	37077	3585	8169	100741	214607	241	111158	66104134	2468556
JL01A485	21	1545	15	50	0	26912	2548	8300	122404	123326	37	5417	70105663	2198449
JL01A472	49	2254	14	0	0	107071	15071	8689	74274	288092	28	11896	52245679	1806165
JL01A475	26	2083	10	0	22	82849	10523	14482	156007	244298	253	17235	73426551	2309996

Setul	207 cor 206Pb/238U		206Pb/238U		208Pb/232Th		207Pb/206Pb		Pb204	Pb206	Pb207	Pb208
Formation	age	+/-1 ster	ratio	+/-1 RSE	ratio	+/-1 RSE	ratio	+/-1 RSE	ppm	ppm	ppm	ppm
LA-4612												
JL01A507	219	15	0.0363	6.8%	0.0158	7.3%	0.0883	12.8%	0.00	3	0	1
JL01A500	452	7	0.0732	1.6%	0.0213	1.7%	0.0618	3.2%	0.00	45	3	20
JL01A526	461	11	0.0746	2.4%	0.0194	3.5%	0.0610	3.6%	0.08	33	2	4
JL01A520	466	8	0.0785	1.7%	0.0237	1.1%	0.0932	3.1%				
JL01A513	501	6	0.0809	1.2%	0.0238	2.4%	0.0585	1.4%	0.00	104	6	5
JL01A512	511	12	0.0832	2.4%	0.0192	2.6%	0.0649	1.1%	0.00	101	7	9
JL01A521	515	6	0.0831	1.2%	0.0228	2.2%	0.0575	1.1%	0.00	114	7	4
JL01A508	518	6	0.0839	1.2%	0.0242	1.4%	0.0600	1.7%	0.00	48	3	17
JL01A503	533	9	0.0861	1.7%	0.0253	1.7%	0.0577	3.1%	0.05	21	1	8
JL01A519	537	6	0.0869	1.2%	0.0257	1.4%	0.0577	1.6%	0.00	43	3	17
JL01A522	550	16	0.0906	2.9%	0.0297	3.2%	0.0728	5.7%	0.00	6	0	1
JL01A509	558	8	0.0905	1.4%	0.0269	1.8%	0.0602	1.6%	0.00	106	6	16
JL01A506	562	7	0.0913	1.3%	0.0269	2.1%	0.0617	2.3%	0.00	27	2	5
JL01A524	565	9	0.0919	1.7%	0.0281	2.6%	0.0612	3.4%	0.00	15	1	2
JL01A502	579	8	0.0942	1.5%	0.0295	2.4%	0.0617	2.1%	0.00	32	2	3
JL01A504	616	10	0.1003	1.6%	0.0285	3.3%	0.0605	3.5%	0.01	13	1	1
JL01A517	627	7	0.1021	1.2%	0.0311	1.8%	0.0608	2.0%	0.00	47	3	6
JL01A514	760	10	0.1252	1.4%	0.0365	1.6%	0.0657	2.7%	0.00	126	8	48
JL01A515	781	9	0.1287	1.2%	0.0369	1.7%	0.0635	1.5%	0.01	55	3	6
JL01A523	801	21	0.1338	2.6%	0.0480	3.7%	0.0749	5.1%	0.00	11	1	3
JL01A511	862	11	0.1431	1.3%	0.0391	1.5%	0.0669	2.7%	0.00	18	1	9
JL01A501	867	9	0.1440	1.0%	0.0446	2.5%	0.0676	0.9%	0.02	162	11	2
JL01A518	893	11	0.1500	1.3%	0.0483	2.0%	0.0765	1.8%	0.05	32	2	5
JL01A525	920	11	0.1544	1.3%	0.0365	2.8%	0.0755	1.2%	0.02	134	10	12
JL01A510	982	13	0.1651	1.3%	0.0464	1.8%	0.0746	1.7%	0.00	172	13	28
JL01A516	1204	34	0.2129	3.0%	0.0710	2.6%	0.1104	2.1%	0.03	41	5	5
JL01A505	1792	26	0.3459	1.5%	0.0922	2.8%	0.1743	0.8%	0.02	248	43	18

Setul Formation (continued)

	Th232	U238	Ti49	Fe56	Hf178	238U/206Pb		207Pb/206Pb		common Pb	206Pb/238U	208Pb/232Th
	ppm	ppm	ppm	ppm	ppm	ratio	+/-1 std err	ratio	+/-1 std err	at age of zirc	age	age
LA-4612												
JL01A507	54	99	92	137	8381	27.58	1.86	0.0883	0.0113	0.851	230	316
JL01A500	849	573	18	101	12274	13.67	0.21	0.0618	0.0020	0.866	455	426
JL01A526	196	410	31	108	12398	13.40	0.33	0.0610	0.0022	0.867	464	389
JL01A520						12.73	0.22	0.0932	0.0029	0.869	487	474
JL01A513	213	1380	19	195	13224	12.36	0.15	0.0585	0.0008	0.870	502	476
JL01A512	470	1263	48	263	14201	12.02	0.29	0.0649	0.0007	0.871	515	385
JL01A521	175	1366	18	109	13812	12.03	0.15	0.0575	0.0007	0.871	515	456
JL01A508	691	583	7	229	13107	11.91	0.15	0.0600	0.0010	0.871	520	483
JL01A503	313	248	14	8	9414	11.61	0.20	0.0577	0.0018	0.872	533	505
JL01A519	628	488	7	25	10940	11.51	0.13	0.0577	0.0009	0.872	537	514
JL01A522	48	68	22	14	10819	11.03	0.32	0.0728	0.0041	0.874	559	591
JL01A509	619	1292	18	587	15437	11.05	0.16	0.0602	0.0010	0.874	559	536
JL01A506	167	297	25	61	13507	10.95	0.14	0.0617	0.0014	0.874	563	538
JL01A524	58	166	13	3	11396	10.88	0.18	0.0612	0.0021	0.875	567	560
JL01A502	94	352	6	14	12701	10.61	0.16	0.0617	0.0013	0.876	580	588
JL01A504	47	127	6	7	11306	9.97	0.16	0.0605	0.0021	0.878	616	568
JL01A517	188	463	5	21	11576	9.79	0.12	0.0608	0.0012	0.879	627	619
JL01A514	1127	929	13	125	11041	7.98	0.11	0.0657	0.0018	0.889	761	725
JL01A515	158	435	3	22	14479	7.77	0.09	0.0635	0.0010	0.891	781	732
JL01A523	77	90	0	9	12893	7.48	0.20	0.0749	0.0038	0.893	809	948
JL01A511	222	127	6	1	10761	6.99	0.09	0.0669	0.0018	0.897	862	775
JL01A501	36	1120	5	185	15659	6.95	0.07	0.0676	0.0006	0.898	867	883
JL01A518	96	211	23	497	11670	6.67	0.09	0.0765	0.0014	0.901	901	953
JL01A525	334	894	61	1365	13056	6.47	0.08	0.0755	0.0009	0.903	926	725
JL01A510	629	1160	48	119	13829	6.06	0.08	0.0746	0.0013	0.907	985	917
JL01A516	70	185	36	570	12021	4.70	0.14	0.1104	0.0023	0.930	1244	1387
JL01A505	203	763	17	172	13440	2.89	0.04	0.1743	0.0014	0.993	1915	1783

Setul Formation (continued)

		207Pb/206Pb		Hg202	Pb204	Pb206	Pb207	Pb208	Th232	U238	Ti49	Fe56	Zr90	Hf178
	+/-1 ster	age	+/-1 ster											
LA-4612														
JL01A507	23	1389	123	15	1	870	71	271	14065	27038	227	7025	41074824	968902
JL01A500	7	666	34	59	0	15652	943	6858	261477	187068	54	6170	48858333	1687682
JL01A526	14	638	39	32	28	11612	676	1458	61097	135228	93	6678	49582819	1730484
JL01A520	5	1493	29	111	21	7641	687	312326	11982313	95434	150	44323	69	296
JL01A513	11	549	15	95	0	64402	3748	2983	116002	798144	99	21147	86746598	3228909
JL01A512	10	771	12	65	0	48637	3127	4013	199029	566888	194	22131	67299721	2690145
JL01A521	10	512	13	25	0	55569	3158	1949	74774	620076	74	9334	68205643	2651826
JL01A508	7	604	19	42	2	25764	1516	8753	326196	291715	33	21448	75039717	2768407
JL01A503	9	517	34	20	23	10293	588	3819	135295	113496	56	705	68637071	1818529
JL01A519	7	517	18	78	0	21740	1243	8363	279190	229658	28	2183	70754670	2178979
JL01A522	19	1008	57	100	0	2767	197	635	19650	29284	87	1125	65198433	1985641
JL01A509	9	611	18	46	0	66446	3969	9805	341206	754985	92	64305	87630965	3807553
JL01A506	11	665	25	36	0	15101	914	2492	82961	156681	121	6011	78977714	3002457
JL01A524	15	646	36	25	0	7794	464	831	26600	80426	56	314	73039532	2343126
JL01A502	14	663	23	74	0	18238	1113	1527	47130	186970	30	1434	79502330	2842017
JL01A504	19	622	38	4	3	6935	412	720	22650	65078	29	703	76975695	2449391
JL01A517	11	633	21	25	2	25950	1550	3206	92238	240927	25	2037	78197021	2547938
JL01A514	12	796	29	199	0	47068	3083	17436	372640	325661	42	8242	52604744	1634777
JL01A515	13	725	16	9	5	27810	1736	3048	70494	205543	14	1987	70938395	2891058
JL01A523	35	1066	52	54	2	6482	487	1962	39502	49325	0	938	81942698	2974079
JL01A511	12	835	28	38	2	9089	600	4401	97120	58912	23	63	69514930	2105478
JL01A501	22	856	9	22	9	79885	5342	793	15696	517098	19	15957	69093210	3044945
JL01A518	19	1107	18	16	25	15553	1172	2269	41168	96304	96	42633	68558011	2252002
JL01A525	20	1081	12	60	10	63413	4704	5348	138826	394044	244	113069	66293590	2436534
JL01A510	16	1057	17	64	0	72470	5321	11355	233784	456907	170	8762	59069066	2299267
JL01A516	37	1806	19	21	9	14636	1594	1794	22061	61744	108	35690	50072050	1694350
JL01A505	49	2599	7	36	9	102907	17789	7259	74404	297197	59	12563	58336117	2206640

Singa Formation	207 cor 206Pb/ 238U		206Pb/ 238U		208Pb/ 232Th		207Pb/ 206Pb		Pb204	Pb206	Pb207	Pb208
LA-3412	age	+/-1 ster	ratio	+/-1 RSE	ratio	+/-1 RSE	ratio	+/-1 RSE	ppm	ppm	ppm	ppm
JL01A561	413	5	0.0667	1.2%	0.0121	1.9%	0.0616	1.7%	0.00	96	6	11
JL01A574	423	6	0.0686	1.4%	0.0191	2.1%	0.0642	1.9%	0.05	53	3	11
JL01A575	425	11	0.0687	2.6%	0.0223	2.4%	0.0608	4.8%	0.00	9	1	4
JL01A580	426	10	0.0688	2.4%	0.0145	3.0%	0.0620	1.9%	0.00	118	7	19
JL01A567	457	11	0.0751	2.3%	0.0264	2.0%	0.0733	3.9%	0.02	43	3	29
JL01A578	463	11	0.0753	2.3%	0.0106	5.5%	0.0646	6.4%	0.00	29	2	2
JL01A573	463	7	0.0755	1.5%	0.0227	2.0%	0.0670	2.3%	0.04	66	4	14
JL01A564	471	12	0.0776	2.6%	0.0187	5.0%	0.0748	4.7%	0.00	104	8	12
JL01A582	516	11	0.0846	2.1%	0.0242	3.1%	0.0705	5.6%	0.01	12	1	8
JL01A565	576	14	0.0961	2.4%	0.0195	2.9%	0.0819	3.9%	0.02	25	2	6
JL01A570	637	10	0.1049	1.7%	0.0296	2.5%	0.0686	3.4%	0.00	40	3	8
JL01A581	703	12	0.1180	1.7%	0.0294	3.8%	0.0824	2.2%	0.10	42	3	4
JL01A577	703	8	0.1178	1.1%	0.0340	1.9%	0.0811	1.0%	0.00	89	7	11
JL01A576	704	9	0.1160	1.3%	0.0339	2.0%	0.0666	1.9%	0.05	63	4	10
JL01A571	706	10	0.1178	1.4%	0.0184	5.5%	0.0772	1.7%	0.00	62	5	8
JL01A563	714	12	0.1173	1.6%	0.0335	1.8%	0.0649	2.9%	0.00	26	2	8
JL01A566	717	15	0.1195	2.1%	0.0358	2.6%	0.0764	3.1%	0.03	54	4	19
JL01A584	742	11	0.1243	1.5%	0.0227	3.2%	0.0793	2.7%	0.01	82	7	9
JL01A572	1612	18	0.2935	1.1%	0.0582	2.8%	0.1275	1.0%	0.11	174	22	6
JL01A583	1857	20	0.3340	1.1%	0.0869	1.4%	0.1140	0.7%	0.00	150	17	13
JL01A568	2062	49	0.3959	2.3%	0.0533	6.3%	0.1699	1.8%	0.01	39	7	2
JL01A562	2295	31	0.4340	1.3%	0.1359	1.8%	0.1586	1.3%	0.00	214	34	42
JL01A579	692	27	0.1154	4.0%	0.0239	7.7%	0.0768	5.2%	0.13	57	4	7
JL01A569	598	8	0.1038	1.4%	0.0270	1.8%	0.1119	1.4%	0.39	161	18	25

Singa Formation	Th232	U238	Ti49	Fe56	Hf178	238U/206Pb		207Pb/206Pb		common Pb	206Pb/238U	208Pb/232Th
LA-3412	ppm	ppm	ppm	ppm	ppm	ratio	+/-1 std err	ratio	+/-1 std err	at age of zirc	age	age
JL01A561	895	1502	69	1216	14044	14.99	0.18	0.0616	0.0010	0.864	416	243
JL01A574	599	817	71	2035	10281	14.58	0.21	0.0642	0.0012	0.865	428	382
JL01A575	172	132	15	265	8861	14.56	0.37	0.0608	0.0029	0.865	428	445
JL01A580	1392	1854	251	5918	11316	14.53	0.35	0.0620	0.0012	0.865	429	290
JL01A567	1195	617	74	4166	11694	13.32	0.31	0.0733	0.0029	0.867	467	526
JL01A578	209	433	27	581	11795	13.28	0.31	0.0646	0.0041	0.867	468	213
JL01A573	646	936	37	799	10459	13.24	0.20	0.0670	0.0015	0.868	469	454
JL01A564	624	1308	44	6536	12514	12.89	0.34	0.0748	0.0035	0.868	482	375
JL01A582	327	157	21	596	9949	11.82	0.25	0.0705	0.0039	0.871	524	484
JL01A565	331	262	43	885	11879	10.40	0.25	0.0819	0.0032	0.877	592	390
JL01A570	272	398	17	733	11269	9.53	0.16	0.0686	0.0023	0.880	643	589
JL01A581	154	383	220	13832	11587	8.48	0.14	0.0824	0.0018	0.886	719	586
JL01A577	305	752	79	1518	13749	8.49	0.10	0.0811	0.0008	0.886	718	676
JL01A576	285	539	15	321	11966	8.62	0.11	0.0666	0.0013	0.885	707	674
JL01A571	589	536	49	9386	10096	8.49	0.12	0.0772	0.0013	0.886	718	368
JL01A563	256	234	24	628	13581	8.52	0.14	0.0649	0.0019	0.886	715	667
JL01A566	566	496	96	2235	12145	8.37	0.18	0.0764	0.0024	0.887	728	710
JL01A584	409	748	142	999	13226	8.04	0.12	0.0793	0.0022	0.889	755	454
JL01A572	92	559	18	643	13594	3.41	0.04	0.1275	0.0013	0.968	1659	1143
JL01A583	142	455	8	127	10958	2.99	0.03	0.1140	0.0009	0.988	1858	1684
JL01A568	36	105	9	596	11049	2.53	0.06	0.1699	0.0031	1.018	2150	1050
JL01A562	314	513	133	1576	12913	2.30	0.03	0.1586	0.0020	1.036	2324	2575
JL01A579	380	575	35	1327	12535	8.67	0.34	0.0768	0.0040	0.885	704	477
JL01A569	952	1698	165	6511	14067	9.63	0.14	0.1119	0.0016	0.880	637	539

Singa Formation

LA-3412	+/-1 ster	207Pb/206Pb age	+/-1 ster	Hg202	Pb204	Pb206	Pb207	Pb208	Th232	U238	Ti49	Fe56	Zr90	Hf178
JL01A561	5	662	18	156	0	37743	2292	4087	306151	543436	226	83144	54804118	2167358
JL01A574	8	749	20	21	23	25068	1595	4980	245372	354174	279	167126	65826995	1906083
JL01A575	11	633	52	74	0	3337	201	1397	56096	45718	45	17329	52425518	1308320
JL01A580	9	674	20	67	0	46418	2869	7375	477436	672619	826	407019	55156754	1757949
JL01A567	11	1021	40	80	6	10871	756	7160	262766	143583	157	183431	35290376	1162172
JL01A578	12	760	67	123	0	12761	809	910	79635	174728	99	44459	61362058	2038453
JL01A573	9	836	24	71	16	30807	1995	6445	263103	403451	144	65200	65439404	1927520
JL01A564	19	1064	47	164	0	8863	652	976	46619	103385	32	97723	11980746	422215
JL01A582	15	944	57	29	7	6932	500	4360	167699	85314	103	61430	82594635	2314486
JL01A565	11	1242	38	45	5	6170	496	1562	71576	59977	90	38333	34718136	1161387
JL01A570	15	887	35	140	0	13433	883	2565	80146	124060	49	43299	47341670	1502448
JL01A581	22	1256	21	0	44	18622	1505	1836	59378	156568	816	1071407	62116222	2027254
JL01A577	13	1225	10	59	0	44667	3561	5178	132907	347210	331	132702	70095668	2714334
JL01A576	13	824	20	12	25	31507	2067	4837	123992	248013	63	27949	69838998	2353547
JL01A571	20	1125	17	58	1	33492	2540	4211	275276	264861	219	878223	75000607	2132464
JL01A563	12	772	30	52	0	12454	802	3945	107667	104197	96	52979	67559901	2583780
JL01A566	19	1105	31	72	18	29691	2273	10305	272471	252895	444	215415	77240330	2641700
JL01A584	15	1179	27	46	7	52495	4154	5315	228175	440949	761	111711	89690211	3341223
JL01A572	32	2064	9	9	44	68287	8599	2228	31585	202380	58	44087	54951210	2103785
JL01A583	24	1864	7	17	0	74232	8345	6173	61231	207306	32	11010	69274108	2138117
JL01A568	67	2557	15	36	8	22767	3758	950	18250	56455	44	60812	81720305	2542753
JL01A562	47	2441	11	172	0	34355	5397	6523	44104	76263	180	44297	22516097	818739
JL01A579	37	1115	52	128	23	10730	802	1228	61901	99256	54	43388	26216193	925534
JL01A569	10	1830	13	34	121	50389	5547	7579	260090	490652	432	356065	43836466	1736668

BRSZ Unit 1

BE-3213	207 cor 206Pb/238U age	+/-1 ster	206Pb/238U ratio	+/-1 RSE	208Pb/232Th ratio	+/-1 RSE	207Pb/206Pb ratio	+/-1 RSE	Pb204 ppm	Pb206 ppm	Pb207 ppm	Pb208 ppm
JA22A085	299.5	3.627872	0.047778	0.012266	0.012666	0.015196	0.055999	0.011509	0.017451	122.2551	6.834055	19.1971
JA22A089	364.7	4.735205	0.058576	0.013013	0.014847	0.019889	0.058978	0.031246	0.009133	41.5556	2.448453	7.452242
JA22A082	366.9	5.141204	0.059241	0.01415	0.018126	0.017789	0.06302	0.022441	0.007998	31.63975	2.008687	8.98301
JA22A086	372.0	5.539818	0.059582	0.01511	0.01795	0.016487	0.056419	0.017654	1.47E-07	46.32164	2.62297	9.34459
JA22A091	684.4	11.95146	0.113838	0.017916	0.026505	0.017674	0.07552	0.01629	1.26E-07	84.50244	6.369132	26.31413
JA22A080	794.7	10.78832	0.132787	0.013988	0.028701	0.017884	0.075489	0.01014	0.014285	84.16506	6.348588	12.44236
JA22A079	901.7	11.54788	0.150529	0.013212	0.045826	0.01747	0.071317	0.012869	0.010336	41.2573	2.945791	6.124712
JA22A083	922.2	11.45357	0.154311	0.012815	0.037236	0.029721	0.072615	0.012625	0.007401	103.0983	7.481802	2.164487
JA22A084	995.2	15.493	0.17274	0.016094	0.030595	0.02506	0.100505	0.009518	0.05881	153.0436	15.3701	11.84385
JA22A088	999.2	18.59839	0.169629	0.019234	0.039615	0.026033	0.082172	0.015976	0.004731	77.24914	6.345609	12.11774
JA22A087	1061.3	13.52599	0.179271	0.013156	0.05032	0.016502	0.076192	0.014708	0.007111	101.8005	7.887931	15.32076
JA22A090	1590.1	20.60503	0.281463	0.01332	0.075367	0.016472	0.103461	0.009422	0.006472	129.8979	13.38086	19.315
JA22A081	2440.4	48.33164	0.461173	0.018569	0.132757	0.018963	0.160447	0.012678	9.8E-08	24.67292	3.951791	7.441494

BRSZ Unit 1

	Th232	U238	Ti49	Fe56	Hf178	238U/206 Pb		207Pb/20 6Pb		Common Pb	206Pb/238U	208Pb/232Th
BE-3213	ppm	ppm	ppm	ppm	ppm	ratio	+/-1 std err	ratio	+/-1 std err	at age of zirc	age	age
JA22A085	1628.555	2710.973	75.64355	970.1446	12856.82	20.93016	0.256722849	0.055999	0.00064452	0.855605324	300.864931	254.4062135
JA22A089	480.7405	686.922	55.02404	707.5988	11266.39	17.07174	0.222149058	0.058978	0.0018428	0.86021573	366.961648	297.8797589
JA22A082	478.1482	515.9756	23.67429	184.9419	7480.934	16.88022	0.238856826	0.06302	0.00141423	0.86050059	371.007537	363.0885552
JA22A086	511.8451	756.341	9.135923	55.73283	11664.89	16.7837	0.253604543	0.056419	0.00099601	0.860646663	373.080538	359.6006119
JA22A091	1102.177	846.333	20.80605	300.5801	11596.97	8.784384	0.157384322	0.07552	0.0012302	0.88433377	695.001102	528.7473955
JA22A080	473.0635	685.919	353.2337	277.5376	12901.93	7.53086	0.105344624	0.075489	0.00076549	0.892798993	803.744954	571.945361
JA22A079	135.5923	278.003	65.47298	236.242	8179.966	6.643217	0.087770352	0.071317	0.0009178	0.900811932	903.930689	905.6400886
JA22A083	65.23247	732.3856	12.95127	982.6821	14986.08	6.48042	0.083048667	0.072615	0.00091674	0.902530301	925.083697	738.949183
JA22A084	362.0525	857.9739	24.81515	1400.058	12028.3	5.789041	0.093169467	0.100505	0.00095665	0.9109564	1027.19133	609.1268736
JA22A088	349.6592	510.9636	189.803	152.9093	14819.53	5.895221	0.113388578	0.082172	0.00131282	0.909527963	1010.06631	785.2603906
JA22A087	342.5814	639.444	10.02098	45.15978	11738.52	5.578151	0.073388185	0.076192	0.00112063	0.913962406	1062.99011	992.3184396
JA22A090	278.0977	493.5167	5.784687	54.49022	9920.103	3.552867	0.047325586	0.103461	0.00097484	0.962194411	1598.72533	1468.654706
JA22A081	59.59942	55.33327	19.60085	9.19822	8024.435	2.168386	0.040264619	0.160447	0.00203419	1.049488154	2444.73303	2519.553072

		207Pb/20 6Pb		Hg202	Pb204	Pb206	Pb207	Pb208	Th232	U238	Ti49	Fe56	Hf178
BE-3213	+/-1 ster	age	+/-1 ster										
JA22A085	3.866052	452.3383	12.77695	34.28245	15.57962	110265.642	6120.08	17203.87	1442787	2603244	600.9881	162225.3	4668483
JA22A089	5.924573	566.2715	34.01737	70.17034	6.645293	30548.9301	1787.279	5442.995	347222.7	537877.4	356.6987	96481.15	3334624
JA22A082	6.459048	708.919	23.85898	25.98585	6.153956	24590.9458	1550.024	6937.548	364966.7	426818.6	161.9547	26641.06	2340699
JA22A086	5.928906	468.9085	19.5419	94.81541	0.0001	31812.2412	1788.613	6376.462	345304.1	553086.3	55.28396	7097.01	3225274
JA22A091	9.345251	1082.376	16.33657	64.75176	0.0001	67874.558	5080.033	20998.82	869905.5	724243.9	147.4487	44789.56	3750561
JA22A080	10.2287	1081.558	10.17085	48.28307	14.56279	86671.4152	6490.692	12732.25	478365.7	751609.9	3199.995	52960.23	5348511
JA22A079	15.82173	966.5084	13.13496	37.4703	9.170633	36973.0913	2620.895	5454.277	119313.8	265070.8	516.0295	39226.64	2950961
JA22A083	21.96198	1003.239	12.81285	0.0001	7.778274	109463.383	7887.053	2283.526	68023	827708.2	121.0653	193396.8	6405610
JA22A084	15.26462	1633.446	8.841951	0.0001	44.72213	117572.625	11723.74	9040.854	273189	701670.9	167.8855	199389	3720120
JA22A088	20.44259	1249.614	15.6356	76.41532	5.070055	83644.3151	6822.494	13036.38	371956.9	589242.4	1811.812	30705.81	6460499
JA22A087	16.37556	1100.13	14.71126	0.0001	7.802055	112839.225	8681.466	16872.96	373037.7	754789.1	97.89762	9282.413	5238482
JA22A090	24.1921	1687.123	8.692801	13.89657	6.532202	132469.788	13550.02	19569.76	278656.4	536134.8	52.03463	10307.82	4073185
JA22A081	47.77763	2460.373	10.7131	50.12188	0.0001	25429.7269	4043.823	7621.341	60323.39	60691.97	177.7685	1756.928	3329489

Karak	207 cor 206Pb/ 238U		206Pb/ 238U		208Pb/ 232Th		207Pb/ 206Pb		Pb204	Pb206	Pb207	Pb208
Formation	age	+/-1 ster	ratio	+/-1 RSE	ratio	+/-1 RSE	ratio	+/-1 RSE	ppm	ppm	ppm	ppm
ME-7213												
JL01A364	232	4	0.0370	1.7%	0.0116	3.1%	0.0582	3.9%	0.06	24	1	3
JL01A347	232	3	0.0369	1.3%	0.0112	1.8%	0.0571	2.5%	0.01	42	2	8
JL01A357	234	4	0.0370	1.6%	0.0123	6.0%	0.0539	3.5%	0.02	35	2	9
JL01A346	234	6	0.0631	2.0%	0.0109	1.2%	0.3864	1.8%				
JL01A363	235	4	0.0373	1.7%	0.0112	2.1%	0.0525	2.8%	0.00	31	2	5
JL01A355	235	3	0.0373	1.3%	0.0115	2.3%	0.0531	2.6%	0.00	70	4	11
JL01A358	237	5	0.0376	2.0%	0.0115	4.0%	0.0541	4.8%	0.01	9	0	1
JL01A371	239	3	0.0378	1.4%	0.0120	2.1%	0.0515	2.8%	0.00	23	1	4
JL01A367	244	7	0.0387	2.7%	0.0115	3.5%	0.0518	8.5%	0.00	7	0	2
JL01A345	246	3	0.0389	1.3%	0.0122	1.5%	0.0523	2.2%	0.02	33	2	9
JL01A343	256	5	0.0405	1.9%	0.0131	3.0%	0.0515	4.2%	0.00	9	0	2
JL01A369	256	5	0.0405	2.0%	0.0129	2.6%	0.0518	4.3%	0.00	7	0	2
JL01A356	258	5	0.0412	2.1%	0.0129	2.8%	0.0580	4.5%	0.01	20	1	3
JL01A366	317	4	0.0504	1.3%	0.0158	1.4%	0.0531	1.6%	0.03	66	4	15
JL01A360	327	5	0.0522	1.6%	0.0157	2.0%	0.0570	2.8%	0.01	53	3	10
JL01A359	349	6	0.0560	1.7%	0.0179	2.1%	0.0592	3.2%	0.00	16	1	5
JL01A368	353	5	0.0564	1.3%	0.0181	1.9%	0.0539	2.9%	0.01	31	2	6
JL01A349	356	9	0.0573	2.6%	0.0178	3.2%	0.0607	5.4%	0.00	9	1	3
JL01A370	362	6	0.0581	1.7%	0.0184	2.1%	0.0587	1.6%	0.00	85	5	13
JL01A350	377	5	0.0602	1.3%	0.0172	2.0%	0.0538	2.4%	0.01	22	1	3
JL01A348	431	5	0.0694	1.2%	0.0213	1.4%	0.0580	1.5%	0.02	64	4	13
JL01A352	470	6	0.0758	1.3%	0.0236	2.0%	0.0586	2.1%	0.00	38	2	6
JL01A353	479	6	0.0773	1.2%	0.0256	1.5%	0.0580	2.0%	0.00	93	5	22
JL01A354	520	7	0.0839	1.4%	0.0267	1.7%	0.0574	2.7%	0.00	17	1	6
JL01A344	869	10	0.1450	1.2%	0.0486	1.8%	0.0713	1.6%	0.01	97	7	14
JL01A365	894	12	0.1499	1.4%	0.0452	1.8%	0.0754	2.1%	0.00	57	4	10
JL01A361	948	10	0.1640	1.1%	0.0424	1.3%	0.0992	0.6%	0.00	319	32	34
JL01A362	960	12	0.1643	1.3%	0.0515	1.6%	0.0897	1.3%	0.01	141	13	41
JL01A351	1504	18	0.2630	1.2%	0.0738	1.9%	0.0947	1.4%	0.00	249	24	40
JL01A342	2411	31	0.4563	1.2%	0.1237	1.7%	0.1614	0.9%	0.02	177	29	16

Karak Formation

	Th232	U238	Ti49	Fe56	Hf178	238U/206Pb	+/-1 std err	207Pb/206Pb	+/-1 std err	common Pb at age of zirc	206Pb/238U	208Pb/232Th
	ppm	ppm	ppm	ppm	ppm	ratio		ratio			age	age
JL01A364	274	639	7	26	13012	27.06	0.45	0.0582	0.0022	0.851	234	234
JL01A347	712	1043	11	66	11255	27.08	0.35	0.0571	0.0014	0.851	234	224
JL01A357	673	867	57	80	11805	27.00	0.43	0.0539	0.0019	0.851	234	246
JL01A346						15.84	0.32	0.3864	0.0069	0.862	395	219
JL01A363	454	795	8	33	10673	26.84	0.44	0.0525	0.0015	0.851	236	225
JL01A355	947	1986	55	40	11765	26.82	0.36	0.0531	0.0014	0.851	236	232
JL01A358	94	217	1	7	10786	26.59	0.53	0.0541	0.0026	0.851	238	232
JL01A371	295	560	4	3	9058	26.46	0.37	0.0515	0.0015	0.851	239	241
JL01A367	200	182	18	33	8081	25.85	0.69	0.0518	0.0044	0.852	245	231
JL01A345	684	810	7	11	10010	25.70	0.33	0.0523	0.0011	0.852	246	245
JL01A343	128	202	6	0	9145	24.72	0.46	0.0515	0.0022	0.852	256	263
JL01A369	119	173	12	0	10633	24.70	0.51	0.0518	0.0022	0.853	256	258
JL01A356	277	498	5	275	10256	24.29	0.50	0.0580	0.0026	0.853	260	259
JL01A366	943	1271	214	47	11892	19.83	0.25	0.0531	0.0008	0.857	317	316
JL01A360	698	1062	17	73	10510	19.15	0.30	0.0570	0.0016	0.857	328	314
JL01A359	275	280	22	19	9801	17.87	0.30	0.0592	0.0019	0.859	351	358
JL01A368	334	526	9	14	10204	17.74	0.24	0.0539	0.0016	0.859	353	362
JL01A349	165	167	7	0	10654	17.46	0.45	0.0607	0.0033	0.860	359	357
JL01A370	746	1539	32	232	14132	17.22	0.29	0.0587	0.0009	0.860	364	368
JL01A350	173	359	16	6	11168	16.62	0.21	0.0538	0.0013	0.861	377	345
JL01A348	608	909	16	64	11545	14.41	0.18	0.0580	0.0009	0.865	433	426
JL01A352	246	465	5	27	11368	13.20	0.18	0.0586	0.0013	0.868	471	471
JL01A353	836	1154	20	37	9951	12.94	0.16	0.0580	0.0012	0.868	480	511
JL01A354	223	191	11	5	11987	11.91	0.17	0.0574	0.0016	0.871	520	532
JL01A344	255	610	8	78	13217	6.90	0.08	0.0713	0.0012	0.898	873	960
JL01A365	222	395	10	42	9760	6.67	0.09	0.0754	0.0016	0.901	900	893
JL01A361	780	1884	84	937	12738	6.10	0.07	0.0992	0.0006	0.907	979	839
JL01A362	812	884	105	635	12320	6.09	0.08	0.0897	0.0012	0.907	980	1016
JL01A351	481	855	250	3883	12363	3.80	0.05	0.0947	0.0013	0.953	1505	1440
JL01A342	130	374	17	59	11536	2.19	0.03	0.1614	0.0014	1.047	2423	2358

Karak Formation

		207Pb/206Pb		Hg202	Pb204	Pb206	Pb207	Pb208	Th232	U238	Ti49	Fe56	Zr90	Hf178
	+/-1 ster	age	+/-1 ster											
JL01A364	7	539	42	34	20	7942	458	1032	83569	207576	20	1543	47374685	1732620
JL01A347	4	496	28	68	5	17827	1026	3592	279303	435503	41	5036	60664685	1918787
JL01A357	15	365	40	49	6	10465	557	2535	185336	253992	146	4295	42646572	1414967
JL01A346	3	3857	13	51	120	5689	2195	267691	21986297	84879	282	21935	961	96
JL01A363	5	306	32	61	0	11218	587	1892	150241	279979	24	2159	51315899	1539512
JL01A355	5	332	30	77	0	44123	2348	6510	543302	1213031	295	4481	88889225	2939157
JL01A358	9	375	54	39	6	3807	199	472	38191	93694	4	552	62915943	1907361
JL01A371	5	265	33	95	0	9998	509	1624	115644	233844	14	246	60956687	1552030
JL01A367	8	276	97	38	3	4081	209	1407	109776	105994	92	3513	84994467	1930635
JL01A345	4	299	25	16	10	16576	862	4285	318523	401715	30	996	72035546	2026437
JL01A343	8	261	48	40	0	4174	208	850	57508	96594	24	0	69366487	1782772
JL01A369	7	275	49	12	0	3573	179	762	53580	82849	49	0	69693099	2083085
JL01A356	7	529	50	39	5	12288	692	2120	156666	300133	27	30420	87750361	2529358
JL01A366	4	332	18	32	16	31095	1642	7019	405196	580843	863	3915	66675078	2228790
JL01A360	6	491	31	82	4	26413	1491	5097	316006	512011	74	6450	70212305	2074006
JL01A359	7	573	35	18	0	9098	527	2757	145095	157520	110	1983	81935229	2257007
JL01A368	7	368	33	26	5	14825	791	2867	143751	240873	35	1178	66771337	1915059
JL01A349	11	628	59	9	0	5590	329	1726	92389	99681	38	0	86537457	2591201
JL01A370	8	556	17	204	0	45467	2616	6946	361987	794570	147	22022	75354233	2993443
JL01A350	7	363	27	0	5	11115	599	1527	79061	174625	70	577	70654648	2217645
JL01A348	6	530	16	0	11	33137	1889	6670	288819	459257	73	5963	73464166	2383528
JL01A352	9	551	23	1138	0	15553	905	2490	91749	185130	16	1942	57860165	1848637
JL01A353	8	528	22	43	0	48886	2849	11408	401855	589941	91	3432	74409542	2080937
JL01A354	9	507	30	17	0	8363	475	3050	101578	92767	47	467	70577943	2377831
JL01A344	18	967	17	10	4	43845	3092	6019	105161	267991	31	6234	63762607	2368347
JL01A365	16	1079	21	8	0	33575	2506	5605	118212	223748	50	4353	82690310	2268501
JL01A361	11	1609	6	56	0	160347	15795	16815	357246	917703	359	83708	70982662	2541356
JL01A362	16	1419	13	90	4	73755	6514	20951	386546	447681	470	58970	73811555	2555967
JL01A351	28	1522	13	86	0	95628	8991	15301	168616	319164	819	265552	54308664	1886943
JL01A342	40	2470	7	71	9	91968	14710	8381	61748	188576	78	5404	73269059	2375296

Semantan	207 cor 206Pb/238U		206Pb/238U		208Pb/232Th		207Pb/206Pb		Pb204	Pb206	Pb207	Pb208
Formation	age	+/-1 ster	ratio	+/-1 RSE	ratio	+/-1 RSE	ratio	+/-1 RSE	ppm	ppm	ppm	ppm
ME-10813												
JA31A146	228	4	0.0362	1.7%	0.0116	2.4%	0.0552	3.1%	0.01	11	1	2
JA31A143	229	5	0.0363	2.1%	0.0103	3.0%	0.0546	4.9%	0.02	10	1	2
JA31A144	230	4	0.0366	1.8%	0.0120	3.1%	0.0585	3.6%	0.04	11	1	2
JA31A139	232	4	0.0369	1.6%	0.0119	2.8%	0.0557	3.5%	0.00	11	1	1
JA31A140	239	4	0.0381	1.8%	0.0117	3.0%	0.0552	4.1%	0.04	15	1	2
JA31A142	255	3	0.0404	1.3%	0.0123	1.8%	0.0515	2.0%	0.00	35	2	7
JA31A145	306	10	0.0494	3.2%	0.0130	4.8%	0.0651	5.6%	0.03	18	1	3
JA31A148	330	5	0.0528	1.4%	0.0150	2.5%	0.0576	2.6%	0.00	24	1	3
JA31A147	788	33	0.1329	4.3%	0.0388	2.6%	0.0829	1.5%	0.00	95	8	8
JA31A141	1145	19	0.1947	1.7%	0.0563	2.1%	0.0794	2.7%	0.00	24	2	6
JA31A138	1572	24	0.2797	1.5%	0.0766	2.2%	0.1082	1.4%	0.00	58	6	7

Semantan	Th232	U238	Ti49	Fe56	Hf178	238U/206Pb		207Pb/206Pb		Common Pb	206Pb/238U	208Pb/232Th
Formation	ppm	ppm	ppm	ppm	ppm	ratio	+/-1 std err	ratio	+/-1 std err	at age of zirc	age	age
ME-10813												
JA31A146	175	296	8	335	9429	27.59	0.47	0.0552	0.0017	0.851	230	232
JA31A143	193	278	17	1369	10005	27.55	0.57	0.0546	0.0027	0.851	230	208
JA31A144	119	284	10	1875	10644	27.32	0.50	0.0585	0.0021	0.851	232	240
JA31A139	114	292	9	3	9066	27.13	0.45	0.0557	0.0020	0.851	233	240
JA31A140	156	370	30	766	10492	26.28	0.46	0.0552	0.0023	0.851	241	234
JA31A142	533	851	2	912	11319	24.76	0.32	0.0515	0.0010	0.852	255	246
JA31A145	231	363	11	549	10861	20.26	0.65	0.0651	0.0037	0.856	311	261
JA31A148	165	428	17	67	10366	18.94	0.27	0.0576	0.0015	0.858	332	301
JA31A147	207	749	16	601	11105	7.53	0.32	0.0829	0.0012	0.893	804	770
JA31A141	116	128	11	32	10340	5.14	0.09	0.0794	0.0022	0.921	1147	1108
JA31A138	82	195	13	54	9767	3.58	0.05	0.1082	0.0015	0.961	1590	1493

Semantan		207Pb/206Pb		Hg202	Pb204	Pb206	Pb207	Pb208	Th232	U238	Ti49	Fe56	Zr90	Hf178
Formation	+/-1 ster	age	+/-1 ster											
ME-10813														
JA31A146	6	421	35	64	3	5716	309	1111	90915	164572	35	31229	83030591	2010209
JA31A143	6	396	55	15	13	5528	298	1125	107683	166042	81	137622	89338024	2293622
JA31A144	7	550	40	21	18	5483	317	775	60090	153458	43	170563	80867758	2209169
JA31A139	7	441	39	50	0	5669	308	743	58165	159997	40	305	82040741	1906795
JA31A140	7	420	46	0	20	6897	363	910	70402	178658	116	62369	72287282	1944757
JA31A142	4	262	23	18	0	17468	877	3452	263738	450682	9	81443	79352788	2304336
JA31A145	12	777	59	6	7	4044	257	689	50296	84637	21	21560	34913414	973438
JA31A148	8	514	28	40	0	11977	679	1348	82576	229052	71	5991	79901352	2127767
JA31A147	20	1266	15	365	0	35196	2872	3063	74931	290880	48	39205	58064584	1656016
JA31A141	24	1183	27	56	0	13798	1082	3723	66360	78962	52	3290	92137931	2443573
JA31A138	33	1769	13	75	0	28092	2989	3280	38809	99292	52	4679	76446426	1913695

Semantan	207 cor 206Pb/238U		206Pb/238U		208Pb/232Th		207Pb/206Pb		Pb204	Pb206	Pb207	Pb208
Formation	age	+/-1 ster	ratio	+/-1 RSE	ratio	+/-1 RSE	ratio	+/-1 RSE	ppm	ppm	ppm	ppm
ME-6512												
NO14A017	230	2	0.0363	1.0%	0.0136	4.2%	0.0507	1.6%	0.00	37	2	1
NO14A015	230	2	0.0365	1.0%	0.0114	1.3%	0.0527	1.2%	0.00	48	3	12
NO14A018	231	2	0.0366	1.1%	0.0111	1.9%	0.0542	1.5%	0.02	21	1	3
NO14A012	232	3	0.0366	1.2%	0.0113	1.3%	0.0506	1.9%	0.01	51	3	19
NO14A016	233	3	0.0368	1.1%	0.0119	1.7%	0.0517	2.0%	0.01	16	1	2
NO14A020	233	14	0.0516	5.7%	0.0586	7.5%	0.2821	4.3%	0.95	52	16	40
NO14A024	233	3	0.0369	1.3%	0.0120	2.4%	0.0507	2.8%	0.01	16	1	2
NO14A023	235	2	0.0371	1.0%	0.0116	1.5%	0.0517	1.3%	0.00	37	2	5
NO14A014	236	3	0.0374	1.4%	0.0114	2.2%	0.0524	2.9%	0.00	21	1	3
NO14A022	238	3	0.0376	1.3%	0.0120	1.7%	0.0527	2.4%	0.01	24	1	4
NO14A011	237	3	0.0374	1.3%	0.0124	2.0%	0.0511	2.2%	0.02	23	1	4
NO14A021	243	3	0.0383	1.2%	0.0121	1.8%	0.0490	1.8%	0.00	16	1	2
NO14A013	243	4	0.0386	1.8%	0.0123	2.5%	0.0549	3.7%	0.00	9	1	2
NO14A019	292	4	0.0464	1.5%	0.0144	3.2%	0.0533	4.2%	0.00	7	0	1
NO14A010	564	6	0.0919	1.1%	0.0299	1.7%	0.0629	1.6%	0.00	26	2	5

Semantan	Th232	U238	Ti49	Fe56	Hf178	238U/206Pb		207Pb/206Pb		Common Pb	206Pb/238U	208Pb/232Th
Formation	ppm	ppm	ppm	ppm	ppm	ratio	+/-1 std err	ratio	+/-1 std err	at age of zirc	age	age
ME-6512												
NO14A017	48	1074	4	5	13344	27.56	0.29	0.0507	0.0008	0.851	230	272
NO14A015	1100	1332	12	28	10198	27.41	0.27	0.0527	0.0007	0.851	231	228
NO14A018	253	568	34	36	11289	27.29	0.29	0.0542	0.0008	0.851	232	222
NO14A012	1763	1504	8	7	12077	27.30	0.32	0.0506	0.0010	0.851	232	228
NO14A016	193	430	12	0	9867	27.18	0.31	0.0517	0.0011	0.851	233	238
NO14A020	1104	1162	7987	3881	11434	19.37	1.10	0.2821	0.0122	0.857	324	1151
NO14A024	138	467	3	8	12369	27.13	0.36	0.0507	0.0014	0.851	233	241
NO14A023	409	1011	5	4	12041	26.94	0.27	0.0517	0.0007	0.851	235	232
NO14A014	275	605	9	1	9890	26.74	0.37	0.0524	0.0015	0.851	237	230
NO14A022	376	697	6	0	11865	26.56	0.34	0.0527	0.0013	0.851	238	240
NO14A011	316	641	11	1	9762	26.70	0.33	0.0511	0.0011	0.851	237	248
NO14A021	170	435	9	0	10347	26.10	0.30	0.0490	0.0009	0.852	242	243
NO14A013	163	262	7	0	10729	25.88	0.46	0.0549	0.0020	0.852	244	246
NO14A019	63	151	13	37	9973	21.57	0.33	0.0533	0.0023	0.855	292	289
NO14A010	171	291	25	772	10993	10.88	0.12	0.0629	0.0010	0.875	567	596

Semantan		207Pb/206Pb		Hg202	Pb204	Pb206	Pb207	Pb208	Th232	U238	Ti49	Fe56	Zr90	Hf178
Formation	+/-1 ster	age	+/-1 ster											
ME-6512														
NO14A017	11	227	38	0	0	36284	1880	611	52402	1253885	24	692	129798885	5006753
NO14A015	3	315	28	44	0	40594	2186	10598	1040283	1348329	61	3153	112360898	3314985
NO14A018	4	379	35	0	15	18981	1044	2591	256151	615614	179	4310	120627164	3934758
NO14A012	3	223	44	0	10	51827	2679	19298	1998628	1823489	48	907	134423930	4702347
NO14A016	4	270	47	0	9	13521	715	1986	185890	442845	60	7	114299457	3261407
NO14A020	86	3375	68	105	783	42745	13229	33890	1010013	1136479	38379	418777	108911250	3595272
NO14A024	6	226	65	21	7	15775	819	1532	146641	532331	18	981	127157561	4533642
NO14A023	3	271	30	15	0	32546	1700	4204	397045	1049465	24	460	115732356	4018246
NO14A014	5	302	67	12	4	21844	1179	3114	318415	748942	55	152	137255779	3928959
NO14A022	4	316	54	0	12	24036	1292	4248	414933	821222	36	6	131341582	4495417
NO14A011	5	245	51	0	18	22219	1159	3620	341378	739966	60	133	127914716	3618453
NO14A021	4	149	43	24	0	14649	729	1844	167775	460400	45	0	117820591	3518193
NO14A013	6	407	82	44	0	9557	530	1935	182086	313279	42	0	132424721	4113613
NO14A019	9	342	96	33	4	6324	338	826	61354	157429	65	4205	116311216	3350429
NO14A010	10	704	35	43	3	22724	1424	4350	166173	302122	123	87391	114808114	3658611

Gua Musang	207 cor 206Pb/238U		206Pb/238U		208Pb/232Th		207Pb/206Pb		Pb204	Pb206	Pb207	Pb208
Formation	age	+/-1 ster	ratio	+/-1 RSE	ratio	+/-1 RSE	ratio	+/-1 RSE	ppm	ppm	ppm	ppm
GM-1112												
JL01A394	210	10	0.0344	4.5%	0.0113	7.9%	0.0809	9.5%	0.00	6	0	1
JL01A388	223	8	0.0364	3.4%	0.0137	4.8%	0.0763	7.8%	0.02	8	1	2
JL01A402	225	4	0.0358	2.0%	0.0122	3.1%	0.0572	4.9%	0.00	10	1	1
JL01A401	225	5	0.0362	2.1%	0.0123	2.9%	0.0652	4.5%	0.00	9	1	1
JL01A404	225	4	0.0359	1.7%	0.0115	2.3%	0.0568	3.8%	0.04	24	1	5
JL01A377	230	4	0.0364	1.8%	0.0114	3.1%	0.0514	4.4%	0.00	6	0	1
JL01A396	232	4	0.0368	1.7%	0.0123	2.2%	0.0557	3.1%	0.03	16	1	3
JL01A381	233	5	0.0370	2.0%	0.0129	2.6%	0.0574	2.7%	0.00	34	2	4
JL01A398	233	4	0.0375	1.8%	0.0129	2.8%	0.0662	4.0%	0.02	12	1	3
JL01A391	234	5	0.0375	2.2%	0.0125	2.1%	0.0611	3.3%	0.03	14	1	5
JL01A386	234	3	0.0371	1.4%	0.0116	2.0%	0.0532	3.0%	0.01	16	1	4
JL01A375	235	3	0.0374	1.3%	0.0123	1.7%	0.0567	1.9%	0.00	44	2	8
JL01A379	235	4	0.0372	1.6%	0.0120	1.6%	0.0524	3.0%	0.00	20	1	6
JL01A395	235	7	0.0376	3.0%	0.0123	5.6%	0.0605	6.5%	0.00	6	0	1
JL01A384	238	3	0.0376	1.3%	0.0121	2.2%	0.0506	3.0%	0.00	20	1	4
JL01A376	241	3	0.0381	1.2%	0.0125	1.8%	0.0520	3.0%	0.00	36	2	8
JL01A393	243	3	0.0385	1.4%	0.0121	2.2%	0.0516	2.7%	0.00	21	1	3
JL01A392	254	4	0.0402	1.7%	0.0121	4.2%	0.0515	3.7%	0.03	11	1	0
JL01A380	262	3	0.0416	1.3%	0.0131	1.8%	0.0534	2.0%	0.02	49	3	9
JL01A389	266	4	0.0423	1.4%	0.0136	2.3%	0.0534	2.5%	0.00	17	1	3
JL01A397	269	3	0.0427	1.1%	0.0133	2.1%	0.0529	1.6%	0.00	51	3	3
JL01A390	275	3	0.0437	1.2%	0.0142	1.9%	0.0532	2.0%	0.00	32	2	4
JL01A378	306	3	0.0491	1.1%	0.0170	1.9%	0.0602	1.8%	0.01	78	5	12
JL01A385	328	4	0.0524	1.4%	0.0167	1.9%	0.0558	2.5%	0.00	18	1	3
JL01A387	350	5	0.0560	1.4%	0.0175	2.0%	0.0562	2.2%	0.00	73	4	10
JL01A403	390	16	0.0678	3.9%	0.0377	5.3%	0.1192	7.7%	0.00	5	1	1
JL01A382	400	7	0.0646	1.8%	0.0205	2.3%	0.0609	3.6%	0.00	11	1	3
JL01A399	1206	12	0.2084	1.0%	0.0509	1.8%	0.0912	0.9%	0.05	342	31	15
JL01A383	1714	23	0.3186	1.3%	0.1084	2.5%	0.1437	1.2%	0.05	173	25	9
JL01A400	535	12	0.0910	2.3%	0.0227	2.0%	0.0983	2.3%	0.22	109	11	31

Gua Musang	Th232	U238	Ti49	Fe56	Hf178	238U/206Pb		207Pb/206Pb		common Pb	206Pb/238U	208Pb/232Th	
Formation	ppm	ppm	ppm	ppm	ppm	ratio	+/-1 std err	ratio	+/-1 std err	at age of zirc	age	age	+/-1 ster
GM-1112													
JL01A394	106	185	11	12	9732	29.10	1.31	0.0809	0.0077	0.850	218	226	18
JL01A388	127	244	16	34	8707	27.50	0.93	0.0763	0.0060	0.851	230	274	13
JL01A402	117	266	9	10	9870	27.97	0.56	0.0572	0.0028	0.851	226	246	8
JL01A401	119	250	8	19	9935	27.64	0.57	0.0652	0.0030	0.851	229	248	7
JL01A404	480	675	25	25	10469	27.89	0.46	0.0568	0.0021	0.851	227	231	5
JL01A377	101	170	10	13	9570	27.50	0.49	0.0514	0.0023	0.851	230	229	7
JL01A396	221	412	6	15	9720	27.14	0.46	0.0557	0.0017	0.851	233	246	5
JL01A381	277	812	27	28	13019	26.99	0.55	0.0574	0.0015	0.851	235	260	7
JL01A398	242	311	28	29	11055	26.65	0.49	0.0662	0.0027	0.851	237	260	7
JL01A391	418	378	58	46	9580	26.68	0.59	0.0611	0.0020	0.851	237	251	5
JL01A386	332	413	16	20	10865	26.94	0.38	0.0532	0.0016	0.851	235	233	5
JL01A375	624	1142	86	29	11240	26.74	0.35	0.0567	0.0011	0.851	237	247	4
JL01A379	524	517	15	16	7190	26.89	0.42	0.0524	0.0016	0.851	235	240	4
JL01A395	67	173	8	22	9339	26.59	0.79	0.0605	0.0039	0.851	238	247	14
JL01A384	304	500	7697	8272	9657	26.59	0.35	0.0506	0.0015	0.851	238	244	5
JL01A376	581	860	14	6	8228	26.22	0.33	0.0520	0.0016	0.852	241	251	4
JL01A393	273	542	5	13	10520	25.97	0.36	0.0516	0.0014	0.852	244	243	5
JL01A392	40	259	3	2	12715	24.89	0.42	0.0515	0.0019	0.852	254	244	10
JL01A380	673	1140	32	7	12342	24.07	0.31	0.0534	0.0011	0.853	262	263	5
JL01A389	241	398	20	307	9275	23.65	0.34	0.0534	0.0013	0.853	267	274	6
JL01A397	236	1142	3	23	13110	23.43	0.27	0.0529	0.0008	0.853	269	267	5
JL01A390	290	698	15	1	11911	22.88	0.28	0.0532	0.0011	0.854	276	284	5
JL01A378	679	1478	8	42	12685	20.36	0.23	0.0602	0.0011	0.856	309	341	6
JL01A385	190	330	45	63	11129	19.08	0.26	0.0558	0.0014	0.858	329	335	6
JL01A387	591	1352	8	64	11905	17.86	0.25	0.0562	0.0012	0.859	351	351	7
JL01A403	38	76	116	16	8626	14.75	0.58	0.1192	0.0092	0.864	423	748	39
JL01A382	135	156	15	7	11110	15.48	0.27	0.0609	0.0022	0.863	403	410	10
JL01A399	290	1568	17	118	12978	4.80	0.05	0.0912	0.0008	0.928	1220	1004	18
JL01A383	73	490	8	81	13004	3.14	0.04	0.1437	0.0017	0.980	1783	2080	53
JL01A400	1412	1260	294	1080	11535	10.99	0.25	0.0983	0.0023	0.874	561	453	9

Gua Musang	207Pb/206Pb		Hg202	Pb204	Pb206	Pb207	Pb208	Th232	U238	Ti49	Fe56	Zr90	Hf178
Formation	age	+/-1 ster											
GM-1112													
JL01A394	1220	93	101	0	1973	142	356	31735	58777	31	681	46544541	1273593
JL01A388	1104	78	35	8	4577	345	899	63219	129012	73	3261	77297019	1892210
JL01A402	499	54	62	0	4146	232	601	45784	110506	32	799	60937562	1691167
JL01A401	782	48	56	0	4817	312	753	56649	127128	37	1821	74557244	2082819
JL01A404	482	42	7	12	8469	464	1837	152808	228306	74	1549	49702826	1463076
JL01A377	261	50	140	1	3060	154	560	43476	77633	40	1075	66672898	1793760
JL01A396	440	34	0	15	7857	427	1357	98315	195117	27	1297	69453522	1898097
JL01A381	507	30	128	0	12967	730	1507	97139	303216	88	1916	54627053	1999307
JL01A398	813	42	34	10	5453	381	1486	98095	134097	105	2307	63187107	1964051
JL01A391	642	36	52	17	7753	464	2764	206571	198899	268	4438	77069172	2075701
JL01A386	337	34	34	5	8104	423	1950	149151	197485	69	1730	69937737	2136373
JL01A375	481	21	135	0	19984	1102	3446	258220	502201	334	2323	64273460	2030729
JL01A379	302	34	77	0	9032	463	2876	214954	225326	59	1313	63749830	1288521
JL01A395	623	70	93	0	2956	174	367	28368	77318	32	1818	65733906	1725929
JL01A384	222	35	64	0	9674	491	1830	135694	237226	32257	722375	69457077	1885769
JL01A376	287	34	51	1	16619	867	3564	246265	388031	54	465	65933691	1525079
JL01A393	269	31	29	0	10547	531	1581	122348	258504	23	1123	69965766	2069369
JL01A392	263	43	0	13	5373	273	238	17998	123887	15	181	70003764	2502576
JL01A380	346	23	108	7	17430	906	3163	215589	388207	95	411	49800078	1727904
JL01A389	346	28	25	1	8848	467	1671	110541	194195	85	27627	71472018	1863753
JL01A397	326	18	46	0	23797	1245	1484	100400	515715	11	1954	66259534	2442376
JL01A390	338	23	63	0	15735	820	2024	130299	333809	64	109	70036694	2345407
JL01A378	611	20	53	5	35809	2140	5402	283741	657109	30	3394	64973421	2316976
JL01A385	445	28	38	1	9098	506	1622	86857	160481	193	5669	71113408	2224967
JL01A387	460	24	155	0	36960	2067	5009	271808	661189	33	5720	71601098	2396400
JL01A403	1944	69	55	1	2611	311	730	18652	40077	541	1533	77531795	1880577
JL01A382	634	39	87	0	4292	256	1161	49278	60593	52	510	56727259	1771783
JL01A399	1451	9	31	12	83573	7569	3647	64100	368309	35	5090	34474275	1258025
JL01A383	2272	10	0	21	73043	10430	3689	27814	198812	30	6055	59427004	2172446
JL01A400	1593	22	114	76	38351	3732	10661	449501	426512	882	67452	49698478	1611947

BRSZ Unit 2	207 cor 206Pb/238U		206Pb/238U		208Pb/232Th		207Pb/206Pb		Pb204	Pb206	Pb207	Pb208
BE-5913	age	+/-1 ster	ratio	+/-1 RSE	ratio	+/-1 RSE	ratio	+/-1 RSE	ppm	ppm	ppm	ppm
JA22A038	203	2.961014	0.032097	0.014679	0.010215	0.01753	0.053353	0.021092	0.022759	34.81955	1.854039	6.978207
JA22A027	209	2.692348	0.033036	0.012994	0.01032	0.015539	0.053622	0.016093	0.001516	66.15228	3.53901	15.47951
JA22A036	209	2.768354	0.033937	0.013342	0.034546	0.022467	0.074292	0.012291	0.131819	87.21819	6.43818	7.444614
JA22A026	222	3.02795	0.035065	0.013743	0.010312	0.025335	0.051196	0.01814	0.031852	43.96695	2.263658	2.268632
JA22A037	226	2.947247	0.035762	0.013123	0.010523	0.017366	0.051075	0.016787	0.002684	40.27844	2.056105	4.704253
JA22A035	371	6.05231	0.059981	0.016505	0.010305	0.019009	0.063111	0.021109	1.73E-07	66.93192	4.269737	6.668526
JA22A032	405	5.031968	0.065136	0.012611	0.020131	0.016472	0.058143	0.015626	0.000581	64.65356	3.780384	10.00383
JA22A034	442	5.706641	0.070946	0.013128	0.022353	0.016793	0.056319	0.019126	0.005116	17.09463	0.960908	4.826285
JA22A033	796	13.03425	0.131802	0.016849	0.034506	0.017642	0.067759	0.017087	1.23E-07	132.3039	8.935536	17.79077
JA22A030	881	11.55055	0.14694	0.013508	0.043428	0.016427	0.070796	0.013957	0.015045	39.28027	2.76696	8.13742
JA22A031	1007	15.02856	0.169819	0.015339	0.051365	0.018238	0.076067	0.022019	9.46E-08	25.32099	1.937965	6.685016
JA22A028	1270	18.85006	0.221565	0.015327	0.057546	0.021005	0.09797	0.01397	0.014154	42.41022	4.148129	10.23933

BRSZ Unit 2	Th232	U238	Ti49	Fe56	Hf178	238U/206Pb		207Pb/206Pb		Common Pb	206Pb/238U	208Pb/232Th
BE-5913	ppm	ppm	ppm	ppm	ppm	ratio	+/-1 std er	ratio	+/-1 std err	at age of	age	age
JA22A038	671.0162	1064.379	6.572986	78.48124	10860.18	31.15567	0.457335	0.053353	0.00112532	0.848971	204	205
JA22A027	1616.421	2150.966	5.781219	17.81795	11857.14	30.26958	0.39333	0.053622	0.00086294	0.849367	210	208
JA22A036	223.5691	2603.157	15.47845	116.1925	14686.22	29.46641	0.393156	0.074292	0.00091311	0.849746	215	686
JA22A026	234.6517	1312.134	5.755784	6.295528	13680.19	28.51806	0.391932	0.051196	0.0009287	0.850222	222	207
JA22A037	475.4629	1184.471	6.771821	11.36437	10184.2	27.96251	0.366956	0.051075	0.00085741	0.850515	227	212
JA22A035	703.6463	1210.613	109.2929	962.5857	13514.28	16.6719	0.275176	0.063111	0.00133223	0.860818	376	207
JA22A032	527.3047	1049.478	20.44093	392.4879	9427.957	15.35255	0.193609	0.058143	0.00090853	0.863033	407	403
JA22A034	214.4802	242.0148	9.128429	1.104454	9834.675	14.0953	0.185047	0.056319	0.00107719	0.865539	442	447
JA22A033	471.8668	970.8774	15.34539	212.1276	11382.48	7.587162	0.127836	0.067759	0.00115779	0.892356	798	686
JA22A030	191.4369	275.369	78.10328	181.2663	12223.01	6.805478	0.091929	0.070796	0.00098806	0.899184	884	859
JA22A031	140.1549	161.3889	4.443597	44.91132	9937.678	5.888626	0.090323	0.076067	0.00167493	0.909615	1011	1012
JA22A028	184.5449	195.2013	15.31812	119.8417	9862.91	4.513355	0.069175	0.09797	0.00136861	0.933669	1290	1131

BRSZ Unit 2		207Pb/206Pb		Hg202	Pb204	Pb206	Pb207	Pb208	Th232	U238	Ti49	Fe56	Hf178
BE-5913	+/-1 ster	age	+/-1 ster										
JA22A038	3.600936	344	23.86449	24.23566	18.89237	29163.17	1540.637	5812.435	550486.8	944181.2	47.88931	12127.44	3659266
JA22A027	3.224685	355	18.17187	101.0414	1.428533	62881.36	3336.956	14636.16	1503998	2162848	47.66234	3121.26	4533431
JA22A036	15.4229	1049	12.38719	11.68808	133.0263	88799.67	6503.14	7538.164	222928.8	2806438	137.0132	21821.45	6015154
JA22A026	5.253287	250	20.87379	0.0001	32.88214	45779.32	2337.966	2349.676	239142.2	1445068	51.96481	1207.884	5729266
JA22A037	3.674151	244	19.33603	58.05959	2.804873	42473.45	2151.062	4933.4	491063.6	1322722	62.10089	2210.734	4320275
JA22A035	3.93898	712	22.43193	45.97917	0.0001	39043.1	2470.931	3868.728	401966.2	747685.2	554.1369	103563.5	3171246
JA22A032	6.635474	535	17.10205	70.60112	0.438568	49207.74	2854.33	7572.845	392960.2	845418.2	135.1155	55079.26	2886448
JA22A034	7.503745	465	21.1865	30.58633	4.8749	16431.56	916.3097	4613.893	201885.2	246272.1	76.24516	195.7842	3802743
JA22A033	12.09706	861	17.72785	0.0001	0.0001	108784.5	7288.688	14548.99	379914.5	845015.5	109.6106	32163.07	3764806
JA22A030	14.11487	952	14.27752	0.0001	14.42669	37994.34	2654.974	7828.876	181285.8	281851.4	655.7577	32321.54	4755716
JA22A031	18.46415	1097	22.0351	125.6662	0.0001	26994.97	2049.595	7088.666	146295.3	182089.4	41.13232	8827.413	4261713
JA22A028	23.75392	1586	13.05723	154.5867	14.95481	45199.58	4385.457	10854.75	192534	220095.2	141.6333	23540.3	4228110

ZIRCON DATING RESULTS FOR IGNEOUS ROCKS

	207 cor 206Pb/238U		206Pb/238U		208Pb/232Th		207Pb/206Pb		Pb204	Pb206	Pb207	Pb208
Granite	age	+/-1 ster	ratio	+/-1 RSE	ratio	+/-1 RSE	ratio	+/-1 RSE	ppm	ppm	ppm	ppm
GM-0113												
JL01A411	193	3	0.0308	1.6%	0.0098	1.8%	0.0622	2.9%	0.07	48	3	21
JL01A419	200	3	0.0374	1.5%	0.0347	3.6%	0.1778	2.7%	0.60	59	11	31
JL01A436	202	4	0.0321	1.9%	0.0101	2.6%	0.0578	4.0%	0.00	34	2	9
JL01A420	202	3	0.0330	1.4%	0.0100	1.8%	0.0782	2.1%	0.07	45	4	13
JL01A415	204	3	0.0344	1.7%	0.0156	2.2%	0.1008	3.1%	0.06	31	3	12
JL01A418	205	3	0.0391	1.2%	0.0275	1.4%	0.1884	1.1%	0.60	65	12	38
JL01A430	208	3	0.0332	1.3%	0.0107	1.4%	0.0614	2.0%	0.03	30	2	12
JL01A421	208	3	0.0332	1.3%	0.0112	1.7%	0.0605	2.3%	0.04	45	3	10
JL01A428	211	3	0.0343	1.2%	0.0160	2.6%	0.0743	2.9%	0.05	46	3	10
JL01A414	215	3	0.0341	1.3%	0.0107	1.6%	0.0533	2.5%	0.00	33	2	11
JL01A410	215	3	0.0345	1.6%	0.0131	2.4%	0.0642	3.9%	0.02	30	2	8
JL01A417	217	5	0.0348	2.1%	0.0124	3.1%	0.0645	4.1%	0.08	32	2	9
JL01A409	218	3	0.0343	1.4%	0.0107	1.8%	0.0504	2.8%	0.00	24	1	7
JL01A413	218	3	0.0360	1.3%	0.0135	1.7%	0.0866	2.5%	0.14	33	3	14
JL01A412	218	4	0.0367	1.7%	0.0161	2.1%	0.0999	2.9%	0.22	33	3	15
JL01A408	221	3	0.0352	1.2%	0.0113	1.4%	0.0584	2.1%	0.01	31	2	12
JL01A429	222	3	0.0369	1.3%	0.0159	2.9%	0.0907	4.0%	0.15	43	4	15
JL01A424	223	3	0.0353	1.2%	0.0109	1.4%	0.0539	2.3%	0.00	32	2	11
JL01A431	224	3	0.0355	1.2%	0.0117	1.4%	0.0546	2.0%	0.02	33	2	13
JL01A425	225	3	0.0356	1.3%	0.0114	1.3%	0.0530	2.2%	0.05	35	2	15
JL01A432	226	3	0.0358	1.4%	0.0114	1.5%	0.0523	2.4%	0.03	23	1	7
JL01A416	228	4	0.0365	2.0%	0.0123	3.3%	0.0610	4.5%	0.00	28	2	9
JL01A426	230	3	0.0366	1.3%	0.0122	1.6%	0.0572	2.6%	0.02	29	2	10
JL01A423	232	7	0.0390	2.8%	0.0204	5.0%	0.0991	4.2%	0.27	66	6	15
JL01A435	232	4	0.0366	1.6%	0.0110	1.7%	0.0500	4.0%	0.00	33	2	11
JL01A434	237	3	0.0380	1.4%	0.0130	1.6%	0.0630	2.3%	0.02	29	2	8
JL01A433	242	3	0.0385	1.3%	0.0123	1.5%	0.0538	2.5%	0.00	34	2	12
JL01A407	250	9	0.0532	3.0%	0.0566	4.8%	0.2590	4.3%	0.22	13	3	9
JL01A427	265	4	0.0419	1.7%	0.0136	1.8%	0.0514	2.6%	0.04	19	1	5
JL01A422	122	2	0.0240	1.4%	0.0182	1.5%	0.2085	1.1%	0.67	67	14	44

Granite	Th232 ppm	U238 ppm	Ti49 ppm	Fe56 ppm	Hf178 ppm	238U/206Pb ratio	+/-1 std err	207Pb/206Pb ratio	+/-1 std err	Common Pb at age of zirc	206Pb/238U age
GM-0113											
JL01A411	1904	1407	14	59	10716	32.44	0.52	0.0622	0.0018	0.848	196
JL01A419	794	1512	16	56	11893	26.73	0.40	0.1778	0.0049	0.851	237
JL01A436	804	969	5	118	12852	31.13	0.58	0.0578	0.0023	0.849	204
JL01A420	1354	1384	19	314	12513	30.28	0.41	0.0782	0.0016	0.849	209
JL01A415	741	908	228	2006	12033	29.11	0.48	0.1008	0.0031	0.850	218
JL01A418	1333	1625	48	95	12040	25.59	0.32	0.1884	0.0022	0.852	247
JL01A430	1092	875	17	58	10957	30.13	0.39	0.0614	0.0012	0.849	211
JL01A421	859	1277	8	9	13072	30.11	0.38	0.0605	0.0014	0.849	211
JL01A428	595	1328	13	0	13326	29.13	0.35	0.0743	0.0022	0.850	218
JL01A414	1032	959	12	1	11366	29.36	0.38	0.0533	0.0013	0.850	216
JL01A410	554	788	18	113	12347	28.94	0.47	0.0642	0.0025	0.850	219
JL01A417	747	981	10	120	12735	28.75	0.60	0.0645	0.0026	0.850	220
JL01A409	696	703	8	7	11372	29.14	0.40	0.0504	0.0014	0.850	218
JL01A413	1008	890	15	98	11088	27.74	0.37	0.0866	0.0022	0.851	228
JL01A412	888	848	20	129	10865	27.23	0.46	0.0999	0.0029	0.851	233
JL01A408	1014	852	14	126	10917	28.44	0.34	0.0584	0.0012	0.850	223
JL01A429	953	1175	17750	2043	12004	27.12	0.34	0.0907	0.0036	0.851	233
JL01A424	950	883	15	24	11115	28.34	0.34	0.0539	0.0012	0.850	224
JL01A431	1085	902	18	7	10794	28.17	0.35	0.0546	0.0011	0.850	225
JL01A425	1299	974	19	9	10197	28.06	0.36	0.0530	0.0012	0.850	226
JL01A432	624	635	16	2	11131	27.97	0.40	0.0523	0.0012	0.851	226
JL01A416	657	683	14	1479	10906	27.37	0.54	0.0610	0.0028	0.851	231
JL01A426	823	780	27	597	10555	27.30	0.34	0.0572	0.0015	0.851	232
JL01A423	655	1538	48	3863	13346	25.67	0.72	0.0991	0.0042	0.852	246
JL01A435	1077	947	14	30	11584	27.29	0.44	0.0500	0.0020	0.851	232
JL01A434	657	773	8	48	12286	26.34	0.37	0.0630	0.0014	0.851	240
JL01A433	947	894	10	88	12003	26.00	0.33	0.0538	0.0013	0.852	243
JL01A407	151	226	52393	49424	11068	18.78	0.56	0.2590	0.0112	0.858	334
JL01A427	334	449	10	6	11388	23.87	0.40	0.0514	0.0013	0.853	265
JL01A422	2462	2799	141	119	12901	41.67	0.58	0.2085	0.0024	0.846	153

Granite	208Pb/232Th age	+/-1 ster	207Pb/206Pb age	+/-1 ster	Hg202	Pb204	Pb206	Pb207	Pb208	Th232	U238	Ti49	Fe56	Zr90	Hf178
GM-0113															
JL01A411	197	4	682	31	0	29	20541	1242	8951	736481	578395	49	4510	60477344	1822381
JL01A419	689	25	2633	23	37	278	27781	5217	14059	334845	677508	63	4675	66017109	2208075
JL01A436	204	5	524	43	31	0	11523	662	3045	243751	312022	13	7038	47577333	1719824
JL01A420	201	4	1153	21	46	34	23251	1788	6666	625480	679419	81	28531	72328484	2545311
JL01A415	313	7	1640	29	96	21	11569	1152	4482	252554	328834	732	134300	53311506	1804041
JL01A418	548	8	2728	9	7	216	23654	4446	13381	435968	564698	149	6133	51201904	1733645
JL01A430	215	3	655	22	3	14	15394	927	6086	501391	427085	75	5263	72034913	2219872
JL01A421	225	4	620	25	32	16	17008	1010	3760	294111	464681	25	613	53622144	1971295
JL01A428	320	8	1049	30	40	27	26012	1906	5279	302060	716178	61	0	79615099	2983868
JL01A414	216	3	342	28	54	0	16381	864	5382	457242	451648	52	76	69330812	2216004
JL01A410	263	6	749	41	76	6	8397	536	2185	139840	211322	42	5577	39442061	1369394
JL01A417	249	8	757	43	19	28	11766	760	3146	243617	340112	32	7693	51046060	1828162
JL01A409	216	4	212	32	35	0	13906	695	4233	366282	392825	37	681	82216313	2629051
JL01A413	271	5	1353	24	0	36	8879	753	3681	244219	229162	34	4641	37894783	1181607
JL01A412	322	7	1622	27	71	33	5180	512	2302	125440	127282	27	3586	22079808	674585
JL01A408	227	3	544	23	23	4	14612	824	5516	432105	385628	56	10508	66561921	2043250
JL01A429	319	9	1441	38	0	83	24320	2200	8393	485436	635667	85311	204684	79838003	2695487
JL01A424	219	3	368	26	38	0	16026	850	5270	425331	419746	64	2078	70134042	2192303
JL01A431	236	3	396	23	35	10	17913	959	7051	528169	466190	82	692	76344283	2317689
JL01A425	230	3	330	25	0	24	17971	949	7547	596999	475208	82	835	71997883	2064730
JL01A432	228	4	297	27	26	16	12584	655	3859	307248	332197	76	222	77208331	2417192
JL01A416	246	8	639	49	45	0	8994	541	2898	193228	213375	40	85414	45998451	1410701
JL01A426	246	4	499	29	15	8	15539	875	5359	397442	400099	124	56731	75703454	2247356
JL01A423	409	20	1607	39	3	47	11741	1116	2592	104982	262140	72	121815	25122626	942967
JL01A435	221	4	193	46	31	0	20336	994	6927	597940	558212	72	3298	87144907	2839435
JL01A434	262	4	708	24	36	11	16843	1046	4853	345661	432299	42	4982	82605470	2854498
JL01A433	247	4	365	28	1	0	18994	1009	6328	472837	474079	48	8666	78347476	2644977
JL01A407	1114	53	3241	34	68	60	3727	945	2529	38236	60864	125140	2460375	39629881	1233430
JL01A427	273	5	259	30	0	22	10051	507	2434	155417	221801	46	527	72969894	2337056
JL01A422	365	6	2894	9	28	318	32069	6556	20941	1065641	1287600	576	10132	67803607	2459989

Granite	207 cor 206Pb/238U age	+/-1 ster	206Pb/238U ratio	+/-1 RSE	208Pb/232Th ratio	+/-1 RSE	207Pb/206Pb ratio	+/-1 RSE	Pb204 ppm	Pb206 ppm	Pb207 ppm	Pb208 ppm
GM-0213												
JL01A457	185	3	0.0320	1.6%	0.0114	2.2%	0.1223	2.4%	0.31	59	7	29
JL01A467	199	4	0.0319	1.9%	0.0132	2.5%	0.0632	3.4%	0.09	44	3	10
JL01A456	200	3	0.0347	1.5%	0.0174	2.3%	0.1235	3.2%	0.13	20	2	9
JL01A452	204	4	0.0331	1.7%	0.0129	2.1%	0.0754	3.0%	0.09	14	1	4
JL01A463	204	4	0.0325	2.0%	0.0115	2.4%	0.0571	3.9%	0.01	16	1	4
JL01A447	209	4	0.0344	1.8%	0.0128	2.2%	0.0827	4.2%	0.13	58	5	23
JL01A448	210	4	0.0348	1.8%	0.0133	2.1%	0.0899	2.8%	0.00	14	1	5
JL01A449	212	3	0.0341	1.4%	0.0115	1.5%	0.0665	2.7%	0.00	30	2	10
JL01A450	215	3	0.0344	1.4%	0.0115	2.0%	0.0606	2.7%	0.05	32	2	7
JL01A464	221	3	0.0463	1.3%	0.0344	1.6%	0.2496	1.4%	0.80	58	14	46
JL01A458	221	3	0.0351	1.2%	0.0121	1.5%	0.0563	1.5%	0.01	71	4	9
JL01A459	222	4	0.0353	1.6%	0.0112	1.7%	0.0575	3.2%	0.00	22	1	8
JL01A466	222	5	0.0354	2.4%	0.0113	2.2%	0.0588	4.1%	0.00	21	1	7
JL01A445	223	4	0.0359	1.7%	0.0128	2.2%	0.0666	3.8%	0.01	10	1	3
JL01A446	224	4	0.0356	1.9%	0.0111	2.2%	0.0568	4.5%	0.04	17	1	4
JL01A443	224	3	0.0359	1.2%	0.0129	1.8%	0.0610	2.7%	0.03	37	2	7
JL01A462	225	4	0.0371	1.8%	0.0162	2.1%	0.0842	2.4%	0.07	26	2	5
JL01A439	226	4	0.0371	1.8%	0.0157	3.9%	0.0809	5.4%	0.08	42	4	12
JL01A455	226	2	0.0357	1.1%	0.0112	1.7%	0.0510	1.5%	0.00	109	6	9
JL01A444	226	4	0.0378	1.7%	0.0162	2.0%	0.0946	2.9%	0.08	15	1	6
JL01A454	227	4	0.0358	1.8%	0.0112	2.2%	0.0480	3.6%	0.03	26	1	6
JL01A442	227	4	0.0368	1.8%	0.0136	2.6%	0.0691	4.5%	0.00	11	1	3
JL01A441	228	4	0.0360	1.8%	0.0111	2.7%	0.0504	4.5%	0.04	12	1	3
JL01A453	231	4	0.0366	1.7%	0.0118	1.8%	0.0533	3.3%	0.02	41	2	14
JL01A465	232	4	0.0366	1.7%	0.0111	1.9%	0.0503	3.1%	0.00	13	1	3
JL01A461	241	7	0.0394	2.8%	0.0174	3.6%	0.0786	5.0%	0.00	6	0	2
JL01A451	244	3	0.0386	1.4%	0.0111	1.5%	0.0514	1.9%	0.01	46	2	12
JL01A460	245	5	0.0389	2.0%	0.0124	2.1%	0.0530	3.4%	0.00	11	1	2
JL01A440	246	10	0.0400	3.9%	0.0105	3.6%	0.0738	6.2%	0.00	12	1	3

Granite	Th232 ppm	U238 ppm	Ti49 ppm	Fe56 ppm	Hf178 ppm	238U/206Pb ratio	+/-1 std err	207Pb/206Pb ratio	+/-1 std err	Common Pb at age of zirc	206Pb/238U age
GM-0213											
JL01A457	2317	1716	310	120	12754	31.23	0.48	0.1223	0.0029	0.849	203
JL01A467	705	1274	18	698	13865	31.36	0.58	0.0632	0.0022	0.849	202
JL01A456	519	585	24	46	11030	28.78	0.44	0.1235	0.0040	0.850	220
JL01A452	296	422	15	10	12691	30.18	0.52	0.0754	0.0023	0.849	210
JL01A463	334	519	16	1373	12518	30.81	0.62	0.0571	0.0022	0.849	206
JL01A447	1885	1819	14	290	11211	29.07	0.51	0.0827	0.0035	0.850	218
JL01A448	377	404	18	1084	11943	28.70	0.53	0.0899	0.0025	0.850	221
JL01A449	830	851	13	12	11873	29.29	0.42	0.0665	0.0018	0.850	216
JL01A450	531	886	18	25	13418	29.06	0.40	0.0606	0.0016	0.850	218
JL01A464	1365	1312	21	1554	11125	21.60	0.29	0.2496	0.0035	0.855	292
JL01A458	731	2021	8	145	13228	28.47	0.33	0.0563	0.0008	0.850	223
JL01A459	723	630	53	361	11839	28.36	0.45	0.0575	0.0019	0.850	223
JL01A466	617	629	11	111	12229	28.29	0.68	0.0588	0.0024	0.850	224
JL01A445	215	268	28	9	11499	27.84	0.48	0.0666	0.0025	0.851	227
JL01A446	315	436	24	224	12050	28.08	0.54	0.0568	0.0026	0.850	226
JL01A443	570	1015	15	18	12820	27.87	0.34	0.0610	0.0017	0.851	227
JL01A462	329	688	11	306	13505	26.93	0.48	0.0842	0.0020	0.851	235
JL01A439	772	1184	9	17	13223	26.97	0.49	0.0809	0.0044	0.851	235
JL01A455	806	3093	8	413	13996	28.00	0.31	0.0510	0.0008	0.850	226
JL01A444	361	392	30	815	11184	26.44	0.45	0.0946	0.0027	0.851	239
JL01A454	580	761	55	73	12577	27.92	0.52	0.0480	0.0017	0.851	227
JL01A442	245	297	36	42	10856	27.20	0.49	0.0691	0.0031	0.851	233
JL01A441	229	341	20	4	11815	27.77	0.51	0.0504	0.0022	0.851	228
JL01A453	1252	1168	8	110	12344	27.36	0.47	0.0533	0.0017	0.851	231
JL01A465	300	346	26	0	11019	27.31	0.46	0.0503	0.0016	0.851	232
JL01A461	90	155	46	252	12278	25.39	0.71	0.0786	0.0039	0.852	249
JL01A451	1029	1150	11	843	12074	25.88	0.37	0.0514	0.0010	0.852	244
JL01A460	196	292	20	12	12028	25.71	0.51	0.0530	0.0018	0.852	246
JL01A440	264	304	38	111	11774	24.97	0.97	0.0738	0.0046	0.852	253

	208Pb/232Th		207Pb/206Pb		Hg202	Pb204	Pb206	Pb207	Pb208	Th232	U238	Ti49	Fe56	Zr90	Hf178
Granite	**age**	**+/-1 ster**	**age**	**+/-1 ster**											
GM-0213															
JL01A457	229	5	1990	21	39	137	26516	3215	12674	928662	730127	1175	9520	63128980	2265101
JL01A467	266	7	714	36	0	35	16768	1029	3920	241416	463008	58	47263	54048991	2108368
JL01A456	349	8	2007	29	0	51	8012	974	3521	189051	226248	84	3319	57337678	1779126
JL01A452	260	6	1078	30	6	37	6350	473	1744	117392	178020	58	760	62499446	2231257
JL01A463	230	6	496	43	30	4	8269	467	1885	153611	253149	69	124778	72533221	2554539
JL01A447	257	6	1263	41	0	80	36327	3099	14329	1054256	1080533	76	31999	87965120	2774175
JL01A448	268	6	1424	27	30	0	6244	553	2225	154266	175509	71	87450	64346688	2161859
JL01A449	232	4	824	28	35	1	11109	717	3638	277307	302140	40	796	52582344	1756275
JL01A450	232	5	626	29	42	22	15773	936	3102	230600	408292	73	2154	68313311	2578554
JL01A464	684	11	3182	11	0	446	33015	8100	25497	692271	706519	100	155844	80001571	2503949
JL01A458	243	4	465	16	49	3	35802	1991	4511	328250	963270	35	12866	70757490	2633237
JL01A459	225	4	509	35	92	1	11223	630	4032	335586	310160	231	33070	73122168	2435439
JL01A466	228	5	560	44	107	0	11082	637	3521	293348	317723	48	10462	75046307	2582083
JL01A445	258	6	825	40	55	7	4957	323	1391	98393	130044	121	855	71849600	2324128
JL01A446	223	5	485	50	0	17	7613	432	1724	127757	188235	91	17955	63864189	2164725
JL01A443	259	5	638	29	34	15	18707	1122	3678	257670	487801	66	1613	71110197	2564256
JL01A462	325	7	1298	24	7	31	10801	907	2243	123669	274328	41	22701	59255356	2251431
JL01A439	314	12	1219	53	170	31	16342	1358	4578	270977	441390	30	1184	55145115	2051009
JL01A455	225	4	240	17	0	2	55277	2772	4455	366649	1493652	35	37103	71645600	2820940
JL01A444	324	6	1520	27	0	42	7468	700	2896	165553	190579	132	73655	72039119	2266245
JL01A454	225	5	99	42	41	13	13506	649	3214	272321	379413	246	6791	73972847	2617219
JL01A442	272	7	903	46	74	0	5694	388	1715	116220	149445	161	3924	74584300	2277608
JL01A441	224	6	213	52	0	24	6875	342	1422	118435	187057	98	397	81270484	2700839
JL01A453	236	4	341	37	41	11	18839	995	6476	520141	515041	31	9022	65405991	2271283
JL01A465	223	4	211	36	39	0	6317	315	1678	132972	162869	110	37	69975505	2169290
JL01A461	349	13	1162	49	48	0	3264	252	816	44034	80813	215	24432	77499505	2677023
JL01A451	224	3	258	21	38	6	22021	1116	5647	443338	525958	45	71640	67777919	2302019
JL01A460	248	5	330	38	51	0	5634	293	1196	86952	137182	83	1039	69762458	2360641
JL01A440	212	8	1037	62	36	0	4783	342	1057	97388	119243	132	8068	58048271	1922370

	207 cor 206Pb/238U		206Pb/238U		208Pb/232Th		207Pb/206Pb		Pb204	Pb206	Pb207	Pb208
Granite	**age**	**+/-1 ster**	**ratio**	**+/-1 RSE**	**ratio**	**+/-1 RSE**	**ratio**	**+/-1 RSE**	**ppm**	**ppm**	**ppm**	**ppm**
GRL-0313												
JA22A055	201	3	0.0338	1.4%	0.0205	5.4%	0.1006	4.4%	0.13	33	3	18
JA22A052	202	3	0.0350	1.4%	0.0130	1.9%	0.1218	2.1%	0.45	87	11	108
JA22A053	203	3	0.0323	1.4%	0.0161	3.1%	0.0602	1.8%	0.05	54	3	3
JA22A046	206	3	0.0326	1.3%	0.0114	2.1%	0.0523	1.8%	0.01	24	1	2
JA22A056	208	3	0.0333	1.4%	0.0137	2.1%	0.0623	1.8%	0.02	55	3	7
JA22A045	208	3	0.0337	1.2%	0.0144	2.4%	0.0708	2.2%	0.06	57	4	12
JA22A048	209	3	0.0330	1.3%	0.0099	2.2%	0.0504	1.1%	0.01	85	4	2
JA22A044	209	3	0.0331	1.2%	0.0100	1.4%	0.0510	1.3%	0.00	49	3	16
JA22A057	211	3	0.0346	1.5%	0.0206	2.9%	0.0812	2.9%	0.08	21	2	4
JA22A054	212	3	0.0337	1.5%	0.0116	2.6%	0.0562	2.6%	0.02	27	2	3
JA22A047	212	4	0.0336	2.0%	0.0106	2.8%	0.0530	3.1%	0.02	26	1	5
JA22A050	213	3	0.0337	1.6%	0.0099	2.8%	0.0517	3.1%	0.02	16	1	2
JA22A049	213	3	0.0336	1.2%	0.0107	1.6%	0.0505	1.3%	0.04	63	3	6
JA22A043	214	3	0.0340	1.2%	0.0113	1.9%	0.0545	1.4%	0.01	80	4	6
JA22A051	240	9	0.0425	3.3%	0.0213	5.6%	0.1391	9.3%	0.14	22	3	14

Granite	Th232 ppm	U238 ppm	Ti49 ppm	Fe56 ppm	Hf178 ppm	238U/206Pb ratio	+/-1 std err	207Pb/206Pb ratio	+/-1 std err	Common Pb at age of zirc	206Pb/238U age	208Pb/232Th age
GRL-0313												
JA22A055	1207	1044	18	396	12281	29.59	0.42	0.1006	0.0044	0.850	214	411
JA22A052	8788	2559	59	69	12233	28.61	0.40	0.1218	0.0025	0.850	221	262
JA22A053	213	1780	67	45	13582	30.93	0.44	0.0602	0.0011	0.849	205	322
JA22A046	136	744	5	9	12552	30.71	0.41	0.0523	0.0009	0.849	207	229
JA22A056	543	1808	19	209	11046	30.05	0.41	0.0623	0.0011	0.849	211	275
JA22A045	823	1725	133	47	10119	29.71	0.36	0.0708	0.0015	0.850	213	289
JA22A048	228	2501	2	1	13302	30.28	0.38	0.0504	0.0005	0.849	209	198
JA22A044	1606	1512	9	9	9471	30.25	0.37	0.0510	0.0006	0.849	210	202
JA22A057	164	600	8	5	11689	28.87	0.43	0.0812	0.0023	0.850	220	412
JA22A054	329	896	48	37	10833	29.72	0.46	0.0562	0.0014	0.850	213	234
JA22A047	516	872	12	7	9981	29.80	0.60	0.0530	0.0016	0.850	213	213
JA22A050	173	506	10	2	11766	29.71	0.48	0.0517	0.0016	0.850	213	199
JA22A049	617	1946	5	2	11408	29.75	0.36	0.0505	0.0007	0.850	213	215
JA22A043	605	2481	7	33	12326	29.41	0.36	0.0545	0.0008	0.850	216	227
JA22A051	892	606	14	132	12910	23.51	0.77	0.1391	0.0129	0.853	269	425

Granite	207Pb/206Pb age	+/-1 ster	Hg202	Pb204	Pb206	Pb207	Pb208	Th232	U238	Ti49	Fe56	Zr90	Hf178
GRL-0313													
JA22A055	1635	41	0	132	32666	3273	17391	1180320	1105415	156	72924	148795341	4929356
JA22A052	1982	19	0	359	69745	8382	85425	6873058	2165682	410	10120	118994349	3927013
JA22A053	613	19	0	51	55751	3291	3267	217314	1965552	605	8749	155260355	5688555
JA22A046	299	20	45	10	22225	1149	1423	124127	736294	43	1558	139238336	4715091
JA22A056	684	19	36	15	55215	3396	6596	531311	1913057	166	38575	148754848	4432367
JA22A045	952	22	54	60	55291	3904	11272	776134	1760821	1116	8378	143603595	3920126
JA22A048	214	12	14	8	72795	3644	1996	191672	2270114	12	130	127681477	4582020
JA22A044	240	14	39	0	45211	2292	14461	1439945	1466528	73	1602	136491347	3487436
JA22A057	1226	28	28	50	12843	1043	2097	96836	383320	41	518	89808953	2831755
JA22A054	462	29	0	22	29263	1628	3713	344710	1015322	446	7319	159380365	4657737
JA22A047	327	35	46	21	28259	1527	5464	558022	1020530	112	1455	164726200	4435533
JA22A050	274	35	0	20	17112	879	1711	180388	571663	92	468	158911040	5044162
JA22A049	216	15	0	36	63907	3209	6323	611351	2085098	46	383	150724534	4638564
JA22A043	393	16	26	12	82566	4435	6571	611930	2712538	59	6330	153879200	5116870
JA22A051	2217	81	49	134	22022	3339	13292	863801	634171	119	24042	147270297	5129014

Granite	207 cor 206Pb/238U age	+/-1 ster	206Pb/238U ratio	+/-1 RSE	208Pb/232Th ratio	+/-1 RSE	207Pb/206Pb ratio	+/-1 RSE	Pb204 ppm	Pb206 ppm	Pb207 ppm	Pb208 ppm
BE-11513												
JA31A153	215	3	0.0340	1.4%	0.0105	1.7%	0.0513	2.2%	0.00	27	1	8
JA31A159	219	4	0.0352	1.9%	0.0116	2.1%	0.0624	3.7%	0.05	15	1	5
JA31A164	220	5	0.0349	2.2%	0.0109	1.9%	0.0559	4.1%	0.01	14	1	6
JA31A155	225	3	0.0356	1.2%	0.0110	1.5%	0.0538	1.8%	0.00	36	2	21
JA31A165	225	3	0.0355	1.3%	0.0110	1.6%	0.0507	2.1%	0.01	36	2	25
JA31A154	225	3	0.0358	1.3%	0.0116	1.7%	0.0563	2.2%	0.00	26	1	10
JA31A151	226	3	0.0357	1.3%	0.0108	1.7%	0.0512	1.9%	0.02	37	2	8
JA31A161	227	3	0.0362	1.3%	0.0112	1.7%	0.0578	2.6%	0.00	31	2	17
JA31A158	227	4	0.0366	1.6%	0.0124	2.0%	0.0659	3.0%	0.04	19	1	8
JA31A156	231	4	0.0364	1.8%	0.0110	1.9%	0.0484	4.0%	0.01	10	0	6
JA31A163	231	4	0.0365	1.7%	0.0116	2.3%	0.0518	3.4%	0.00	17	1	4
JA31A162	231	3	0.0365	1.5%	0.0111	1.9%	0.0496	3.2%	0.05	23	1	7
JA31A152	232	4	0.0367	1.6%	0.0112	1.8%	0.0518	2.7%	0.01	25	1	12
JA31A160	241	5	0.0381	1.9%	0.0122	2.3%	0.0524	3.8%	0.04	24	1	14
JA31A157	258	5	0.0408	2.1%	0.0134	2.6%	0.0498	6.4%	0.00	18	1	11

Granite	Th232 ppm	U238 ppm	Ti49 ppm	Fe56 ppm	Hf178 ppm	238U/206Pb ratio	+/-1 std err	207Pb/206Pb ratio	+/-1 std err	Common Pb at age of zirc	206Pb/238U age	208Pb/232Th age
BE-11513												
JA31A153	754	790	6	19	11292	29.41	0.40	0.0513	0.0011	0.850	216	212
JA31A159	431	459	14	3780	10772	28.45	0.54	0.0624	0.0023	0.850	223	233
JA31A164	593	407	11	62	9190	28.63	0.64	0.0559	0.0023	0.850	221	220
JA31A155	1825	985	8	93	10150	28.07	0.35	0.0538	0.0010	0.850	226	221
JA31A165	2263	1025	5	49	9329	28.14	0.37	0.0507	0.0010	0.850	225	220
JA31A154	859	718	12	18	10379	27.93	0.36	0.0563	0.0012	0.851	227	232
JA31A151	691	1046	4	8	11703	27.99	0.35	0.0512	0.0010	0.850	226	218
JA31A161	1506	888	824	2392	9407	27.63	0.36	0.0578	0.0015	0.851	229	225
JA31A158	626	520	162	18562	10519	27.34	0.44	0.0659	0.0019	0.851	232	249
JA31A156	489	284	13	2	9096	27.46	0.49	0.0484	0.0020	0.851	231	222
JA31A163	376	489	6	16	11213	27.41	0.47	0.0518	0.0017	0.851	231	234
JA31A162	644	648	6	10	10915	27.42	0.40	0.0496	0.0016	0.851	231	224
JA31A152	1075	731	10	161	10271	27.27	0.45	0.0518	0.0014	0.851	232	225
JA31A160	1188	698	9	20	9650	26.22	0.51	0.0524	0.0020	0.852	241	246
JA31A157	700	399	7	6	9665	24.54	0.51	0.0498	0.0032	0.853	258	269

Granite	207Pb/206Pb age	+/-1 ster	Hg202	Pb204	Pb206	Pb207	Pb208	Th232	U238	Ti49	Fe56	Zr90	Hf178
BE-11513													
JA31A153	254	25	24	0	13530	684	4149	371915	417768	25	1708	78859538	2290227
JA31A159	688	40	0	26	8233	499	2660	230763	263863	62	361603	85502008	2371894
JA31A164	447	45	43	6	6563	358	3094	283473	208293	45	5273	76079902	1802585
JA31A155	361	20	0	0	18129	968	10694	911250	526864	34	8327	79758709	2082998
JA31A165	225	24	47	4	19832	988	13869	1240390	602486	24	4802	87273408	2099670
JA31A154	464	24	65	0	13332	741	5363	434850	389711	51	1672	80912236	2160322
JA31A151	252	22	0	11	18727	949	3870	339325	550052	16	698	78505977	2361845
JA31A161	522	28	63	0	16694	948	9059	804844	508616	3696	227772	85181105	2064509
JA31A158	802	31	13	15	8201	526	3341	268784	239311	587	1424465	68563475	1856990
JA31A156	118	48	16	4	5269	248	2847	242237	150846	53	139	79110147	1851896
JA31A163	277	38	0	0	9862	502	2474	209992	293126	27	1585	89050428	2573780
JA31A162	175	38	0	25	12712	618	3984	354927	382829	26	966	87860984	2471478
JA31A152	278	31	40	6	13506	686	6201	559608	407935	42	15037	83231801	2198098
JA31A160	304	44	0	26	15076	774	8640	727562	458248	44	2199	97676845	2427963
JA31A157	184	75	76	0	7211	352	4287	279821	170907	23	443	63771127	1586525

LA ICP-MS Solution				
Sample	**Au (ppm)**	**Au (ppb)**	**% Analytical Error**	**Limit of Quantification**
GM-0912	0.034	34	7.7	0.005
GM-1012	0.014	14	9.3	0.005
GM-1112	0.017	17	9.2	0.005
GM-1212	0.022	22	9.0	0.005
GM-1312	0.020	20	7.9	0.005
KL-0512	0.051	51	6.2	0.005
BE-2212	0.039	39	7.0	0.005
BE-2312	0.033	33	9.0	0.005
BE-2412	0.017	17	7.1	0.005
BE-2512	0.024	24	10.1	0.005
BE-2612	0.020	20	10.2	0.005
BE-2712	0.003	3	DL<x<DQ	0.001 < x < 0.005
ME-5912	0.020	20	8.0	0.005
ME-6612	0.018	18	8.5	0.005
KL-0112	0.023	23	7.2	0.005
KL-0212	0.033	33	9.1	0.005
KL-0312	0.025	25	9.3	0.005
KL-0412	0.042	42	22.1	0.005
CH-0612	0.012	12	9.7	0.005
CH-0712	0.017	17	11.4	0.005
TP-1412	0.017	17	13.4	0.005
TP-1512	0.014	14	12.2	0.005
TP-1612	0.003	3	DL<x<DQ	0.001 < x < 0.005
PJ-1812	0.042	42	8.5	0.006
PJ-1912	0.041	41	14.9	0.006
PJ-2012	0.028	28	12.1	0.006
LA-2812	0.040	40	9.3	0.006
LA-2912	0.042	42	10.5	0.006
LA-3012	0.057	57	11.1	0.006
LA-3112	0.046	46	8.8	0.006
LA-3212	0.049	49	8.4	0.006
LA-3312	0.042	42	7.9	0.006
LA-3412	0.046	46	9.1	0.006
LA-3512	0.048	48	8.3	0.006
LA-3612	0.062	62	8.6	0.006
LA-3712	0.053	53	8.7	0.006
LA-3812	0.046	46	11.4	0.006
LA-3912	0.048	48	11.7	0.006
LA-4012	0.065	65	16.6	0.006
LA-4112	0.057	57	11.0	0.006
LA-4212	0.119	119	8.4	0.006
LA-4312	0.039	39	35.3	0.006
LA-4412	0.022	22	10.2	0.006
LA-4612	0.017	17	13.9	0.006
LA-4712	0.014	14	21.4	0.006
LA-4812	0.005	5	DL<x<DQ	0.002 < x < 0.007
LA-4912	0.101	101	10.9	0.007
LA-5012	0.075	75	11.4	0.007
LA-5112	0.017	17	14.7	0.007
LA-5212	0.004	4	DL<x<DQ	0.002 < x < 0.007
LA-5412	0.011	11	20.3	0.007
LA-5512	0.042	42	13.0	0.007
LA-5612	0.034	34	13.1	0.007
LA-5712	0.040	40	13.7	0.007
ME-6212	0.030	30	12.4	0.007
ME-6312	0.024	24	17.3	0.007

APPENDIX C

ROCK CATALOGUE

Utas#	Field Number	Collector	Year	Contact details	Stored at	Class	Type	Rock Name	Ore model	Commodity
179490	LA-2812	Makoundi, Charles	2015	c.makoundi@utas.edu.au, charlesmakoun	Compactus	Sedimentary	clastic	Sandstone	Sedimentary rock hosted	Gold
179491	LA-2912	Makoundi, Charles	2015	c.makoundi@utas.edu.au, charlesmakoun	Compactus	Sedimentary	clastic	Shale	Sedimentary rock hosted	Gold
179492	LA-3012	Makoundi, Charles	2015	c.makoundi@utas.edu.au, charlesmakoun	Compactus	Sedimentary	clastic	Shale	Sedimentary rock hosted	Gold
179493	LA-3112	Makoundi, Charles	2015	c.makoundi@utas.edu.au, charlesmakoun	Compactus	Sedimentary	clastic	Sandstone	Sedimentary rock hosted	Gold
179494	LA-3212	Makoundi, Charles	2015	c.makoundi@utas.edu.au, charlesmakoun	Compactus	Sedimentary	clastic	Shale	Sedimentary rock hosted	Gold
179495	LA-3312	Makoundi, Charles	2015	c.makoundi@utas.edu.au, charlesmakoun	Compactus	Sedimentary	clastic	Sandstone	Sedimentary rock hosted	Gold
179496	LA-4612	Makoundi, Charles	2015	c.makoundi@utas.edu.au, charlesmakoun	Compactus	Sedimentary	clastic	Sandstone	Sedimentary rock hosted	Gold
179497	LA-4712	Makoundi, Charles	2015	c.makoundi@utas.edu.au, charlesmakoun	Compactus	Sedimentary	clastic	Sandstone	Sedimentary rock hosted	Gold
179498	LA-4812	Makoundi, Charles	2015	c.makoundi@utas.edu.au, charlesmakoun	Compactus	Sedimentary	clastic	Sandstone	Sedimentary rock hosted	Gold
179499	LA-4912	Makoundi, Charles	2015	c.makoundi@utas.edu.au, charlesmakoun	Compactus	Sedimentary	clastic	Sandstone	Sedimentary rock hosted	Gold
179500	LA-5012	Makoundi, Charles	2015	c.makoundi@utas.edu.au, charlesmakoun	Compactus	Sedimentary	clastic	Sandstone	Sedimentary rock hosted	Gold
179501	LA-3412	Makoundi, Charles	2015	c.makoundi@utas.edu.au, charlesmakoun	Compactus	Sedimentary	clastic	Sandstone	Sedimentary rock hosted	Gold
179502	LA-3512	Makoundi, Charles	2015	c.makoundi@utas.edu.au, charlesmakoun	Compactus	Sedimentary	clastic	Shale	Sedimentary rock hosted	Gold
179503	LA-3612	Makoundi, Charles	2015	c.makoundi@utas.edu.au, charlesmakoun	Compactus	Sedimentary	clastic	Shale	Sedimentary rock hosted	Gold
179504	LA-3712	Makoundi, Charles	2015	c.makoundi@utas.edu.au, charlesmakoun	Compactus	Sedimentary	clastic	Shale	Sedimentary rock hosted	Gold
179505	LA-3812	Makoundi, Charles	2015	c.makoundi@utas.edu.au, charlesmakoun	Compactus	Sedimentary	clastic	Shale	Sedimentary rock hosted	Gold
179506	LA-3912	Makoundi, Charles	2015	c.makoundi@utas.edu.au, charlesmakoun	Compactus	Sedimentary	clastic	Shale	Sedimentary rock hosted	Gold
179507	LA-4012	Makoundi, Charles	2015	c.makoundi@utas.edu.au, charlesmakoun	Compactus	Sedimentary	clastic	Shale	Sedimentary rock hosted	Gold
179508	LA-4112	Makoundi, Charles	2015	c.makoundi@utas.edu.au, charlesmakoun	Compactus	Sedimentary	clastic	Shale	Sedimentary rock hosted	Gold
179509	LA-4212	Makoundi, Charles	2015	c.makoundi@utas.edu.au, charlesmakoun	Compactus	Sedimentary	clastic	Sandstone	Sedimentary rock hosted	Gold
179510	LA-4312	Makoundi, Charles	2015	c.makoundi@utas.edu.au, charlesmakoun	Compactus	Sedimentary	clastic	Sandstone	Sedimentary rock hosted	Gold
179511	LA-4412	Makoundi, Charles	2015	c.makoundi@utas.edu.au, charlesmakoun	Compactus	Sedimentary	clastic	Sandstone	Sedimentary rock hosted	Gold
179512	LA-5112	Makoundi, Charles	2015	c.makoundi@utas.edu.au, charlesmakoun	Compactus	Sedimentary	clastic	Sandstone	Sedimentary rock hosted	Gold
179513	LA-5212	Makoundi, Charles	2015	c.makoundi@utas.edu.au, charlesmakoun	Compactus	Sedimentary	clastic	Sandstone	Sedimentary rock hosted	Gold
179514	LA-5312	Makoundi, Charles	2015	c.makoundi@utas.edu.au, charlesmakoun	Compactus	Sedimentary	clastic	Sandstone	Sedimentary rock hosted	Gold
179515	LA-5412	Makoundi, Charles	2015	c.makoundi@utas.edu.au, charlesmakoun	Compactus	Sedimentary	clastic	Sandstone	Sedimentary rock hosted	Gold
179516	LA-5512	Makoundi, Charles	2015	c.makoundi@utas.edu.au, charlesmakoun	Compactus	Sedimentary	clastic	Shale	Sedimentary rock hosted	Gold
179517	LA-5612	Makoundi, Charles	2015	c.makoundi@utas.edu.au, charlesmakoun	Compactus	Sedimentary	clastic	Sandstone	Sedimentary rock hosted	Gold
179518	LA-5712	Makoundi, Charles	2015	c.makoundi@utas.edu.au, charlesmakoun	Compactus	Sedimentary	clastic	Shale	Sedimentary rock hosted	Gold
179519	BE-2212	Makoundi, Charles	2015	c.makoundi@utas.edu.au, charlesmakoun	Compactus	Sedimentary	clastic	Sandstone	Sedimentary rock hosted	Gold
179520	BE-2312	Makoundi, Charles	2015	c.makoundi@utas.edu.au, charlesmakoun	Compactus	Sedimentary	clastic	Sandstone	Sedimentary rock hosted	Gold
179521	BE-2412	Makoundi, Charles	2015	c.makoundi@utas.edu.au, charlesmakoun	Compactus	Sedimentary	clastic	Sandstone	Sedimentary rock hosted	Gold
179522	BE-2512	Makoundi, Charles	2015	c.makoundi@utas.edu.au, charlesmakoun	Compactus	Sedimentary	clastic	Sandstone	Sedimentary rock hosted	Gold
179523	BE-2612	Makoundi, Charles	2015	c.makoundi@utas.edu.au, charlesmakoun	Compactus	Sedimentary	clastic	Sandstone	Sedimentary rock hosted	Gold
179524	BE-2712	Makoundi, Charles	2015	c.makoundi@utas.edu.au, charlesmakoun	Compactus	Sedimentary	clastic	Sandstone	Sedimentary rock hosted	Gold
179525	BE-2813	Makoundi, Charles	2015	c.makoundi@utas.edu.au, charlesmakoun	Compactus	Sedimentary	clastic	Shale	Sedimentary rock hosted	Gold
179526	BE-2913	Makoundi, Charles	2015	c.makoundi@utas.edu.au, charlesmakoun	Compactus	Sedimentary	clastic	Sandstone	Sedimentary rock hosted	Gold
179527	BE-3013	Makoundi, Charles	2015	c.makoundi@utas.edu.au, charlesmakoun	Compactus	Sedimentary	clastic	Shale	Sedimentary rock hosted	Gold
179528	BE-3113	Makoundi, Charles	2015	c.makoundi@utas.edu.au, charlesmakoun	Compactus	Sedimentary	clastic	Sandstone	Sedimentary rock hosted	Gold
179529	BE-3213	Makoundi, Charles	2015	c.makoundi@utas.edu.au, charlesmakoun	Compactus	Sedimentary	clastic	Shale	Sedimentary rock hosted	Gold
179530	BE-3313	Makoundi, Charles	2015	c.makoundi@utas.edu.au, charlesmakoun	Compactus	Sedimentary	clastic	Shale	Sedimentary rock hosted	Gold
179531	BE-3513	Makoundi, Charles	2015	c.makoundi@utas.edu.au, charlesmakoun	Compactus	Sedimentary	clastic	Shale	Sedimentary rock hosted	Gold
179532	BE-3613	Makoundi, Charles	2015	c.makoundi@utas.edu.au, charlesmakoun	Compactus	Sedimentary	clastic	Shale	Sedimentary rock hosted	Gold
179533	BE-3713	Makoundi, Charles	2015	c.makoundi@utas.edu.au, charlesmakoun	Compactus	Sedimentary	clastic	Shale	Sedimentary rock hosted	Gold
179534	BE-3913	Makoundi, Charles	2015	c.makoundi@utas.edu.au, charlesmakoun	Compactus	Sedimentary	clastic	Shale	Sedimentary rock hosted	Gold
179535	BE-4013	Makoundi, Charles	2015	c.makoundi@utas.edu.au, charlesmakoun	Compactus	Sedimentary	clastic	Shale	Sedimentary rock hosted	Gold
179536	SEL-R103	Makoundi, Charles	2015	c.makoundi@utas.edu.au, charlesmakoun	Compactus	Sedimentary	clastic	Shale	Sedimentary rock hosted	Gold
179537	SEL-R076	Makoundi, Charles	2015	c.makoundi@utas.edu.au, charlesmakoun	Compactus	Sedimentary	clastic	Shale	Sedimentary rock hosted	Gold
179538	ME-5912	Makoundi, Charles	2015	c.makoundi@utas.edu.au, charlesmakoun	Compactus	Sedimentary	clastic	Shale	Sedimentary rock hosted	Gold
179539	ME-6612	Makoundi, Charles	2015	c.makoundi@utas.edu.au, charlesmakoun	Compactus	Sedimentary	clastic	Shale	Sedimentary rock hosted	Gold
179540	ME-6412	Makoundi, Charles	2015	c.makoundi@utas.edu.au, charlesmakoun	Compactus	Sedimentary	clastic	Shale	Sedimentary rock hosted	Gold
179541	ME-6512	Makoundi, Charles	2015	c.makoundi@utas.edu.au, charlesmakoun	Compactus	Sedimentary	clastic	Shale	Sedimentary rock hosted	Gold
179542	ME-9313	Makoundi, Charles	2015	c.makoundi@utas.edu.au, charlesmakoun	Compactus	Sedimentary	clastic	Shale	Sedimentary rock hosted	Gold
179543	ME-9413	Makoundi, Charles	2015	c.makoundi@utas.edu.au, charlesmakoun	Compactus	Sedimentary	clastic	Shale	Sedimentary rock hosted	Gold
179544	ME-9513	Makoundi, Charles	2015	c.makoundi@utas.edu.au, charlesmakoun	Compactus	Sedimentary	clastic	Shale	Sedimentary rock hosted	Gold
179545	ME-9613	Makoundi, Charles	2015	c.makoundi@utas.edu.au, charlesmakoun	Compactus	Sedimentary	clastic	Shale	Sedimentary rock hosted	Gold
179546	ME-9713	Makoundi, Charles	2015	c.makoundi@utas.edu.au, charlesmakoun	Compactus	Sedimentary	clastic	Shale	Sedimentary rock hosted	Gold
179547	ME-9813	Makoundi, Charles	2015	c.makoundi@utas.edu.au, charlesmakoun	Compactus	Sedimentary	clastic	Shale	Sedimentary rock hosted	Gold
179548	ME-9913	Makoundi, Charles	2015	c.makoundi@utas.edu.au, charlesmakoun	Compactus	Sedimentary	clastic	Shale	Sedimentary rock hosted	Gold
179549	ME-10013	Makoundi, Charles	2015	c.makoundi@utas.edu.au, charlesmakoun	Compactus	Sedimentary	clastic	Shale	Sedimentary rock hosted	Gold
179550	ME-10113	Makoundi, Charles	2015	c.makoundi@utas.edu.au, charlesmakoun	Compactus	Sedimentary	clastic	Shale	Sedimentary rock hosted	Gold
179551	ME-10213	Makoundi, Charles	2015	c.makoundi@utas.edu.au, charlesmakoun	Compactus	Sedimentary	clastic	Shale	Sedimentary rock hosted	Gold
179552	ME-10313	Makoundi, Charles	2015	c.makoundi@utas.edu.au, charlesmakoun	Compactus	Sedimentary	clastic	Shale	Sedimentary rock hosted	Gold
179553	ME-10813	Makoundi, Charles	2015	c.makoundi@utas.edu.au, charlesmakoun	Compactus	Sedimentary	clastic	Shale	Sedimentary rock hosted	Gold
179554	GM-0912	Makoundi, Charles	2015	c.makoundi@utas.edu.au, charlesmakoun	Compactus	Sedimentary	clastic	Shale	Sedimentary rock hosted	Gold
179555	GM-1012	Makoundi, Charles	2015	c.makoundi@utas.edu.au, charlesmakoun	Compactus	Sedimentary	clastic	Shale	Sedimentary rock hosted	Gold
179556	GM-1112	Makoundi, Charles	2015	c.makoundi@utas.edu.au, charlesmakoun	Compactus	Sedimentary	clastic	Sandstone	Sedimentary rock hosted	Gold
179557	GM1212	Makoundi, Charles	2015	c.makoundi@utas.edu.au, charlesmakoun	Compactus	Sedimentary	clastic	Shale	Sedimentary rock hosted	Gold
179558	GM-1312	Makoundi, Charles	2015	c.makoundi@utas.edu.au, charlesmakoun	Compactus	Sedimentary	clastic	Shale	Sedimentary rock hosted	Gold
179559	KL-0112	Makoundi, Charles	2015	c.makoundi@utas.edu.au, charlesmakoun	Compactus	Sedimentary	clastic	Shale	Sedimentary rock hosted	Gold
179560	KL-0212	Makoundi, Charles	2015	c.makoundi@utas.edu.au, charlesmakoun	Compactus	Sedimentary	clastic	Shale	Sedimentary rock hosted	Gold
179561	KL-0312	Makoundi, Charles	2015	c.makoundi@utas.edu.au, charlesmakoun	Compactus	Sedimentary	clastic	Shale	Sedimentary rock hosted	Gold
179562	KL-0412	Makoundi, Charles	2015	c.makoundi@utas.edu.au, charlesmakoun	Compactus	Sedimentary	clastic	Shale	Sedimentary rock hosted	Gold
179563	KL-0512	Makoundi, Charles	2015	c.makoundi@utas.edu.au, charlesmakoun	Compactus	Sedimentary	clastic	Shale	Sedimentary rock hosted	Gold
179564	TP-1112	Makoundi, Charles	2015	c.makoundi@utas.edu.au, charlesmakoun	Compactus	Sedimentary	clastic	Shale	Sedimentary rock hosted	Gold
179565	TP-1412	Makoundi, Charles	2015	c.makoundi@utas.edu.au, charlesmakoun	Compactus	Sedimentary	clastic	Sandstone	Sedimentary rock hosted	Gold
179566	TP-1512	Makoundi, Charles	2015	c.makoundi@utas.edu.au, charlesmakoun	Compactus	Sedimentary	clastic	Shale	Sedimentary rock hosted	Gold
179567	TP-1612	Makoundi, Charles	2015	c.makoundi@utas.edu.au, charlesmakoun	Compactus	Sedimentary	clastic	Shale	Sedimentary rock hosted	Gold
179568	PJ-1812	Makoundi, Charles	2015	c.makoundi@utas.edu.au, charlesmakoun	Compactus	Sedimentary	clastic	Shale	Sedimentary rock hosted	Gold
179569	PJ-1912	Makoundi, Charles	2015	c.makoundi@utas.edu.au, charlesmakoun	Compactus	Sedimentary	clastic	Shale	Sedimentary rock hosted	Gold
179570	PJ-2112	Makoundi, Charles	2015	c.makoundi@utas.edu.au, charlesmakoun	Compactus	Sedimentary	clastic	Shale	Sedimentary rock hosted	Gold
179571	BE-4813	Makoundi, Charles	2015	c.makoundi@utas.edu.au, charlesmakoun	Compactus	Sedimentary	biogenic	Chert	Sedimentary rock hosted	Gold
179572	BE-4913	Makoundi, Charles	2015	c.makoundi@utas.edu.au, charlesmakoun	Compactus	Sedimentary	biogenic	Chert	Sedimentary rock hosted	Gold
179573	BE-5013	Makoundi, Charles	2015	c.makoundi@utas.edu.au, charlesmakoun	Compactus	Sedimentary	biogenic	Chert	Sedimentary rock hosted	Gold
179574	BE-5113	Makoundi, Charles	2015	c.makoundi@utas.edu.au, charlesmakoun	Compactus	Sedimentary	biogenic	Chert	Sedimentary rock hosted	Gold
179575	BE-5213	Makoundi, Charles	2015	c.makoundi@utas.edu.au, charlesmakoun	Compactus	Sedimentary	biogenic	Chert	Sedimentary rock hosted	Gold
179576	BE-5313	Makoundi, Charles	2015	c.makoundi@utas.edu.au, charlesmakoun	Compactus	Sedimentary	biogenic	Chert	Sedimentary rock hosted	Gold
179577	BE-5413	Makoundi, Charles	2015	c.makoundi@utas.edu.au, charlesmakoun	Compactus	Sedimentary	biogenic	Chert	Sedimentary rock hosted	Gold
179578	BE-5513	Makoundi, Charles	2015	c.makoundi@utas.edu.au, charlesmakoun	Compactus	Sedimentary	biogenic	Chert	Sedimentary rock hosted	Gold
179579	BE-5613	Makoundi, Charles	2015	c.makoundi@utas.edu.au, charlesmakoun	Compactus	Sedimentary	biogenic	Chert	Sedimentary rock hosted	Gold
179580	BE-5813	Makoundi, Charles	2015	c.makoundi@utas.edu.au, charlesmakoun	Compactus	Sedimentary	biogenic	Chert	Sedimentary rock hosted	Gold
179581	BE-6013	Makoundi, Charles	2015	c.makoundi@utas.edu.au, charlesmakoun	Compactus	Sedimentary	biogenic	Chert	Sedimentary rock hosted	Gold
179582	BE-6213	Makoundi, Charles	2015	c.makoundi@utas.edu.au, charlesmakoun	Compactus	Sedimentary	biogenic	Chert	Sedimentary rock hosted	Gold
179583	BE-6313	Makoundi, Charles	2015	c.makoundi@utas.edu.au, charlesmakoun	Compactus	Sedimentary	biogenic	Chert	Sedimentary rock hosted	Gold
179584	BE-6613	Makoundi, Charles	2015	c.makoundi@utas.edu.au, charlesmakoun	Compactus	Sedimentary	biogenic	Chert	Sedimentary rock hosted	Gold
179585	GM-0113	Makoundi, Charles	2015	c.makoundi@utas.edu.au, charlesmakoun	Compactus	igneous	plutonic	Granite	Granite hosted	Gold
179586	GM-0213	Makoundi, Charles	2015	c.makoundi@utas.edu.au, charlesmakoun	Compactus	igneous	plutonic	Granite	Granite hosted	Gold
179587	GRL-0313	Makoundi, Charles	2015	c.makoundi@utas.edu.au, charlesmakoun	Compactus	igneous	plutonic	Granite	Granite hosted	Gold
179588	BE-11513	Makoundi, Charles	2015	c.makoundi@utas.edu.au, charlesmakoun	Compactus	igneous	plutonic	Granite	Granite hosted	Gold

Utas#	Latitude	N/S	Longitude	E/W	Country	State	Mine/Prospect	Eon	Era	Period/System	Formation	Environment	Tectonic Setting
179490	6.43	N	99.727	E	Malaysia	Langkawi	Outcrop	Phanerozoic	Palaeozoic	Cambrian-Ordovician	Machinchang	Delta	Continental margin
179491	6.431	N	99.728	E	Malaysia	Langkawi	Outcrop	Phanerozoic	Palaeozoic	Cambrian-Ordovician	Machinchang	Delta	Continental margin
179492	6.431	N	99.73	E	Malaysia	Langkawi	Outcrop	Phanerozoic	Palaeozoic	Cambrian-Ordovician	Machinchang	Delta	Continental margin
179493	6.431	N	99.73	E	Malaysia	Langkawi	Outcrop	Phanerozoic	Palaeozoic	Cambrian-Ordovician	Machinchang	Delta	Continental margin
179494	6.431	N	99.731	E	Malaysia	Langkawi	Outcrop	Phanerozoic	Palaeozoic	Cambrian-Ordovician	Machinchang	Delta	Continental margin
179495	6.43	N	99.733	E	Malaysia	Langkawi	Outcrop	Phanerozoic	Palaeozoic	Cambrian-Ordovician	Machinchang	Delta	Continental margin
179496	6.443	N	99.882	E	Malaysia	Langkawi	Outcrop	Phanerozoic	Palaeozoic	Ordovician-Silurian	Setul	deep water	Continental margin
179497	6.443	N	99.882	E	Malaysia	Langkawi	Outcrop	Phanerozoic	Palaeozoic	Ordovician-Silurian	Setul	deep water	Continental margin
179498	6.443	N	99.882	E	Malaysia	Langkawi	Outcrop	Phanerozoic	Palaeozoic	Ordovician-Silurian	Setul	deep water	Continental margin
179499	6.443	N	99.882	E	Malaysia	Langkawi	Outcrop	Phanerozoic	Palaeozoic	Ordovician-Silurian	Setul	deep water	Continental margin
179500	6.443	N	99.882	E	Malaysia	Langkawi	Outcrop	Phanerozoic	Palaeozoic	Ordovician-Silurian	Setul	deep water	Continental margin
179501	6.286	N	99.729	E	Malaysia	Langkawi	Outcrop	Phanerozoic	Palaeozoic	Pennsylvanian-Permian	Singa	glacial	Continental island arc
179502	6.286	N	99.727	E	Malaysia	Langkawi	Outcrop	Phanerozoic	Palaeozoic	Pennsylvanian-Permian	Singa	glacial	Continental island arc
179503	6.286	N	99.727	E	Malaysia	Langkawi	Outcrop	Phanerozoic	Palaeozoic	Pennsylvanian-Permian	Singa	glacial	Continental island arc
179504	6.268	N	99.733	E	Malaysia	Langkawi	Outcrop	Phanerozoic	Palaeozoic	Pennsylvanian-Permian	Singa	glacial	Continental island arc
179505	6.268	N	99.733	E	Malaysia	Langkawi	Outcrop	Phanerozoic	Palaeozoic	Pennsylvanian-Permian	Singa	glacial	Continental island arc
179506	6.268	N	99.733	E	Malaysia	Langkawi	Outcrop	Phanerozoic	Palaeozoic	Pennsylvanian-Permian	Singa	glacial	Continental island arc
179507	6.269	N	99.733	E	Malaysia	Langkawi	Outcrop	Phanerozoic	Palaeozoic	Pennsylvanian-Permian	Singa	glacial	Continental island arc
179508	6.29	N	99.783	E	Malaysia	Langkawi	Outcrop	Phanerozoic	Palaeozoic	Pennsylvanian-Permian	Singa	glacial	Continental island arc
179509	6.29	N	99.783	E	Malaysia	Langkawi	Outcrop	Phanerozoic	Palaeozoic	Pennsylvanian-Permian	Singa	glacial	Continental island arc
179510	6.283	N	99.765	E	Malaysia	Langkawi	Outcrop	Phanerozoic	Palaeozoic	Pennsylvanian-Permian	Singa	glacial	Continental island arc
179511	6.283	N	99.765	E	Malaysia	Langkawi	Outcrop	Phanerozoic	Palaeozoic	Pennsylvanian-Permian	Singa	glacial	Continental island arc
179512	6.426	N	99.915	E	Malaysia	Langkawi	Outcrop	Phanerozoic	Palaeozoic	Pennsylvanian-Permian	Singa	glacial	Continental island arc
179513	6.426	N	99.915	E	Malaysia	Langkawi	Outcrop	Phanerozoic	Palaeozoic	Pennsylvanian-Permian	Singa	glacial	Continental island arc
179514	6.426	N	99.915	E	Malaysia	Langkawi	Outcrop	Phanerozoic	Palaeozoic	Pennsylvanian-Permian	Singa	glacial	Continental island arc
179515	6.426	N	99.915	E	Malaysia	Langkawi	Outcrop	Phanerozoic	Palaeozoic	Pennsylvanian-Permian	Singa	glacial	Continental island arc
179516	6.402	N	99.82	E	Malaysia	Langkawi	Outcrop	Phanerozoic	Palaeozoic	Pennsylvanian-Permian	Singa	glacial	Continental island arc
179517	6.401	N	99.82	E	Malaysia	Langkawi	Outcrop	Phanerozoic	Palaeozoic	Pennsylvanian-Permian	Singa	glacial	Continental island arc
179518	6.412	N	99.824	E	Malaysia	Langkawi	Outcrop	Phanerozoic	Palaeozoic	Pennsylvanian-Permian	Singa	glacial	Continental island arc
179519	3.605	N	101.902	E	Malaysia	Pahang	Outcrop	Phanerozoic	Palaeozoic	Devonian	BRSZ Unit 1	Flysch	Recycled orogen
179520	3.605	N	101.902	E	Malaysia	Pahang	Outcrop	Phanerozoic	Palaeozoic	Devonian	BRSZ Unit 1	Flysch	Recycled orogen
179521	3.59	N	101.901	E	Malaysia	Pahang	Outcrop	Phanerozoic	Palaeozoic	Devonian	BRSZ Unit 1	Flysch	Recycled orogen
179522	3.59	N	101.901	E	Malaysia	Pahang	Outcrop	Phanerozoic	Palaeozoic	Devonian	BRSZ Unit 1	Flysch	Recycled orogen
179523	3.59	N	101.901	E	Malaysia	Pahang	Outcrop	Phanerozoic	Palaeozoic	Devonian	BRSZ Unit 1	Flysch	Recycled orogen
179524	3.591	N	101.901	E	Malaysia	Pahang	Outcrop	Phanerozoic	Palaeozoic	Devonian	BRSZ Unit 1	Flysch	Recycled orogen
179525	3.605	N	101.902	E	Malaysia	Pahang	Outcrop	Phanerozoic	Palaeozoic	Devonian	BRSZ Unit 1	Flysch	Recycled orogen
179526	3.605	N	101.902	E	Malaysia	Pahang	Outcrop	Phanerozoic	Palaeozoic	Devonian	BRSZ Unit 1	Flysch	Recycled orogen
179527	3.605	N	101.902	E	Malaysia	Pahang	Outcrop	Phanerozoic	Palaeozoic	Devonian	BRSZ Unit 1	Flysch	Recycled orogen
179528	3.605	N	101.902	E	Malaysia	Pahang	Outcrop	Phanerozoic	Palaeozoic	Devonian	BRSZ Unit 1	Flysch	Recycled orogen
179529	3.605	N	101.902	E	Malaysia	Pahang	Outcrop	Phanerozoic	Palaeozoic	Devonian	BRSZ Unit 1	Flysch	Recycled orogen
179530	3.605	N	101.902	E	Malaysia	Pahang	Outcrop	Phanerozoic	Palaeozoic	Devonian	BRSZ Unit 1	Flysch	Recycled orogen
179531	3.605	N	101.902	E	Malaysia	Pahang	Outcrop	Phanerozoic	Palaeozoic	Devonian	BRSZ Unit 1	Flysch	Recycled orogen
179532	3.605	N	101.902	E	Malaysia	Pahang	Outcrop	Phanerozoic	Palaeozoic	Devonian	BRSZ Unit 1	Flysch	Recycled orogen
179533	3.605	N	101.902	E	Malaysia	Pahang	Outcrop	Phanerozoic	Palaeozoic	Devonian	BRSZ Unit 1	Flysch	Recycled orogen
179534	3.605	N	101.902	E	Malaysia	Pahang	Outcrop	Phanerozoic	Palaeozoic	Devonian	BRSZ Unit 1	Flysch	Recycled orogen
179535	3.605	N	101.902	E	Malaysia	Pahang	Outcrop	Phanerozoic	Palaeozoic	Devonian	BRSZ Unit 1	Flysch	Recycled orogen
179536	4.538	N	101.732	E	Malaysia	Pahang	Selinsing Gold Mine	Phanerozoic	Mesozoic	Carboniferous	Selinsing	deep water	-
179537	4.538	N	101.732	E	Malaysia	Pahang	Selinsing Gold Mine	Phanerozoic	Mesozoic	Carboniferous	Selinsing	deep water	-
179538	3.546	N	102.518	E	Malaysia	Pahang	Outcrop	Phanerozoic	Mesozoic	Triassic	Semantan	deep water	Oceanic island arc
179539	3.588	N	102.349	E	Malaysia	Pahang	Outcrop	Phanerozoic	Mesozoic	Triassic	Semantan	deep water	Oceanic island arc
179540	3.526	N	102.309	E	Malaysia	Pahang	Outcrop	Phanerozoic	Mesozoic	Triassic	Semantan	deep water	Oceanic island arc
179541	3.526	N	102.309	E	Malaysia	Pahang	Outcrop	Phanerozoic	Mesozoic	Triassic	Semantan	deep water	Oceanic island arc
179542	3.588	N	102.349	E	Malaysia	Pahang	Outcrop	Phanerozoic	Mesozoic	Triassic	Semantan	deep water	Oceanic island arc
179543	3.588	N	102.349	E	Malaysia	Pahang	Outcrop	Phanerozoic	Mesozoic	Triassic	Semantan	deep water	Oceanic island arc
179544	3.588	N	102.349	E	Malaysia	Pahang	Outcrop	Phanerozoic	Mesozoic	Triassic	Semantan	deep water	Oceanic island arc
179545	3.588	N	102.349	E	Malaysia	Pahang	Outcrop	Phanerozoic	Mesozoic	Triassic	Semantan	deep water	Oceanic island arc
179546	3.588	N	102.349	E	Malaysia	Pahang	Outcrop	Phanerozoic	Mesozoic	Triassic	Semantan	deep water	Oceanic island arc
179547	3.588	N	102.349	E	Malaysia	Pahang	Outcrop	Phanerozoic	Mesozoic	Triassic	Semantan	deep water	Oceanic island arc
179548	3.588	N	102.349	E	Malaysia	Pahang	Outcrop	Phanerozoic	Mesozoic	Triassic	Semantan	deep water	Oceanic island arc
179549	3.588	N	102.349	E	Malaysia	Pahang	Outcrop	Phanerozoic	Mesozoic	Triassic	Semantan	deep water	Oceanic island arc
179550	3.588	N	102.349	E	Malaysia	Pahang	Outcrop	Phanerozoic	Mesozoic	Triassic	Semantan	deep water	Oceanic island arc
179551	3.588	N	102.349	E	Malaysia	Pahang	Outcrop	Phanerozoic	Mesozoic	Triassic	Semantan	deep water	Oceanic island arc
179552	3.588	N	102.349	E	Malaysia	Pahang	Outcrop	Phanerozoic	Mesozoic	Triassic	Semantan	deep water	Oceanic island arc
179553	3.588	N	102.349	E	Malaysia	Pahang	Outcrop	Phanerozoic	Mesozoic	Triassic	Semantan	deep water	Oceanic island arc
179554	4.839	N	101.961	E	Malaysia	Pahang	Outcrop	Phanerozoic	Mesozoic	Triassic	Gua Musang	deep water	Continental island arc
179555	4.839	N	101.961	E	Malaysia	Pahang	Outcrop	Phanerozoic	Mesozoic	Triassic	Gua Musang	deep water	Continental island arc
179556	4.839	N	101.961	E	Malaysia	Pahang	Outcrop	Phanerozoic	Mesozoic	Triassic	Gua Musang	deep water	Continental island arc
179557	4.839	N	101.961	E	Malaysia	Pahang	Outcrop	Phanerozoic	Mesozoic	Triassic	Gua Musang	deep water	Continental island arc
179558	4.839	N	101.961	E	Malaysia	Pahang	Outcrop	Phanerozoic	Mesozoic	Triassic	Gua Musang	deep water	Continental island arc
179559	4.163	N	102.032	E	Malaysia	Pahang	Outcrop	Phanerozoic	Mesozoic	Triassic	Gua Musang	deep water	Continental island arc
179560	4.189	N	102.057	E	Malaysia	Pahang	Outcrop	Phanerozoic	Mesozoic	Triassic	Gua Musang	deep water	Continental island arc
179561	4.132	N	102.009	E	Malaysia	Pahang	Outcrop	Phanerozoic	Mesozoic	Triassic	Gua Musang	deep water	Continental island arc
179562	4.191	N	102.057	E	Malaysia	Pahang	Outcrop	Phanerozoic	Mesozoic	Triassic	Gua Musang	deep water	Continental island arc
179563	4.291	N	102.061	E	Malaysia	Pahang	Outcrop	Phanerozoic	Mesozoic	Triassic	Gua Musang	deep water	Continental island arc
179564	4.18	N	102	E	Malaysia	Pahang	Outcrop	Phanerozoic	Mesozoic	Triassic	Gua Musang	deep water	Continental island arc
179565	4.18	N	102	E	Malaysia	Pahang	Outcrop	Phanerozoic	Mesozoic	Triassic	Gua Musang	deep water	Continental island arc
179566	4.18	N	102	E	Malaysia	Pahang	Outcrop	Phanerozoic	Mesozoic	Triassic	Gua Musang	deep water	Continental island arc
179567	4.18	N	102	E	Malaysia	Pahang	Outcrop	Phanerozoic	Mesozoic	Triassic	Gua Musang	deep water	Continental island arc
179568	4.1	N	102.004	E	Malaysia	Pahang	Outcrop	Phanerozoic	Mesozoic	Triassic	Gua Musang	deep water	Continental island arc
179569	4.1	N	102.004	E	Malaysia	Pahang	Outcrop	Phanerozoic	Mesozoic	Triassic	Gua Musang	deep water	Continental island arc
179570	4.1	N	102	E	Malaysia	Pahang	Outcrop	Phanerozoic	Mesozoic	Triassic	Gua Musang	deep water	Continental island arc
179571	3.52	N	101.921	E	Malaysia	Pahang	Outcrop	Phanerozoic	Mesozoic	Triassic	BRSZ Unit 2	deep water	Continental margin
179572	3.52	N	101.921	E	Malaysia	Pahang	Outcrop	Phanerozoic	Mesozoic	Triassic	BRSZ Unit 2	deep water	Continental margin
179573	3.52	N	101.921	E	Malaysia	Pahang	Outcrop	Phanerozoic	Mesozoic	Triassic	BRSZ Unit 2	deep water	Continental margin
179574	3.52	N	101.921	E	Malaysia	Pahang	Outcrop	Phanerozoic	Mesozoic	Triassic	BRSZ Unit 2	deep water	Continental margin
179575	3.52	N	101.921	E	Malaysia	Pahang	Outcrop	Phanerozoic	Mesozoic	Triassic	BRSZ Unit 2	deep water	Continental margin
179576	3.519	N	101.921	E	Malaysia	Pahang	Outcrop	Phanerozoic	Mesozoic	Triassic	BRSZ Unit 2	deep water	Continental margin
179577	3.519	N	101.921	E	Malaysia	Pahang	Outcrop	Phanerozoic	Mesozoic	Triassic	BRSZ Unit 2	deep water	Continental margin
179578	3.519	N	101.921	E	Malaysia	Pahang	Outcrop	Phanerozoic	Mesozoic	Triassic	BRSZ Unit 2	deep water	Continental margin
179579	3.519	N	101.921	E	Malaysia	Pahang	Outcrop	Phanerozoic	Mesozoic	Triassic	BRSZ Unit 2	deep water	Continental margin
179580	3.519	N	101.921	E	Malaysia	Pahang	Outcrop	Phanerozoic	Mesozoic	Triassic	BRSZ Unit 2	deep water	Continental margin
179581	3.519	N	101.921	E	Malaysia	Pahang	Outcrop	Phanerozoic	Mesozoic	Triassic	BRSZ Unit 2	deep water	Continental margin
179582	3.519	N	101.921	E	Malaysia	Pahang	Outcrop	Phanerozoic	Mesozoic	Triassic	BRSZ Unit 2	deep water	Continental margin
179583	3.519	N	101.921	E	Malaysia	Pahang	Outcrop	Phanerozoic	Mesozoic	Triassic	BRSZ Unit 2	deep water	Continental margin
179584	3.519	N	101.921	E	Malaysia	Pahang	Outcrop	Phanerozoic	Mesozoic	Triassic	BRSZ Unit 2	deep water	Continental margin
179585	4.888	N	101.982	E	Malaysia	Pahang	Outcrop	Phanerozoic	Mesozoic	Triassic	Central Belt	Plutonic	Continental margin
179586	4.888	N	101.982	E	Malaysia	Pahang	Outcrop	Phanerozoic	Mesozoic	Triassic	Central Belt	Plutonic	Continental margin
179587	6.35	N	99.666	E	Malaysia	Pahang	Outcrop	Phanerozoic	Mesozoic	Triassic	Central Belt	Plutonic	Continental margin
179588	4.01	N	101.959	E	Malaysia	Pahang	Outcrop	Phanerozoic	Mesozoic	Triassic	Central Belt	Plutonic	Continental margin